UNIVERSITY OF SOUTHAMPTON

Tectonic and Chemical Evolution of a Late Proterozoic Gold Deposit, Gebeit Mine, Northern Red Sea Hills, Sudan.

A thesis presented for the Degree of Doctor of Philosophy

by

ANTONY STARLING

Department of Geology, University of Southampton

December 1990

UNIVERSITY OF SOUTHAMPTON

ABSTRACT

FACULTY OF SCIENCE

GEOLOGY

Doctor of Philosophy

Tectonic and Chemical Evolution of a Late Proterozoic Gold Deposit, Gebeit Mine, Northern Red Sea Hills, Sudan.

by Antony Starling

The Gebeit Gold Mine in the Northern Red Sea Hills of Sudan is a late-Proterozoic mesothermal, shear zone-hosted, gold-quartz vein deposit. It is situated on the western margin of the accreted oceanic island arc terranes which comprise the central area of the Pan-African, Nubian-Arabian Shield. The deposit is hosted by low-K tholeiite to calc-alkaline, basaltic andesites of the Gebeit Volcanic Group. At Gebeit, four main accretion-related deformation events have been recognised:

i) D_1, NE-trending regional upright folding,
ii) D_2, the main phase of dextral strike-slip shearing, accommodated along regional, NE-trending ductile phyllonite shear zones which subdivided the region into elongate (≈5x30km) tectonic blocks.
iii) D_3, a minor phase of NW-directed folding and thrusting, which was followed by renewed dextral strike-slip shearing, and
iv) D_4, a switch from dextral to sinistral strike-slip deformation followed by NE-directed thrusting and folding.

The ENE-trending quartz veins which host the gold mineralisation were emplaced during late-D_2 dextral shearing and were subsequently folded and fragmented by D_3 and D_4 deformation phases. Together with three phases of Pan-African dyke-emplacement, fluid flow and vein formation were controlled by secondary extensional Riedel shear zones which were preferentially developed across the Gebeit Block. Gold mineralisation was immediately preceded by a phase of pervasive ankerite metasomatism which sealed the main Riedel shears and restricted mineralisation to secondary, parallel, adjacent shear zones. Formation of the V_1 lode veins was pre-dated by emplacement of calc-alkaline, diorite dykes, and post-dated by a transitional phase of calc-alkaline to alkaline dolerite dykes.

Six phases of veining are evident but gold is confined either to gold-only fractures or on the surfaces of vein sulphides within the massive V_1, blue quartz veins. Gold has not been observed in association with wallrock sulphides. Wallrock alteration consists of sulphidation (Fe-As-sulphides) and sericitisation together with varying degrees of carbonatisation (calcite), and is characterised by significant additions of K_2O (± Rb, Ba), MgO, Fe_{tot}, Cr, Ni, As, Au, ± CaO and MnO, with concomitant depletion of Na_2O and Sr. The alteration assemblages, incorporated with fluid inclusion data, indicate that the ore fluids at Gebeit comprised H_2O-CO_2 fluids (X_{CO_2} ≈0.1) of low salinity and low Eh, and near neutral pH, at 250-300°C. Oxygen isotope analyses indicate that fluid compositions remained fairly constant for most of the accretion-related deformation (fluid $\delta^{18}O$ estimated at 2.4-8.7‰). The fluids were probably metamorphic in origin but may have had a magmatic input. Fluid pressure estimates of 2.0 to 3.9kb (≈7-12km depth) are consistent with evolution at the brittle-ductile transition at greenschist facies grade. Available evidence, although limited, suggests that phase separation was the main gold precipitation mechanism.

CONTENTS LIST

PART 3 - STRUCTURAL GEOLOGY

Chapter 5 Structural Geology

PART 4 - MINERALISATION: PARAGENESIS AND ALTERATION

Chapter 6 Mineralisation I: Vein Paragenesis and Ore Mineralogy

PART 5 - SUMMARY, DISCUSSION AND CONCLUSIONS

List of Figures

Chapter 1

Chapter 2

Chapter 3

Chapter 4

Chapter 5

Chapter 6

Chapter 7

Chapter 8

List of Tables

Chapter 1

Chapter 2

Chapter 3

Chapter 4

Chapter 5

Chapter 6

Chapter 7

List of Plates

Acknowledgements

Ecce opus! Well here it is, finished at last. On the academic side I am very grateful to my tireless supervisor Dr Bob Foster for his friendship and enthusiasm, and whose work schedule never ceases to amaze me. At Southampton I wish to thank Drs Andy Barker, Rex Taylor, Steve Roberts, Andy Gize and Ian Croudace for lending a sympathetic ear or two and the ever cheerful technical support, especially from Robin, Bob and Barry. I am also grateful to Dr Norman Charnley at Oxford for help with the probe, Dr Tony Fallick at SURRC for isotope analyses, and Prof. Charlet at Mons, Belgium, for the thermoluminesence data.

I wish to thank everyone at Greenwich Resources especially John Gaskell and Peter Bridges and to the staff at Gebeit, including John Lovell, Rod, Don, Dave, Crazy Pete, Cliff, Jack, Steve A., Duncan G., Bill B., Alan B., Brian Williams, Geoff Templeton, Tag, Karim, and Mo'oawia (to name but a few), for helping the months to pass so quickly. I am also grateful to Dick Fletcher at Robertson Research and to the people of Gebeit village for giving me a new outlook on life.

I've learnt alot about many things during the past few years and I extend my gratitude to the members of the now acceptable post-grad Escape Committee at Southampton for making the PhD process very pleasant indeed. In particular I would like to thank Slap for taking life as it comes, Spiney McHooligan for being positive (however loud), Jerry-man for enjoying life (especially during opening hours, Hurrah!), Phil for ubiquitously making his presence felt and Mr E. Blackadder in his various guises for helping it all make sense (and the porpoise?). In addition, Marko, Dr Big Nose, 40p, Al, Jamie, Dr Scroat and Dickie deserve a special mention. I also thank the other members of staff at Southampton for not taking me to court over my EC magazine articles (perhaps they haven't read them yet).

I am grateful for the financial support of a NERC grant, Greenwich Resources plc, Suzanne Wood and my parents. I must also thank John Wood for the "office supplies".

Lastly, but most importantly, I thank Suzanne and my family for their patience and understanding and without whom this would not have been possible.

"Tectonic and Chemical Evolution of a Late Proterozoic Gold Deposit, Gebeit Mine, Northern Red Sea Hills, Sudan."

PART ONE

INTRODUCTION

"And the gold of that land is good."

Genesis 2:12

Chapter 1

Introduction, Project Objectives, Location and History

1.1 Introduction

World gold production in terms of geological time is markedly polarised into Archaean deposits and deposits of Phanerozoic and Tertiary age. Approximately 20% of the world's gold production (ancient and modern) has come from Archaean greenstone terranes, a further 40% from the Witswatersrand goldfields (Woodall, 1988), and the bulk of the remaining production from Palaeozoic turbidites, placers and Tertiary epithermal deposits. The majority of Precambrian deposits studied in Canada, Australia and Zimbabwe have been shown to be largely of late Archaean age (2.8-2.6 Ga) and associated with rift-related (back-arc marginal basin?), tholeiitic volcanic greenstone successions (Colvine et al., 1984,1988; Kerrich, 1986; Groves et al.,1984,1985, 1987; Foster, 1985,1987,1988). This compares with the linear fold belt/convergent boundary characteristics which are predominant in most Palaeozoic and Tertiary gold deposits. However, convergent boundary characteristics have now been recognised in some of the Australian Archaean deposits (Groves,1988). The real or apparent paucity of significant gold mineralisation in the Proterozoic remains enigmatic. This may be due, in part, to the lack of extensive exploration resulting from the geographical or political remoteness of the bulk of Proterozoic terranes (e.g. Antarctica, Africa, and South America). There is the possibility, however, that tectonic styles in the Proterozoic may not have been appropriate for the generation of large-scale Archaean-type gold deposits and only continued research into Proterozoic terranes and deposits may resolve this problem.

The Gebeit Gold Mine in the Red Sea Hills of Northern Sudan is a late Proterozoic, shear-zone-hosted, lode gold deposit occurring in calc-alkaline, volcanic arc assemblages. The nature of the tectonic controls, mineralisation, and alteration of the Gebeit deposit bears many similarities to mesothermal Archaean lode gold deposits (e.g. Colvine et al., 1984). This indicates that, although the Proterozoic

may have been a transitional phase between Archaean and modern plate tectonic regimes, it is likely that common fluid processes prevailed.

1.2 Project Initiation

The N.E.R.C.-supported topic "Tectonic and Chemical Evolution of a Late Proterozoic Gold Deposit, Gebeit Mine, Northern Red Sea Hills, Sudan" is a CASE award with Minex Minerals (Sudan) Ltd, a subsidiary of Greenwich Resources plc. This studentship was allocated for the period October, 1985, to September, 1988, and was supervised by Dr R.P. Foster. The project is focused on the Gebeit Gold Mine which has been worked by various companies intermittently from 1903 to the present. Pharonic surface workings, however, indicate that mining may have started as far back as 1500 BC (Gaskell, 1985). Gebeit lies in an area where numerous gold prospects have been reported but, due to the remoteness of the region, exploration and general reconnaissance mapping has largely been restricted to interpretation of aerial photographs and Landsat data. As a result of the poor geological understanding of the area, this project was initiated by Greenwich Resources and the Department of Geology at the University of Southampton in order to identify the geological setting and elucidate the precise controls on the gold mineralisation.

1.3 Method of Study

The project commenced with an initial six-month field season based at Gebeit with a subsequent three-month field season ten months later. During both field seasons, structural and lithological mapping was undertaken on surface (2km^2 at 1:1000) and underground (Wadi Lode, 4 Level, 1:250), along with detailed sampling of vein material, altered and unaltered host rocks and intrusive lithologies. These two field periods were augmented by laboratory studies at the University of Southampton comprising polished block and thin section work, X-ray diffraction and fluorescence analyses, and scanning electron microscope investigations and fluid inclusion studies. In addition, background gold and stable isotope analyses, electron micro-probe, and thermoluminescence studies were completed outside the department. Full details of analytical techniques, limits of detection and precision are listed in Appendix A.

1.4 Project Objectives

Initial fieldwork by Robertson Research (1985) indicated that the gold-sulphide mineralisation at Gebeit was stratabound, confined to chert horizons between two volcanic complexes. Previous descriptions, however, suggested it was a volcanic hosted vein-type deposit (Gass, 1955; Ruxton, 1956; Whiteman, 1971; El Boushi, 1972). The early stages of fieldwork undertaken as part of the present project showed that the auriferous mineralisation was structurally controlled and exhibited a protracted and complex history of tectonism, magmatism and fluid flow. The availability of drillcore data, ease of underground access and problems with transport dictated that field studies be concentrated on Gebeit. The lack of any detailed geological work in the area meant that the project could not be confined to a detailed study of any one aspect until the overall geological framework had been defined. Hence, the project objectives can be summarised as follows:

1) to define the petrography and geochemistry of the unaltered volcanic and intrusive rocks in order to add to the scant regional database and to act as a control when considering variations due to deformation and mineralisation;
2) to determine the metamorphic and structural evolution of the Gebeit area;
3) to resolve the tectonic, magmatic and fluid evolution of the deposit;
4) to detail the alteration facies and petrological and chemical variations due to mineralisation;
5) to ultimately develop a unifying model for the evolution of the deposit, define the controls on mineralisation and produce an exploration strategy for the area;
6) to lastly compare and contrast the tectonic and chemical styles of the Gebeit deposit in relation to established models for the more extensively studied Archaean lode deposits.

1.5 Location, Climate and Topography

Gebeit al Ma'adin is situated at 36° 23' 30"E, 21° 03' 30"N in the Red Sea Hills Province (Jubal Al Bahr Al Ahmar) of north-east Sudan, approximately 100km west of the Red Sea coast and 730km north-east of the Sudanese capital Khartoum (Fig.1.1). The area around Gebeit is classified as a hammada-type semi-desert with the edge of the Nubian

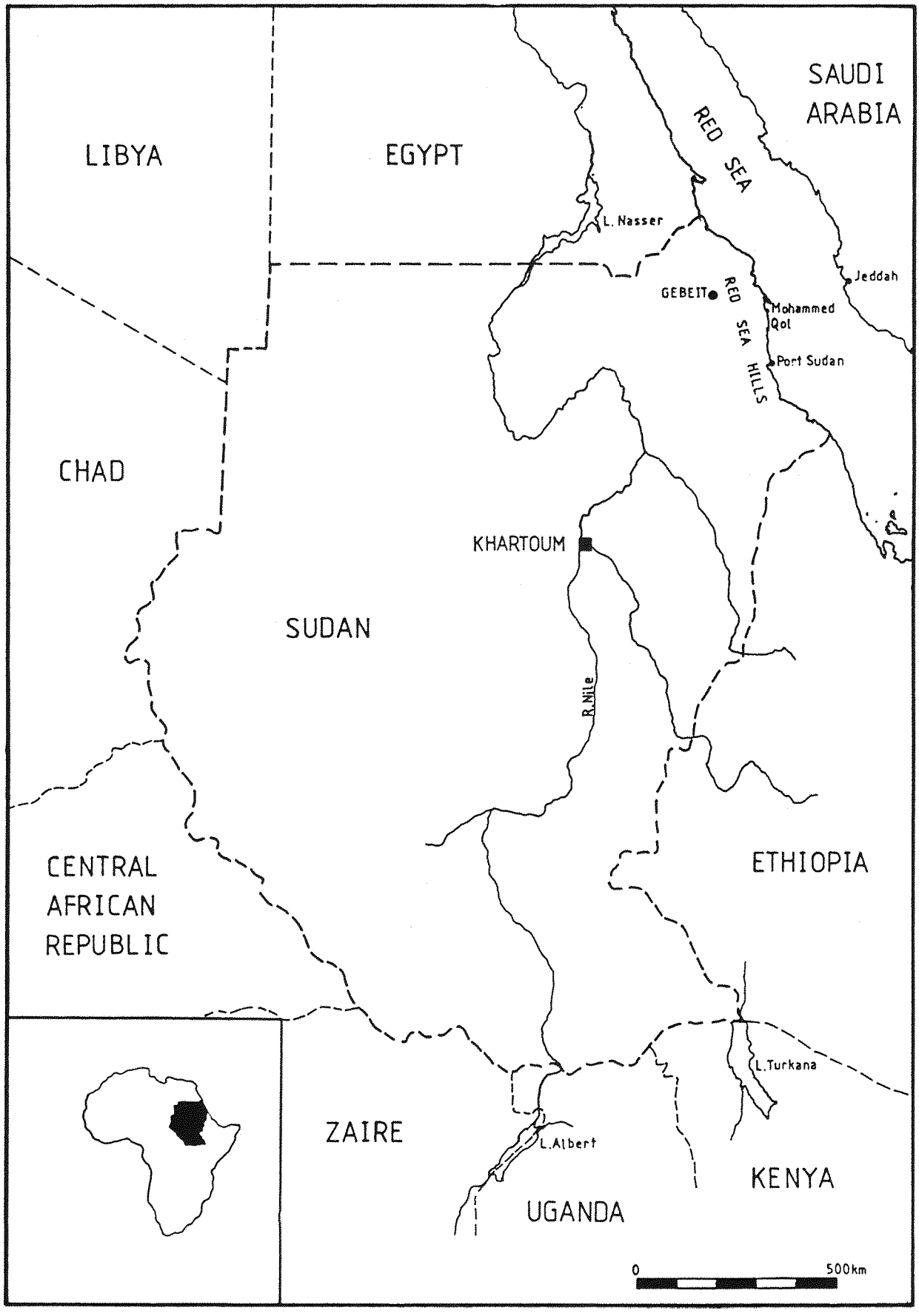

Figure 1.1 Location Map of Gebeit al Ma'adin

desert lying approximately 15km to the west. Rainfall averages 137mm a year and occurs as violent thundery showers. Much of this water is lost by surface run-off and evaporation but the water table is fairly high at Gebeit and often breaks the ground surface during the winter months. Maximum shade temperatures vary between 20°C in the winter to around 42-45°C during the summer. Vegetation, which is confined mainly to the wadis, is sparse and is characterised by Acacia tortillis, Acacia etabaica, Acacia nilotica and Maerua crassifolia desert scrub. The greenstone belt topography is rugged but relatively flat, locally varying between 550m and 850m above sea level, but can reach up to 2200m in the younger granitic areas (e.g. Jebel Asotriba, 2216m). The hills are generally rounded and invariably covered in a blanket of coarse scree with most lithologies weathering to a dark brown or black desert varnish. The main wadis follow basement structural trends and produce a NE-NW trellis-type drainage system supplied by sub-dendritic tributaries (Fig.1.2). A N-S-trending watershed roughly follows the 35° line of longitude. Wadis to the west of this divide tend to drain westwards to the Nile and wadis to the east flow to the Red Sea. Though the wadis can be very wide (up to 1km), they are usually shallow with less than 5m of wadi alluvium overlying a layer of weathered bed rock which can be 15-30m thick (B.Williams,pers. comm.,1986; Fletcher, 1985). The Northern Red Sea Hills region is only sparsely populated. The Sofaya-Gebeit area is occupied by the Bisharin and Amarar tribes, sub-tribes of the nomadic Beja people, who graze sheep, goats and camels and occasionally grow sorghum (dura). The village of Gebeit has a population of about three hundred and provides the majority of the mine work force.

1.6 History of Mining

Gold has reportedly been mined in the Sudan for over 3000 years and mining activity dates back to the time of the Middle and New Kingdoms of Ancient Egypt (Vercoutter, 1959; Whiteman,1971). Gold initially came from Wadi Allaqi, a tributary of the Nile close to the present Egyptian border, and when these resources began to dwindle the ancient prospectors moved further afield. Vercoutter (1959) stated that the areas of Kush and Wawat (the Ancient Egyptian areas of Northern Sudan) were not mined before Middle Kingdom times (1900 BC) and Gebeit was probably not developed until the reign of Pharoah Thutmose III (1500 BC, Gaskell, 1985). The earliest reference to

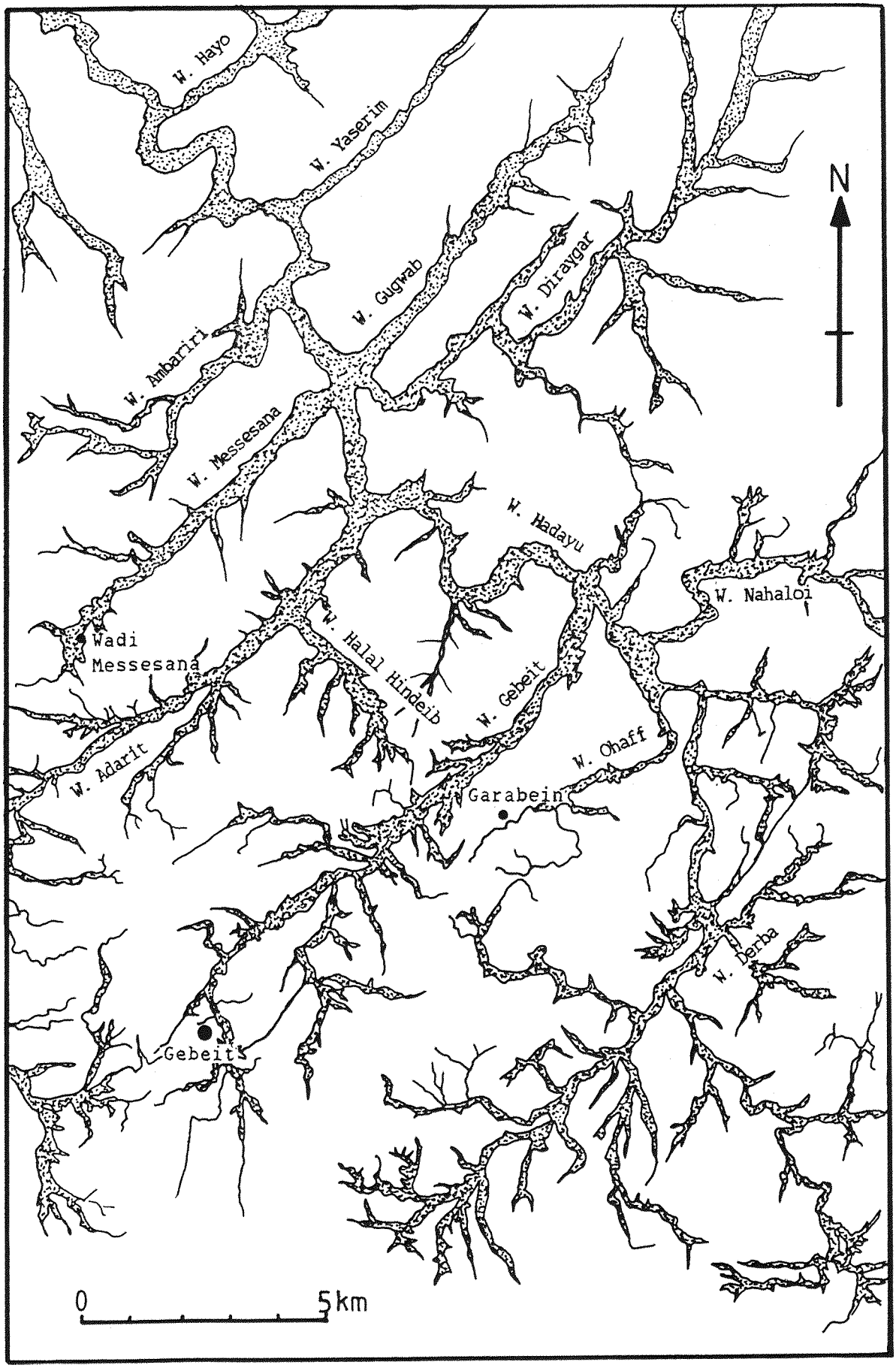

Figure 1.2 Structurally-controlled trellis drainage pattern of the Northern Red Sea Hills around Gebeit.

Gebeit was by Mr Theodore Bent (1896) who noted at least 700-800 small dry-built miners' huts distributed up to 2 miles along Wadi Gebeit, the area being littered with hundreds of crushing stones. There was a large open pit and evidence of extensive quarrying and underground stopes worked along outcrops but these were not fully surveyed until 1929. It appears that a small stream had once flowed down the valley and cave drawings at Salala depicting long-horn cattle and fossil evidence (Mawson and Williams, 1984) suggest there was a wetter climate in the past allowing the region to support a settled population. From old maps and descriptions it is estimated that the ancients did not mine below 50m but they are believed to have extracted 100,000-150,000 tonnes of ore at an average gold grade of 30g of gold per tonne of rock (g/t) along with an indeterminable amount of alluvial material (Gaskell, 1985).

According to Whiteman (1971), modern gold prospecting is considered to have started in the 1820's with the expeditions of Mohammed Ali Pasha and his son Ismail to the alluvial area of Beni Shangul near the Ethiopian border in their search for gold and slaves. These expeditions, however, ended with little success 30 years later. In 1899, following the formation of the Condominium Government, Egyptian financial interests were attracted to the Sudan and the impression that vast unexploited mineral resources existed, fostered by knowledge of Ancient Egyptian gold, drew many prospectors and mining companies. Modern mining methods were introduced to the Sudan mainly by British companies searching for gold in the early 1900's and by 1940, eight mines had been opened. These included; the Onib group of mines i.e. Oyo, Micraff and Shishiteib, (Kassala Gold Mines (Sudan) Ltd, 1934-1937); Garabein/ Ohaff (Garabein Mining Syndicate, 1932-1935); Aberkateib, and Umm Nabardi (Sudan Gold Fields Ltd, 1902-1942). Due to finance and mining problems, however, only Gebeit survived.

1.6.1 Gebeit Mining History

The following brief account is derived from the incomplete mine records at Gebeit collated by Robertson Research (1983) and Roberton (1987). During this period Gebeit's name has varied and so several variations exist (e.g. Gabait, Jabet). A summary of past production at Gebeit is given in Table 1.1

Period	Tonnes of Ore	Kg of Gold	Grade (g/t)
1500 BC-1903	100-150,000*	3000-4500*	30*
1903 - 1921	68,267	2643.76	38
1934 - 1942	100,000	1300.00	13
1947 - 1954	48,900	342.13	7
1954 - 1975	32,000	48.20	1.5
1988 - 1989	16,537(t) 30,801(o)	16.59 146.26	1.0 4.75
Min. Total	396,505	7500.00	15.71

* denotes estimated figure (t)=tailings, (o)=ore

Table 1.1 Summary of gold production at Gebeit - ancient and modern.

Gebeit was revived in 1903, when a prospecting license, covering 8000 sq. miles around Gebeit, was first granted to the Gabait Mining Syndicate following a visit by Mr C.G. Alford on a prospecting tour. At the end of 1904, a mining lease had been acquired by Sudan Mines Ltd and mining continued intermittently to September 1908. During this period, mining was confined to a 0.5m thick zone, 10-25m below the surface with grades reaching up to 217 g/t.

In 1911, the Gabait Tributing Syndicate was formed and new machinery was installed at Gebeit including a 5-stamp crushing battery with gold recovery by mercury on a copper amalgamation table. By 1914, mining had extended down to 34m below surface and 92.8kg of gold had been recovered from 1498 tons of ore at an average grade of 62 g/t. In 1917 a cyanidation plant was built and a new branch of the orebody was discovered grading at 31 g/t. Production continued to 1928 at a break-even grade of 15 g/t with workings developed on a south-easterly dipping lode folded into a shallow antiformal structure. This activity realised approximately 2550kg of gold from 50,000 tons of ore (average grade exceeding 45 g/t) and 42,000 tons of tailings (5 g/t). During the period 1914-1928, many of the existing shafts were sunk including

the main 45° decline. The operation was suspended in January 1930 due to the financial crisis of 1929.

In 1931, Auruns Ltd was formed to acquire the option on Gebeit and a new counter-current cyanidation plant was installed to treat 60,000 tons of tailings grading at ≈5 g/t. On January 1st, 1933, the company was re-registered as Sudan Gold Mines, then incorporated as Gabait Gold Mine Ltd and the mine re-opened. Mining steadily increased up to 1936, when 197kg of gold and 20kg of silver were recovered from 9299 tons of ore at a cut-off grade of 10.5 g/t. Production ceased in 1942 due to supply difficulties. From 1932-1942, a total of 1300kg gold was recovered from 100,000 tons of ore with workings extending down to 250m below surface.

From 1948-1953, Atbai Gold Ltd was formed and gold recovery reverted from cyanidation to amalgamation resulting in 342.13kg of gold from 48900 tons of ore (an average grade of 7 g/t). The decline in production and grades continued when the mine was bought by the El Aliab Mining and Prospecting Company, a private Sudanese company, in 1954. Up to 1975, 48.2kg of gold were recovered from 32,000 tons of ore using hand amalgamation.

On 17th June, 1978, Minex Inc. (a subsidiary of Greenwich Resources) signed an exploration agreement for a large area of Northern Sudan with the Sudanese Government and detailed exploration work commenced at Gebeit in January, 1982. A Sudan-Minex joint venture was formed in December 1982 with mining leases granted to cover the 6 km^2 around Gebeit. The majority of exploration at Gebeit was confined to the broadly triangular area between Wadi Gebeit and Wadi East Gebeit. A mine grid system was produced and the area subdivided into separate prospects (Fig 1.3). All lithological mapping, including this study, was based on the mine grid as detailed topographic maps were then not available.

In 1983, construction work commenced on four 350-tonne cyanide leach vats capable of treating 2-3000 tonnes per month on a 15-17 day leach cycle. Continued percussion and diamond drillhole exploration delineated unworked portions of known orebodies designated as the X,Y, and A lodes (Fig.1.4). The 45° inclined main shaft was refurbished and deepened to 140m vertical depth in 1985/6 to gain access to the newly discovered Wadi Lode and mining commenced on 4 level and 5 level (80m and 120m vertical depths respectively). A new 300 tonne-per-day mill was commisioned in late 1987. The mill consisted of crushing, fine grinding, gravity concentration, and sulphide flotation circuits for

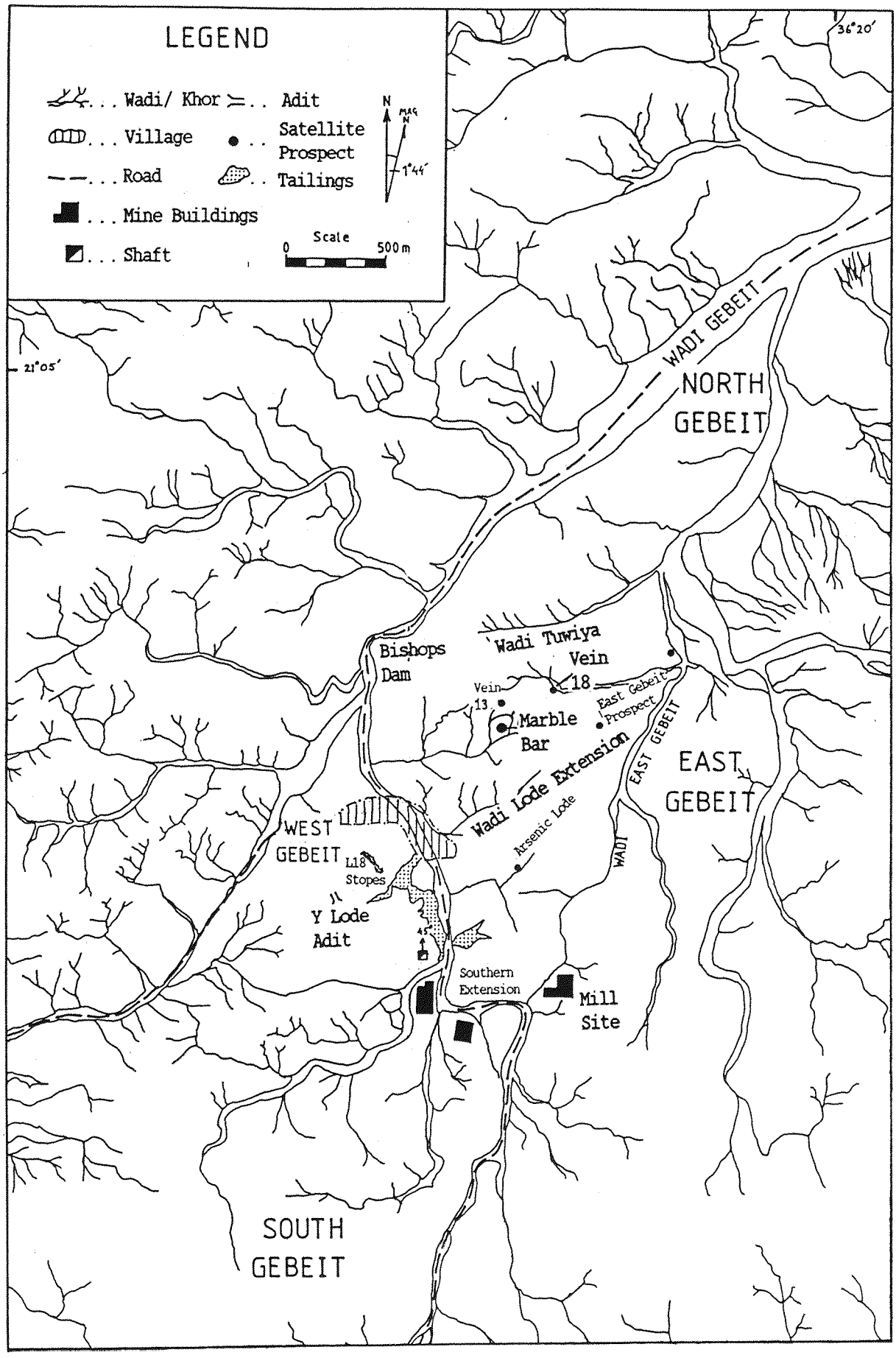

Figure 1.3 Location plan of Gebeit Mine area.

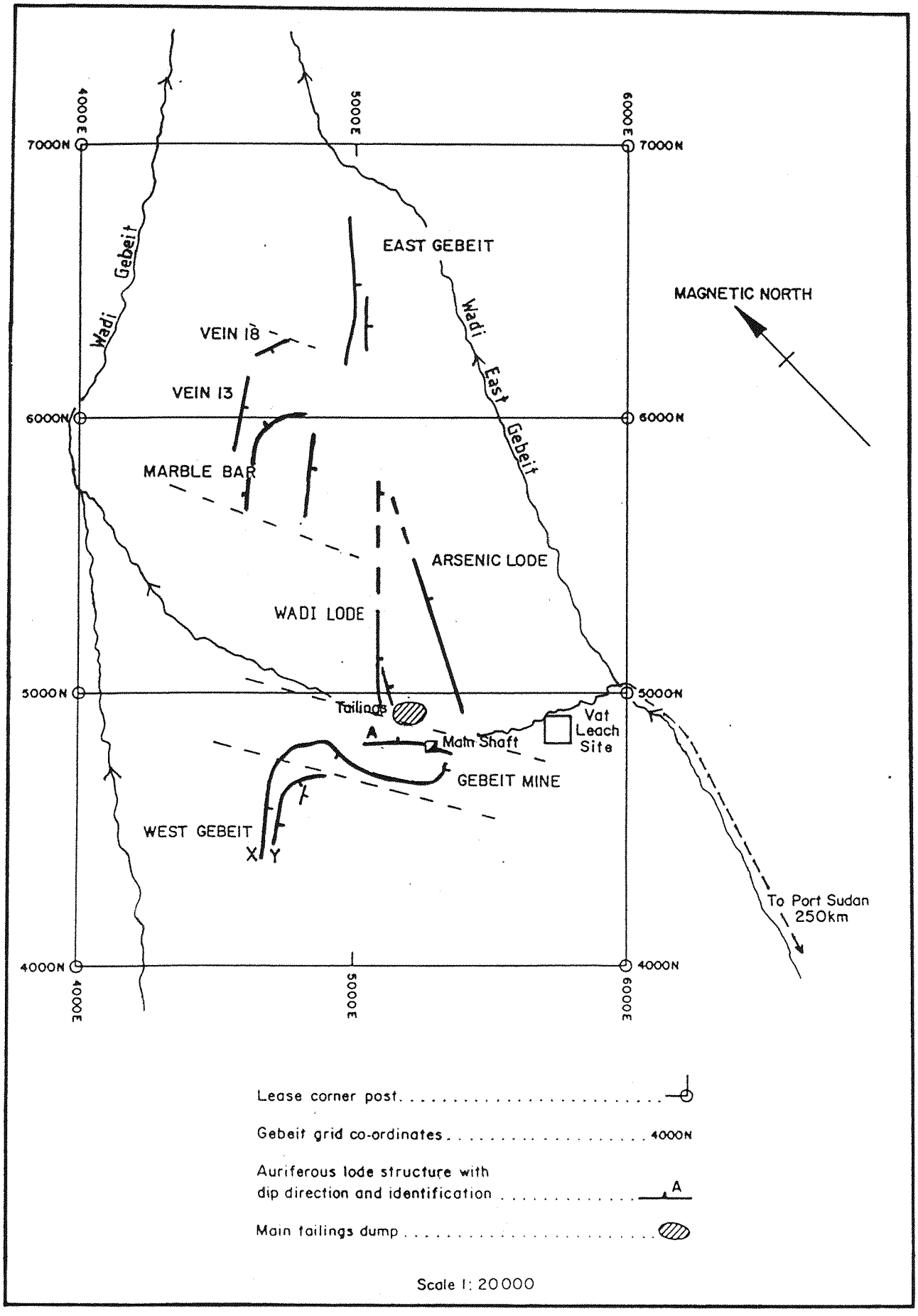

Figure 1.4 Plan of main lode veins at Gebeit.

non-oxidised ore, with gold recovery by intensive leach in a Merril-Crowe plant.

Continued underground exploration of the Wadi Lode, however, revealed extensive faulting of lode veins, greatly reducing ore reserves amenable for stoping. Although the genesis and evolution of the deposit had been established, sufficiently undeformed new reserves could not be located and in March 1990 Gebeit was once again closed.

1.7 Thesis Structure

The research programme discussed in the following chapters was established to evaluate the controls on mineralisation in order to facilitate mine and regional scale exploration. A brief summary of the main discussion points is given at the end of each chapter. Specific locations in the Gebeit mine area refered to in the text are denoted by grid co-ordinates corresponding to the mine grid, which is orientated at 45° to north.

Chapter 2 is a continuation to the introduction and describes the regional and local geological setting.

Chapters 3 and 4 deal with the petrography and geochemistry of the volcanic and intrusive rocks at Gebeit, providing an indication of the tectonic setting and magmatic and metamorphic evolution of the area. The host-rock data also adds to the scant regional database and acts as a control when considering hydrothermal alteration reactions.

Chapter 5 details the structural evolution of the area and elucidates the structural controls on mineralisation and the subsequent deformation of lode veins.

Chapter 6 considers the paragenesis of the various vein sets with emphasis on the ore and vein mineralogy of the early, gold-bearing, blue quartz veins. The results of fluid inclusion and stable isotope studies are also discussed.

Chapter 7 deals with the petrography and geochemistry of the altered wallrocks, quantifying the variations due to mineralisation. Collation with the data from Chapter 6 provides estimates of fluid temperatures and fluid compositions and defines the fluid evolution of the area.

The conclusions drawn from the work are summarised and discussed in Chapter 8 outlining the tectonic, magmatic and fluid histories. A unifying model is then presented for the geological evolution of the Gebeit gold deposit.

1.7.1 Maps

As a guide to the overall lithological and structural trends, four geological maps of the mine area at different scales, produced during this study, have been included. These comprise:

a) drainage and general geology of the Gebeit area based on aerial photograph interpretation and reconnaissance mapping,
b) a synoptic sheet of the northern half of the Gebeit block compiled from this study and from maps produced by Robertson Research and Greenwich Resources,
c) a map of the mine area north of the main shaft including the areas of Wadi Lode Extension, Vein 18, Vein 13, Marble Bar, East Gebeit, and Bishops Dam, and
d) an underground map of the Wadi Lode exposed along 4-level.

Original maps of the mine area were produced by tape and compass traverses which were surveyed at a later date. Large-scale maps of the Gebeit area were based on drainage traces traced from air photographs.

Chapter 2

Regional Geology and Previous Work

2.1 Introduction

The late-Proterozoic lithologies of the Northern Red Sea Hills comprise part of the Nubian-Arabian Shield, a terrane which forms the Upper Proterozoic crust across Sinai, Eastern Egypt, Sudan, Ethiopia, Somalia and east into Western Saudi Arabia and the Yemen. The true extent of this basement is obscured by Phanerozoic cover and may continue further south and west to include parts of Uganda and Kenya (Fig.2.1). It is now widely accepted that the Nubian-Arabian Shield evolved largely by accretion of progressively maturing, intra-oceanic, island arc terranes (Greenwood et al.,1976; Bakor et al.,1976; Frisch & Al-Shanti,1977; Gass,1977,1979,1982) as part of widespread late-Proterozoic to early-Palaeozoic diastrophism (900-600 Ma). The effects of this period of intense crustal deformation and remobilisation can be traced throughout Gondwanaland but were especially important in the structural evolution of Africa (Stern and Hedge,1985) which Kennedy (1964) termed the "Pan-African Thermo-Tectonic Episode". There were probably, however, several diachronous events as opposed to a single "Pan-African episode" (Jackson and Ramsay,1980).

In this chapter, the tectonic evolution of the Northern Red Sea Hills is discussed together with previous work in the region. Structural studies at Gebeit indicate that gold mineralisation occurred as part of a protracted tectonic history related to the complex interaction of several terranes. Hence, consideration has been given to the development of the whole of the Nubian-Arabian Shield and to the neighbouring Pan-African belts which may have interacted with it.

2.2 Evolution of the African Craton

As with all other continental crustal plates, the African craton has undergone protracted accretion of Proterozoic mobile belts around early Archaean nucleii. In the period extending from 1200 Ma to the

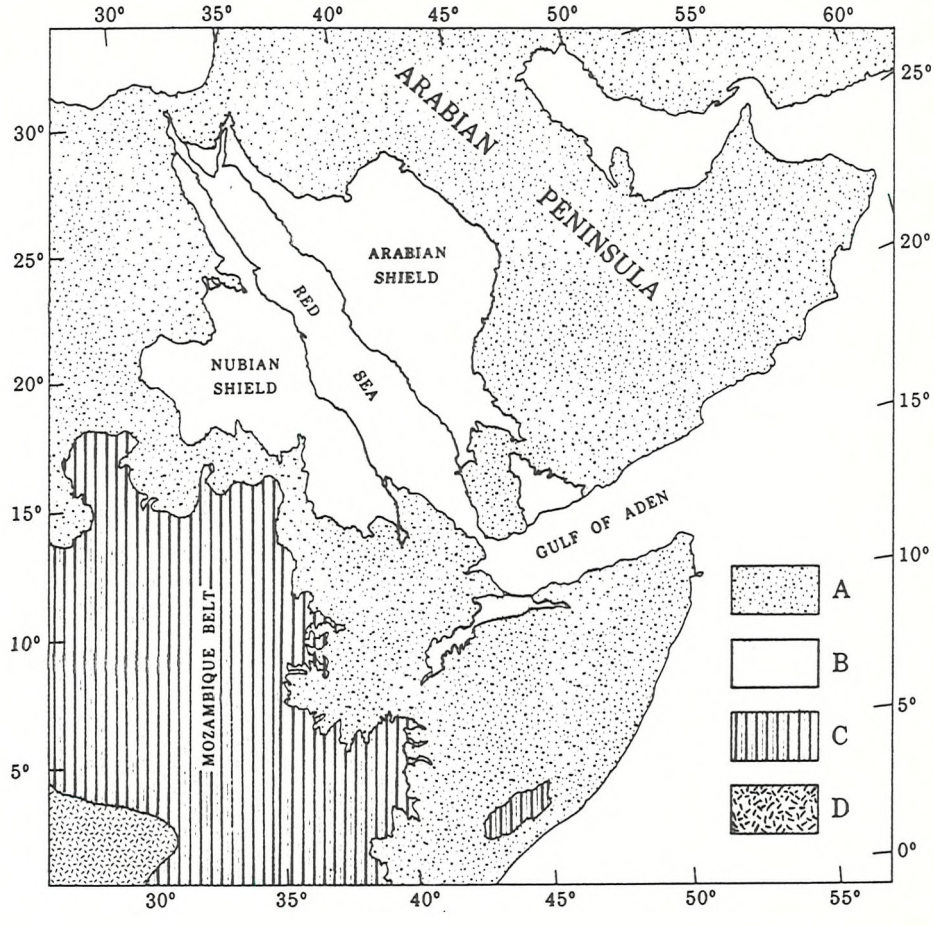

Fig.2.1 Location map showing Phanerozoic cover rocks (A), outcrop of the Nubian-Arabian Shield (B), the Mozambique Belt (C), Archaean rocks of the African Craton (D, after Stoeser & Camp, 1985)

end of the Proterozoic (≈550 Ma), a series of mobile belts formed in several continents by the accretion of various terranes to form Gondwanaland. The numerous mid- to late-Proterozoic fold belts identified in the African craton (Fig.2.2) fall broadly into three phases of orogenesis, namely

a) the Eburnean/Ubendian (2000-1850 Ma),
b) the Kibaran/Lurian (1375-1100 Ma), and
c) the Pan-African (950-550 Ma).

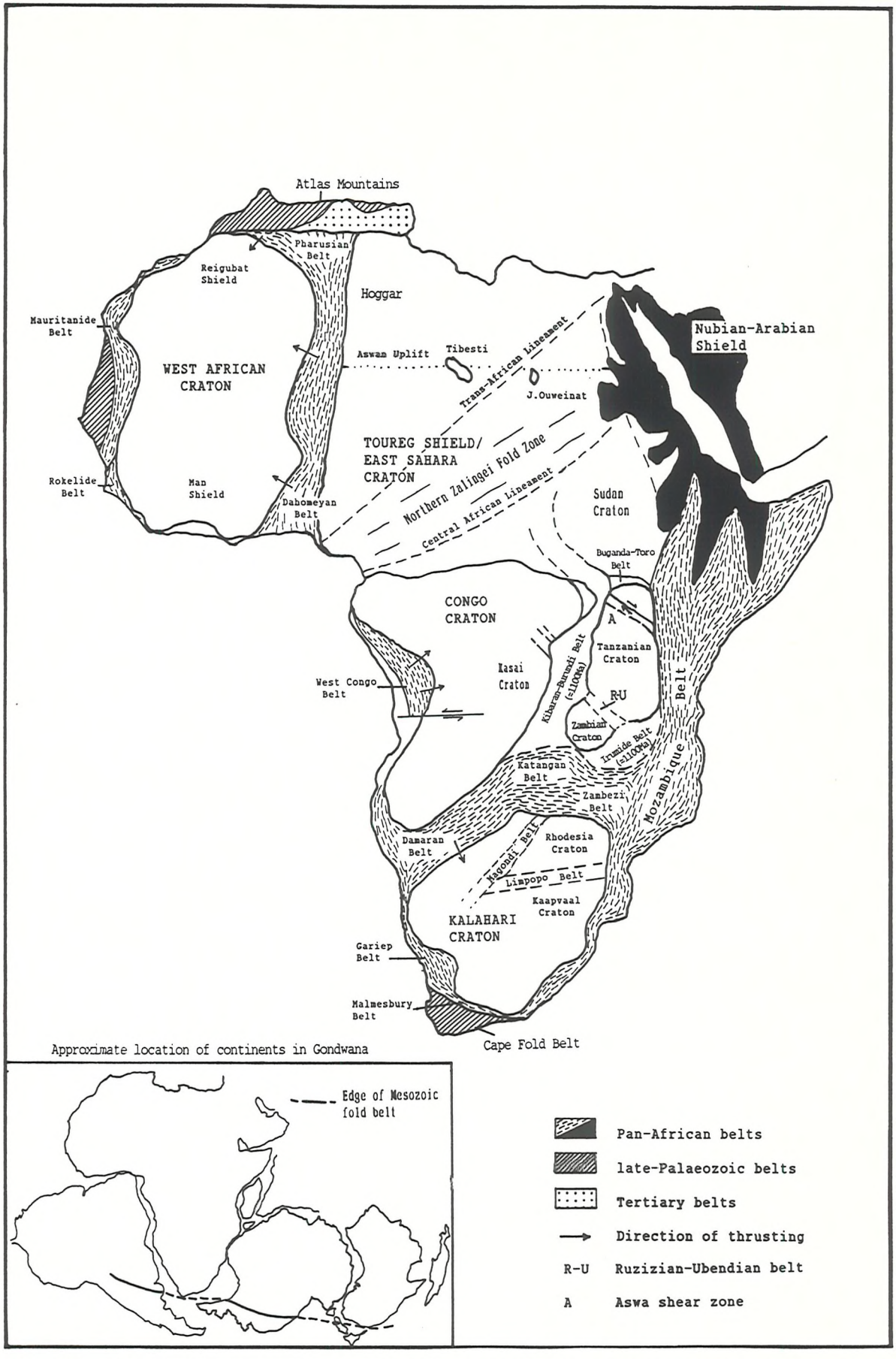

Fig.2.2 Simplified sketch map showing the main structural elements of the African Craton (after Seyfert & Sirkin,1973; Windley,1984; Kröner,1977, 1979; Rogers et al.,1978; Caby et al.,1981; Schandelmeier & Harms,1987)

The Eburnean cycle was coincident with a collision between Africa and Laurentia (Morgan and Briden,1981), and stabilisation of the East Sahara and West African cratons (Leblanc, 1981) and included development of;

i) the Ruzizian-Ubendian Belt and the Buganda-Toro Belt between the Zambian, Tanzanian and Sudan cratons (Kröner,1977; Shackleton, 1986),
ii) the Magondi Mobile Belt in north-west Zimbabwe (Treloar,1988), and
iii) the Northern Zalingei Folded Zone, which purportedly separates the Eburnean and Sudan cratons (Schandelmeier and Harms,1987; Schandelmeier et al.,1987).

During the Kibaran cycle, collision along the Irumide/ Lurio belt and the Kibaran-Burundi belt joined the Tanzania and Zambia cratons with the Kasai craton to form the Congo Craton. By the beginning of the Pan-African cycle, four major cratonic areas had evolved; the West African Craton (comprising the Reguibat Shield and the Man Shield); the Congo Craton; the Kalahari Craton (composed of the Zimbabwean/Rhodesian and Kaapvaal cratons), and the East Sahara Craton. Throughout the late-Proterozoic to early-Cambrian Pan-African orogenic cycle, these cratonic areas were consolidated to form the present day African craton with only minor additions during the late-Palaeozoic and Tertiary (the Cape Fold Belt and Atlas Mountains, Fig.2.2).

Including the Nubian-Arabian Shield, twelve Pan-African belts have been identified in Africa (Kröner, 1979), the more notable of which include the the Dahomeyan and Pharusian belts (the Hoggar/Touareg Shield), and the Mozambique belt. It is necessary to briefly evaluate the tectonic evolution of these two major late-Proterozoic belts as they were contemporaneous and interacted with the Nubian-Arabian Shield and its adjacent cratons.

2.3. The Pharusian-Dahomeyan Belt

The Hoggar Shield of the central Sahara underwent a multi-stage rifting and collisional history of a full Wilson cycle between 900 and 550 Ma (Caby et al.,1981). This trans-Saharan, north-south trending mobile belt extends along the eastern and northern boundaries of the West African craton from Adrar des Iforas (Mali) and Hoggar (Algeria)

to Anti-Atlas (Morocco) and resulted from the collision between the West African craton and the East Sahara craton (Fig.2.2 & 2.3). It comprises the Dahomeyan belt as part of the Nigerian Shield in the south and the Pharusian belt in the north which forms the western edge of the Touareg Shield (Bertrand and Caby,1978; Black et al.,1979; Caby,1982).

The Pharusian belt in the east comprises up to 6 km of volcaniclastic sediments with island arc calc-alkaline volcanics and batholiths and passes laterally eastwards into the Cordilleran-type continental margin domains of Hoggar-Aïr and Hoggar-Ténéré. The Hoggar-Ténéré domain acted as an early active continental margin until it was stabilised around 730 Ma as a pre-Pan-African north-west-trending fold belt intruded by syn- to late-tectonic calc-alkaline batholiths (Caby and Andrepoulos-Renaud,1987). This domain is separated from the Pharusian belt by the central Hoggar-Aïr domain - a polycyclic area consisting of reactivated ancient gneisses intruded by Cordilleran-type plutons.

Initial collision of the western branch of the Pharusian belt occurred in a north-south direction probably linked to the southward subduction and obduction at 685±15 Ma of the Bou Azzer ophiolites (788±9 Ma) and the overlying calc-alkaline volcanics of the Anti-Atlas, Morocco, on to the West African passive continental margin (Leblanc,1981,1984). Eastward subduction culminated in a final east-west collision and nappes of the passive margin sediments were thrusted westwards on to the West African craton, with the suture zone delineated by the Gourma-Dahomeyan Frontal Thrust.

Post-collisional, east-west shortening (580-540 Ma, Liégeois et al.,1987) produced conjugate strike-slip, brittle fault systems east of the suture in the recently created shield. This involved considerable lateral displacements along major shear zones caused by eastward indentation of the more rigid West African craton (Ball,1980) - a situation analogous to the rigid indenter tectonic model proposed by Molnar and Tapponnier (1975) for the Himalayan-Tibetan region. This has been suggested as the mechanism for the development of the Najd fault system in the Nubian-Arabian Shield (Stoeser and Camp,1985).

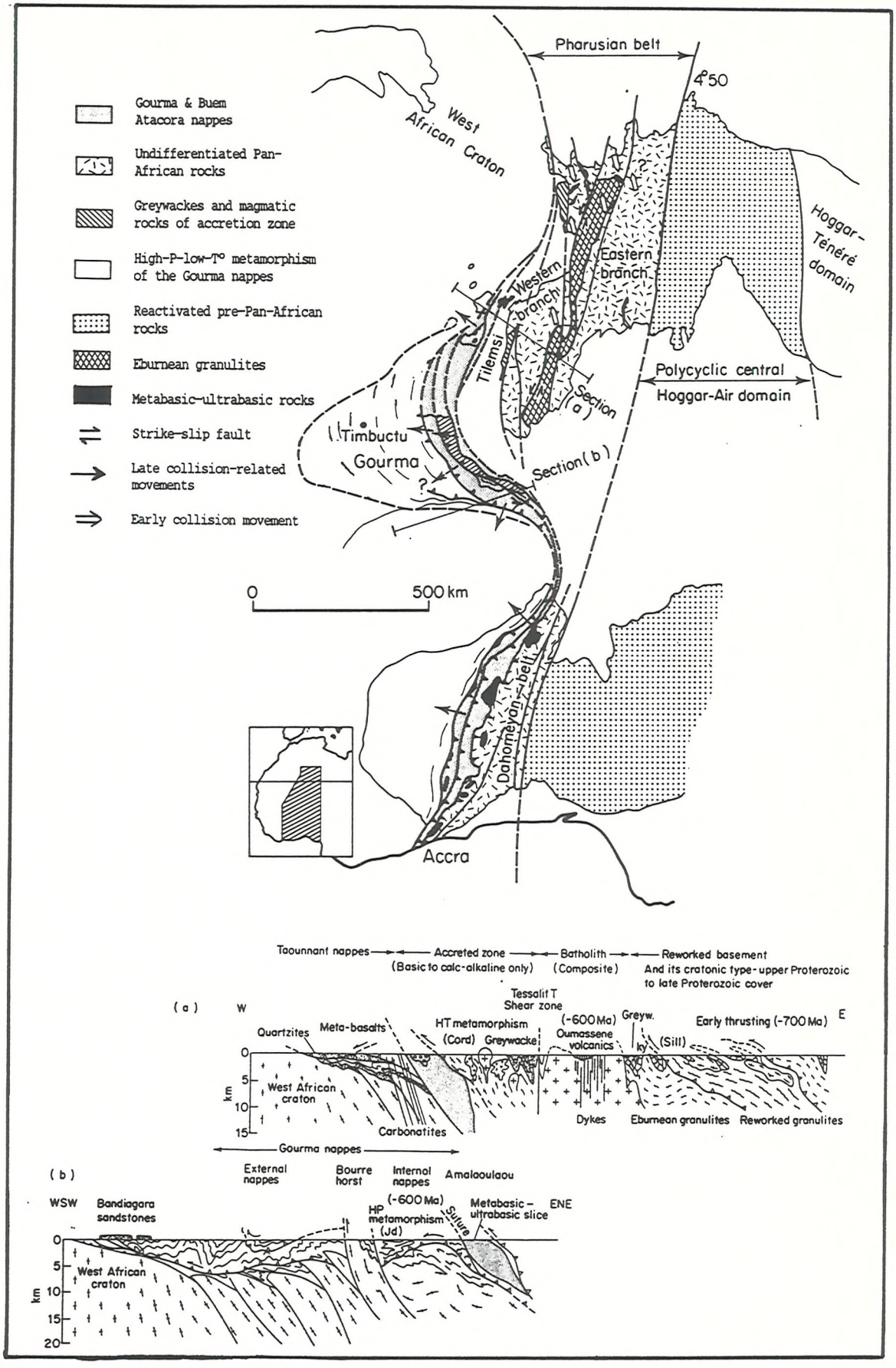

Fig.2.3 Simplified sketch map of the Pharusian-Dahomeyan belt and schematic cross-sections a: northern Adrar des Iforas; b: the Gourma nappes (after Caby et al.,1981).

2.4 The Mozambique Belt

The Mozambique belt (Holmes,1951) is the longest mobile zone in the African continent, extending along the East African coast from Mozambique to Ethiopia and Somalia. This belt largely comprises high-grade granitoid gneisses and metasediments indicative of crustal thickening, and has been considered to be a zone of ensialic crustal mobility (Kröner,1977). Reappraisal, by Shackleton (1986), however, has shown it to be a deeply eroded, Himalayan-type belt with post-collisional thrusts that have penetrated into the Archaean gneissic basement which probably underlies the metasedimentary sequences (Kazmin,1971). A multi-stage continental collision involving intense and complex deformation is envisaged, producing Alpine-type recumbent thrusts, imbricates and isoclinal fold structures (Vearncombe,1983; Shackleton, 1986).

Palaeomagnetic evidence from apparent polar wandering paths indicates that the Mozambique belt represents a collision between the previously separated continental plates of east and west Gondwana (McWilliams,1981; Fig.2.2,inset). This produced north-south folding of the pre-Pan-African basement gneisses of Northern Somalia and generated basaltic and dioritic magmatism on the eastern flank (west of Madagascar) due to westward subduction of the East Gondwana plate (Warden and Daniels, 1984; the Asiatica plate of Vail,1983). North-west-trending stretching lineations in the western part of the belt, together with an overall westward vergence and the identification of three probable, easterly-dipping, ophiolite-bearing sutures (Sekerr, Baragoi and Moyale-Shakiso), infer a north-west/south-east direction of plate motion. The ophiolite belts have been tentatively correlated with sutures in the Nubian-Arabian Shield (Shackleton,1979; Vearncombe,1983) and substantiated by satellite imagery interpretation and lithological mapping (Fig.2.4; Berhe and Rothery,1986). However, stretching lineations in the central zones have a north-south trend which is interpreted to result from post-collisional ductile shear parallel to the plate boundaries after transverse plate motion became impossible (Shackleton and Ries,1984) -a process which appears to have also occurred in the western Nubian Shield along the Oko shear zone (Almond and Ahmed,1987).

The contrast between the greenschist facies, island arc assemblages of the Nubian-Arabian Shield and the high-grade gneisses and metasediments of the Mozambique belt can be attributed to

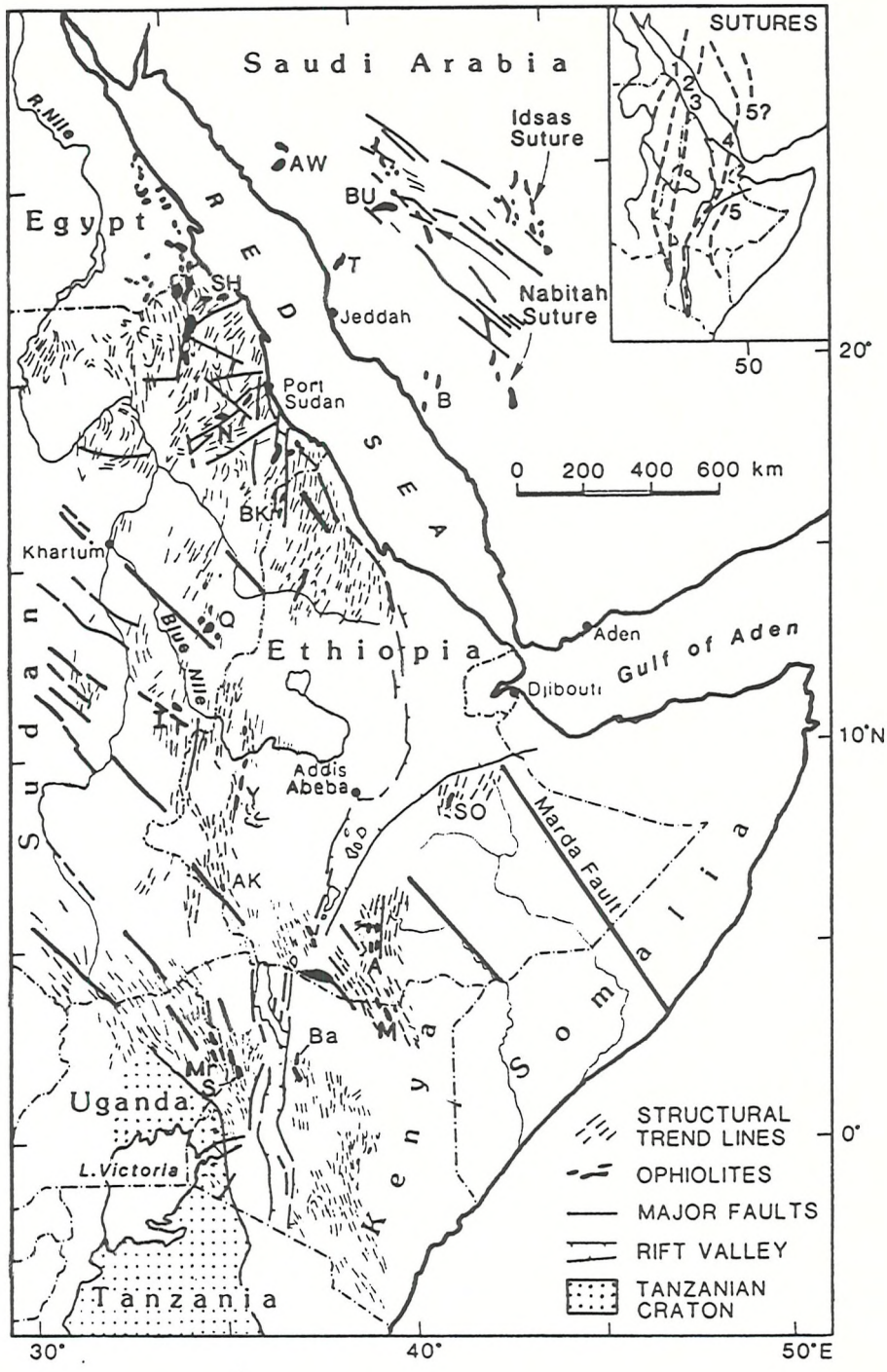

AW = Jebel al Wask
BU = Bi'r Umq
T = Jebel Thurwah
B = Bishah
SH = Sol Hamid

N = Nakasib
BK = Baraka
Q = Qala al Nahal
I = Ingessana
Y = Yubdo
Mr = Moroto

AK = Akabo
So = Soka
A = Adola
M = Moyale
S = Sekerr
Ba = Baragoi

Fig.2.4 Sketch map of the ophiolite belts of north-east Africa and their correlation (from Berhe & Rothery,1986).

differences in age or depth of erosion. In Kenya and Tanzania, the western margin of the belt is clearly defined by a generally easterly-dipping mylonite zone which truncates or transposes the east-west structures of the Archaean Tanzanian craton. Further north, however, the nature of the contact with the Nubian-Arabian Shield remains unclear. The Mozambique belt bifurcates in Southern Ethiopia and the amphibolite grade paragneisses which make up the belt are separated by tholeiitic and calc-alkaline volcanics, immature clastics, and ophiolitic slices derived from the closure of island arc basins (Warden,1982).

The belt continues north into south-west Arabia where it is truncated by a north-west-trending shear zone and to the north-west there is a transition from the Mozambique gneisses to the rocks of the Arabian-Nubian Shield. Almond (1984) considered the major features of the Mozambique belt to be Eburnean in age (2000±200 Ma) which formed a foreland and local basement to rocks of the Nubian-Arabian Shield. Tentative structural evidence suggests that north-trending folds characteristic of the Nubian-Arabian Shield post-dated the north-east structure of the Mozambique belt (Warden,1982). Although scant geochronological data indicate that the suture ophiolites and the collisions of the Mozambique belt in Tanzania are late-Proterozoic in age (Shackleton,1986), the belt was undoubtedly polycyclic and comprises a complex assemblage of Proterozoic belts of different ages (i.e. of Eburnean, Kibaran and Pan-African age) which, in southern Tanzania, define successive orogenic fronts from west to east (Shackleton,1979). It is probable that the older belts were reactivated and overprinted by intense Pan-African deformation and metamorphism due to the collision of East Gondwana (ca.700 or 600-550 Ma, Warden,1982) and subsequently their geochronological signatures were largely obliterated. This would suggest that the various phases of Pan-African orogenesis in East Africa comprised:

a) the reactivation of the Mozambique belt, which separated Archaean crustal segments, and
b) the eventual collision of the East Gondwana plate ranging from a continental collision in the south to the softer collisions by closure of oceanic island arc basins in the north (the Arabian-Nubian wedge of Vail,1983).

2.5 Evolution of the Nubian-Arabian Shield

Calc-alkaline arc assemblages were first recognised in the Arabian Shield by Jackaman in 1972. However, contrasting views for the evolution of the African Shield i.e. continental accretion and progressive cratonisation (Clifford,1970) versus the ensialic formation of younger belts in older shields (Kröner,1977) initially realised two tectonic models for the Nubian-Arabian Shield (Al-Shanti & Roobol,1979) namely:

a) a pre-plate tectonic ensialic model where the magmatic stratigraphic groups sit on a sialic basement; and

b) a plate tectonic model where magmatic arcs (± sialic basement) were juxtaposed by subduction of intervening oceanic crust and are now joined along ophiolitic sutures.

The identification of several discontinuous, linear, ophiolite belts (Brown & Coleman,1972; Bakor et al.,1976; Greenwood et al.,1976) resulted in an eventual general acceptance of the magmatic arc plate tectonic model (Fig.2.5). Early models progressed from the ideas of a single ensimatic arc for the Arabian Shield (Greenwood et al.,1976; Fleck et al.,1980) or multiple arcs with sialic basement (Garson & Shalaby,1976; Stern,1981) to a model of crustal growth by accretion of closely spaced oceanic island arc terranes (Bakor et al.,1976; Neary et al.,1976; Al-Shanti & Mitchell,1976; Gass,1977,1979, 1981; Frisch & Al-Shanti,1977; Shackleton,1977; Engel et al.,1980). Research in the region revealed an abundance of volcaniclastic sequences and related sediments, the ubiquitous presence of calc-alkaline volcanic and plutonic rocks with generally low initial $^{87}Sr/^{86}Sr$ ratios of 0.702-0.704, isotopic ages of <1200 Ma, and $^{143}Nd/^{144}Nd$ values consistent with original derivation from oceanic crust between 900 and 600 Ma (e.g. Stern,1981; Dixon,1981; Jackson & Ramsay; 1980; Gass,1977,1979; Vail,1978; Klemenic & Poole, 1982). Brown (1980) estimated heat production during the Pan-African to be 1.4-1.7 times that of the present day and indicated that Upper Proterozoic arcs would have had similar dimensions (±10%) to current narrow arc systems (100-150 km from trench to back arc basin). A subsequent comparison by Gass (1982) suggested that up to ten or more collided arcs could be accommodated in the 1500 km north-south or east-west extent of the Nubian-Arabian Shield.

Although the apparent absence of older continental crust within the Shield initially indicated its origins by arc accretion, early-

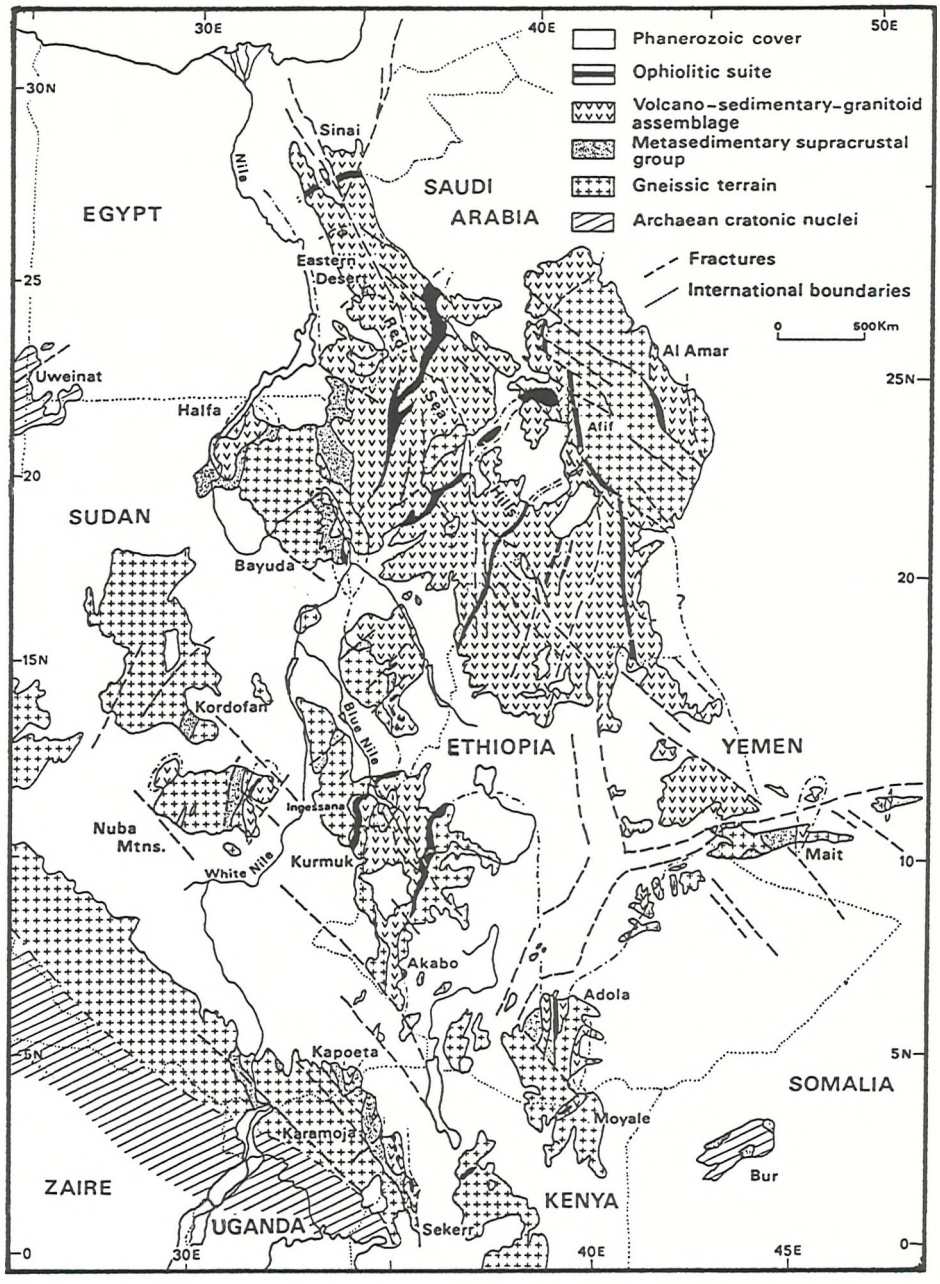

Fig.2.5 Palinspastic sketch map of NE Africa showing its subdivision in to separate terranes by linear ophiolite belts (from Vail,1987b).

Proterozoic continental crust, ironically, was identified in the eastern Arabian Shield (Stacey et al.,1980), possibly marking the eastern boundary of the oceanic arc terranes. Further research has resulted in the identification of several oblique arc/ continental terranes and their sutures in Saudi Arabia (Camp,1984; Stoeser & Camp, 1985) which have been correlated across the Red Sea into north-east Africa (Vail,1983,1985b). Many of these plates display complex and protracted tectonic histories due to their interaction and collision and have been intruded by various syn- to late-orogenic, post-orogenic and anorogenic intrusions. Many areas of the Shield, especially in the Sudan, however, are still poorly understood because of remote

conditions and lack of exposure, and require concentrated research to completely define the evolutionary history of the Shield.

2.5.1 Boundaries of the Nubian-Arabian Shield

The Nubian-Arabian Shield forms the late-Proterozoic basement of Eastern Egypt, Ethiopia, Sudan and Western Saudi Arabia but its true limits are largely obscured by Phanerozoic sedimentary cover. This restriction, coupled with a paucity of geochronological data means that, in most parts of the Shield, the nature and position of the boundary between the Pan-African oceanic island arc system and any older foreland continental basement remains equivocal. In the west, the boundary lies somewhere between the granulite facies Archaean basement exposed on the borders of Sudan, Libya and Egypt at Jebel Uweinat (Figs.2.2 & 2.5; 2670 Ma, Klerkx and Deutsch, 1977; Harris et al.,1984) and the late-Proterozoic greenschist facies calc-alkaline juvenile arc lithologies in the Eastern Desert of Egypt and the Red Sea Hills of Sudan.

In the Eastern Desert of Egypt, as with the other arc terranes of the Shield, very low initial Sr ratios ($^{87}Sr/^{86}Sr=0.7026$) and very low LIL and REE abundances preclude the existence of any pre-existing continental crustal material (Stern,1981). The dating, however, of granitic and arkosic cobbles in rare conglomerate bands within the 600-700 Ma volcaniclastic and greywacke assemblages show a wide range of ages (1.1-2.3 Ga, U-Pb on zircons) and are considered to be derived from adjacent pre-Pan-African continental areas to the west and/or south (Dixon,1981). In addition, the continental affinities of some granitic rocks near Aswan are consistent with a proximal continental margin near the western boundary of the exposed Nubian Shield (Fig.2.6; Gillespie & Dixon,1983). Elsewhere in Egypt, gneisses originally considered to be older continental crust (Hume,1934; Schürmann,1966; Abdel-Monem & Hurley,1979; Shimron,1980), are principally exposed in the three areas of Sinai (Wadi Feiran), Central Eastern Desert (Meatiq Dome), and South Eastern Desert (Migif-Hafafit). Subsequent geochronological and isotopic studies in these areas, however, have shown that pre-Pan-African continental crust was not involved in generating the gneisses (Sturchio et al.,1983; Harris et al.,1984; Stern & Hedge,1985; Stern & Manton,1987) and there is still no evidence for either a pre-Pan-African stable foreland or reworked pre-Pan-African basement in northernmost Afro-Arabia east of the River Nile.

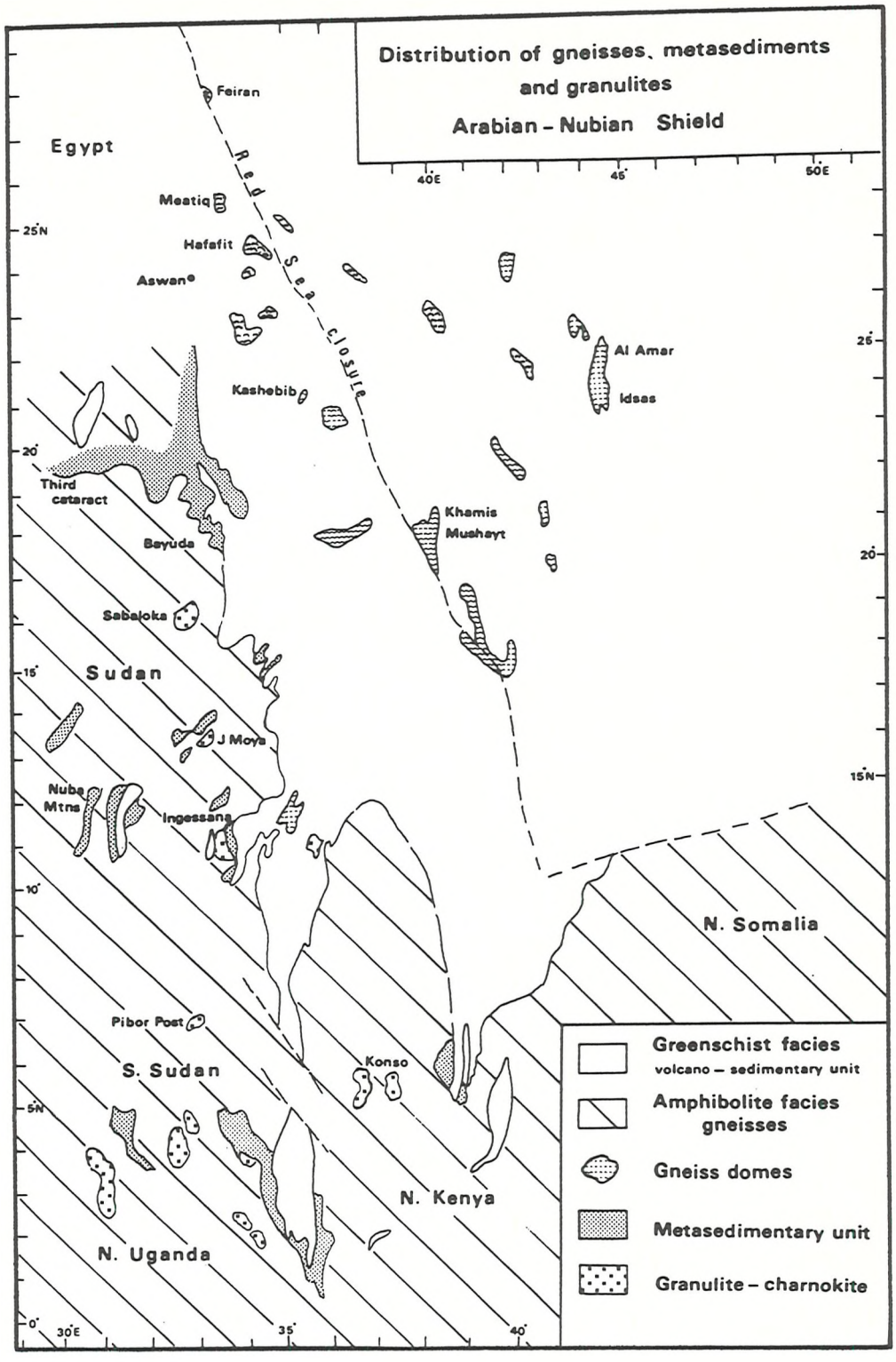

Fig.2.6 Sketch map of the Nubian-Arabian Shield showing the distribution of gneisses, metasediments and granulites (from Vail,1983).

To the south in Sudan, high-grade gneisses (Grey Gneiss Group; Vail,1979) found with amphibolite grade metasediments (Metasedimentary Group; Vail,1979) along the Nile in the Bayuda desert, at Sabaloka and in the Blue Nile Province (the Tin Group; Vail & Hughes,1987) were tentatively correlated with the granulitic gneisses at Jebel Uweinat and considered to represent the remobilised pre-Pan-African continental margin (Vail,1976,1979; Almond,1980,1982). This delineated the continental margin and western limit of the Nubian Shield which was assumed to occur roughly along the Nile Valley on a north-south trend. Subsequent geochemical and geochronological studies (Harris et al.,1984; Ries et al., 1985; Kröner et al.,1987) contradict the previous hypotheses and indicate that the gneisses are of similar age to the greenschist facies arc volcanics. However, detrital zircon ages from 870 Ma sediments at Sabaloka range from ≈1000Ma to 2650Ma, indicating sedimentary input from the ancient shield close to the west. Although the granulite and gneiss complexes have been disputed as the remobilised margin to the African craton, the occurrence of continental margin shelf deposits in the form of the amphibolite grade metasediments on the edges of the Nubian Shield appear to be indicative of its close proximity, especially in the absence of good exposure, and isotopic and geochronological data (Fig.2.7).

Problems due to lack of dating around the Nubian Shield and uncertainties in the evolution and age of the Mozambique belt have resulted in a poor understanding of the limits of the Nubian Shield in Ethiopia. Hence, only tenuous correlations of the Metasedimentary and Grey Gneiss Groups with the Mozambique belt and its possible continuation into north-east Africa have been made (Almond,1980,1982; Kröner et al.,1987). Consequently, on the western side of the Nubian Shield, boundary definition between the late-Proterozoic fold belt and an older craton is still ambiguous but appears to lie west of and close to the Nile valley on a roughly north-south trend.

Although initial evolutionary models for the Arabian Shield were based on the accretion of oceanic arc systems, the existence of a pre-Pan-African sialic basement had been reported underlying parts of the eastern Arabian Shield (Baubron et al.,1976; Delfour,1979; Nawab,1979; Schmidt et al.,1979). The ages and nature of this basement were largely inferred on geological grounds and were inconclusive (Kröner et al.,1979; Stacey et al.,1980; Engel et al.,1980; Duyverman & Harris,1982; Duyverman et al.,1982). The initial lead isotope data from the Halaban-Al Amar region of the eastern Arabian Shield exhibited

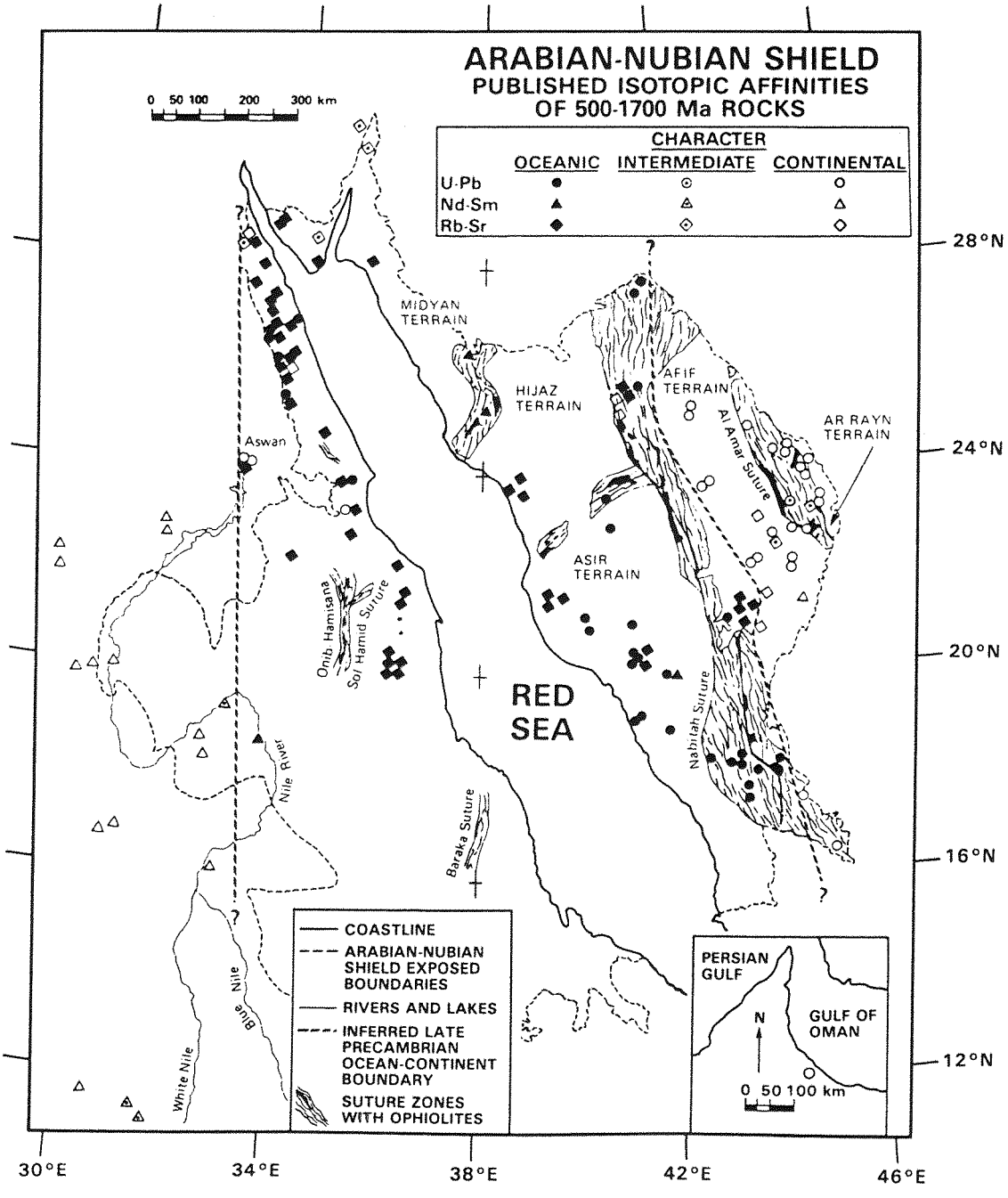

Fig.2.7 Isotopic data for Precambrian rocks of the Nubian-Arabian Shield compiled by Dixon and Golombek (1988).

a continental crustal component of at least early Proterozoic age (2100 Ma; Stacey et al.,1980). Follow-up studies (U-Pb zircon, feldspar common Pb,whole-rock Sm-Nd and Rb-Sr) indicated an evolved early Proterozoic continental crustal basement component of 1800-1600 Ma age (Fig.2.7; Stacey & Stoeser,1983; Stacey et al.,1984; Stacey & Hedge,1984) but no definitive evidence was presented. Similar lead isotope data from massive sulphide deposits in the Arabian Shield were published by Bokhari & Kramers (1982) who did not accept the conclusion of a lower older continental crust. However, the identification of

2000 Ma zircons in a trondhjemite along the Al Amar fault by Calvez et al. (1983) lent further support to the original assertion of a pre-Pan-African basement. As with the Egyptian Desert, although an older basement is suggested, no source terrain within the exposed Saudi Arabian Shield has been identified.

Within the Halaban-Al Amar region of the eastern Shield, Delfour (1980) recognised three north-south-trending geological provinces bounded by fault zones: the Afif province in the west, the Ad Dawadimi province in the centre, and the Ar Rayn province in the east. To the north Johnson and Vranas (1984) defined another terrane composed of metamorphosed arc-derived volcano-sedimentary rocks with a distinctive north-east magnetic grain which have been dated at ≥735 Ma and comprise the Ha'il terrane (Fig.2.8).

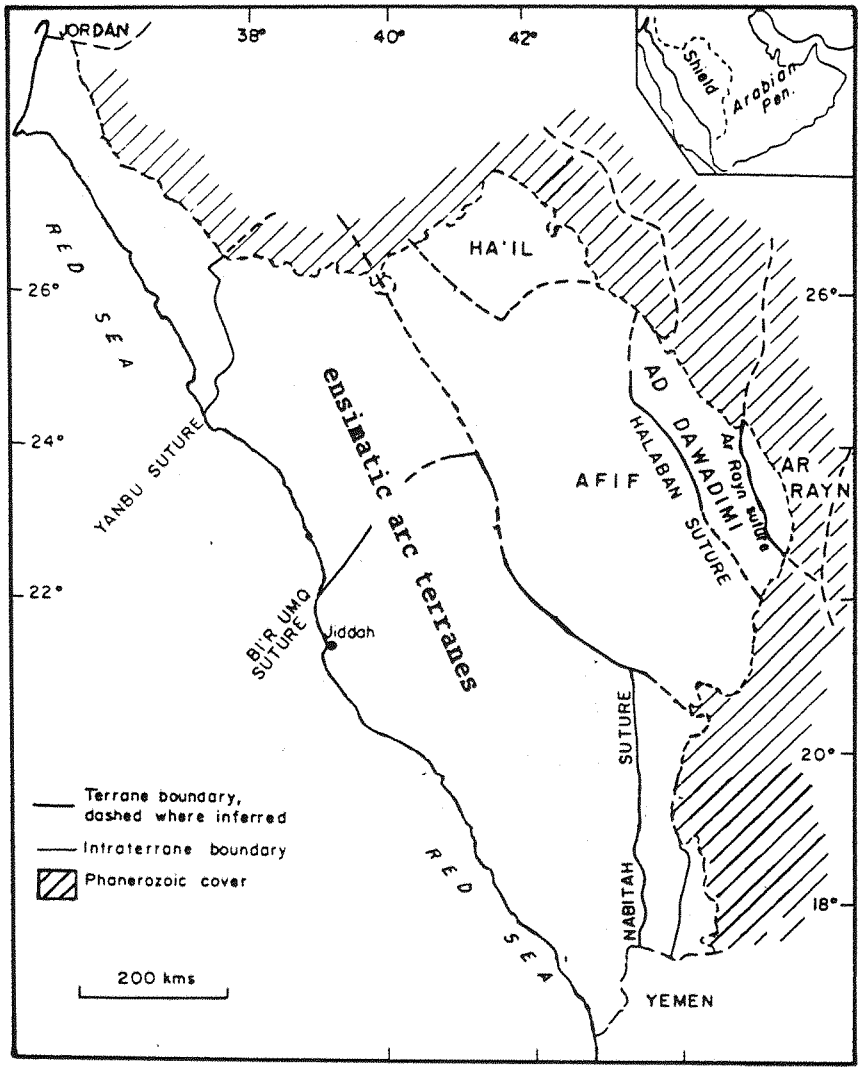

Fig.2.8 Sketch map of the Arabian Shield outlining the main terrane boundaries (after Johnson et al., 1987).

The Afif terrane consists of post-orogenic granites (640-580 Ma) and intermediate to felsic volcanic rocks and molasse-type sediments (≈660-600 Ma) that unconformably overlie a crystalline basement (the As Sawda Domain of Delfour,1979). The basement complex is composed of felsic gneiss, sparse paragneiss and schist, and voluminous intermediate plutonic lithologies (Stoeser & Camp,1985). Dating and correlation of metasediments and volcanics in the Afif terrane (Mahanid, Khida, and Kabid Formations 1839±14Ma; and Siham Group) has produced direct evidence for a late-Proterozoic continental microplate and active continental margin in the eastern Saudi Arabian Shield (Stacey & Agar,1985; Agar,1985; and White,1985).

The Ar Rayn province occurs in the eastern-most part of the Halaban-Al Amar region and is largely concealed by Phanerozoic sediments. It is separated from the Afif terrane by the Ad Dawadimi province which Stoeser & Camp (1985) termed the Al Amar(-Idsas) suture (Fig.2.7). This province comprises a 40 km wide zone of deformed clastic sediments (chlorite-sericite schists of the Abt Formation) intercalated with fault-bounded mafic-ultramafic complexes collectively known as the Urd Group (Stacey et al.,1984). The Urd Group appears to form a broad synclinorium with the ophiolite complexes at the base but there is uncertainty concerning the polarity of subduction (east or west) and whether the clastic sediments and ophiolitic mélange constituted an accretionary wedge (Al-Shanti & Mitchell,1976; Stacey et al.,1984) or a back arc basin (Nawab,1979; Al-Shanti & Gass,1983). Pallister et al. (1988), however, consider the Ad Dawadimi province as a separate microplate on the basis of it being bounded by fault zones containing ophiolitic material (Urd/Halaban and Al Amar-Idsas sutures) and U-Pb zircon dating suggests there is a possibility that the ophiolitic rocks of the Al Amar-Idsas suture may be considerably older than those of the Urd suture.

The Ar Rayn terrane is composed primarily of syn-tectonic tonalitic gneisses and a group of calc-alkaline volcanic rocks (Al Amar Group) which pre-dated suturing, probably representing arc magmatism (Stoeser & Camp,1985). Camp et al. (1984) pointed out that the rocks either side of the Abt schist basin are distinct in terms of seismic and magnetic characteristics, metallogenic signature, and Pb-isotope characteristics, and, therefore, cannot be rifted fragments of the same arc complex. The Al Amar arc in the Ar Rayn terrane indicates that initial subduction was to the east with the Abt schist representing an accretionary complex that formed in an arc basin. Collision, however,

may have initiated westward subduction beneath the eastern margin of the Afif terrane producing the arc magmatism of the "Sawda arc" (680-670 Ma; Stoeser & Camp, 1985).

To the west, the boundary of the Afif microplate and the north-east-trending oceanic arc terranes is delineated by the north-south-trending province of the 100-200 km wide Nabitah mobile belt (Fig.2.9).

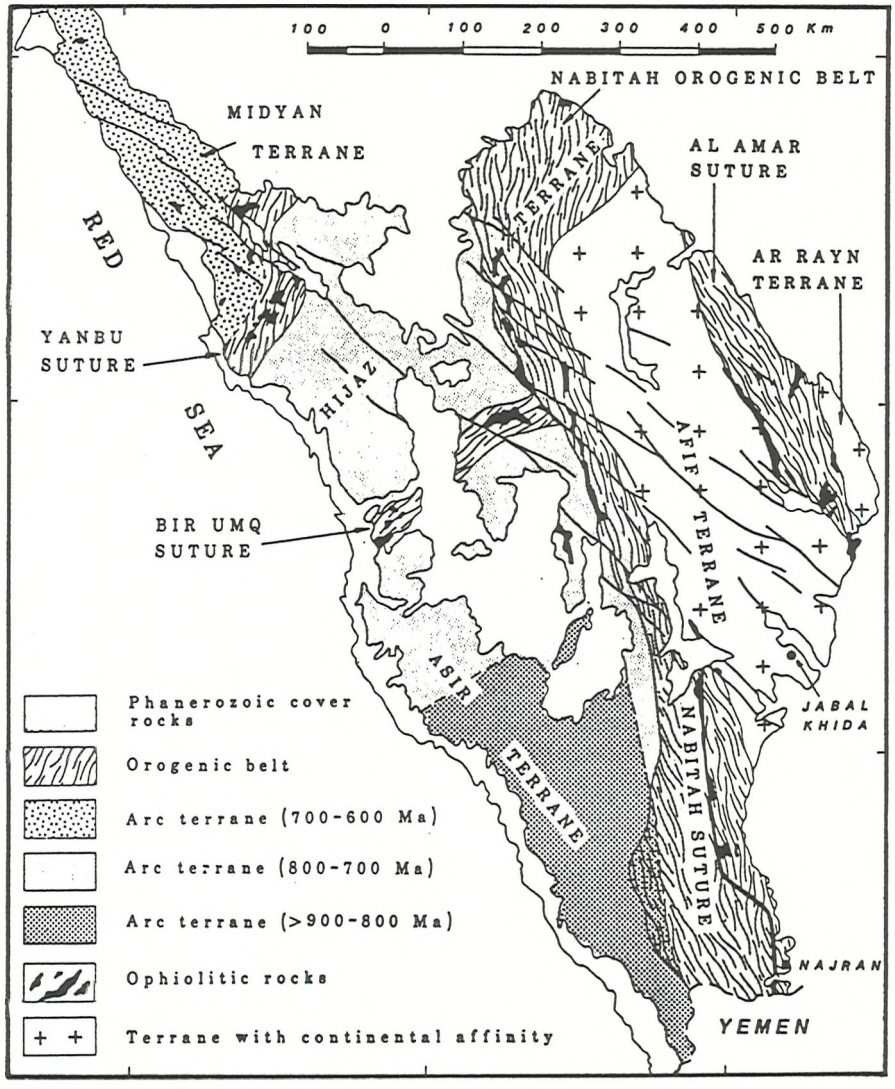

Fig.2.9 Sketch map of the Arabian Shield showing the relationship between the continental and oceanic-arc terranes (from Stoeser & Camp,1985).

This belt contains a centrally located ophiolitic zone (Bir Tuluhah, Ad Dafinah, Tathlith and Hamdah complexes) which Schmidt et al. (1979) called the Nabitah suture. Stoeser et al. (1984) considered the Nabitah belt as a zone between two composite allochthonous microplates, namely the pre-accreted intraoceanic Hijaz-Asir arc province to the

west and, to the east, the Afif microplate with its early-Proterozoic microplate enclosed by volcanic and plutonic rocks (Hulayfah volcanic complex >720 Ma; Nuqrah volcanic complex >820 Ma; Siham arc and basin >720 Ma; Farshah volcanic complex) similar to those of the Hijaz. The stratigraphy and palaeogeography of the Siham Group continental margin metasediments is consistent with easterly directed subduction (Agar,1985). Collision between the more primitive western arc terranes and the more evolved continental margin arc complex of the Afif microplate (Schmidt et al.,1979) resulted in superimposition of the eastern part of the belt over the Afif continental margin by eastward directed thrusting (Stoeser & Camp,1985; Agar,1985). This collision, known as the the Nabitah orogeny, has been dated at 680-640 Ma (Stoeser et al.,1984) and culminated in the final suturing of the western margin of the Afif microplate.

The Afif and Ar Rayn terranes have been interpreted as exotic continental fragments that may represent rifted fragments of the early-Proterozoic Mozambique belt surrounded by larger oceanic-arc terranes. (Stoeser & Camp,1985; Kröner,1985; Pallister et al.,1987). Compilation of available isotopic data by Dixon and Golombek (1988) suggest that the eastern quarter of the exposed Arabian Shield is largely of continental affinity. Post-thrusting igneous complexes with acquired continental isotopic signatures indicate the oceanic-arc material of the Al Amar-Idsas suture zone to be limited to thin sheets over a continental margin basement as purported by Stacey et al. (1984). Geochemical trends in A-type (late-stage anorogenic) granites in the exposed Arabian Shield show increasing continental influence to the east (Stuckless,1987) and high lead ratios from Oman and Yemen also indicate derivation from early-Proterozoic or Archaean crust (Stacey et al.,1980; Stacey & Stoeser,1983). Although there are no basement exposures in the Phanerozoic cover further east in Saudi Arabia, the isotopic data suggest the obscured basement in this area to consist of pre-existing continental crust. The presence of narrow, late-Proterozoic, oceanic-arc terranes flanked by older continents are suggestive of a Wilson cycle (Dixon & Golombek,1988). New volume estimates for the arc terranes indicate the growth rate of the Nubian-Arabian craton between 950-640 Ma to be 10-20% of the modern global rate (Pallister et al., 1988: Dixon & Golombek,1988) and that the anomalously high growth rates for the continental crust postulated by Reymer and Schubert (1984,1986) are not required.

2.5.2 Ophiolites, Sutures and the Oceanic Arc Complexes

Numerous arc-arc and arc-continent sutures have been identified in the Nubian-Arabian Shield on the basis of recognition and correlation of ophiolite complexes (Brown & Coleman,1972) and their association with calc-alkaline volcanic rocks of island-arc affinity (Fig.2.10).

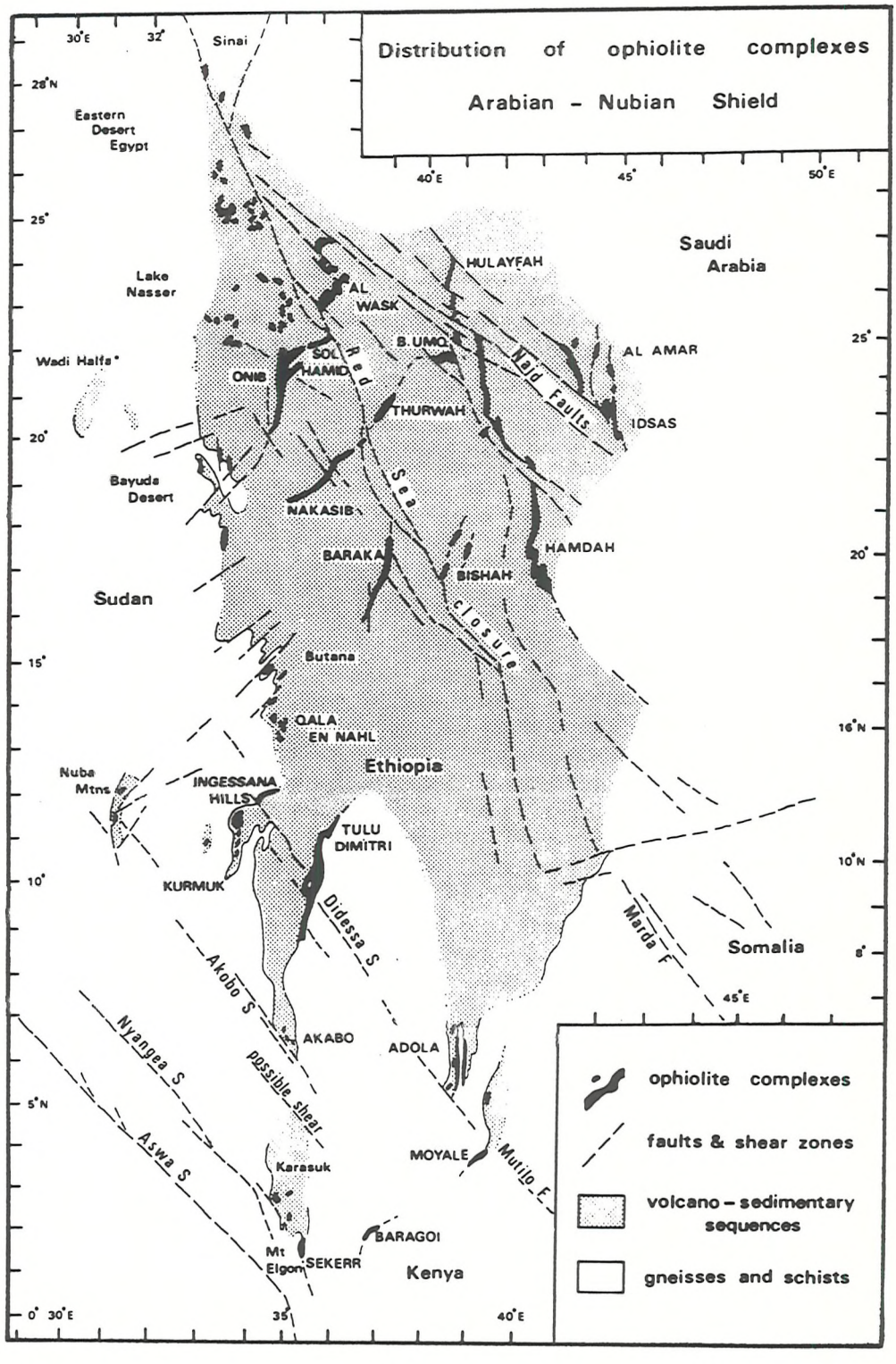

Fig.2.10 Distribution of ophiolite complexes in the Nubian-Arabian Shield (from Vail,1983).

In Saudi Arabia almost complete and intact ophiolite sequences have been described at Jabal al Wask (Bakor et al.,1976), in the Al Amar-Idsas zone (Al-Shanti & Mitchell,1976), and along the Nabitah mobile belt (Hulayfah-Hamdah zone), at Bir Umq (Frisch and Al-Shanti,1977) and at Jebel Thurwah (Nassief et al.,1984). These have recently been comprehensively reviewed and dated by Pallister et al. (1988). On the western side of the Nubian-Arabian Shield, probable, though less well documented, complexes have been described from the Eastern Desert of Egypt (Garson & Shalaby,1976; Dixon,1980; Shackleton et al.,1980; Nasseef et al.,1980; Ries et al.,1983), in Sudan (Fitches et al.,1983; Vail,1983; Hussein et al.,1984; Kröner,1985; Steiner,1987), Ethiopia (Kazmin et al. 1978) and Kenya (Shackleton, 1977). Early tentative correlations of outcrops of ophiolitic affinity in Saudi Arabia indicated that the belts which represented possible palaeo-sutures trended north-westwards (Greenwood et al.,1976; Bakor et al., 1976) despite the recognition in north-east Sudan and western Saudi Arabia of a general north to north-east trend to the basement (Gass,1955; Neary et al.,1976). A detailed structural traverse across the Eastern Desert of Egypt (Shackleton et al.,1980; Ries et al.,1983) showed the ophiolitic complexes there to comprise an allochthonous ophiolitic mélange which originated as a trench olistostrome before being tectonically transported in a north-west direction. Hence, a justifiable correlation with the Arabian ophiolites could not be made.

Different criteria have been used, in addition to the correlation of ophiolitic complexes, to identify individual Pan-African arc systems. These include: regional variations in the geochemical characteristics of magmatic rocks (Greenwood & Brown,1973; Gass,1977; Gass & Nasseef, 1980), zones of distinctive lithological and/or metamorphic character (Ramsay et al.,1979), and zones of characteristic mineralisation (Shanti & Roobol,1979; Vail,1985). Gass (1982) reappraised the above criteria and opted to use linear granitic zones, best developed in north-eastern Sudan, to mark the plutonic cores of eroded arc axes, the north-south to north-east-south-west orientations of which coincided broadly with many of the ophiolite zones and structural trend lines (Vail, 1979). Following the identification of terranes of continental affinity by Stacey et al. (1984) in the eastern Arabian Shield and the delineation of two north-east-trending arc systems (Hijaz and Asir) by Camp (1984) in the western Arabian Shield, Stoeser and Camp (1985) synthesised the data to define at least five oblique and geologically distinct terranes (microplates) in the

Arabian Proterozoic basement (Figs.2.9). It is likely that these five microplates are composed of numerous units that should be defined as separate terranes similar to those of Johnson and Vranas (1984) who proposed ten such terranes. A similar conclusion was drawn by Vail (1985a,1985b) who demonstrated good correlation of the arc terranes of western Arabia across the Red Sea closure line into north-east Africa but with some uncertainty on the western side of the Nubian Shield (Fig.2.11). Vail (1987) and Johnson et al. (1987) further subdivided the three arc microplates of Camp (1984) into seven or eight oceanic terranes distinguished by oblique ophiolite belts or fracture zones considered to represent probable Proterozoic suture zones.

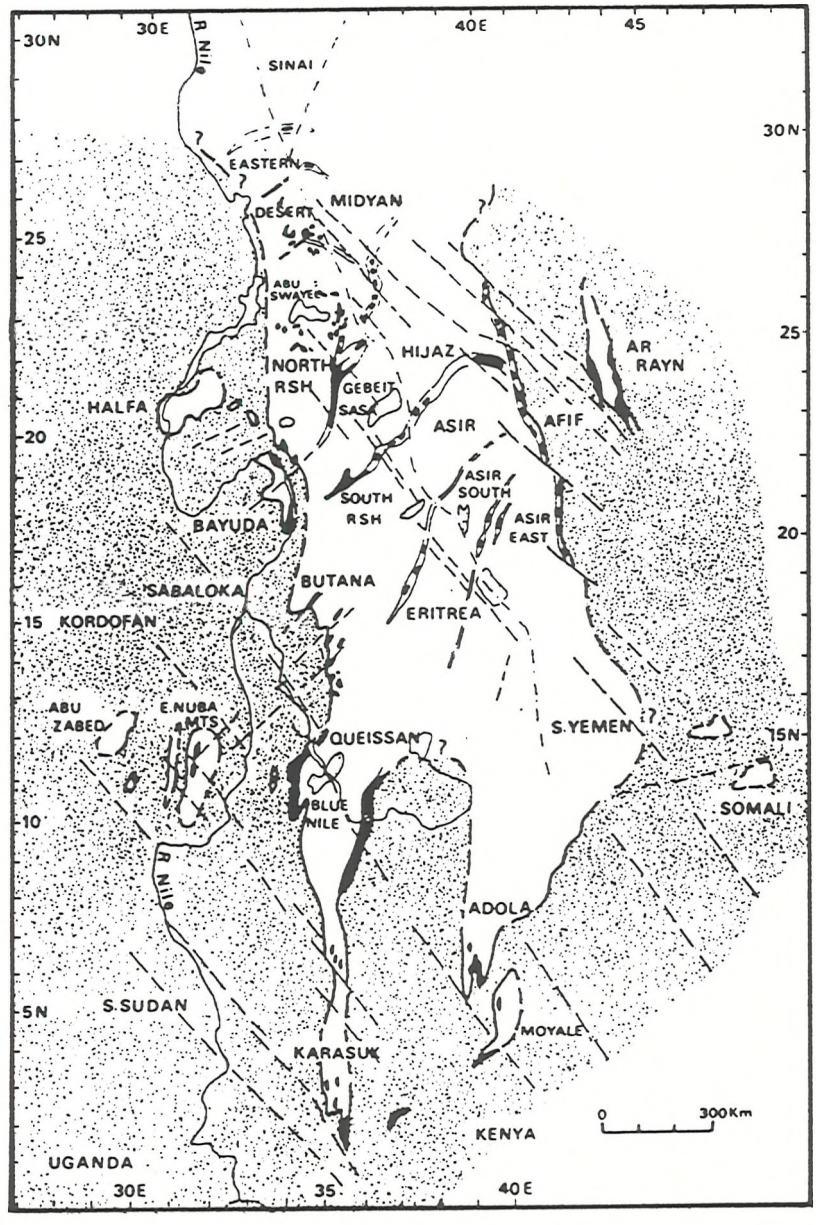

Fig.2.11 Map of the correlation of Arabian arc terranes (unornamented) with arc terranes of the Nubian Shield (from Vail,1987a).

Recent studies of shear zones in the Sudan by Almond and Ahmed (1987; Almond et al.,1984) have indicated that the north-east-trending arc systems of the central Shield terminate to the west, as they do along the Nabitah mobile belt in the eastern Shield, against the north-south-trending Abirkitib shear zone which Almond and Ahmed believe represents a suture zone between the central Gebeit-Hijaz arc and an immature arc to the west, close to the African continental margin (see Fig.2.20). The resulting tectonic pattern comprises a narrow central zone of north-east-trending oceanic-arc terranes bounded by regions of older continental crust and associated continental margins (Fig.2.11). The orientation of the arc terranes and the Mozambique Belt controlled the subsequent rift trends of the Red Sea and the East African Rift. Stoeser and Camp (1985) recognised three ensimatic island arc terranes separated by arc-arc sutures: the southern, composite Asir terrane; the central Hijaz terrane; and the northernmost Midyan terrane (Fig.2.9).

2.5.2.1 The Asir Island Arc System

The Asir island arc system is separated from the Hijaz terrane to the north by a north-east-trending suture zone delineated by the ophiolite localities of Bi'r Umq, Thurwah and Khor Nakasib (Fig.2.10; Al-Rehaili & Warden,1980; Nassief et al.,1984; Vail,1979) and is commonly termed the Bi'r Umq-Port Sudan suture. It is a narrow (20 km wide) belt of highly deformed, greenschist facies, arc-related lithologies together with amphibolite, gneiss, and dismembered ophiolite complexes contained in isoclinal folds and north-west-dipping allochthonous, imbricate thrust sheets (Camp,1984; Stoeser & Camp,1985; Pallister et al.,1988). The suture extends for 600 km from the Nabitah mobile belt to at least 150 km south-west of Port Sudan and has been dated 820-870 Ma. It may also continue further north, transposed along the western side of the Nabitah belt, to define the northern half of the Nabitah suture (Bir Tuluhah ophiolite 823-847 Ma, Pallister et al.,1987). South of the Bi'r Umq-Port Sudan suture lies the Asir arc system of Camp (1984) who identified several lithostratigraphic and tectonic provinces conforming to fore-arc, arc and back-arc environments with at least two generations of arc magmatism (Fig.2.12). A palaeo-accretionary prism, accretionary basin, frontal arc, inter-arc basin and remnant arc have been recognised (Camp,1984), prompting other workers (e.g. Vail,1985a,b; Johnson et al.,1987) to subdivide the Asir terrane into several volcanic complexes (Table 2.1).

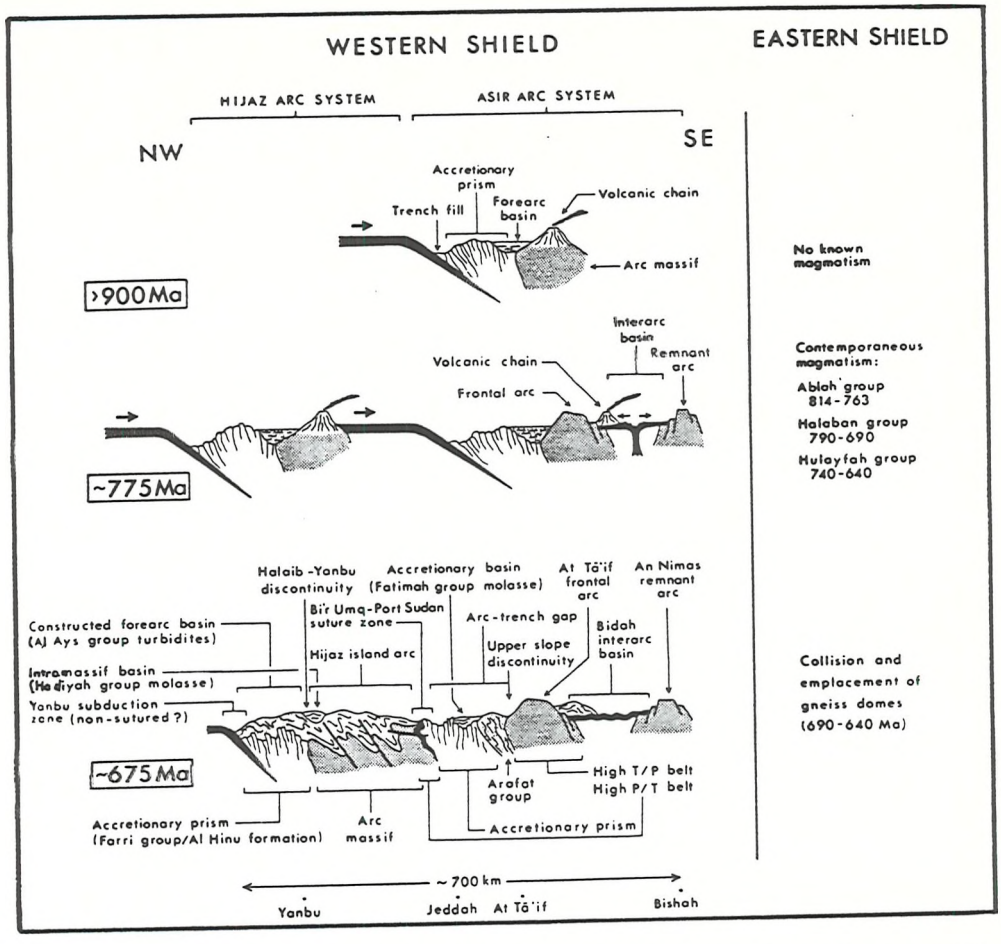

Fig.2.12 Structure of the Asir and Hijaz arc terranes along a NW-SE section immediately east of the Red Sea (from Camp, 1984).

Stoeser & Camp (1985)		Johnson et al. (1987)	Vail (1985)
Accretionary prism	Jiddah-At Ta'if	Jiddah volcanic complex (pre-816 to 760 Ma)	
Fatimah Discontinuity		Upper-slope Discontinuity	Asir-South Red Sea Hills
At Ta'if frontal arc		Al Lith Complex (>890-?820 Ma)	
		Afaf suture	
Biddah inter-arc basin	Asir	Bidah-Hali volcanic complex (pre-900 to ?830Ma)	Asir South-Eritrea
		Ablah volcanic rift (?795-720Ma)	
An Nimas remnant arc		Abha-Bishah volcanic complex (?912-797Ma)	Asir East
Tarib arc		Khadra-Ishmas volcanic complex (785-725Ma)	

Table 2.1 Subdivisions of the Asir arc terrane of Stoeser & Camp (1985).

The accretionary prism and frontal arc (the At Ta'if frontal arc) are separated by an upper-slope discontinuity (Fatimah Discontinuity) and collectively they, possibly, constitute a paired metamorphic belt. The area south-east of the At Ta'if zone is interpreted as an inter-arc basin (Bidah Inter-arc Basin) with its associated remnant arc (An Nimas Remnant Arc) further to the south being delineated by the north-east-trending, fault-bounded trondjhemite block of the An Nimas Batholith (Camp,1984).

The back-arc area is dominated by a metabasalt-greywacke-chert assemblage comprising the Baish Group (primarily basalt but locally bimodal low-K tholeiitic volcanics) and the Bahah Group (contemporaneous volcaniclastic and epiclastic sediments). This domain contains the oldest rocks in the Asir dated at 820-900 Ma (Marzouki et al.,1982). Ocean-floor ultramafic and mafic rocks contained in major faults between the At Ta'if frontal arc and the An Nimas remnant arc represent the thin oceanic floor produced during spreading of the inter-arc basin. This zone is delineated by the Afaf suture, separating the At Ta'if-Jiddah terrane and the Asir terrane of Johnson et al. (Fig.2.13; 1987). The Afaf suture separates regions of north-east-trending structures in the At Ta'if-Jiddah terrane from north-south trends in the Asir terrane and has been correlated with the Baraka ophiolite which forms the northern boundary to the Asir South-Eritrea terrane of Vail (Fig.2.11; 1985a,b).

At the eastern edge of the Asir terrane lies a north-south-trending zone of volcanic and intrusive rocks of an island arc complex produced by westward directed subduction below the older Bidah inter-arc complex and dated at 785-725 Ma (Camp, 1984; Johnson et al.,1987). This arc termed the Khadra-Ishmas complex by Johnson et al. (1987) was designated the Tarib arc by Stoeser and Camp (1985). It is deemed to be coeval with secondary arc volcanism due to continued south-easterly-directed subduction beneath the Ta'if region (Fig.2.14). Similar lithologies are found in the Malahah-Yafikh and Wassat volcanic complexes exposed east of the Nabitah suture (the older Junaynah suture of Pallister et al., 1987) and constitute the Malahah-Najran composite terrane which is dated at ≥732 Ma and encompasses the high-grade mélange and basin deposits (Nabitah suture of Pallister et al.,1987) of the Tathlith terrane (Fig.2.13; Johnson and Vranas,1984).

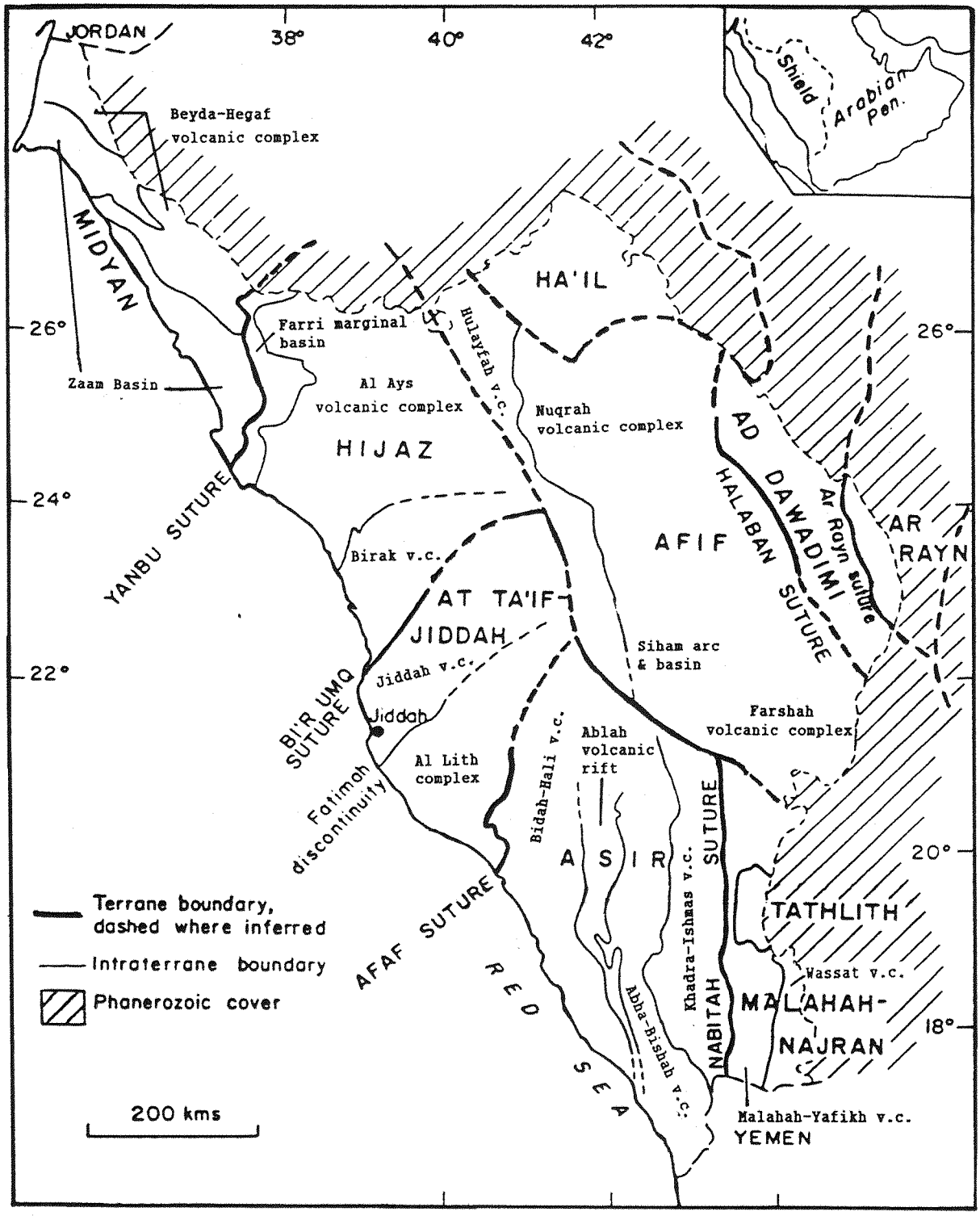

Fig.2.13 Late-Proterozoic accreted tectonostratigraphic terranes in the Arabian Shield (after Johnson et al., 1987).

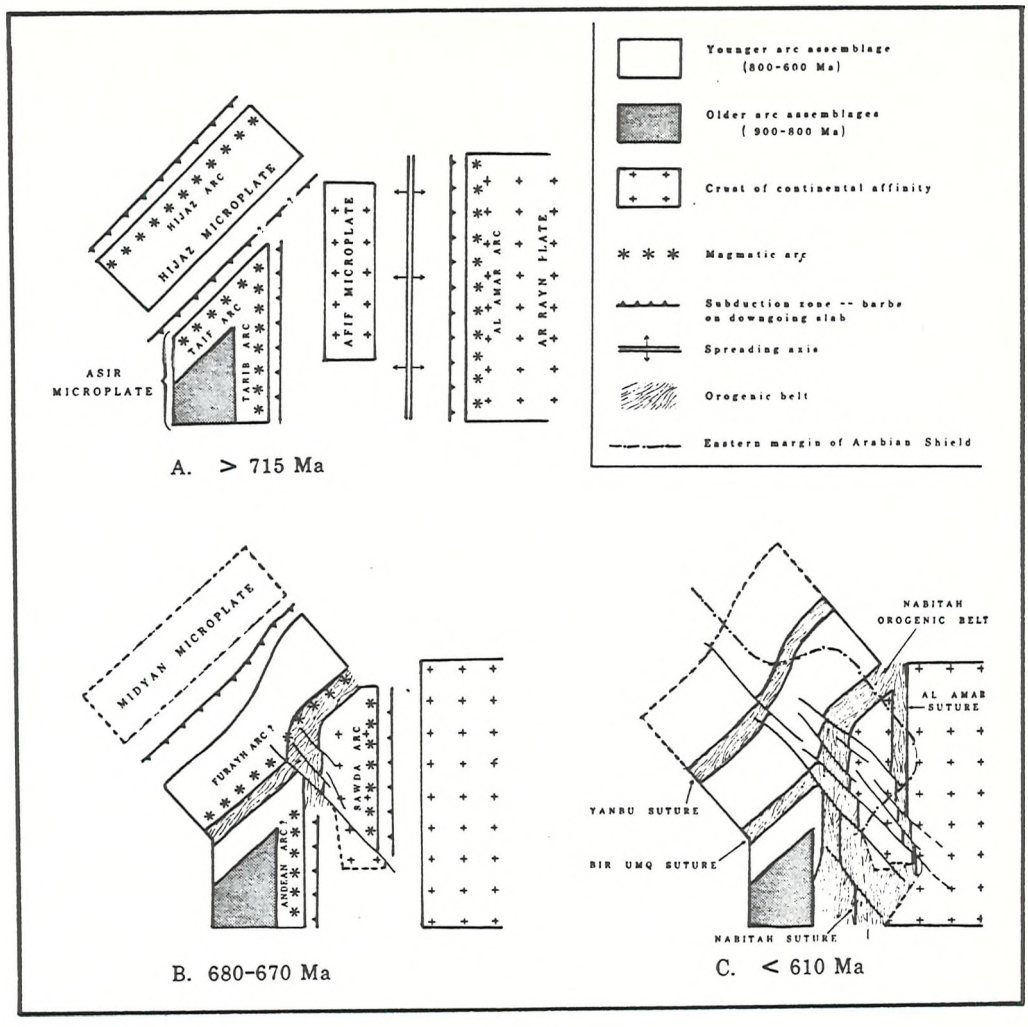

Fig.2.14 Evolution of the Arabian Shield (from Stoeser & Camp,1985).

2.5.2.2 The Gebeit-Hijaz Island Arc Terrane

To the north of the Bi'r Umq-Port Sudan suture lies the Hijaz island arc terrane which contains three superimposed magmatic assemblages (Camp,1984) and is correlated with the Gebeit terrane of Vail (1985a,b). The north-western edge of the Hijaz is defined by Halaib-Yanbu suture connecting the ophiolites of Jabal Ess (Shanti & Roobol,1979) and Jabal al Wask (Bakor et al.,1976) in the Arabian Shield, and Sol Hamid (Hussein,1977; Fitches et al.,1983) and Wadi Onib (Hussein et al.,1984; Nassief et al.,1984) in the Nubian Shield (Fig.2.10).

In Arabia, it is a zone composed of highly deformed greenschist to amphibolite grade volcano-sedimentary assemblages (Al Hinu Formation) that are often associated with ultramafic lithologies and believed to be the strongly metamorphosed equivalent of the Farri Group (Camp,1984). The Al Hinu Formation and the Farri Group collectively

represent the strongly deformed accretionary prism of the Farri marginal basin subsequently intruded by a suite of pre-accretionary tonalites dated at 796-743 Ma (Johnson et al.,1987). The Jabal al Wask and Jabal Ess ophiolites have been dated at 743±24 Ma and 782±38 Ma respectively (Claesson et al., 1984) and their trace element geochemistry suggests they are back-arc in origin (Bakor et al.,1976; Pallister et al.,1985).

The Farri Group is unconformably overlain by a forearc sequence of turbiditic sediments and minor volcanics of the sedimentary facies of the Al Ays group (Fig.2.12; Kemp,1981). The Al Ays Group dated at 735-705 Ma covers most of the Hijaz terrane (Fig.2.13) and is intruded by gabbro-diorite-tonalite-granodiorite batholiths elongated in parallel to the Yanbu suture (Camp,1984). To the south-east the Al Ays succession is predominantly volcanic consisting of mostly sub-aqueous, arc facies, calc-alkaline basalts (Matran Formation) which become increasingly silicic up section (Camp,1984). Dating of plutonic lithologies indicates that arc magmatism continued up to 715 Ma when the north-east trending Samran fold belt was produced by arc collision along the Bi'r Umq suture between 700 and 680 Ma (Stoeser & Camp,1985). Unconformably overlying the Al Ays Group fore-arc turbidites to the south-west are basalts and andesites of the Furayh and Hadiyah Groups which were generated through Andean-type magmatism (Furayh Arc) by continued south-east subduction beneath the Hijaz terrane (Fig.2.14) and deposited subaerially in a north-east trending intramassif basin (Camp,1984; Stoeser & Camp,1985).

The oldest volcanics in the Hijaz cut by intrusives dated 870-800 Ma (Al-Shanti et al.,1984) are exposed along the southern margin of the terrane as the Birak Group where they are associated with ophiolites of the Bi'r Umq suture zone. The Birak volcanic complex comprises low-K tholeiitic mafic volcanic, and volcaniclastic rocks intruded by arc-related calc-alkalic diorites, granodiorites and tonalites (Johnson et al., 1987).

In Sudan, the Sol Hamed ophiolite dips steeply and faces south-east indicating a south-easterly dipping subduction zone (Fitches et al.,1983). The volcanic/sedimentary polarity and the structural vergence of the belt in Saudi Arabia led Camp (1984) to concur with south-east directed subduction. The ophiolite complex at Sol Hamid is unconformably overlain by a greenschist facies volcaniclastic series of andesites, dacites, tuffs, volcaniclastic sediments, turbidites and limestones (Nafirdeib Series of Ruxton,1956; Oyo Series of Gass,1955)

dated at 712±58 Ma which were deposited on the flanks of an emergent island arc (Fitches et al.,1983). At Wadi Onib shear zones and ophiolites define a Y-shaped pattern (Fig.2.10) where the north-east trending Halaib-Yanbu suture is transposed/truncated by the north-south-trending Abirkitib shear zone which contains dismembered ophiolites (Hussein et al.,1984) and is regarded as a rejuvenated suture (Almond & Ahmed,1987). To the west of the Abirkitib suture lies a north-south belt of low-grade metavolcanics and metasedimentary rocks backed by a zone of high-grade shelf metasediments. It has been termed the Gabgaba terrane by Kröner et al. (1989) and the North Red Sea Hills terrane by Vail (1985b), and has been interpreted as an immature island arc marginal to the Proterozoic African continent (Almond & Ahmed,1987).

2.5.2.3 The Midyan Island Arc Terrane

The area north of the Halaib-Yanbu suture, termed the Midyan terrane (Stoeser & Camp,1985) is poorly understood and in Saudi Arabia the older formations have been subdivided into the volcaniclastic, turbidite and shale continental edge deposits (Zaam Group, Silasia Formation, Alqunnah and As Safra Groups) of the Zaam basin and the mafic to felsic, low-K to calc-alkaline, volcanics and volcaniclastic rocks of the Bayda-Hegaf volcanic complex (Fig.2.13; Clark, 1985; Johnson et al.,1987). Both groups have been intruded by arc-related diorites and tonalites which constrain minimum ages to 800-725 Ma and pre-710 Ma respectively. In the Eastern Desert Of Egypt, Ries et al. (1983) defined four different tectonic units separated by structural contacts which comprise;

a) the lowest group of continentally derived, shallow water, arkosic metasediments exposed as gneisses in the Meatiq and Hafafit areas;
b) an ophiolitic mélange (containing the Older Metavolcanic Group of Stern, 1981) separated from the lowest unit by a mylonite zone;
c) a predominantly andesitic group of calc-alkaline volcanics (Younger Metavolcanic Group of Stern,1981) thrusted over the ophiolitic mélange but with the upper members possibly erupted in situ; and
d) unconformable, molasse-like, sediments of the Hammamat Group.

Lineations and fabrics in the ophiolitic lithologies indicate north-west directed transport; however, the nearest suture at Sol Hamid

would require transport of the ophiolite masses a distance of 300 km and hence a nearer unrecognised suture may exist (Ries et al.,1983). In addition, epiclastic sediments in the north of the Bayda-Hegaf volcanic complex in Arabia indicate a palaeo-continental margin to the far north (Johnson et al.,1987). An east-west belt of ultramafic complexes extending from southern Sinai into the northern Midyan terrane (Fig.2.10) may represent another suture zone (Clark,1985).

Although primitive volcanics older than 725 Ma are present (Clavez et al.,1983) the Midyan terrane is dominated by mature, calc-alkaline, magmatic rocks younger than 680 Ma (639-612 Ma Dixon,1979; Stern,1979) and possibly as young as 575 Ma (Stern & Hedge,1985), suggesting arc ma gmatism was active much later than the other terranes. Stern and Hedge (1985) recognised three distinctive basement terranes in the Eastern Desert of Egypt, namely, the North-Eastern Desert, the Central-Eastern Desert, and the South-Eastern Desert, all of which are separated by significant discontinuities which Vail (1987a) identified as distinct, possibly suture-bound, terranes.

Dating of the Eastern Desert lithologies suggests that, to a first approximation, the locus of intense magmatism appears to have migrated north with time, i.e. the basement broadly youngs to the north, similar to the Arabian Shield arc assemblages (Stern & Hedge,1985; Stoeser & Camp,1985). The Dokhan volcanics of the Northern Eastern Desert dated at 602±13 Ma are evidence for still younger volcanic activity and their geochemistry has prompted Stern & Hedge (1985) to invoke an arguable phase of crustal extension, possibly related to the formation of Infracambrian rift basins linked by the sinistral Najd fault system, which was active from 630-550 Ma (Husseini,1988). The change in geochemistry of the volcanic groups suggests that suturing of the Hijaz and Midyan terranes may not have occurred until sometime after 630 Ma (Stoeser & Camp, 1985).

2.6 Accretion and Deformation of the Nubian-Arabian Shield

The final ages of suturing between the various terranes are difficult to ascertain and can only be bracketed by the ages of the suture ophiolite complexes and rocks that intrude or are deposited over these sutures (Pallister et al.,1988) (Table 2.2).

Suture	Terranes	Collision (Ma)	Units Dated	References
Fatimah Discontinuity	Jiddah & At Ta'if	775–755	syn-kinematic granites	Fleck,1981
B'ir Umq–Port Sudan	Hijaz & At Ta'if	775–750 to 700–675	syn-kinematic gneisses overlapping Furayh Group	Duyverman et al.,1980 Stoeser & Camp,1985
Afaf	Jiddah-At Ta'if & Asir	730	foliated granites along suture	Kröner et al.,1984
Halaib–Yanbu	Hijaz & Midyan	676–672 to 640–630	syn-kinematic granites calc-alkaline "stitching granites"	Hedge,1984 Calvez et al.,1983
Nabitah North	Afif & Hijaz	started at 700	overlapping Furayh Group	Johnson et al.,1987
Nabitah South	Afif & Asir	640–630	syn-kinematic plutons	Stoeser & Camp,1985
Al Amar–Idsas /Ar Rayn	Ar Rayn & Ad Dawadimi	670–640	syn-kinematic plutons	Stacey et al.,1984
Urd/ Halaban	Afif & Ad Dawadimi	670–640	syn-kinematic plutons	Stacey et al.,1984
Abirkitib–Onib	(Hijaz)–Gebeit & Gabgaba	$\geqslant$700	syn-kinematic plutons	Almond & Ahmed,1987 Stern et al., 1989

Table 2.2 Summary of suturing dates for the Nubian-Arabian Shield.

The general younging of the basement from south to north, seen in Arabia (Stoeser & Camp,1985) and in the Egyptian basement (Stern & Hedge,1985), is reflected in a progressive accretion and cratonisation sequence in which early collision within the Asir group of terranes (760-730 Ma) was followed by suturing of the Hijaz, northern Afif, and Asir terranes (720-670 Ma; Fig.2.14) and culminated in the contemporaneous collision of the Midyan terrane and the north-south-trending continental and marginal terranes at the eastern and western boundaries of the shield (670-630 Ma).

Deformation within each of the terranes and their suture zones is controlled by the original orientation of the composite units that form each terrane and the subsequent collision with adjacent microplates. The predominant structures within the arc terranes comprise north-east-trending fold and thrust belts (e.g. Samran belt), whereas the bounding marginal Afif, Ar Rayn, and Ad Dawadimi terranes, the Nabitah mobile belt and the area west of Abirkitib (Gabgaba/Northern Red Sea Hills terrane; Kröner et al., 1989) display structures with north-south trends (Fig.2.15). Marginal zones of the arc terranes close to the Nabitah and Abirkitib sutures display secondary north-south structures superimposed on early arc-accretion trends.

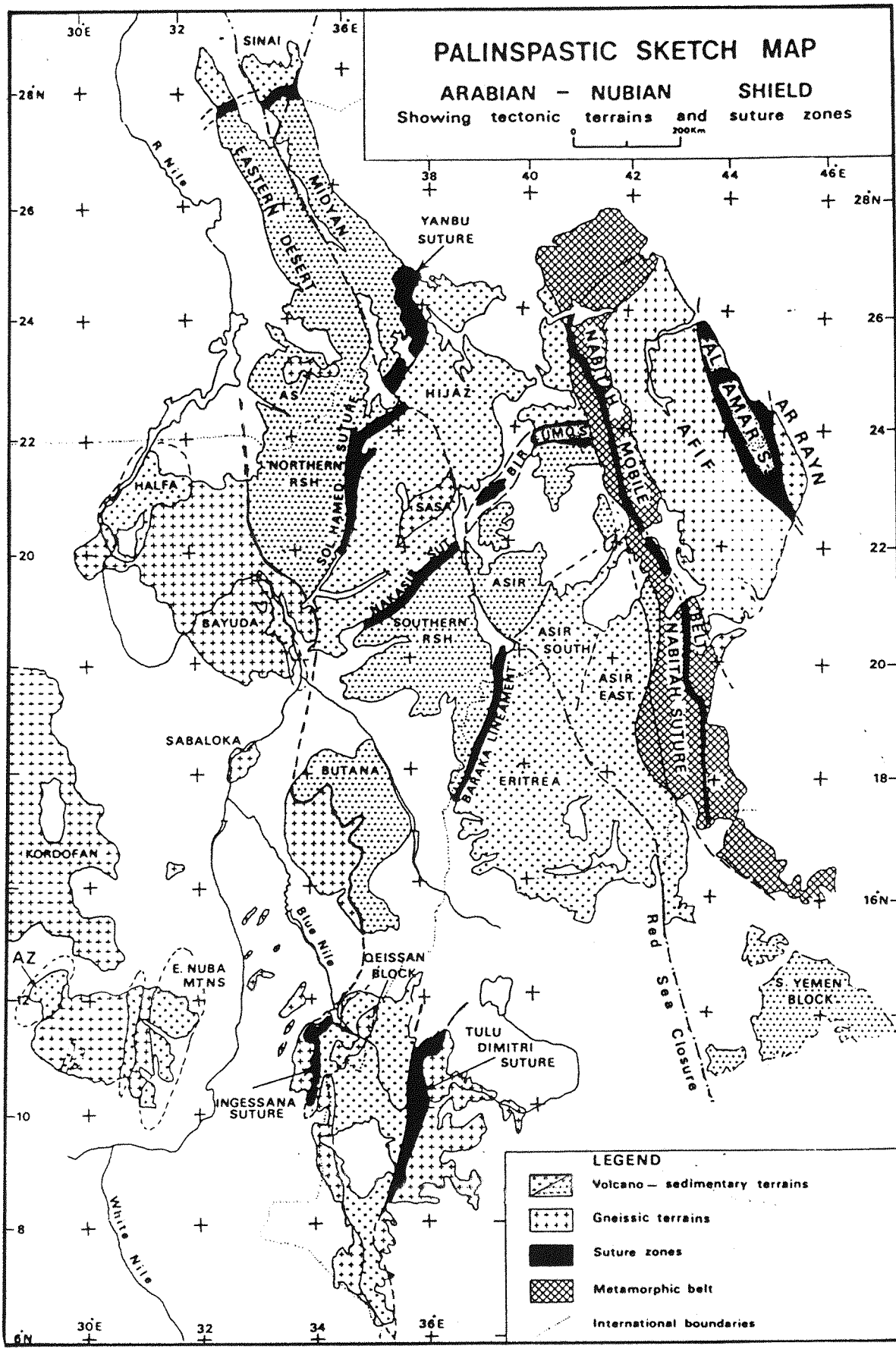

Fig.2.15 Post-accretion orientation of the component terranes of the Nubian-Arabian Shield (from Vail,1985b).

Early east-west trending major folds have been identified in western Ethiopia (Geba Phase; Kazmin et al.,1979), in northern Kenya (Samburu Phase, Berhe & Rothery,1986), in the southern Arabian Shield (Moore,1983,1984; Agar,1985) and in the north-eastern Arabian Shield (Beurrier & Villey,1984) where they are overprinted by open, north-south folds related to the later phases of accretion.

In the Eastern Desert of Egypt, several phases of deformation are evident on north-west and north-east trends and at the Wadi Hafafit Culmination, Elbayoumi and Greiling (1984) claim to have identified eleven deformation episodes. The majority of the deformation appears to be related to north-west-directed tectonic transport during folding and thrusting (Ries et al.,1983; Greiling,1987). It is not clear, however, whether folds and thrusts identified on a north-west trend pre-dated the north-east trending deformation (Soliman et al.,1982; Abdel-Khalek & Abdel-Wahed,1982), post-dated it (Ries et al., 1983) or occurred before and after the main arc collision event (Elbayoumi & Greiling,1984; Greiling,1987). Estimation of the timing of accretion in the region suggests that collision of the Midyan terrane with the Hijaz terrane was contemporaneous with suturing of the marginal arc terranes and the terranes of continental affinity to the east and west, producing locally complex interactions and deformations on both trends.

Similarly, in the Sudan, the ophiolite complex at Sol Hamid has been thrust to the north-east following obduction and deformation on a north-east trend (Fitches et al.,1983). Post-dating emplacement of the Bi'r Umq-Port Sudan ophiolites, two further ductile shearing phases have been identified. These comprise modification of the Nakasib-(B'ir Umq-Port Sudan) shear zone suture by dextral shearing with a large strike-slip component, followed by sinistral strike-slip shearing along a north-south trend typified by the braided Oko shear zone (see Fig. 2.20; Almond & Ahmed,1987). The accretion of the arc terranes, with the subsequent collision of the north-south trending marginal microplates, effectively ended accretion of the Shield and these deformation events were followed by development of the Najd fracture system and widespread emplacement of post-orogenic granites.

Collision of the Nubian-Arabian Shield and Mozambique Belt to the east and the West African Craton to the west is considered to have reactivated parts of the early- to mid-Proterozoic East Sahara Craton, east of the Archaean basement at Jebel Uweinat (Schandelmeier et al.,1987). The reactivated north-east-trending structures include the Northern Zalingei Fold Zone, the Trans-Africa Lineament, the Bir

Safsaf-Aswan Uplift System, and the Central African Lineament (Fig. 2.16) in which Pan-African dextral wrench faulting has been observed and linked as a possible conjugate system of the Najd event (Schandelmeier et al.,1987; Schandelmeier & Harms,1987).

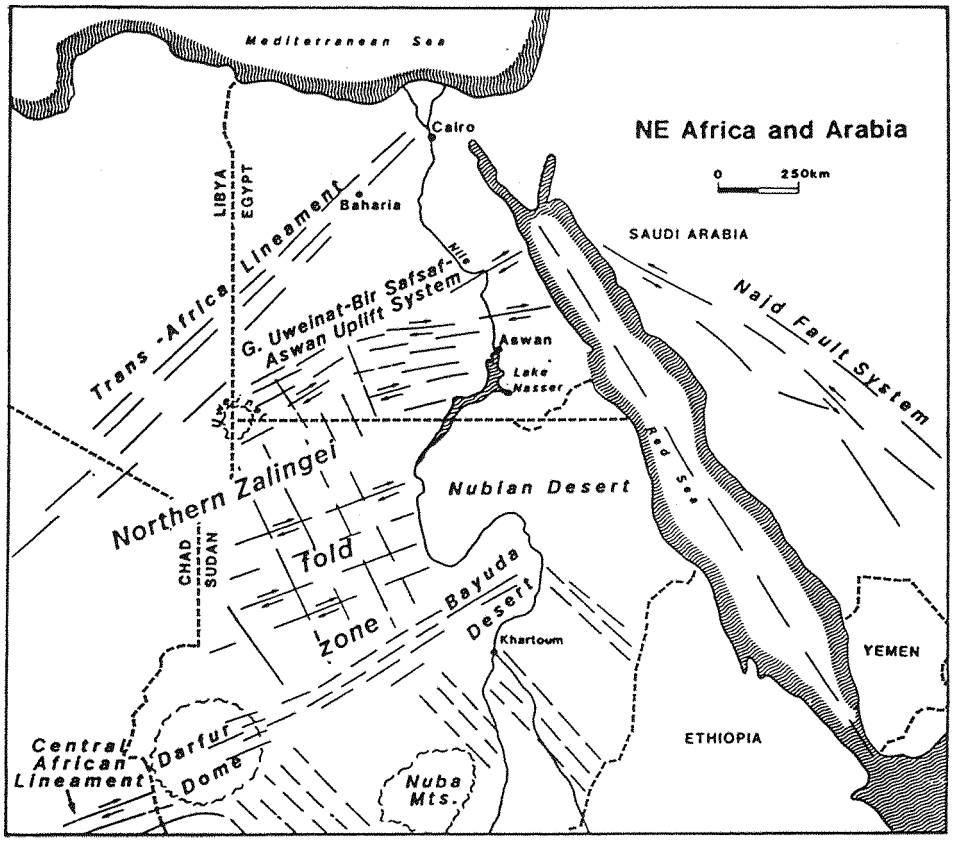

Fig.2.16 Early- to mid-Proterozoic structures reactivated during the Pan-African (after Schandelmeier et al.,1987).

2.7 Post-Accretion Evolution of the Nubian-Arabian Shield

The Najd fracture system comprises a north-west-trending group of strike-slip faults which traverse the northern part of the Arabian Shield into Egypt (as the Duwi Shear zone; Moore,1979). It forms a zone 300-400 km wide and, although its extent is obscured by Phanerozoic sedimentary cover, it has a strike length of between 1200 and 2000 km (Fig.2.17; Brown & Jackson,1960). Displacement across individual faults varies from 2 to 25 km but produce a cumulative sinistral diplacement of 240-300 km (Brown,1972). The age of Najd faulting has been constrained to between 640 to 540 Ma by the dating of fault bounded and cross-cutting intrusions (e.g. Hufrayh complex, Haml Batholith) and by volcanosedimentary sequences (e.g. Bani Ghayy Group, 620-608 Ma; Murdama Group,615-595 Ma) deposited into fault-bounded graben (Fleck et al.,1976; Davies,1984; Stacey et al.,1984; Agar,1987).

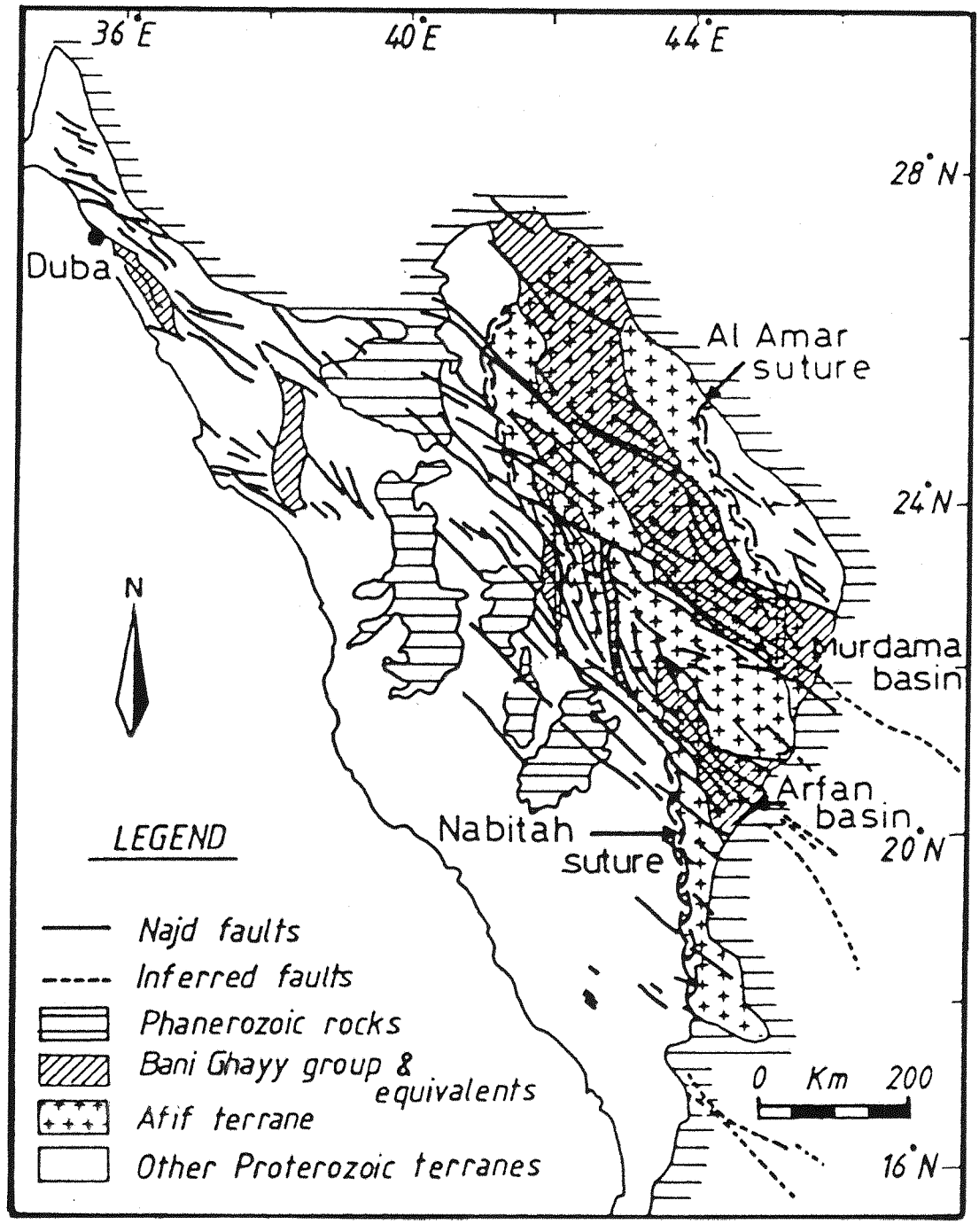

Fig.2.17 Sketch map of the Arabian Shield showing the major faults of the Najd fracture system (from Agar,1987).

Moore (1979) demonstrated the earliest phase of faulting to be ductile/brittle-ductile followed by the main brittle faulting event. Analysis of the major and secondary structures of the fault system, i.e. normal and reverse faults, thrusts, folds, graben structures and dyke complexes, by Agar (1987) indicated that components of dextral as well as sinistral shear existed. Hence, the Najd episode appears to have consisted of two phases, namely:

i) an early dextral ductile event from 640 to 600 Ma together with greenschist facies regional metamorphism which was possibly related to the final phase of collision along the Al Amar-Idsas suture;

ii) a second phase of brittle movement from 600 to 540 Ma, culminating in an overall sinistral displacement of up to 300 km (Agar,1987).

The origin of the Najd system is generally considered to be due to tectonic reactivation (Johnson et al.,1987), likened by many to the intracratonic phase that followed the collision of the Indian and Asian plates (Tapponier & Molnar,1976), with the Ar Rayn terrane acting as the rigid indenter (e.g. Schmidt et al.,1979; Stoeser & Camp,1985). Stern (1985) has criticised this model and stated that the Najd system consists of transform faults which accommodated a north-east-trending rift zone in Egypt which was active between 600 and 540 Ma. The deformation style of the Najd system does not appear to comply with the rigid indenter model in that the strike-slip fault system remains parallel throughout its length and does not converge on the corners of the rigid Ar Rayn plate along with the difficulty of explaining the initial dextral episode. Suturing of the Nubian-Arabian Shield was virtually complete by 625 Ma and at around 600 Ma there was a transition from post-orogenic bimodal calc-alkaline ring complexes, distinguished as Younger Granites from the larger syn-to late-tectonic batholithic complexes, to the plugs and ring complexes of anorogenic alkali granites and quartz syenites (Neary et al.,1976; Almond,1979; Harris,1982; Vail,1982,1985c,1989). In Saudi Arabia, syenites were emplaced between 620 and 550 Ma and alkali granites from about 680 to 517 Ma (Stoeser,1986).

The widespread intrusion of anorogenic alkali granites and syenites is indicative of a phase of crustal relaxation and extension which is supported by the identification of Infracambrian (600-540 Ma) rift basins on both sides of the Najd system in northern Egypt (Stern,1985), southern Oman, Pakistan and the Arabian Gulf (Fig.2.18; Husseini,1988). The early phase of ductile dextral shearing (640-600 Ma) has thus been attributed to the continental collision of the Ar Rayn plate which was followed by sinistral brittle shearing with the onset of rifting from 600 to 540 Ma (Husseini,1988).

Following the end of tectonic activity in the area, the Nubian-Arabian neocraton subsided and was peneplaned on a regional scale.

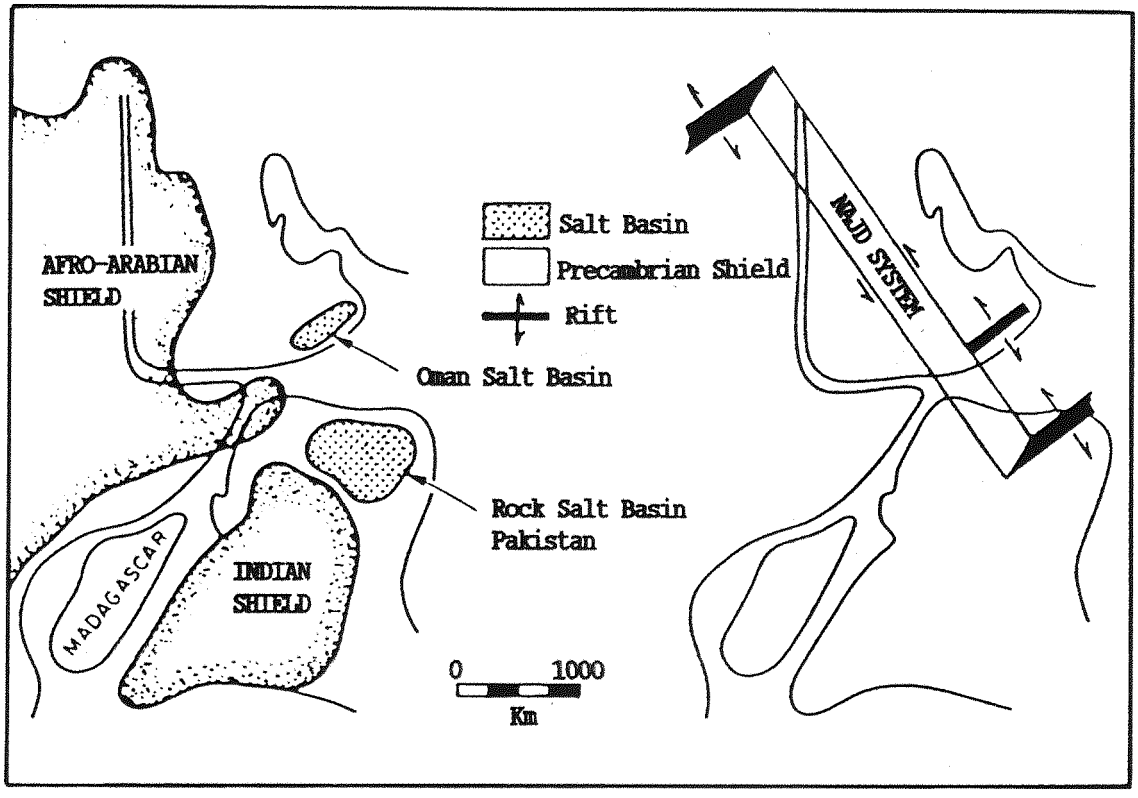

Fig.2.18 Infracambrian rift basins related to the Najd fault system (after Husseini,1988).

Throughout the Palaeozoic, the general northward dip of the African continental platform was rapidly transgressed by Palaeozoic seas southward to the north-western Sudanese border around Jebel Uweinat (Klitsch,1987; Fabre, 1988). Sedimentation dominated by fluvial and shallow marine sheet sandstones was, in part, controlled by a north-west structural relief and by basins formed from reactivation of the north-east trending Trans-African and Central African lineaments (Nagy et al.,1976; Wycisk, 1987). Collision of Gondwana with northern continents during the Carboniferous produced an east-west-trending uplift through Jebel Uweinat and Aswan, resulting in deposition of glacial and continental fluvial sediments into a large but shallow basin to the south. From the late-Jurassic onward, sedimentation was of predominantly continental sheet sandstone sequences of the Nubian Formation, with marine transgressions migrating further south during the Cretaceous in response to further reactivation of north-east- and north-west-trending Precambrian structures (Klitsch,1987; Wycisk,1987). The onset of the break up of Pangea, initiated in the Permian, is the likely cause of the earliest phase of rift related magmatism dated at around 250 Ma (Table 2.3).

Phase	Period	Age (Ma)	Cause	Associated Volcanism
1	Permian	≈250	Initiation of the break-up of Pangea	anorogenic alkali-basalt syenite & trachyte magmatism
2	≈Neocomian to late-Albian	160-130 to 98	Initial opening of Sth Atlantic & rifting of Benue Trough	
3	Turonian to late-Senonian	90 to 65	Opening of South Atlantic	
4	late-Eocene to Oligocene	40 to 25	Propogation of Red Sea rift from Gulf of Aden to the Gulf of Suez	Cenozoic volcanics along the Central African shear zone
intra-cratonic sag	from middle Miocene	15	Opening of Red Sea along Dead Sea Transform, Gulf of Aqaba	

Table 2.3 Summary of late-Phanerozoic and Cenozoic phases of extension in Sudan.

Three further phases of rifting, beginning in the late-Jurassic, were controlled by dextral reactivation of the Central African shear zone and resulted in the formation of four north-west-trending basins in southern Sudan, namely; the Bagarra, the Muglad, the Melut and the Blue Nile basins (Fig.2.19; Schull,1988).

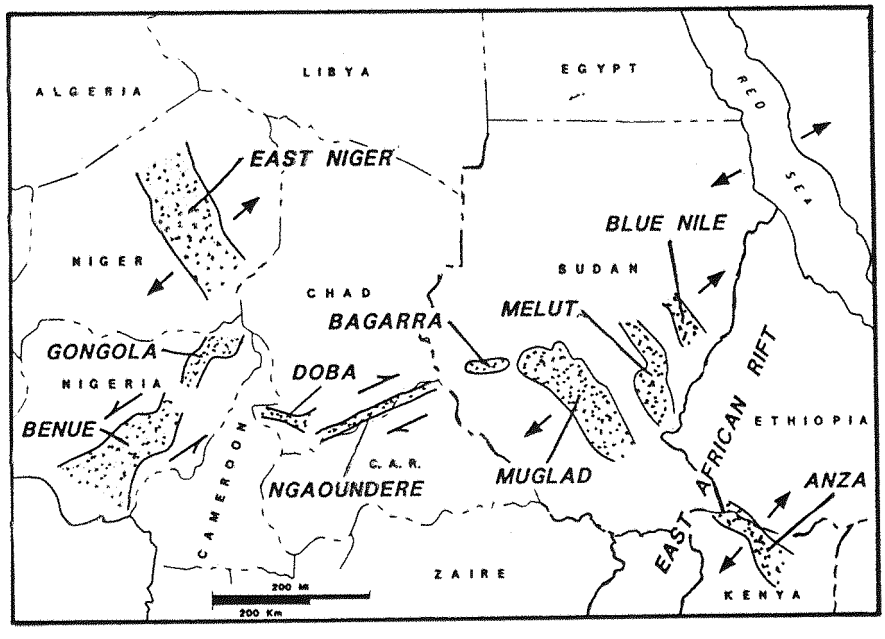

Fig.2.19 Regional tectonic map of central Africa showing the major rift basins and structures associated with the break-up of Pangea (from Schull,1988).

In eastern Sudan and Egypt, phases of anorogenic alkali basalt-trachyte magmatism dated at 150-89 Ma (Vail,1987a) and 104-80 Ma (Greiling et al.,1988) were focused by reactivated north-south structures (Oko shear zone and the Onib-Hamisana shear zone) and probably correspond to the first two rifting events (Medani & Vail,1974; Almond & Ahmed,1987). The third phase, from the Eocene to the Oligocene, was confined to the eastern side of the African Shield (Girdler,1985) with continued deposition into the southern Sudan basins (Schull,1988). The Central African shear zone was once again reactivated and can be traced across Sudan by the north-east line of Cainozoic volcanic rocks from Gebel Marra to the Central Bayuda Desert (Schandelmeier et al.,1987). This phase of extension ceased in the Sudan when increased lithospheric strength in the Mediterranean continental margin prevented further rifting to the north-west and opening continued along the Dead Sea Transform along the Gulf of Aqaba (Steckler & ten Brink,1986).

2.8 Geology of the Northern Red Sea Hills around Gebeit al Ma'adin

The majority of geological research on the Nubian-Arabian Shield has been concentrated in Saudi Arabia and consequently the geological database for the Northern Red Sea Hills Province at present remains more limited. Present understanding of the Red Sea Hills area is derived from the work of several authors dating back to the studies of Gass (1955), Ruxton (1956), Gabert et al. (1960) and Kabesh (1962), which were synthesised by Whiteman (1971). The basic stratigraphic interpretation for the area produced by Gass (1955) changed very little up to the succession published by Vail (1979; Table 2.4a) in which the units underlying the volcano-sedimentary assemblages (formerly the Oyo, Nafirdeib, Salala, and Odi Series) were subdivided into the amphibolite grade meta-sediments of the Metasedimentary Group and the quartzo-feldspathic gneisses of the Grey Gneiss Group (formerly the Primitive or Kashebib Series and not represented in the Red Sea Hills). The acid through to basic lavas, pyroclastics, and associated greywackes, marbles, shales, quartzites and conglomerates that comprise the volcano-sedimentary sequences have been described and correlated from various parts of the province (e.g. the Oyo Series of Gass,1955 and the Nafirdeib Series of Ruxton,1956). The range of descriptions, however, indicated that there are rapid lateral and vertical variations which prompted Vail (1979) to use the overall term of Greenschist Assemblage, later called the Nubian-arc-system metavolcanics by El-Nadi (1984).

GASS (1955)	RUXTON (1956)	GABERT, RUXTON & VENZLAFF (1960)	KABESH (1962)	VAIL (1979)
ASOTERIBA VOLCANICS (acid lavas, tuffs)				
(dykes) YOUNGER GRANITES	(acid, basic sills and dykes) RED GRANITE	(dykes) YOUNGER GRANITE	(dykes) YOUNGER GRANITES	(dykes) YOUNGER IGNEOUS ACTIVITY (gabbro, granite, syenite) CENTRAL VOLCANIC GROUP (HOMOGAR) (acid volcanics)
	INJECTION GRANITES		GREY GRANITES	
	AWAT SERIES (acid volcanics, sediments)	AWAT SERIES (acid volcanics, sediments)	AWAT SERIES (acid volcanics, sediments)	GREENSCHIST ASSEMBLAGE (serpentinites)
BASIC INTRUSIVES (gabbro, troctolite, pyroxenite)	BASIC INTRUSIVES	BASIC INTRUSIVES	GABBROS	
BATHOLITHIC GRANITE (assimilation granite)		BATHOLITHIC GRANITE	DIORITES AND EPIDIORITES	BATHOLITHIC GRANITOIDS
OYO SERIES (metasediments, intermediate-acid volcanics)	NAFIRDEIB SERIES (basic and intermediate volcanics, sediments)	NAFIRDEIB SERIES SALALA SERIES (intermediate volcanics, sediments)	NAFIRDEIB SERIES (intermediate volcanics, sediments)	GREENSCHIST ASSEMBLAGE (meta-volcanics, sediments and ultrabasics)
GRANITE GNEISS (+ schists, volcanics)	PRIMITIVE SERIES BASIC DYKE SWARMS (acid gneiss, schists, etc)	KASHEBIB SERIES (paragneisses)	GNEISSES (para- and orthogneisses)	METASEDIMENTARY GROUP
				GREY GNEISS GROUP

Table 2.4a Stratigraphic subdivisions for NE Sudan according to previous workers (from Vail et al.,1984).

(9) Unconsolidated sedimentary cover and coastal marine deposits

(8) Anorogenic intrusive masses and complexes

(7) Sediments of the Nubian Sandstone Formation

(6) Post-orogenic intrusions and complexes

(5) Syn-orogenic batholiths

(4) Volcanic-sedimentary sequences

(3) Ophiolite belts

(2) Amphibolie facies metasediments and gneisses

(1) Grey gneisses and granulites

Table 2.4b Stratigraphic subdivision of Embleton et al. (1982)

Advances in the understanding of geological processes allied to plate tectonic theory and the evolution of the Shield (e.g. Greenwood et al.,1976; Neary et al.,1976) lead to rationalisation of the stratigraphy by Almond (1982) and Embleton et al. (Table 2.4b; 1982) who divided the rocks into nine major units within which there may be a substantial temporal overlap. The recent recognition of discrete tectonic terranes in the Arabian Shield (Camp,1984; Stoeser & Camp,1985; Johnson & Vranas,1984) has been paralleled in the Nubian Shield mainly by the research of Vail (1983,1985a,b,1987a) and co-workers and by Almond (1982,1984,1987) and co-workers.

Gebeit Gold Mine is situated in the north-western corner of the Hijaz oceanic-arc terrane approximately 100 km south-west of the ophiolite complex of the north-east trending Halaib-Yanbu suture at Sol Hamid and 120 km east of the north-south Onib-Hamesana suture at Abirkitib (Fig.2.20). Although sixty percent of the areal extent of the province comprises intrusive granitoids, the area around the mine complex comprises greenschist facies, basic to intermediate, volcanic and volcano-sedimentary rocks. This Proterozoic basement displays a strong north-east-trending structural grain and has been intruded by syn- to late-tectonic, post-tectonic, calc-alkaline complexes and anorogenic syenite and alkali granites (formerly the Batholithic Granites and Younger Granites of Gass,1955). The volcano-sedimentary succession is separated from the Halaib-Yanbu suture by a north-east trending zone of syn-orogenic granitoid plutons aggregated to form a batholith which intrudes and envelopes the Onib-Hamesana suture as the Serakoit batholith. This batholithic zone, along with syn-orogenic batholiths to the south-east of Gebeit, has been preferentially intruded by several dyke swarms of doleritic to microgranite composition dated at around 725 Ma (Vail et al.,1984). Conversely, the later calc-alkaline post-orogenic complexes are concentrated in bands parallel to the ophiolite zones and preferentially intrude the volcano-sedimentary assemblages (Vail,1982). To the south of Gebeit lies the Sasa Plain where amphibolite-grade paragneisses (high-grade shelf metasediments) are exposed and are believed to represent original shelf deposits derived from the Nile craton, possibly as a detached micro-continental block (Vail,1987a; El-Nadi,1987). Mapping of the Red Sea Hills by previous workers including the Soviet-Sudanese project (Ahmed, 1984) has been augmented by Landsat MSS Imagery Interpretation (Geosurvey,1983). These studies demonstrate that widescale faulting on NW-SE, N-S, and E-W trends has occurred in addition to the north-

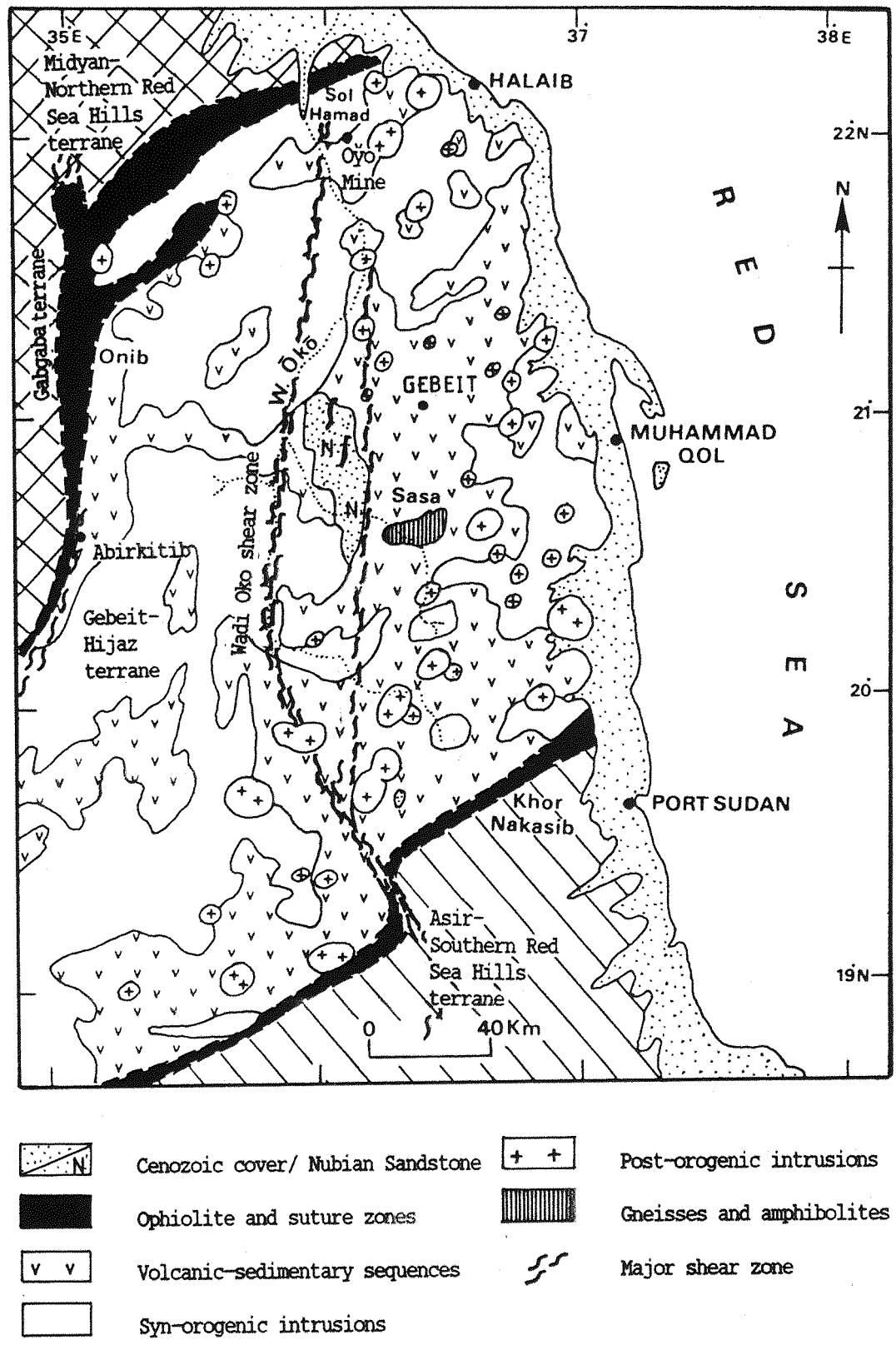

Fig.2.20 Geological sketch map of Gebeit-Hijaz terrane in north-east Sudan (after Vail et al.,1984; Almond & Ahmed,1987).

east-trending folding and faulting associated with arc-accretion events. Field-based studies of ductile shear zones by Almond and Ahmed (1987) indicate that the Nakasib shear zone of the Bi'r Umq-Port Sudan suture was reactivated dextrally following obduction and, with the Onib-Hamesana suture, subsequently was deformed by later north-south-trending Oko and Abirkitib shear zones. West of the Sasa Plain is a block of Cretaceous(?) Nubian Formation sandstone preserved in a north-south graben produced by further reactivation of the Oko shear zone. This shear zone also controlled Tertiary alkali basalt-syenite volcanicity (Almond & Ahmed,1987) and implies that the region has undergone a protracted and complex tectonic history including reactivation of older structures.

Gold prospects and limited mining activities are evident throughout the province which has a long history of mining and exploration dating back to the Pharoahs. Even though the auriferous quartz veins are generally confined to the volcano-sedimentary areas, mineralisation was originally considered to be related to the intrusion of the Younger (post-orogenic) Granites (Whiteman,1971; El-Boushi, 1972). Although the precise controls on mineralisation have not been established, Vail (1978) indicated that the veins were controlled mainly by north-east trending fractures, post-dating all major folding and metamorphism but pre-dating emplacement of post-orogenic intrusions (Vail,1978; Almond et al.,1984). The paucity of geological information on the Red Sea Hills Province coupled with the complexity of the basement geology has constrained this study, primarily, to an evaluation of the geological evolution of the Gebeit area in order to define the exact controls on mineralisation.

"Tectonic and Chemical Evolution of a Late Proterozoic Gold Deposit, Gebeit Mine, Northern Red Sea Hills, Sudan."

PART TWO

GEBEIT LITHOLOGIES: PETROGRAPHY AND GEOCHEMISTRY

CHAPTER 3

Gebeit Volcanic Group

3.1 Introduction

Greenschist facies, andesitic, oceanic arc, meta-volcanics are the host lithologies to gold mineralisation at the Gebeit Mine and in the immediate satellite prospect areas. Whole rock and mineral Sm-Nd data yield a late Proterozoic (Pan-African) age of between 832±26 and 871±73 Ma (Reischmann et al.,1986) and these lithologies reportedly display the geochemical affinities of calcalkaline andesites, consistent with a regional genetic model of an oceanic arc accreted terrane (Jackaman, 1972; Greenwood et al.,1976; Al-Shanti & Mitchell,1976; Bakor et al., 1976; Gass,1977,1979,1981; Frisch & Al-Shanti,1977; Shackleton,1977, 1986).

Within the mine sequence, three main lithotypes can be distinguished petrographically and geochemically and these have been further subdivided on a textural basis. The lithologies comprise:

i) aphyric and plagioclase-phyric volcanics, consisting of:

   a) fine, laminated, tuffs, and
   b) coarse flows and tuffs,

ii) hornblende-, clinopyroxene-, and plagioclase-phyric volcanics, which consist of:

   a) massive and basal cummulate flows,
   b) fine to coarse tuffs, and
   c) lapilli-tuffs and agglomerates,

iii) black, carbonaceous, pyritic shales.

Because of the inherent difficulties in correlating ancient volcanic sequences across the Nubian Shield, the stratigraphic

succession around Gebeit has been logged and is here designated the Gebeit Volcanic Group (GVG).

3.2 Field Descriptions

Virtually all outcrops of the volcanic lithologies are coated in a dark brown to black desert varnish, which is enhanced by the relatively high ferromagnesian contents of these rocks (see 3.6.1). As a result, mapping is restricted to chip-sampling all definable units although an estimation of grain size can be made from the smoothness of surface textures. Because of the additional structural complexities, recognition of lateral extents, correlation of individual beds, and definition of depositional types have proved to be very difficult. Classification of pyroclasts and rock-types is taken from Schmid (1981) and Fisher and Schmincke (1984).

Well-bedded volcaniclastics, which generally occur at lower topographic levels, have sharply defined bedding planes with beds ranging from laminae <3 mm to beds 5 m thick. The majority, however, lie between 1 and 50 cm in thickness. Grain size varies from very fine, grey-green, laminated, flinty tuffs to coarse (average grain size, 2 mm), often plagioclase-phyric, more thickly bedded, grey-green tuffs. The aphyric tuffs are often grouped in sets of laminae from 50 cm to 5 m, which commonly are separated by single, coarse, plagioclase-phyric, volcaniclastic beds, from 5 cm to 5 m thick (see section 3.5.2, Fig.3.2). Carbonaceous black volcaniclastic shales are seen interbedded with the fine tuff horizons in drill core and underground, but have only been observed in two locations on surface at Gebeit (Bishops Dam; 4200E,5600N and Wadi Lode Extension; 5100E,5500N). Graded bedding is evident in these lithotypes and relationships with other sedimentary structures, e.g. scours and flame structures (see 3.3.1), indicate that grading is usually normal although rare examples of reverse grading have been observed.

Hornblende-, clinopyroxene-, and plagioclase-phyric, green, volcanics form the higher topographic features and produce a coarse, blocky scree outcrop, which hinders estimation of bed thicknesses. Lava and pyroclastic flows, lapilli-tuffs, and agglomerates can be identified, with individual members ranging from 20 cm to 10 m thick, however lateral variations in depositional style and thickness have not been ascertained. Untectonised bombs and lapilli from these units are generally sub-angular to sub-rounded, 2 to 50 cm in diameter, and

contain < 25% matrix. Some lithotypes display sub-rounded ejecta, commonly harder than the matrix on weathered outcrops, indicating they are agglomerates. Conversely, with the sub-angular varieties the ejecta are not prominent or are preferentially weathered suggesting that flow breccias are also present (Moseley, 1983). Sub-rounded, sometimes composite, amygdales up to 15 mm in diameter, containing quartz, carbonate, chlorite and zoisite, are relatively common in the flow horizons and many of the larger pyroclastic fragments are intensely vesiculated. Rare, fine agglutinated pyroclasts have been observed with highly weathered matrices and probably represent scoria deposits.

3.3 Depositional Structures

3.3.1 Aphyric and Plagioclase-Phyric Tuffs

In the aphyric and plagioclase-phyric tuffs, graded bedding and lamination is a common feature and is better developed in the coarser, plagioclase-phyric units (Plate 3.1a & b). The lower contacts of each lamination and bed, although often very sharp, are generally irregular due to scour and flame structures. These are most prominent where coarse tuffs overlie shale units (Plate 3.1c). The relationship between bedding and the scour and flame structures indicates that grading is normal and is evident in beds from 1 to 30 cm thick. Ripples and cross-lamination have been observed and often the upper surfaces of laminae and beds are truncated by local unconformities (Plate 3.1c). Rare sub-angular clasts of fine laminated tuffs occur generally parallel to bedding and range in size from 2 to 35 cm. At Garabein, angular to sub-rounded, matrix-supported, chaotic, rip-up clast units are common at the base of the coarser, more massive beds (Plate 3.1d). As well as minor syn-depositional micro-faulting, slump folds, 5 to 100 cm in length, have been observed at Garabein (Plate 3.1e), and Gebeit. Syn-depositional, north-east-trending folding is also evident in the form of an angular unconformity e.g. as seen at: 5350E,5450N; 5480E,5520N; and 4730E,6460N where gentle, upright folding of the lower fine tuffs (interbedded with hornblende-phyric lavas at 4730E,6460N) are overlain by relatively flat-lying hornblende-phyric agglomerate. The plagioclase-phyric and aphyric rocks have been dated as possibly older than the hornblende-phyric rocks (871±73Ma and 832±26Ma respectively; Reischmann et al.,1986). This suggests that the

Plate 3.1 Depositional structures of the Gebeit Volcanic Group.

a) Interbedded coarse and fine aphyric andesitic tuffs displaying normal graded bedding and a clast of fine, laminated tuff (Vein 18, 4500E,6300N)

b) Fine, laminated aphyric andesitic tuff showing dewatering structures (D), good sorting, sharp basal contacts, and normal graded bedding indicative of deposition in a submarine environment (Bishops Dam, 44200E,5700N).

c) Finely laminated andesitic tuffs and minor shales showing fine cross-lamination (C), dewatering flame structures (F), and erosional basal contacts (E), Garabein Mine.

d) Chaotic rip-up clast unit displaying angular clasts of fine, laminated tuffs and shales in a coarse andesitic pyroclastic flow, Garabein Mine.

e) Syn-sedimentary slump fold showing NW-vergence, from interbedded fine laminated and coarse andesite tuffs. East Gebeit (5600E,7400N; lens cap scale = 5cm).

f) Erosional contact (C) of a coarse hornblende-phyric andesite flow (top) cross-cutting fine laminated aphyric tuffs, Wadi Lode Extension (5150E, 4550N; lens cap scale = 5cm).

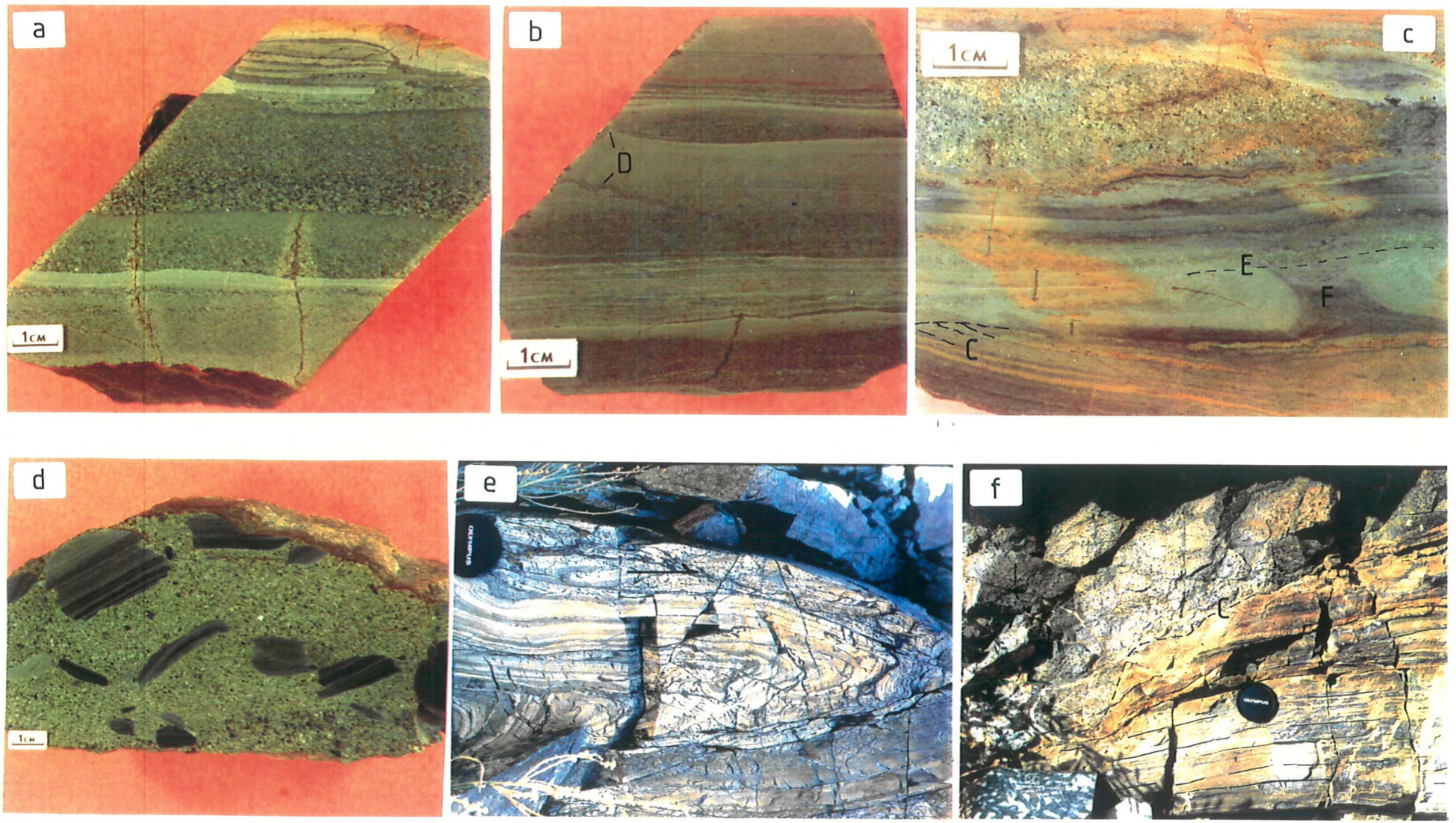
a
1cm
b
D
1cm
c
1cm
E
F
C
d
1cm
e
f
C

sequence at Gebeit is not inverted and that there may have been a significant hiatus between the deposition of the plagioclase-phyric and aphyric rocks and the hornblende-phyric lavas and agglomerates.

Many of the sedimentary structures evident in these volcaniclastics are very similar to the textures of the water-lain tuffaceous units of the Borrowdale volcanics in the Lake District (Moseley, 1983) and, in addition to being interbedded with carbonaceous shales, indicate a predominantly submarine depositional environment (see 3.7).

3.3.2 Hornblende-, Clinopyroxene-, and Plagioclase-Phyric Volcanics

In contrast to the lower succession dominated by the aphyric and plagioclase-phyric tuffs, the upper hornblende- and clinopyroxene-phyric volcanics mainly comprise flows and agglomerates with subordinate tuff and basal cummulate units. Where observed, the relationship between flows and underlying fine tuff beds show both conformable and erosional contacts (Plate 3.1f). Pillow lavas have been reported in the area (Yassin and Ahmed, 1984; Robertson Research, 1983). Breccias are evident but the host matrices are usually coarse-grained (2-10mm) and appear to represent autoclastic flow breccias. No distinct, unequivocal pillow structures, hydroclastic or similar, large-scale quench textures, suggestive of a submarine dominated depositional environment, have been observed. Occasionally, however, finely brecciated flows occur with pale coloured, very fine-grained, aphanitic matrices indicative of rapid quenching (Plate 3.2a). Bombs and lapilli in the agglomeratic beds are rounded, highly vesiculated, and often have well-developed tails. Sag textures have been identified (Plate 3.2b) and are due to subaerial tephra fall-out into unconsolidated fine tuff laminae with some bombs displaying quenched rims.

3.4 Petrography

Samples of all the sub-groups of the volcanic lithologies have been examined as thin sections for mineralogical and textural information followed up by random powder X-ray diffraction analysis to aid mineral identification. Surface and drill core samples have been studied in order to define a set of specimens which display the least alteration and hence can be used to characterise the geochemistry.

Plate 3.2 Petrography and textures of the Gebeit Volcanic Group.

a) Finely-brecciated hornblende-phyric andesite flow, Marble Bar (4600E, 5900N).

b) Contact (C) between upper hornblende-phyric, andesitic agglomerate and unconsolidated fine, aphyric tuffs. Lowest clast shows fine, quenched rim and sag texture in deformed tuffs, mill site (5700E, 4700N).

c) Photomicrograph (CN) of micro-porphyritic texture in fine, aphyric andesite tuff (field of view 4mm; DDH 21,21m).

d) Photomicrograph (PPL) of the contact between graphitic shale (top) and fine plagioclase-phyric tuff showing pyrite grains with, quartz pressure shadows, sub-parallel to S_2 fabric (c; field of view 8mm; DDH 34,79m).

e) Photomicrograph (CN) of plagioclase-phyric andesitic tuff (field of view 10mm; DDH 22, 08m).

f) Hornblende-phyric (Hb) and clinopyroxene-phyric (Cp) andesite flow, (DDH 21, 130m).

g) Photomicrograph (CN) of hornblende-phyric andesite showing replacement of clinopyroxene phenocryst (Cp) by fine-grained actinolite, chlorite, and calcite (field of view 15mm;DDH 21,130m).

h) Vesiculated hornblende-phyric andesite flow showing plagioclase micro-phenocrysts (pl; DDH 43, 223.7m).

CN = crossed Nicols, PPL = plane-polarised light.

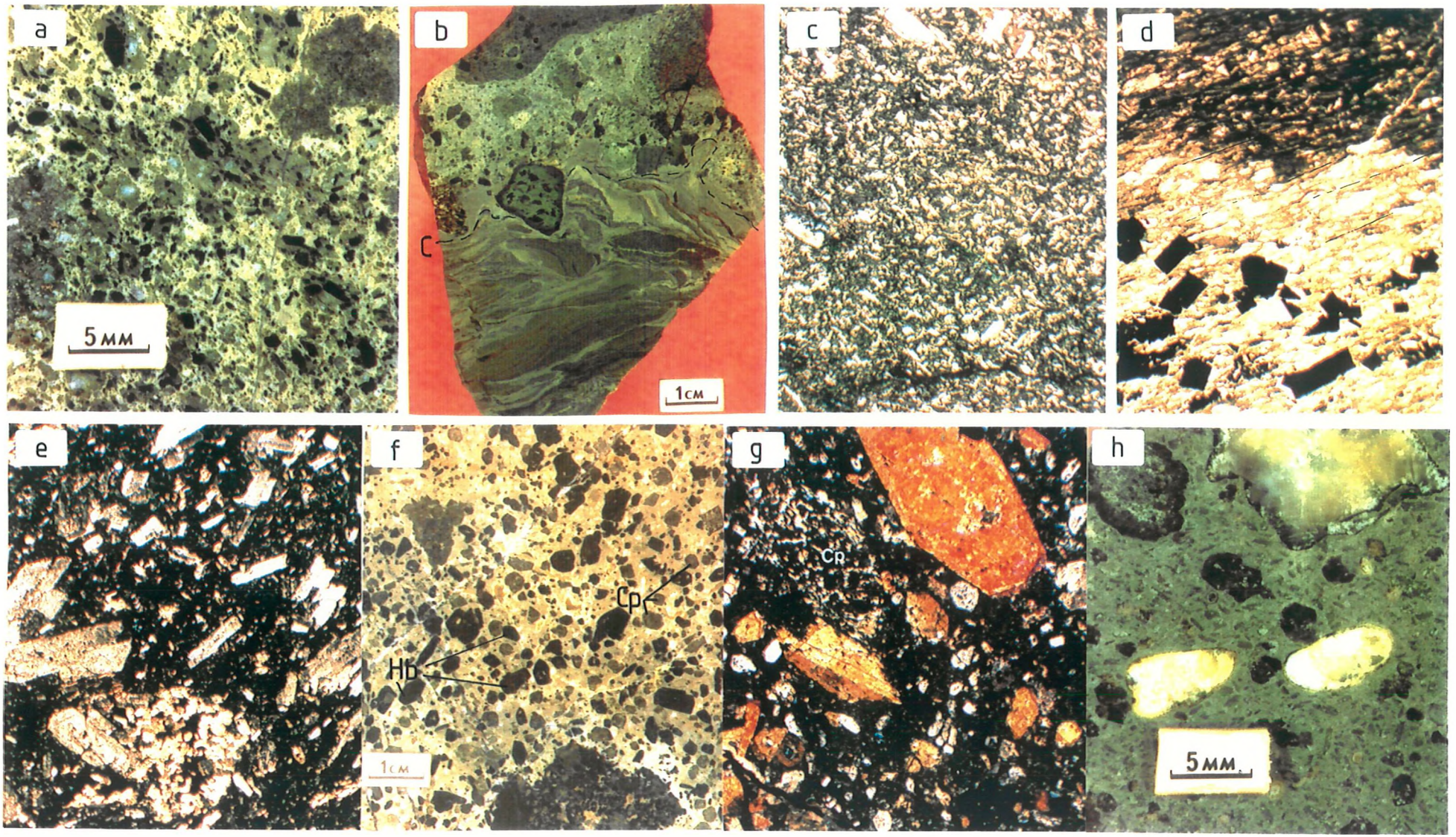
a
5 мм
b
C
1см
c
d
e
f
Cpx
Hb
1см
g
Cpx
h
5 мм

From petrographic studies, the original classification of the Gebeit volcanics (i.e. crystal tuff, fine, medium and coarse lithic tuff, banded tuff, lapilli tuff, and tuffaceous schist (Robertson Research, 1983) has been discarded as many of these igneous terms were employed to describe variably sheared and hydrothermally altered basaltic andesites. As a result, the broad field-based sub-divisions of aphyric tuffs, plagioclase-phyric volcaniclastics, shales, and hornblende-, clinopyroxene-, and plagioclase-phyric volcanics have been retained. In this chapter, only igneous textures and mineralogies are discussed; structural textures and mineralogical changes due to hydrothermal alteration are discussed in Chapter 7.

3.4.1 Aphyric Laminated Tuffs and Shales

The aphyric tuffs are generally very fine-grained, ranging from a micro-porphyritic texture (Plate 3.2c) to a cryptocrystalline consolidated ash where no crystallite phases are readily identifiable using thin-section petrography. The finest tuffs appear to be volcaniclastic in origin rather than being altered holohyaline lithotypes; however, the very fine grain size makes estimation of the amount of subsequent alteration by sea water and hydrothermal fluids difficult to assess. The coarser texture consists of equant albitic plagioclase crystals, up to 0.5mm, in a trachytic matrix of albite laths up to 0.2mm. The mineralogy of the groundmass and the very fine-grained lithologies, determined by X-ray diffraction studies, comprises fine-grained chlorite, quartz, albite, epidote, sericite and calcite ± apatite ± opaques. The larger feldspar grains show minor alteration to chlorite and sericite. In contrast to the other lithotypes, both the aphyric volcanics and the shales show sericite peaks on X-ray diffraction traces indicating a sericite content of at least 5 vol%. As these rocks are very similar, geochemically, to the porphyritic volcanics, the high sericite contents probably represent a higher degree of alteration. The finer-grained tuffs would be more susceptible to sea-floor and diagenetic alteration especially in a predominantly submarine depositional environment (Suthren,1985). The majority of the tuffs investigated are crystal-rich which may be attributed to both pyroclastic and epiclastic processes (Cas & Wright,1987)

The finest tuff units are found finely interbedded with laminae and beds of shale. The mineralogy of the shales is essentially the

same as the aphyric tuffs but they display a very dark colouration (Plate 3.2d) due to the presence of fine grained graphite, which was not detectable using XRD methods. This has been reported as "up to 1% elemental carbon" (Robertson Research, 1983). The change from shales to aphyric tuffs is gradational and feldspar laths (up to 0.2mm) are evident in laminae with a lower graphite content. These tuffaceous bands within the shale often contain horizons of early, euhedral pyrite cubes (up to 2mm in diameter) parallel to bedding and oblique to the tectonic fabric suggestive of primary, syngenetic pyrite.

3.4.2 Plagioclase-Phyric Volcanics

Mineralogically, the plagioclase-phyric volcanics are coarser grained equivalents of the aphyric tuffs and are composed of albite, quartz, chlorite, epidote, and calcite ± apatite ± rutile ± dolomite ± opaques. The plagioclase phenocrysts are albitic in composition, occur up to 4mm in length and seriate as well as porphyritic textures are displayed (Plate 3.2e). Carlsbad, albite and sawtooth deformation twinning are common and, in the freshest samples, alteration of the phenocrysts is restricted to minor, fine-grained, chlorite and sericite. This alteration occurs along cleavage traces and is most often concentrated at the grain centres, indicating original normal zonation. Generally all grains are intact with only the largest phenocrysts appearing fractured. The fine-grained, often trachytic, groundmass contains fine feldspar laths up to 0.5mm in length, together with fine, pervasive chlorite, epidote, calcite and quartz. In the more altered sections, the albite microlites in the groundmass are pseudomorphed by carbonate. Vesiculation is relatively common and amygdales (from 0.2 to 5mm) are infilled by quartz, carbonate and chlorite.

3.4.3 Hornblende-, Clinopyroxene-, and Plagioclase-Phyric Volcanics

This lithology displays similar textures and mineralogy to the plagioclase-phyric volcanics with the addition of euhedral phenocrysts of hornblende and clinopyroxene (Plate 3.2f). In the flow units, the hornblende phenocrysts are up to 12mm long with the clinopyroxene phases generally finer grained (0.5 to 4mm). The hornblende phenocrysts are predominantly fresh, usually range from 0.5 to 6mm, and display twinning and the brown pleochroism indicative of an original

igneous amphibole (Plate 3.2g). Minor alteration to chlorite and carbonate occurs along cleavages. In coarse grained samples, hornblende can be zoned and commonly shows ophitic and sub-ophitic texture with plagioclase. Clinopyroxene phenocrysts range from 0.5 to 4mm and, unlike the fresh hornblende, are usually altered to patchy chlorite, calcite and actinolite. Actinolite commonly occurs as a fibrous replacement of crystal rims and cleavage planes separating patches of chlorite, calcite, quartz and relict clinopyroxene. As a consequence, in hand specimen the pyroxene phases are not always evident in the chloritic grey-green groundmass and some of the pyroxene- and plagioclase-phyric beds may have been mapped in this study and by previous workers as purely feldspar-phyric lithologies. Plagioclase occurs as a phenocrystic phase but is subordinate to the mafic phases (0.2 to 2mm) and is often more altered. Groundmass mineralogies comprise albite, quartz, chlorite, actinolite, calcite, hornblende, epidote and zoisite ± apatite ± rutile ± opaques.

Vesiculation is common and more pronounced than the plagioclase-phyric lithologies, with vesicles more irregularly shaped, up to 15mm across, and with coarse radiating zoisite crystals round the rims in addition to the usual infill of chlorite, quartz and carbonate (Plate 3.2h). Seriate as well as porphyritic textures occur and trachytic texture is often evident in the groundmass along with preferential alignment of vesicles. Rare cumulate basal flows, as observed at the logged section (see 3.5.2), are coarse (2 to 5mm), equigranular, and comprise euhedral hornblende, clinopyroxene (generally altered to fibrous actinolite) and minor plagioclase grains with intersertal chlorite.

The well-rounded tephra of the agglomerate and lapilli-tuff units are usually highly vesiculated and fine grained but retain a micro-porphyritic texture in contrast to cryptocrystalline host matrices. The angular to sub-angular tephra of the breccia units display only minor vesiculation and are coarsely porphyritic. Host matrices are either cryptocrystalline, showing fine compaction structures, possibly due to welding, or are of similar grain size and texture as the clasts. This suggests that pyroclastic, possibly hydroclastic, and autoclastic (flow brecciation) depositional mechanisms were active to produce both fine-and coarse-grained textures respectively. In both agglomeratic and breccia units, ejecta composition is petrographically consistent with the host and hence most of the clasts appear to be juvenile or cognate in origin.

3.4.4 Metamorphism

From the mineralogy of the relatively unaltered lithologies, an estimate of the peak metamorphic grade can be made. Pervasive alteration of the groundmass to chlorite, epidote, zoisite, albite and calcite, replacement of clinopyroxene by actinolite, calcite, and chlorite ± epidote, and pervasive albitisation of the plagioclase feldspars indicate a peak metamorphic grade of greenschist facies (Miyashiro 1973). The brown colouration and euhedral habit of the hornblende phenocrysts (Plates 3.2f & g) implies that these are original high temperature igneous phases (as opposed to lower temperature, green-blue, metamorphic hornblendes, Miyashiro, 1973) and hornblende has acted metastably during metamorphism (Barker, pers. comm.,1987). In addition, the lack of biotite suggests that metamorphism of these metabasites was confined to lower greenschist facies. The presence of actinolite also signifies a relatively low P_{CO_2} during metamorphism; at higher P_{CO_2}, actinolite breaks down to form calcite and chlorite (Miyashiro, 1973).

3.5 Stratigraphy

Assessment of the volcano-sedimentary belts in the Central Arabian Shield (Jackson & Ramsay,1980; Roobol *et al.*,1983) resulted in the subdivision of the stratigraphy into three sequences namely:

i)"Sequence C", >900 Ma; the oldest volcano-sedimentary belts of chemically immature bimodal suites of low-K tholeiites and sodic dacite and rhyolite depleted in lithophile elements and similar to immature island arcs such as the Tonga-Kermadec and Lesser Antilles arcs. This sequence contains greenschist to amphibolite facies metamorphic rocks derived from fine-grained terrigenous clastic assemblages interbedded with the volcanic/volcaniclastic rocks that were deposited in a marine basin marginal to but some distance from a continental landmass (Jackson & Ramsay,1980). These rocks were deformed and intruded by ≈900 Ma old diorite plutons (Darbyshire *et al.*,1983) and include rocks assigned to the Baish, Bahah, Ajal/Siham, Arafat and Hali Groups.

ii)"Sequence B", 900-700 Ma; comprises several volcano-sedimentary

complexes which locally contain allochthonous mafic and ultramafic rocks interpreted to be ophiolites. This sequence consists mainly of greenschist facies rocks intruded by composite calc-alkaline batholiths ranging between ≈850-700 Ma in age. The lavas are predominantly calc-alkaline and low-K arc-tholeiite series, slightly more mature in composition than sequence C, with higher lithophile element contents comparable with Pacific island arc averages (Jackson & Ramsay,1980; Darbyshire et al.,1983; Roobol et al.,1983).

iii)"Sequence A", 700-570 Ma; contains coarse-grained terrigenous clastic sediments locally interbedded with fluviatile to shallow-marine carbonates and sub-aerially deposited rhyolite-dominated volcanics. The voluminous lavas are generally calc-alkaline or high-K calc-alkaline lavas with moderately high lithophile element abundances comparable to volcanic arcs such as those of Central America and Indonesia which are transitional between island arcs and continental margin volcanics. This succession is weakly metamorphosed and intruded by ≈600 Ma granite plutons.

Although the volcano-sedimentary belts of the Nubian-Arabian Shield are characterised by rapid lateral and vertical lithological variations, there is a high degree of similarity in the lithological character and gross structure (Jackson,1980). This is a result of apparent common depositional environments and processes throughout the Shield in which a broad development can be seen from extensive marine basins which received detritus from both continental and immature island-arc sources (sequence C) through diachronous volcano-sedimentary basins related to maturing intraoceanic arc systems (sequence B), to shallow marine to subaerial depostion of sediments and calc-alkaline to alkaline volcanics (sequence A) on continental basement (Jackson & Ramsay, 1980). It has been recognised, however, that the Shield comprises distinct tectonostratigraphic terranes that have intrinsic geological histories and are separated by major crustal discontinuities. Mapping in contiguous regions has produced a plethora of stratigraphic names but the probable independent and diachronous evolution of the various terranes means that direct correlation of similar facies is unrealistic unless supported by accurate age data. The recognition of progressively maturing arc facies within each terrane indicates that the Nubian-Arabian Shield evolved in terms of superimposed volcanic arcs as opposed to the juxtapositioning of

oceanic arcs as suggested by Gass (1977) and Shackleton (1979).

Johnson et al. (1987) identified a series of autochthonous, unconformable, post-accretion, "overlap sequences" ranging in age from 760 to 570 Ma that were deposited diachronously over the Shield and obscure previously accreted terranes and terrane boundaries. These consist of a number of structural environments, namely:

a) Successor basins which occur above terrane boundaries; an example is the Furayh Group (700-675 Ma) of conglomerate, sandstone and mafic volcanics which were deposited in a successor basin above the sutures joining the Hijaz, At Ta'if-Jiddah (Northern Asir), and Afif terranes. Similar sequences include the Fatimah Group (704-675 Ma) in the At Ta'if-Jiddah composite terrane and the Thalbah (670-640 Ma) and Amlas Formation within the Midyan terrane.

b) Crustal downwarp basins; such as the elongate Murdama basin across the Afif, Ad Dawadimi and Ha'il terranes which contains a thick succession of shallow-marine to fluviatile, volcaniclastic and epiclastic rocks of the Murdama, Jurdhawiyah and Hibshi Groups with marginal, mature, calc-alkaline volcanics (sequence A, Jackson & Ramsay, 1980) dated at 631 Ma. The contraction and downwarp of basement rocks following thermal expansion during syn-accretionary granite emplacement is seen as a likely basin-generating mechanism.

c) Pull-apart basins; in which subaerial and shallow-water sequences were deposited in ensialic, fault-controlled grabens, delineated by the north-west-trending, sinistral, strike-slip faults of the post-accretionary Najd system. They include the Jibalah and Bani Ghayy (630-610 Ma) Groups and the Minawah Formation (≈575 Ma) of clastic, epiclastic and volcaniclastic sediments interbedded with bimodal volcanic rocks typical of lavas in continental rifting environments.

3.5.1 Stratigraphy of the Northern Red Sea Hills

The stratigraphy of the Red Sea Hills is poorly understood owing to the complexities of the late-Proterozoic granite-greenstone basement and the remoteness of the region. Several attempts have been made to correlate the greenstone belt volcanics in the area under various collective terms, i.e. Oyo Series (Gass, 1955), Nafirdeib Series (Ruxton, 1956; Gabert et al.,1960; Kabesh, 1962) and the Nubian arc system meta-volcanics (NAM) (El Nadi, 1984,1987). Although the volcanic and sedimentary groups of the Nubian-Arabian shield may be

linked in terms of common genetic processes, it is unwise to attempt to erect regional stratigraphies within the Northern Red Sea Hills, let alone across supposed plate boundaries into adjacent terranes. As Vail (1987a) has rightly pointed out, these lithologies do not extend over great distances and hence stratigraphic nomenclature should be confined to a local scale (Embleton et al.,1982; Klemenic et al.,1985).

Geological mapping of the Gebeit-Sofiya area (Dunganab Sheet 36-1) by a joint Soviet-Sudan team (Ahmed,1984) divided the greenstone lithologies into a metasedimentary suite consisting of sandstone, marble, quartzite and conglomerates ± basic volcanics (Salala area) and a volcanic suite (Gebeit area) (Fig.3.1). The volcanic suite, comprising andesite and basalt tuffs, flows and agglomerates, were further subdivided into a lower succession of volcanics and interbedded slates, greywackes and marbles, as at Gebeit, and an upper volcanic succession ± metasediments.

Recent Landsat imagery of the basement around Gebeit Mine has recognised two further subdivisions of the Precambrian volcano-sedimentary lithologies, termed PG1 and PG2 (Geosurvey, 1983), which were previously defined by Ruxton (1956) as the Nafirdeib Series and the older, Primitive System, respectively. In the field, the low relief, PG2 tuffaceous slates contrast markedly with the massive, blocky, high-relief, PG1 volcanics. The north-easterly dipping contact between these two units, 4-5km to the south and south-east of Gebeit, is sharply defined by shear zones (30-50m wide) where PG1 is over-thrust on to PG2 (Fig.3.1). El-Nadi (1984, 1987) defined the PG2 rocks as metagreywacke-dominated, volcanogenic metasediments of low metamorphic grade, with interbedded meta-basic schists possibly representing basic sills and flows. Consideration of the transitional-element geochemistry of the interbedded volcanics prompted El-Nadi (1984, 1987) to suggest that the sediments were possibly derived by erosion of an earlier or proto-Nubian arc with deposition in a marginal basin. El-Nadi also correlated the PG1 volcanics with the Homogar Volcanic Group (250 km south of Gebeit) (Klemenic et al.,1985) under the genetic term of Nubian-arc system metavolcanics (NAM). Although extensive rhyolites were identified in addition to the syn-orogenic, intrusive/extrusive rhyolite complexes by Landsat imagery, these have not been verified by the field-based Soviet-Sudanese mapping (Ahmed, 1984).

As all observed gold mineralisation in the area occurs within the PG1 volcanic group, all stratigraphic, petrographic and geochemical

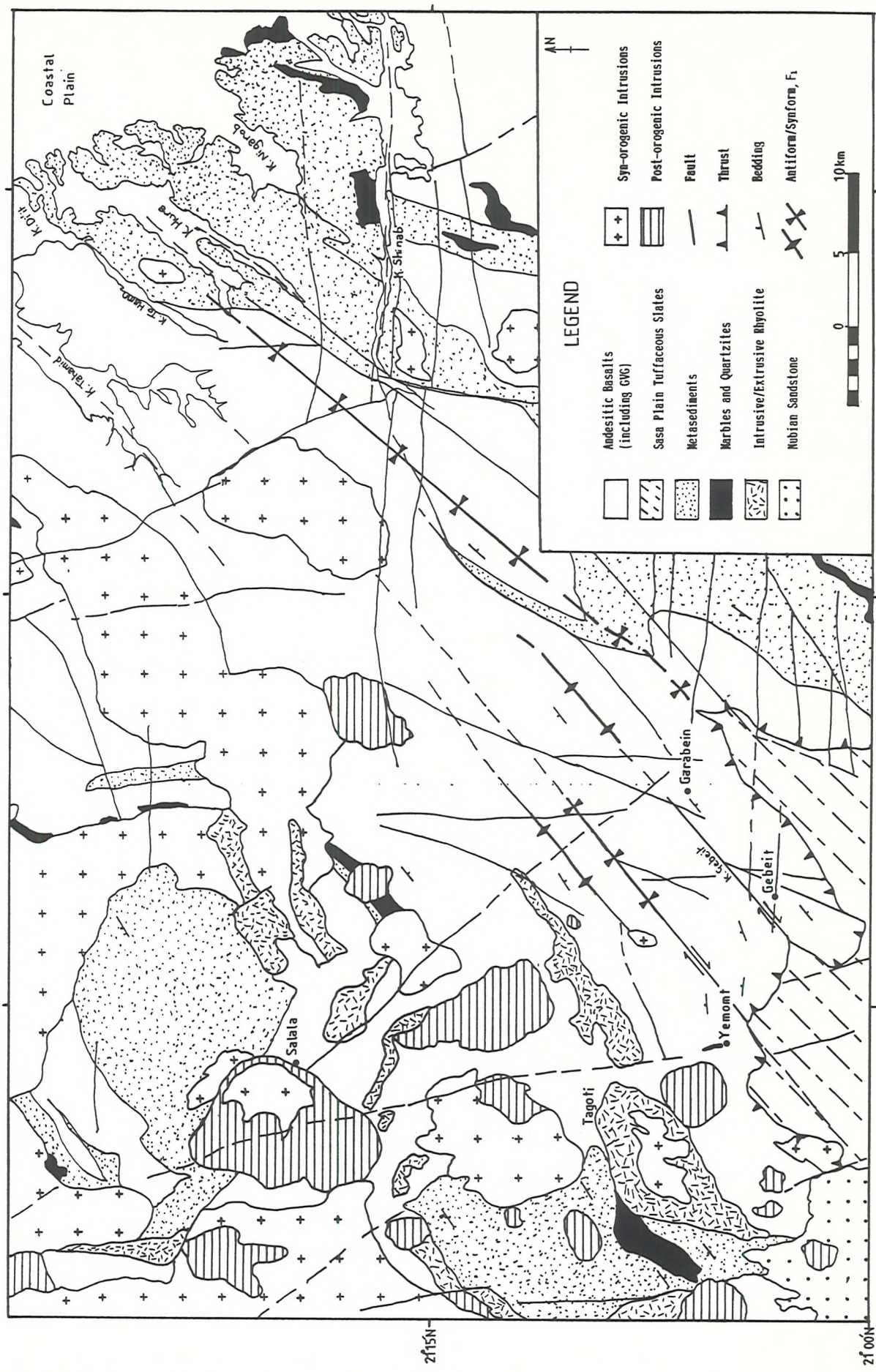

Fig.3.1 Geology of the area around Gebeit with emphasis on extrusive lithologies and structure (this study and after Geosurvey,1983; Ahmed,1984).

investigations undertaken in this study have concentrated on the PG1 group. From geological mapping of the PG1 volcanics in the immediate mine area, (this study, Robertson Research 1983-1985, Greenwich Resources 1985-1987), with reconnaissance mapping and sampling up to 15 km from the mine, a local stratigraphy has been realised. Using the type of stratigraphic nomenclature employed by Embleton et al., (1982); Klemenic et al., (1985); and Vail (1987a), the PG1 volcanics studied at Gebeit have been termed the Gebeit Volcanic Group (GVG).

3.5.2 Stratigraphy of the Gebeit Volcanic Group

Establishment of a stratigraphic sequence for a succession dominated by volcanics must be generalised and restricted to a relatively small area. Because of the structural complications in the mine area, a well exposed section at the southern margin of the GVG outcrop was logged (Fig.3.2) and then compared with mine-scale and reconnaissance mapping. The logged section, 2.5 km south-east of Gebeit on the Gebeit-Muhammad Qol road, appears to be fairly characteristic of the overall succession and can be correlated at least 15 km to the north-west at Garabein Mine. The main belt of volcanics extends 10 km west to the contact with the predominantly granitic belt north of Tagoti. The rocks appear to become more subaerial in character both east and west of Wadi Gebeit with the succession dominated by agglomerates and lavas together with discontinuous, north-east-trending belts of metasediments, quartzites and marbles. The consistency in stratigraphy to the north-east along strike and the rapid lithological variation perpendicular to strike may be due solely to F_1 folding or may also reflect deposition controlled by north-east-trending, elongate, marginal basins.

The broad stratigraphy at Gebeit comprises a lower succession of fine, well-bedded, aphyric and plagioclase-phyric pyroclastics which grade into an upper sequence dominated by hornblende-, and clinopyroxene-phyric agglomerates, lapillistones, and flows (Fig.3.3). Shear zones delineate the lower limit of the succession and generally within these zones lapilli-tuffs and agglomerates can be identified which display strong fabric-development in the matrix but minor deformation to the clasts. Because of the apparent repetition in the succession across the Gebeit block, it is uncertain whether these agglomerates within the shear zones form the lowest identifiable unit of the stratigraphy or are from the upper agglomerate-dominated part of

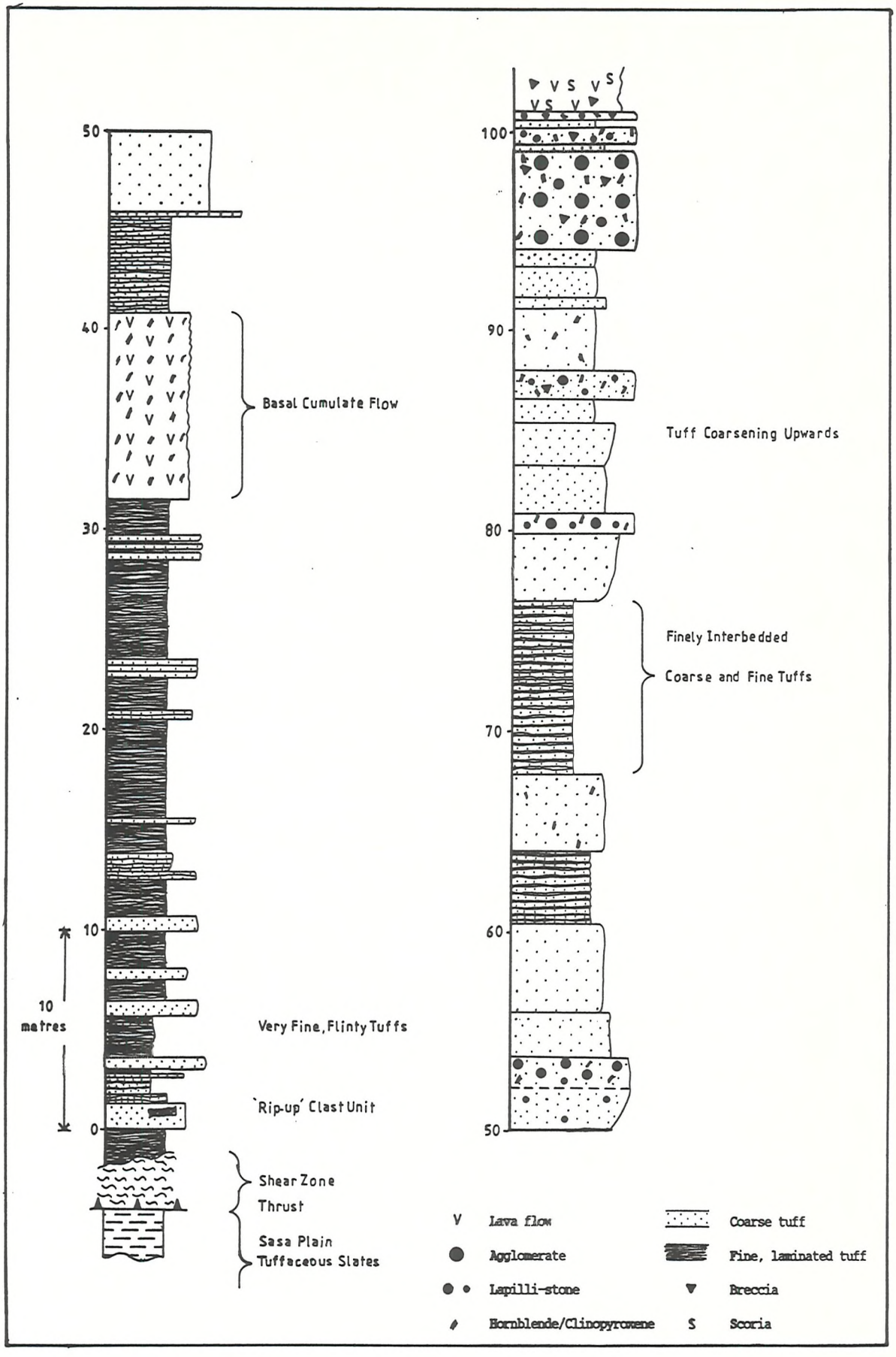

Fig.3.2 Stratigraphic log of the Gebeit Volcanic Group, 2.5km south-east of Gebeit. Bedding trends 340°N/50°E.

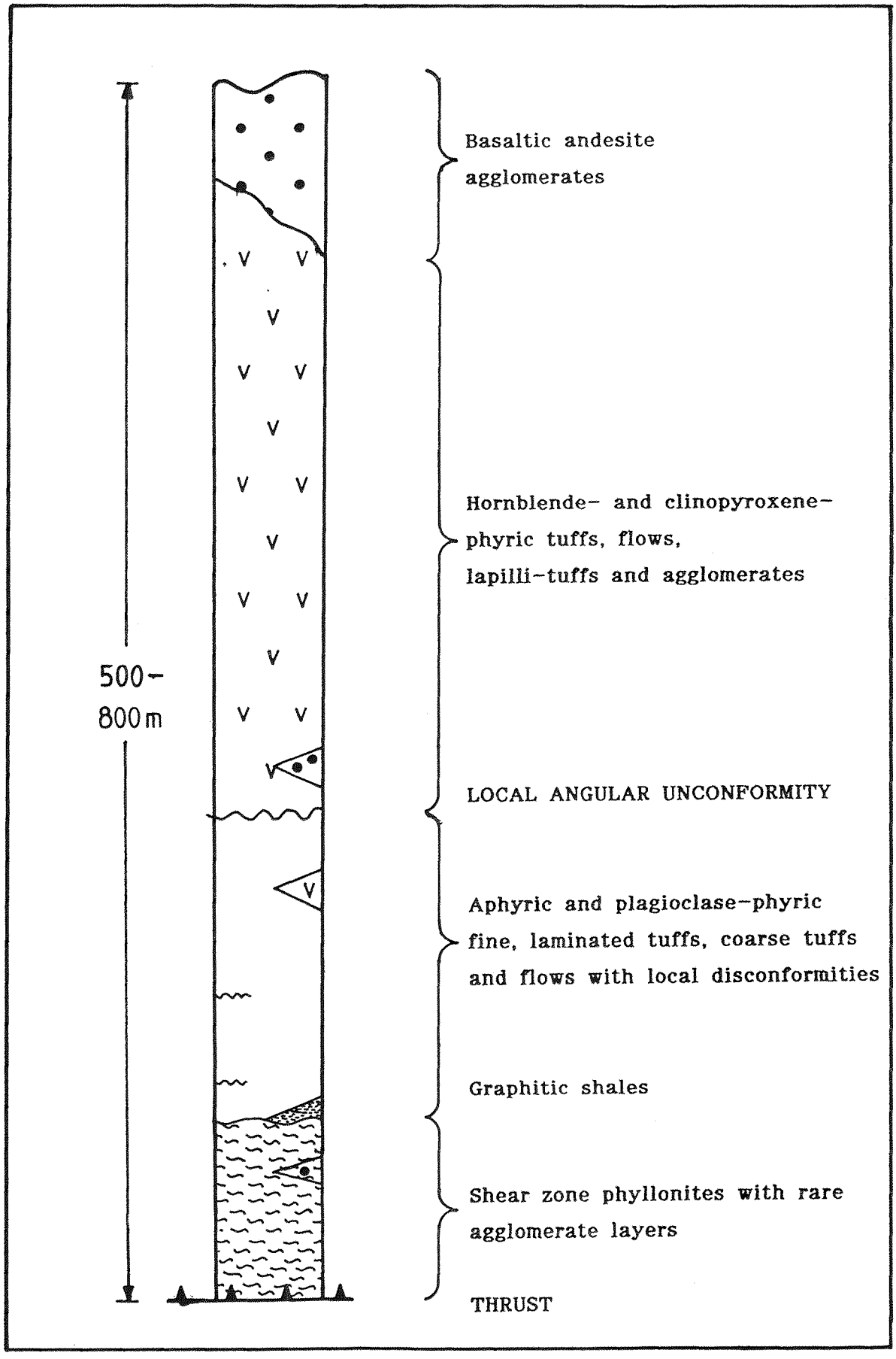

Fig.3.3 Generalised stratigraphic log for the Gebeit Volcanic Group in the Gebeit Mine area.

the succession. Graphitic shales are evident at Gebeit, interbedded with aphyric tuffs at the base of the succession. They consistently occur along the hanging wall of many of the major shear zones and appear to be significant in the siting and localisation of these structures. As a consequence of the preferential deformation of the shale units, they vary considerably in thickness. However, drill intersections of relatively undeformed rocks suggest some shale beds exceed 50 cm in thickness.

At Garabein, the sequence of interbedded shales and tuffs is thicker. The relatively more abundant sedimentary structures (e.g. slump folds, cross-lamination, rip-up clast beds) and rock types indicate a more submarine-dominated depositional environment than at Gebeit. Further up the succession, coarser pyroclastic lithologies become predominant along with a gradual increase in the abundance of agglomerate, lapilli-tuff and flow units. At the transition zone from aphyric and plagioclase-phyric tuffs to the hornblende-phyric lithlogies, the laminated tuffs are sometimes observed interbedded with flows and agglomerates. The top of the stratigraphic sequence is composed of thick (>1m) but laterally variable agglomerates which form the tops to many of the hills, especially to the west of Bishop's Dam.

Because of the problems of abundant upper scree-cover, desert varnish, and structural complexities, estimation of the thicknesses of various units and of the overall succession must be approached with caution. The lower contacts to the defined stratigraphic succession are invariably structural and the apparent repetition in stratigraphy between the Wadi Gebeit, Wadi Lode and Wadi East Gebeit shear zones is considered to be a structural repetition rather than a stratigraphic cyclicity. Thus, due to the effects of thrusting and folding, the observed succession may not represent the true depositional sequence and as a result any estimations represent a maximum thickness. Mapping indicates that the Gebeit Volcanic Group sequence in the mine area is generally 500 to 800 m thick. However due to the localised nature of pyroclastic deposition, significant lateral variations will occur.

3.6 Geochemistry of the Gebeit Volcanic Group

Geochemical analyses of relatively fresh samples of all lithotypes were undertaken for two main reasons, namely:

i) to act as a control when comparing major and minor element

mobilities in alteration zones, and

ii) to add to the limited geological database for Proterozoic volcanic lithologies in the Red Sea Hills.

Samples that displayed minimal hydrothermal alteration and veining were taken for analysis and were examined in thin section prior to processing. However, alteration was difficult to identify in the cryptocrystalline groundmasses and in the aphyric lithologies and, consequently, some samples may have contained the products of incipient alteration. All surface samples were cleaned of any desert varnish.

3.6.1 Geochemical Effects of Desert Varnish

Desert varnish forms a dark brown-black coating up to 0.1 mm thick on the exposed surfaces of outcrops in the Red Sea Hills. Studies of desert varnishes in Southern California (Engel and Sharp,1958) have indicated that varnish-formation is primarily a weathering process involving the dissolution, transportation and precipitation primarily of Mn, Fe, Ti, Ba and Sr, together with many other trace elements. Engel and Sharp (1958) considered that most elements are derived from local sources and are transported in solution or by ionic diffusion through moisture films. This is enhanced in the Red Sea Hills due to the relatively high water table, the predominance of mafic lithologies, and the wetter climate that is known to have existed historically (Mawson & Williams,1984).

In addition to iron and manganese, Ti, Ba, and Sr are the most abundant trace elements in desert varnish, followed by Cu, Ni, Zr, Pb, V, Co, La, Y, B, Cr and Sc ± Nb and it appears that most trace elements are considerably enriched (Engel and Sharp,1958). This possible source of contamination is of particular importance because of the relatively low abundances of the high field strength (HFS) elements (Nb, Ti, Zr, Y) in oceanic island arc mafic volcanics (Gill,1981) and their use as immobile elements for characterising altered lithologies (Pearce and Cann, 1973).

Rates of varnish-formation vary widely with local conditions from hundreds or thousands of years to as little as twenty-five (Engel and Sharp,1958). At Gebeit, old grindstones which are considered to be Pharonic in age (from the reign of Tutmose III; Gaskell, 1986) also display desert varnish which sets the upper time limit of formation to three and a half thousand years.

3.6.2 General Geochemical Characteristics of the Gebeit Volcanic Group

Previous workers have variably classified the Gebeit Volcanic Group as silicic volcanics (El-Boushi, 1972), andesites and greywackes (Ruxton, 1956; Robertson Research, 1983), and basalts and basaltic andesites (El-Nadi, 1984, 1987 ; Reischmann et al.,1986). Petrographic studies of these volcanics indicate that they are basaltic to andesitic in composition; however, distinction into three sub-groups suggests there may be significant geochemical variations. Discrimination of magma type using the Jensen cation plot (Fig.3.4; Jensen,1976) suggests the GVG rocks are tholeiitic andesites, and major and minor element analyses of the Gebeit Volcanic Group (Appendix B) indicate a general accordance with basic andesites (Table 3.1). Comparison of the Gebeit lithologies with basic andesites (Table 3.1) illustrates, with the exception of SiO_2, the good correlation in major and trace element geochemistry. The more definitive geochemical characteristics are summarised in Table 3.2. The andesitic nature of the GVG suggests a convergent plate boundary tectonic setting.

The Gebeit volcanics have Ba/La ratios ≥15 which is consistent with all volcanic rocks erupted at destructive plate margin boundaries (in contrast to Ba/La values of 4-15 for MORB). The Ba/La ratios for the GVG are relatively high (Table 3.2) and tend to be higher in low-K volcanics compared to high-K rocks. The Ba/La ratio is also higher in island arc rocks compared to rocks derived from thicker continental margins and increases with differentiation (Gill, 1981). Comparison of K_2O, Rb, and K/Rb, and Zr/Nb ratios suggest that the hornblende-phyric rocks of the GVG are low-K in character relative to the medium- to high-K nature of the plagioclase-phyric and aphyric volcanics (Gill,1981).

3.6.3. Geochemistry of Orogenic Andesites

Andesites are associated with convergent plate boundaries and are normally classified as intermediate hypersthene-normative volcanic rocks with SiO_2 between 53% and 63%. Andesitic magmas usually contain 2-5 wt% water which is released on eruption. This volatile loss causes precipitation and generates the porphyritic textures characteristic of andesitic rocks. The high phenocryst content (20-50vol%), the low settling rates of some phenocrysts, the high yield strength of

Fig. 3·4

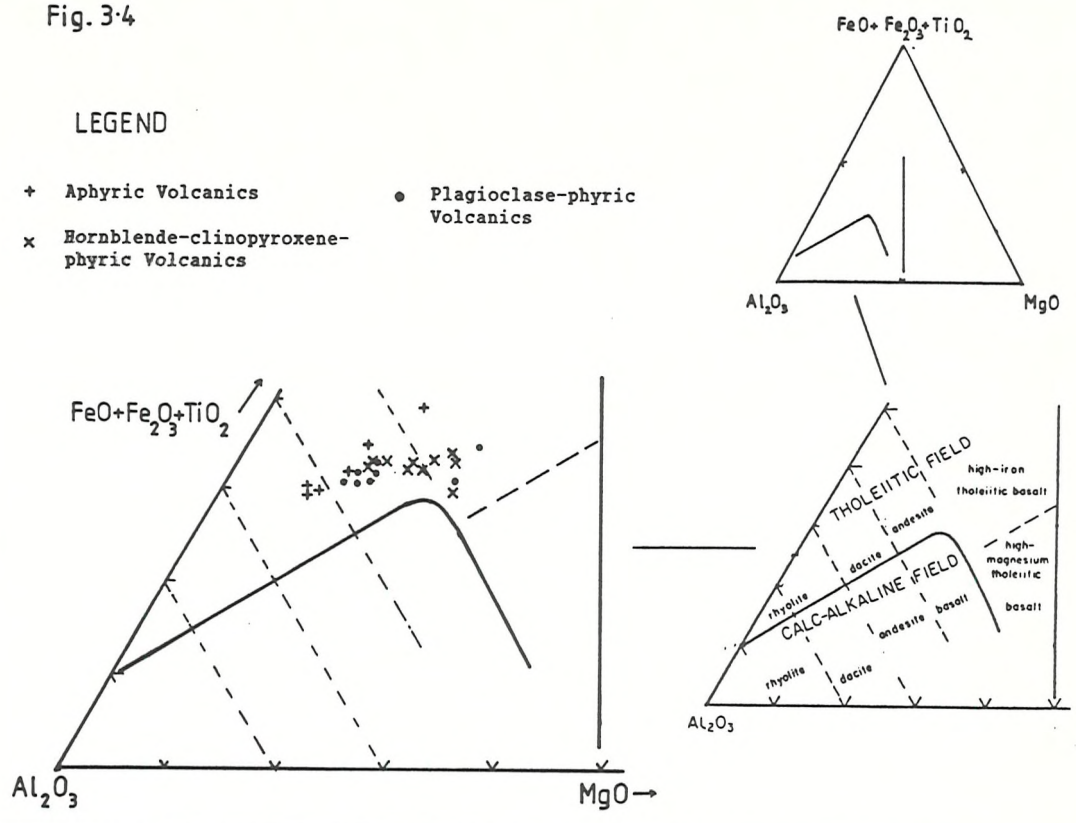

Fig. 3·5

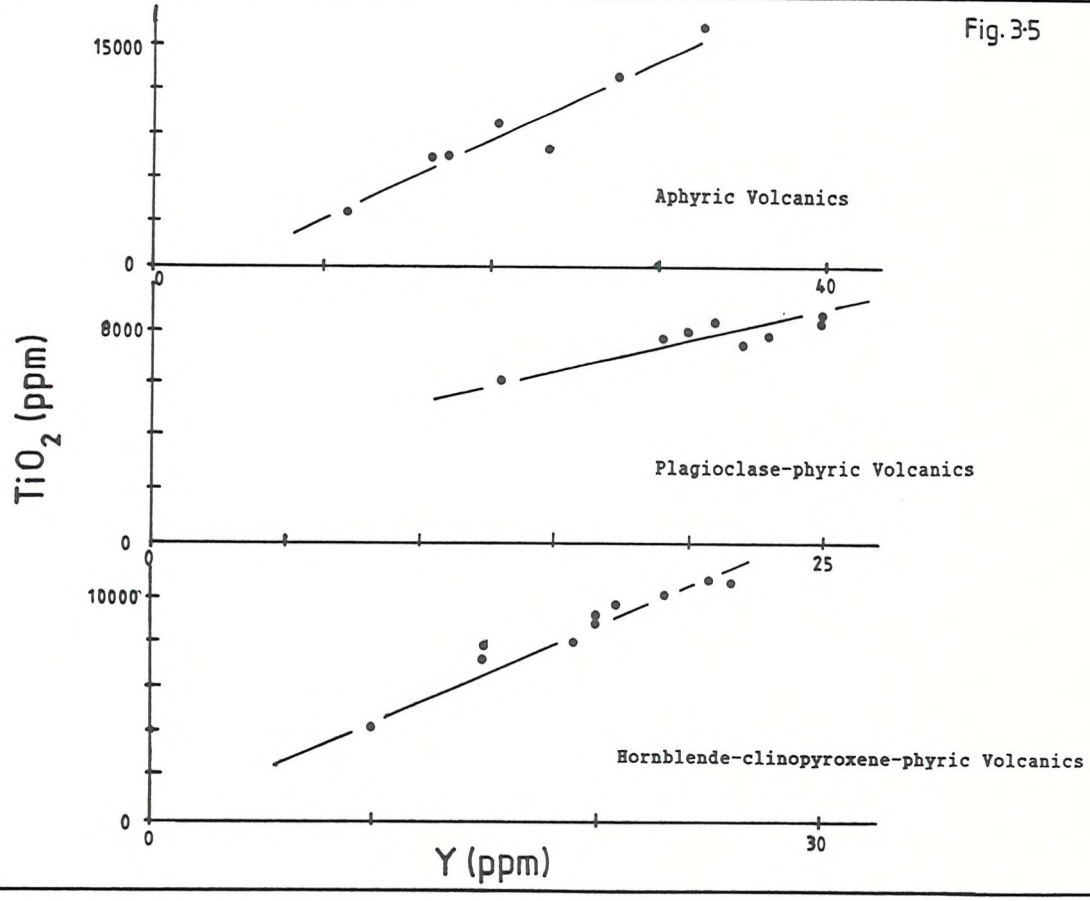

Fig.3.4 Jensen cation plot of the Gebeit Volcanic Group (after Jensen,1976).

Fig.3.5 TiO_2 vs. Y plots for the Gebeit Volcanic Group demonstrating the isochemical behaviour of the immobile elements.

	Basic Andesites						Gebeit Volcanic Group		
	Low-K		Medium-K		High-K		Hb/Cpx Phyric	Plag. Phyric	Aphyric Tuffs
	Thol.	Calcalk.	Thol.	Calcalk.	Thol.	Calcalk.	n=10	n=8	n=8
SiO2(%)	55.4	55.0	55.5	55.0	54.4	55.2	47.14	50.87	46.44
TiO2	0.57	0.52	0.81	1.1	0.73	0.92	0.83	0.82	0.58
Al2O3	17.6	17.3	17.7	17.4	19.4	15.9	17.01	17.01	17.39
Fe2O3	2.6	3.4	4.4	8.4*					
FeO	7.5	5.8	4.0		7.4*	7.3*	10.19*	9.51*	8.54*
MnO	0.19	0.16	0.18		0.20		0.18	0.15	0.11
MgO	4.2	5.4	3.4	4.2	3.0	5.5	6.07	4.60	2.92
CaO	11.0	9.4	8.0	7.5	8.7	9.6	10.77	6.19	6.85
Na2O	1.8	2.8	4.0	3.8	3.7	2.9	2.33	2.72	4.15
K2O	0.4	0.46	1.6	1.1	2.1	2.7	0.20	1.87	1.79
P2O5	0.08	0.17	0.35		0.36		0.24	0.21	0.10
LOI	0.55				0.35		4.51	7.03	6.51
Total	100.0	100.3	100.0	98.5	100.3	100.0	99.47	101.01	95.37
FeO*/MgO	2.3	1.6	2.4	1.8	2.4	1.3	1.5	1.86	2.6
Rb(ppm)	6	5	25	25	50	68	<2	48	33
Sr	235	380	810	501	605	583	560	301	323
Ba	100	105	250	226	690	670	73	308	298
K/Rb	555	735	535	365	348	328		323	450
Pb	1.8	1.0	5			12	4	4	<3
Th	0.2	0.1	1.3		8.1	5.3	<3	<3	<3
U	0.2	0.1	0.6		2.0	1.3	<5	<5	<5
La	1.8		11	17	22	15	<6	9	6
Ce	4.7		24	42		33	<10	16	<10
Y	17	16	17		25	22	22	22	17
Zr	28	38	81		98	111	57	73	58
Nb	0.6		4		5	7	3	5	3
Ni	13	34	6	20	3	45	52	19	15
Cr	15	76	9	196	8	220	180	41	38
V	310	225	178		260	190	317	283	240
Cu	145	88	46	41	38	66	58	19	42
Zn	89	76	74	104			81	81	80

* Total Fe calculated as FeO or Fe2O3
LoI = Loss on Ignition
<3 = Below Lower Limit of Detection

Table 3.1 Average compositions of Gebeit Volcanic Group lithotypes and comparison with basic andesites of both tholeiitic and calc-alkaline affinities (after Gill, 1981)

		Gebeit Volcanic Group		
	Orogenic Andesites[1]	Hb/Cpx Phyric	Plag. Phyric	Aphyric Tuffs
K_2O % high K med K low K	>1.8 0.75-1.8 <0.75	0.01-0.69	0.8-2.7	1.4-2.3
TiO_2 %	0.8-1.0	0.67-0.98	0.61-0.95	0.49-0.73
Al_2O_3 %	16.0-18.0	16.0-18.7	14.1-18.4	15.7-19.6
P_2O_5 %	0.05-0.3	0.19-0.30	0.16-0.24	0.09-0.11
Zr ppm	50-150	40-70	59-100	51-66
Y ppm	20-25	19-26	19-25	15-19
Nb ppm	<5	3-4	4-5	2-4
Sr ppm	100-1000	289-987	246-368	177-444
Rb ppm high K low K	5-100 1-5	<2-10	19-72	27-42
Ni ppm	<40	28-84	12-24	9-19
Zn ppm	50-100	56-95	73-88	72-96
Cu ppm	10-150 (60)	28-82	<2-42	26-68
Ba/La	>15		18-63	46-70
K/Rb high K low K	250 1000	361-573	312-349	430-460
Zr/Nb high K low K	10-20 40	13-22	12-25	16.5-28
FeO/MgO calcalk. thol.	<2.2 >2.2	1.1-1.9	1.2-2.3	2.4-2.9

Table 3.2 Summary of characteristic major and minor element variations of orogenic andesites and comparison with Gebeit Volcanic Group lithologies ([1]after Gill, 1981).

andesitic magma, and the possibility of magma-mixing during andesite genesis suggest that some samples may not have been homogenous liquids. Some phenocrysts, therefore, may not have precipitated from the liquid in which they occurred at eruption (Gill, 1981). As a result, scatter of data can occur in element-element diagrams and variation diagrams may represent mixing lines rather than lines of liquid descent.

Geochemically, arc volcanics are characterised by the enrichment of large ion lithophile (LIL) elements (Rb, Ba, K, Th, & Sr) over the high field strength (HFS) elements (Nb, Ta, Zr, Hf, Ti, Y, & Yb) relative to mid-ocean ridge basalt (MORB). Calc-alkaline volcanics can be differentiated from arc tholeiites by a greater magnitude of LIL enrichment along with additional variable enrichments of Ce, P and Sm (Pearce, 1982). It is not possible to derive island arc tholeiites and calc-alkaline basalts from mantle with trace element and isotopic properties similar to the source of N-MORB. Furthermore, partial melting or high level fractional crystallisation cannot produce the observed LIL/HFS element ratios (Saunders and Tarney, 1984). From studies of oceanic island arcs (Ringwood,1974; Pearce,1982,1983; Saunders and Tarney,1979,1984; Pearce et al.,1984) the selective enrichments in Sr, K, Rb, Ba, Th ± Ce ± Sm ± P and the relative lack of enrichment of Ta, Nb, Hf, Zr, Ti, Y and Yb have been attributed to mantle source modification by a subduction component of aqueous and siliceous fluids derived from an underlying subducting slab undergoing dehydration. Additionally, the mantle wedge source regions become gradually depleted in all incompatible elements due to extraction by repeated arc magma production and the continuous transfer of LIL elements from the adjacent subducting slab serves to rapidly increase the LIL/HFS element ratio. Continental margin basalts carry an additional geochemical component which contains Nb, Ta, Zr and Hf and is assumed to be derived from trace element-enriched, metasomatised, sub-continental lithosphere. This results in higher concentrations of Nb and Ta relative to Zr and Hf, along with higher concentrations of Zr and Hf relative to Y and Yb.

3.6.4 Immobile Element Discrimination Diagrams

Despite the fresh appearance of the analysed samples, relatively low SiO_2 values suggest that some degree of major element mobility may have occurred. Certain minor and trace, high field strength (HFS), elements (Ti, Zr, Y, Nb, Ce, Ga), which have low ratios of ionic charge

to ionic radius, i.e. ionic potential, have been shown to be generally immobile in aqueous fluids (Cann, 1970; Pearce and Cann, 1973) and behave incompatibly during most partial melting and fractional crystallisation events (Pearce, 1982). As a result, rocks which have undergone secondary alteration processes or metamorphism can be characterised by comparison with fresh volcanics (Winchester and Floyd, 1977; Floyd and Winchester, 1978). Plots of the immobile elements (Ti,Zr,Nb,Y) for the GVG (e.g. Ti vs. Y; Fig.3.5) show good positive correlations that indicate these elements have behaved isochemically. The Gebeit Volcanic Group lithologies have been plotted on established geochemical grids (Figs.3.6-3.10) in order to classify them geochemically, to indicate petrogenetic affinities and to identify a possible tectonic setting. Despite petrographic differences, all the GVG lithologies plot closely together in the basaltic andesite and sub-alkaline basalt fields (Fig.3.6).

Plots of immobile elements (Ti,Zr,Y, and Cr) on discrimination diagrams confirm that the GVG rocks are characteristic of volcanic arc basalts rather than mid-ocean ridge basalts (MORB; Fig.3.7) and are not of within-plate affinity (Fig.3.8). Figures 3.8 and 3.9 also indicate that the hornblende-clinopyroxene-phyric volcanics are low-K tholeiites (K_2O;0.01-0.69wt%) compared with the calc-alkaline plagioclase-phyric and aphyric rocks (K_2O; 0.80-2.7wt%). On each plot, one or two samples occur in the MORB field but no single sample plots consistently as a mid-ocean ridge basalt. Given that the Gebeit Volcanic Group rocks are volcanic arc in origin, the Zr/Y vs. Zr plot (Fig.3.10) suggests that the GVG rocks were erupted as part of an oceanic island arc and not in a continental margin environment. The Zr/Y ratio is a measure of within-plate enrichment and not alkalinity (Pearce, 1982); thus, continental margin and within-plate lavas, derived from metasomatised sub-continental lithosphere similarly enriched in Nb, Zr, Ta, and Hf, plot in the same field. Continental margin lavas also have a subduction component.

These inferences are supported by comparison with basalts from other tectonic settings (Table 3.3). The GVG has low TiO_2 values (<1%) and low abundances of Cr, Ni, Zr, Y, and Nb relative to basalts from within-plate and mid-ocean ridge environments. The lack of any silicic volcanics, Y values of 20-25 ppm, and low Ni, <40 ppm also indicate that the GVG were not erupted through thick continental crust, supporting an oceanic arc setting.

Fig. 3·6

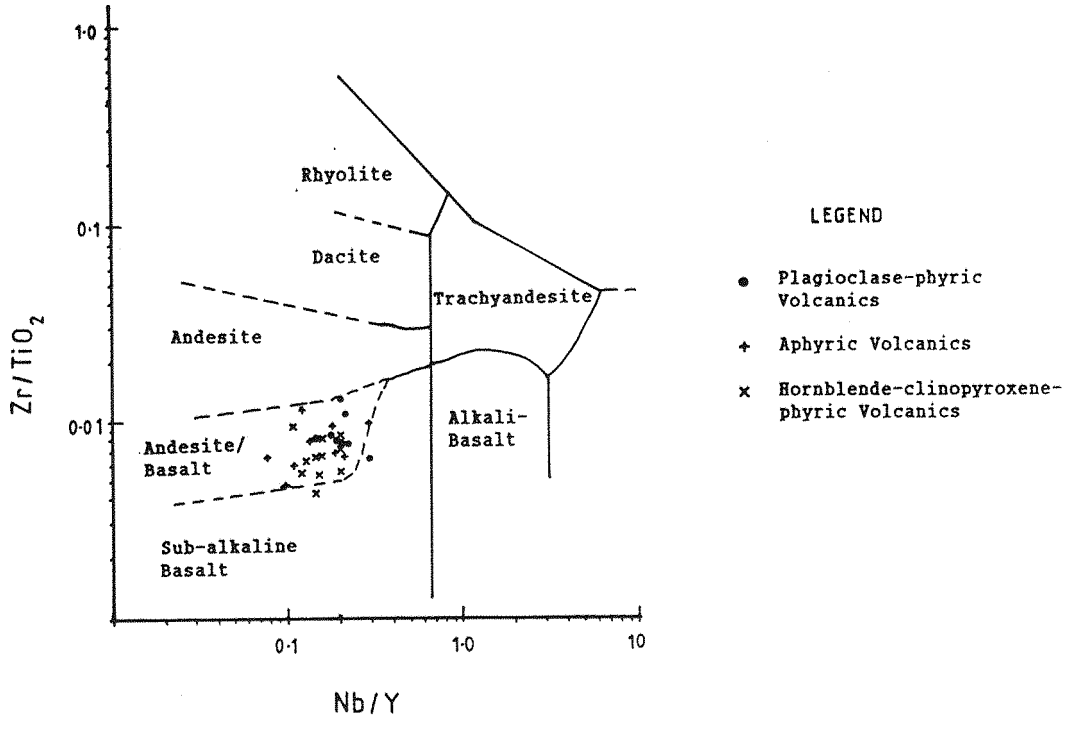

Fig. 3·7

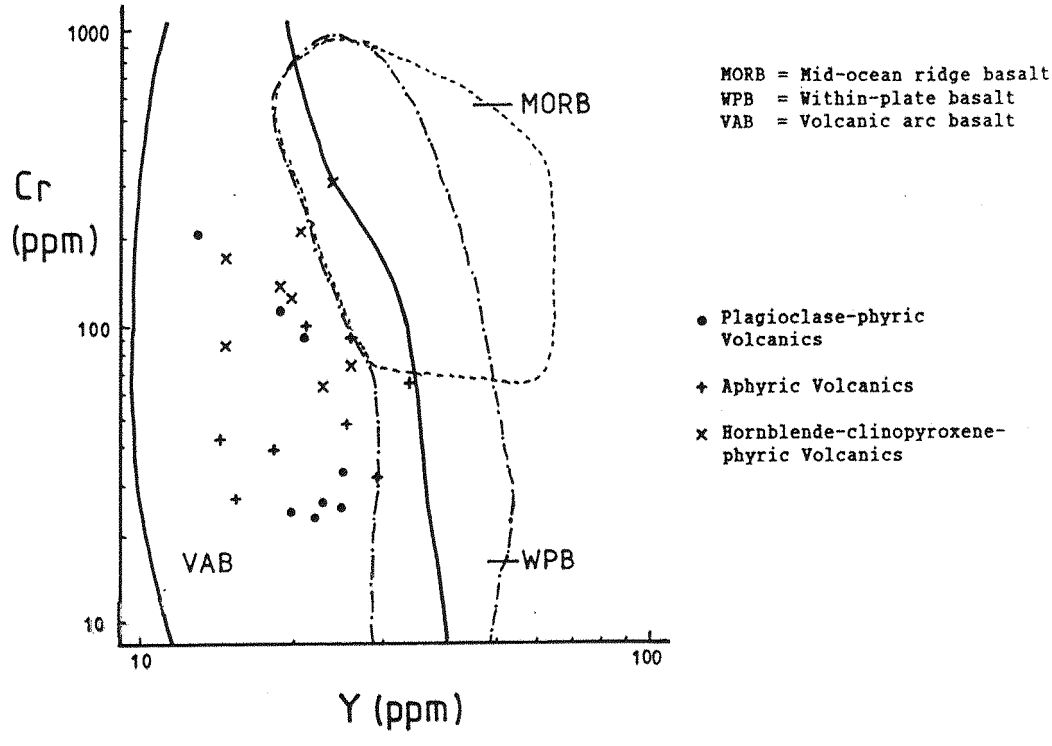

Fig.3.6 Zr/TiO_2 vs. Nb/Y discrimination plot showing the andesitic basalt affinities of the Gebeit Volcanic Group (after Winchester & Floyd,1977).

Fig.3.7 Cr vs. Y plot showing the volcanic arc affinities of the Gebeit Volcanic Group (after Pearce,1982).

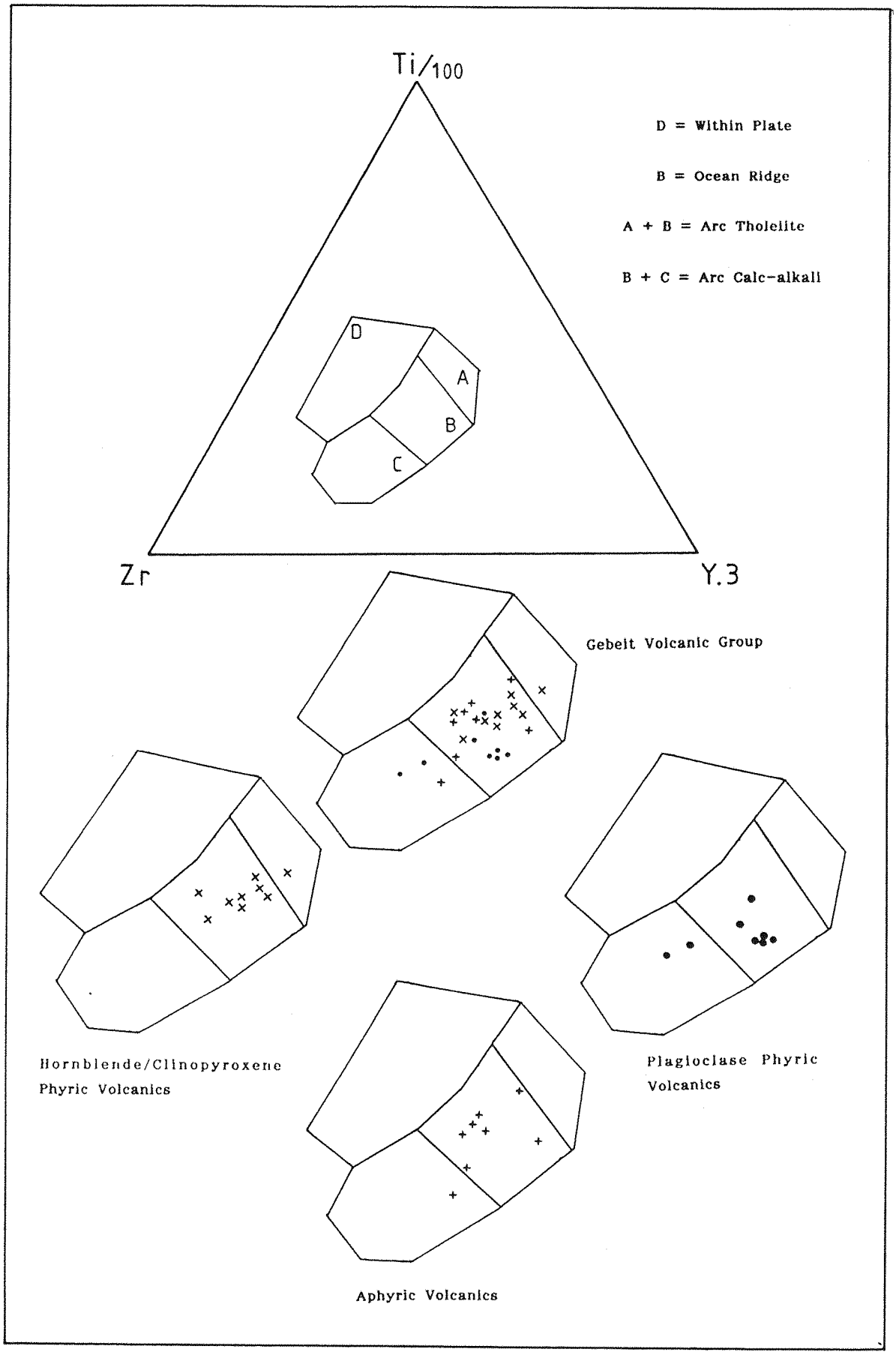

Fig.3.8 Discrimination diagram for the Gebeit Volcanic Group using Ti, Zr, and Y. In conjunction with Fig.3.7, the hornblende-phyric rocks are more arc tholeiitic compared to the aphyric and plagioclase-phyric calc-alkaline rocks (after Pearce & Cann,1973).

Fig.3.9

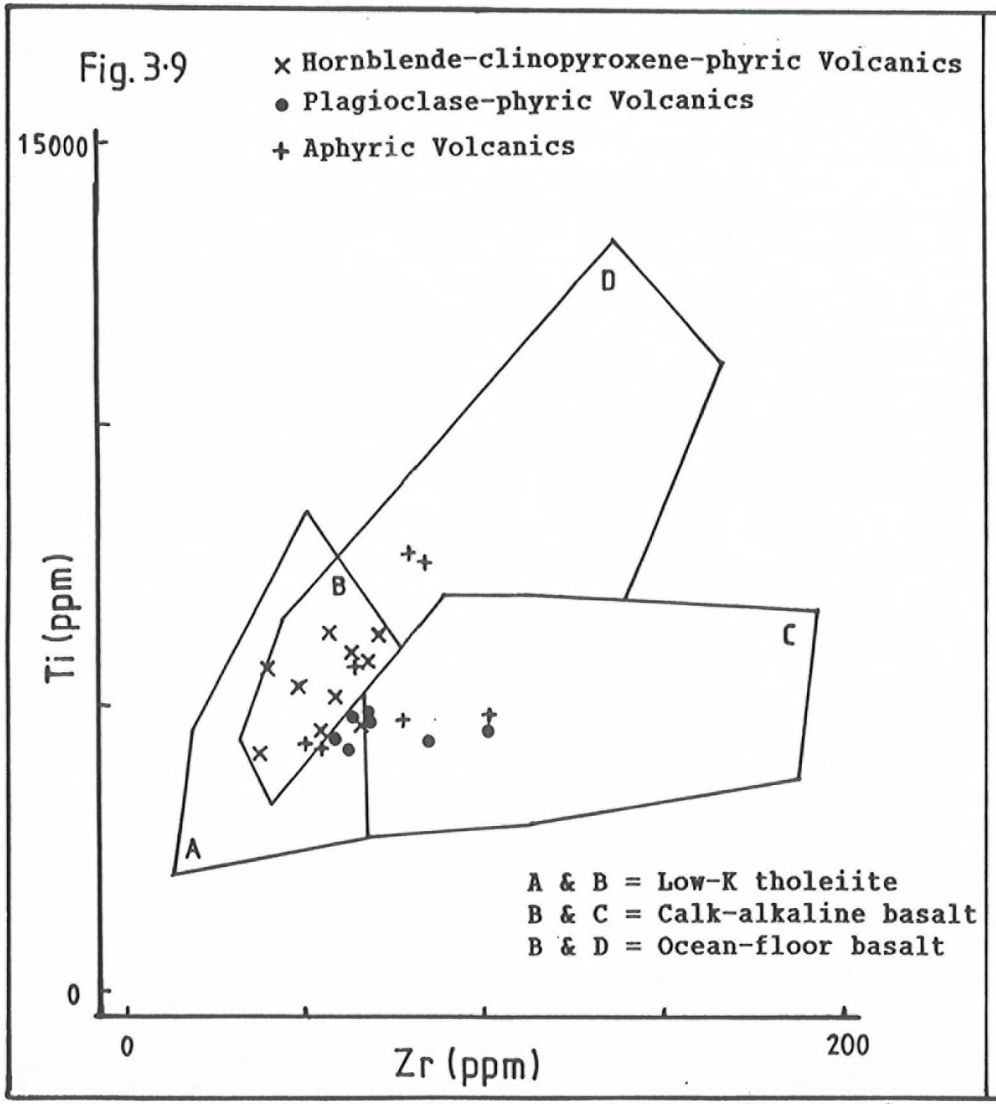

Ti vs. Zr discrimination diagram for the Gebeit Volcanic Group indicating the calc-alkaline affinities of the plagioclase-phyric and aphyric rocks and the arc tholeiite affinities of the hornblende-phyric rocks (after Pearce & Cann,1973).

Fig.3.10

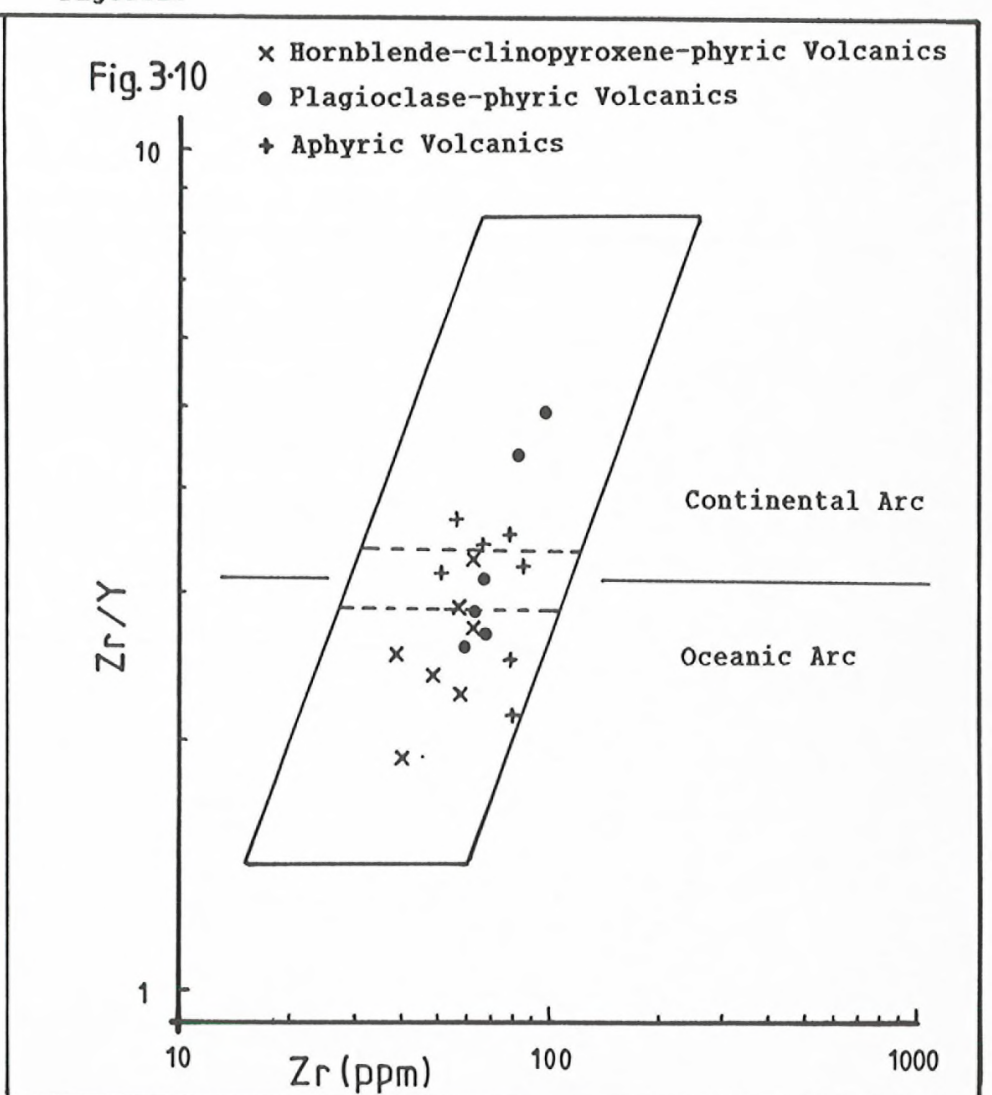

Zr/Y vs. Zr discrimination plot for the Gebeit Volcanic Group indicating oceanic arc affinities (after Pearce,1983).

	Mid-Ocean Ridge		Within-Plate		Volcanic-Arc			Gebeit Volcanic Group		
	Thol.	Trans.	Thol.	Alkaline	Thol.	Calcalk.	Shosh.	Hb/Cpx	Plag.	Aphyric
K_2O(%)	0.20	(0.51)	(0.5)	(1.5)	0.43	0.94	2.51	0.20	1.87	1.79
Rb(ppm)	(2)	(6)	(7.5)	(40)	4.7	23	51	<2	48	33
Ba(ppm)	(20)	(60)	(100)	(600)	60	260	609	73	308	298
TiO_2(%)	1.40	1.39	2.23	2.90	0.84	0.98	0.94	0.83	0.82	0.58
Zr(ppm)	90	96	149	213	40	71	87	57	73	58
P_2O_5(%)	0.12	0.18	0.25	0.64	0.08	0.19	0.44	0.24	0.21	0.10
Ce(ppm)	11	23.3	31.3	96.8	6.94	29.3	50.2	<10	16	<10
Nb(ppm)	4.6	16	13	84	1.7	2.7	8.4	3	5	3
Sr(ppm)	121	196	290	842	231	428	934	560	301	323
Ni(ppm)	(90)	(130)	(70)	(90)	18	50	14	52	19	15
Y(ppm)	33	25	26	25	17	22	22	22	22	17
Cr(ppm)	251	411	352	536	111	160	100	180	41	38

( ) Estimated values (no compilation available)

Table 3.3 Chemical characteristics of mid-ocean ridge (MORB), within-plate, volcanic arc basalts (Pearce, 1982), and Gebeit Volcanic Group basaltic andesites.

	Average post-Archean shale 1.	2.	Average GVG shale n=5
SiO_2(%)	62.8	61.6	56.8
TiO_2	1.0	1.0	0.56
Al_2O_3	18.9	18.3	17.5
FeO	6.5	7.4	
Fe_2O_3			8.4
MnO	0.11	0.13	0.06
MgO	2.2	2.7	2.3
CaO	1.3	4.2	4.8
Na_2O	1.2	1.1	4.4
K_2O	3.7	3.4	2.0
P_2O_5	0.16	0.22	0.15
Σ	99.9	100.1	97.0
LOI	6.0		7.0
Ba(ppm)	650	580	207
Rb	160	140	35
Sr	200	450	199
Pb	20	20	17
La	38	40	10
Ce	80	50	16
Y	27	30	24
Th	14.6	11	<3
U	3.1	3.2	<5
Zr	210	200	97
Sn	4.0	6	<6
Nb	19	20	4
Mo	1.0	2	5
Cr	110	100	188
V	150	130	225
Ni	55	95	35
Cu	50	57	52
Zn	85	80	118
Ga	20	19	21

Table 3.4 Average composition of Gebeit Volcanic Group shale compared with average post-Archaean shales (1.= terrigenous shale, excluding carbonate components; after Taylor & McClennan, 1985 and 2.= after Krauskopf,1967).

3.6.5 MORB-Normalised Discrimination Plots

Reischmann et al. (1986) have suggested that the aphyric and plagioclase-phyric volcanics of the GVG are tholeiitic and were erupted in a back arc environment, whereas they believe that the hornblende-phyric lithologies are calc-alkaline in character. If this is the case, then some of the GVG rocks may be expected to display some of the geochemical characteristics of mid-ocean ridge basalts (Saunders & Tarney,1984).

Major and trace element variations relative to MORB are best displayed using spider plots (Pearce,1982) with the geochemical data for the GVG normalised to N-MORB (normalising values and analytical precision are given in Appendices A & B). The analytical data for the GVG are, however, restricted by relatively high detection limits under standard operating conditions (Appendix A) for low abundance elements like Ce (<10 ppm), Nb (<2 ppm), Th (<3 ppm), and La (<6 ppm) when compared with their normalising values (10 ppm, 3.5 ppm, 0.2 ppm, and 3 ppm respectively). This creates a problem with diagnostic immobile elements such as Ce and Th which only appear on plots when enriched relative to MORB and, in the case of Nb, can also have large analytical errors due to abundances of as little as 3-4 ppm. Further limitations are imposed as other diagnostic elements such as Ta, Hf, Sm, Yb and Sc have not been analysed. Although detailed geochemical studies for modelling igneous processes were beyond the time constraints of this project, the distinctive geochemistry of the GVG does allow some degree of characterisation.

Although the various lithotypes of the GVG display minor differences, the overall trends are consistent. All groups show a flat trend of the HFS elements, parallel but depleted relative to MORB, an enrichment of the large ion lithophile (LIL) group (i.e. Sr, K, Rb, Th and Ba) and variable enrichments of Ce and P.

In both sets of spider diagrams of the Gebeit Volcanic Group, the aphyric and plagioclase-phyric volcanics display very similar trends and their corresponding plots are virtually congruent (Figs. 3.11a & 3.11b). Although the aphyric tuffs often show more chemical variability (possibly due to alteration), both groups display marked LIL enrichments, flat depleted HFS element trends and enrichments in Ce and P compatible with calc-alkaline, island arc affinities.

The hornblende-phyric volcanics have similar but much flatter patterns (Figs. 3.11c) along with variable, large scale potassium

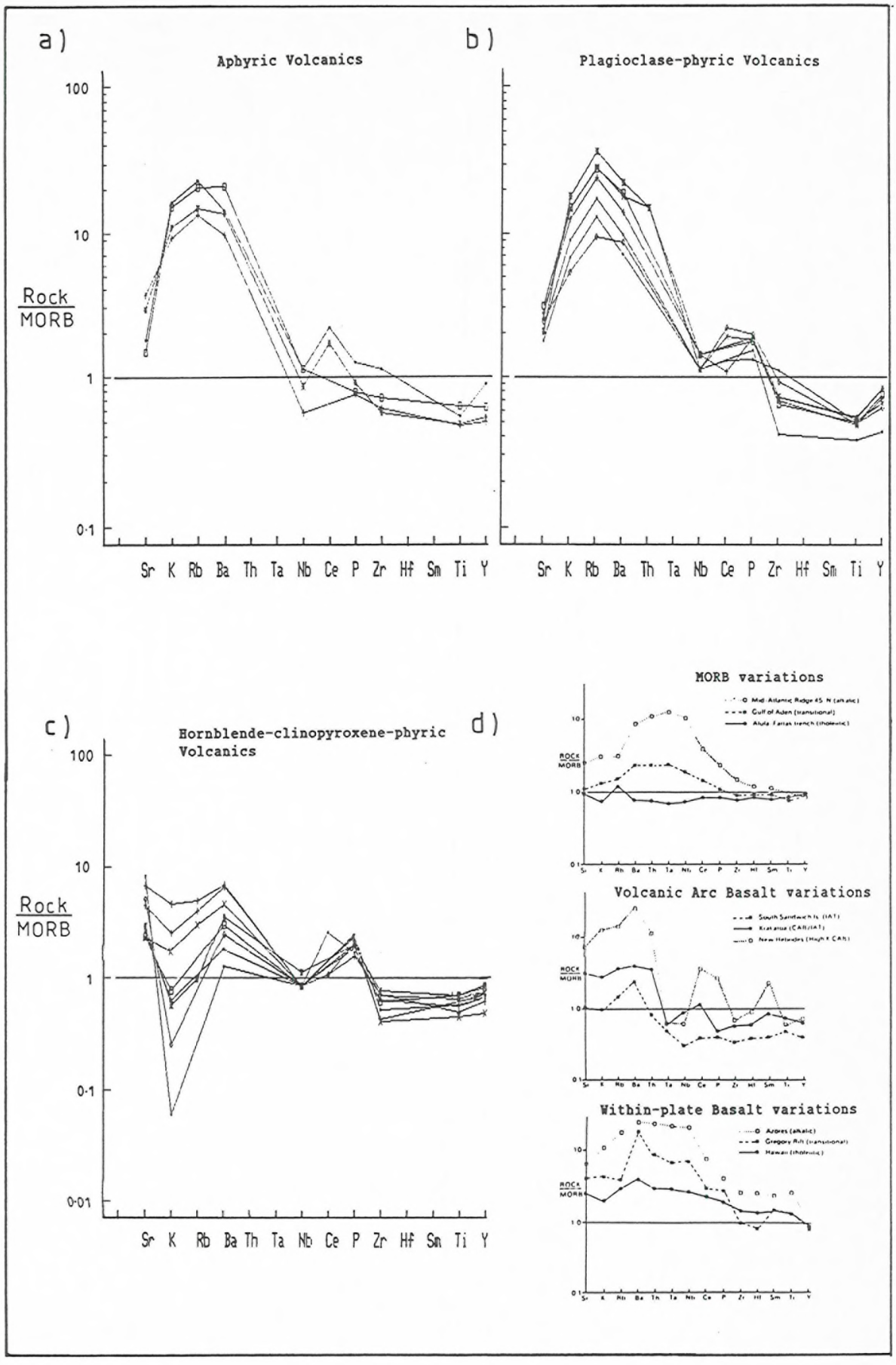

Fig.3.11 (Mid-oceanic ridge basalt) MORB-normalised plots for the Gebeit Volcanic Group (a-c) and comparison (d) with basalts of different tectonic settings demonstrating the volcanic arc affinities of the GVG (after Pearce,1982).

depletion in addition to the relatively lower abundance of LIL elements. The hornblende-phyric rocks still, however, display HFS element-depletion and higher Ce and P values characteristic of arc-derived magmas. Comparison with the volcanic arc basalt variations (Fig.3.11d) suggests that the hornblende-phyric rocks represent a low-K lithology, transitional between calc-alkaline and arc tholeiite in composition and concurs with the immobile element discrimination plots. These characteristics contradict Reischmann et al. (1986) who considered the plagioclase-phyric and aphyric rocks to be tholeiitic.

3.6.6 Seawater Alteration of Basalts

Low temperature interaction between seawater and basalt has been shown to cause variable enrichment in basalts of Mg, K, Rb, Sr, U and Cs ± Ba (Hart et al., 1974; Mitchell & Aumento, 1977) and under extreme conditions the light rare earth elements (LREE) (Ludden & Thompson, 1979; Terrell et al., 1979). Higher grades of alteration and metamorphism (greenschist to amphibolite grade) may result in leaching of Ca, Mg, Sr, Cr, and Ni (Dostal & Dupuy, 1987). Although the GVG has undergone lower greenschist facies metamorphism, the intimate spatial and temporal association of the plagioclase- and hornblende-phyric volcanics indicates that any differences in LIL element contents are unlikely to be attributed to metamorphic processes. If the variations in LIL element contents are not due to original igneous compositional differences or hydrothermal alteration, then the environments of deposition of the two lithotypes may be distinct. Depositional textures (sections 3.3 & 3.7) suggest that the aphyric tuffs and probably the plagioclase-phyric rocks were deposited sub-aqueously as opposed to the predominantly subaerial deposition of the hornblende-phyric lithologies. Therefore, the plagioclase and aphyric rocks may have been preferentially enriched by seawater alteration but the low K levels seen in the hornblende-phyric group (assuming no depletion due to alteration) are of igneous origin. There is, however, no petrographic evidence to indicate that the plagioclase-phyric rocks are altered in preference to the hornblende-phyric volcanics. In addition, there are differences in the immobile (HFS) elements between the three groups indicating igneous differentiation. The non-labile trace element abundances, depletions and enrichments compatible with arc lavas imply that LIL element enrichment in the GVG should be observed. Saunders and Tarney (1984) consider Th to be immobile under low levels

of alteration and further detailed work on the Th abundances of these rocks (only detectable at >15x background under normal operating conditions) could ascertain whether the LIL element variations are primary or due to secondary alteration. Determination of Ta, Hf, Sm, and Yb abundances would also enhance the geochemical characterisation of the GVG.

3.6.7 Carbonaceous Shales

Comparison of GVG shales with estimates of average post-Archean shale (Table 3.4, p.3-28) shows relative depletions of major, immobile and trace elements, with the exception of CaO, Na_2O, Cr, V, and Zn. High field strength elements such as Zr, Ti, Nb, Y, La, Ce, and large ion lithophile elements, e.g. Ba, Rb, K_2O, and Th, all show much lower relative abundances. The overall geochemistry is similar to the volcanic members of the GVG with additional organic material now in the form of graphite. The organic content probably originates from blue-green algae within the submarine basin. The close correlation of chemistry with the volcanic units together with the observed, graded tuffaceous horizons suggests that direct deposition of volcanic ash, as well as products from the erosion of the arc itself, acted as the main source of material.

3.6.8 Comparison of the Gebeit Volcanic Group to other volcanic assemblages in the Red Sea Hills.

The transitional, low-K to calc-alkaline nature of the GVG differs from the more calc-alkaline Kadaweb volcanics, 110 km south of Gebeit (Klemenic et al., 1985). Age determinations on both groups indicate that the Gebeit group is older (871±73 to 832±26 Ma, Reischmann et al., 1986) than the Kadaweb group (723±4 Ma, Klemenic,1985) and differences in chemistry suggest the Kadaweb suite was derived from a more mature arc system. The Kadaweb volcanics have been compared to the younger Homogar Volcanic Group (671 Ma; Klemenic et al.,1985), 250 km south of Gebeit, which appears to be more evolved than the Kadaweb group and is believed to have been extruded along a transitional arc or continental margin (Klemenic et al.,1985). Although data are scarce, the apparent increase in arc maturity with decreasing age displayed by the Gebeit, Kadaweb and Homogar Volcanic Groups in the Red Sea Hills, is consistent with the model of Roobol et al. (1983) for the Central Arabian Shield

(3.5). This comprises progressively maturing volcanic arcs from early, immature, low-K, tholeiitic arcs (sequence C) through more mature, low-K tholeiite and calc-alkaline arcs (sequence B) to mature arcs transitional between island arcs and continental margins. The geochemistry and age of the Gebeit Volcanic Group conforms with the sequence B volcano-sedimentary complexes of Roobol et al. (1983).

3.7 Depositional Environment

From the variation in lithology, depositional structures, and textures, the general Gebeit Volcanic Group stratigraphy appears to define an upwardly coarsening and shallowing sequence which represents a transition from a submarine to a subaerial depositional environment, similar to that proposed for the Kadaweb Volcanic Group (Vail et al., 1984). Trace element discrimination plots indicate an oceanic island arc setting and, although volcanic vents may be subaerial, submarine deposition is also likely. The transitional low-K/ calc-alkaline characteristics of the hornblende phyric volcanics compared with the calc-alkaline character of the plagioclase phyric and aphyric lithologies, and the absence of any MORB-type chemical signature contradict the observations made by Reischmann et al. (1986) that the plagioclase phyric volcanics are back-arc basinal in origin. However, the Gebeit Volcanic Group is well preserved and it is likely that it was deposited in a marginal basin as volcanics on the arc axis tend to get uplifted and eroded. To the north-west of Gebeit, the linear, north-east-trending zone of syn-tectonic granitoid batholiths are considered to represent the plutonic core of an eroded arc axis (Gass,1982). The north-west boundary of this granitoid zone is defined by the Bi'r Umq-Port Sudan suture which is believed to represent a zone of south-east directed subduction (Fitches et al.,1983; Camp,1984). By analogy with present day marginal basins, the area around Gebeit thus correlates with the palaeo-back-arc basin but geochemical signatures suggest the GVG was largely derived from the volcanic arc (to the north-west?) and not from back-arc spreading. Thus, a back-arc depositional environment is postulated but not on the basis of geochemistry.

The calc-alkaline nature of the lower plagioclase and aphyric units imply that highly explosive eruptions created large volumes of ash (Fischer & Schminke, 1984) deposited with shales into adjacent basins producing the characteristics of submarine fall-out tephra

(Table 3.5). Rip-up clast units suggest that debris (pyroclastic?) flows were active which, along with slumping and cross-lamination, may be either primary depositional textures or due to reworking by currents (Fig.3.12). The apparent lack of widespread hydroclastic textures, the high vesiculation in agglomerates and flows, and the presence of basal cumulate flows and crystal-rich volcaniclastics indicate that the upper eruptive source was subaerial and nearby. Because the Gebeit succession appears to grade in most cases directly from submarine to subaerial, the environment of deposition was probably within and around a shallow marine basin on the slopes of the arc.

The north-east-trending marble and quartzite belts 15km east and west of Gebeit suggest shallower water conditions compared to the lower sequence of the GVG. Quartzites have also been identified 8 km from Gebeit (Wadi Yemomt) interbedded with volcanic horizons and these are reported to indicate palaeo-basin margin areas (Gass, 1955).

Characteristics of submarine fallout tephra
- Distribution of fallout sheets may be modified by water currents. - Thickness of single layers <50 cm. Thick layers with many thin laminae may be multiple fall units. - Normal grading from crystal and lithic rich bases to shard-rich tops. - Basal contacts sharp. - Structures on land-based outcrops may include post-depositional thickening, thinning and flow structures, especially if diagenetically altered. - May include water escape structures and load or slump structures. - Sorting generally good. - Tephra is commonly interbedded with pelagic, calcareous or siliceous oozes, or with terrigenous muds and silts depending on proximity to land. Terrigenous materials are commonly turbidites. - Ancient tephra layers on land often interbedded with non-volcanic or tuffaceous shale or siltstone.

Table 3.5 Characteristics of submarine fallout tephra also displayed by lower succession of Gebeit Volcanic Group (after Fischer and Schminke, 1984).

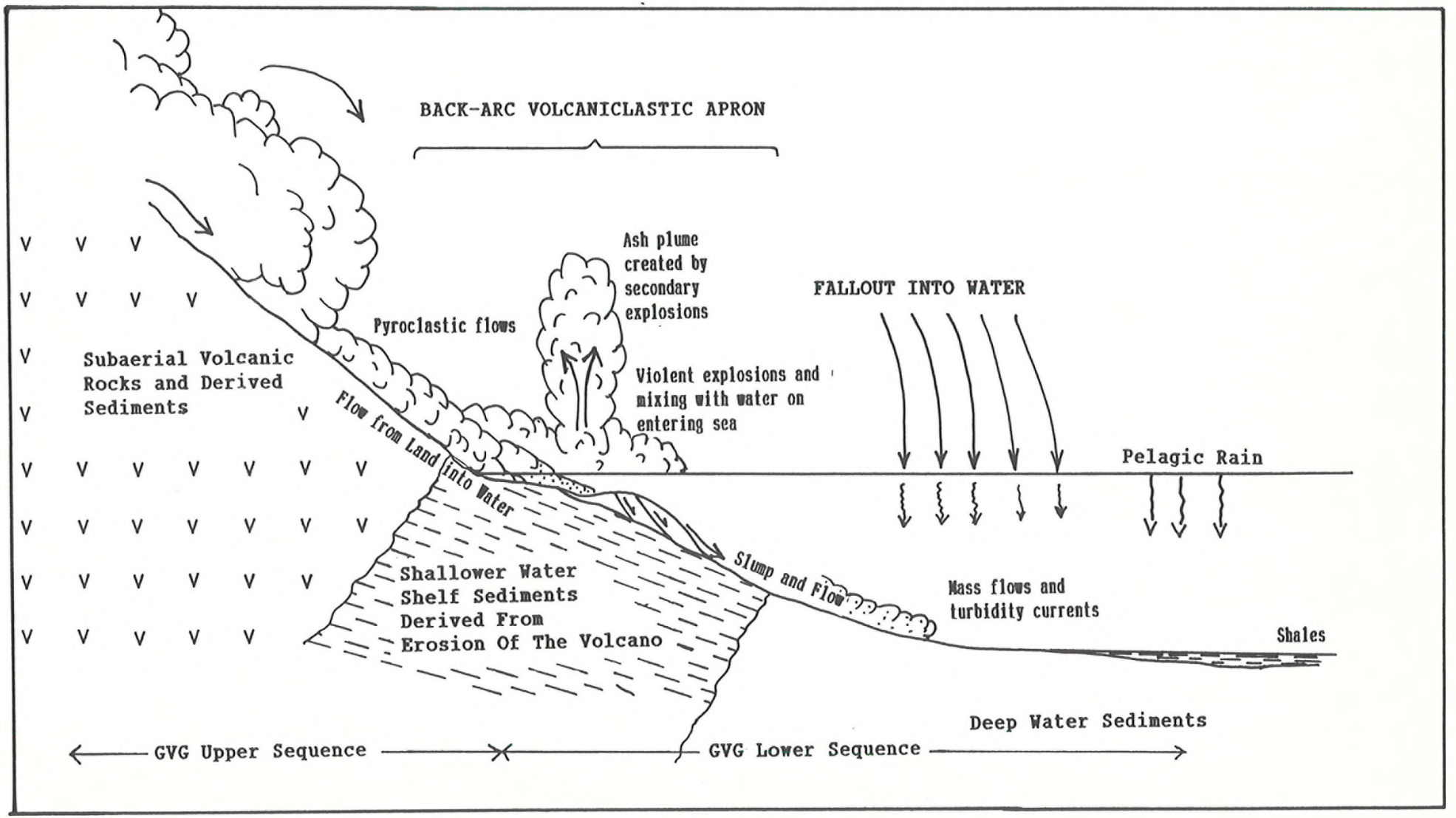

Fig.3.12 Depositional environment proposed for the Gebeit Volcanic Group (after Fisher,1985; Fisher & Schmincke,1984; Cas & Wright,1987)

3.8 Summary of the Gebeit Volcanic Group

Due to difficulties in stratigraphic correlation, the local succession has been designated the Gebeit Volcanic Group. The essential characteristics of the volcanic lithologies at Gebeit are:

i) three distinguishable petrographic groups:
   a) plagioclase phyric and aphyric fine and coarse tuffs,
   b) hornblende- and clinopyroxene-phyric tuffs, flows, lapilli-tuffs and agglomerates.
   c) minor carbonaceous shales,

ii) All volcanic lithologies plot as upper Proterozoic, oceanic, island arc basaltic andesites, transitional between low-K tholeiite and calc-alkaline in affinity.

iii) The stratigraphy represents a shallowing sequence from the submarine-deposited aphyric and plagioclase phyric tuffs and black shales at the base, to the predominantly subaerial hornblende phyric flows, tuffs and agglomerates at the top.

iv) The Gebeit Volcanic Group appears to have been deposited in a shallow marginal back-arc basin on the south-eastern flank of a relatively immature, palaeo-oceanic arc.

v) Metamorphism was to lower greenschist facies grade.

Chapter 4

Intrusive Lithologies

4.1 Introduction

Generally, granitoids comprise up to 60% of the outcrop area within the Red Sea Hills and contiguous terranes. However, known sites of gold mineralisation are generally restricted to the volcanic successions. Although large-scale mapping (1:250000, Geosurvey,1983; 1:100000, Technoexport,1978) has not identified any intrusive complexes within the Gebeit area, detailed mapping of the area around the mine (1:1000, Robertson Research,1983; this study) and reconnaisance mapping of satellite gold prospects has shown that several phases of intrusive magmatism are present.

Owing to the structural complexity of the Gebeit area, the earliest formed structures, including those which focussed and now host economic gold mineralisation, have been continually reactivated. As a result of the protracted tectonic and magmatic evolution of the area, various distinct phases of dyke and stock emplacement have been identified which pre- and post-dated auriferous vein formation. The inter-relationship between structure, vein-formation and intrusive magmatism can be used to determine the age of mineralisation more specifically.

In order to elucidate the pre- to post-collisional magmatic evolution, the petrography and geochemistry of each intrusive group has been characterised. At Gebeit, at least four distinct phases of dyke and stock emplacement are evident;

a) an early calc-alkaline dolerite, microdiorite, granodiorite, tonalite association,
b) an intermediate, late-tectonic, phase of dolerites and granodiorites with more evolved, transitional geochemical signatures,
c) post-tectonic, within-plate, alkaline gabbro, dolerite, sodic-trachyte, and alkali-granite which probably comprise more than one phase of intrusion, and

d) a late phase of ultra-potassic trachyte dykes.

Comparisons and possible correlations have also been made with established petrographic, geochemical and geochronological data of intrusive suites in the Northern Red Sea Hills in order to constrain the timing and nature of emplacement of the Gebeit intrusive lithologies. However, as the intrusions at Gebeit form only a relatively minor component, it is beyond the scope of this project to analyse these units in great detail.

4.2 Plutonic Magmatism in the Nubian-Arabian Shield

In the Nubian and Arabian Shields, plutonic assemblages have been broadly assigned to two phases of emplacement known as Older and Younger Granites (Almond,1979). In Saudi Arabia, where the majority of research has been concentrated, the older granitoids (900-715 Ma) have been subdivided into an early trondjhemite association and a slightly younger calc-alkaline granodiorite association (Table 4.1; Greenwood et al.,1976; Jackson et al.,1984; Jackson,1986a). The older trondjhemite association, comprising calcic gabbro-diorite or gabbro-diorite-tonalite-trondjhemite suites, are depleted in K, Ba, Ce, F, Li, La, Nb, Rb, Y and Zr relative to the more evolved granodiorite assemblage of gabbro-diorite-tonalite-granodiorite ± monzogranite (Marzouki et al.,1982). The early arc-stage plutonic magmas were controlled by subduction-related processes and were emplaced in contemporary, immature to mature, island arcs (Brown,1982; Brown et al., 1984). These associations represent the products of mantle (gabbro-diorite) and crustal (tonalite-trondjhemite-granodiorite) partial melting, modified by fractionation processes (Jackson,1986a), and in the Nubian Shield are recognised as the batholithic, predominantly granodiorite, assemblages of the Eastern Desert of Egypt (715-665 Ma; Stern & Hedge,1985) and the Red Sea Hills, Sudan (c.815-724; Neary et al.,1976; Klemenic,1988). In the Northern Red Sea Hills, the north-east-trending syn-orogenic batholiths are composed of biotite-hornblende lithologies which developed from early gabbro-diorite-granodiorite plutonism to more evolved granites at c.700 Ma. Both groups have significantly low K_2O, Rb, Nb and Y contents (Neary et al.,1976), similar to the calc-alkaline Arabian assemblages. Numerous orogenic to post-orogenic dyke swarms, ranging from basalt to rhyolite in composition, have been identified in the Red Sea Hills, and these preferentially intrude the orogenic batholiths and post-orogenic ring complexes (Vail et

	Petrologic Association	Rock Types	Melting Process	Protolith
'Island arc stage'	Trondjhemite association	tonalite, trondjhemite, minor gabbro	simple fusion	immature,low-K tholeiitic arc
	Granodiorite association	gabbro,diorite, tonalite and granodiorite	simple fusion	mature, calc-alkaline, arc crust
'Post-accretion stage'	Monzogranite association	monzogranite, granodiorite, syenogranite	simple fusion	mature,island arc & continental crust
		gabbro,syenite & anorthosite	reaction melting and hybridisation	
	Alkali-feldspar granite association	alkali-feldspar granite and syenogranite	simple fusion	continental crust, previously fused mature arc and continental crust
	Alkali-granite association	alkali granite, alkali-feldspar granite and syenite	simple fusion	

Table 4.1 Formation and evolution of late-Precambrian plutonic associations in the Arabian Shield, also applicable to the Northern Red Sea Hills (after Jackson et al., 1984; and Jackson, 1986a).

Complex	Lithology	Age, Ma
Jebel Tagoti	Coarse microcline granite	552
Jebel Um Arad	Granophyric biotite granite	508
Salala	Ring complex: Anorthositic Gabbro	550,517
	Granite	542
	Syenite	462,411
	Nepheline syenite	226
Jebel Ankur	Gabbro	237
	Syenite	144,115
Jebel Erbairi	Aegerine-quartz syenite	147

Table 4.2 Summary of the main post-orogenic and anorogenic complexes dated around Gebeit, 21°00'-21°30'N, 36°00'-37°00'E (after Gass, 1955; Vail,1976; Neary et al.,1976). Locations are detailed in Figure 4.1.

al.,1984). The various generations have variable orientations (NW-SE, N-S and E-W), with the basic dykes usually being older, and some have been dated at between 740 Ma (Whiteman,1968), 725±23 Ma (Vail et al.,1984) and 660±19 to 616±18 Ma (Vail & Hughes,1977).

Post-orogenic magmatism in Saudi Arabia is confined to the period 700-517 Ma and comprises monzogranite-syenite and alkali-feldspar granite associations in addition to an alkali granite association (Jackson et al.,1984). Crustal fusion events, allied with variations in the nature of the protolith (i.e. tholeiitic and calc-alkaline island arc crust and continental crust), the degree of melting, and differentiation have resulted in a great diversity of rock types. Low-K tonalites are considered to be produced from primitive tholeiitic arc crust whereas moderately potassic to potassic, I-type monzogranites, syenogranites, granodiorites and alkali-feldspar granites are derivatives from fusion and differentiation of calc-alkaline arc crust and continental crust (Jackson et al.,1984). Post-collisional partial melting of a crust relatively deficient in water and radio-elements is unlikely under normal geothermal gradients, and the large-scale, post-orogenic crustal fusion event has been attributed to the introduction of large volumes of mafic magma into the lower and middle crust (Jackson et al.,1984; Hildreth,1981; O'Halloran,1985). Reaction melting involving alkali basic magma was probably an important process in the formation of gabbro-anorthosite-syenite intrusions, rocks of the monzogranite association (monzogranite, granodiorite, syenogranite and quartz monzonite) and the bimodal series of Sequence A volcanics (Jackson,1986a; see 3.5). Residual protoliths remaining after the extraction of initial fusion products are poor in volatiles and alkalis and rich in refractory phases such as calcic plagioclase, pyroxene, amphibole, sphene, magnetite, apatite and zircon (Collins et al.,1982). Compared with a subduction environment, within-plate magmatism has no equivalent hydrous volatile reservoir and, consequently, volatile phases are enriched in CO_2 and F. Input of sufficient volatiles from a degassing mafic magma coupled with further heat input allows re-melting of the residual refractory protoliths to occur (Jackson,1986a). High field strength (HFS) elements (e.g. REE, Nb, Y, and Zr) complex with CO_2 and F producing HFS element-rich residual melts of the alkali (A-type) granite association which also tend to be low in Ca, Al, and Mg due to their retention in refractory calcic-plagioclase and pyroxene (Harris,1982).

Similarly, in the Red Sea Hills, post-orogenic alkaline plutonism

occurred from c.530-500 Ma during the later stages of subduction-related magmatism coincident with the emplacement, in zones parallel to suture zones, of calc-alkaline, gabbro-granite ring complexes (Delany,1955; Vail,1973,1976,1982,1989; Vail & Kuron,1978; Harris, 1982). There are, however, certain differences between alkaline magmatism in the Nubian and Arabian portions of the shield. Anorogenic alkali granite-syenite ring complexes formed in two further cycles in the Nubian Shield (phase 2 and 3 of the Younger Granites; Harris,1982) around 250-222 Ma (central Sudan) and 150-89 Ma (eastern Sudan) with the latter event being accompanied by north-south-trending trachyte and microsyenite dyke swarms (Stoeser & Elliot,1980; Vail,1985c). The main post-orogenic, calc-alkaline and anorogenic, alkaline ring complexes and circular masses which occur within the volcanic succession around Gebeit are summarised in Table 4.2 and shown in Fig.4.1. These complexes comprise late- to post-orogenic gabbros and granites dated at 550-508 Ma (Tagoti, Um Arad and Salala) and anorogenic gabbros and syenites ranging from 237 to 115 Ma in age (Salala, Ankur and Erbairi; Vail,1976).

4.3 Petrography and Field Descriptions of the Gebeit Suites

Field mapping of the intrusive lithologies is considerably easier than the Gebeit Volcanic Group rocks as most phases tend to follow major structural trends along wadis. The basic dykes tend to create saddles across ridges and depressions in outcrops of the shear zone phyllonites. Conversely, the more acidic intrusions often stand proud of the host volcanic rocks. In most cases, especially with the earlier phases of intrusion, classification of the Gebeit rocks has been hindered by pervasive propylitic alteration and by the fine-grained nature of many of the lithologies. The intrusions, dominated by various phases of dyke emplacement, were subdivided in the field by lithology and relation to local structural controls, and have subsequently been classified and grouped using thin section petrography, X-ray diffraction studies, and trace element geochemistry.

4.3.1 Phase 1 Dolerites, Microdiorites and Related Intrusions

In the immediate mine area defined by the shear zone boundaries of the Gebeit tectonic block, this suite comprises an intrusive phase of

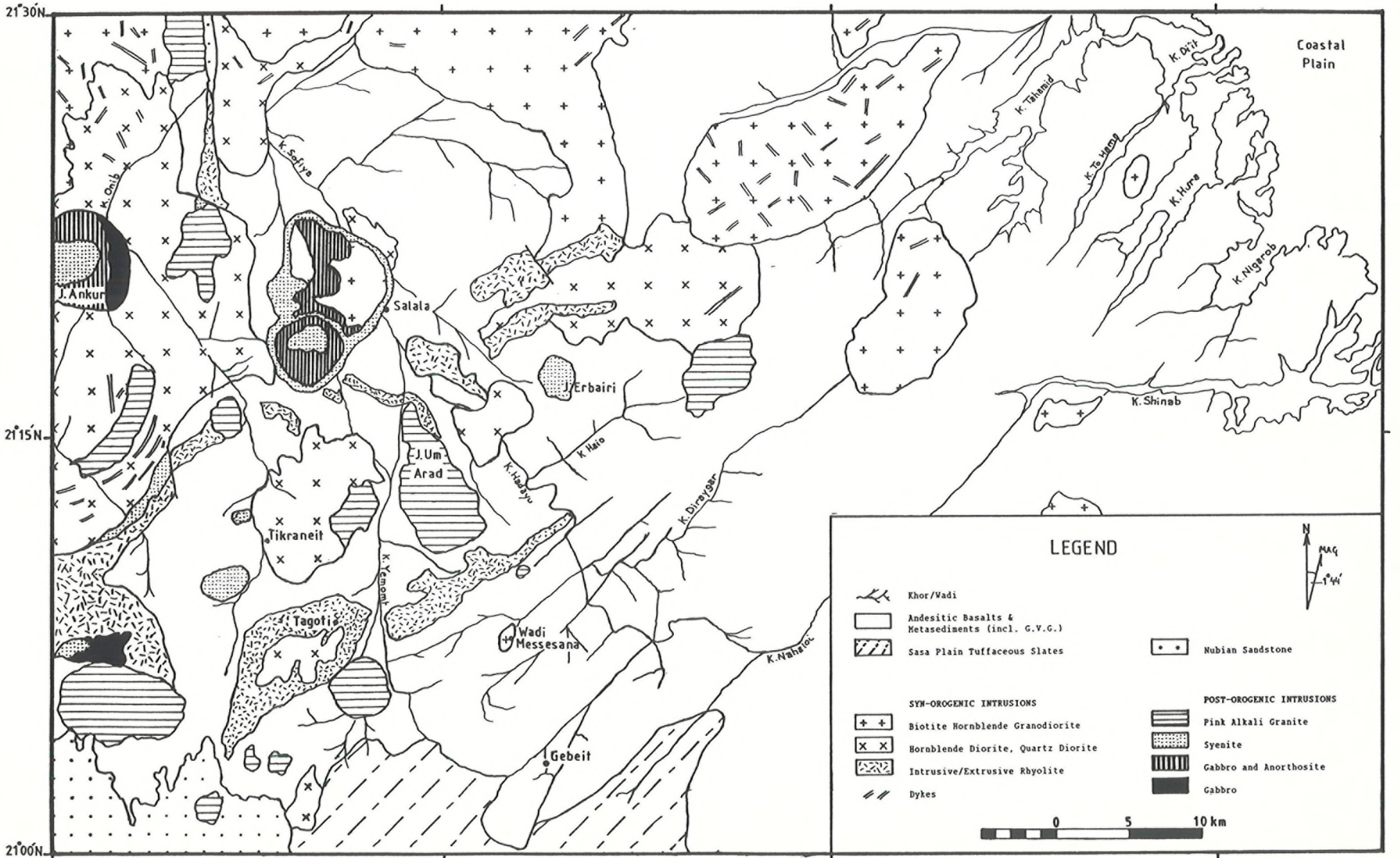

Fig.4.1 Geology of the area around Gebeit with emphasis on the intrusive lithologies (this study and after Gass,1955; Whiteman,1971; Neary et al.,1976; Geosurvey,1983; Ahmed,1984).

dolerite and microdiorite dykes which are confined to many of the major north-east-trending, carbonatised shear zones (Fig.4.2). They invariably occur parallel to the main c-fabric of these shear zones and, though not pervasively deformed, these units have undergone at least one further phase of faulting and/or folding. The early emplacement of these dykes along the shear zones has proved invaluable in identifying post-D_2 structures which can otherwise be fairly cryptic. Although the more leucocratic microdiorites can be distinguished from the finer-grained, darker dolerites, they cannot be separated in terms of age of emplacement. Outcrops along the Wadi Lode shear zone from Wadi Lode Extension to West Gebeit (Plate 4.1a, Fig.4.3 along grid line 5000E) are often fragmented, having been affected by north-south-trending normal faulting, white quartz veining, and stacking due to north-east-trending, imbricate thrusting (5050E, 5300N; 4900E,5400N).

At West Gebeit (4700E,4900N), a phase 1 dolerite dyke, which lies parallel to the steep main NNE-trending c-fabric, is transected by a shallow south-easterly dipping, coarse cleavage (5-15 cm) with associated fine white quartz-carbonate stringers. Along the centre of this dyke runs a vein of coarse-grained sericite and along strike to the south-west the dyke is isoclinally folded and faulted around shallow, north-east- and north-south-trending axes. Similar structures have been observed along strike-parallel shear zones at Bishops Dam (4000E,6000N-4500E,6500N) and along the North Gebeit shear zone at the confluence of Wadi Gebeit and Wadi East Gebeit (Fig.4.2; 4000E,8250N). At these localities the lower surfaces of the dykes appear to have been reactivated as fault surfaces and are now defined by quartz veining (see 5.6.2). In areas where the shear zones have undergone pervasive carbonate alteration, the dykes also display varying degrees of alteration, indicating that emplacement occurred prior to the main phase of carbonate alteration.

In thin section, the slightly coarser-grained, equigranular (1-2mm) microdiorites are generally propylitised, composed of quartz, euhedral to subhedral albitic plagioclase feldspar (50-60%), and minor sericite and epidote with chlorite (20-30%), calcite and iron oxides replacing all the original ferromagnesian phases (Plate 4.1b). The more mafic dolerites comprise the same mineralogy but contain higher amounts of chlorite and iron oxides and less quartz. To the east of Marble Bar (4840E,6050N), the dolerite intruded along the shear zone that forms the southern limit to the prospect contains a more

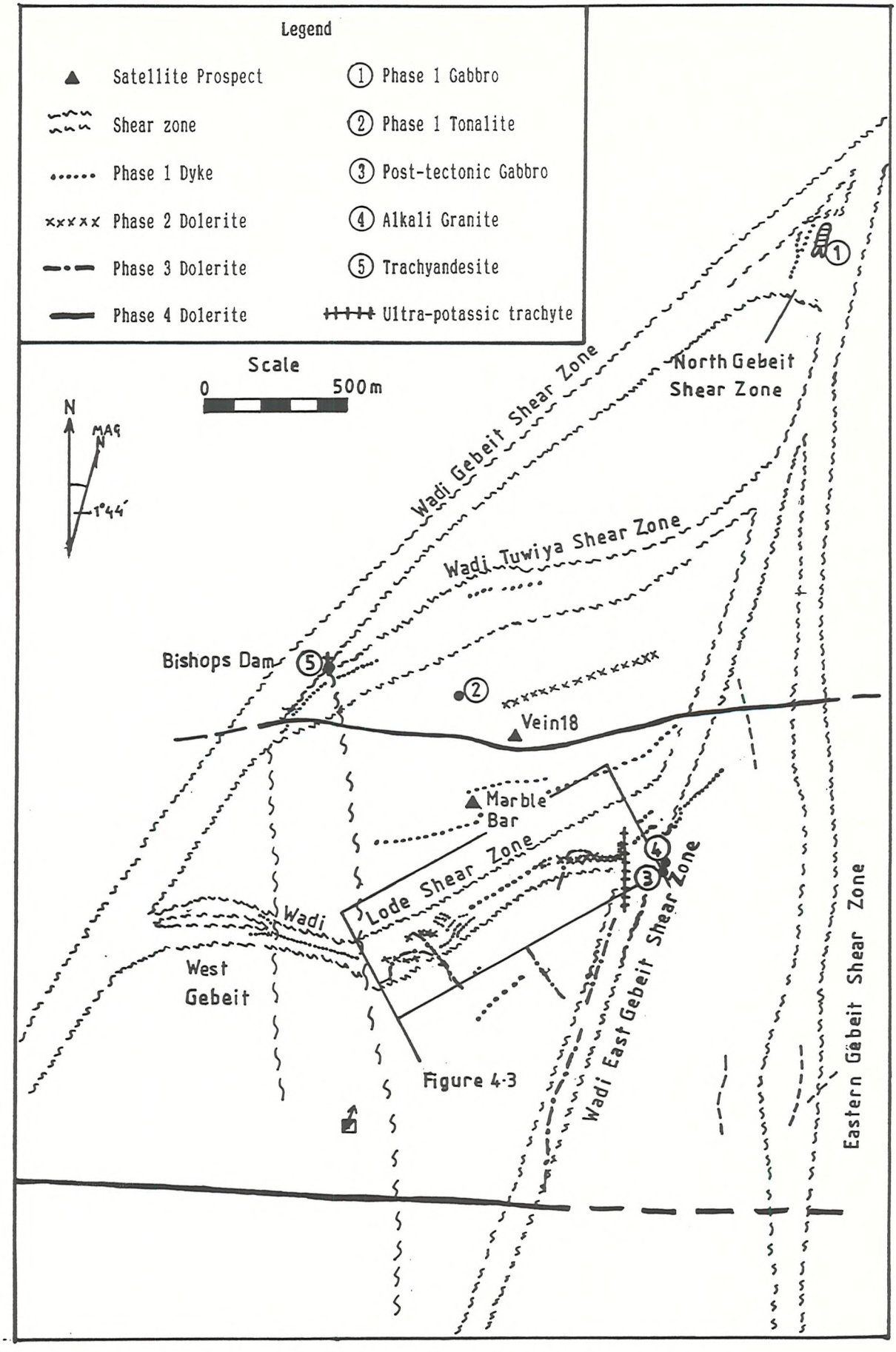

Fig.4.2 Location map of intrusions in the Gebeit area showing the close association between intrusions and D_2 shear zones.

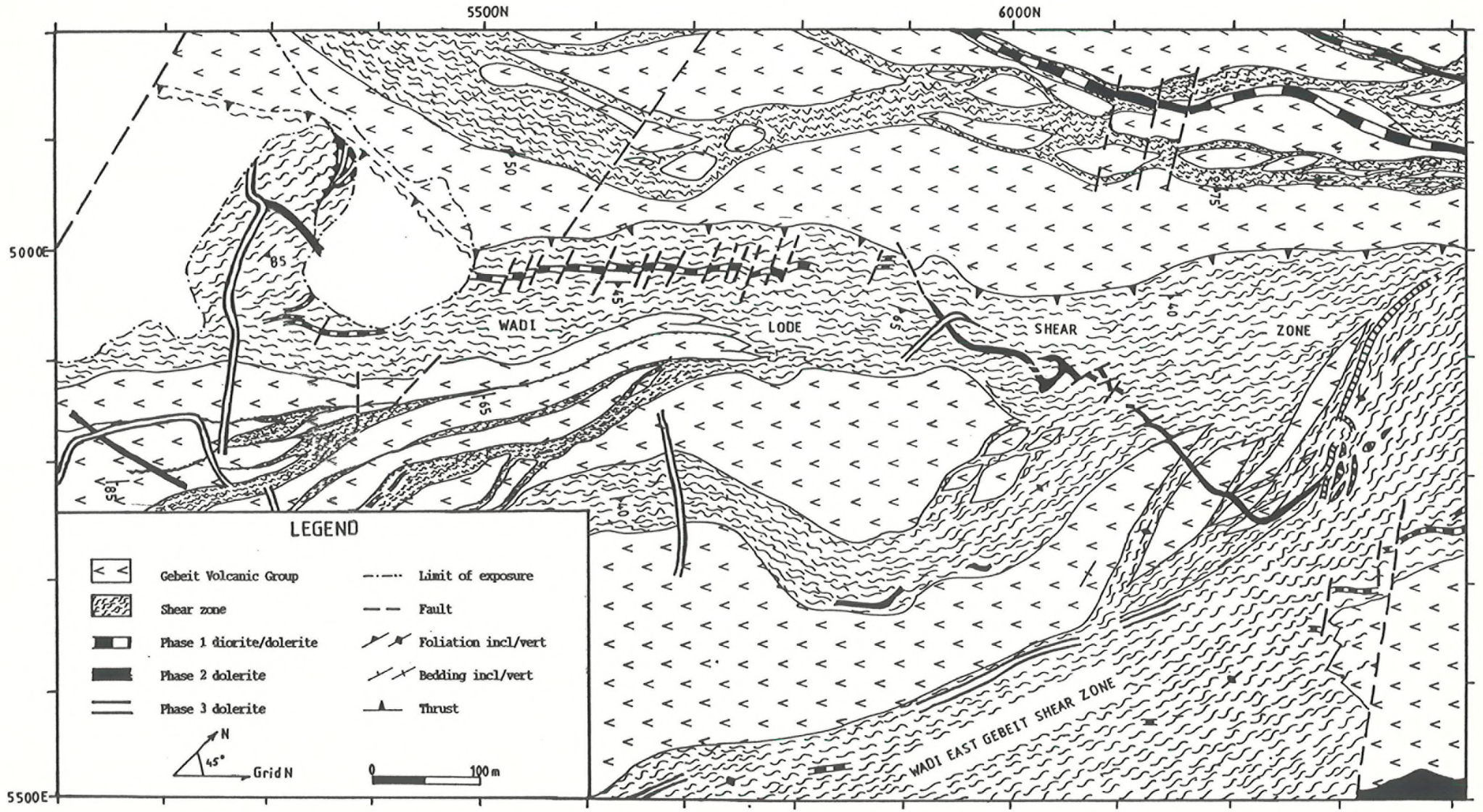

Fig.4.3 Map of the Wadi Lode Extension (4800-5500E,5100-6400N), showing the controls and relationships of the dykes from Phases 1 to 3.

Plate 4.1 Structural control and petrography of the phase 1 calc-alkaline dykes at Gebeit.

a) View south-east from Marble Bar (4900E, 5700N) towards the red ankerite phyllonites of the Wadi Lode shear zone (5000E,5750N to 5000E, 5200N) showing the phase 1 calc-alkaline diorite dyke (Di) and its fragmentation by D_2 antithetic shears (s) (see Fig.4.3).

b) Hand specimen (left) and photomicrograph (CN; right) of phase 1 micro-diorite dyke from the Wadi Lode shear zone showing incipient carbonatisation (cb; field of view of photomicrograph 5mm).

c) Photomicrograph (CN) of phase 1 hornblende-actinolite dolerite from Marble Bar (4850E,6000N; field of view 15mm).

CN = crossed Nicols, PPL = plane-polarised light.

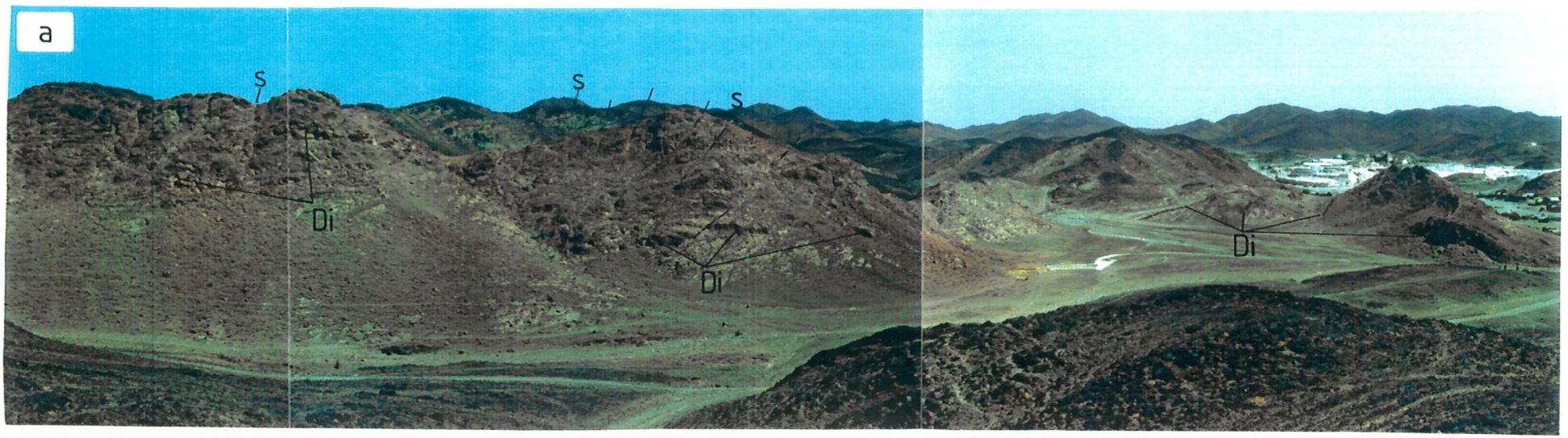
a
S
S
S
Di
Di
Di

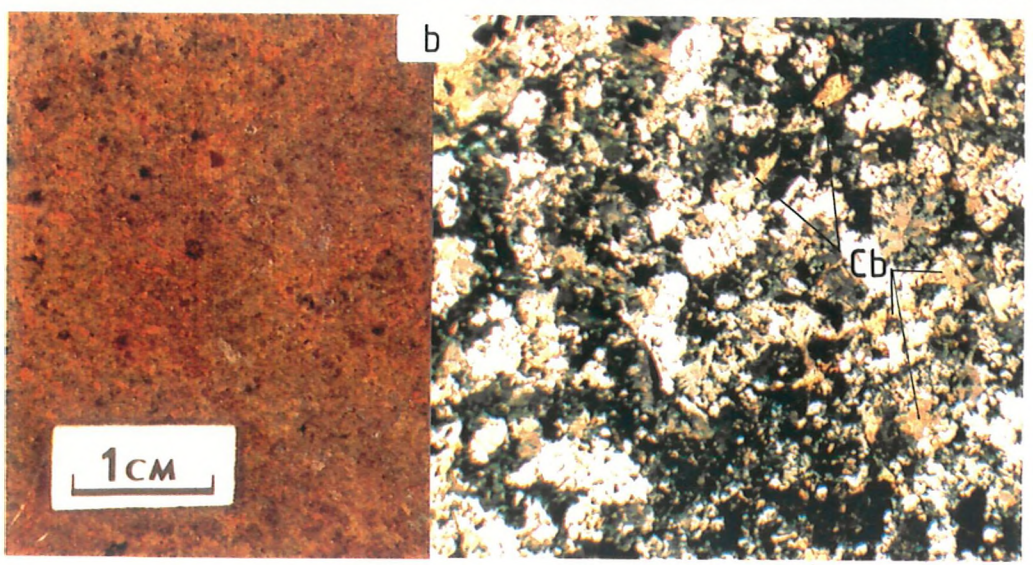
b
1см
Cb


c

leucocratic, less altered centre in which the original euhedral hornblende (up to 3mm long) and biotite phases are only partially replaced (uralitised) by actinolite and chlorite (Plate 4.1c). The most highly altered dykes, located in blocky carbonatised chlorite phyllonites which comprise the shear zones, are paler in colouration due to a similar but much less intense carbonate metasomatism. Where carbonate is present, ankerite is the dominant phase but this alteration is far less pervasive than that observed in the phyllonites (see 7.8) and probably reflects the much less permeable nature of the unsheared massive dykes.

In addition to the dolerite and microdiorite dykes are two small intrusive bodies which appear to be contemporaneous with phase 1 and have been classified as such due to their geochemical affinities (see 4.4.1). At the junction of Wadi Gebeit and Wadi East Gebeit lies an elongate (100m x 10m), possibly folded, medium-grained gabbro which strikes parallel to the main fabric (Fig.4.2). It comprises the characteristic greenschist facies assemblage of saussuritised calcic plagioclase and hornblende with relict pyroxenes altered to epidote, actinolite and chlorite and groundmass grains of epidote, zoisite, actinolite, chlorite and calcite. The lack of pervasive carbonate alteration of this intrusion, however, suggests it was emplaced after the main phase of carbonatisation.

The timing of intrusion of phase 1 lithologies can be constrained to post-dating the formation of north-east-trending shear zone fabrics during D_1 and early-D_2 deformation and pre-dating a phase of intense carbonate alteration followed by thrusting. This indicates that emplacement of phase 1-type intrusions at Gebeit occurred at roughly the same time as the auriferous mineralisation. Although wide-scale carbonate alteration is characteristic of many gold deposits world-wide (e.g. Colvine et al., 1984), the intense carbonatisation at Gebeit does not occur in association with the lode veins and hence may not be coeval with the main stage of gold mineralisation (see Chapter 7). Thus, as no contact between dykes of proven phase 1 affinity and auriferous lode veins has been observed, the exact timing of emplacement of phase 1 dykes relative to the main gold precipitation event is unclear.

At the two small Pharonic satellite prospects of Wadi Messesana and Tikraneit (Fig.4.1), elongate bodies of calc-alkaline granodiorites and diorites respectively form the host lithologies. Mineralisation is confined to shear zone-hosted auriferous white quartz veins which trend

NE (Wadi Messesana) and NW (Tikraneit), indicative of a phase of intrusion prior to the gold mineralisation. Although both prospects appear to have the same structural controls as at Gebeit, suggesting a coeval development, fluid inclusion and stable isotope studies could not be used (see 6.9 and 6.10) to confirm this. At the Vein 18 area of Gebeit (Fig.4.2), however, a small (25x25 m) tonalite body has been intruded through the fabric of the south-easterly dipping shear zone east of Wadi Tuwiya and contains rounded xenoliths (up to 30 cm long) of vein quartz. This indicates that emplacement of the earliest phases of plutonism in the area were approximately synchronous with mineralisation, occurring before and after formation of the auriferous veins.

4.3.2 Phase 2 Dolerites and Related Intrusions

This phase of emplacement was initially defined by the cross-cutting relationships displayed at the north-south phyllonite ridge immediately east of Gebeit village (Fig.4.3; 4900-5000E,5300-5400N). At this location, the thrust structures which displace the phase 1 microdiorite dyke are cross-cut by an east-west-trending undeformed dolerite dyke enveloped by massive white quartz veins. This second phase of dyke intrusion is itself transected by a north-west-trending vesicular dolerite related to a third phase of dolerite intrusion. Intrusions of this intermediate second phase of magmatism cannot be differentiated from the other dolerites petrographically but tend to occupy reactivated extensional structures, trending E-W, oblique to the shear zone c-fabric.

Phase 2 dolerite dykes observed underground always cross-cut the auriferous quartz veins (see Fig.5.15) and display fine (<1 cm) chilled margins (Plate 4.2a). The dyke outcroping at 5150E,5130N (Fig.4.3) can be traced down to intersections at 4 and 5 levels of the Wadi Lode, confirming emplacement after thrusting. Although post-dating mineralisation, the fine-grained dolerites are often hydrothermally altered, resulting in a quartz, chlorite, albitic plagioclase, sericite and Fe-calcite ± epidote mineralogy. These dykes are late-tectonic in age but are affected by late, minor, north-west-and east-west-trending normal faults and north-east-trending dextral faulting which probably occurred as a result of reactivation of D_2 structures during post-D_3 strike-slip deformation (see 5.6.1). The phase 2 dolerite at the end of the Wadi Lode Extension (Fig.4.3; 5100E, 6000N) is confined to the

Plate 4.2 Petrography of the alkaline intrusions at Gebeit.

a) Contact of phase 2 dolerite (showing 2-3cm chilled margins) and graphitic shales exposed on 4-level Wadi Lode (see Fig.5.15).

b) Photomicrograph (CN) of fresh phase 4 analcime-olivine dolerite at Vein 18 (4600E,6150N; field of view 15mm).

c) Photomicrograph (CN) of post-tectonic, anorthositic olivine-analcime gabbro showing minor alteration of clinopyroxene and olivine and saussuritisation of the plagioclase (Wadi East Gebeit, 5500E, 6500N; field of view 20mm)

d) Photomicrograph (CN) of altered vesicular phase 3 alkaline dolerite from Wadi East Gebeit (5400E,6020N; field of view 8mm).

e) Photomicrograph (CN) of alkali-granite from East Gebeit (5500E,6400N) showing ferriferous orthoclase with interstitial quartz, and sericite with minor aegirine and chlorite (field of view 27mm).

f) Photomicrograph (CN) of late ultra-potassic trachyte dyke from Wadi East Gebeit (5150E,6350N) showing sanidine phenocrysts sets in a trachytic groundmass of sanidine laths with minor interstitial quartz, sericite, aegirine, and chlorite (field of view 12mm).

CN = crossed Nicols, PPL = plane-polarised light.

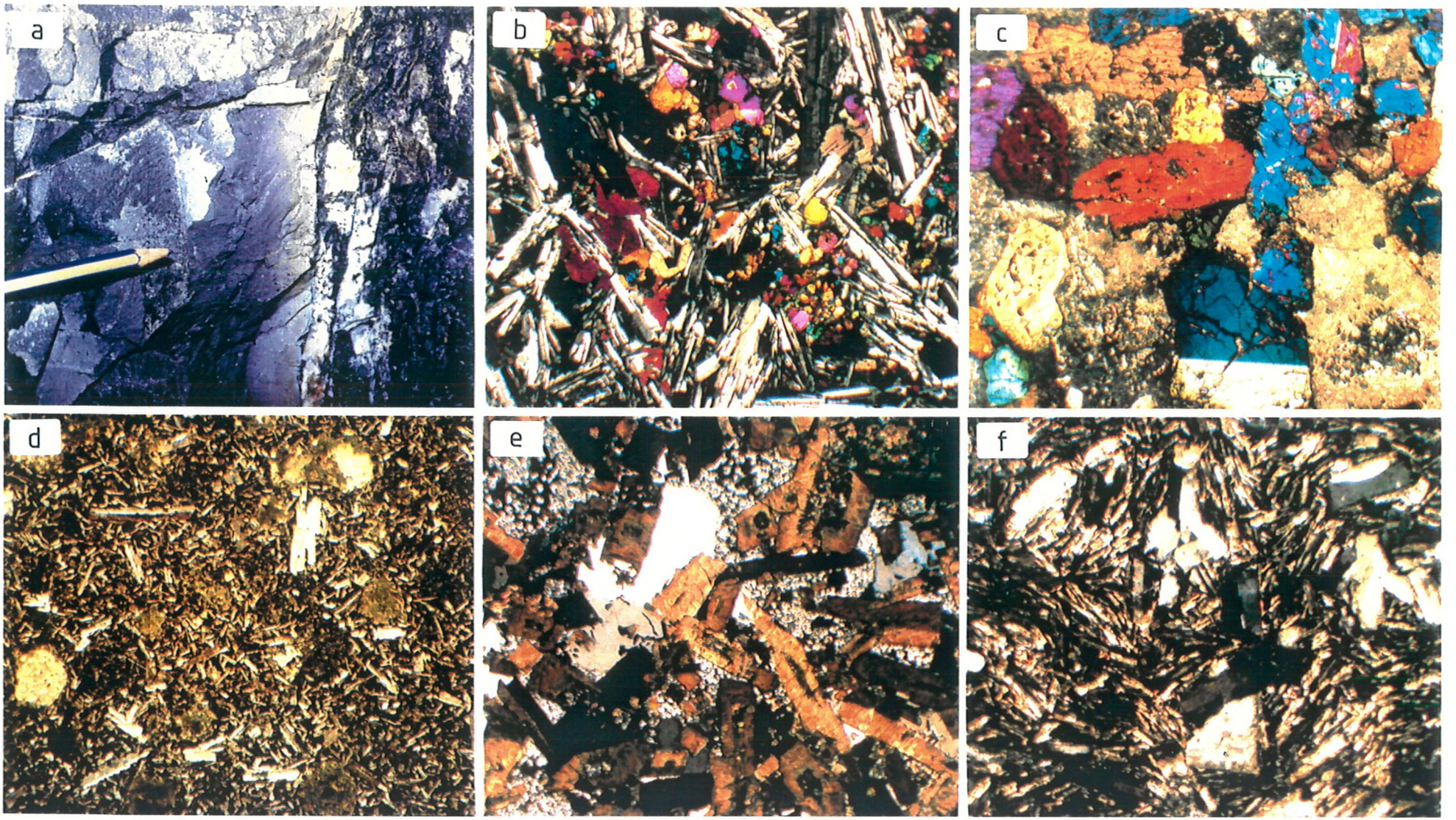
a
b
c
d
e
f

Wadi Lode shear zone and is also transected at 90° by a phase 3 dolerite. The orientation of the phase 2 dyke within the shear zone and its fragmentation by dextral D-shears parallel to the c-fabric suggest that emplacement was coeval with the post-D_3 dextral deformation (see Fig.5.16). As the east-west-trending, phase 2 dolerites are late-tectonic in age, they may belong to the same phase of east-west-trending basic dykes dated at 740±80 Ma (Whiteman,1968) which intrude the batholithic granites.

At Tagoti West, a vertical granodiorite dyke trending NNE, has been intruded into sheared andesitic tuffs parallel to a massive white quartz vein, indicative also of structural reactivation. Similarly, 4 km to the south-west of Gebeit on the Sasa Plain, a 30 m wide, southerly-dipping biotite-granodiorite dyke appears to have been emplaced along an ENE-trending reactivated thrust structure. In both cases, the mineralogy comprises quartz, sericitised albitic plagioclase, chlorite, carbonate and epidote with the addition of actinolite at Tagoti and euhedral biotite in the Sasa Plain dyke.

4.3.3 Post-Tectonic Dolerites

The post-tectonic phase(s) of dolerite dyke emplacement produced a series of north-west-, north-south-, north-east- and east-west-trending dykes which partly cross-cut and in places reactivate the older structures. Although grouped together as post-tectonic alkaline dolerites, these intrusions probably represent more than one phase of emplacement. At Vein 18 (4620E,6250N) the dyke which transects the northern end of the prospect is a coarse-grained, east-west-trending, fresh olivine-analcime dolerite in which even the olivine crystals show no evidence of alteration (Plate 4.2b). The undersaturated nature of this coarse-grained intrusion, coupled with its lack of any observable alteration, suggests it is relatively young and may be related to the post-30 Ma alkali basalts associated with the opening of the Red Sea (Gass,1955; Harris, 1982).

Similarly, a coarse-grained anorthositic olivine-analcime gabbro which outcrops on the eastern side of Wadi East Gebeit (5500E,6400N) also displays minimal chlorite and serpentine alteration of olivine grain rims and saussuritisation of the plagioclase (Plate 4.2c). This differs markedly from the other post-tectonic dolerites which tend to be finer grained, vesicular dolerites (Plate 4.2d) and have variable north-west to north-east trends. These dykes have intruded reactivated

structures such as the Wadi East Gebeit shear zone (Fig.4.3; 5500E, 5600N to 5300E, 6150N) and the reactivated north-east-trending thrusts at the Wadi Lode and Wadi Lode Extension (5150E,5200N and 5100E,5950N). At the southern end of the Wadi East Gebeit shear zone (≈5800E,5100N) the intruded dyke both parallels and cross-cuts the main shear zone fabric. This intrusion is a much coarser-grained (plagioclase 5-30mm), anorthositic gabbro which shows fine, pervasive alteration of the plagioclase phenocrysts and hematitic replacement of the interstitial mafic phases. The dyke is accompanied by coarse drusy carbonate (calcite and ankerite) veins parallel to the shear zone c-surfaces indicating repeated late-stage extension of the shear zone structures during early D_4 sinistral shearing (see 5.7.1).

The other, finer, dykes show variable alteration ranging from chlorite and serpentine replacement of the mafic phases to the addition of quartz and calcite. If these altered alkaline dykes are all of the same age, as seems likely, then they appear to represent a change to within-plate magmatism during post-collisional deformation and may be coeval with the gabbros at Salala dated at 517-550 Ma.

4.3.4 Non-specific Alkaline Intrusions

A few intrusions which can be clearly identified as being post-tectonic in age have been included in this group due to the lack of any structural or age dating criteria with which to sub-divide them. At Gebeit, these comprise a sodic trachyte at the western boundary of the Gebeit Volcanic Group and the tuffaceous slates of the Sasa Plains, and a commenditic alkali-granite at the eastern edge of Wadi East Gebeit (5500E,6400N). The sodic-trachyte occurs as a north-west trending dyke, dipping gently to the south-west at Wadi Yemomt, 4km west of Gebeit. This very fine-grained intrusion comprises riebeckite, aegerine, plagioclase and orthoclase and contains a pronounced igneous foliation. Conversely, the alkali-granite at East Gebeit is exposed as a coarse-grained (3-12mm), reddish brown, elliptical, intrusion (40x20m) composed of euhedral ferriferous orthoclase laths with interstitial quartz and sericite and minor chlorite, aegirine and Fe-oxides (Plate 4.2e) The poor exposure and close proximity of this intrusion to the anorthositic analcime-olivine gabbro suggest it may be part of a concealed multiple intrusion such as the gabbro-syenite ring complexes exposed at Salala and Jebel Ankur.

4.3.5 Late Potassic Trachytes

A set of trachyte dykes have been intruded into the north-south-striking sections of the Wadi East Gebeit and A Lode shear zones at East Gebeit and Bishops Dam (Figs.4.2 & 4.3). These dykes are petrographically similar to the alkali-granite at East Gebeit and are possibly coeval. They are composed of sanidine phenocrysts (5-9mm) set in a trachytic groundmass of sanidine laths (0.5-3mm) with interstitial quartz, sericite, aegirine and chlorite (Plate 4.2f). The dykes at East Gebeit show no obvious signs of alteration but the more basic trachy-andesite dyke at Bishops Dam is finer grained and textures are partially obscured by Fe-oxide staining. These dykes have been separated from the other alkaline intrusions because of their ultra-potassic geochemistry, trachytic textures and north-south orientation. The consistent N-S trend suggests they belong to the extensive, Mesozoic, anorogenic trachyte and microsyenite dyke swarms which are concentrated along a belt parallel to the Red Sea coast in reactivated shears similar to the Oko shear zone (see Fig.2.20; Vail et al.,1984; Almond & Ahmed,1987).

4.4 Geochemistry of the Gebeit Intrusives

Although the Gebeit intrusions have not been dated, structural relationships, correlation with intrusions studied throughout the Northern Red Sea Hills (e.g. Neary et al.,1976; Vail,1985c), and changes in the geochemical characteristics of the various lithologies allow the Gebeit rocks to be fitted into an evolutionary framework. Progressive variations in chemistry, especially in the different phases of dolerite emplacement, are largely reflected in changes in trace element concentrations. Due to the high degrees of hydrothermal alteration experienced by the older units, classification of these rocks was mainly achieved using trace element discriminant analysis. The analytical techniques employed and data precision are listed in Appendix A and a complete database of geochemical analyses can be found in Appendix B.

4.4.1 Phase 1 Intrusions

The geochemistry of the earliest phase 1 intrusions is very similar to the trends seen in the extrusive calc-alkaline Gebeit

Volcanic Group (3.6). When plotted on Zr/TiO_2-Nb/Y discriminant diagrams (Winchester & Floyd,1977), four separate groups emerge which correspond directly to the gabbros, dolerites, microdiorites and granodiorites/tonalites defined petrographically (Fig.4.4). These are distinct from the later phases of intrusion, a feature which is emphasised on fractionation trend diagrams (Fig.4.5). The calc-alkaline nature of the phase 1 suite is reflected in the low concentrations of TiO_2, P_2O_5, Nb, Y, Zr, Ce, La, Rb, and K_2O (Tables 4.3 & 4.4), similar to the low-K tholeiite and immature calc-alkaline Gebeit volcanics, and is indicative of primitive island arc plutonism. As expected, all the rocks plot within the volcanic arc field using discriminant Rb, Y, Nb, Ti, Zr diagrams for basic rocks (Pearce & Cann,1973; Meschede,1986; Fig.4.6) and granitic rocks (Pearce et al.,1984; Fig.4.7).

When normalised against ocean ridge granites the granitoid lithologies all plot as volcanic arc granites but the granodiorites from Wadi Messesana and Tikraneit appear to be more evolved than the Vein 18 tonalite and display higher Zr, Nb, Y, Rb, K_2O and TiO_2 values (Fig.4.8). This may reflect either age differences and/or source variations for the granitoids possibly as a result of increasing arc maturity with time (Brown et al.,1984). All lithologies are related to subduction-controlled magmatism and were probably emplaced as part of the plutonic phase of active arc formation. Classification of the granitic rocks using the normative albite-anorthite-orthoclase ternary diagram (Fig.4.9), however, indicates that the Vein 18 tonalite has trondjhemitic affinities (Ramsay et al.,1986) but, like the phase 1 diorites, is too basic (i.e. SiO_2 <68%, FeO_t+MgO >3.4%) to be classified strictly as a trondjhemite (Jackson,1986b).

Other granitic rocks of both phases 1 and 2 plot as granodiorites and granites and significantly contain higher concentrations of Zr, Nb, La, Ce, Rb and K_2O analogous to the granodiorite association recognised in Saudi Arabia. Notably, the only calc-alkaline granitic rock identified and sampled within the immediate mine area was the trondjhemitic Vein 18 sample which contrasts geochemically with the granitoids of granodioritic affinity which were sampled in satellite prospect and marginal areas (Sasa Plain, Wadi Messesana, Tikraneit, Tagoti West, Yemomt). Although only a limited number of samples were taken, no intrusions of trondjhemite affinity were identified outside Gebeit. This contrast may reflect the more primitive, low-K nature of the Gebeit Volcanic Group at the mine and suggests that the partially

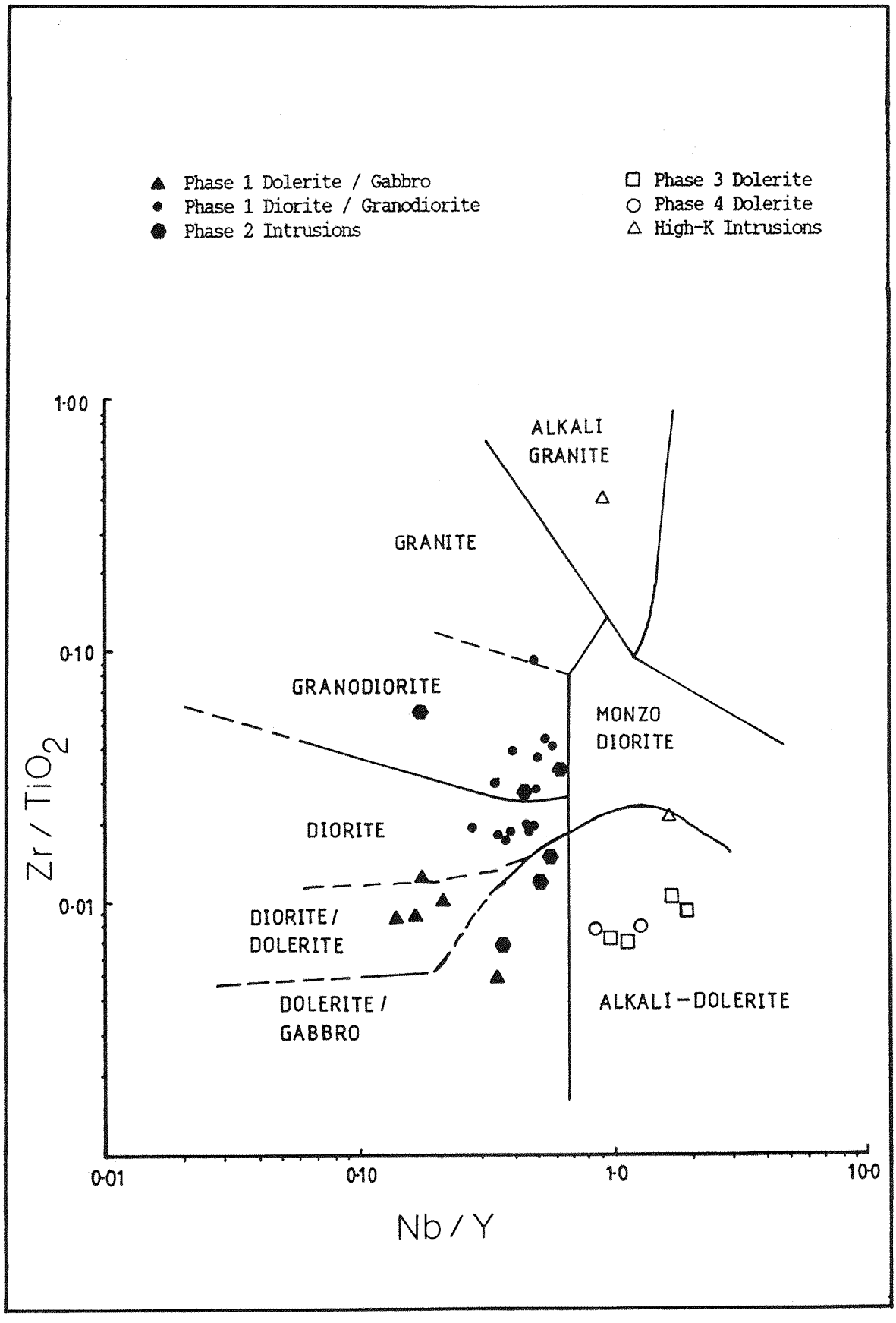

Fig.4.4 Zr/TiO_2 vs. Nb/Y discrimination plot for the Gebeit intrusions (after Winchester & Floyd,1977).

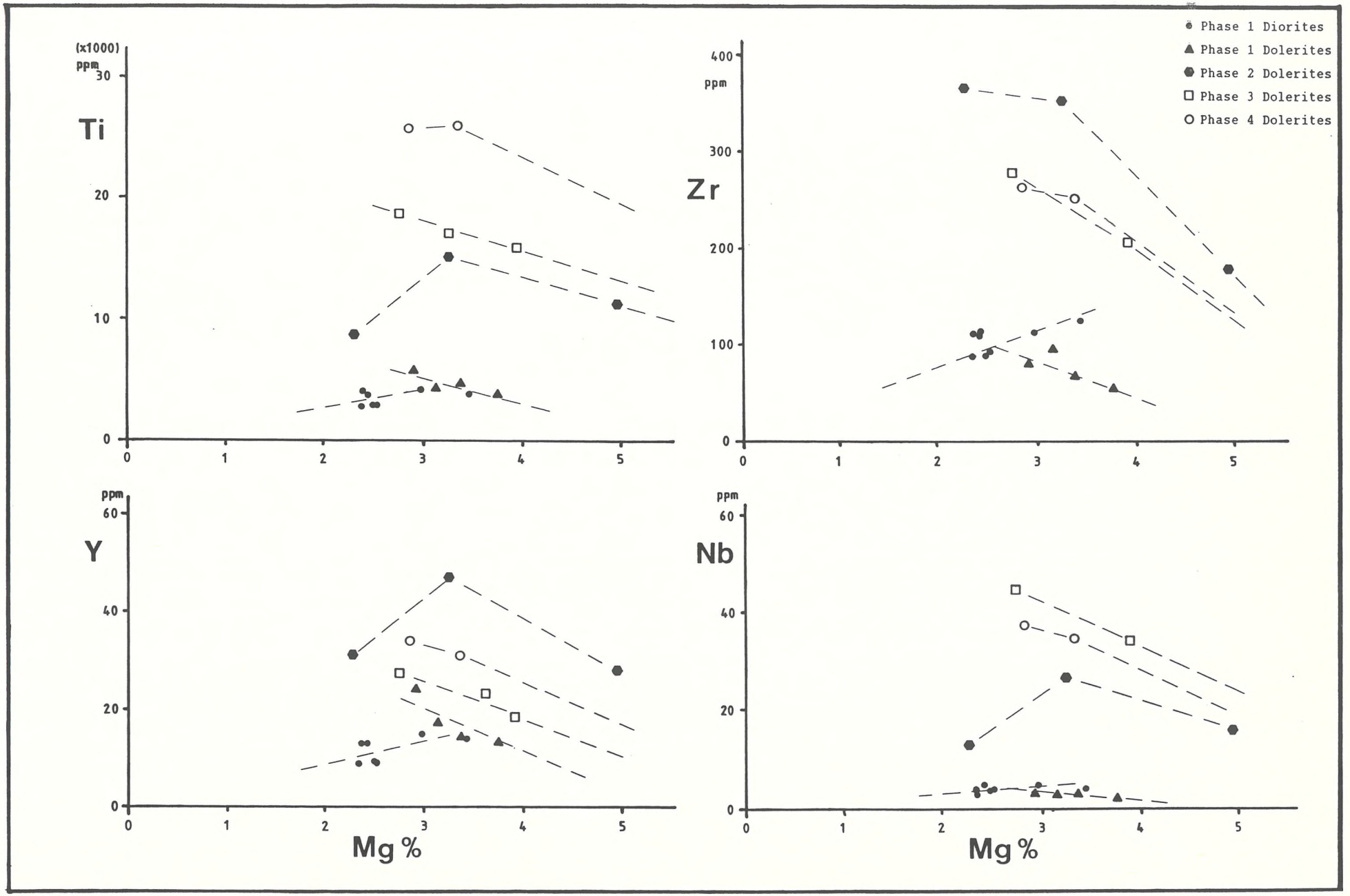

Fig.4.5 Fractionation diagrams for the basic dykes at Gebeit demonstrating four distinct phases of magmatism.

	Phase 1		Phase 2		Phase 3	Phase 4
	Dolerite n=4	Diorite n=7	Dolerite n=2	Diorite n=2	Dolerite n=4	Dolerite n=2
SiO_2 (%)	51.1	56.1	47.3	54.6	43.9	44.2
TiO_2	0.7	0.6	2.1	1.5	2.7	4.0
Al_2O_3	17.8	15.7	14.6	15.7	14.9	15.6
Fe_2O_3*	9.0	5.9	11.5	8.8	11.8	15.3
MnO	0.2	0.1	0.1	0.1	0.1	0.2
MgO	5.5	4.5	6.8	3.8	5.5	5.1
CaO	8.7	3.8	6.9	4.3	7.4	7.7
Na_2O	3.6	6.5	2.2	3.7	2.5	3.6
K_2O	0.7	0.4	1.8	2.6	2.3	1.2
P_2O_5	0.2	0.2	0.7	0.7	0.6	0.8
ΣH_2O	1.9	6.0	5.0	3.7	7.5	1.4
Total	99.4	99.8	99.0	99.7	99.2	99.1
Rb(ppm)	8	5	35	31	49	16
Sr	610	253	445	503	360	671
Ba	190	402	503	661	601	503
Pb	3	5	<3	8	<3	<3
Th	<3	<3	<3	<3	4	3
U	<5	<5	<5	<5	<5	<5
La	<6	10	31	35	35	36
Ce	10	14	53	65	53	63
Y	19	12	38	31	23	33
Zr	68	103	264	366	242	257
Nb	3	4	22	13	40	37
Ga	24	22	24	24	27	28
Ni	42	36	125	48	88	61
Cr	215	170	160	83	85	40
V	239	151	194	163	153	160
Cu	<2	24	52	42	47	41
Zn	73	74	121	129	135	129
As	30	20	<7	<7	17	<7

* Total Fe calculated as Fe_2O_3
ΣH_2O = Loss on Ignition
<3 = Below Lower Limit of Detection

Table 4.3 Comparison of Average Major and Trace Element Geochemistry for Basic and Intermediate Intrusive Suites at Gebeit.

	Syn-tectonic		Transitional	Post-Tectonic
	Tonalite n=1	Granodiorite n=2	Granodiorite n=3	Na-trachyte n=1
SiO_2 (%)	66.4	66.9	61.9	62.7
TiO_2	0.4	0.6	1.0	0.1
Al_2O_3	16.2	15.6	15.6	17.4
Fe_2O_3*	3.3	3.7	5.8	4.3
MnO	0.7	0.1	0.1	0.2
MgO	2.4	1.3	1.4	0.0
CaO	3.2	1.9	2.9	0.7
Na_2O	4.9	4.4	4.6	7.9
K_2O	0.4	3.4	3.1	4.7
P_2O_5	0.1	0.2	0.3	0.01
ΣH_2O	2.1	1.2	2.5	1.3
Total	100.1	99.3	99.2	99.2
Rb(ppm)	7	92	57	224
Sr	535	326	347	25
Ba	174	697	841	62
Pb	<3	8	7	21
Th	<3	8	<3	43
U	<5	<5	<5	10
La	<6	20	33	200
Ce	<10	35	73	368
Y	11	17	45	107
Zr	110	227	462	1742
Nb	4	8	17	275
Ga	19	24	26	60
Ni	41	28	35	15
Cr	368	34	20	7
V	69	56	54	<5
Cu	30	23	27	<2
Zn	41	37	95	247
As	<7	45	<7	15

* Total Fe calculated as Fe_2O_3
ΣH_2O = Loss on Ignition
<3 = Below Lower Limit of Detection

Table 4.4 Comparison of Average Major and Trace Element Geochemistry for Granitoid Intrusive Suites at Gebeit.

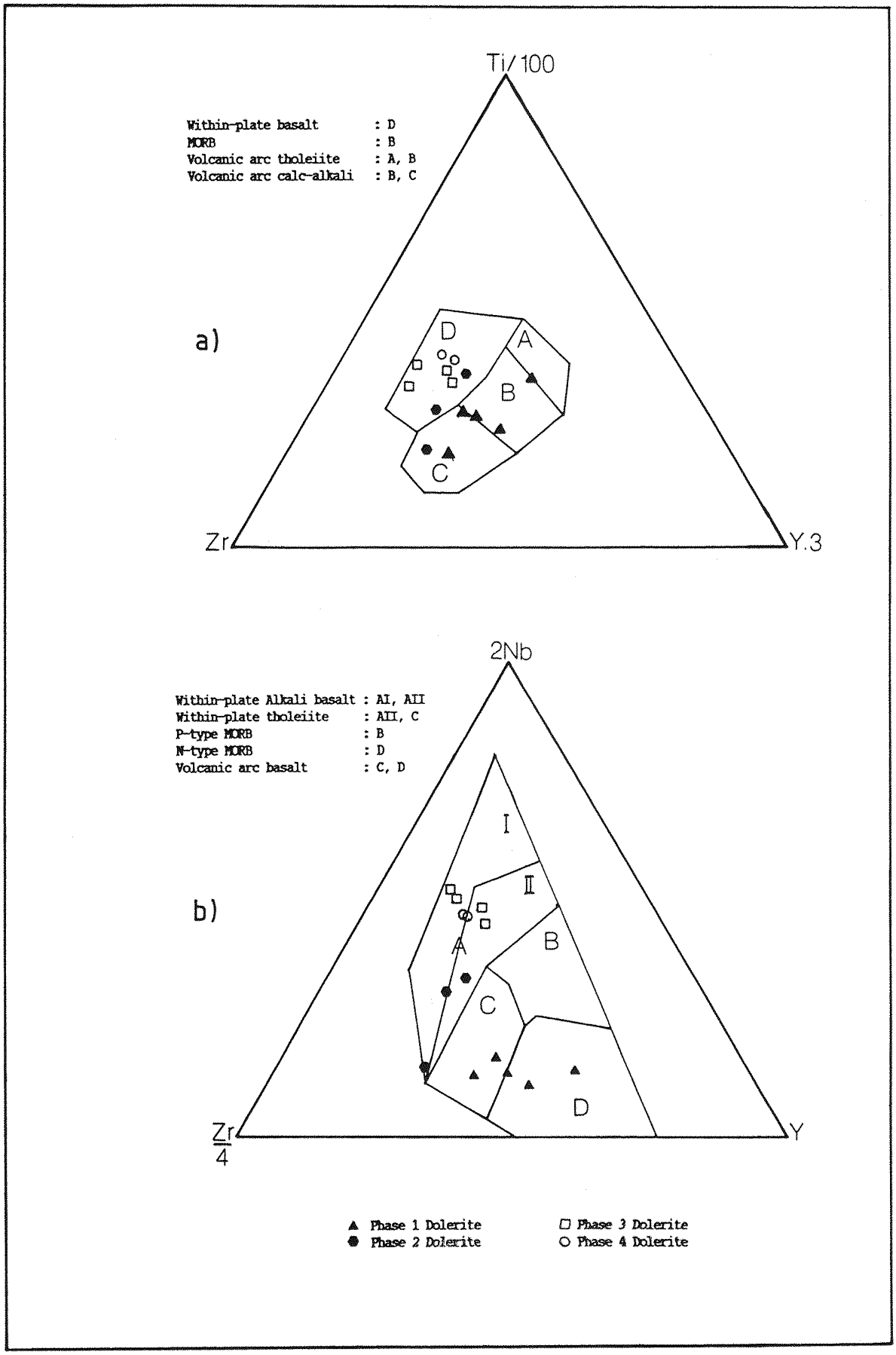

Fig.4.6 Discrimination plots using Ti,Zr,Y, and Nb for the basic dykes at Gebeit showing the transition from calc-alkaline to within-plate affinities during emplacement of phases 1 to 4 (a. after Pearce & Cann,1973; b. after Meschede,1986).

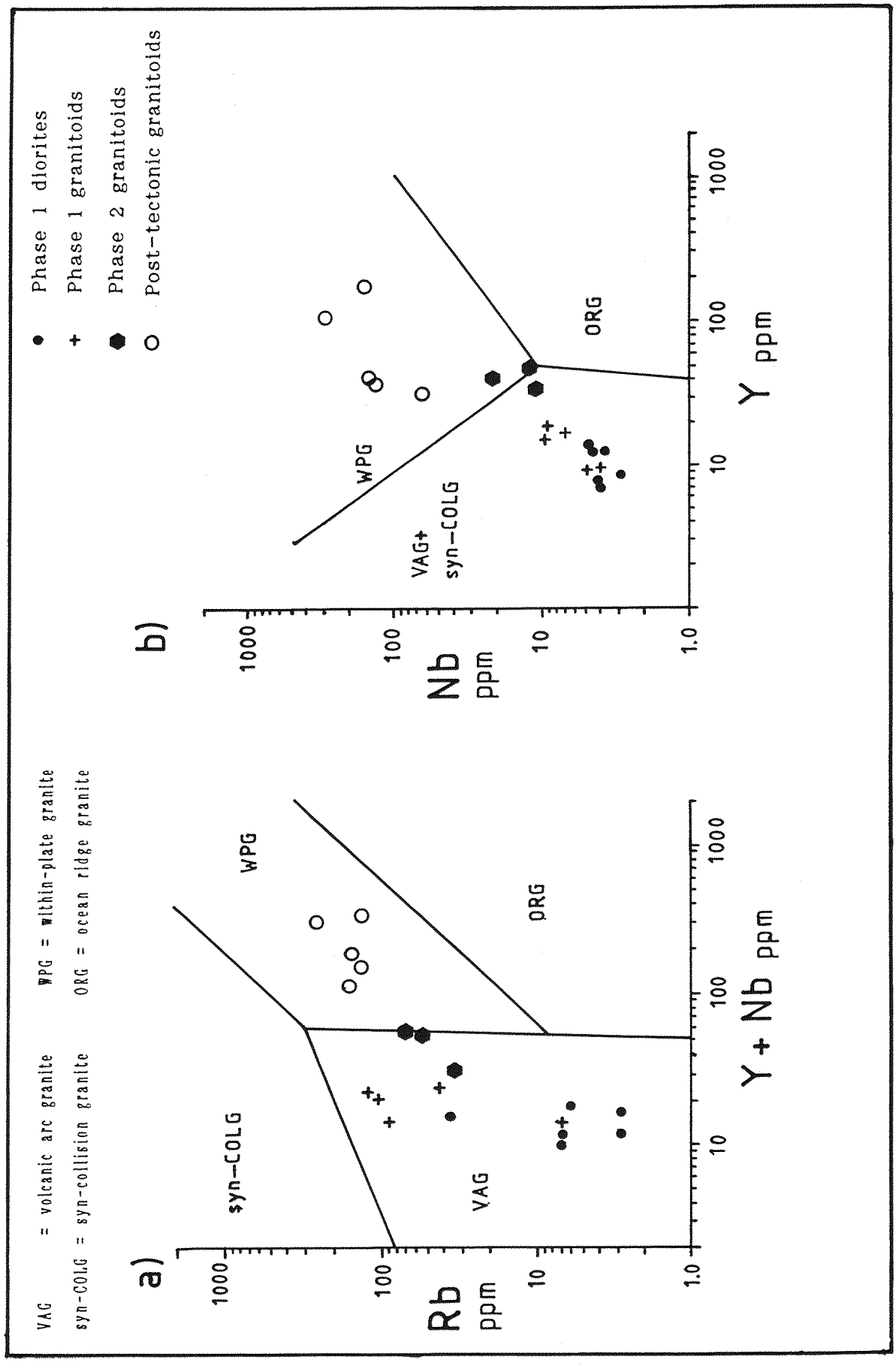

Fig.4.7 Discrimination plots using Rb, Nb, and Y for the granitoid intrusions at Gebeit showing the transition from calc-alkaline to within-plate affinities (after Pearce et al.,1984).

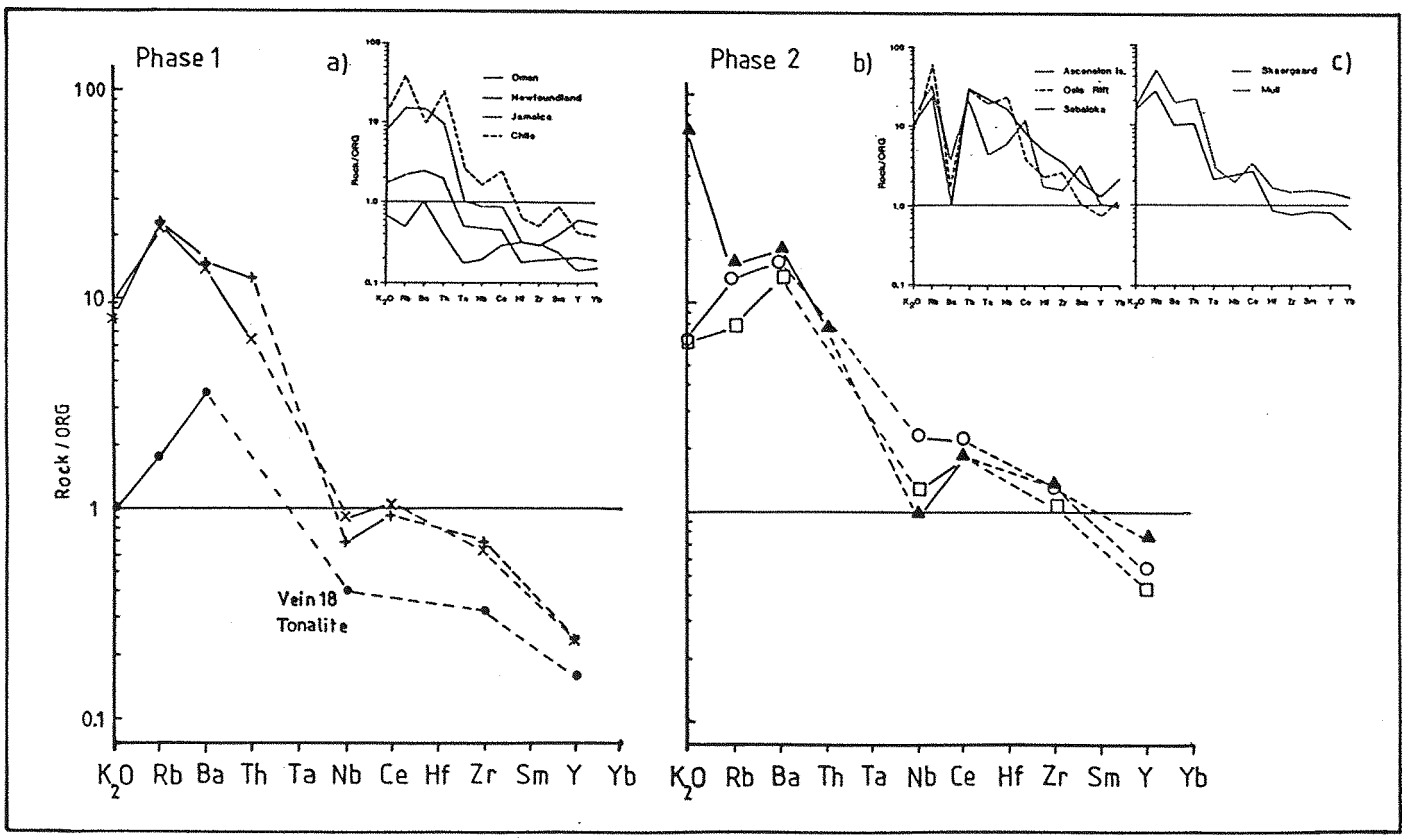

Fig.4.8 (Ocean-ridge granite) ORG-normalised multi-element plots for phase 1 and 2 granitoids at Gebeit compared with volcanic arc granite variations (a), within-plate granite variations (b), and granites from attenuated crust (c; after Pearce et al.,1984).

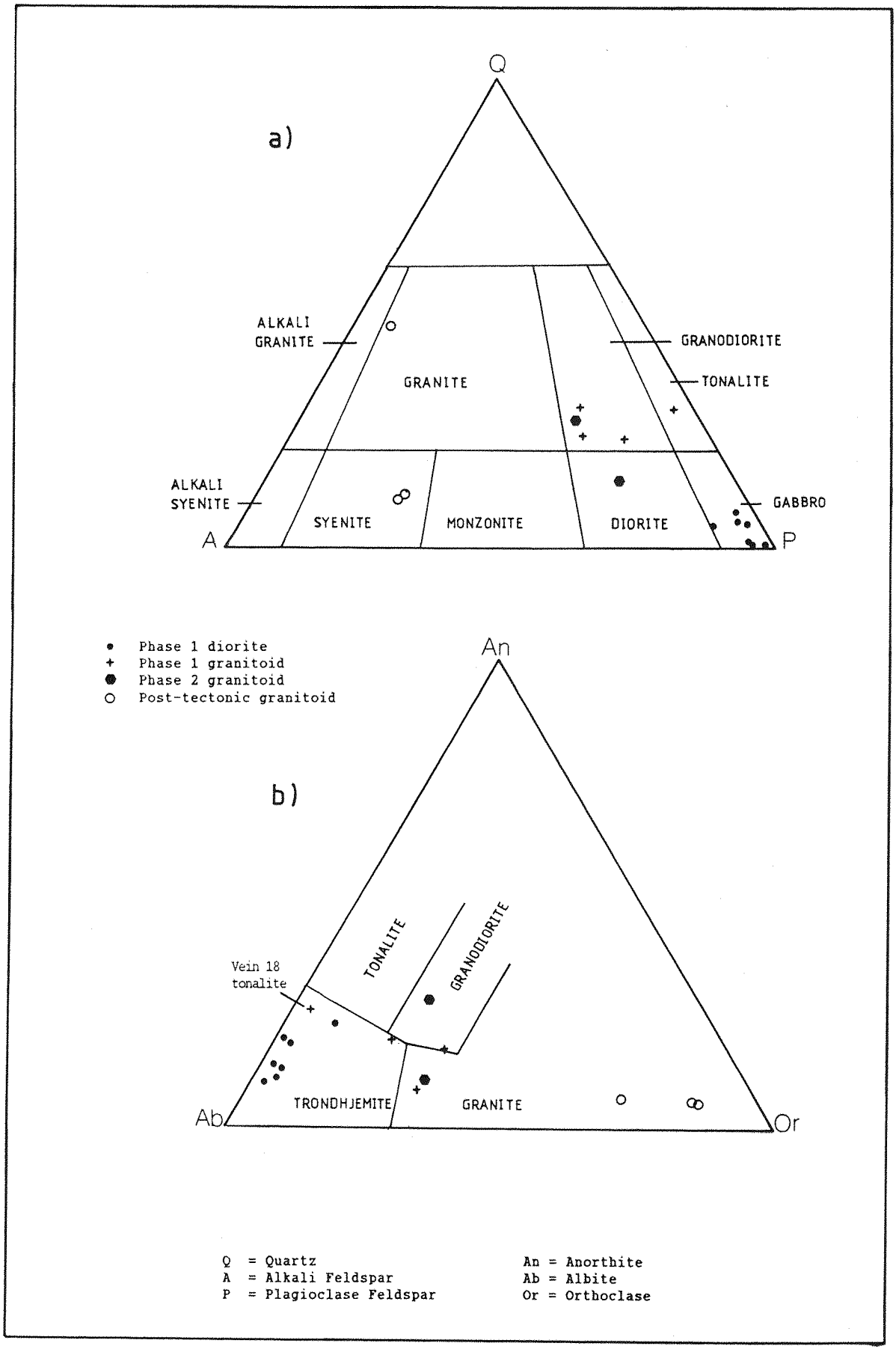

Fig.4.9 Ternary plots for the felsic intrusions at Gebeit showing the change in composition from syn- to post-orogenic magmatism (a. after Streckeisen,1976; b. after Barker,1979).

fused crustal precursors to the granodioritic association were more evolved, mature, arc volcanics.

North-east-trending, strike-slip shears transect the Wadi Messesana and Tikraneit bodies and host minor, gold-bearing veins. This indicates that the north-east-trending accretion-related deformation was still active following emplacement of these more evolved granodioritic rocks. In Saudi Arabia, the granodiorites of this association are seen to post-date rocks of the trondjhemite association (Jackson et al., 1984). Field relations between shearing, mineralisation and trondjhemite emplacement at Gebeit (i.e. the Vein 18 tonalite), however, infer that this phase of magmatism post-dates auriferous mineralisation. The two alternative conclusions to be drawn from this are that either:

a) magmatic evolution was diachronous and was geochemically controlled by the host volcanics. The granodioritic rocks at Wadi Messesana and Tikraneit may, in this case, have been mineralised contemporaneously with Gebeit followed by intrusion of the more primitive Gebeit trondjhemitic suite, or
b) there is more than one phase of gold mineralisation in the area.

The north-east-trending shear zones which host the auriferous veins at Gebeit and at the satellite prospects appear to be of the same age. However, vein textures are different and at Tikraneit mineralisation is accompanied by intense cupriferous alteration (up to 1.5% Cu). This suggests that either more than one auriferous precipitation event occurred, or ore fluid chemistry was significantly different at Tikraneit. As the two magmatic phases are mutually exclusive, spatially, in the Gebeit area, then it is probable that magmatism and possibly mineralisation were diachronous. As both prospects were investigated only briefly, resolution of this problem is, unfortunately, beyond the scope of this study.

4.4.2 Phase 2 Intrusions

Samples from this intrusive suite are chemically and temporally intermediate between the calc-alkaline arc intrusions of phase 1 and the alkaline within-plate rocks of the later post-tectonic suites. The transitional nature of the geochemistry is reflected in chemical variations evident in the dolerites of phases 1 to 3. Phase 2 dolerites display higher TiO_2, Fe_2O_3, K_2O, P_2O_5, Y, Zr, Nb, Ga, La, Ce, and Rb contents relative to the phase 1 dolerites (Table 4.3) and

although having Nb/Y <1 (alkalinity index, Fig.4.4), they plot largely in the within-plate field (Fig.4.6). Generalised discrimination parameters for tholeiitic and alkalic basalts indicate that these intrusions are alkaline (i.e. TiO_2 >1.8 wt%, P_2O_5 >0.25 wt%, Zr/P_2O_5 <0.06; Floyd & Winchester,1975), but not to the same extent as the dolerites of phases 3 and 4. Peraluminous (Al_2O_3>($CaO+Na_2O+K_2O$) granitic rocks of the granodiorite association appear to be transitional between volcanic-arc and within-plate rocks (Table 4.4, Fig.4.7) and when normalised against ocean ridge granites they display the HFS element enrichment trends with characteristics of both volcanic arc and within-plate granites (Fig.4.8). As not all the trace elements required for the discrimination plot were determined, the geochemical affinities of these rocks remains equivocal. Post-tectonic granitoids with similar compositions from the Red Sea Hills 120-250km to the south of Gebeit (Kadaweb, Shabateb, Erheib and Tehilla granites; Klemenic & Poole,1988) have been interpreted as more evolved, calc-alkaline granites derived from a volcanic arc margin. These intrusions have been dated between c. 717 and 555Ma. and suggests that the second episode of plutonism at Gebeit may have represented a late- to post-tectonic phase of magmatism that marked the transition to within-plate magmatism.

4.4.3 Anorogenic Alkaline Dolerites

These post-tectonic within-plate alkaline dykes (Figs.4.4 & 4.6) represent an end member of a transition series from calc-alkaline to alkaline basic magmatism and display the highest enrichment of HFS elements relative to the dolerites of phases 1 and 2 (Table 4.3). The progressive within-plate enrichment trends are demonstrated by increases in TiO_2, Fe_2O_3, K_2O, P_2O_5, Y, Zr, Ga, La, Ce, Rb and Nb and an overall decrease in Na_2O. Petrographically the unaltered undersaturated dolerites appear to be younger and in some of the discriminant plots they can be geochemically distinguished as a separate group (Fig.4.6). This is due to significantly higher TiO_2 (3.9-4.1%), Y (31-34 ppm), Fe_2O_3 (>14.8%), P_2O_5 (>0.75%) and Na_2O (>3.5%) values compared to the altered alkaline dolerites (TiO_2, 2.5-2.9%; Y, 18-28 ppm; Fe_2O_3, <12.8%; P_2O_5,<0.66% and Na_2O, <2.7%), a feature which is reflected in their fractionation trends (Fig. 4.5). This implies that four distinct phases of dolerite magmatism can be defined at Gebeit which show a progressive change from the saturated,

calc-alkaline, volcanic-arc-related dolerites of phase 1 to the, alkaline, within-plate dolerites of the third and fourth phases. The undersaturated phase 4 dolerites are probably associated with the more recent (<30 Ma) phases of Red Sea rifting.

4.4.4 Anorogenic Alkaline Granitoids

Alkaline rocks of this association contain the highest HFS element concentrations of all lithotypes studied and comprise the alkali-feldspar granite at East Gebeit (5450E,6500N), the sodic-trachyte at Yemomt, and the ultra-potassic (K_2O/Na_2O >3, molar ratio) trachyte and trachy-andesite at East Gebeit and Bishops Dam (Table 4.5). The sodic trachyte has comparable trace element characteristics to the alkali granite but is so alkaline, i.e. Nb/Y=3.6, that it does not plot on a Zr/TiO_2-Nb/Y discrimination diagram and is noticeably enriched in Na_2O similar to the syenites at Salala (Neary et al.,1976). The north-south-trending trachytic dykes reflect the predominant sanidine feldspar mineralogy with very high K_2O values of >9%. However, as the ratio K_2O/Al_2O_3 is <1, they are not deemed to be perpotassic (Bergman, 1987). These rocks are too low in MgO (<5 wt%) and too high in Al_2O_3 (>12%) to be classified as lamproites (sensu stricto) but the high K_2O/Na_2O (4-24) and K_2O/Al_2O_3 (0.6) ratios, coupled with enrichment in Ba (892-1291ppm), suggest that this suite may be the fractionated derivatives (Bergman, 1987). The alkali granite at East Gebeit, like the ultrapotassic trachytes, is also high in K_2O (6.53%), but contains much lower Al_2O_3 (9.6%) and higher Fe_2O_3 and TiO_2 levels, indicative of a lamproitic affinity. The much higher HFS element concentrations compared with the K-rich trachytes implies they are not consanguineous but does not negate a similar mode of formation. If indeed these rocks are fractionated lamproites, a refractory, K-metasomatised, mantle-peridotite source is inferred with water as the main volatile species in contrast to CO_2-rich alkali basalts (Bergman, 1987). In addition, lamproite suites tend to be localised at the margins of continental cratons in areas that overlie fossil Benioff zones, a situation analogous to the Nubian Shield. The ultra-potassic trachytes have been correlated with the extensive north-south, trachyte-syenite dyke swarms considered to be 150-89 Ma in age (Vail,1987a). They represent an extensional phase related to Red Sea rifting which reactivated north-south-trending deep crustal fractures such as the Oko (Almond & Ahmed,1987) and Gebeit shear zones.

	Mesozoic Ultra-potassic Suite		
	Trachyandesite n=1	Trachyte n=2	Alkali Granite n=1
SiO_2 (%)	47.8	62.0	70.7
TiO_2	1.6	0.06	0.3
Al_2O_3	15.7	15.7	9.6
Fe_2O_3*	8.0	3.7	7.5
MnO	0.1	0.1	0.1
MgO	3.3	0.9	0.3
CaO	5.3	2.1	1.4
Na_2O	0.4	2.1	0.9
K_2O	9.9	9.6	6.5
P_2O_5	1.0	0.03	0.04
ΣH_2O	5.9	3.2	2.2
Total	99.0	99.3	99.6
Rb(ppm)	185	162	146
Sr	119	60	22
Ba	1291	897	264
Pb	3	11	9
Th	6	11	22
U	<5	<5	6
La	51	90	88
Ce	98	149	190
Y	36	38	186
Zr	385	786	1742
Nb	62	137	173
Ga	24	34	40
Ni	20	10	14
Cr	14	89	286
V	10	<5	10
Cu	2	<2	<2
Zn	118	137	96
As	<7	<7	<7

* Total Fe calculated as Fe_2O_3
ΣH_2O = Loss on Ignition
<3 = Below Lower Limit of Detection

Table 4.5 Comparison of Major and Trace Element Geochemistry for Mesozoic Ultra-potassic Intrusions at Gebeit.

4.5 Summary of the Gebeit Intrusive Suites

Intrusions comprise a minor part of the late-Proterozoic crust around Gebeit mine but continued deformation and reactivation of large scale structures resulted in a protracted and diverse magmatic history (Table 4.6). The general evolution comprises;

i) an early gabbro-diorite-tonalite-trondjhemite, low-K, calc-alkaline suite, predominantly consisting of dolerite and microdiorite dykes. These intrusions are confined to the fabrics of the main Gebeit shear zones and are syn-to post-mineralisation in age but pre-date later thrusting events.

ii) This was accompanied, or possibly post-dated, by a more evolved, calc-alkaline, diorite-granodiorite suite which contain shear zone-hosted auriferous mineralisation at two satellite prospects but are not observed within the Gebeit mine area.

iii) Following a phase of north-westerly directed thrusting, east-west trending dolerite dykes and diorite-granodiorite dykes were emplaced along partially reactivated thrust structures during a second phase of dextral strike-slip shearing. All lithotypes display geochemical signatures transitional between volcanic arc and within-plate magmatism.

iv) Several phases of alkaline, late-orogenic to anorogenic, within-plate plutonism have been identified at Gebeit but cannot be accurately dated. These consist of;

a) north-east to north-west trending alkaline dolerites partly intruded along reactivated structures which may be coeval with early D_4 sinistral shearing, and alkali sodic trachytes;

b) north-south-trending, ultra-potassic trachyte and trachy-andesite dykes which are confined to the reactivated sections of the major shear zones. These dykes are of lamproitic affinity and are probably Mesozoic (150-89 Ma) in age;

c) east-west-trending, undersaturated analcime-olivine dolerite dykes which transect all structures and are probably of Cainozoic age (<30 Ma).

Intrusion	Dyke Trends	Host Structures	Geochemical Affinity	Tectonic Setting
Phase 1 diorites dolerites tonalites	NE-SW	parallel to fabric D_2 dextral strike-slip extensional shears	immature, low-K/ calc-alkaline	coeval with arc magmatism (approx. coeval with Au min^n.)
Phase 2 dolerites diorites	E-W	oblique to fabric D_2 shear zones associated with late-D_3 dextral shearing	transitional between evolved calc-alkaline & within-plate	late-tectonic volcanic arc margin (post-dating Au mineralisation)
Phase 3 dolerites	NW-SE N-S & NE-SW	NW-trending normal faults and reactivated D_2 & D_3 structures	alkaline within-plate	post-tectonic
Ultra-potassic trachytes	N-S	reactivated major Pan-African shear zones	alkaline high-K within-plate	Mesozoic phase of early Red Sea extension
Phase 4 dolerites	E-W	E-W-trending regional normal faults	alkaline undersaturated within-plate	associated with Recent (<30Ma) Red Sea rifting

Table 4.6 Summary of the main phases of intrusion at Gebeit.

"Tectonic and Chemical Evolution of a Late Proterozoic Gold Deposit, Gebeit Mine, Northern Red Sea Hills, Sudan."

PART THREE

STRUCTURAL GEOLOGY

Chapter 5

Structural Geology

5.1 Introduction

The interaction of oceanic-arc, continental and continental-margin micro-plates during the accretion and evolution of the Nubian-Arabian shield has resulted in a complex and protracted tectonic history. The Proterozoic basement in the Northern Red Sea Hills province displays a strong north-east grain but fault sets on N/S, NW/SE and E/W trends with associated perturbations in the north-east-trending fold and fault patterns indicate more than one deformation episode has occurred (Geosurvey,1983). Unfortunately, in the Nubian-Arabian Shield, structural studies have been the most neglected of all disciplines and in order to understand the processes of vein formation and the effects of later deformation episodes, elucidation of the structural history of the area is essential.

In addition to the recent Red Sea rift related structures, four distinct deformational episodes have been identified. These comprise:

a) D_1 - compression about NW/SE axes to produce upright, regional folds F_1,
b) D_2 - dextral strike-slip deformation along NE-trending phyllonitic shear zones,
c) D_3 - minor NE-trending, F_3 folding accompanied by NW-directed thrusting and dextral reactivation of D_2 shears, and
d) D_4 - sinistral reactivation of D_2 shears followed by NE-directed thrusting and N-S to NW-trending F_4 folding.

Although four distinct deformation phases have been distinguished, they collectively represent the protracted tectonic evolution of the Gebeit area during late-Proterozoic island arc accretion. The D_2 phase of strike-slip tectonism is the dominant mode of deformation interspersed with the other phases and marks a progression from a ductile to a brittle regime. Other than alluvial prospects, gold

mineralisation in the province appears to be confined to relatively early, north-east-trending quartz vein sets. The intrinsic control on gold mineralisation at Gebeit is the availability of extensional sites for fluid access during D_2 dextral shearing. Mining of the auriferous lodes has been complicated due to the overprinting by the later deformation events, D_3 and D_4, which have laterally and vertically fragmented an otherwise fairly continuous vein system. As a result, structural studies have largely been confined to the immediate mine area in order to define the precise controls on lode vein formation, to differentiate non-auriferous veins, and to evaluate the subsequent degree and direction of lode offset.

5.2 Regional Structure

The region is bounded to the north and south by the north-east trending Halaib-Yanbu and Nakasib/Port Sudan-Bi'r Umq sutures, respectively, which define the Gebeit-Hijaz arc terrane (see section 2.8, Fig.2.20). The overriding north-east trend of this late-Proterozoic basement fold and fault system is compatible with a genetic model of arc accretion along a north-east-trending axis and is intruded by large syn- to late-tectonic composite batholiths and minor post-tectonic ring complex intrusions (Fig.5.1). The area appears to be dominated by complex interactions between the north-east-trending faulting and folding, indicating large strike-slip displacements in addition to thrusting. The western limit of the Hijaz-Gebeit terrane is delineated by the Abirkitib/Hamisana shear zone which marks a transition from the north-easterly deformation trends in the Gebeit terrane to the north-south upright, isoclinal structures in the westerly Gabgaba /Northern Red Sea Hills terrane, as part of the Midyan arc system (Almond & Ahmed,1987; Stern et al.,1989).

Large-scale structural analysis of the Northern Red Sea Hills region has been derived through extrapolation of field observations to Landsat MSS image interpretation maps compiled by Geosurvey (1983), aerial photographs and Soviet-Sudanese survey maps (e.g. Ahmed,1984). From aerial photography, the broad association between the north-east-trending folding and faulting in the Gebeit terrane suggests that they are contemporaneous; however, fold axes are evidently offset by some of the north-east faults and hence the relationship is not completely clear. The north-east faults display a range of trends (approximating to 045°, 020° and 360°) in the form of fault splays which appear to

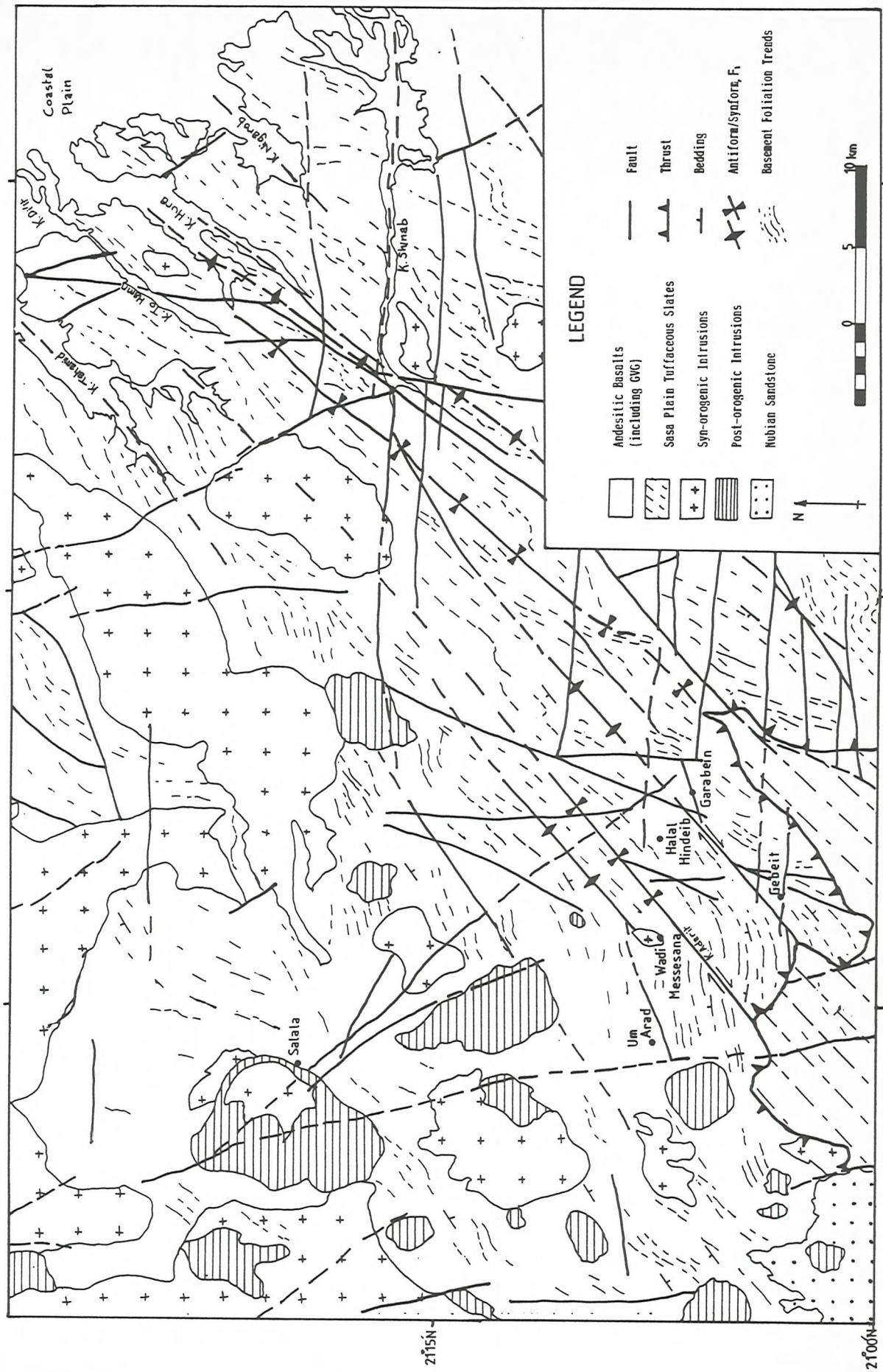

Fig.5.1 Geology of the area around Gebeit with emphasis on structure (this study and after Geosurvey,1983; Ahmed,1984).

relate to the same system. In addition, a large dextral offset along Wadi Adarit indicates a phase of north-east-trending, strike-slip tectonism which post-dates regional folding. As well as minor north- to NW-trending faults whose relation is unclear, Geosurvey confirmed a second major fracture trend, approximately E-W (080°-095°), which appears to cut every mapped rock unit with no apparent displacement and may be due to regional crustal extension induced by tectonic uplift (Nur, 1982).

5.3 Local Structure

The coarse blocky nature of the volcanic lithologies in the Northern Red Sea Hills tends to obscure the more minor structural trends and only regional-scale folding and deformations with significant components of strike-slip displacement can be identified using remote sensing-type techniques (i.e. Landsat Imagery and aerial photography). Aerial photograph analysis (1:40,000 scale) of the immediate mine area coupled with field observations and reconnaissance mapping show that within the Gebeit Volcanic Group (PG1 greenstone group, defined by Geosurvey) several tectonic blocks can be delineated. Each block displays an apparent difference in orientation of internal structures and to the south-west their boundaries are defined by phyllonitic brittle-ductile shear zones which are clearly visible on air photographs (Fig.5.2). For this study, the four main blocks around Gebeit have been named after their satellite prospects and comprise from north-west to south-east the Um Arad-Messesana, the Halal Hindeib, the Gebeit, and Garabein blocks.

Gebeit is located at the centre of a broadly triangular shaped, north-east-trending block, 10km x 2.5km, bounded on all sides by carbonate-altered phyllonitic shear zones. Deformational fabrics are largely restricted to these major and subsididary shear zones whereas the intervening volcanics display no apparent tectonic foliations. Similar shear zones cross-cut the block at low angles to the margins which, on close inspection, are evidently part of the same shear system, implying a strike-slip shear zone array. Splay-patterned faults and dextral offsets are evident in the surrounding blocks, indicating that the dextral phase of deformation is not restricted to the Gebeit block alone but appears to be ubiquitous in the region and has been reported from the Nakasib shear zone (see section 2.8; Almond & Ahmed,1987).

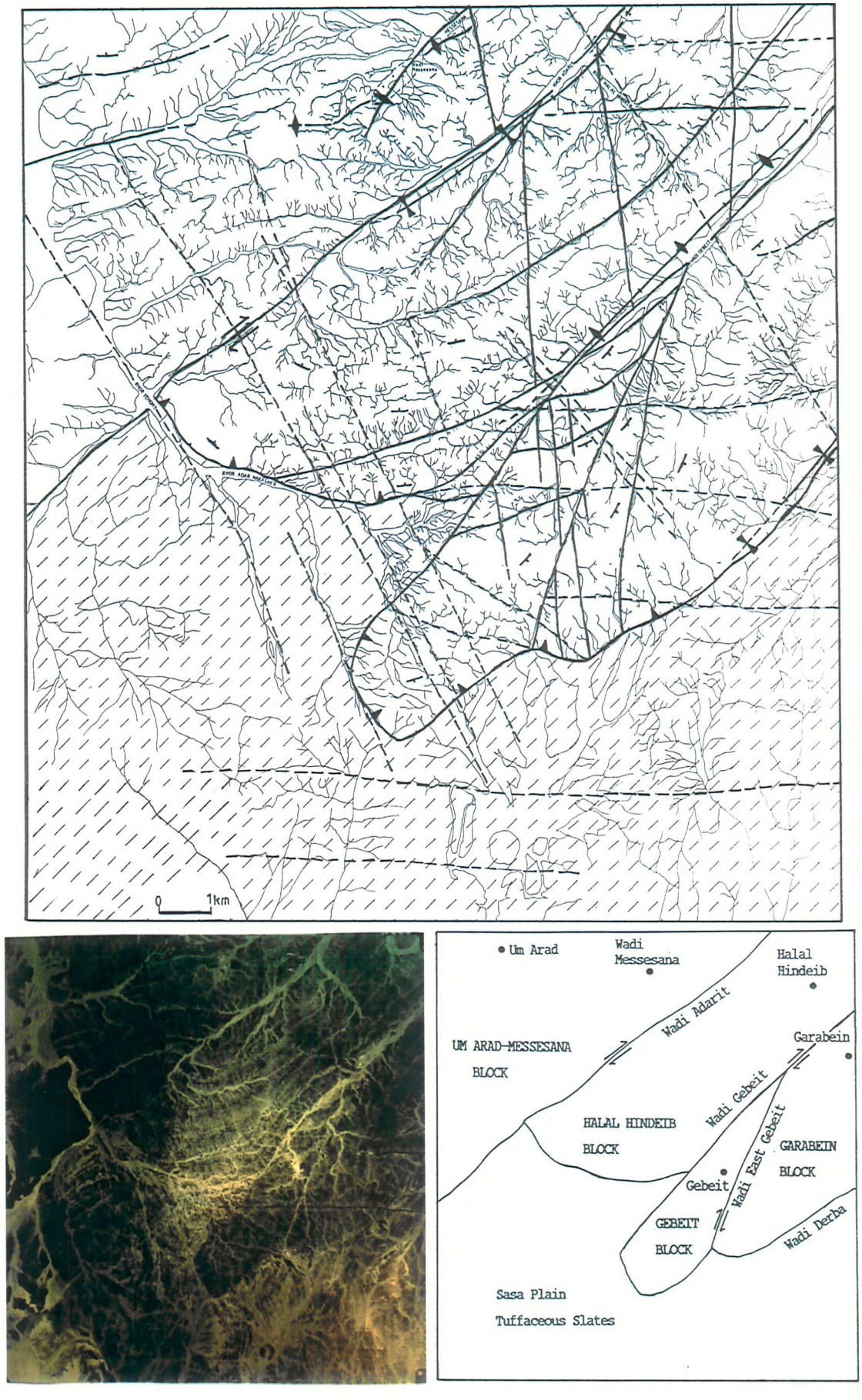

Fig.5.2 Photo-geological interpretation of the area around Gebeit showing the delineation of the various tectonic blocks. (Dashed lines denote late extensional faults).

North-east-trending antiforms and synforms can be identified (El Boushi, 1972) which parallel the 045°N shear zones and have been attributed to a regional folding event, F_1 (see section 5.4). At the junction of the Um Arad-Messesana and Halal Hindeib blocks, 5km to the north-west of the mine, these bedding-strike ridges in both blocks are rotated towards the sub-parallel Wadi Messesana and Khor Adarit faults, indicating a component of dextral, strike-slip shear (Figs.5.1 & 5.2). Restoration of the strike ridges to their original north-east trend indicates that a minimum of 1.5 to 2 km of lateral movement has been accommodated along this zone. At the south-western edge of the Gebeit block, the strike ridges are similarly deflected to the north-west. In the Garabein block, south-east of the Gebeit block, the main structural trend is north-south to north-easterly and, in the field, a clear change in fabric orientation is observed across the boundary of the Wadi East Gebeit shear zone. Because of the lack of previous structural studies to act as a framework, mapping (scale,1:1000) was confined to the immediate mine area where some underground exposure provided good 3-dimensional control.

5.4 D_1 Deformation Phase

The first phase of deformation, D_1, appears to have generated regional folds, F_1, of 5 to 8 km wavelength with north-easterly aligned fold axes (Fig.5.1). These folds have been defined from Landsat imagery (Geosurvey 1983) and aerial photography (El Boushi 1972) and are essentially cryptic in the field. Although D_3 and D_4 events disturb bedding trends on the small scale (<1m-100m), large scale (>3km) variations in the direction of dip of bedding (NW and SE) around Gebeit with consistent directions of bedding strike substantiate an early folding event. The nature of the folding appears to be upright and relatively open but no estimate of vergence can be made.

Within the Gebeit and Garabein blocks, bedding generally strikes north-east and dips to the south-east but immediately north-west of Bishops Dam (Fig 1.3) in the Halal Hindeib block, the direction of dip changes to the north-west indicating that the axis of a major antiform is congruent with Wadi Gebeit. Similarly, to the north-west there appears to be a synclinal axis running along Wadi Adarit and, to the south-east, the axis of another major synclinal structure (identified by Technoexport,1978 and Geosurvey,1983) coincides with Wadi Derba.

The parallel association between this phase of folding, the north-

east-trending shear zones, and the later dextral movement along the same structures suggest that shearing parallel to the fold axes may have accompanied F_1 folding during the D_1 deformation event and that the resulting shear zones were subsequently reactivated during the dextral D_2 phase. The timing of formation of the pervasive north-east-trending basement grain must pre-date the main dextral strike-slip episode as it is deformed by this later event (Fig.5.2; dextral movement along Wadi Adarit). Similarly, the north-east orientation of the F_1 folds are incompatible with formation synchronous to dextral strike-slip shear. Shearing of phase 2 dykes shows that dextral shearing also occurred at Gebeit after D_3 deformation (see 5.6.2). Although the D_3 folding and thrusting locally appears to be a relatively minor event, it cannot be completely ruled out as the main phase of regional folding. However, angular unconformities of hornblende-phyric lavas overlying gently folded aphyric tuffs (e.g. 5350E,5450N) and bedding parallel, syn-sedimentary slump folding of deep water tuffs (see Plate 3.1e) within the local stratigraphy suggest that north-west-directed compression was initiated at an early stage, during sedimentation. As bedding is generally steep and orientated sub-parallel to the extensional strike-slip shear zones, uplift must have occurred prior to shear zone initiation.

Reischmann (1986) has attributed the dextral deflection along Wadi Adarit to an unspecified north-east folding event. However, the plunge of such folding would have to be very steep to produce the observed outcrop pattern and is also inconsistent with the regional F_1 folding.

5.5 D_2, Dextral Strike-slip Deformation Phase

The regional folding event, F_1, was post-dated by a strike-slip deformation phase, D_2, along a north-east trend. Phyllonitic ductile shear zones were developed, possibly through the reactivation of D_1 shear zones, and these shear zones define the boundaries of the various tectonic blocks. From large-scale structures (e.g. Wadi Adarit), small-scale kinematic indicators (see section 5.5.2), and the geometry of the shear zone arrays, the strike slip event was largely dextral in sense, corroborating evidence for dextral slip on the regional scale (i.e the Nakasib shear zone). The first observable phases of quartz vein formation (V_1 and V_2) and dyke intrusion occurred during this deformation event and the timing of their emplacement is constrained by overprinting by the later D_3 and D_4 deformation phases.

5.5.1 Phyllonite Shear Zones

The sheared rocks which form the linear fault zones are more highly deformed towards the centre of each shear zone where steeply dipping, pervasive schistose planar foliations are developed. These braided shear zones are up to 200m in width and the longer faults, including the Wadi Gebeit shear zone, can be traced for a minimum distance of 15km. Landsat MSS images indicate these faults extend to the Red Sea coast and may continue into the Arabian Shield (Fig.5.1). The anastamosing shears incorporate elongate pods, up to 400 m long (Fig.4.3; 4850E,5500-5900N), of much more weakly deformed lithologies, which are identifiable as sheared basaltic andesites. The most highly deformed lithologies display s-c foliations and are composed of fine-grained chlorite, quartz, albite, calcite, ankerite and sericite. The schistose nature of these rocks (see Plates 5.2 & 5.3) and their associated micro-structures are characteristic of mylonites, as defined by White & Baxter (1987) and were produced as a result of ductile reworking within the shear zones. From the terminology of fault rocks outlined by Sibson (1977), the predominance of chlorite in the Gebeit lithologies suggests that they should be classified as phyllonites.

Many of the shear zones are characterised by an intense red-brown colour in weathered outcrop due to a phase of ankeritic alteration which is exclusively confined to the sheared lithologies (Plates 5.1 & 5.2a). This ranges from the incipient replacement of chlorite by ankerite and sericite along cleavage planes to a pervasive replacement of all chlorite and the obliteration of the phyllonitic planar foliations to form a cohesive, blocky, ankerite-rich rock. As a result of the obscured cleavage, the most altered lithologies have been previously mapped as marbles, rhyolitic volcanics, or as dykes. However, petrographic and trace element geochemical analyses across these zones show them to be composed of mylonitised andesitic basalt volcanics (see section 7.8). This large-scale carbonate alteration can be identified on air photographs and has been understandably mistaken on Landsat imagery as an intrusive lithology (Fig.5.3).

The Gebeit block is bounded by the Wadi Gebeit Fault to the north-west and by the Wadi East Gebeit Fault to the south-east and on aerial photographs, both shear zones appear to curve very gently towards the south (Fig.5.2). Similar shear zones cross-cut the block at low angles (22° to 31°) to the margins but cannot be traced outside the Wadi Gebeit and Wadi East Gebeit Faults and are evidently part of the same

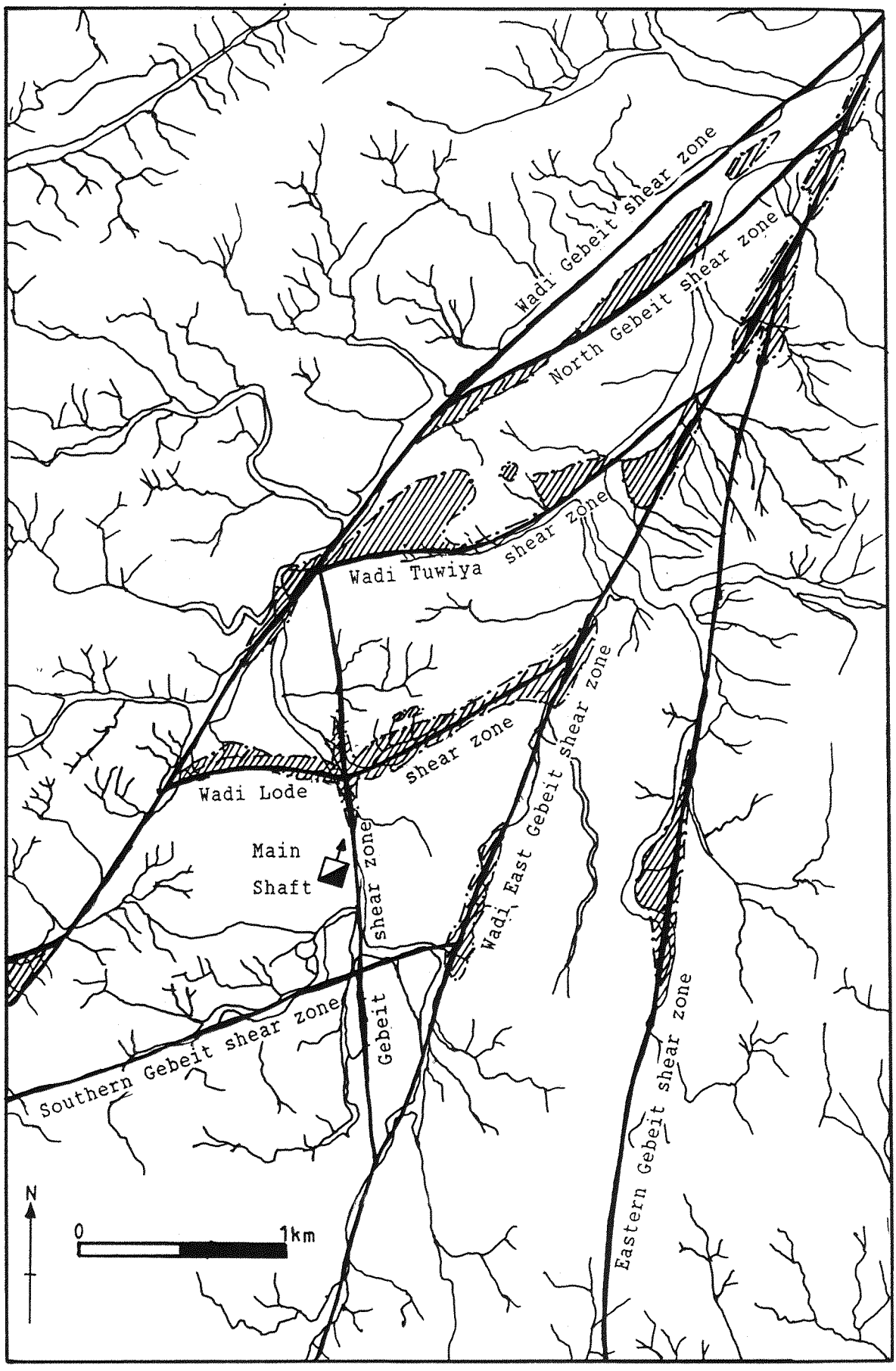

Fig.5.3 Sketch map of the Gebeit block showing the main phyllonite outcrops.

Plate 5.1 Major D_2 shear zones of the Gebeit block.

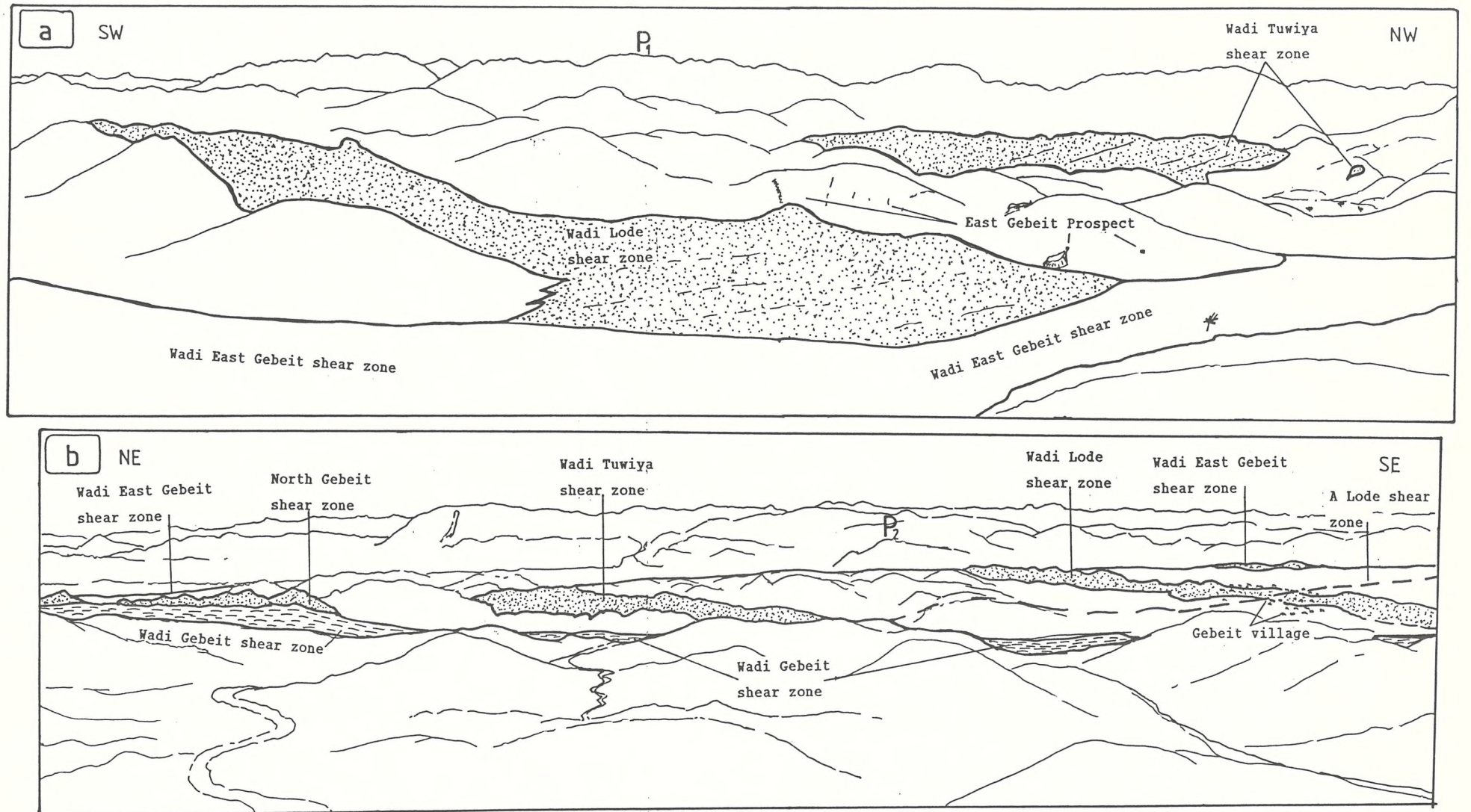

P_1 = view-point for 5.1b, P_2 = view-point for 5.3a. Shaded areas = blocky ankerite phyllonite.


a

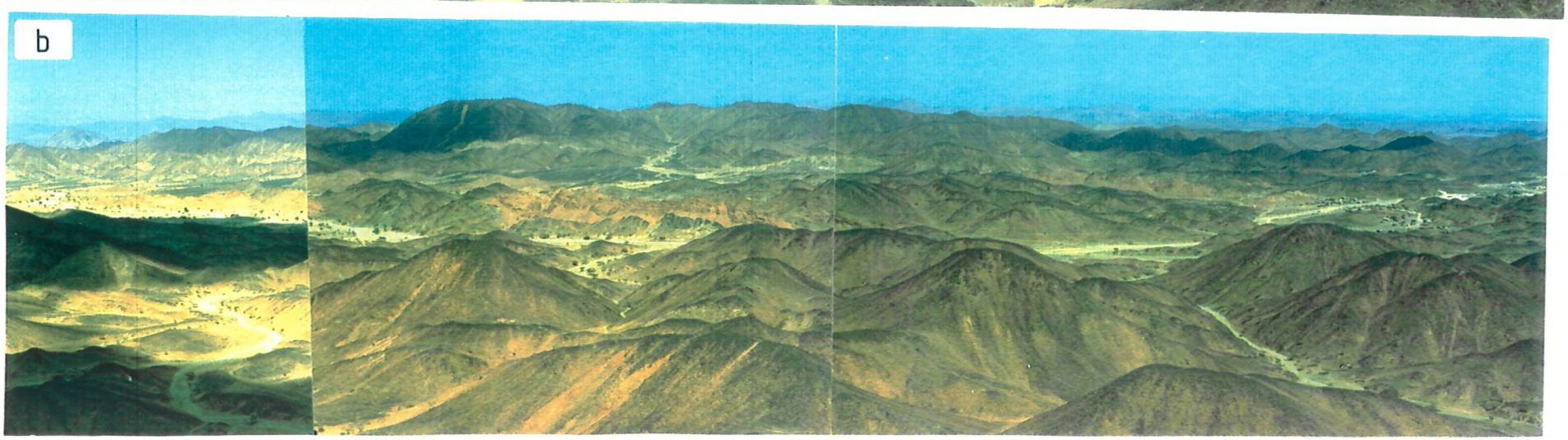
b

shear system (Plate 5.2a). The shear zone geometry and alignment patterns conform to a dextral strike-slip simple shear system which has been verified using micro to macro-scale kinematic indicators.

5.5.2. Shear Zone Characteristics and Kinematic Indicators

As development of the phyllonites occurred relatively early in the deformation history, most of the subsequent strain has been taken up along these zones. Unlike the blocky undeformed volcanics, the phyllonites exhibit well developed structures and are invaluable in deciphering the subsequent tectonic history. Generally the shear zone fabrics at Gebeit are vertical (e.g. Wadi East Gebeit Fault, see Plate 5.3a) or dip steeply (>60°) to the south-east but lower angle dips are observed due to rotation by the later folding and thrusting events. Stretching lineations are generally masked, as are many of the small-scale kinematic indicators, by the later pervasive carbonate alteration event. However, in the rare cases where they are observed, they are orientated sub-parallel to the strike of the shear zones and substantiate the predominantly strike-slip mode of deformation. Some of the fault zones contain irregular, coarser horizons of rounded, prolate clasts which at each location (i.e. Garabein, East Gebeit, Gebeit village at 4700E,4800N, and 5100E,5400N) are elongated parallel or sub-parallel to the strike. Because of the roundness and common vesicular nature of these clasts, they are considered to represent sheared agglomerates as opposed to a fragmented more resistant unit or a dismembered dyke. Measurements of the orthogonal axial lengths of these clasts show low ratios in the region of 2.7:1.3:1 (R_f; X:Y:Z) indicative of low amounts of strain (Appendix C). Furthermore, high values of R_i (≈2.3:1.5:1) indicate that a significant proportion of the ellipticity seen is due to the original shapes of the clasts produced during deposition. These agglomerates are matrix supported and the intense deformation displayed by the chlorite phyllonite matrices suggests that the bulk of the strain during shear zone formation was partitioned into the matrix. However, some of the sheared lapilli-tuff units display clasts elongated up to ten times their width (Plate 5.2b), confirming much higher strain conditions.

Foliation varies from a single continuous cleavage to a spaced (3-10 mm) cleavage but often a reticulate pattern is observed due to two, low-angle, apparently conjugate cleavages which define s- and c-foliations typical of mylonites (Plate 5.2d; Berthé et al.,1979; Lister

Plate 5.2 The Wadi Tuwiya Shear Zone at Bishops Dam and fabrics of the shear zone phyllonites.

a) Junction of the Wadi Gebeit and Wadi Tuwiya shear zones at Bishops Dam (4100E,5500N) showing the chlorite phyllonites of the Wadi Gebeit shear zone (WG) separated from the ankerite phyllonites of the Wadi Tuwiya (WT) by a lens of undeformed andesitic volcanics (A). The trend of the A Lode shear zone is also delineated by a topographic low.

b) Chloritic phyllonite composed of sheared andesitic agglomerate displaying extensive ductile deformation and the development of D_2 sheath folds whose axes are delineated (Wadi Lode Extension; 5000E, 5950N; see Fig 5.9).

c) S-c-foliation in the ankerite phyllonites near the base of the Wadi Lode shear zone (5000E, 5600N) indicating a dextral sense of shear.

d) Lozenge-shaped microlithons produced by a combination of carbonatisation and intersecting s-c-fabrics indicating dextral shear, Wadi Tuwiya shear zone (4600E,6900N).

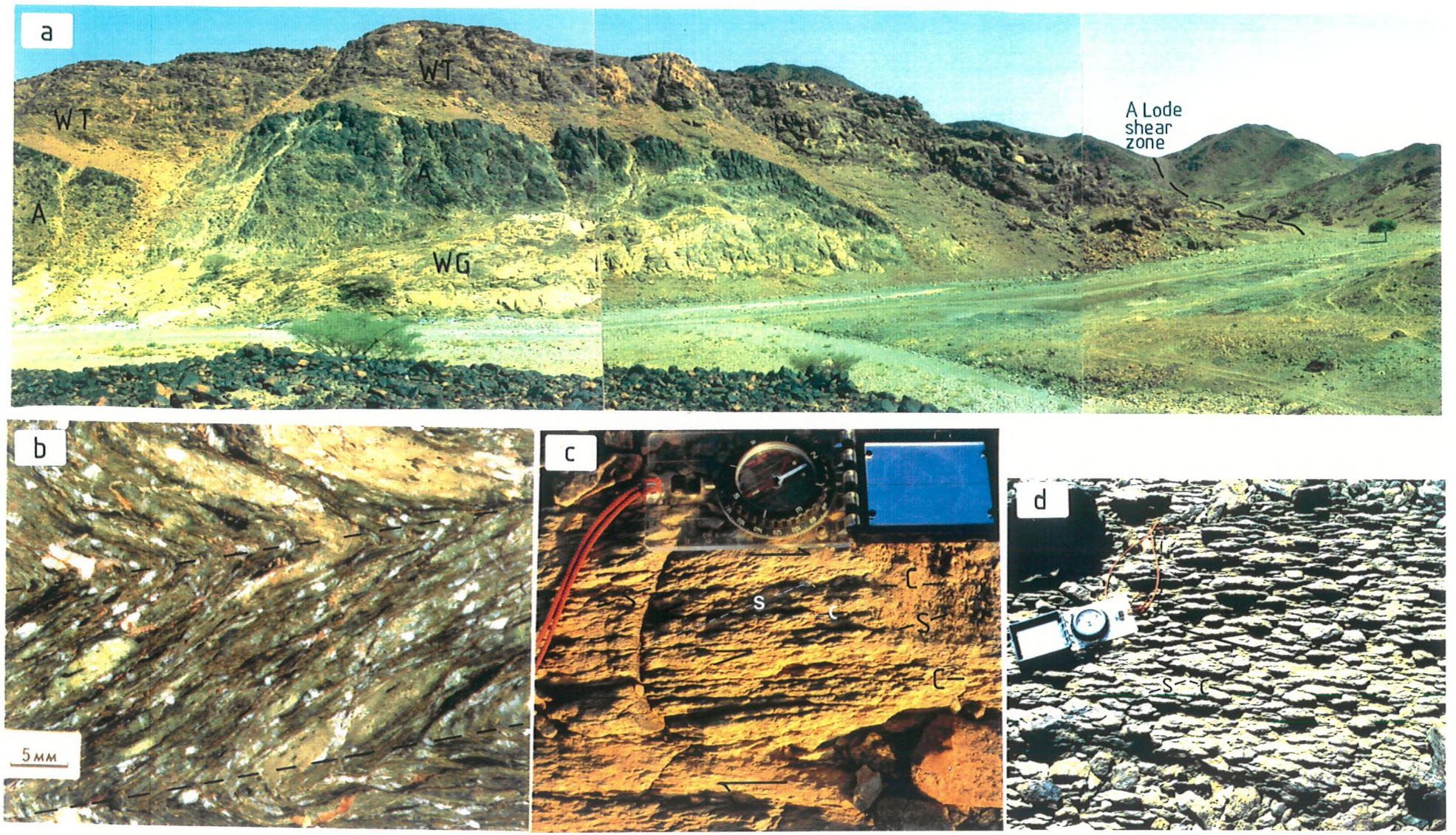
a
WT
WT
A
A
WG
A Lode
shear
zone
b
5 мм
c
C
S
S
C
C
d
S
C

& Snoke,1984). Occasionally, minor (<50mm wavelength) isoclinal sheath folds occur parallel to the s-surfaces (Plate 5.2b) but vary from 0-90° in plunge, suggestive of fold rotation during deformation (White & Baxter,1987). Where the cleavage is continuous and pervasive, the c-surfaces sometimes appear to post-date the s-surfaces. The s-foliations are orientated at 25-30° to the margins of the shear zones in a north-north-east trend (010-020°N), indicating a dextral sense of shear (Plate 5.2c). In the zones where cleavage is spaced, lensoid microlithons up to 80mm long and 12mm wide are preserved (Plate 5.2d).

Quartz-calcite veinlets between 13mm and 2mm wide, are occasionally developed in the extensional (R-shear) shear band orientation (Plate 5.3b,c) and are thickened at the junctions with the c-surfaces. These veins are transected by pressure solution cleavages parallel to the s-surfaces (Plate 5.3b) and by extensional, high-angle, sinistral, X shears (Plate 5.3c). These orientations are reflected on a larger scale (10-100m) where the weakly deformed parallelogram-shaped pods enclosed by the north-east-trending shear zones are defined by shears in R- and P-shear (s-surface) orientations producing the anastamosing trends.

The first phase of emplacement of the syn-tectonic, dolerite-microdiorite dykes was confined to the shears in the 070°N orientation, parallel to the c-foliations, demonstrating the overall extensional nature of the shears in this orientation. The dykes are generally fragmented and offset, up to 2.5m, by a set of widely spaced (0.5-10m), high-angle, shear surfaces (see Plate 3.1a; Fig.5.4). Usually these occur as extensional kink bands up to 15 cm wide, which are confined to the shear zones, and all indicate an opposite (sinistral) sense of shear. They appear to be coeval with a similar set of low-angle (east-west-trending) shears which are sometimes intruded by the transitional phase 2 dolerite dykes (Fig.5.4). These synthetic and antithetic shears (Riedel and X shears) represent later secondary planar fabrics identified here as "extensional crenulation cleavages" (Platt,1979; Platt & Vissers,1980) or "shear-band cleavage" (White et al.,1980). This is indicative of the departure from progressive simple shear where the bulk flow field is partitioned and slip on the s-surfaces leads to the formation of coaxial deformation domains, common in strongly anisotropic micaceous rocks such as phyllonites (Platt, 1984). Although difficult to differentiate, these shear bands are not obscured and appear to post-date the carbonate metasomatism phase. The large scale replacement by carbonate during deformation, concentrated

Plate 5.3 The Wadi East Gebeit Shear Zone and D_2 kinematic indicators.

a) View south-west along Wadi East Gebeit showing the restriction of pervasive ankerite metasomatism (red ridge) to a narrow zone 3-5m wide.

b) Low-angle V_1 quartz-calcite veins developed along extensional Reidel shears (C') in carbonatised phyllonite and transected by low-angle pressure solution s-foliation (S) indicating a dextral sense of shear. Note thickening of veins at C'-C fabric intersections (I) and incipient folding of early veins (1) cut by unfolded lower angle veins (2; Bishops Dam, 4000E, 5800N).

c) As for 5.3b) but note high-angle extensional crenulation shears (i.e. antithetic shear, X).

d) Photomicrograph (CN) of asymmetric augen in chlorite phyllonite showing s-c-foliations and extensional calcite veining indicating a dextral sense of shear (Wadi Lode Extension; 5200E,6000N; field of view 3mm).

e) Photomicrograph (PPL) of altered hornblende phenocrysts showing high angle extension fractures (f) and development of minor asymmetric chlorite pressure shadows indicating a dextral sense of shear (Vein 18, 4400E,5900N; field of view 4mm).

CN = crossed Nicols, PPL = plane-polarised light.


a

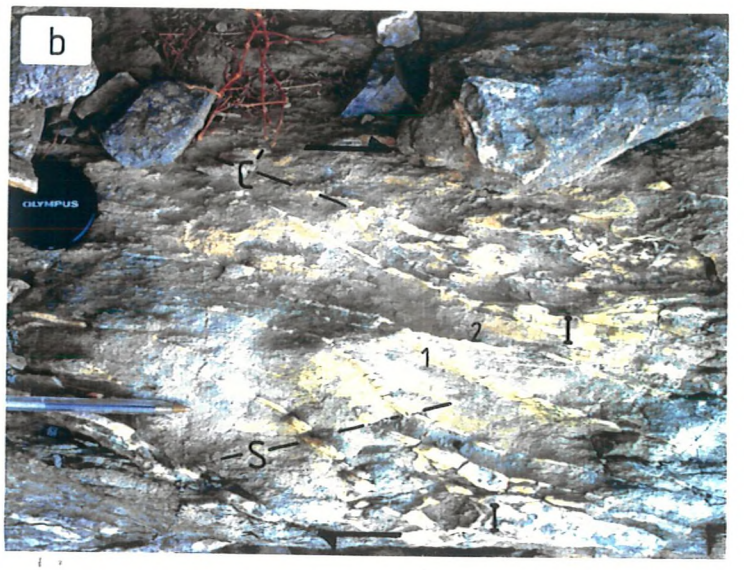
b
OLYMPUS
2
1
S


c

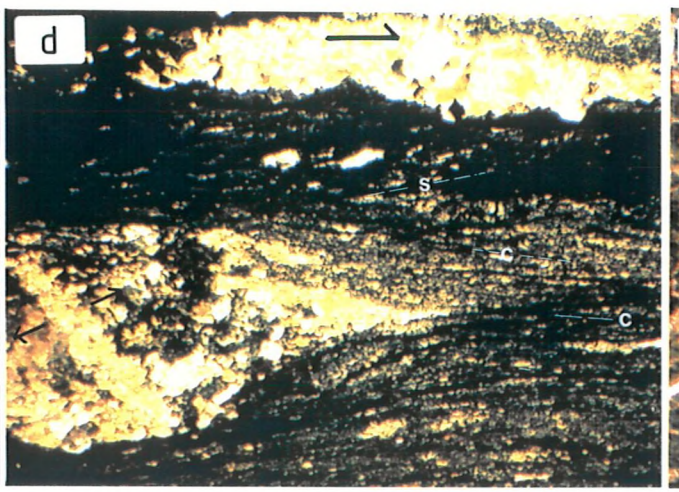
d
s
c
c


e
Chl
f
f

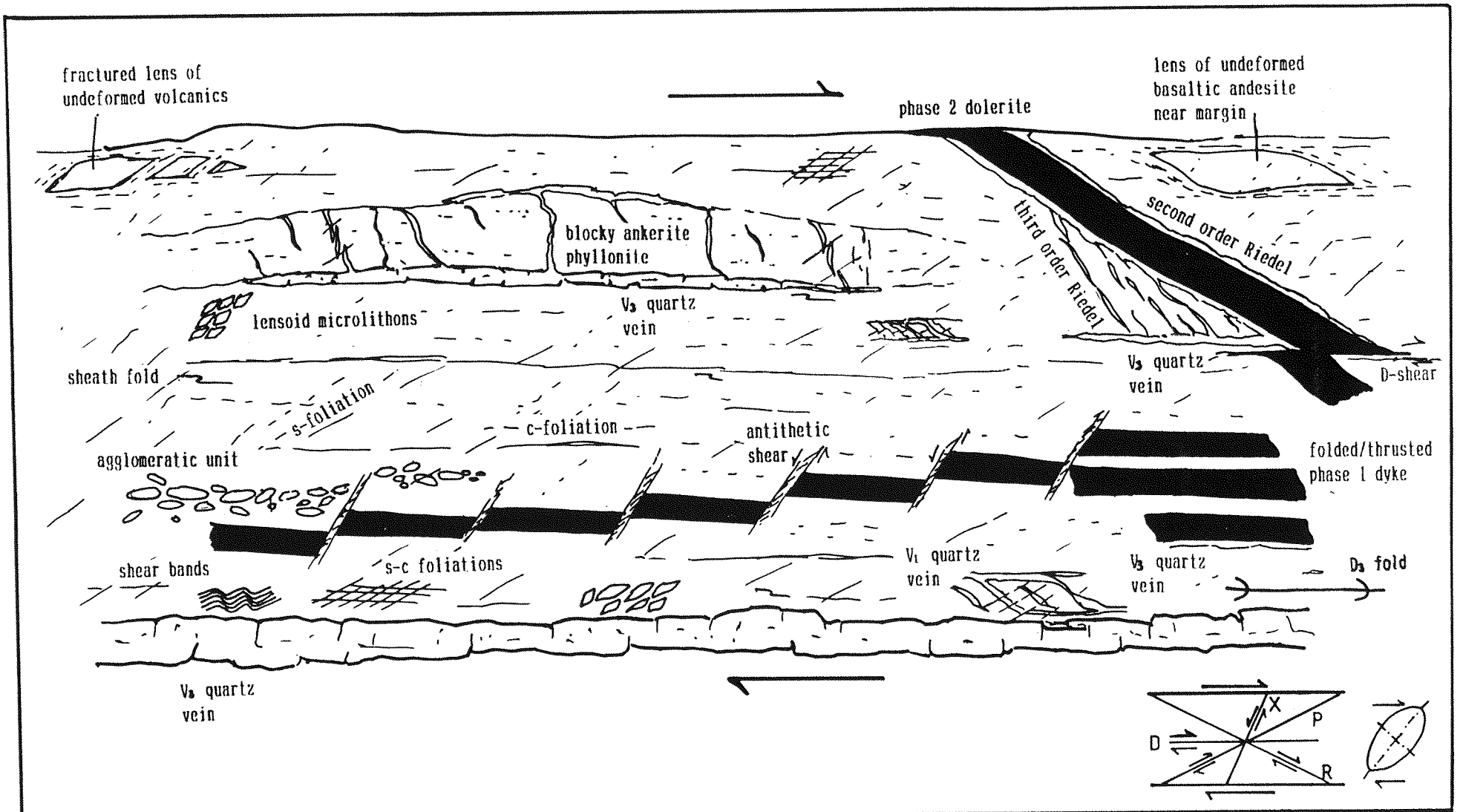

Fig.5.4 Characteristics of the phyllonite shear zone produced during dextral shear.

initially along the foliation surfaces, would probably result in a significant change in the mechanical properties of the shear zone and possibly initiated more brittle behaviour along the s-surfaces with the development of the extensional crenulation cleavages.

In most cases, the phyllonite samples are too friable or are too obscured by carbonate metasomatism for petrographic studies and only the more incipiently deformed samples can be examined. The 0.03-0.8mm-wide cleavage domains are delineated by fine-grained chlorite with minor biotite and are gradational into the microlithons composed of fine-grained (<0.1mm) chlorite, albite, quartz and calcite. Asymmetric augen of quartz-albite-calcite and s-c foliations in the finer-grained lithologies also indicate a dextral sense of shear (Plate 5.3d), and recrystallisation textures predominate over sub-grain development in the quartz grains. In the coarse hornblende-clinopyroxene-phyric volcanics where only a weak fabric is developed, the long axes of the hornblende phenocrysts are generally flattened and rotated into parallelism with the foliation. Often these grains display high-angle extensional fractures and minor chloritic pressure shadows due to dextral shear (Plate 5.3e). The smaller plagioclase grains show little evidence of deformation but the chlorite-actinolite pseudomorphs of the pyroxene phenocrysts form elongate patches sub-parallel to the foliation.

Similar micro-structures have been observed underground in altered host-rocks adjacent to the major auriferous veins. These kinematic indicators indicate that gold mineralisation and wallrock alteration were synchronous with dextral shear and are fully discussed in Chapter 6. The occurrence of dynamic recrystallisation, sub-grain development, micro-veining, and pressure shadows is indicative that both crytal-plastic and diffusive mass transfer processes were active during ductile deformation but the formation of s-c shear surfaces due to strain localisation suggests that these textures were produced in the semi-ductile regime (Shimamoto,1989) within the brittle-ductile transition (Sibson,1977).

5.5.3. The Gebeit Shear Zone System

The small-scale kinematic indicators, outlined above, show that the shear zones at Gebeit were produced during dextral, strike-slip, simple shear. Experimental shearing of clay blocks (e.g. Riedel,1929; Tchalenko,1970) has shown that shear zones are composed of a system of

shears on a lower scale. The orientations and sense of shear of the shear zones within the Gebeit block indicate they conform to a dextral shear zone array and D, R (Riedel), and P shears can be identified (Fig.5.5). These shear zones, along with later Red Sea rift related north-west and east-west structures e.g. Wadi Hadayu (see Fig.1.2), control the wadi drainage pattern on the local scale and probably on the regional scale. Within the Gebeit block, three major Riedel shears trending 070°N are evident: the Wadi Lode shear zone, on which Gebeit village is sited; the Wadi Tuwiya shear zone; and the North Gebeit shear zone, with a possible fourth Riedel (South Gebeit shear zone) to the south of the mine (Fig.5.5).

In the Gebeit block, only the Riedel shears are pervasively carbonate altered (see Plates 5.1 & 5.2a), implying they are preferential sites for large scale fluid movement, and as a result tend to appear as topographic highs, unlike the P shears. All the known auriferous veins are hosted by numerous parallel but subordinate, anastamosing shear zones from 2 to 20m wide which lie on either side of each main Riedel shear. The main zone of mineralisation on which the Gebeit mine is based lies immediately south-east of the Wadi Lode shear zone and comprises steeply south-east-dipping, blue-grey quartz veins hosted by shear zones showing a variable intensity of deformation. The veins are offset in both sub-vertical and sub-horizontal planes due to late-D_2, D_3 and D_4 deformation and consequently several lodes have been distinguished, namely the X, Y, A, Wadi and Arsenic Lodes (Fig.5.6; see Fig.5.18). Further north, the satellite prospects of Marble Bar, Vein 13, Vein 18 and East Gebeit, which lie in between the Wadi Lode and Wadi Tuwiya shear zones, have only been exploited by surface pitting (Marble Bar, Vein 18 and Vein 13) or exploration adits (East Gebeit). The structural control of the lode veins and their subsequent fragmentation by the later deformation events constrain the mineralisation phase as synchronous with early dextral strike-slip tectonism (see Chapter 6). Similarly, intrusion of the first phase of dyke emplacement, parallel to the c-foliation of the 070°-trending shears, confirms the extensional nature of these shears. Within an ideal shear zone array, the tensional and compressional components would lie oblique (approximately 20°) to the P and R shears (Fig.5.5) but at Gebeit, tensional features, i.e. syn-tectonic dykes and massive quartz veins, occur parallel to the Riedel shears. This is probably due to the northward convergence of the boundaries of the Gebeit array at 25° in which the ranges of possible shear orientations from the Wadi

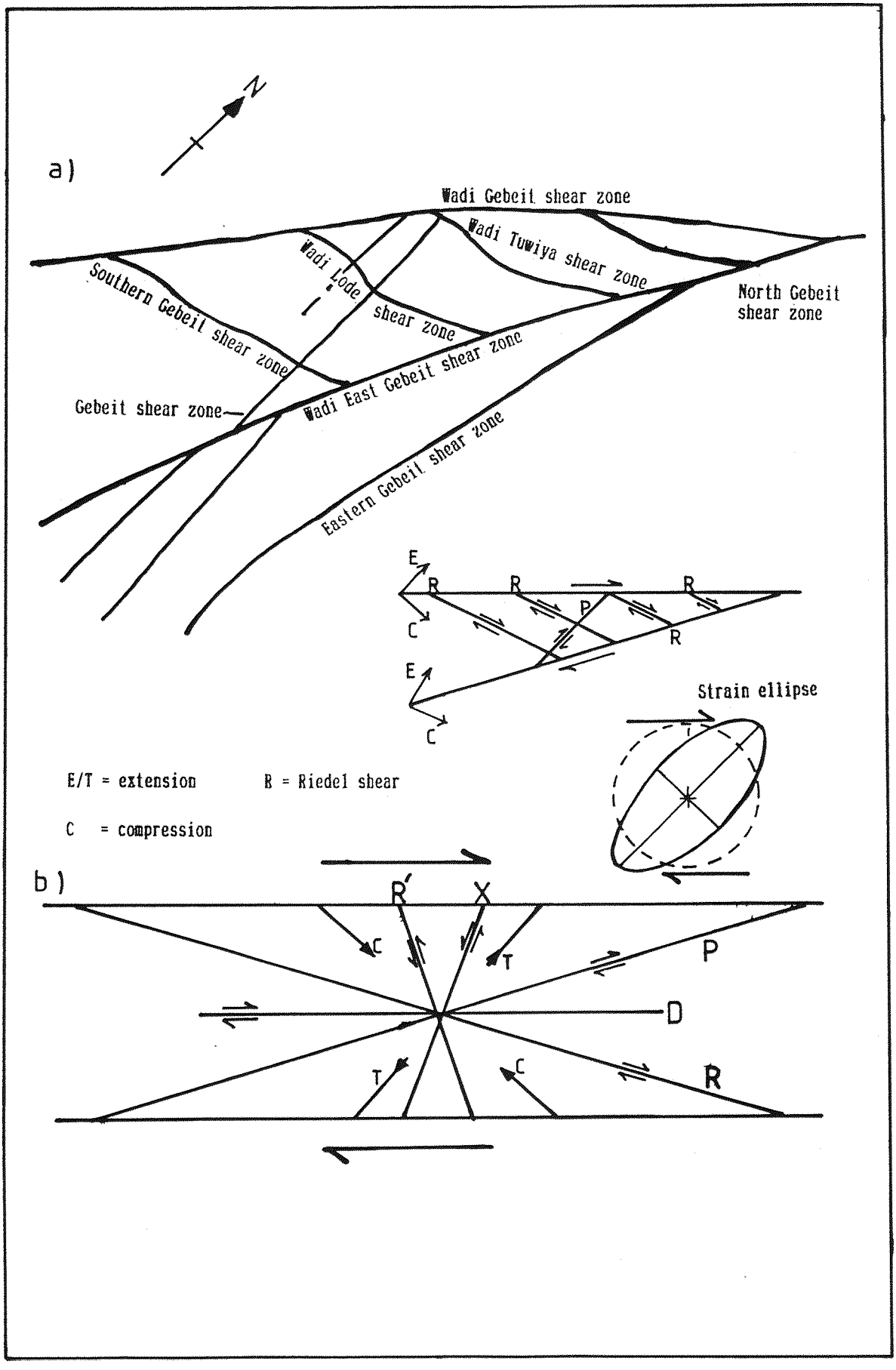

Fig.5.5 Geometry of the Gebeit shear zones (a) and their comparison with a dextral shear zone array (b) allowing identification of extensional and compressional shears.

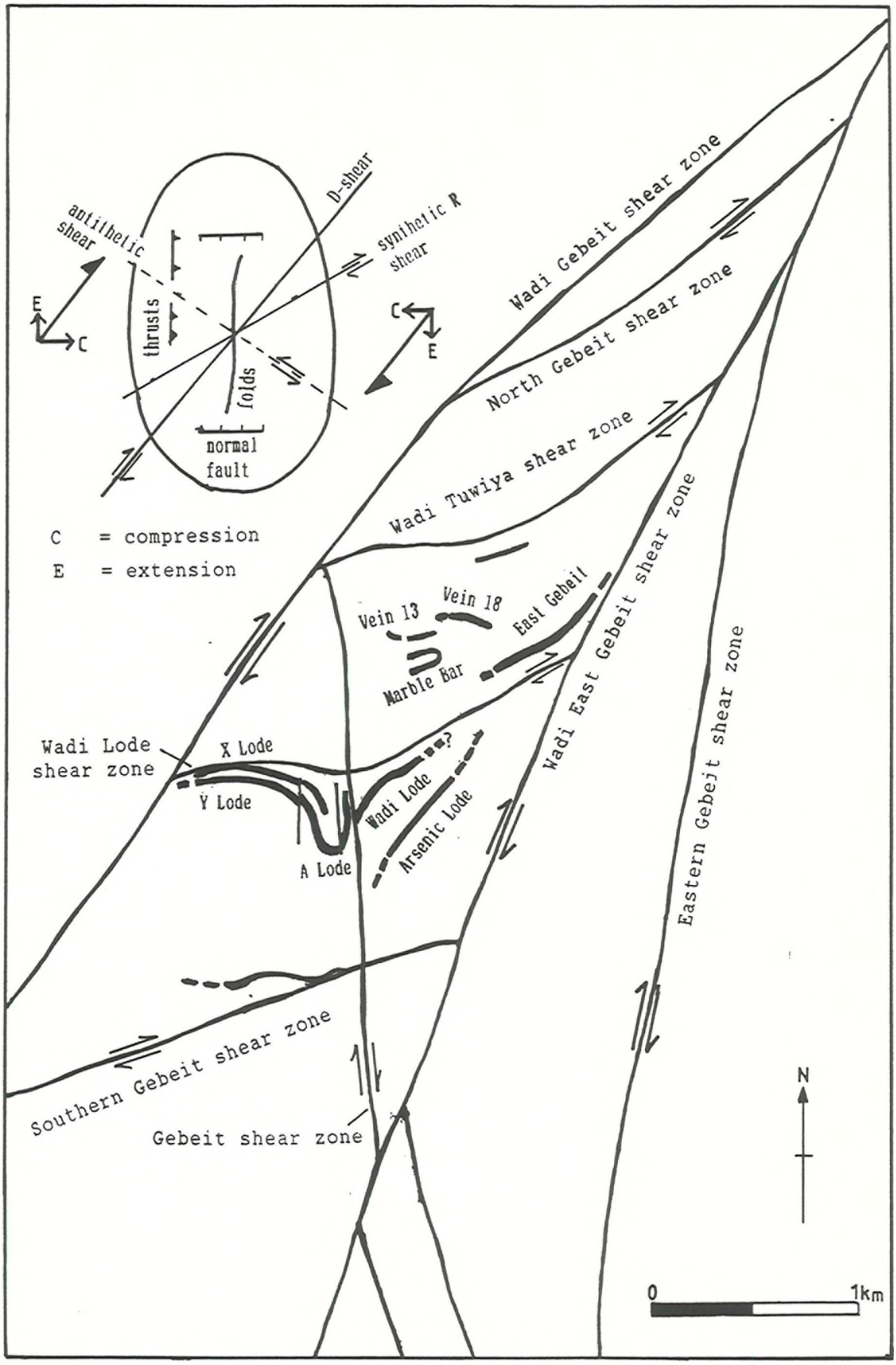

Fig.5.6 Orientation of the main veins at Gebeit in parallel with the extensional Riedel shears.

Gebeit and Wadi East Gebeit faults overlap the tensional (065-090°N) and Riedel (045-070°N) components.

Within the Riedel shears, the intensity of deformation appears to be polarised between the finer-grained phyllonites and the weaker deformation textures observed in the coarse-grained lavas and agglomerates; however, the degree of tectonic reworking is difficult to gauge in the finer tuffaceous units. All of the Riedel shears and auriferous V_1 veins at Gebeit tend to be developed within the fine-grained tuffs and shales towards the base of the stratigraphic succession or are confined to the thin tuffaceous units of the upper lava- and agglomerate-dominated succession (e.g. Marble Bar, see Fig. 5.11; Y Lode, see Fig.5.18). The loci of shear zone development may, therefore, have been controlled and concentrated by the fine-grained tuffaceous horizons which would tend to be preferentially deformed.

The main P shear at Gebeit is the north-south-trending Gebeit shear zone which intersects the Wadi Lode shear zone at the village and, although not widely exposed, appears to be approximately 15 to 25m wide. Like the other minor P shears, which have been identified from aerial photographs and by mapping, alteration is minimal and no syn-tectonic dykes or veins have been observed. Although no mineralisation occurs along the Gebeit fault at the intersection with the auriferous shears, parallel to the Wadi Lode shear zone, the original structural relationships are difficult to determine due to the repeated reactivation of these structures during later deformation events.

The Wadi East Gebeit shear zone differs from the other block-bounding shears in that intense deformation and alteration is restricted to a relatively narrow vertical zone 30-50 m wide which trends 020°N (Plate 5.3a). Approximately 750m east of the Wadi East Gebeit shear zone another prominent shear zone, similar to the Riedels at Gebeit, trends 010°N. This shear zone, termed the Eastern Gebeit shear zone, extends from the southern limit of the Garabein block to an intersection with the Wadi East Gebeit shear, 500m south of the junction of the Wadi Gebeit and Wadi East Gebeit shears (Figs.5.2,5.3, & 5.5). The width of the zone varies from 30m to 200 m and foliation dips steeply to the east. S-c foliations, stretching lineations, and extensional crenulation cleavages, similar to those seen at Gebeit, indicate a dextral sense of strike-slip shear along this zone but no pervasive carbonate alteration is evident except at the intersection with the Wadi East Gebeit shear zone.

At the northern-most end of Wadi East Gebeit, several isolated

outcrops of ankeritic phyllonite are located at the projected intersections of the Wadi East Gebeit shear zone and the Riedel shear zones (Fig.5.3), implying that these intersections were sites of enhanced fluid flow.

The nature of the intersection of the Wadi East Gebeit and the Eastern Gebeit shears is not clear but the predominant 020°N foliation of Wadi East Gebeit shear appears to merge with the 010°N-trending Eastern Gebeit fault zone, indicating they were coeval. The Gebeit fault can be traced south across the Wadi East Gebeit shear into the Garabein block, suggesting that early in the D_2 phase the Gebeit block was part of the Garabein block and subsequently became detached. The orientation of the Wadi East Gebeit shear zone indicates that it was initiated as a P-shear between the parallel Wadi Gebeit and Wadi Derba shear zones. The Eastern Gebeit may have been formed as a P-shear between the Wadi East Gebeit and Wadi Derba shear zones when the Gebeit block had become a separate entity (Fig.5.7).

As the Gebeit Riedel shears are located towards the northern end of the Gebeit block where the Wadi East Gebeit and Eastern Gebeit shear zones converge, it is difficult to determine whether they extend across to the Eastern Gebeit shear or terminate against the Wadi East Gebeit shear. Areas of weakly carbonatised phyllonite, intruded by phase 1 diorite dykes, outcrop immediately east of the Wadi Lode shear zone (around 5500E, 6900N) and indicate that the Riedels extend to the Eastern Gebeit shear zone. This suggests that the Eastern Gebeit shear zone may have been formed before the Wadi East Gebeit shear zone. However, the phyllonite zones along the centre of Wadi East Gebeit are not pervasively carbonatised like the Riedel shears west of Wadi East Gebeit shear zone and the Eastern Gebeit shear zone may not have been active during later shearing. As pervasive carbonate alteration along both the Wadi East Gebeit and Eastern Gebeit shear zones is restricted to their intersection with other structures (Fig.5.3), it appears that, like the Gebeit shear zone, enhanced fluid flow did not occur along these structures.

The strike ridges in the southern part of the Garabein block are rotated southwards into a north-south trend, apparently folded against the Wadi East Gebeit and Eastern Gebeit shears. This may have been due to a cessation of movement along the Eastern Gebeit shear zone which prompted further deformation along the Wadi East Gebeit shear zone. The complex area between the Wadi East Gebeit and Eastern Gebeit shear zones contains predominantly north-north-east-(010-020°N) trending

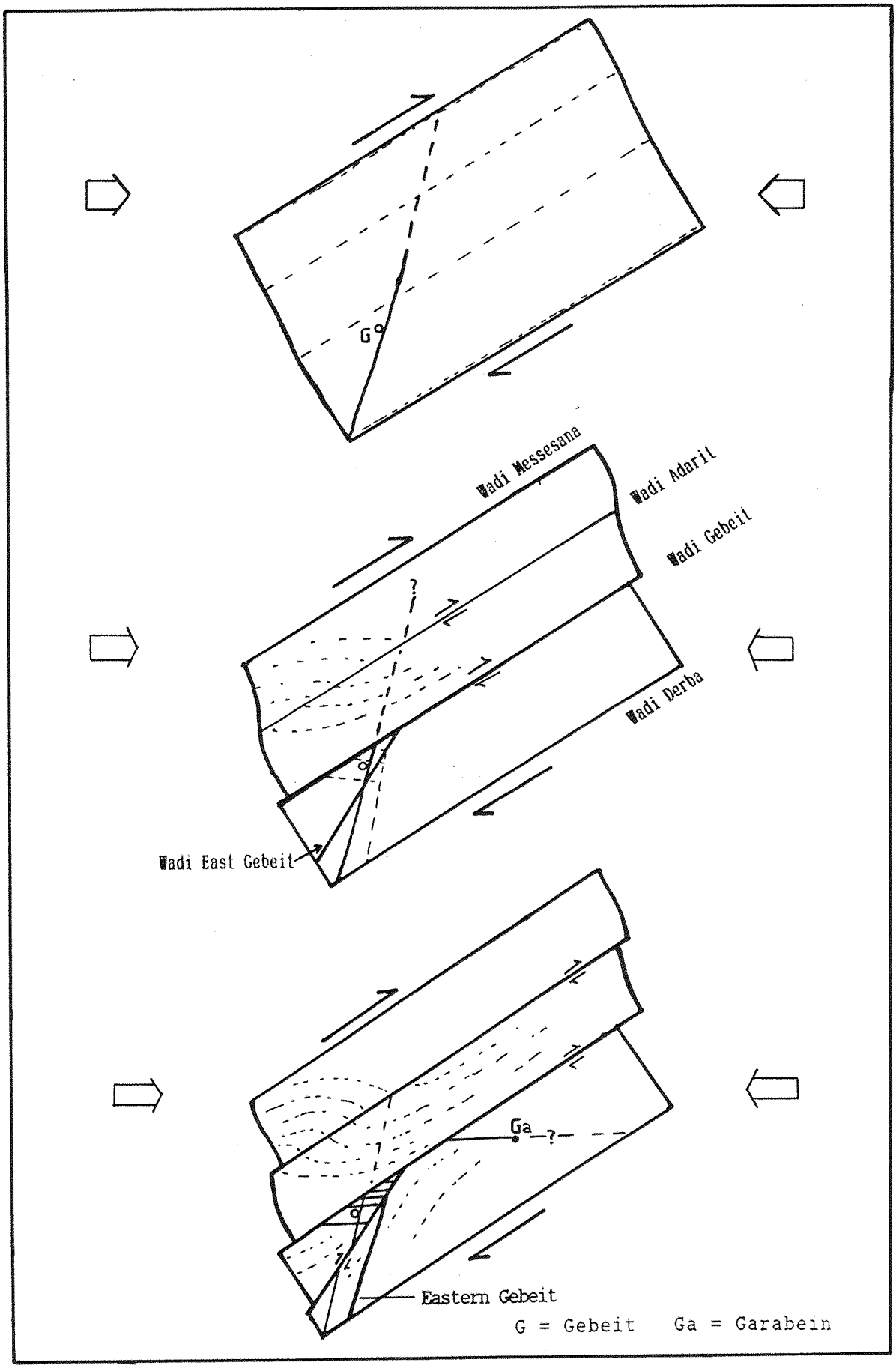

Fig.5.7 Sequence of shear zone formation at Gebeit during D_2 dextral shear.

structures and there are no major shears evident between the bounding shear zones other than the apparent continuation of the Gebeit fault to the south. Twelve kilometres north-east of Gebeit lies the satellite prospect of Garabein which is smaller than Gebeit but is the only other prospect in the area that was developed into a mine. The east-north-east trending auriferous quartz veins at Garabein are shear-hosted and lie parallel to a 070°N-trending shear zone (Wadi O'Haff). There is minimal pervasive carbonate alteration along this shear but its orientation suggests that, like Gebeit, the mineralisation at Garabein is controlled by east-north-east-trending Riedel shears related to a north-east-trending phase of dextral shearing.

The parallelism of the P- and R-shears at Gebeit with other fault splays in the area (Fig.5.1) suggests that similar shears were developed in the adjacent blocks as components of the 045°N-trending shear zone system with the north-south faults, e.g. the Gebeit fault, produced from the interaction of the 045°N-trending shear zones and their associated subsidiary shears. The dominance of the Riedel and D-shears in the Gebeit array produces sigmoidal lozenge-shaped blocks within the Gebeit block, especially at the northern end and is characteristic of an extensional strike-slip duplex (Fig.5.8; Woodcock & Fischer,1986).

The 045°-trending shear zones, which define the various tectonic blocks, extend to the southern margin of the Gebeit Volcanic Group outcrop where they change strike to form the continuous south-western boundary with the Sasa Plain tuffaceous slate (PG2) assemblages (Figs. 5.1 & 5.2). On these margins the shear zone foliations strike north-west and, as with the slate assemblages further west, dip at around 35° underneath each block. The north-east-trending bedding in the Gebeit Volcanic Group, likewise, is rotated to a NW strike, dipping to the north-east. The dextral sense of shear identified in the north-east-trending shear zones and their continuation round the south-western margins indicate that the blocks were transported to the south-west, eventually overriding the Sasa Plain slate assemblages. This implies that the north-east-trending, dextral, strike-slip shear zones acted locally as lateral ramps to south-westerly-directed thrusting induced by a regional phase of dextral deformation. The unexplained south-west directed thrusting observed in the Eastern Desert of Egypt, where north-west-directed thrusting is the predominant style of deformation (see section 2.6; Elbayoumi & Greiling,1984), is probably related to an early, dextral, strike-slip phase.

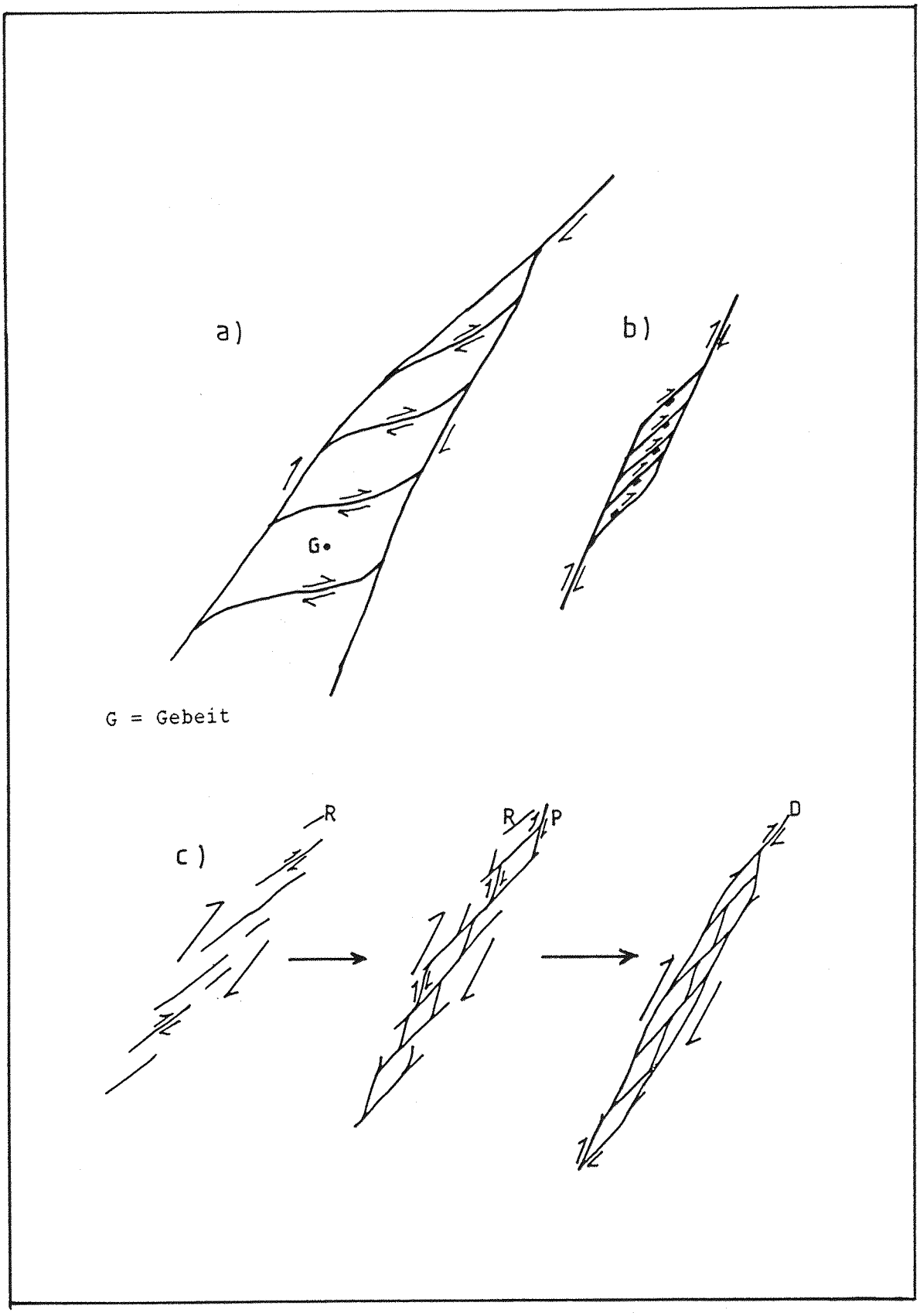

Fig.5.8 Comparison of the Gebeit shear zone array (a) with an extensional strike-slip duplex (b) and the sequence of extensional duplex development along a straight shear zone (c) (after Woodcock & Fischer,1986).

5.6 D_3, North-east-trending Folding and Thrusting

The third deformation phase recognised at Gebeit comprises north-east-trending (045°-060°N) folding and thrusting which occurred sub-parallel to the 070°N Riedel shear orientation. Stretching lineations parallel to the strike of foliation in the shear zones demonstrate a purely strike-slip mode of shearing during D_2 deformation and there is no evidence for transpression. As the Riedel shears are extensional in nature, folding and thrusting on this trend cannot be reconciled to the D_2 dextral strike-slip phase and has been designated as a separate phase within the framework of arc accretion. Thrusting appears to be largely restricted to a fold-accommodation process and seems confined to the partial reactivation of the D_2 Riedel structures which consequently makes the thrusts difficult to trace. The majority of thrusts generally exhibit minor displacements of less than 2 m but are usually closely spaced and in many cases are identified by the offset or repetition of dykes and veins.

The shear zone margins at Gebeit tend to be gradational with their limits set by the recognition of a relatively unsheared, continuous, protolith. The exposed footwall contacts of the the Wadi Lode and Wadi Tuwiya shear zones, however, are very sharp and mark the boundary between blocky, undeformed andesitic basalts and upper shear zone phyllonites (e.g. Plate 5.2a). These basal contacts dip at relatively shallow angles (25-45°) to the south-east and are sometimes delineated by massive white quartz veins up to 80 cm thick (5050E,6000-6300N). In contrast with the general steep dip of the shear zone fabrics, foliations in these areas dip variably from 20° to vertical and north-west-facing recumbent folds are common. Where the contact is well defined at Bishops Dam and the Wadi Lode extension, the phyllonite outcrops trend 050°N, oblique to the main 070°N trend of the Riedel shears and the sharp lower boundaries of these phyllonites appear to be thrust contacts produced by local décollement during folding. Along the phyllonite ridge which forms a topographic high, parallel and north-west of Wadi Tuwiya, D_4 folding has resulted in localised preferential erosion through the shear zone (4400E,6600-6900N). The underlying undeformed volcanics, with steeply dipping (135°N/80°) north-east-trending bedding are exposed, with the Wadi Tuwiya shear zone phyllonites preserved as a small klippe ≈50 x 20 m which dips at 45-50° to the south-east (Fig.5.3).

Further east along strike, the 030°N-trending foliation abuts

sharply against blocky undeformed volcanics along a 070°N-trending fault plane dipping at 60° south (Plate.5.4a). Slickensides are very poorly developed at the intersection but localised, minor, upright folding sub-parallel to the trend of the fault indicates it is an oblique ramp related to D_3 thrusting. A similar structure at the southern end of the shear zone at Bishops Dam occurs within 017°N-trending phyllonites and has been identified due to its locally anomalous 070°N trend (Plate 5.4b). This thrust rapidly changes dip along a 1.5 m perpendicular section from 60° to 32°, parallel to the south-east dip of the footwall phyllonites and demonstrates the localised nature of D_3 thrusting. Thin (10-25 mm) quartz-carbonate veins are developed along the trust plane along with tensional veins normal to the fault surface. Slickensides trend 330-340°N and small recumbent footwall folds trend 040°N, indicating a north-west direction of transport.

At the north-eastern end of the Wadi Lode shear zone a topographic depression provides a cross-section through the contact area along 5950N (Fig.5.9). Along a 50m section line perpendicular to the strike, a minimum of twelve thrusts can be identified dipping at 25-60° to the south-east with the steeper, and presumably older, thrusts furthest from the contact. Many of the carbonate phyllonite blocks bounded by the thrusts have north-east-trending parallel joint sets orientated perpendicular to the fault surface. Often these joints are infilled by massive, white, quartz ladder veins, up to 30 mm wide, some of which are gently folded. Low angle (<40°) reverse kink bands, which dip to the north-west, commonly intersect fine (8-15 mm) quartz-carbonate veins generated along the thrust surfaces and indicate a component of back-thrusting. Although most of the phyllonites are cohesive and blocky due to pervasive carbonate metasomatism, there are two thrust-bounded lensoid pockets of recumbently folded (050°N), dark green, chlorite phyllonite, indicating that the carbonate alteration event preceded D_3 deformation. As the non-carbonate altered phyllonites are highly sheared, it is unlikely that they represent preferentially unaltered protolith blocks and are probably derived from the shear zone footwall. The movement on each thrust is difficult to quantify due to a lack of identifiable marker horizons but the deviation of the zone from the presumed 070°N Riedel shear trend indicates a combined displacement across the whole zone of less than 150m. The thrusts are difficult to trace individually to the south-west as they strike sub-parallel to the foliation and reactivate low angle c-surfaces.

Plate 5.4 D_3 structures in the shear zone phyllonites.

a) View north at East Gebeit (4500E,7000N) showing the D_2 fabric of the Wadi Tuwiya shear zone (left) abutting against undeformed andesitic volcanics along a D_3 oblique thrust ramp.

b) Section through Wadi Tuwiya shear zone at Bishops Dam (4000E,5900N) showing a high-angle D_3 frontal thrust ramp with minor V_3 veining (hammer scale = 40cm).

c) North-east-trending F_3 isoclinal recumbent fold in sheared andesites in footwall of Wadi Lode shear zone (4900E,5500N).

d) North-east-trending, open, recumbent F_3 folding of ankerite phyllonites at southern end of Wadi Gebeit shear zone.

e) High-angle V_3 NW-trending extensional veins in ankerite phyllonites at Bishops Dam (4000E,6000N).

f) East-west-trending, second order V_3 Riedel veins (R_2) along margin of phase 2 dolerite (Do) linked by third order V_3 Riedel veins (R_3) to V_3 vein along D-shear (Wadi Lode shear zone, 4950E,5325N; width of dyke ≈1m), indicative of late-D3 dextral shear.


a

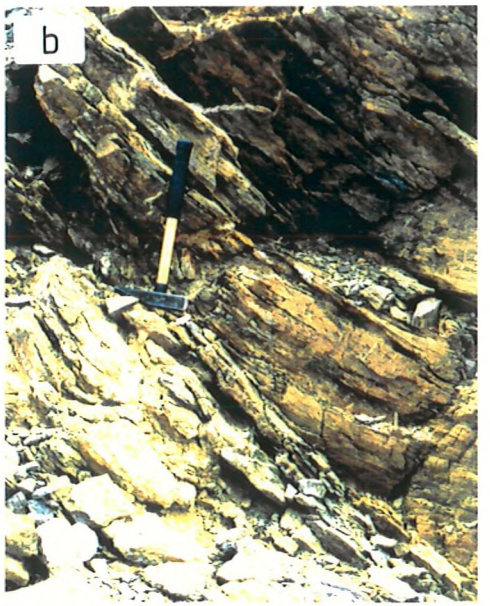
b

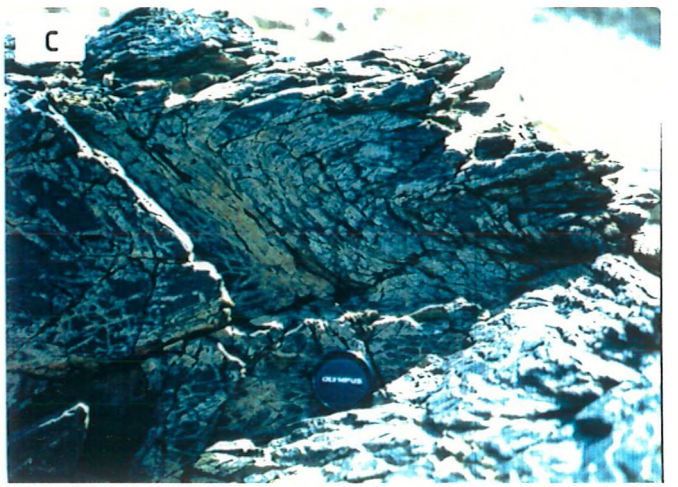
c

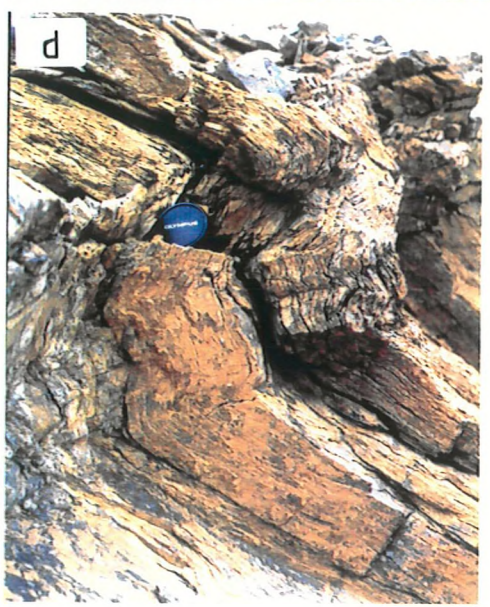
d


e

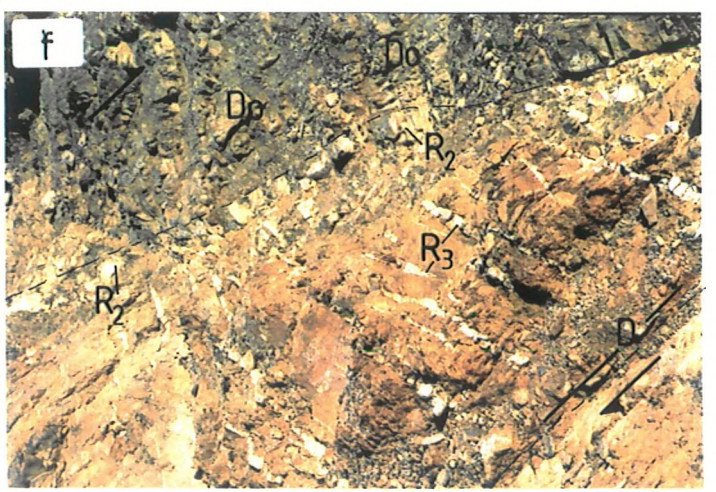
f
D0
D0
R2
R3
R2
D

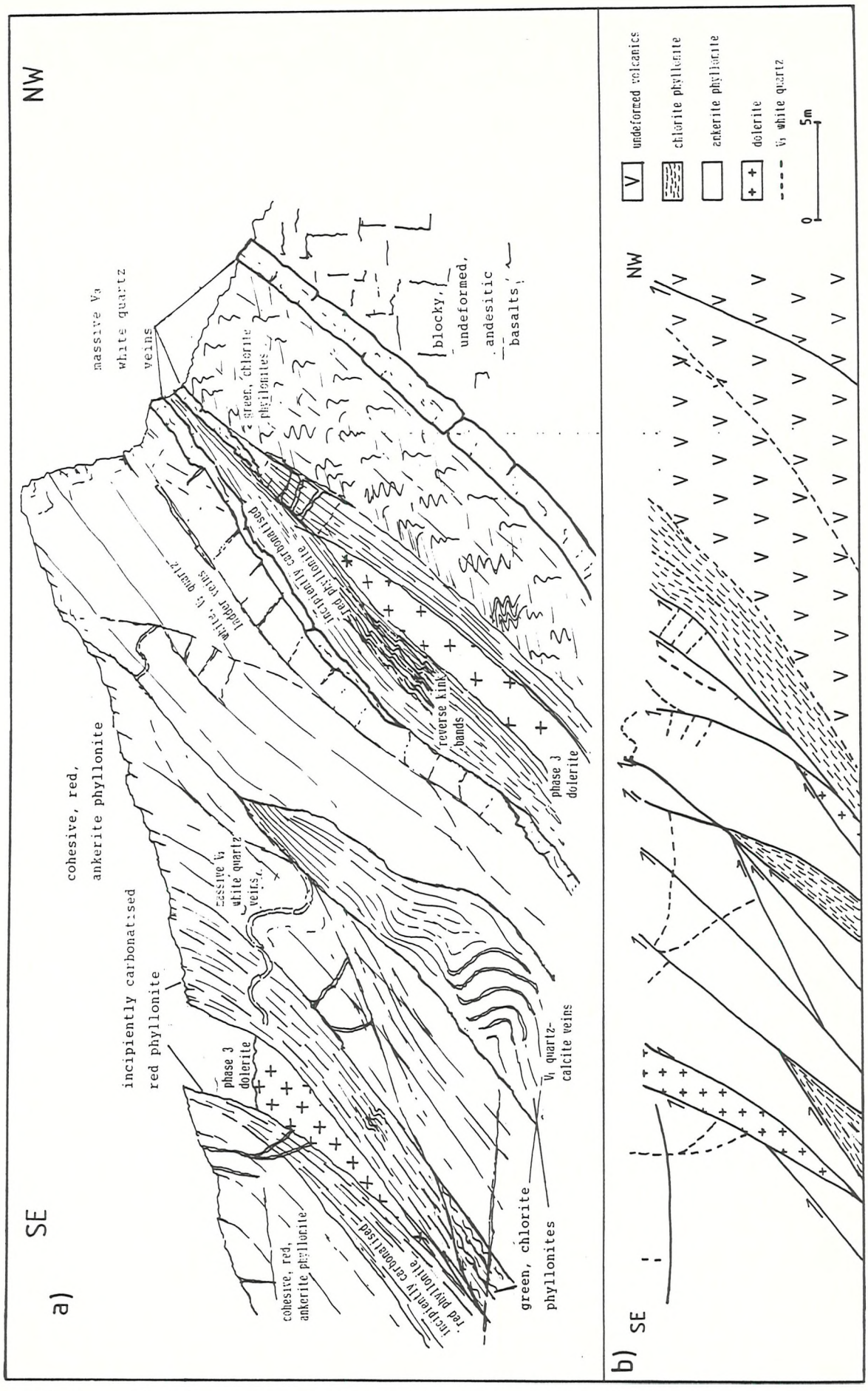

Fig.5.9 Sketch section (a) and measured section (b) normal to strike at the northern end of the Wadi Lode shear zone showing the effects of D_3 thrusting.

Recumbent parabolic folds (15-45 cm wavelength) trending 030-050°N occur in the sheared footwall volcanics at a few locations (e.g. 4900E, 5500N; Plate 5.4c). Recumbent folds on the same trend are evident within the shear zone phyllonites (Plate 5.4d) but vary from 50cm wide (Wadi Lode extension 5100E,5800N) and 1.5m wide (Vein 18, 4450E,6300N) to folds many tens of metres in wavelength at the northern end of Wadi Tuwiya (4600E,6950N). Often a weak local axial planar cleavage is developed through the fold hinges, with dip ranging from horizontal to shallow (<40°) to the south-east. The smaller-scale recumbent folds sometimes show minor displacements along these axial planar surfaces due to shearing across the lower fold limbs. The relatively open form of these folds, their formation in weakly deformed lithologies, their consistent north-easterly strikes and straight hinge lines preclude their origins as sheath folds. Sheath folds would parallel foliation trends and plunge steeply or lie upright in shear zones with steep fabrics; however, all these folds are recumbent irrespective of the original dip of the host foliation. East of Marble Bar (4900E,5600N), an outcrop of carbonate altered phyllonite, possibly another klippe, comprises a sub-vertical D_2 foliation (70° to SE) transected by a coarse, sub-horizontal, (<20° to SE) crenulation cleavage, S_3. Cleavage spacing varies between 5cm and 20cm and produces small, recumbent, chevron folds and kink bands up to 18cm wide which give an overall north-west sense of vergence (Fig.5.10).

Within Marble Bar prospect itself (4700E,5900N) the central area consists of a rim of tuffaceous phyllonite and quartz-carbonate veining which dips away on all sides from a central block of massive andesite lavas (Fig.5.11). This dome structure is the result of folding on two trends i.e. north-east and north-north-west related to D_3 and D_4 deformation phases, respectively. Folding on the north-east trend (045°N) reflects a fairly gentle open and upright style of folding but a small (1.2m) monocline on the western side of the prospect indicates north-westerly vergence. Drilling at the prospect has shown that the south-easterly dipping shear zone and quartz vein of Vein 13 propect, west of Marble Bar, is the continuation of the Marble Bar shear defining a minor synform along grid line 5100E.

Further south towards the intersection of the Wadi Lode shear zone and the Gebeit Fault (4900-5100E,5350N), a phase 1, syn-tectonic microdiorite dyke is, in two locations, repeated three times by south-east-directed back-thrusting (see Fig.4.3). Thrusting appears to have been controlled by the lower dyke-phyllonite interface with ramp

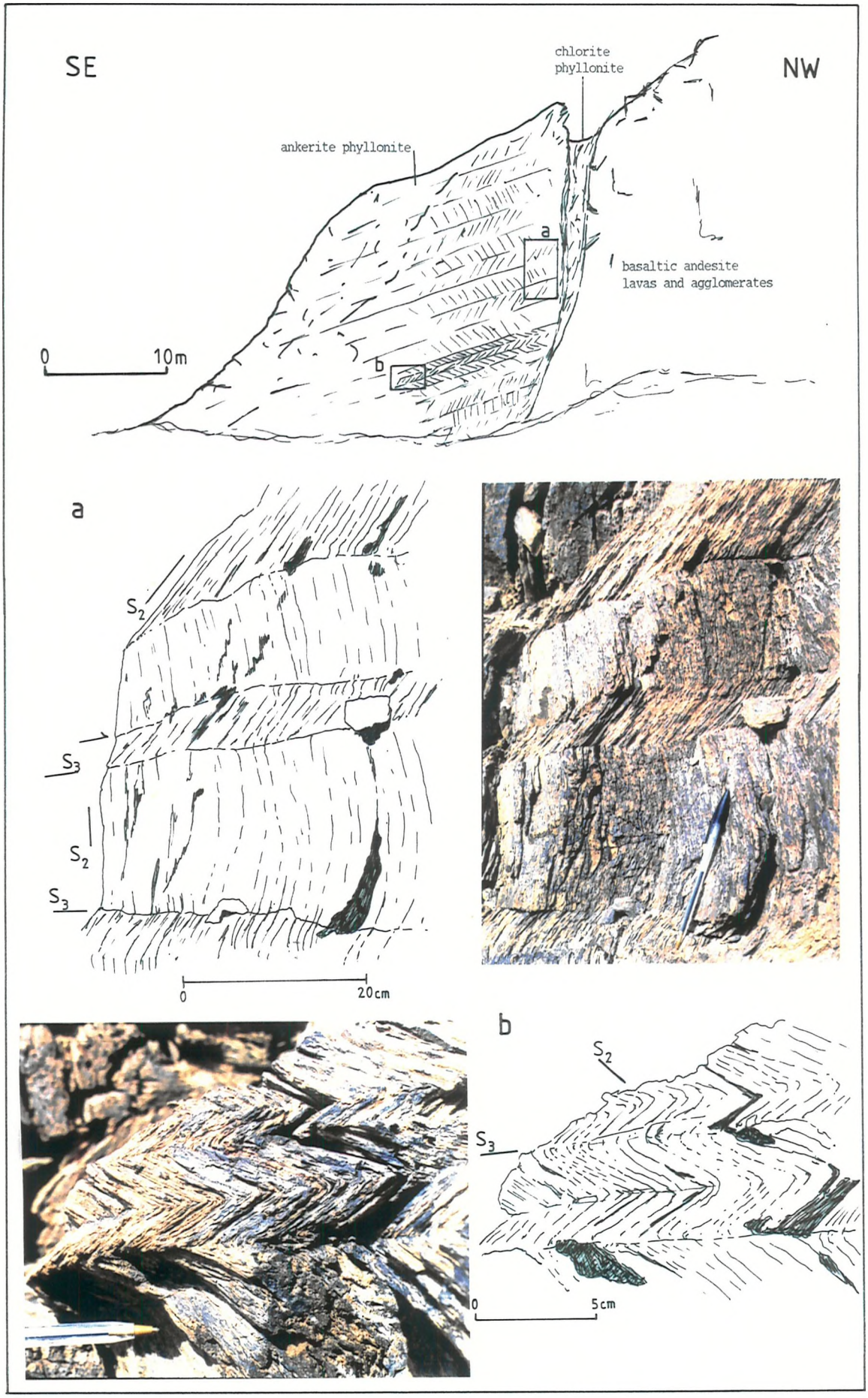

Fig.5.10 D_3 thrust structures in the klippe of ankerite phyllonite 100m north of the Wadi Lode shear zone.

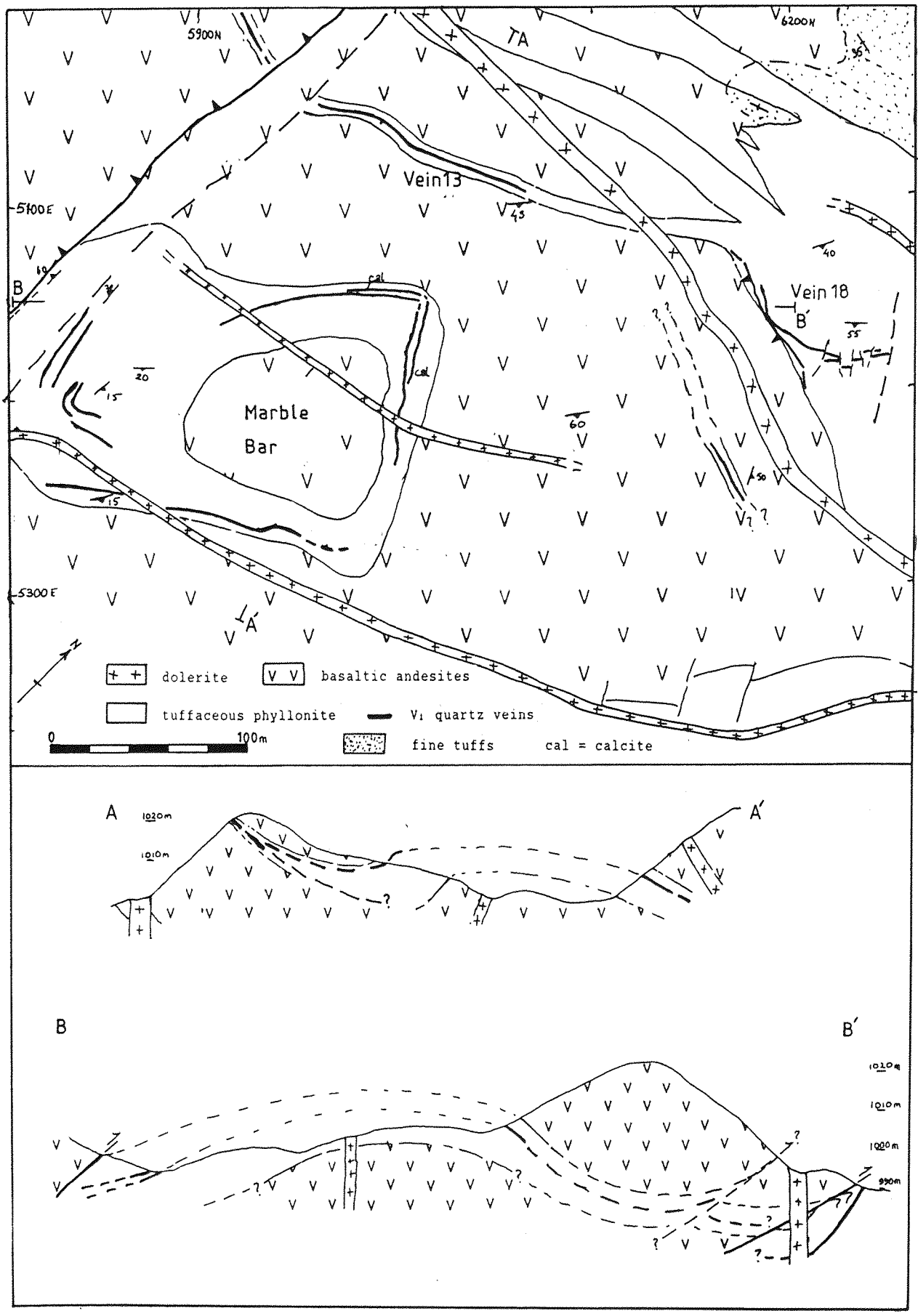

Fig.5.11 Sketch map and cross-sections of the Marble Bar, Vein 13, and Vein 18 propects showing the effect of D_3 and D_4 folding.

propagation at 45° to the upper dyke surface. The initiation of thrusts is common along the upper and lower surfaces of more competent layers within the preferentially reactivated phyllonite shear zones and occurs along lode veins and units of blocky carbonatised phyllonite as well as dykes (Fig.5.12). A similar mechanism of thrusting along the footwall of the shear zone accounts for the incorporation of wedges of non-carbonatised phyllonite along the base of the blocky, ankeritic phyllonite outcrops (Fig.5.9).

150 m south-west of the mine centre (5300E,4450N), a short exploration decline (-45°) has been driven at the base of a thick north-west-trending (116°N) quartz vein complex which is up to 2 m in thickness and extends in continuous outcrop for nearly 300 m. The veins lie approximately 500 m south-west of, and parallel to, the outcrop of the Y Lode but are apparently uneconomic. The outcrop comprises a set of 3 early blue, V_1, quartz veins of 0.75 m combined thickness intruded by a sub-parallel, 1.5m thick, massive, white quartz V_3 vein. The veins are hosted by ferruginous phyllonite and appear to lie parallel to the foliation but the shear zone extends less than 20 cm from the vein margins. The blue quartz tends to form the upper and lower boundaries of the vein complex but cross-cutting veins of the much thicker white quartz indicates the blue quartz is the older of the two. The intruding white quartz veinlets are orientated either parallel to the margin of the blue quartz vein or at 30-40° clockwise from it, suggesting formation under dextral strike-slip shear (Fig.5.13 inset). The cross-section provided by the decline, however, shows that the lower exposed blue quartz veins and hosting shear, which initially dip at 52° to the south-west, shallow out 5 m down dip and are transected by the footwall of the white quartz (Fig.5.13). The blue quartz and enveloping sheared tuffs display fracture cleavages parallel, normal and 30° to the vein margins which are usually infilled by the white quartz. The ferruginous alteration is confined to the shear zone immediately adjacent to each blue vein and does not occur as a halo to the white quartz.

The structural relationships infer that the Riedel-parallel shear zone and blue quartz veins were gently folded prior to the emplacement of the white quartz vein. The thickness of the white quartz vein and the orientations of the cross-cutting veinlets suggest that the white quartz vein was not formed during D_3 folding or thrusting but was emplaced under extensional, dextral, strike-slip shear which partially reactivated the shear zone. The thick white quartz veins which occur

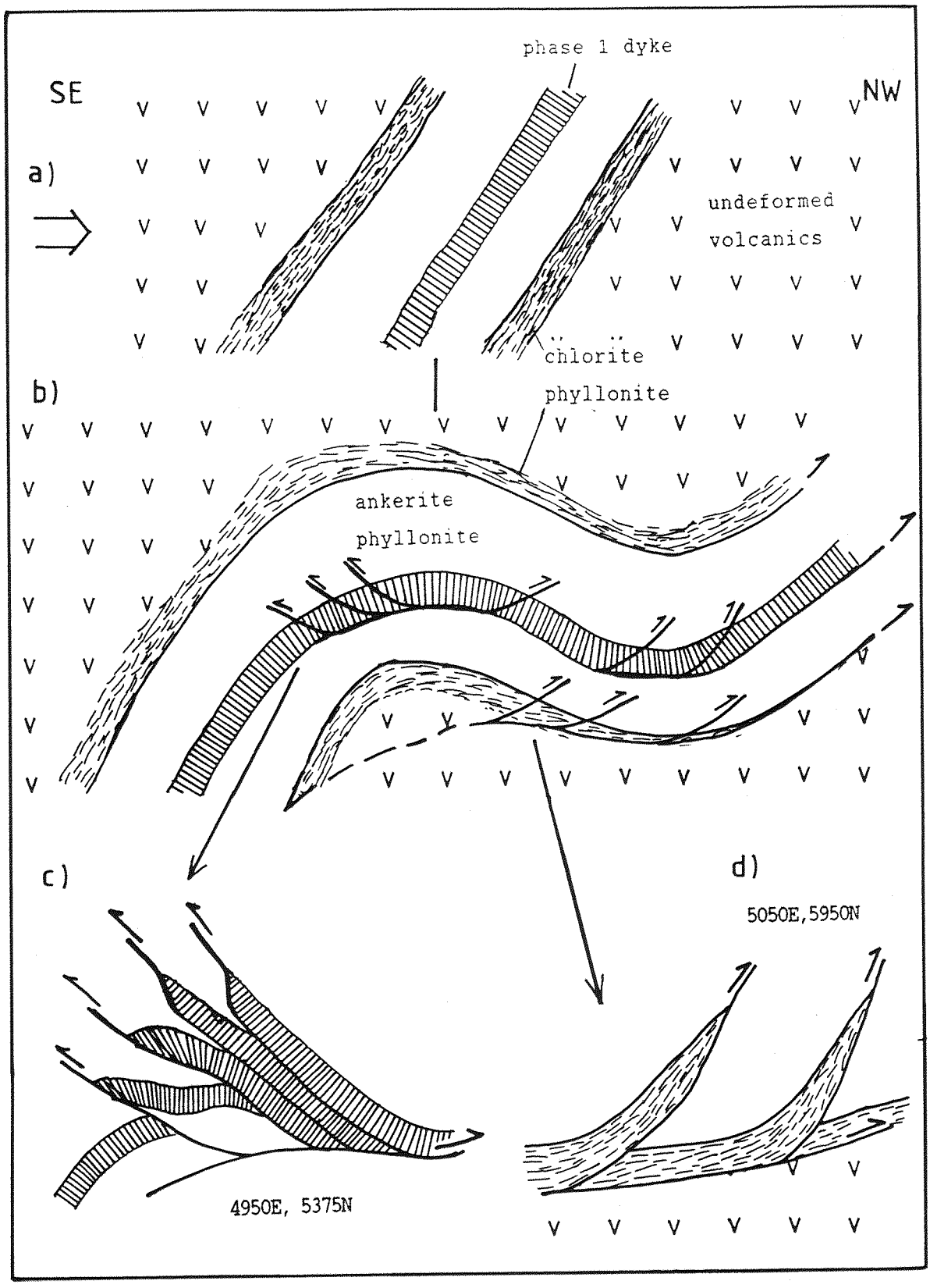

Fig.5.12 Sketch sections of a Gebeit Riedel shear showing the effects of D_3 folding (a-b). Thrust ramp propogation along the base of more competent units such as blocky, carbonatised phyllonite or phase 1 dykes produces stacking of dykes by back-thrusting (c) or lenses of chlorite phyllonite between cohesive ankeritic phyllonite (d).

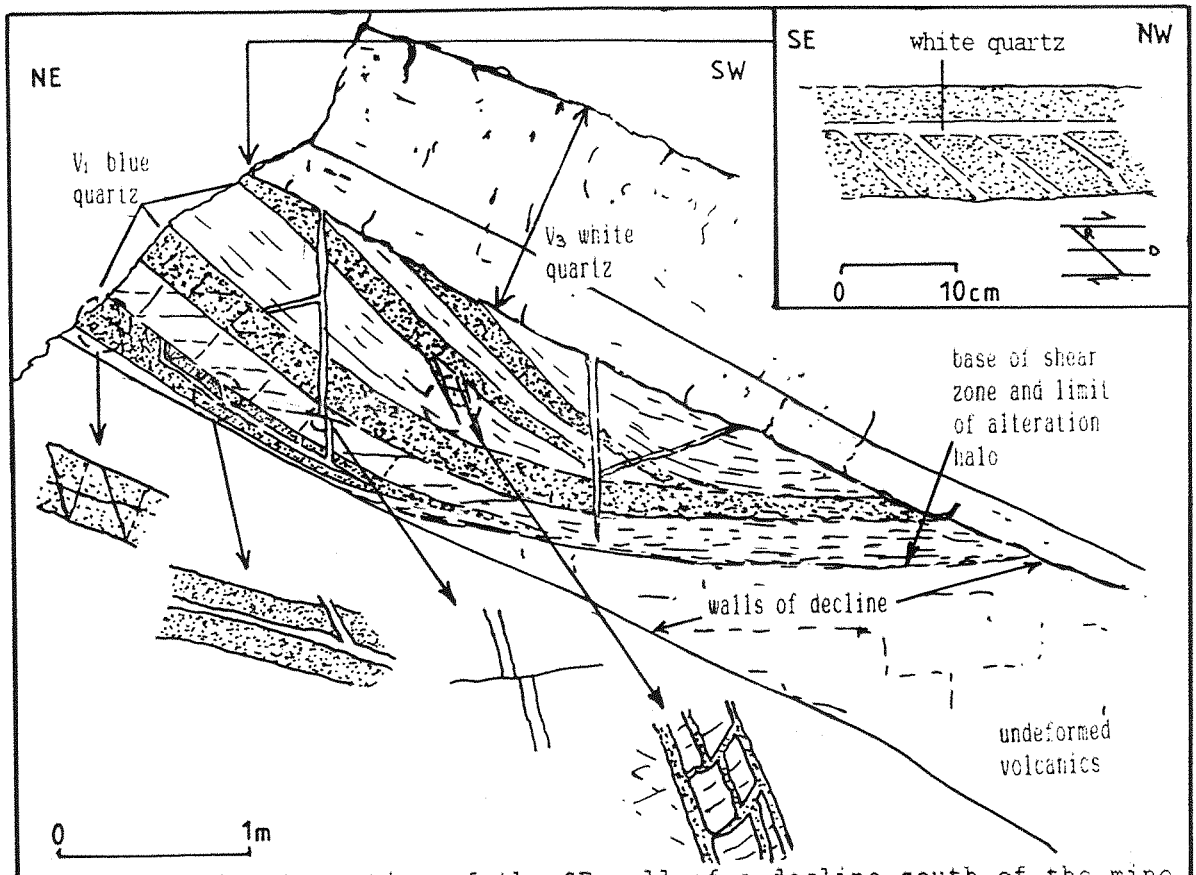

Fig.5.13 Sketch section of the SE wall of a decline south of the mine showing the relationship of the V_1 and V_3 quartz veins. Inset, sketch section parallel to strike.

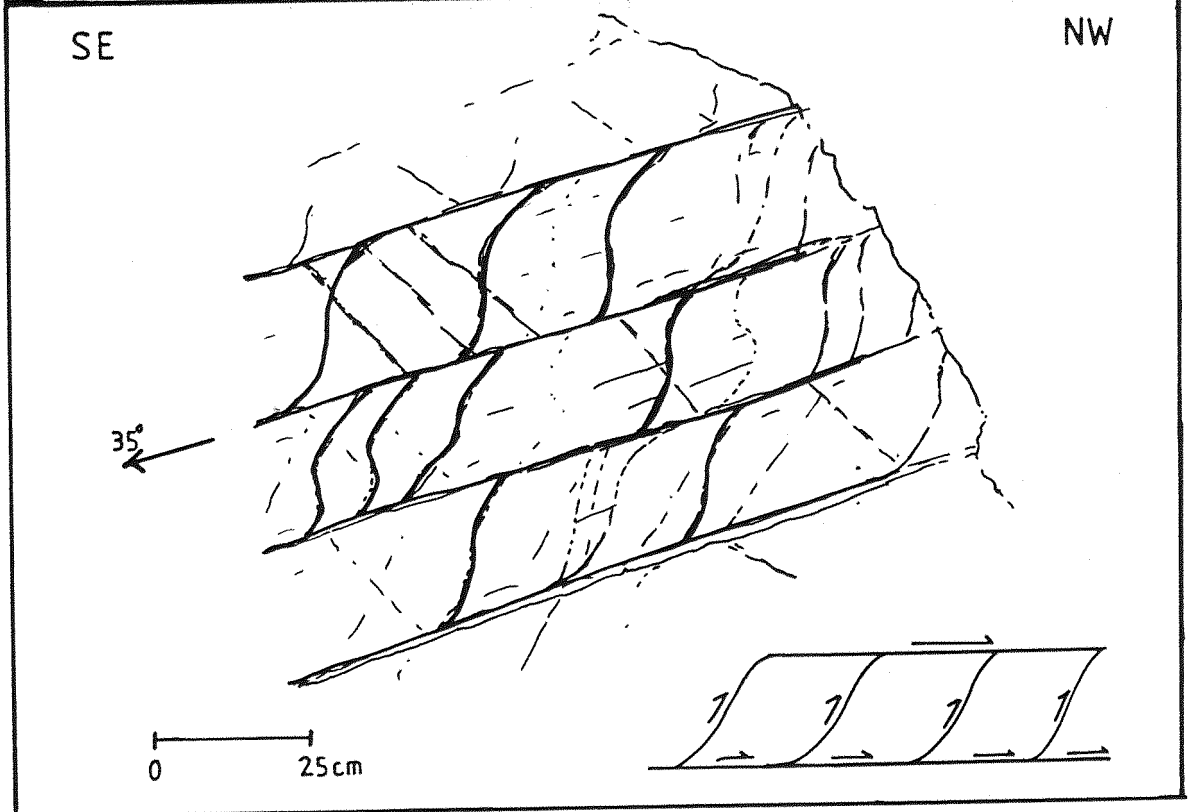

Fig.5.14 Sketch of D_3 thrust duplexes developed in andesitic tuffs at Garabein mine, 12km north-east of Gebeit.

towards the bases of the Wadi Lode and Wadi Tuwiya shear zones were probably emplaced during this second phase of dextral slip.

5.6.1. D_3 Deformation Beyond the Gebeit Block

Thrusting is not restricted to the Gebeit block alone and has been observed in the adjacent tectonic blocks, usually trending north-east. At Garabein, the north-east- (040°N) striking vertical bedding contains two vertical- to steep south-easterly-dipping fine cleavages trending 000°N and 035°N which are probably related to D_2 dextral shearing (i.e. s-c surfaces). These are transected by two low-angle (35-40°) later, coarser, foliations, which trend 040-060°N dipping to the south-east, and 330°N dipping to the south-west, and which probably represent D_3 and D_4 phases respectively. The south-east-dipping D_3 fracture cleavage tends to be localised, unlike the more pervasive D_2 foliations, and is associated with groups of closely spaced thrust surfaces (<40cm apart) which occur in both sheared and unsheared tuffaceous volcanics. The thrusts are often connected by sigmoidal imbricate thrust surfaces forming small-scale duplexes indicative of north-west-directed deformation (Fig.5.14).

Similarly, ENE-trending structures hosting blue quartz veins, identified immediately south of Um Arad prospect, display discrete parallel white quartz veins adjacent to the blue veins. This indicates that continued structural reactivation related to D_2 dextral shearing was not restricted to Gebeit.

5.6.2 Post-D_3 Dextral Shearing

In places where the D_2 foliation dips at shallow angles due to D_3 folding (e.g. Bishops Dam), later, steeply-dipping fabrics due to late-D_3 dextral shearing produce extensive pencil cleavages. This second phase of dextral strike-slip tectonism following D_3 deformation is confirmed by the emplacement of the east-west-trending, phase 2 dolerite dykes which display transitional calc- alkaline to alkaline geochemical affinities. Immediately north-east of the Gebeit and Wadi Lode shear zone intersection (see Fig.4.3; 5175E,5150N), one of these sub-vertical dykes can be traced down to 4 Level of the Wadi Lode where it cross-cuts the auriferous veins. Although the dyke is not affected like the lodes by D_3-related folding or thrusting, it is offset by foliation-parallel dextral shearing and folding (Fig.5.15).

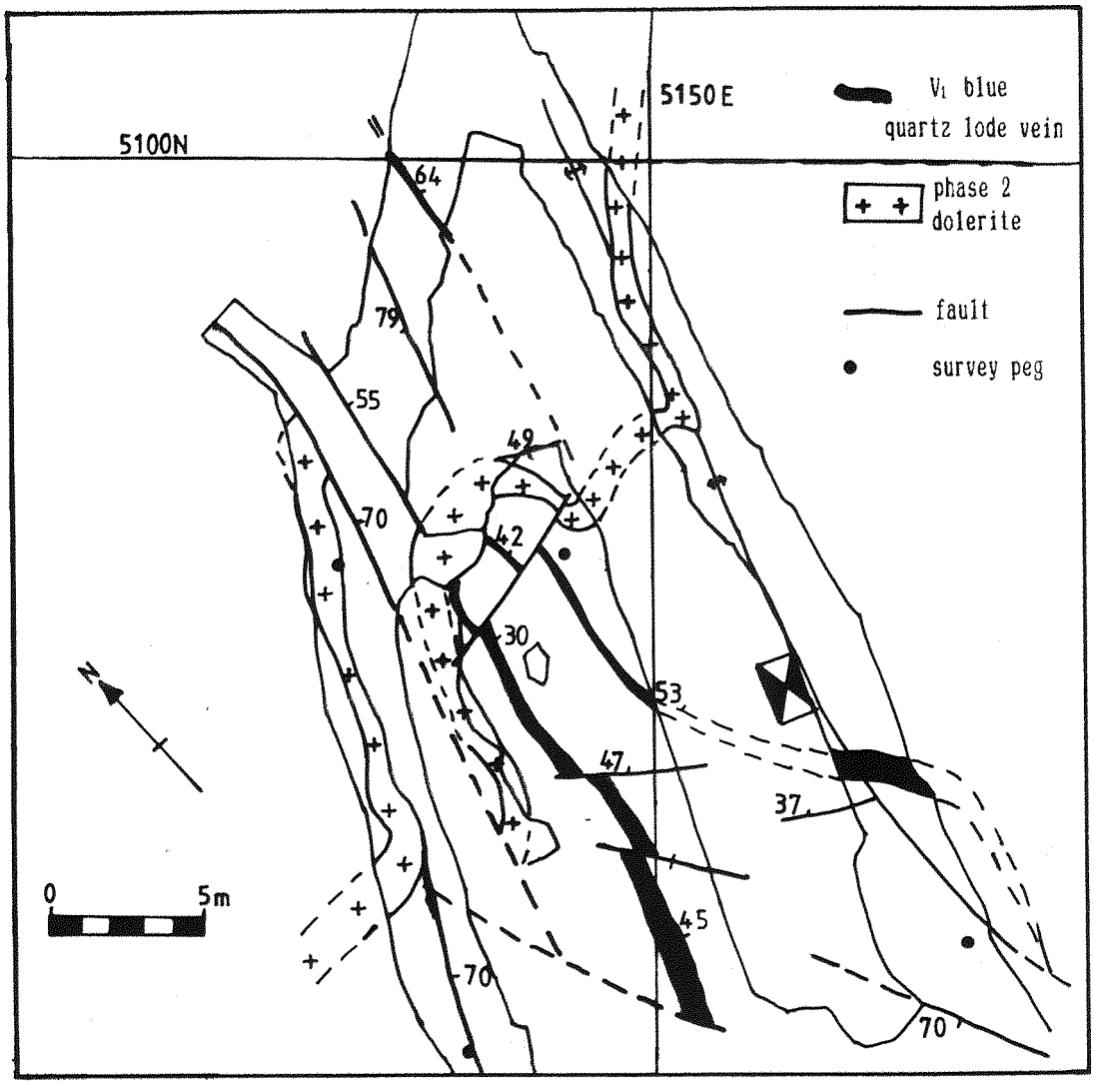

Fig.5.15 Sketch map of a section of the Wadi Lode exposed on 4-level (mapped by Greenwich Resources).

Restoration of the dyke indicates that a combined displacement of 15 m due to dextral folding and faulting occurred parallel to the strike of the shear zone across the exposed 25 m zone. This figure is a minimum estimate as sinistral reactivation associated with early D_4 deformation may have recovered some of the dextral displacement.

300 m to the north, within the Wadi Lode shear zone (4950E,5300N), another phase 2 dyke cross-cuts the back-thrusts which repeat the phase 1 microdiorite dykes (see Fig.4.3). This dyke is bounded on both sides by parallel, massive, white, V_3 quartz veins from 5-23 cm wide, implying that the structure has been reactivated at least once. High-angle (50-60°) discontinuous veinlets link these veins to massive white quartz veins generated parallel to the c-surfaces (Fig.5.4). The coeval formation of these vein sets is compatible with extension during dextral strike-slip shearing. From the regional scale (tens of km)

through outcrop scale (1-10m) to the scale of thin sections (0.1-10cm), second and third order shears are evident. The east-west-trending veins and dykes lie along the extensional Riedel surfaces relative to the margins of the Wadi Lode shear zone, which is itself a Riedel shear. Similarly, the link veins occur along second order extensional shears relative to the east-west veins (see Plate 5.4f, Fig.5.4).

Similar vein sets occur in the blocky altered phyllonites at Bishops Dam where north-east-trending white quartz veins, preferentially developed parallel to the less ductile horizons, are linked by irregular, second order, extensional (Riedel orientation) veins which dip at >65° clockwise from the margin of the fractured unit (Plate 5.4e; Fig.5.4). The small white Riedel veins formed in the phyllonites during early dextral shearing, which are initially similar in appearance, dip at <45° to the c-foliation, are often carbonate infilled, and are transected at 90° by a pressure solution cleavage. These veinlets are also often strongly sigmoidal in shape and occasionally offset by shearing along c-surfaces. The length and relatively high angles of the later Riedel veins contrast with the earlier Riedel veins. The later veins are not cut by pressure solution cleavages, indicating that dextral shear was accommodated by fewer, discrete, shear surfaces. These surfaces appear to have been preferentially reactivated along the margins of less ductile units such as the pervasively carbonatised, blocky, phyllonites, the early lode veins, and syn-tectonic dykes (Plate 5.4f, Fig.5.4).

The relationship between emplacement of the phase 2 dykes and the later dextral shear-related, white quartz veins is unclear. As the dykes are often bounded on both sides by veining, it would appear that the dykes were intruded first since it is not likely that the dykes would be emplaced along the centres of pre-existing quartz veins. Further dextral movement following dyke intrusion is evident and could account for the late-stage vein orientations. The dykes, however, are not cut by this veining which infers that reactivation occurred along the dyke margins.

5.7 D_4 Deformation, Easterly Directed Folding and Thrusting

The final phase of accretion-related deformation commenced when post-D_3, dextral, strike-slip shearing was reversed to a late phase of sinistral displacement prior to NNW-trending folding accompanied by eastward-directed thrusting.

5.7.1. Early D_4 Sinistral, Strike-slip Shearing

Sinistral reactivation of the D_2 shear zones produced extensional veins (V_4) within the main shear zones perpendicular to those generated during post-D_3 dextral deformation. The sinistral sub-vertical quartz veins are distinct from earlier veining as they cross-cut all previous structures and contain coarse, sericite selvages. These veins are most concentrated along the northern end of the Wadi Lode shear zone (5000E,5600-5900N) where they appear to reactivate some of the north-south-trending, antithetic shears but are usually orientated obliquely on a 010°N trend. These veins are not confined to the shear zones and extend, undeformed, for several hundred metres, indicating that they were formed relatively late in the arc accretion-related deformation.

Composed of massive white quartz, they are up to 30 cm wide and also display 1-2 cm wide bands of coarse sericite flakes which grow normal to the vein walls. The selvages commonly form along the margins and centres of the quartz veins and occasionally occur as multiple layers. The veins are not heavily jointed like the earlier quartz veins and extend up to 350 m south from the base of the Wadi Lode shear zone to the south-eastern limit of shear zone formation (along 5250E).

At the northern end of the Wadi Lode ridge (5000E,5900N), the east-west-trending, phase 2, dolerite dyke is intersected by a north-south-trending, untectonised, phase 3, alkaline dyke which partially reactivates the D_3 thrust structures (see Fig.4.3). Another phase 3 dolerite occurs sub-parallel to the foliation at the southern end of the Wadi East Gebeit shear zone, indicating this structure was reactivated during sinistral shear. Eastwards along strike, the phase 2 dyke is offset by both sinistral and dextral 025°N-trending shears. This demonstrates that between D_2 and D_4 deformation phases, intrusive magmatism evolved from calc-alkaline to alkaline in character. Emplacement of the respective dykes was controlled by discrete, cross-cutting structures (Fig.5.16) confirming that the various deformation phases outlined were distinct and not produced by a single, dextral,strike-slip deformation event.

Sinistral shearing of the steeper lode veins resulted in vein-parallel extension by brittle dextral microfractures, 6-15 mm wide, at high-angles to the vein margins (Fig.5.17, Plate 6.1c), similar to those produced in displaced broken grains described by Simpson & Schmid (1983). The more shallow-dipping veins tend to be intersected and sinistrally displaced by steeper (>70°), thin, NE-trending fault zones.

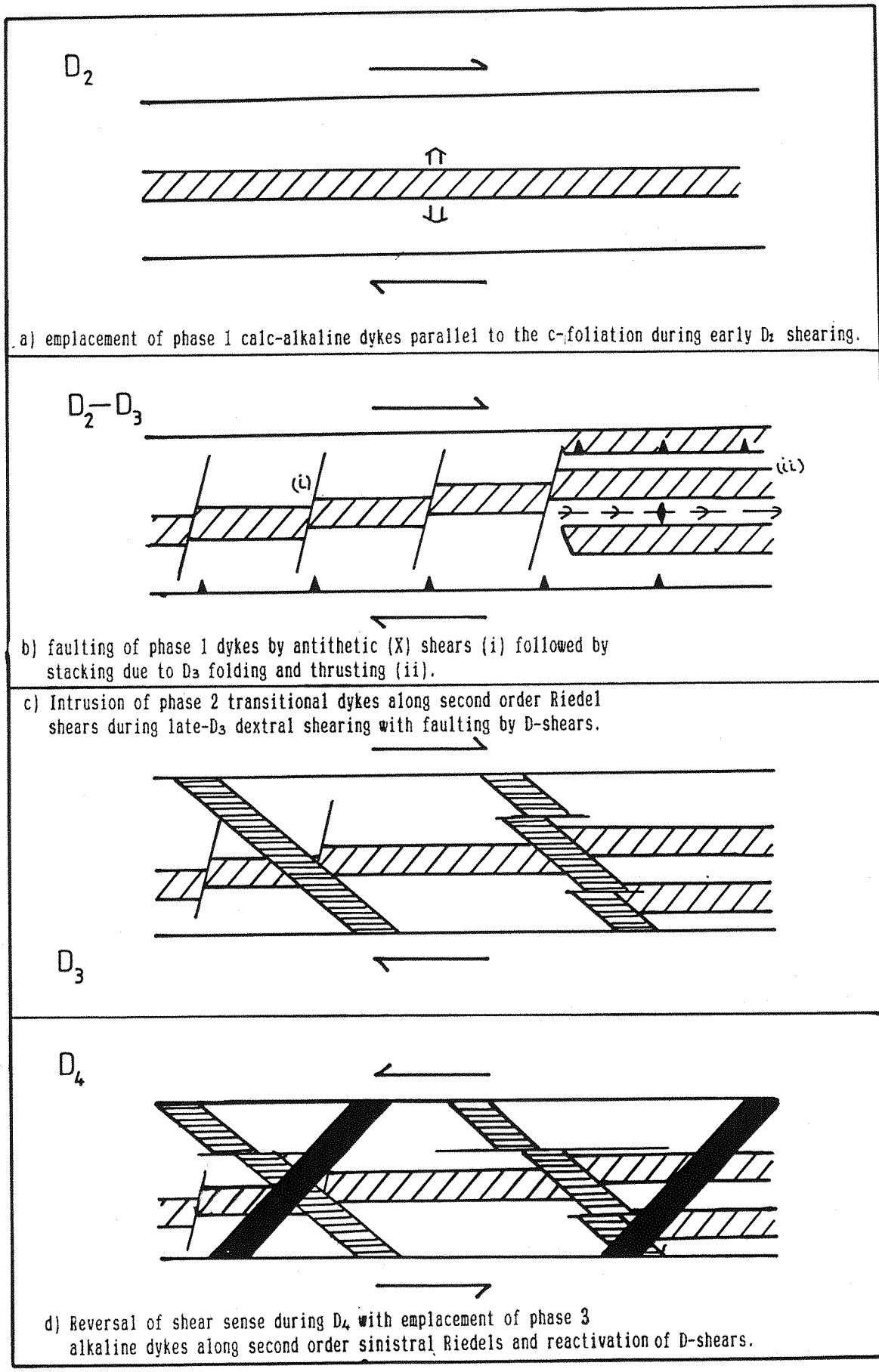

Fig.5.16 Diagram of a Gebeit Riedel shear zone showing the control of emplacement of dyke phases 1,2, and 3 during strike-slip shear.

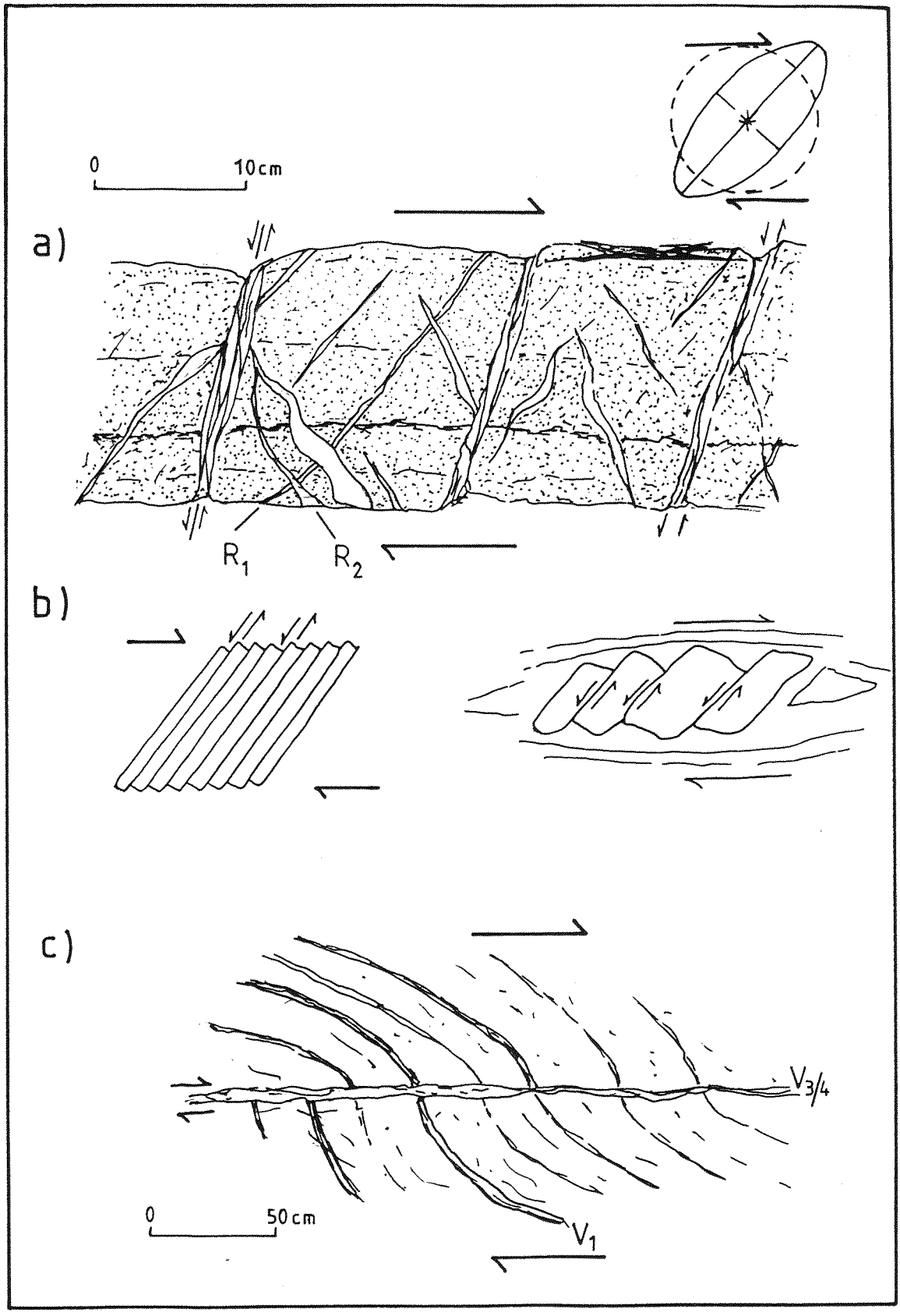

Fig.5.17 Late-shear structures displayed in the roof of the Wadi Lode 4-level. As the sketches are drawn looking up dip, all shear criteria are reversed. Blue auriferous quartz (a) is cross-cut by early white quartz Riedel veins (R_1) due to D_2-D_3 dextral shearing. These are transected by later Riedel veins (R_2) and antithetic shears due to early D_4 sinistral shear. Comparison is made with the sheared stack of cards model and a fractured grain in a ductile matrix (b; after Simpson & Schmid,1983). 5.17c demonstrates the sinistral shearing of foliation parallel V_1 quartz stringers.

5.7.2. D_4 Folding and Thrusting

The main phase of D_4 deformation followed early sinistral strike-slip shearing and produced large NNW-trending (≈340-350°N), gently to moderately inclined folds which tend to verge to the east. The largest of these evident is the antiform centred on the mine complex (Fig.5.18; 5000E,4900N) which folds the Wadi Lode shear zone and the main mineralised zones about a NNW-trending axis (between 4950E,5000N and 5300E,4800N). Although the folded mineralised zone appears to represent a continuous zone, the fold axis is delineated by faulting which separates the A Lode from the Y and X Lodes to the south-west.

The A Lode dips more steeply (45-50° to the east) than the Y and X lodes (25° west), showing an easterly vergence. At the fold hinge, the flat-lying X Lode abuts against the steeply dipping A Lode which continues to outcrop and suggests the shear zone hosting the A lode was reactivated as a reverse fault (A Lode Fault) during D_4 folding. The main part of the fold is bracketed by the Gebeit shear zone and the Western Boundary fault which originated as P-shears to the dextral system and may have been reactivated during D_4 to control the north-south folding. The south-east dip of the shear zones, lode veins and bedding produced by D_3 folding makes the antiform appear to plunge to the south.

Although folding in this orientation would be compatible with east-west-directed compression during dextral strike-slip shearing (see Fig.5.6), the folding and displacement of the Wadi Lode and subsidiary shear zones indicates it is a later event. The late-D_3 white V_3 quartz veins which parallel the phase 2 dolerite dyke near Gebeit village (4900E,5300N) can be traced westward into the village wadi where they are folded on a 350°N trend into tight, upright, synforms and antiforms which appear to plunge to the south at 60°.

Further north, a second antiform at Marble Bar combines with the the north-east-trending D_3 folding to produce the dome-shaped fold interference structure (Fig.5.11). At the southern margin of the prospect, the blue-grey auriferous veins dip beneath a north-south-trending structure which dips at 55° to the west. The phyllonites, where this structure enters Wadi Tuwiya (4400E,6100N) to the north, are recumbently folded on the hanging wall and display an easterly sense of vergence. The phyllonites which host the veining at Marble Bar display north-south-trending, reverse kink bands (2-4 mm wide) and minor thrust faults which dip to the west (Plate 5.5a), indicating that easterly-

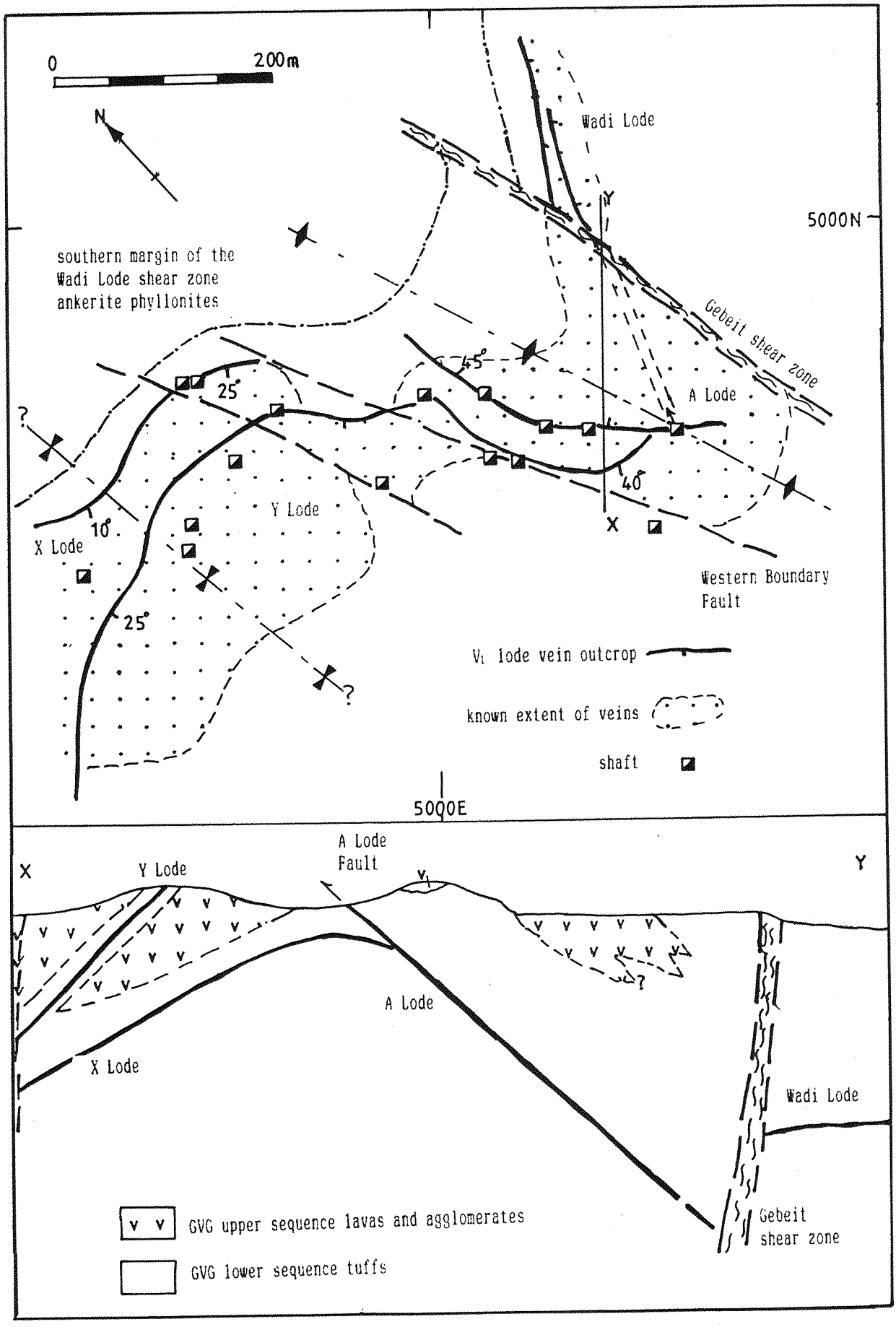

Fig.5.18 Sketch map and cross section of the Gebeit mine area showing the effect of D_4 folding and the subdivision of the lodes.

Plate 5.5 D_4 structures and deformation of the V_1 lode veins.

a) Easterly-verging, N-S-trending D_4 reverse kink bands in oxidised sulphidic phyllonite from Marble Bar (4650E,5950N).

b) NE-verging D_4 chevron folds with axial planar cleavage in ankerite phyllonites at southern end of Wadi Gebeit shear zone.

c) NE-trending D_4 back-thrust and box fold in ankerite phyllonites at southern end of Wadi Gebeit shear zone.

d) Incipiently carbonatised phyllonite from southern end of Wadi Gebeit shear zone showing orthogonal S_3 and S_4 crenulation cleavages on S_2 foliation surface.

e) South view of V_1 lode vein abutting against D_3 high-angle brittle fault (lateral ramp?) at southern end of Wadi Lode, 4-level.

f) NW-view of V_1 lode vein of the Y Lode (eastern end, main adit) hosted by thin oxidised sulphidic phyllonite envelope showing boudinage and extensional veins (R) in the footwall due to D_2 and/or D_3 shearing. As view is up dip overall sense of shear is dextral.

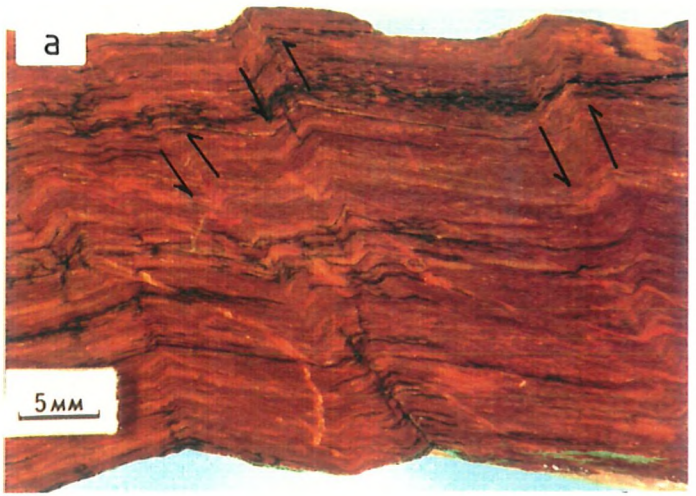
a
5 мм

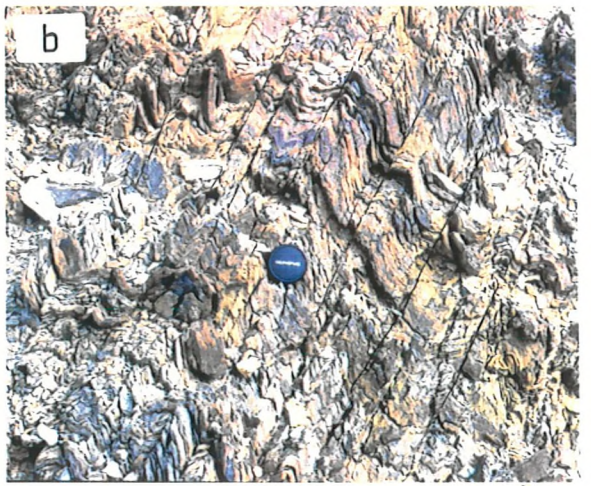
b

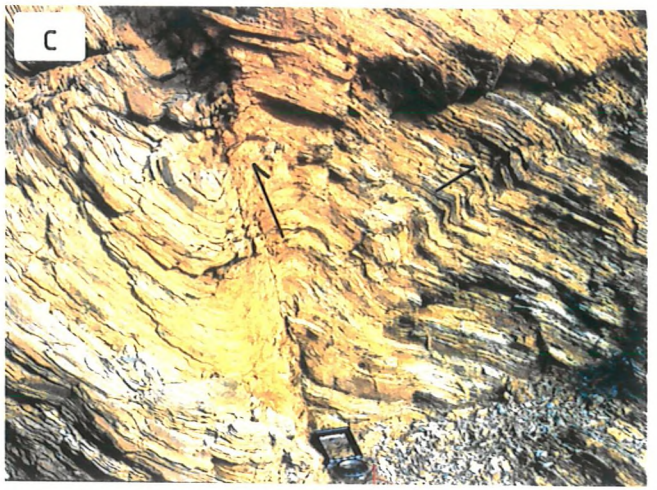
c

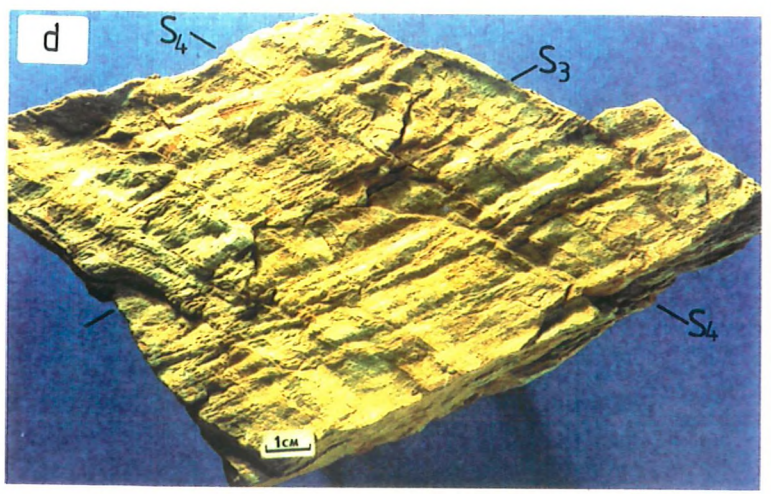
d
S4
S3
S4
1см

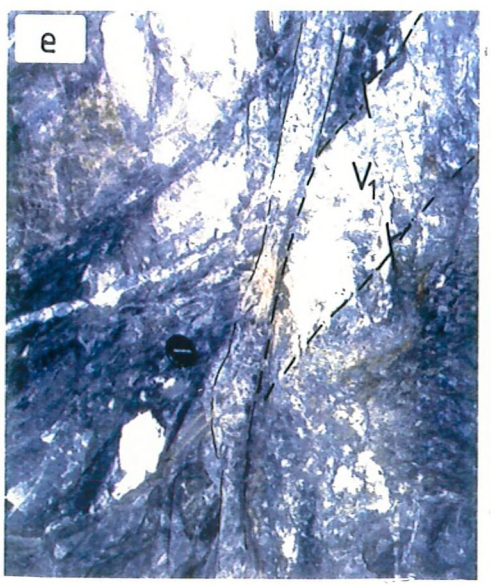
e
V1

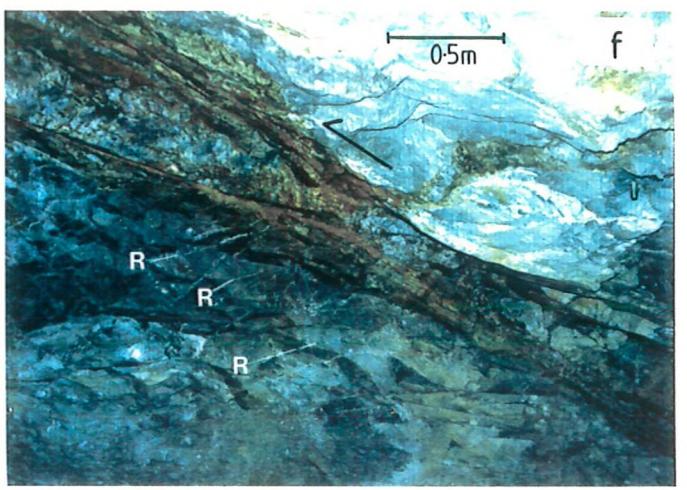
0·5m
f
R
R
R

directed thrusting accompanied D_4 folding. Similarly, at the north-east end of the prospect, the lode veins dip east into the hill which separates Marble Bar from the east-north-east trending veins at Vein 18 prospect.

The auriferous veins at Vein 18 are stacked in discontinuous outcrops, repeated by north-east-trending D_3 folds and thrusts which dip to the south-east (Fig.5.19). The dips of these veins vary along strike from 30 to 70° and overall strike of the veins changes from 080°N to 050°N to the north-east. The D_3 structures are intersected by 0.25 to 0.75m-wide, upright folds and steep faults, trending 340 to 360°N, which have minor offsets (1-3 m) but no consistent sense of displacement. The hanging-wall of the uppermost vein is defined by an ENE-trending, parabolic, recumbent fold, 1.3 m wide, which is truncated on its upper limb by a thrust plane. The thrust plane, which dips gently at 25° to the south-south-east, separates the lower shear zone phyllonites from upper, massive, andesite lavas.

The thin unit (3-5m) of tuffaceous phyllonite which hosts the mineralisation at Vein 18 appears to be part of the same folded structure as Marble Bar and Vein 13. Structurally, however, Vein 18 sits 10-15m lower than Marble Bar, and the north-south folding at Marble Bar coupled with the upper thrust boundary at Vein 18 suggests that Marble Bar was thrusted above Vein 18 during D_4 folding (Fig. 5.19). This folding appears to have produced smaller-scale folds in the Vein 18 lodes which was also accompanied by minor faulting.

The phyllonites along the southern side of Wadi Tuwiya (4500E, 6500N) contain 50-150mm wide, eastward-verging, reverse kink bands which dip at 35-60° west, parallel to minor thrust faults. As the kinks and folds do not plunge to the north or south, they cannot be related to sinistral shearing and have the wrong sense of shear to be D_2-related sheath folds. Minor reverse kink bands occur throughout the phyllonites in most of the shear zones and all give an easterly sense of vergence. At West Gebeit, closely spaced, ENE-directed, imbricate thrusts in the phyllonites produce complexly deformed zones (Fig.5.20).

Preferential erosion through the shear zone phyllonites at the thrust window in the Wadi Tuwiya shear zone (4400E,6700N) appears to represent another interference structure due to NE-SW- and N-S-trending folding. The adjacent N-S-striking phyllonites dip away from the axis, which tends to confirm the presence of a 340-360°N-trending antiform. A progressive change in the foliation to a NE-SW-strike further south suggests a synformal structure exists, as anticipated, between the

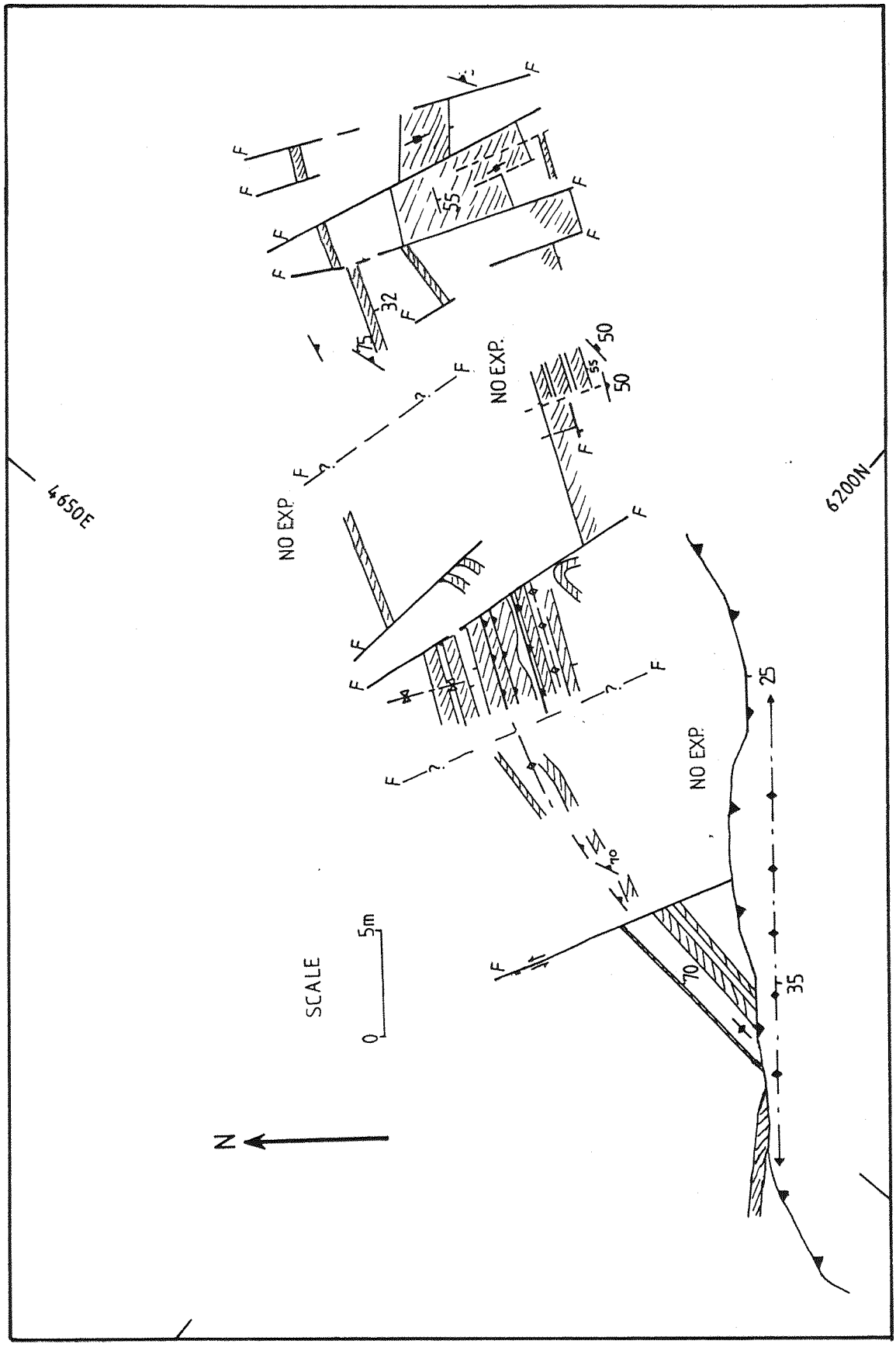

Fig.5.19 Sketch map of the V_1 veins which comprise Vein 18 prospect.

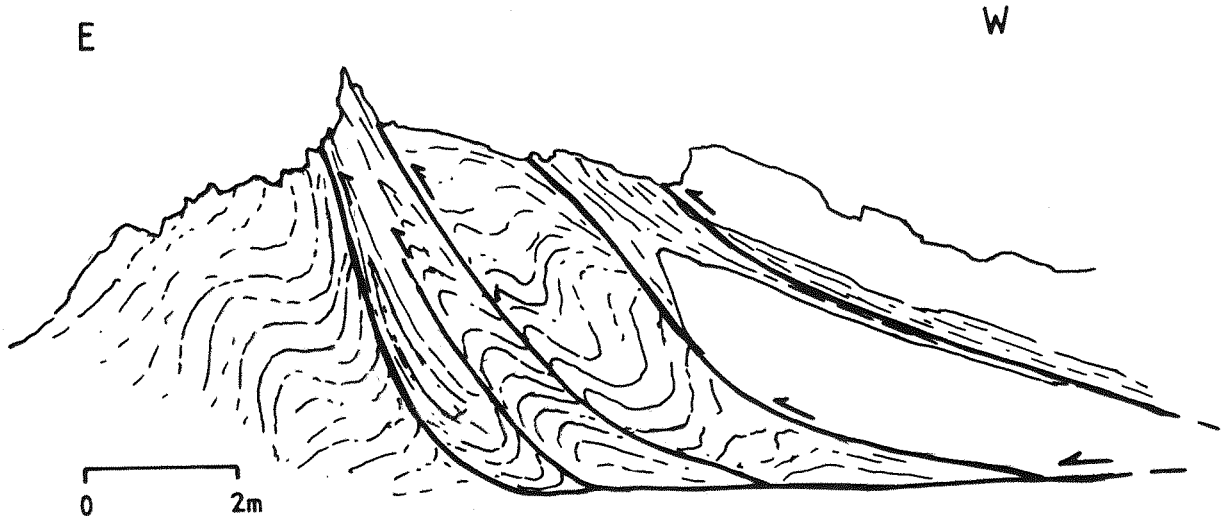

Fig.5.20 NNE-directed, imbricate, D_4 thrusts in the phyllonites of the Wadi Lode shear zone at West Gebeit (4675E, 4800N).

thrust window and Marble Bar, coinciding with Vein 18 (Fig.5.21).

The three antiforms noted at Marble Bar, Wadi Tuwiya and at the mine suggest that D_4 deformation produced easterly-verging folds of 400-500m wavelength and, like D_3, was accompanied by localised thrusting. As with the thrusting associated with D_3 folding, D_4 thrusts seem to be fairly steep (up to 65°) as only the high angle ramps tend to be visible within the phyllonites, acting primarily as contractional faults due to décollement during folding. The thrusts appear to be largely restricted to the shear zones and indicate that local thrusting within the phyllonites was a common accommodation process during folding.

5.7.3. D_4 Deformation Outside the Gebeit Block

At the intersection of the Hindeib and Gebeit blocks and the Sasa Plain slate assemblages, south-west of Gebeit village, the phyllonites which border the blocks are well exposed. At this location, recumbent, north-east-trending folds of D_3 age are overprinted and refolded by 340-350°N-trending D_4 folds. These folds range from upright to westerly dipping (45°) chevron and polyclinal open folds from 7 to 50cm wavelength and all have a strong axial planar cleavage (Plate 5.5b). These folds are associated with low-angle, easterly-directed thrusts, back-thrusts, kink bands, and box folds and are parasitic to 100-200m wavelength, upright folds (Plate 5.5c). At this location S_2, S_3, and

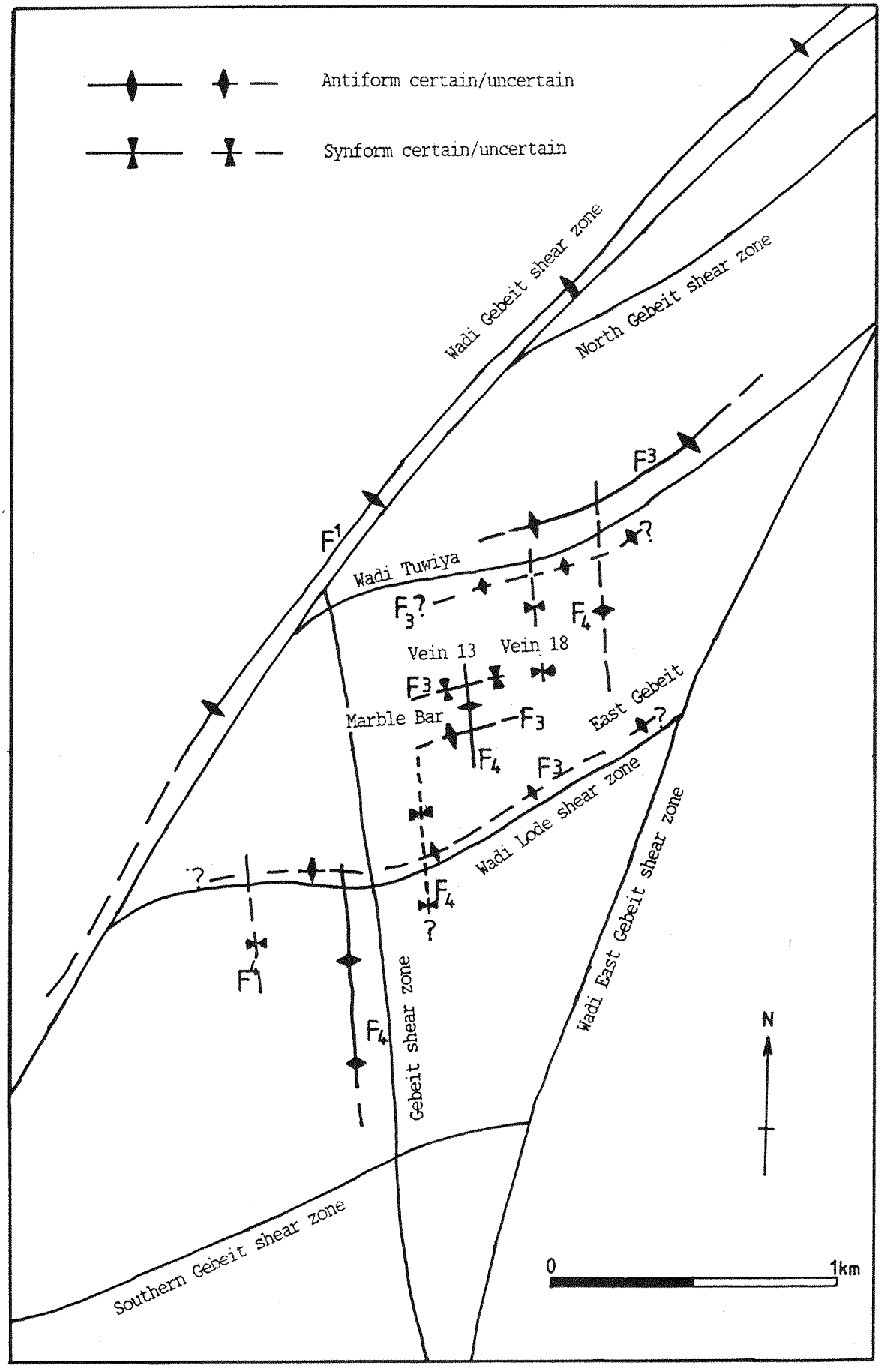

Fig.5.21 Sketch map of the Gebeit block showing the location and trends of late-Proterozoic, accretion-related folding.

S_4 foliations are mutually perpendicular producing two orthogonal crenulation cleavages on the S_2 surfaces (Plate 5.5d). Similar structures occur at Garabein, where a strong S_4 cleavage is developed on a 330-340°N trend dipping at 35-40° to the west.

Throughout the area, the relatively undeformed rocks of the Gebeit Volcanic Group occur as coarse, blocky outcrops produced by well-defined orthogonal joint surfaces. The spacing of these joints varies from 30cm to 150cm and the trends usually parallel the D_2 to D_4 foliations (i.e. NE-, N-S-, and NW-trending) thus, defining a coarse fracture cleavage.

5.8 Post-Pan-African Structures

Following the late-Proterozoic deformation phases associated with arc collision during accretion of the Nubian-Arabian Shield, this neocratonic area remained inactive until the early stages of the break up of Pangea, culminating in the rifting of the Red Sea (see section 2.7). The early phases of rifting reactivated the northern end of the Wadi East shear zone at the intersections with the Wadi Lode and Wadi Tuwiya shear zones and resulted in the intrusion of the ultra-potassic trachyte dykes considered to be 100Ma in age. The main effect of rifting at Gebeit produced normal faulting on north-west and east-west trends. The sub-vertical north-west and east-west faults which cross-cut the Wadi Lode have variable displacements between 5cm and 130cm. These faults tend to partially reactivate some of the structures they cross, producing extensional cavities and geodes which are infilled by coarse, drusy carbonates. Joints are also well developed on this trend and are infilled with carbonates and minor sulphides (pyrite and chalcopyrite). However, not all north-west-trending joints and foliations are post-Pan-African in age as north-west lineations are produced by the intersection of secondary D_2 shears with the flat-lying, north-east-trending, D_2 shear zone foliations (Fig.5.22).

Drusy carbonate veins also occur in outcrop at Vein 18 and along the lower end of the Wadi East Gebeit shear zone. Several major north-west-trending faults can be traced for up to 25 km across the area including Wadi Hadayu and Wadi Yemomt/Sofiya which, with the Oko shear zone (see Figs.2.20, 4.1 & 5.1), probably controlled the siting of the Salala ring complex.

East-west faults form a significant group of faults in the Northern Red Sea Hills and extend for over 60 km inland from the coast

and cross-cut the Nubian sandstone outcrops 10 km west of Gebeit. Two main east-west faults cross the Gebeit block through Vein 18 and the main mine complex and host the phase 4 undersaturated, alkaline olivine dolerites (see Fig.4.2).

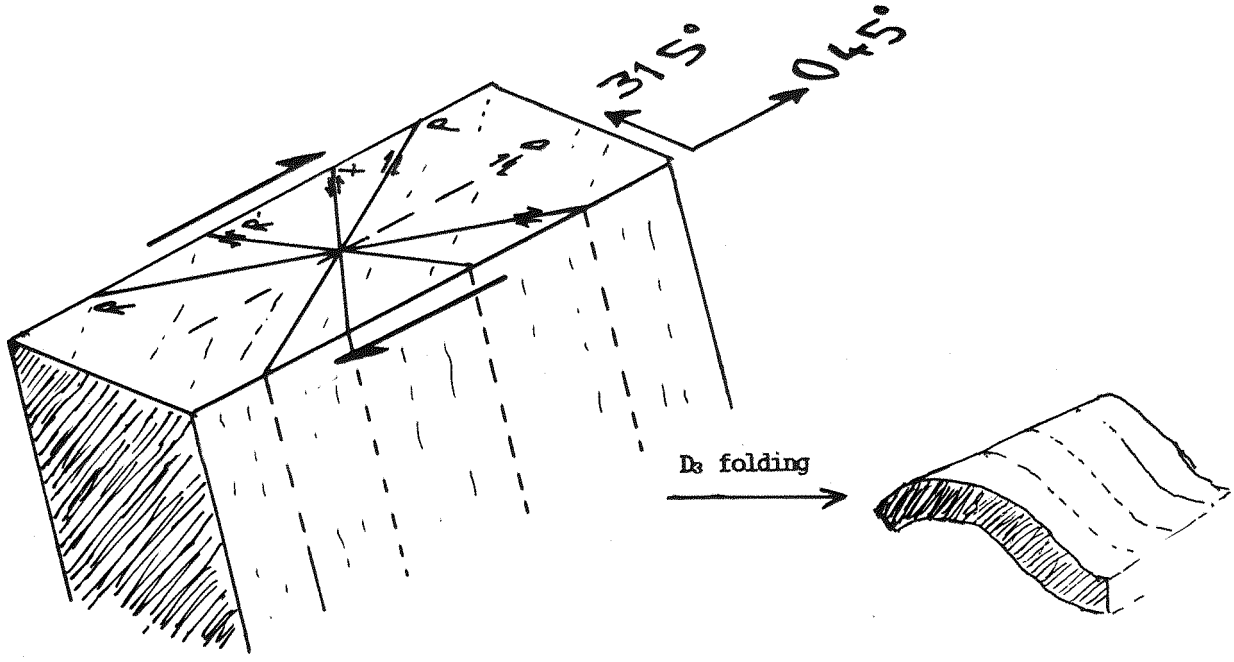

Fig.5.22 North-west-trending intersection lineations produced on D_2 foliation surfaces.

5.9 V_1 Quartz Vein Deformation Trends

The V_1 auriferous veins exposed underground commonly display marked variations in dip along strike and are frequently truncated by structures and veins of varying orientation and dip. Overall, the scale of vein fragmentation appears to decrease to the east and west away from the Wadi Lode-Gebeit shear zone intersection and ranges from the complex multiple offsets of the central mine area to the almost continuous, single, planar veins of the western X and Y lodes. In plan, the Wadi Lode veins (Fig.5.23) show D_2-D_3 dextral and D_4 sinistral offsets related to steep faults which trend sub-parallel to the lodes. Close to the Gebeit shear zone, the host structures and veins of the Wadi Lode trend NNE (020°N), forming part of the eastern limb of the main F_4 fold which traverses the mine (see Fig.5.18). Cross-sections of the lode vein intersections, however, also show the effects of D_3 folding and thrusting (Fig.5.23). The recumbent open folds, secondary veining and north-west-trending slickensides on the listric thrust surfaces confirm that these structures belong to a separate deformation event and are not rotated D_2 structures.

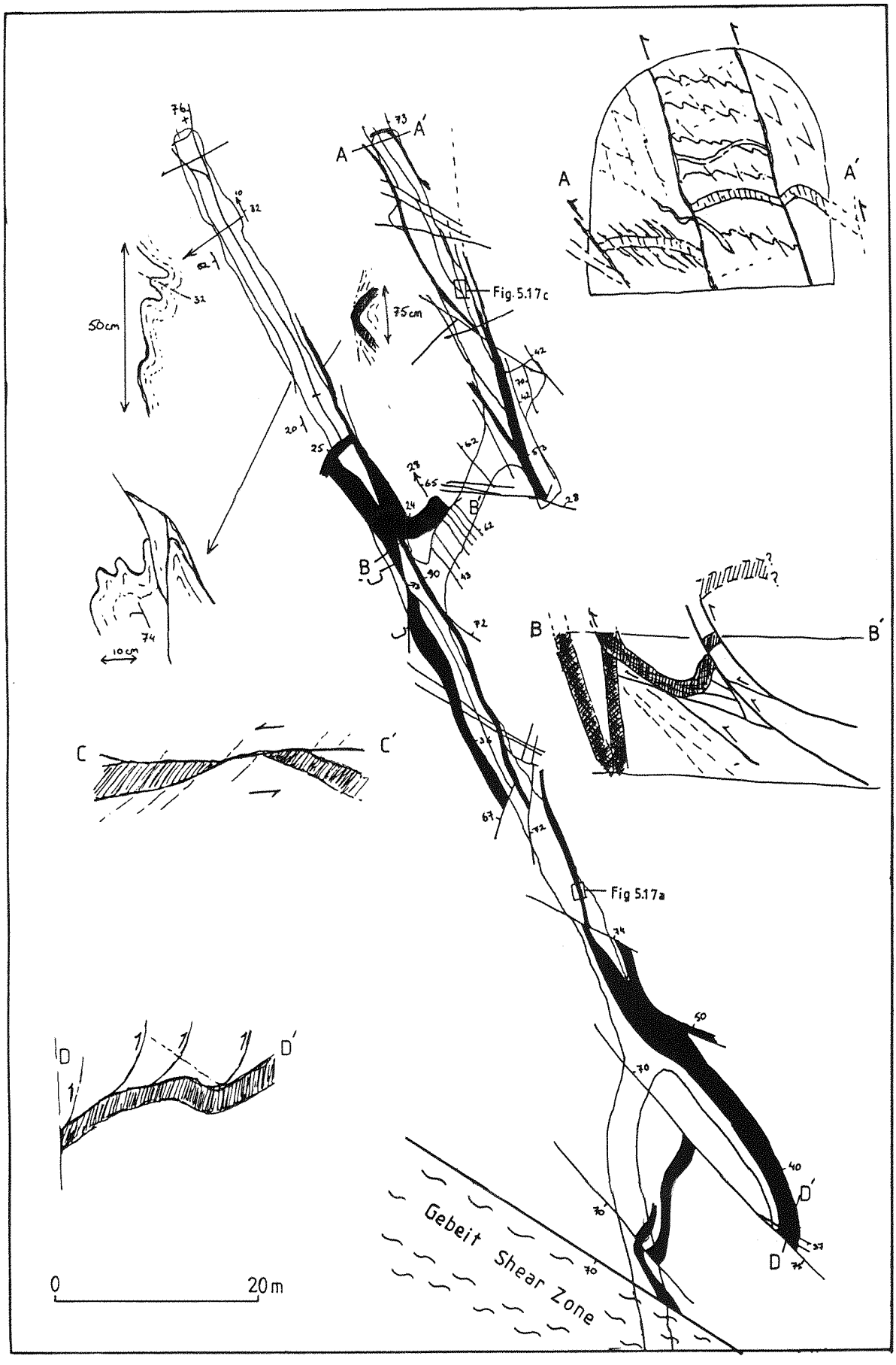

Fig.5.23 Map of the Wadi Lode 4-level with sketch sections showing the deformation of the V_1 auriferous, blue, quartz veins (shown in black).

Many of the later structures which boudinage and fragment the lodes (Plates 5.5e,f) appear to have been initiated along the vein-wallrock interface, similar to the thrusted phase 1 dykes and blocky ankerite phyllonites in the D_2 shear zones (Fig.5.12). This is accompanied by later white, V_3, quartz veining which cross-cuts the blue, V_1 quartz lode veins (see section 6.2) and occurs along the interface between the V_1 veins and the altered wallrocks. In addition to fragmentation by later deformation (Plate 5.5e) , the V_1 quartz veins also vary considerably in thickness, both laterally and vertically, and in many cases pinch out along steep D_2 structures.

The combined effects of the D_2 to D_4 deformation phases resulted in zones of sub-parallel, stacked veins, seen as small double- and triple-decked stopes in the A Lode old workings, interspersed by areas of little or no apparent veining. The lack of extensive, continuous lode zones results in a considerable reduction of ore reserves amenable to stoping and increases exploration costs. Although individual offsets along each fault surface is generally less than a few metres, the close spacing of the cross-cutting structures can combine to produce much larger (>10m) displacements. The lodes show considerable variation in thickness and because bedding trends and thicknesses in the volcanic lithologies are irregular, correlation of drill-hole and underground lode intersections is greatly hindered.

5.10 Structural Summary

The complex interaction of oceanic-arc terranes and terranes of continental affinity in the region has resulted in a protracted tectonic history. At Gebeit four deformation episodes have been recognised (Table 5.1). These comprise:

i) the earliest D_1 phase of arc accretion, when regional north-east-trending F_1 folds were produced throughout the region;

ii) the main D_2 phase of dextral, strike-slip deformation accommodated by major, north-east-trending, brittle-ductile, phyllonite shear zones. These shear zones subdivided the rocks of the Gebeit Volcanic Group into a series of discrete, north-east-trending, tectonic blocks. Several Riedel and P shears were formed within the Gebeit block. Fluid flow was preferentially focussed by the extensional Riedel shears which hosted the auriferous V_1 blue quartz veins, minor V_2 calcite-albite veins and phase 1 calc-alkaline dykes.

Phase	Folding	Faulting	Intrusive Magmatism	Veins	Tectonic Setting
D_1	NE-SW, F_1 upright regional	minor shearing along fold axes?	—	—	early arc accretion & obduction ?
D_2	rotation of D_1 fabric into dextral wrench folds	dextral strike-slip along brittle-ductile shear zones	phase 1 calc-alkaline diorites and dolerites	V_1 blue quartz V_2 albite-calcite	initiation of collision marginal N-S terranes
D_3	upright open to recumbent isoclinal, NW-verging F_3	minor NW-directed thrusts with F_3 folding	—	—	late-collision & obduction of arc terranes
late-D_3	—	dextral strike-slip shearing	phase 2 calc-alkaline to alkaline	V_3 massive white quartz	final collision of NE-trending arc terranes and N-S-trending, marginal, continental terranes
early D_4	—	sinistral strike-slip shear	phase 3 alkaline dolerites	V_4 quartz-sericite	
D_4	F_4 open to isoclinal NE-verging	NE-directed thrusts and kink bands	—	V_5 quartz along thrusts	
post-D_4	—	NW-trending normal faults	—	V_6 drusy carbonates	rifting due to the break-up of Pangea culminating in rifting of the Red Sea
	—	reactivated N-S shear zones	alkaline trachytes	—	
	—	regional post-Nubian normal faults	undersaturated alkaline dolerites	—	

Table 5.1 Summary of the structural evolution of the Gebeit area and its possible correlation to regional tectonism.

Strike-slip deformation was probably induced by east-west-directed compression due to the simultaneous collision of the northern arc terranes and the north-south-trending continental terranes to the east and west (see Figs.2.7 & 2.10).

iii) The D_2 deformation was interupted by a phase of north-west-directed D_3 folding and thrusting which was concentrated along the D_2 shear zones and resulted in deformation of the V_1 veins and phase 1 dykes.

iv) D_3 was followed by renewed north-east dextral shearing which controlled the emplacement of phase 2, transitional calc-alkaline to alkaline, dykes and V_3, massive, white quartz veins and further fragmented the V_1 lodes. The block-bounding shear zones formed the south-west margin to the Gebeit Volcanic Group where they are thrust over the Sasa Plain tuffaceous slate assemblages, believed to represent part of a continental margin arc terrane (El Nadi,1984).

v) The final stages of arc accretion commenced with a switch from dextral to sinistral strike-slip deformation, probably due to collision with the marginal arc terranes to the west. This phase of strike-slip deformation reactivated the D_2 shears, controlling the emplacement of the phase 3 alkaline dykes and V_4 quartz-sericite veins and deforming the earlier veins and dykes.

vi) Accretion-related deformation ended with the D_4 phase of eastward-directed folding and thrusting which folded the north-east-trending, V_1 lodes into NNW-trending antiforms and synforms.

vii) Several phases of extension, related to the break-up of Pangea and the rifting of the Red Sea (see section 2.7; Table 2.3), produced faults on E-W and NW-SE trends and reactivated many of the N-S-trending Pan-African structures. At Gebeit reactivated N-S faults host the alkaline trachyte dykes similar to the Oko shear zone (see section 4.4.3). E-W faults host the late, phase 4, undersaturated, alkaline, dolerites. NW-trending normal faults cross-cut and partially reactivate the late-Proterozoic structures but usually have displacements of <50cm. Some of these NW structures may have been coeval with reactivation of the N-S shear zones and controlled the siting of many of the post-tectonic ring complexes (e.g. Salala; Fig.5.1).

"Tectonic and Chemical Evolution of a Late Proterozoic Gold Deposit, Gebeit Mine, Northern Red Sea Hills, Sudan."

PART FOUR

MINERALISATION: PARAGENESIS AND ALTERATION

Chapter 6

Mineralisation I: Vein Paragenesis and Ore Mineralogy

6.1 Introduction

Structural studies at Gebeit indicate that gold mineralisation is largely confined to an early phase of north-east-trending, shear-zone hosted, blue quartz veins which lie parallel and adjacent to major Riedel shear zones. The main target of mining and exploration has been the area immediately south of the Wadi Lode shear zone where known reserves comprise a continuous narrow belt of veining approximately 1 km in strike length. These south-east-dipping blue quartz veins have been fragmented by the subsequent D_3 and D_4 deformation phases to produce a complex lode pattern, with multiple orebodies designated as the X, Y, A and Wadi lodes (see Fig.5.18). It is this complexity which hinders mine-scale exploration. Several generations of quartz and calcite vein sets are evident in addition to the auriferous, blue, quartz veins (see Fig.6.11). In many cases these have been distinguished by texture, mineralogy and structural location, and often the relative ages have been determined indirectly from these geological relationships. The separate vein sets identified comprise:

V_1 - massive blue-grey quartz veins ± calcite, tourmaline, gold and sulphides formed during D_2 dextral strike-slip shearing;
V_2 - late-D_2 calcite and albite ± chlorite veins;
V_3 - coarse white quartz veins related to late-D_3 dextral shearing;
V_4 - N/S-trending, coarse, milky quartz and sericite veins due to early D_4 sinistral shearing;
V_5 - minor white quartz veinlets emplaced along D_4 thrust surfaces;
V_6 - post-tectonic, NNW- to E/W-trending, drusy carbonate veins ± sulphides.

These various vein sets demonstrate a protracted and variable fluid history that developed with the changing deformation styles and P-T conditions. The overprint of later fluid phases has proved to be a

problem in deciphering the wallrock alteration patterns associated with mineralisation and are discussed in the next chapter. This chapter outlines and characterises the mineralogy and paragenesis of the separate vein types with emphasis on the earliest phase of auriferous vein mineralisation.

6.2 V_1 Blue Quartz-Calcite Veins

The earliest veins recognised at Gebeit consist of north-east-trending quartz veins which contain variable amounts of calcite up to a maximum of 60%. V_1 veins are distinct from the later sets of quartz-carbonate veining due to a characteristic blue colouration which varies from blue-white to dark blue-grey. Braided phyllonitic shear zones of varying width, which parallel the Wadi Tuwiya and Wadi Lode Riedel shear zones, invariably host V_1 veining. The veins generally occur parallel to the shear zone c-surfaces and vary in thicknesses from 2-5mm wide stringers to the massive 1.2 m thick veins exposed on 4-level of the Wadi Lode (see Fig.5.23). Some minor V_1 veining, in the form of 2-10 mm wide calcite-quartz stringers, occurs in the Wadi Tuwiya and Wadi Lode shear zones but the majority of veins are confined to subordinate marginal shears (see 7.6.1). There is no apparent positive correlation between shear zone and vein thicknesses associated with the increase in shear zone widths towards the Wadi Tuwiya and Wadi Lode shears zones. In some sections of the Y Lode, the host shear zones comprise thin chlorite phyllonite envelopes <15 cm wide around blue quartz veins from 15-50 cm thick (see Plate 5.5f). However, gold mineralisation appears to occur exclusively within the V_1 veins which are enveloped by propylitic alteration haloes of variable widths.

6.2.1 Internal Structures and Textures

Varying styles of vein-formation and degrees of subsequent deformation are displayed by the veins grouped into the V_1 category. The large quartz veins which constitute the Wadi, X, Y and A lodes are commonly fragmented and discontinuous both laterally and vertically. Because of the more competent nature of the veins relative to the sheared and hydrothermally altered host volcanics, fault surfaces commonly form the upper and lower vein surfaces (see Fig.5.12), making it difficult to establish a representative wallrock alteration profile. Veins more than 10 cm thick usually contain microbands of wallrock

parallel to the vein-rock interface. Thicknesses of wallrock laminae range from 0.25 to 5mm and are spaced at 2-50mm intervals. These are particularly well developed in the shale horizons where wallrock slivers are spaced at 1-5mm intervals (Plate 6.1a); however V_1 veins are rarely thicker than 50mm due the relative plasticity of the shales during shearing. Wallrock inclusions are important sites for precipitating gold and sulphides and are more significant as a guide to grade than overall vein thicknesses (Plate 6.1b & c). These textures indicate an antitaxial crack-seal type mechanism for vein growth (Durney & Ramsey, 1973; Ramsay,1980a). The successive assimilation of wallrock material into veins produces a blue-grey banding parallel to the vein margins due to the replacement of wallrock chlorite by fine-grained tourmaline (Plate 6.1c).

Sub-parallel discontinuous quartz veinlets and stringers are commonly developed within the alteration haloes of the larger veins. These are generally orientated parallel to the main veins and the main c-foliation but also lie at a low angle (<40°) to this trend, perpendicular to the local shear extension directions, along second order Riedel structures (Fig.6.1). Subordinate stringers generated within less deformed, coarser tuff horizons tend to display a much wider variety of trends up to 60° from the main veins (Plate 6.1d). Small calcite crystals up to 1.2mm long often occur along the vein margins and are generally orientated at high angles to the walls (Plate 6.1e).

The walls of the smaller veins tend to have stepped margins at up to 25° from the overall vein trend (Fig.6.1). Some veins clearly display growth fibres orientated at between 25° and 65° to the vein walls, the fibres lying parallel to the elongation of pressure shadows developed around wallrock sulphide grains. Although some sulphide mineralisation occurs in the veins, the major part is concentrated in the wallrock alteration haloes, especially in the zones of visible bleaching (Fig.6.2). The asymmetry of some of the chlorite, quartz, carbonate and secondary sulphide pressure shadows indicates that deformation occurred by dextral simple shear. The oblique growth fibres and stepped margins of the smaller veins indicate that vein formation progressed by initial development of en échelon P- and R-surfaces followed by precipitation of quartz-calcite vein material during extension sub-parallel to the P-surfaces (Fig.6.1). Some of the apparent growth fibres, on close inspection, are fracture planes across the quartz vein and are generally infilled by fine-grained calcite.

Plate 6.1 Textures of the V_1 quartz veins.

a) Minor V_1 quartz vein developed in graphitic shales from Wadi Lode 4-level showing crack-seal vein texture due to the entrainment of laminae of altered wallrock. Fine white patches in upper veins comprise calcite grains along vein margins and lowest vein shows high-angle calcite-infilled fractures.

b) Close-up of V_1 blue quartz vein showing concentration of gold (Au) grains along lamina of entrained wallrock (Wadi Lode 4-level).

c) V_1 vein margin from the roof of 4-level Wadi Lode showing partial entrainment of wallrock lamina by antitaxial, crack-seal vein growth and banding parallel to the vein margin due to alteration of wallrock stringer. Vein is transected by late brittle fracture due to early-D_4 sinistral shearing (as sample viewed up dip of lode, shear sense is reversed; see Fig.5.17).

d) Fine V_1 quartz veins developed in coarse andesitic tuff from the footwall of the Wadi Lode 4-level. Top vein shows oblique growth fibres indicating an overall dextral sense of shear.

e) V_1 quartz-calcite vein in altered hornblende-phyric andesite showing calcite grains orientated sub-perpendicular to the vein margin (Wadi Lode 4-level).

f) Early blue V_1 quartz veins (1) along c-foliation (main vein) and along extensional (Riedel structures, C' fabric) showing infill of secondary (V_3?) white quartz veins (2) parallel to extensional structures (Wadi Lode, 4-level).

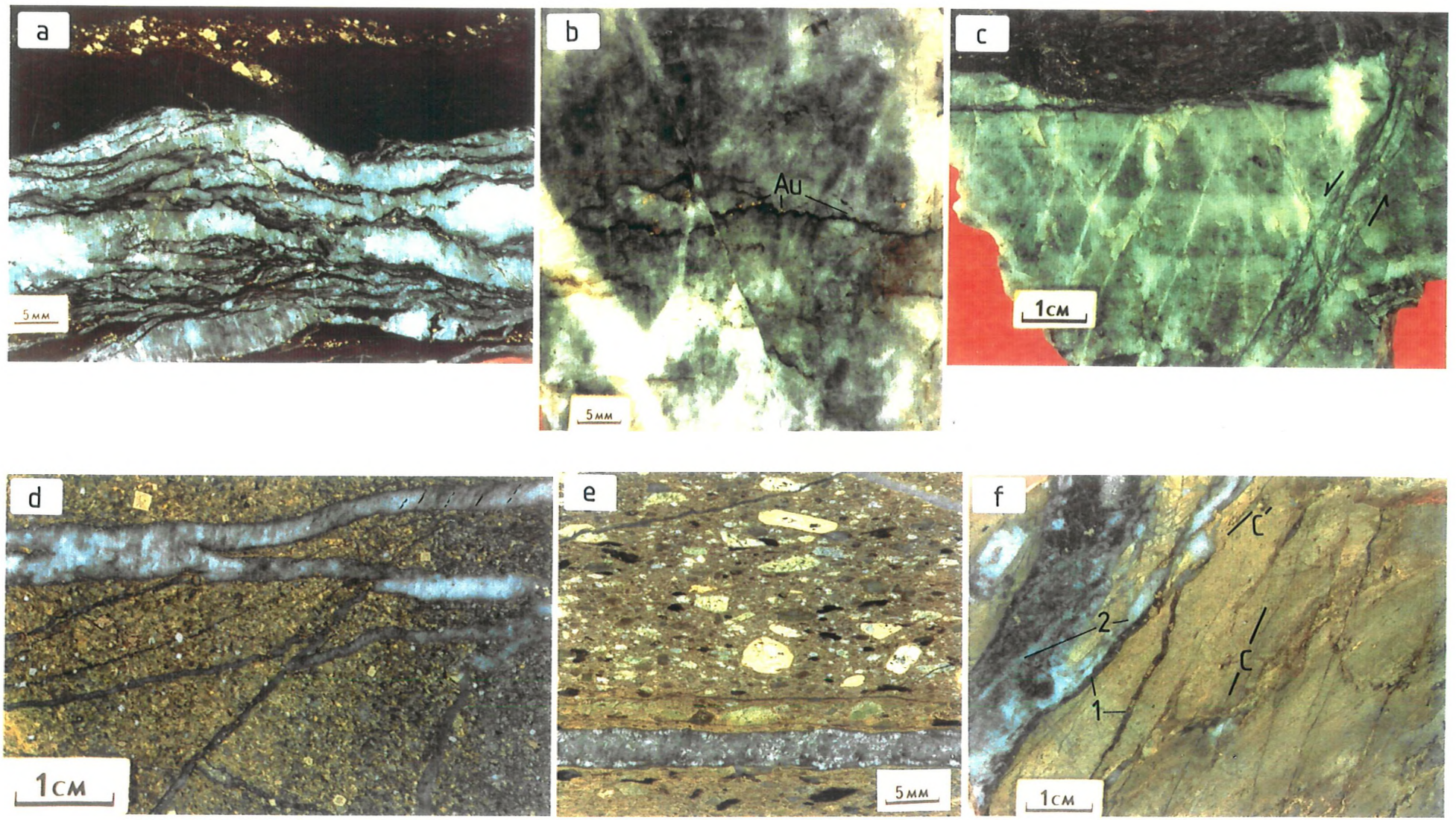
a
5мм
b
Au
5мм
c
1см
d
1см
e
5мм
f
C'
C
2
1
1см

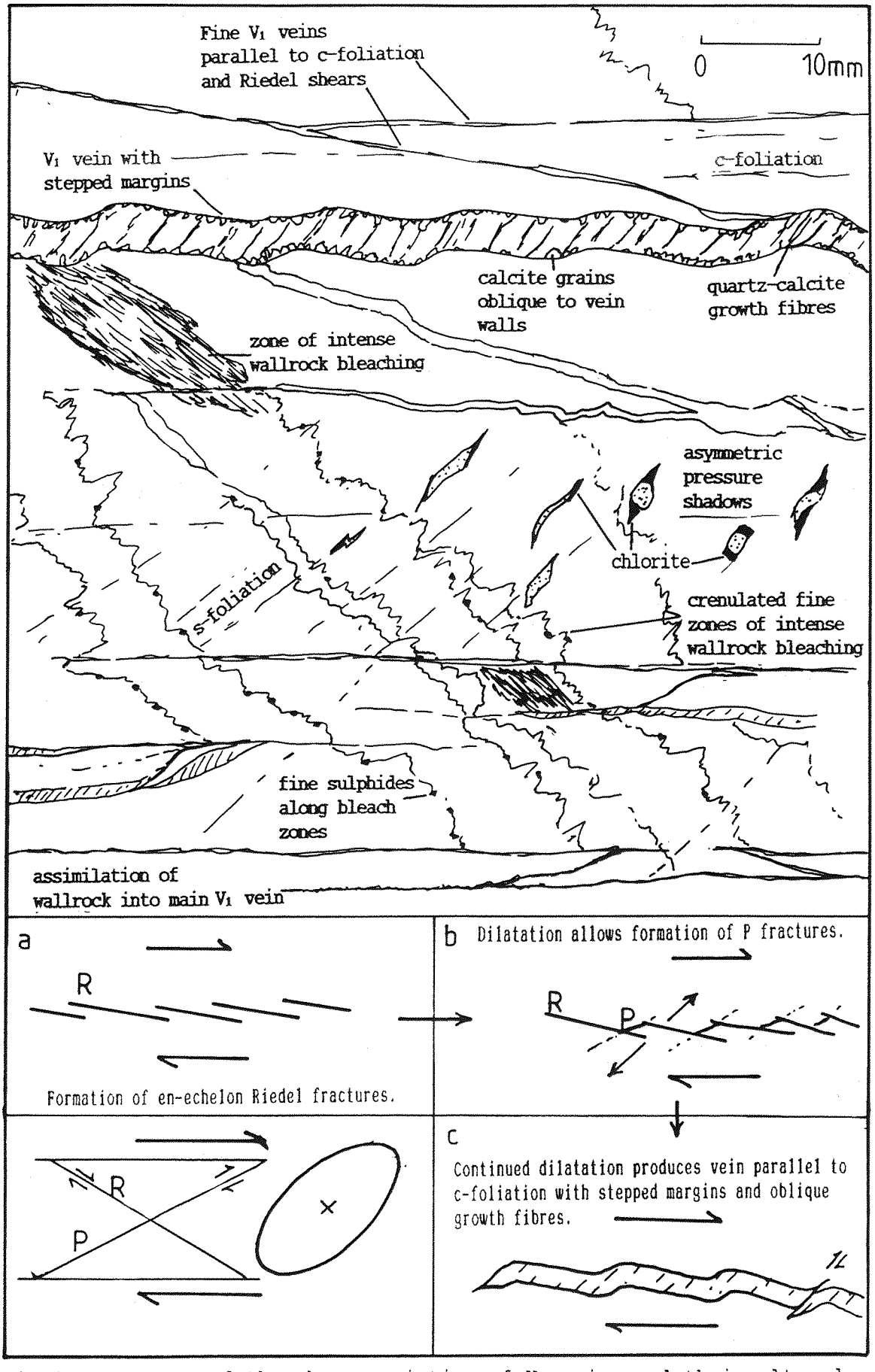

Fig.6.1 Summary of the characteristics of V_1 veins and their altered margins together with formation of stepped vein margins (a-c; after Gammond,1983).

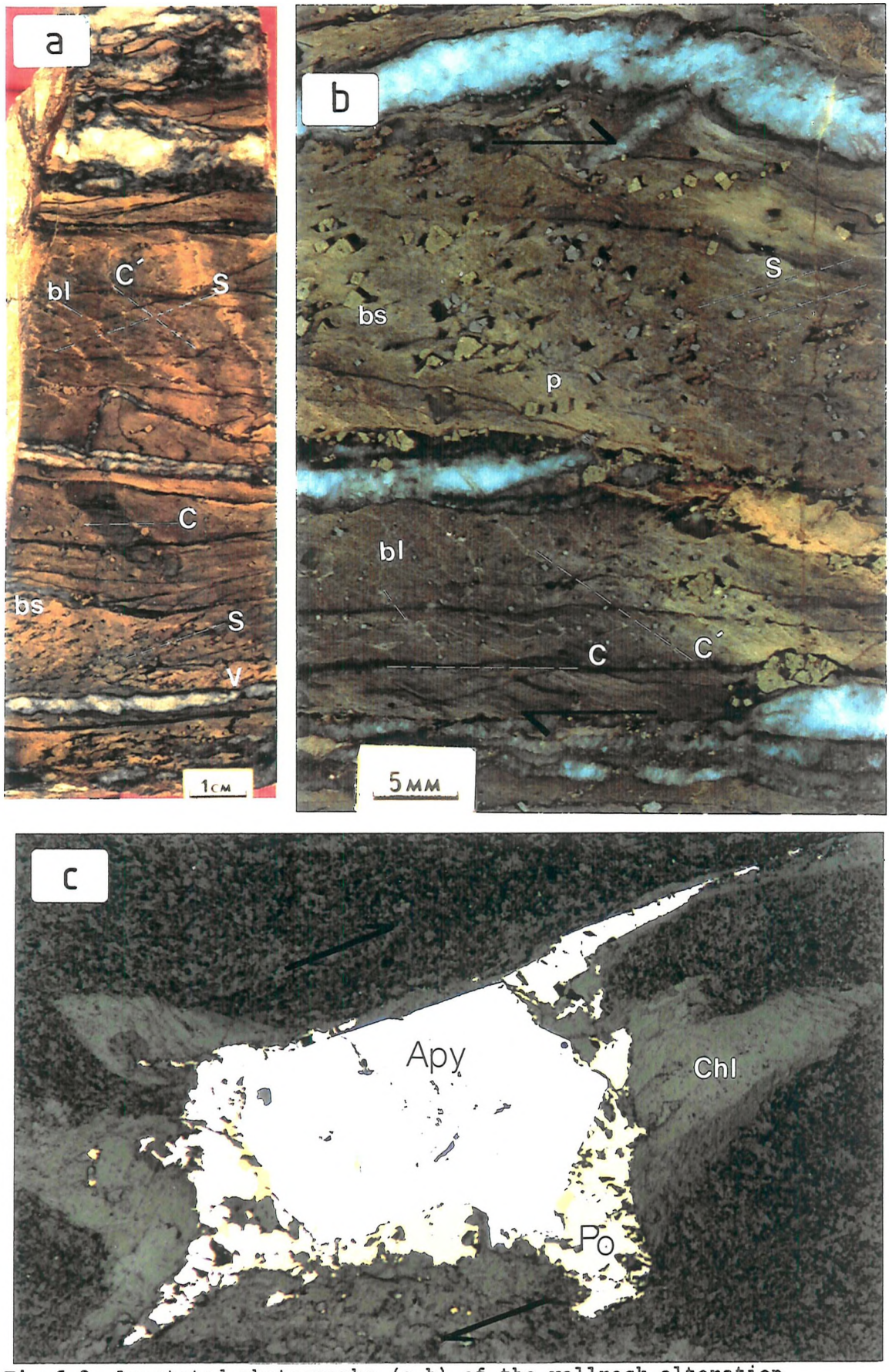

Fig.6.2 Annotated photographs (a,b) of the wallrock alteration adjacent to a V_1 lode vein (Wadi Lode 4-level) showing: sulphide rich bleached zones (bs), and fine zones of bleaching along Riedel (C') micro-shears; veins with stepped margins (V) parallel to the c-fabric (C); and arsenopyrite grains (c; Apy) grains with elongate pressure shadows (p) of chlorite (chl) and pyrrhotite (Po) indicating formation during dextral simple shear (see Figs.6.1, 6.3, and 6.4).

The predominantly quartz-filled veins display a range of deformation textures from brecciation to the development of deformation bands and lamellae, sub-grains, and dentate grain margins together with new, recrystallised grains (see Plate 6.2a-d). All of the V_1 blue quartz veins show some evidence of deformation and the range of textures probably reflects repeated changes in strain rate during vein formation.

In addition to the delineation of P-surfaces in the alteration zones by the alignment of pressure shadows, Riedel surfaces are visible in the form of fine, parallel zones of intense bleaching orientated at high angles to the P-surfaces (Figs.6.1 & 6.2). These microbands are usually <0.1 mm thick, lie about 2-5mm apart, and are crenulated by the P-surfaces. The intense bleaching indicates that local fluid movement was preferentially channelled along these surfaces during syn-deformational mineralisation and increased fluid access to the more distal parts of the alteration haloes.

All of the small-scale kinematic indicators observed within the alteration zones demonstrate that vein growth accompanied deformation during dextral simple shear. As the thickest veins lie parallel to the c-foliation, the host shear zones must have been orientated normal to the regional extension direction. This supports the hypothesis that economic, auriferous, quartz vein mineralisation at Gebeit was controlled structurally by preferential channelling of fluid flow along localised Riedel structures during early dextral strike-slip shear.

The dark blue colouration of the earliest quartz veins enables successive generations of quartz veining to be easily recognised. In the smaller veins, secondary blue-white quartz infill occurs along the upper or lower vein interface (Plate 6.1f) similar to the antitaxial vein growth process observed in the large quartz lodes. In some cases the earlier quartz is fractured and infilled at low angles to the vein wall parallel to the second order Riedel shears. In the thicker lode veins, however, coarse white veins up to 65 mm thick cross-cut the early blue quartz and entrained laminae of wallrock at steeper angles up to 60° from the vein margins (see Plate 6.3d & e). Quartz fibres normal and angled to the fracture surfaces demonstrate that hybrid shear-extension processes due to dextral shear were active during later quartz precipitation. The contrasting styles of quartz fracturing relative to the antitaxial veins of the early V_1 veins suggest that the later quartz may be related to the V_3 veins formed during late-D3, dextral shearing.

6.2.2 V_1 Vein Mineralogy

The V_1 veins are chiefly composed of massive quartz but in the smaller veins calcite becomes a more significant component. Fine-grained calcite (10-150µm) usually occurs around fractured quartz grains and the degree of fracturing is more pronounced in the smaller veinlets and stringers. At the margins of the sheared quartz zones, small, secondary, twinned albite crystal laths are often found intergrown with the calcite. In many veins (Plate 6.2a-e), extensive brittle fracturing forms discrete planar cross-cutting calcite veins. In the large lode veins, the calcite is much coarser (0.2-1.5 mm) and is frequently associated with gold grains (see Plate 6.6). When found in mineralised samples, calcite is confined to isolated rectangular pockets that often terminate against wallrock stringers and appear to represent late-stage fracture infill. Fine-grained calcite is also more rarely observed close to gold grains in strained quartz in which wide-scale, sub-grain development and recrystallisation has occurred (Plate 6.2d). Although primary calcite grains up to 1.2 mm long have been observed as small crystals on vein walls, the majority of the fracture-hosted calcite post-dates quartz precipitation. The composition of the carbonate vein phases were identified as calcite using X-ray diffraction studies and confirmed by microprobe analysis.

In addition to the quartz and calcite in the larger veins, fine laminae of entrained wallrock material are evident. In contrast to the chloritic phyllonites, these corrugated layers comprise quartz, tourmaline, sericite, rutile and arsenopyrite ± gold (Plate 6.2e), sometimes bounded by a muscovite-tourmaline envelope. The fine, pleochroic, tourmaline grains (5-50 µm long) are generally euhedral and prismatic to acicular in habit, displaying no preferred orientation. When not confined by a muscovitic envelope, the tourmaline crystals extend out into the surrounding quartz vein matrix, indicating formation synchronous with the vein quartz (Plate 6.2f). Deformation of the tourmaline is restricted to minor fracturing of the longer crystals. The fine grain size of the tourmaline grains hinders accurate studies by microprobe; however, two analyses (Appendix H) indicate the tourmaline to be intermediate in composition between schorl and dravite ($Fe/Fe+Mg \approx 0.4$). Abundant sericite occasionally occurs intergrown with tourmaline parallel to the margins of the wallrock laminae.

Plate 6.2 Mineralogy of the V_1 quartz veins.

a-b) Photomicrograph (CN) of Deformed V_1 quartz veins from Lode Profile 1 showing the development of deformation lamellae (l) and sub-grains (s) and transected by later calcite-infilled fractures (0.50-1.00m from lode, field of view 5mm).

c) Photomicrograph (CN) of V_1 (?) quartz vein adjacent to phase 1 dolerite dyke showing brittle fracturing and infill by fine grained calcite (Wadi East Gebeit; 4950E, 6600N, field of view 7mm).

d) Photomicrograph (CN) of V_1 blue quartz vein from the Y Lode (Raise 9) showing fracture hosted gold grain (Au) in deformed quartz and calcite (field of view 4mm).

e) Photomicrograph (CN) of altered wallrock lamina in V_1 blue quartz vein (Wadi Lode 4-level) showing prismatic tourmaline grains (grey) with interstitial subhedral to anhedral arsenopyrite grains (white; field of view 2.5mm).

f) Photomicrograph (PPL) of altered wallrock inclusion in V_1 quartz vein comprising abundant acicular tourmaline crystals growing into the host vein quartz (Wadi Lode 4-level; field of view 5mm).

CN = crossed Nicols, PPL = plane-polarised light.

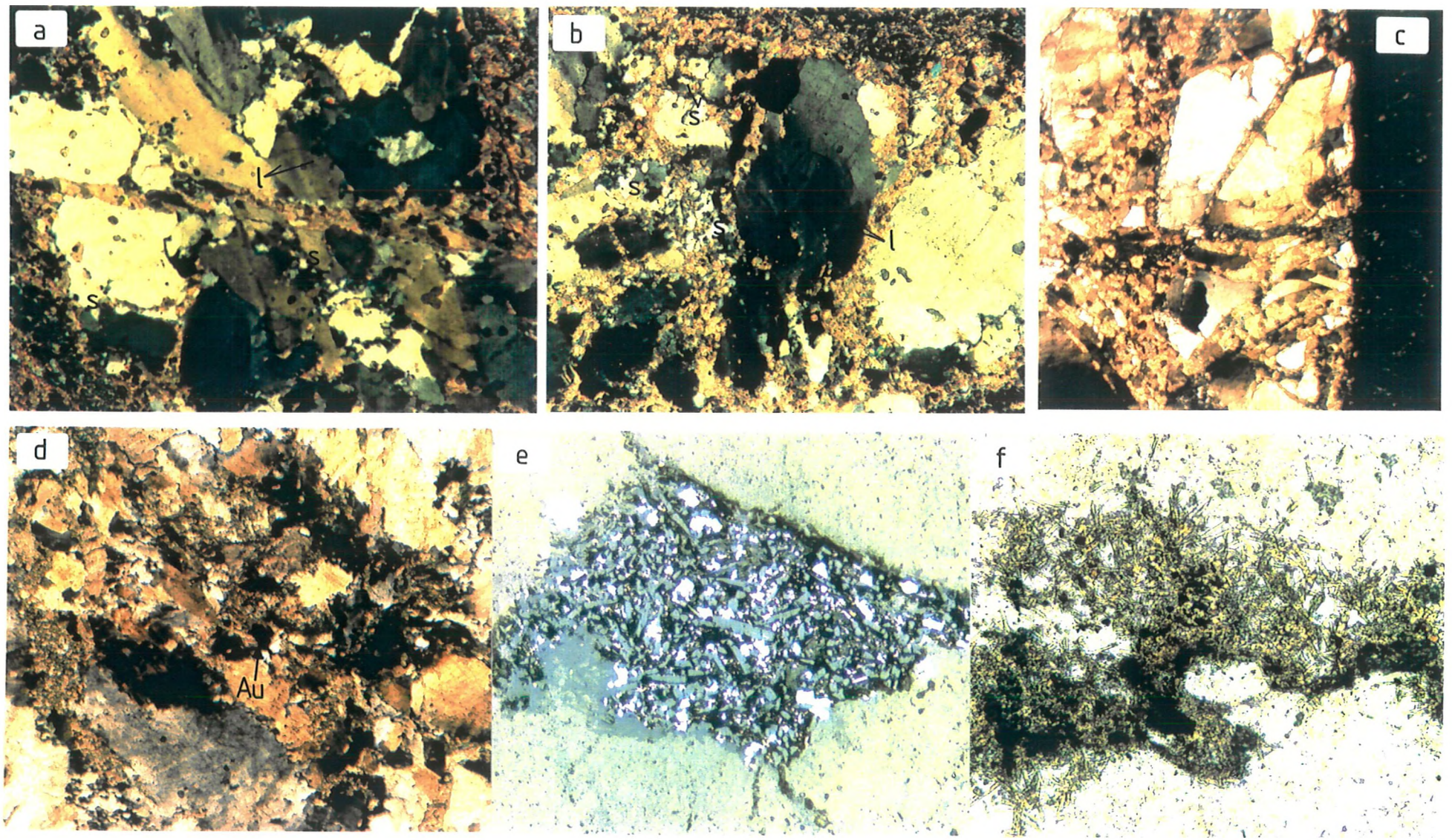
a
l
s
s
b
s
s
s
l
c
d
Au
e
f

6.3 V_2 Calcite-Albite Veins

The second type of veins which has been identified within the lode alteration profile consists of minor extension-shear albite-calcite veins. These veins are generally <10mm wide and comprise euhedral plagioclase laths up to 2.5mm long orthogonal to the vein margins with coarse calcite intergrown along the vein centres (Plate 6.3a). The albites display well developed albite twinning, and multiple crystals growing from a single point form a variolitic-type texture. Many of the longer laths are strongly curved and stepped twin planes indicate growth under combined extension and vein-parallel simple shear (Plate 6.3b). Some quartz grains are evident but albite tends to form >90% of the total vein silicates. The albites also show evidence of brittle fracture and often exhibit fine-grained calcite along fractures and grain boundaries. The coarse late calcite-infill usually displays strong deformation lamellae and appears to be coeval with the fine interstitial carbonate. Small calcite-only veinlets also occur with low-angle growth fibres which display a large component of simple shear (Plate 6.3c).

At Marble Bar, a thick (30-60 cm) coarse calcite vein lies parallel to the V_1 quartz vein in the northern part of the prospect and has previously been referred to as a marble (Robertson Research, 1983). As no wallrock carbonate alteration occurs at Marble Bar, it seems likely that the calcite veining represents a separate vein stage. Similar late coarse calcite veins are found along the Wadi Lode and Wadi Tuwiya shear zones and are probably related to the pervasive carbonatisation of these zones. The V_2 phase of veining appears to be coeval with the late-stage albite-calcite fracture-infill identified within the V_1 auriferous quartz-calcite veins. As no fluid inclusion or stable isotope studies have been undertaken on the V_2 veins, it is not certain how the albite-calcite veins relate to the tectonic and fluid evolution of the deposit. There are no sulphides, tourmaline or gold associated with this phase of veining. However, the similarity of growth and deformation textures compared with the V_1 veins suggest relatively early development. Occasionally, the V_2 veins contain patches of late coarse fibrous to vermicular chlorite which cross-cuts the calcite-filled fractured albites and occurs along the V_2 vein margins. This late phase of chloritisation is generally restricted to the V_2 veins and, although apparently genetically related, it may represent a later fluid phase.

Plate 6.3 Mineralogy and textures of the V_2, V_3, and V_4 veins.

a) Photomicrograph (CN) of left margin of V_2 albite-calcite vein showing curved albite crystals with stepped twin planes orthogonal to the vein margin with coarse calcite infilling the vein centre. Section shows sinistral shear sense but sample taken from non-orientated drill core (Lode Profile 1, 2.00m from lode; field of view 5mm).

b) Photomicrograph (CN) of close up of 6.3a showing stepped twin plane in V_2 albite grain (field of view 0.5mm).

c) Photomicrograph (CN) of V_2 calcite vein showing low-angle growth fibres (A-A') and stepped vein margins indicating growth during dextral simple shear (sample taken from non-orientated drill core; Lode Profile 1, 4m from lode; field of view 3mm) .

d) V_1 blue quartz vein cut by steep V_3 white quartz veins which display orthogonal growth fibres (ladder texture).

e) View south-east at V_1 quartz vein of the Wadi Lode (4-level) showing large extensional V_3 white quartz vein and near-orthogonal antithetic veins suggesting formation during late-D_3 dextral shear (pen scale = 14cm).

f) View east at north-south-trending, vertical V_4 white quartz vein (20cm wide) with coarse sericite margins (Wadi Lode Extension; 5000E,5800N).

CN = crossed Nicols, PPL = plane-polarised light.

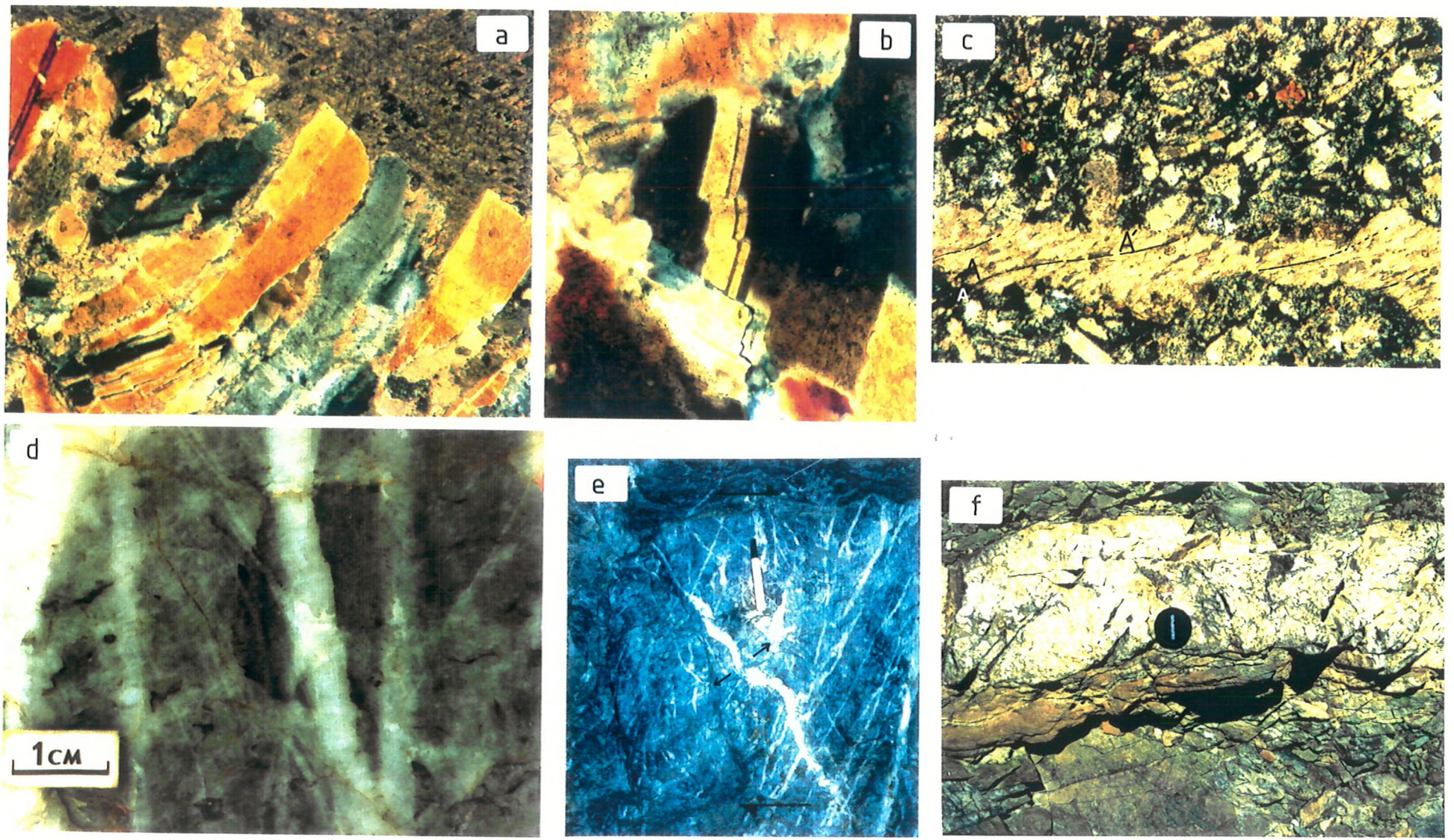
a
b
c
A
A'
A
A
d
1см
e
f

6.4 V_3 White Quartz Veins

This phase of veining brackets the coarse, massive white quartz veins which parallel the V_1 veins, produced during D_3 thrusting and late-D_3 dextral reactivation of the D_2 shear zones. Veining in this phase varies from the 80cm thick veins (see Fig.5.13) such as occur at the basal contact of the Wadi Lode shear zone, to the fine white quartz veinlets which cross-cut the V_1 blue auriferous veins (Plate 6.3 d,e). These veins are composed almost entirely of coarse quartz which is milky due to abundant sub-micron size fluid inclusions. Deformation textures range from undulose extinction to deformation bands, lamellae and sub-grain development but the white quartz is always less strained than adjacent blue quartz material. Recrystallisation at the contact between the blue and white quartz makes boundaries, which are clear in hand specimen, difficult to pin-point in thin section. Unlike the V_1 veins, V_3 veins do not have discrete and extensive alteration envelopes and do not display widespread ribbon-quartz texture from entrained wallrock laminae. As this phase of quartz veining is invariably white and not associated with carbonate alteration, the V_3-related fluids probably did not contain the significant quantities of CO_2 seen in V_1 inclusions.

The V_3 veins which cross-cut the blue V_1 auriferous veins usually display a ladder texture due to quartz growth fibres orientated at high angles to the sharply defined vein margins (Plate 6.3d). No gold or sulphide mineralisation has been observed within these veinlets or in any of the V_3 quartz veins, and extensive cross-veining of V_1 lodes produces a dilution effect resulting in lower gold contents, as seen at the southern end of the Wadi Lode (4 Level; Plate 6.3e, see Fig.5.23).

6.5 V_4 Quartz-Sericite Veins

The steep V_4 veins, formed during early D_4 sinistral strike-slip shearing, are consistently aligned on a north-south trend and are distinct both texturally and mineralogically from the other shear-related quartz veins. The veins are variable in thickness, generally <25 cm wide, and are composed of milky white quartz and sericite. Coarse mica selvages, up to 30 mm wide, usually form the vein margins and less commonly the centres of the V_4 veins (Plate 6.3f). These consist of muscovite flakes up to 20 mm long which are orientated orthogonal to the vein walls. The white quartz which forms the bulk of

these veins is relatively coarse-grained (5-15 mm) and displays only minimal effects of strain (undulose extinction, sutured grain boundaries). Occasional small patches (<15mm across) of finely intergrown biotite and dravite appear in the quartz as an opaque blue colouration. The milky colour of the quartz itself is due to numerous parallel trails of secondary sub-micron sized fluid inclusions. As with all the shear-related veins at Gebeit, the fluid inclusion populations are too small to be analysed using current thermometric techniques.

6.6 V_5 Thrust Plane Veins

The V_5 veins comprise a small set of thin irregular white quartz veins (usually <10 cm thick) which occur along the D_4 thrust planes. These veins have not been studied petrographically but have been separated from the other shear-related quartz veins by field relations and disparate stable isotope data which indicate a change in fluid source and composition at the end of accretion-related deformation.

6.7 V_6 Post-Tectonic Drusy Carbonate Veins

The youngest vein set identified at Gebeit consists of sub-vertical drusy carbonate veins (1-15cm wide) and joint infills (<2cm) which generally trend north-west to east-west. These V_6 veins tend to cross-cut all late-Proterozoic structures and veins but sometimes partially reactivate northerly trending D_1-D_4 faults. The east-west to north-west trend of these veins reflects the large scale normal faulting seen throughout the Northern Red Sea Hills which is considered to be associated with Red Sea rifting. The coarse calcite-infilled normal faults which transect the Wadi Lode often display geodes, up to 40 cm wide, containing manganiferous, dog tooth spar calcite, where the fault planes are stepped (see Fig.6.11). The fault and joint planes which cut the veins and alteration zones usually contain abundant euhedral pyrite (± chalcopyrite) grains up to 15 mm across which appear to be locally remobilised from the wallrock alteration haloes.

Fossiliferous (gastropods), red, arsenic-rich (1.25% As), calcite cements occur on the surface exposures of Wadi Lode extension fault surfaces. Similarly, the widespread formation of alluvium cemented by white, limestone calcretes along wadi bases, indicates that carbonates have been remobilised along fault zones by recent ground waters.

6.8 Ore Mineralogy

In addition to the mineral assemblages produced by wallrock alteration, the ore mineralogy of the Gebeit lodes primarily comprises gold, arsenopyrite, pyrite and pyrrhotite, with lesser amounts of chalcopyrite, gersdorffite (NiAsS), sphalerite, and apatite. Gold chiefly occurs in the V_1 quartz veins, concentrated along wallrock stringers and at the vein-wallrock interface, but also extends into the alteration envelope. Economic grades have been encountered in shear zones where extensive veining has not locally developed (e.g. Marble Bar), indicating firstly, that the auriferous mineralisation is not exclusively hosted by the main veins and, secondly, that it is ultimately controlled by the north-east-trending shear zones.

6.8.1 Vein Sulphides

Arsenopyrite and, to a lesser degree, pyrite are the main sulphide phases developed in the quartz veins and are more or less restricted to the wallrock laminae. Vein sulphide contents are very low compared to the alteration haloes and usually constitute less than 0.1 wt %. Arsenopyrite is the predominant sulphide within the entrained wallrock inclusions, forming mutual intergrowths with euhedral prismatic tourmaline (Plate 6.2e). The textures of the arsenopyrite grains suggest they have grown as interstitial fill to the tourmaline grains. The anhedral to subhedral grains rarely exceed 1mm in size (generally 0.05-0.5 mm) and contain much fewer silicate inclusions relative to the sulphides developed in the alteration envelopes. Arsenopyrite grains which are not precipitated in or on the wallrock inclusions tend to be euhedral equant crystals in contrast to the prismatic habit common in the wallrock alteration haloes (see Plate 6.4). Qualitative SEM studies show some of the arsenopyrite to contain minor amounts of nickel, and occasionally inclusions of the nickel-arsenic sulphide gersdorffite (NiAsS) have been identified. Pyrite is much more common in the vein sulphides precipitated along the vein-wallrock interface, suggesting that the bulk of the sulphide iron is derived from altered wallrock silicates. Pyrite crystal surfaces in contact with the wallrock tend to show irregular bases often with enclosed silicate grains (Fig.6.3a).

Pyrrhotite is rare in vein material, forming minor rounded inclusions up to 30µm in diameter within vein-margin pyrite grains.

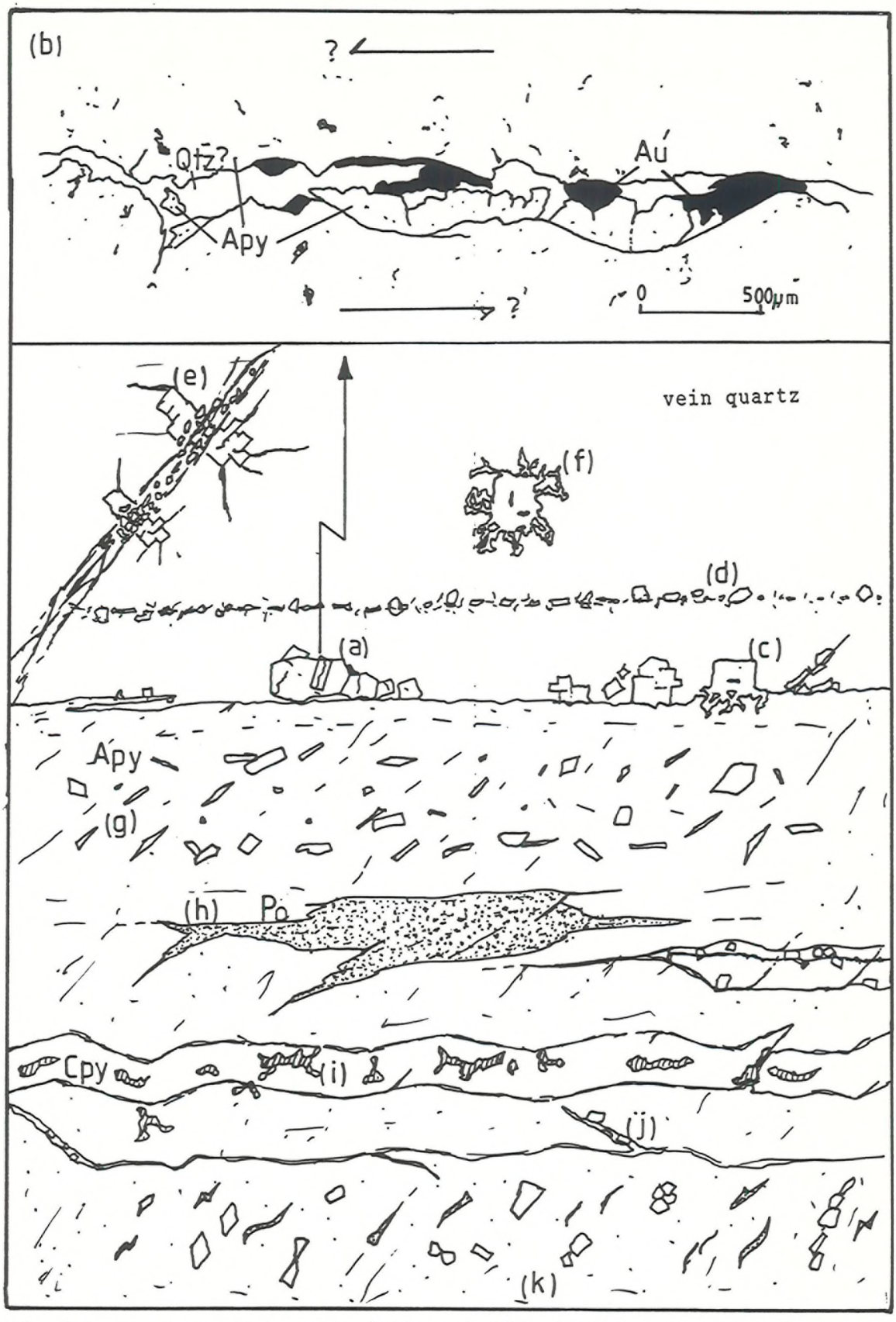

Fig.6.3 Summary of characteristic sulphide textures associated with V_1 and V_2 veins observed along 4-level Wadi Lode.

a) fractured arsenopyrite along V_1 vein wall hosting native gold (b), c) pyrite showing irregular intergrowth with altered wallrock, d) fine subhedral arsenopyrite along altered wallrock stringer, e) euhedral arsenopyrite grains transected by late brittle fractures, f) flame-like pyrite grain margins due to brecciation of host quartz, g) prismatic arsenopyrite orientated parallel to s-and c-foliations in wallrock alteration halo, h) massive pyrrhotite lens in altered wallrock, i) anhedral chalcopyrite within V_2(?) calcite vein, j) pyrite along V_1 Riedel veinlet, k) sulphides with pressure shadows parallel to the s-foliation.

Similarly, chalcopyrite is restricted to fine inclusions within composite gold-arsenopyrite grains, occurring as discrete rounded blebs <50µm in size adhered to the surfaces of gold and arsenopyrite grains. Chalcopyrite, however, is most common in V_1 extension-shear veinlets where coarse calcite predominates over quartz as the gangue phase. It takes the form of late-stage anhedral cuspate grains from 20 to 450µm in length. Sphalerite has been identified as fine 15-20 µm inclusions within V_1 vein sulphides (mainly pyrite) but is not observed in the majority of samples. In some vein sections, apatite and, less commonly, rutile have been identified, using the SEM, in close association with fine-grained gold grains. These generally lie within or close to altered wallrock stringers and probably comprise a minor part of the alteration envelope assemblage.

The range of textures displayed by the sulphide grains and their host vein minerals indicate that sulphide precipitation was protracted and, in part, synchronous with deformation. Arsenopyrite and pyrite grains in the early strained quartz veins tend to show evidence of brittle fracturing which ranges from elliptical sub-grain formation at cuspate sulphide-sulphide grain boundaries to complete fragmentation of original grains (Fig.6.3e). Some late subhedral pyrite grains display irregular flame-type margins due to growth into brecciated host quartz matrix and may post-date the phase of gold mineralisation.

6.8.2 Wallrock Sulphides

Although the same sulphide mineral assemblage is found in the wallrock alteration haloes, the abundances and textures are significantly different. Arsenopyrite and pyrite are the predominant sulphides, as in the veins, but pyrrhotite and chalcopyrite are much more abundant. These sulphides are most concentrated in the 5-50 cm thick bleached zones adjacent to the V_1 veins (Fig.6.2), however, not all zones of bleaching contain large quantities of sulphide. Sulphide-poor bleached zones tend to have higher abundances of fine stringer veins, with sulphides developed along the veins walls but largely absent from intervening wallrock.

Pyrite and arsenopyrite grains generally vary between 0.1 and 2.5 mm but can reach 7.5 mm in size. Silicate and oxide inclusions such as rutile (relict ilmenite?), quartz, albite and chlorite are abundant in the equant grains relative to vein sulphides, indicating replacement of wallrock minerals such as magnetite. The most intense areas of

sulphide precipitation comprise 2.5-4 wt% sulphides with highly variable relative abundances of arsenopyrite, pyrite and pyrrhotite. In some lode alteration profiles (see 7.5), arsenopyrite is the dominant sulphide, producing arsenic anomalies of over 10,000 ppm As, equivalent to 2.5 wt% arsenopyrite. Arsenopyrite crystals are usually prismatic and vary in shape from rhombic to acicular. Crystal shapes are normally euhedral, and the z-axes of the more elongate grains show preferred orientations parallel to local foliation trends (Fig.6.3; see Plate 7.1). Fluid access and alteration of less deformed volcanics appears to have been controlled by foliation and often produces thin parallel trails of arsenopyrite crystals 0.1-1mm in size along spaced cleavage domains.

Pyrite comprises up to 60% of the sulphide phases and grains vary considerably in size (0.1-7.5 mm) and texture (euhedral simple cubes a{100} to fine anhedral composite granules). Although arsenopyrite and pyrite are common in the alteration haloes, arsenopyrite is closely restricted to vein envelopes and the main shear zones whereas pyrite occurs in the more incipiently sheared volcanics. Sulphide zones with both pyrite and arsenopyrite in abundance (Fig.6.2) usually contain significantly more pyrrhotite (± chalcopyrite, ± sphalerite), than observed elsewhere in the mineralisation profile. Chalcopyrite can constitute up to 5% total sulphides but is generally found as small inclusions within pyrite, pyrrhotite and, more rarely, within arsenopyrite. Sphalerite is rare and confined to small irregular inclusions mainly hosted by pyrite.

Pyrrhotite contents vary from 5 to 25% total sulphides and in a few samples, at the margins of the alteration zones, forms 80% of all sulphide phases. The pyrrhotite-rich samples comprise foliation-parallel massive lenses 1 to 6mm thick, interdigitated with chlorite. Small euhedral pyrite cubes often form the cores to these patches and chalcopyrite is common. The pyrrhotite is usually crystalline with grain sizes around 30-60µm.

As with the oblique growth fibres and orientations of the V_1 veins, wallrock textures indicate that the bulk of sulphide precipitation was synchronous with deformation. In contrast with the vein sulphides, brittle fracturing is limited but pressure shadows are commonly developed; this reflects the differences in competency between quartz-rich veins and the chlorite-calcite-sericite-albite-quartz wallrock assemblage. The pressure shadows vary from 0.2 to 0.75xlength of sulphide grains and are chiefly composed of fibrous chlorite,

although quartz, calcite and sericite shadows also occur (Fig.6.2). They are developed around the more equant grains as none are observed bracketing acicular or prismatic arsenopyrite. The orientation of the shadows normal to micro-vein trends and the oblique growth of vein fibres confirm deformation by dextral simple shear. The elongated chlorite fringes define the local s-foliation trends and some sulphides display asymmetric chloritic shadows which indicate a dextral sense of shear. The arsenopyrite grains sometimes have secondary overlapping pressure shadows composed of massive pyrrhotite and minor amounts of chalcopyrite (Fig.6.4). These shadows, together with pyrrhotite and chalcopyrite infilling fractures within the arsenopyrite grains, suggest that the ductile pyrrhotite was extensively remobilised. The pyrrhotite displays a rectangular crystal shape which coincides with the primary chloritic pressure shadows suggesting it has pseudomorphed pyrite. Pyrrhotite grains with no arsenopyrite cores are smeared along the s-foliation suggesting that some of the early euhedral pyrrhotite-pyrite pseudomorphs were preserved by replacement of their cores with arsenopyrite. Subsequent deformation partially remobilised the relatively ductile pyrrhotite into secondary pressure shadows.

6.8.3 Gold Mineralisation

Within the lode veins, gold occurs in a number of precipitation sites which broadly fall into two associations, namely,

i) with sulphides in, or close to, altered wallrock inclusions, and
ii) as free grains in zones of deformed quartz, often with calcite.

Gold often occurs with vein sulphides along entrained laminae of altered wallrock but has not been observed in any of the sulphide assemblages within the wallrock alteration envelope. Vein-wallrock profile samples show that gold grades tend to decrease very rapidly outside vein margins. Significant anomalies of 0.1-6g/t (ppm) are evident up to 5m from the veins and are controlled by the width of the shear zones. Many of the minor shear zones which parallel the Wadi Lode and Wadi Tuwiya shear zones display limonitic/ hematitic gossans after pyrite and arsenopyrite even though extensive quartz-calcite veins are not developed. Trench sampling across these zones by Robertson Research (1982-3) revealed sub-economic gold grades of ≤0.1-3.6g/t (e.g. Southern Extension area; 4800E,5600N to 5300E,5000N). This suggests that auriferous wallrock mineralisation occurs as sub-

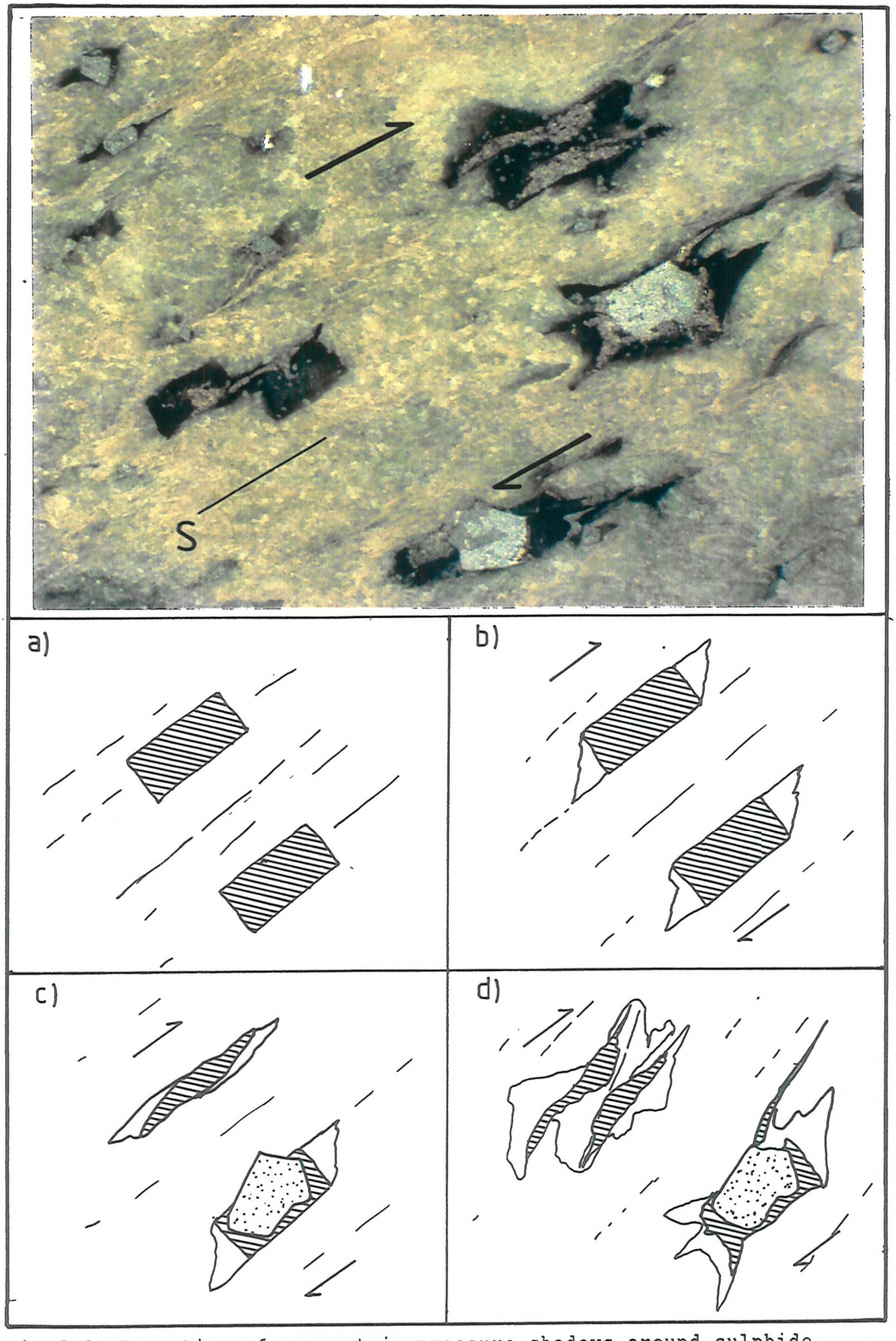

Fig.6.4 Formation of asymmetric pressure shadows around sulphide grains in altered footwall tuffs, Wadi Lode 4-level (see Fig.6.2).
a) pyrite (?) pseudomorphed by pyrrhotite along s-foliation,.
b) formation of asymmetric chlorite pressure shadows during dextral shear,
c) replacement of some pyrrhotite grains by arsenopyrite,
d) flattening and shearing of pyrrhotite grains and formation of secondary chlorite-pyrrhotite-chalcopyrite pressure shadows around arsenopyrite.

micron scale inclusions in sulphides and/or hosted by fine quartz-calcite stringers. Background and economic gold grade distribution is discussed fully in chapter 7.

The gold associated with vein sulphides tends to be hosted by arsenopyrite within V_1 quartz veins but is also associated with pyrite at the vein-wall rock interface (Plate 6.4). The intergrown gold and sulphides exhibit a wide range of textures due to precipitation and subsequent deformation. Gold grains often appear as inclusions in sulphide minerals but sulphides are only rarely observed within gold. Occasionally, acicular tourmaline crystals up to 5µm long are found within gold and sulphides along altered wallrock laminae (Plate 6.4d). Gold inclusions range from ≤1 to 60µm and generally occur towards the periphery of host sulphide grains, especially in the largest sulphide crystals (Plate 6.4e). The smallest gold inclusions are less than 8µm across and are irregular to sub-spherical in shape. Larger gold grains tend to be elongate and have regular straight edges suggesting they infill spaces between sulphide grain aggregates (Plate 6.4c). In gold-sulphide composite grains, the majority of gold occurs as grains adhered to sulphide surfaces but in areas where both free gold and gold-sulphide grains occur only a minor amount of gold occurs as inclusions (Plate 6.4a).

Many of the auriferous vein samples contain free gold within zones of strained quartz in which sulphide grains are notably absent. At least some of the gold, however, is entrained by larger quartz grains which remain unrecrystallised, suggesting that gold mineralisation pre-dated quartz deformation. As no secondary quartz precipitation is evident, it is unlikely, given the large fluid volumes necessary to precipitate ore-grade mineralisation, that the gold grains were precipitated from late-stage fluids channelled along the narrow strain zones. As a result, an SEM study was made of these gold grains to determine whether they displayed any evidence of shearing (Plate 6.5). In order to liberate the grains without producing any mechanical deformation through processing, three samples of high grade quartz vein material were digested using established palynological hydrofluoric acid dissolution techniques (Phipps & Playford,1984).

The free grains vary in size from 10-1000µm (rarely up to 3.5mm) and textures range from small sub-spherical grains with negative crystal imprints to elongate more planar grains with fine filigree margins (Plate 6.5a & b). Although the flatter grains are more abundant in the more deformed veins, there are no textures which can

Plate 6.4 Gold mineralisation associated with V_1 vein sulphides.

a) Photomicrograph (RL) showing gold (yellow) and sulphide (arsenopyrite; white) mineralisation adjacent to tourmaline rich wallrock lamina (W, top left to bottom right) and calcite infilled fracture (Ct, left -marked by cleavage pits) from blue V_1 quartz vein, Wadi Lode 4-level (field of view 3.5mm).

b,c) Photomicrographs (RL) close-up of 6.4a showing most of the gold associated with sulphides occurs on sulphide grain faces (i), infilling spaces between sulphide grains (ii). Larger gold grains in sulphides tend to have straight edges (iii) indicating late gold precipitation between sulphide grains.

d) Photomicrograph (CN left, RL right) showing gold grains (Au) at the junction of a tourmaline-rich wallrock lamina and the base of calcite infilled fracture in a V_1 quartz vein (Wadi Lode 4-level) (Apy = arsenopyrite; field of view 1.5mm).

e) Photomicrograph (RL) of V_1 vein margin show native gold (left, yellow) and gold on the margins of pyrite (py) and arsenopyrite (apy) grains, (Wadi Lode 4-level; field of view 1.5mm).

CN = crossed Nicols, RL = reflected light.

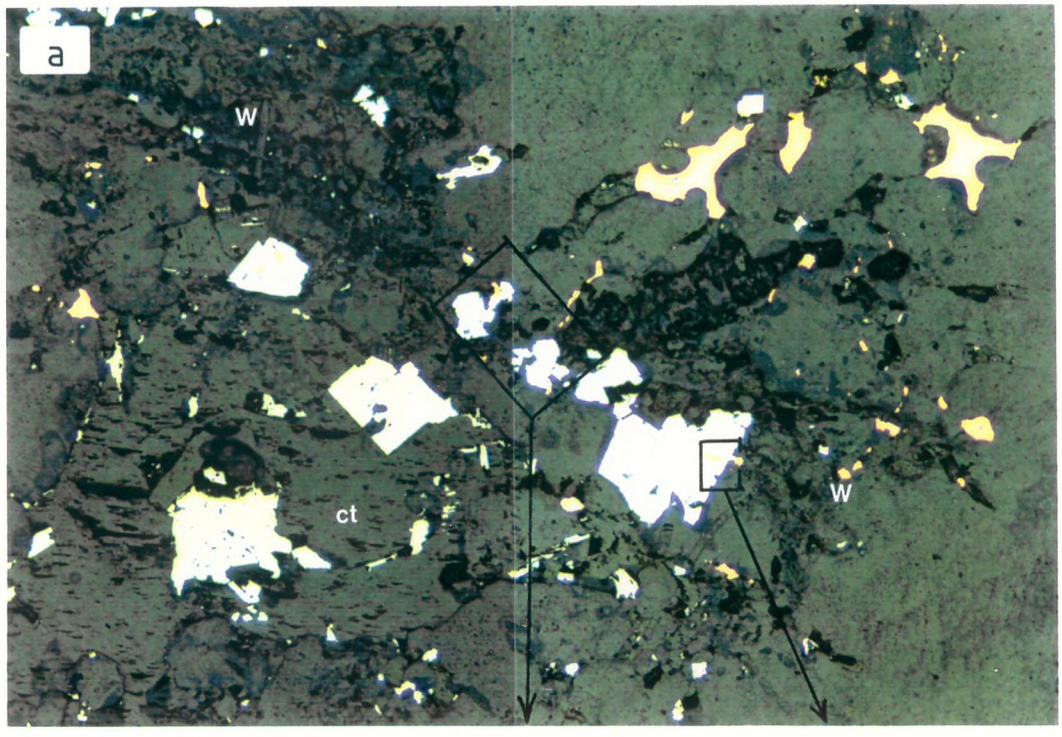
a
W
ct
W

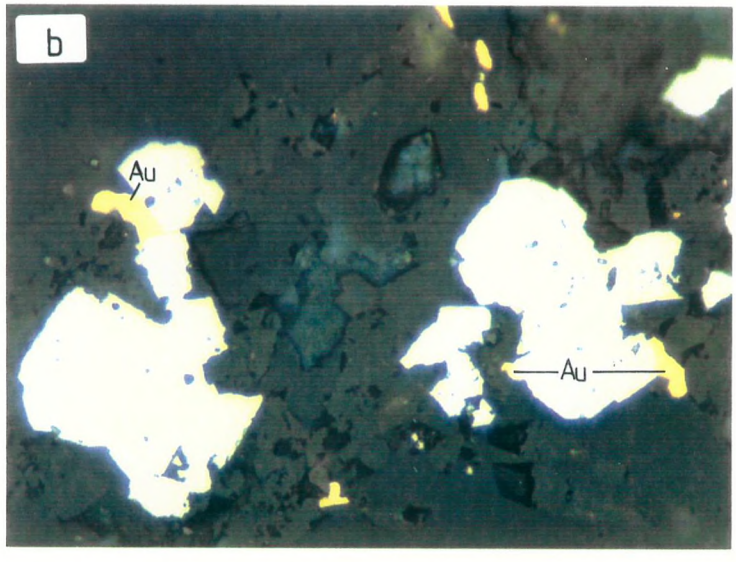
b
Au
Au

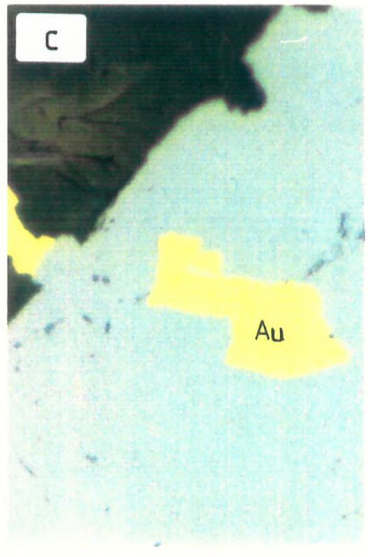
c
Au

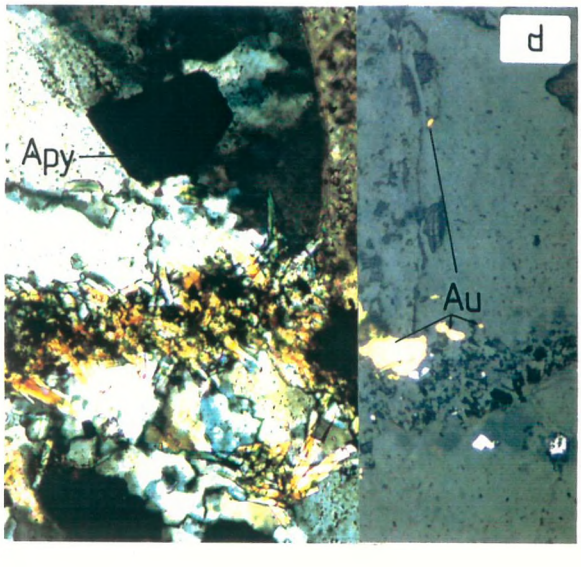
Apy
d
Au

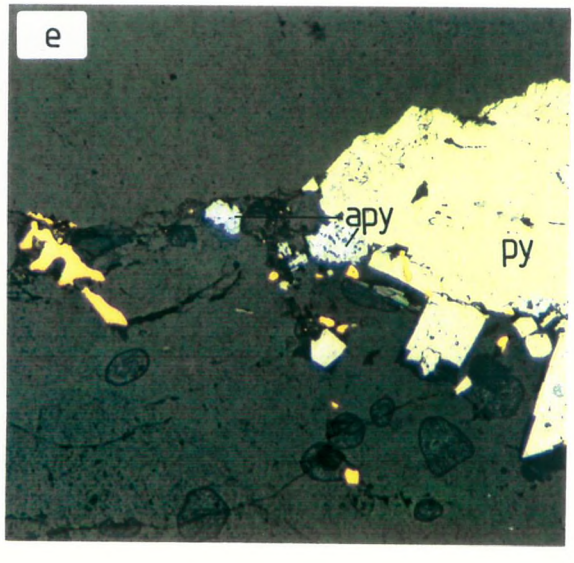
e
apy
py

Plate 6.5 Back-scattered electron (BSE) images of gold and gold-sulphide grains from the V_1 quartz veins.

a) Gold grain showing fine filligree crystal ends (scale bar = 200µm).

b) Close-up of gold grain showing negative crystal imprints and minor chalcopyrite (scale bar = 20µm).

c) Fine gold grains on the faces and edges of hydrothermally etched arsenopyrite grains (scale bar = 200µm).

d) Large composite gold-arsenopyrite-pyrite grain with gold filling the interstitial spaces between euhedral to subhedral sulphide grains (scale bar = 800µm).

e) Euhedral arsenopyrite grains with gold as discrete domal grains (bottom) and as a uniform coating with fine ends (top; scale bar = 20µm).

f) Central arsenopyrite grain with domal gold grain on crystal edge showing close association with tourmaline (Tm; scale bar = 30µm).

g) Elongate platy gold grains forming a pressure shadow on the corner of a euhedral arsenopyrite grain (upper surface folded over; scale bar = 100µm).

h) Close-up of folded grains (6.5g) showing the fine platy nature of the gold grains indicating interstitial growth between euhdral sulphide grains (scale bar = 20µm).

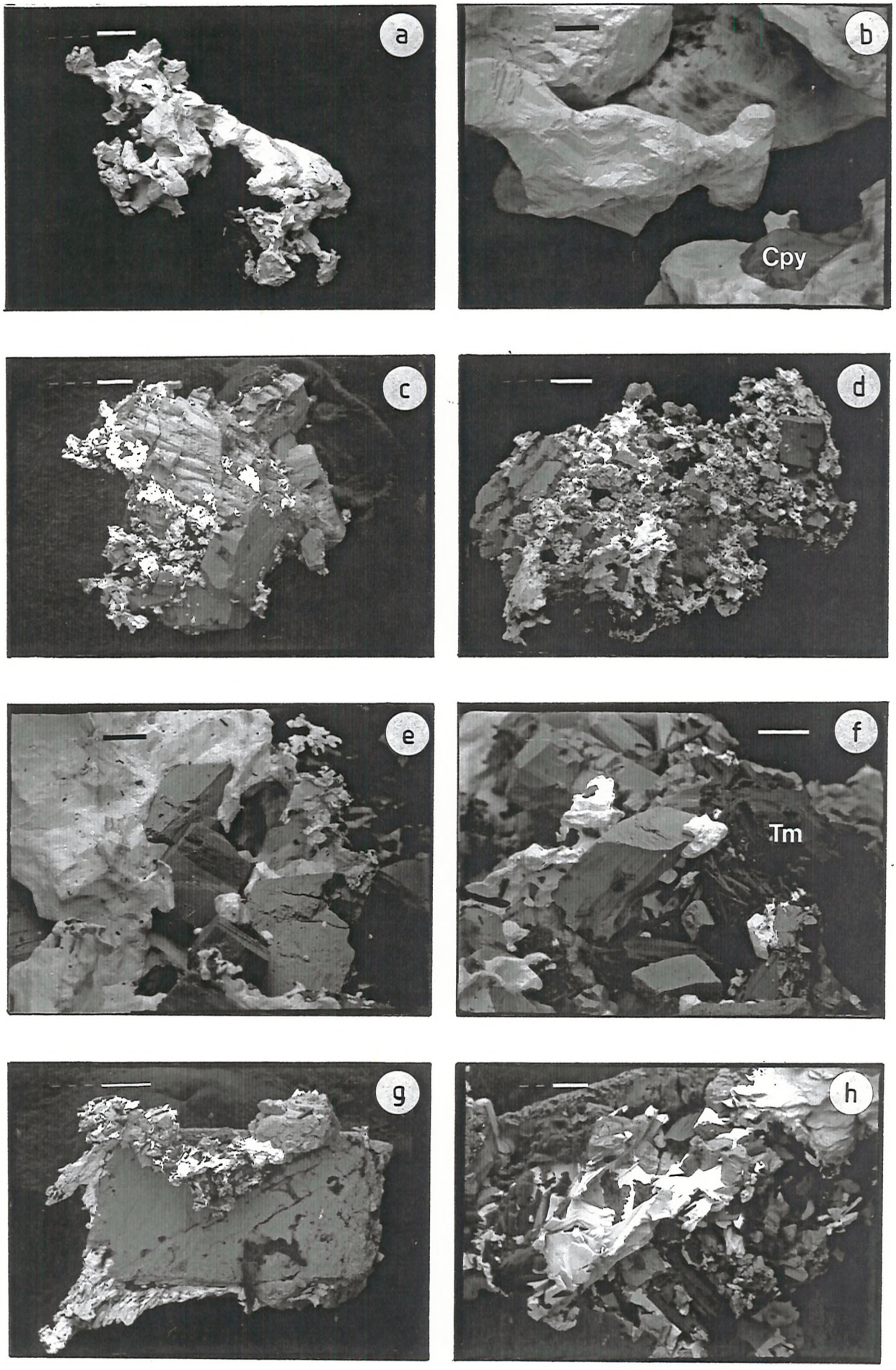
a
b
Cpy
c
d
e
f
Tm
g
h

definitely be ascribed to shearing of the highly ductile gold. In some hand specimens, however, gold occurs as fine grains which appear smeared across fracture surfaces, indicating that some gold grains have been strained. Qualitative EDX analyses of the gold show relatively low silver contents, which confirms earlier analytical studies that indicated 6-13% Ag (average of 10%; Robertson Research,1983). It is not known what other minor elements are alloyed with the gold but the relatively high fineness of ≈900 enhances the ductility of the Gebeit grains.

In addition to liberating free gold grains, HF acid dissolution produced numerous composite gold-pyrite-arsenopyrite grain aggregates (Plate 6.5c & d) up to 6mm long, as pyrite (and presumably arsenopyrite) is not etched by this technique (Neuerberg,1961). The gold forms discrete anhedral, domal to filigree grains distributed across the sulphide grain surfaces and occasionally predominates to form a thick layer which blankets the sulphide grains (Plate 6.5e). Tourmaline, which is only very weakly affected by HF dissolution (Deer et al.,1966), is evident as nests of euhedral prismatic crystals intergrown with gold (Plate 6.5f). Thin-section studies of composite gold-sulphide grains show most of the gold occurs on the surfaces of the sulphide grains, producing planar surfaces at the gold-sulphide interface (Plate 6.4c). Sequential leaching of the sulphides using H_2O_2 confirms that the gold is adhered to the surface and reveals thin planar gold grains that have infilled the interstices of subhedral to euhedral sulphide grain aggregates.

Gold and sulphides show evidence of synchronous precipitation as is expected with destabilisation of gold-thio complexes within the estimated P-T range of the Gebeit mineralisation (Seward,1973). However, much of the gold appears to post-date precipitation of iron-bearing sulphides. This has been attributed to physical adsorption of the charged aqueous gold species on the sulphides followed by reduction-driven chemisorption of the gold species to precipitate the native gold (Starling et al.,1989):

$$Au(HS)_2 + e^- \dashrightarrow Au + 2HS^-$$

Siting of the gold is controlled by crystal edges and defects of pyrite and other sulphides which act as semiconductors with gold predominantly adsorbed by p-type and mixed n-p-type pyrites (Mironov et al.,1981; Colvine et al.,1984). Rarely, some gold occurs as fine elongate grains normal to the corners of some arsenopyrite crystals in the form of a

pressure shadow (Plate 6.5g & h) indicating that, although some of the auriferous mineralisation may post-date the sulphides, it was synchronous with shear deformation.

Many of the free gold grains not associated with sulphides in V_1 veins occur at the margins of coarse, calcite-filled fractures (Plate 6.6). These grains vary from sub-spherical to stellate and irregular in shape. The host quartz is usually strained and, although the calcite often displays deformation lamellae, fine calcite occurs along quartz grain boundaries and in cross-cutting fractures. On initial observation, the gold appears to be contemporaneous with the late calcite; however, in almost all cases the gold is attached to the quartz fracture rim and extends into the host quartz matrix (Plate 6.6a,b, & f). Many grains are totally enclosed by the larger relict quartz and petrographic studies in reflected light and under crossed nicols show the quartz fracture margins to be brecciated (Plate 6.6c & d). As most of the free gold is hosted by strained and/or fractured quartz (Plate 6.6e) and paradoxically appears to be coeval with it, the gold grains may have exerted a control on deformation. The presence of ductile gold grains within a highly brittle quartz matrix would generate significant heterogeneities during brittle deformation, preferentially propogating fractures to and away from the gold grains.

The same ductility contrast between gold and sulphides may account for the occurrence of gold hosted by fractures in sulphides. In two samples, gold occurs coating both sides of fractures in pyrite but in places appears to have been squeezed between the two surfaces where the fractures are constricted (Fig.6.3). The centres of the fractures are infilled by quartz or silicates which are probably secondary. This suggests that the gold pre-dated or was precipitated very early in fracture formation, affirming the intimate association between gold and vein sulphides.

6.9 Fluid Inclusions

Samples of quartz vein material from lode veins, numerous satellite prospects, and from the later phases of vein formation at Gebeit have been investigated for potential fluid inclusion studies. The aim of fluid inclusion analysis would be to characterise the fluid evolution at Gebeit and to compare and contrast the nature of mineralising fluids from the various satellite areas. Initial petrographic studies on 25 samples of the quartz material, however,

Plate 6.6 Gold in sulphide-poor quartz and along calcite-infilled fractures in the V_1 quartz veins.

a,b) Photomicrographs (RL left, CN right) of gold (yellow) at margins of a fracture (i) infilled by coarse calcite, attached to brecciated quartz grains (ii), and enclosed by strained vein quartz in V_1 blue quartz vein (Wadi Lode 4-level; field of view 2mm).

c,d) Photomicrographs (RL left, CN right) of cuspate gold grains (yellow) along grain boundaries of strained V_1 quartz which shows extensive sub-grain development (g; Wadi Lode 4-level; field of view 1mm).

e) Photomicrograph (CN) of elongate gold grains (Au) hosted by brittle fracture in relatively undeformed V_1 quartz (Wadi Lode 4-level; field of view 2mm)

f) Photomicrograph (RL) of gold grains (Au) in V_1 quartz vein at margin of rectangular calcite-infilled fracture and totally enclosed within host quartz showing propogation of fractures to and away from gold grains (Wadi Lode 4-level; field of view 1.5mm)

CN = crossed Nicols, RL = reflected light.

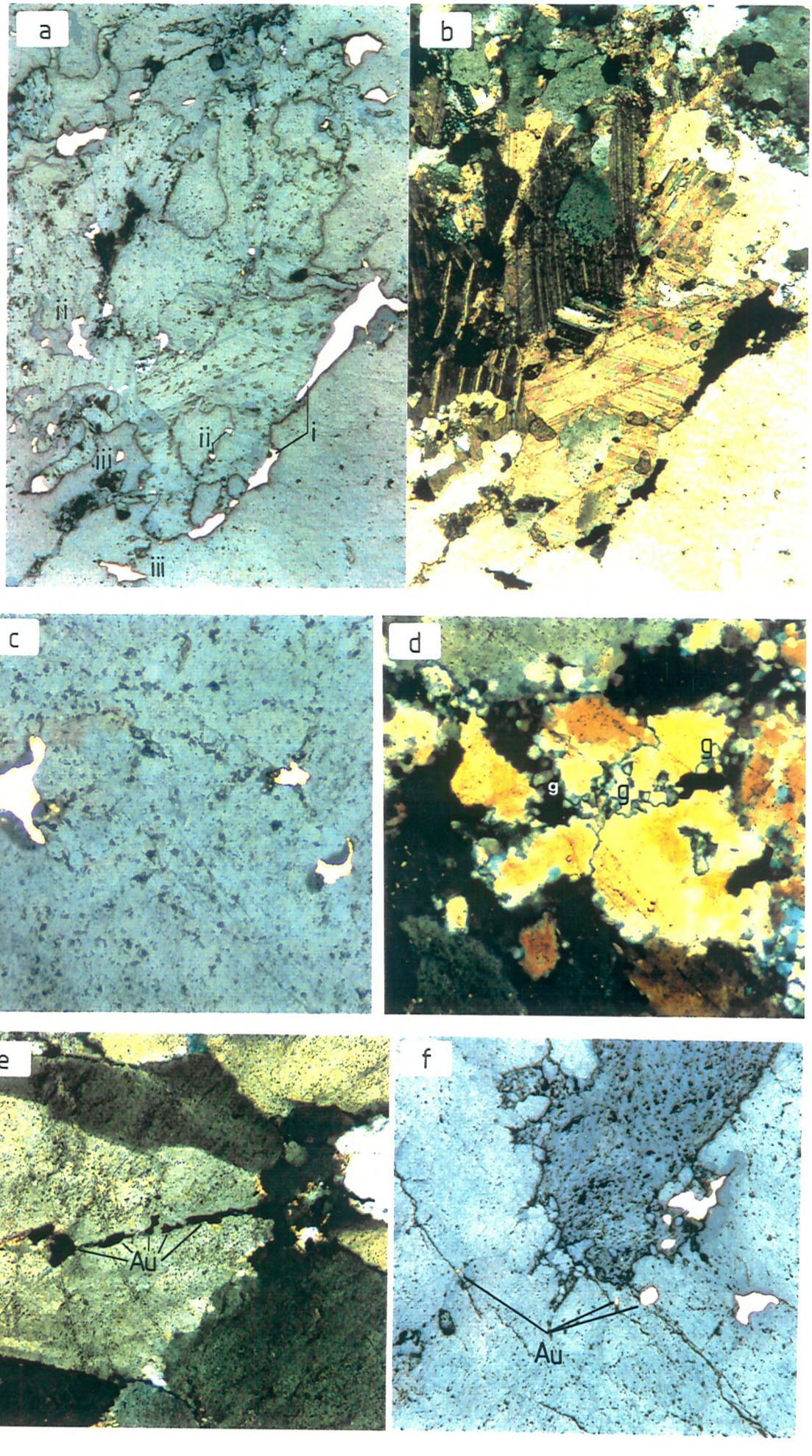
a
i
ii
iii
ii
iii
b
c
d
g
g
g
e
Au
f
Au

showed that the majority of inclusions are less than 2.5 μm in size and can only be resolved using the highest magnifications available (800x). No daughter mineral phases are evident in any of the inclusion types identified but CO_2-bearing inclusions are common. Unfortunately, the long working distance objective lenses necessary on microscopes modified to incorporate a fluid inclusion stage reduces resolution to the point where most of the Gebeit samples cannot be analysed.

Significantly, the only two samples with inclusions >5μm consisted of quartz vein material hosted by granitoids: mineralised quartz veins hosted by sheared granodiorite at Wadi Messesana and quartz vein xenoliths in the tonalite at Vein 18. The larger inclusions found exclusively at these two sites possibly reflect the preservation of original vein textures by the granitoid host rocks.
There are, however, a few problems with using samples from these localities, namely:

i) although Wadi Messesana was an ancient prospect, no gold was observed in the vein material sampled and it cannot be directly correlated with the Gebeit mineralisation,

ii) the quartz xenoliths at Vein 18 may represent plucked lode vein material incorporated during igneous emplacement, but without visible gold mineralisation and comparison with lode inclusion data this cannot be confirmed,

iii) data collected from these samples is biased towards the larger inclusions >5μm.

Nevertheless, a preliminary investigation was carried owing to the strong similarity of inclusion types seen in the Wadi Messesana and Wadi Lode, Y and A lode samples. Analytical techniques are described in Appendix A and all fluid inclusion data are tabulated in Appendix D.

6.9.1 Wadi Messesana Prospect

This minor gold prospect lies approximately 6km NNW of Gebeit and consists of an auriferous white quartz vein hosted by a north-east trending shear zone within a late-tectonic granodiorite. The 750m long elliptical intrusion lies along the base of Wadi Messesana in the core of an antiform as part of the Wadi Messesana shear zone (see Fig.5.1). Most of the original 30-60 cm wide vein has been extracted by Pharonic mining activity, indicating at least some gold enrichment. As with the samples from the other prospect areas, the Wadi Messesana quartz is fairly milky and is cross-cut by numerous, very fine fractures and

inclusion trails. There are, however, several patches of more translucent quartz which contain irregular to negative-crystal-shaped inclusions up to 15μm in size (Fig.6.5; see Plate 6.7a). From the primary inclusions (group I), defined by isolated random distributions, a range of compositions exist which can broadly be subdivided into three categories:

i) two phase aqueous liquid-vapour inclusions with degree of fill F=0.95, ± CO_2,
ii) two phase aqueous-CO_2 liquid inclusions, F=0.30-50,
iii) CO_2-rich liquid inclusions + H_2O, F=0.60-0.80.

The CO_2-rich nature of many of the primary inclusions was confirmed on cooling of the Wadi Messesana samples which produced a third gaseous CO_2 phase in the liquid CO_2 phase. Because of the small size of the inclusions and problems with clouding of the stage at low temperatures, temperatures of final melting of CO_2 could not be accurately measured. It is, therefore, not known whether other phases such as CH_4 are present.

Homogenisation of the CO_2 phases to liquid CO_2 ranged from -2.2 to 19.7°C (x=12.3, σ_n=6.5, n=13), indicating an average CO_2 density of 0.85 gcm^{-3} (Fig.6.6a). Final melting temperatures of >0°C for most of the aqueous-rich inclusions, evident by a final movement by the vapour bubble, indicated the formation of gas hydrates (clathrates) due to the presence of small amounts of CO_2. Clathrate melting temperatures of 3.2-4.9°C (x=3.9, σ_n=0.69, n=5) show the salinity of the aqueous phase to be between 9 and 11 wt% NaCl (Fig.6.6b).

As with the freezing of small inclusions, total homogenisation temperatures were not easy to determine, especially with the CO_2-rich inclusions, and samples had to be repeatedly cooled to determine whether the inclusions had completely homogenised. Gradual bubble growth on cooling indicated that complete homogenisation had not been reached in contrast to rapid nucleation at much lower temperatures (20-50°C below T_h). Although total homogenisation temperatures for all three types occur in the range 235-294°C, the CO_2-rich inclusions tend to have slightly higher temperatures (x=271.2, σ_n=19.8) relative to the more aqueous types (x=253.3, σ_n=11.2). This slight discrepancy may be due to the relatively small sample number (n=12) and the possibility that leakage has occurred from the more CO_2-rich inclusions. Several of the CO_2-rich inclusions leaked before homogenisation at 230-295°C

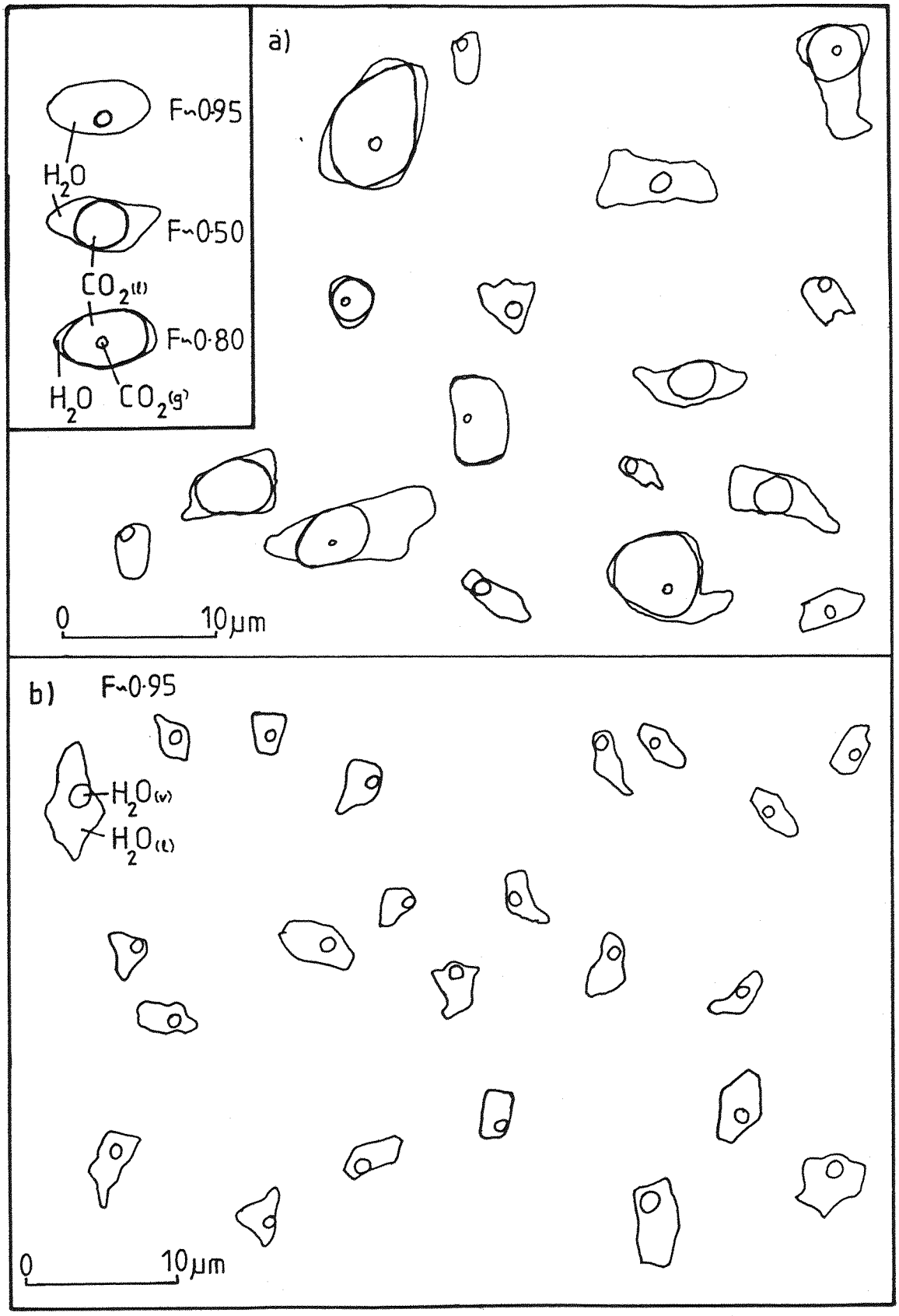

Fig.6.5 Sketches of the primary fluid inclusions observed in granitoid-hosted quartz samples from Wadi Messesana (a) and Vein 18 (b).

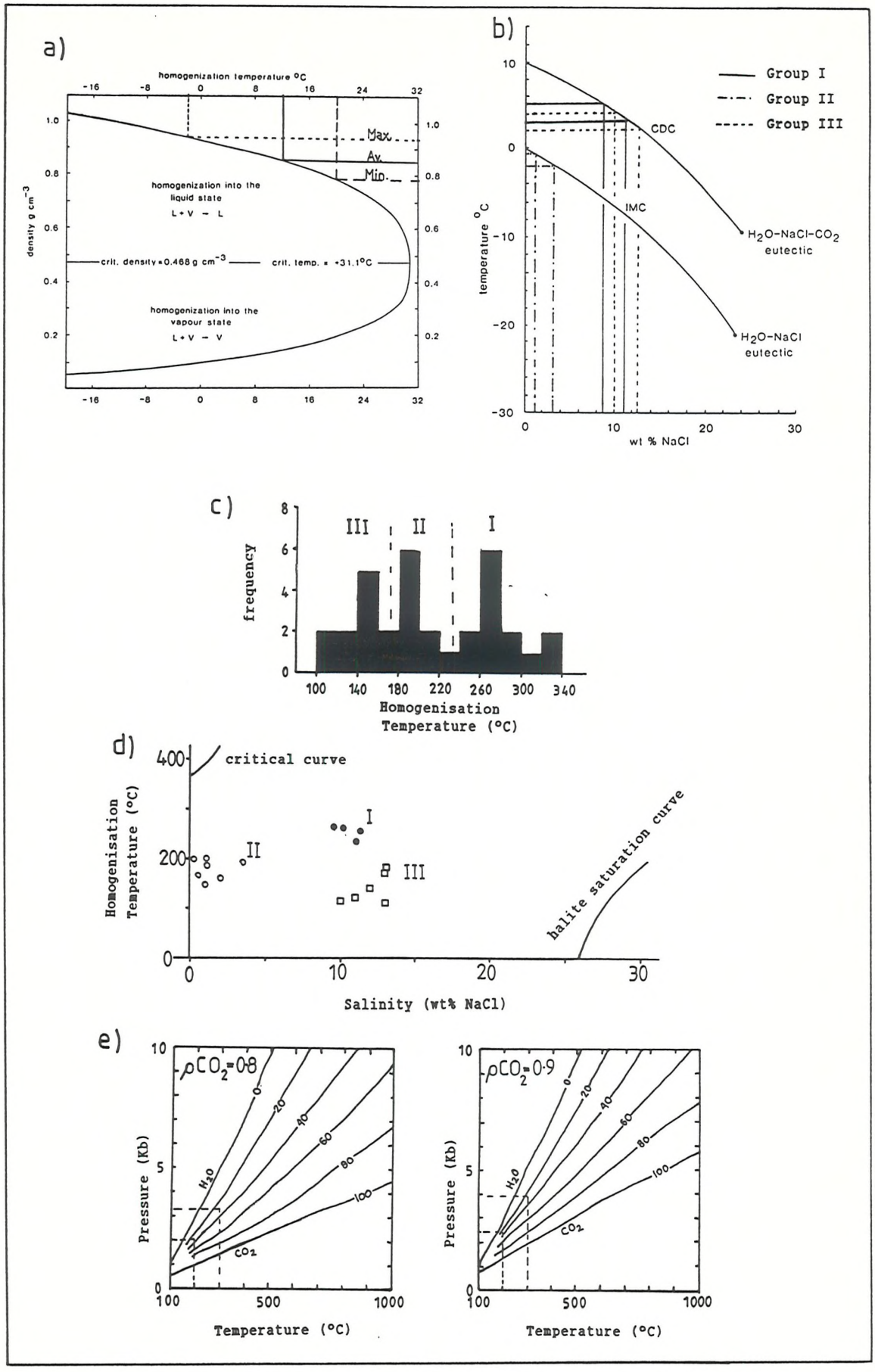

Fig.6.6 Fluid parameters determined from the Wadi Messesana inclusions: CO_2 density (a) and salinity (b; after Shepherd et al.,1985); T_h vs. frequency (c) and T_h vs. salinity (d) showing three possible fluid inclusion populations; (e) bulk H_2O-CO_2 fluid isochores indicating fluid pressures of 2.0-3.9Kb (after Brown & Lamb,1986).

and others appeared to homogenise by fading of the meniscus at temperatures up to 340°C.

Using estimates of the degrees of fill and density of the main inclusion types, percentage mole fractions of CO_2 can be calculated. For the mixed CO_2-H_2O inclusions which homogenised by meniscus fade, 50 volume% CO_2 (= 46 wt%) equates to a mole fraction of 26%. The CO_2-rich inclusions contain up to 80% CO_2 (77 wt% CO_2), which is equivalent to 58 mole%. The CO_2 content of the H_2O-rich inclusions varies from 25% (10 mole%) to those inclusions in which CO_2 is not visible but is detectable by the formation of gas hydrates during freezing. As less than 5 wt% (2 mole %) CO_2 is very difficult to detect in aqueous inclusions (Shepherd et al., 1985), the CO_2 content of the H_2O-rich inclusions appears to vary, approximately, from 2 to 10 mole %.

The variation of phases and apparent isothermal formation of the three inclusion types suggests they may represent the heterogenous trapping of immiscible H_2O-CO_2 fluids, fluid mixing, or the products of variable inclusion leakage or necking down. Sub-solvus unmixing would result in progressively more pure H_2O- and CO_2-rich fractions during cooling, typified by fluids of 2-10 mole % and 60 mole % CO_2 (Fig.6.7), respectively, in the Wadi Messesana sample. These values appear to coincide with expected compositions derived from the H_2O-CO_2 solvus, (Hendel & Hollister,1981; Bowers & Helgeson,1983); however, the shape of the solvus in T-X space is variable depending on NaCl content and, to a lesser degree, pressure.

Critical homogenisation by meniscus fade is also indicative of compositions close to the critical point, around 26 mole % CO_2. Superficially the data appear to satisfy many of the criteria for fluid immiscibility (Ramboz et al.,1982) but it must be emphasised that the inclusions analysed are close to the limits of resolution and represent a small, possibly biased, sample set. If phase separation is the cause of the variable phase CO_2-H_2O inclusions, then the temperature of homogenisation equals trapping temperature ($T_h=T_t$), implying trapping temperatures of around 230-270°C for the Wadi Messesana samples. Preferential partitioning of saline phases into the aqueous phase during unmixing would produce artificially high values of wt % $NaCl_{eq}$, suggesting that original fluid salinities could have been well below 10 wt % $NaCl_{eq}$. P-T bulk fluid isochore diagrams have been calculated for coexisting H_2O-CO_2 in the H_2O-CO_2(±NaCl) system (Brown & Lamb,1986) for application to fluid inclusion studies of Canadian Archaean gold deposits. Plotting the Wadi Messesana primary inclusion data for CO_2

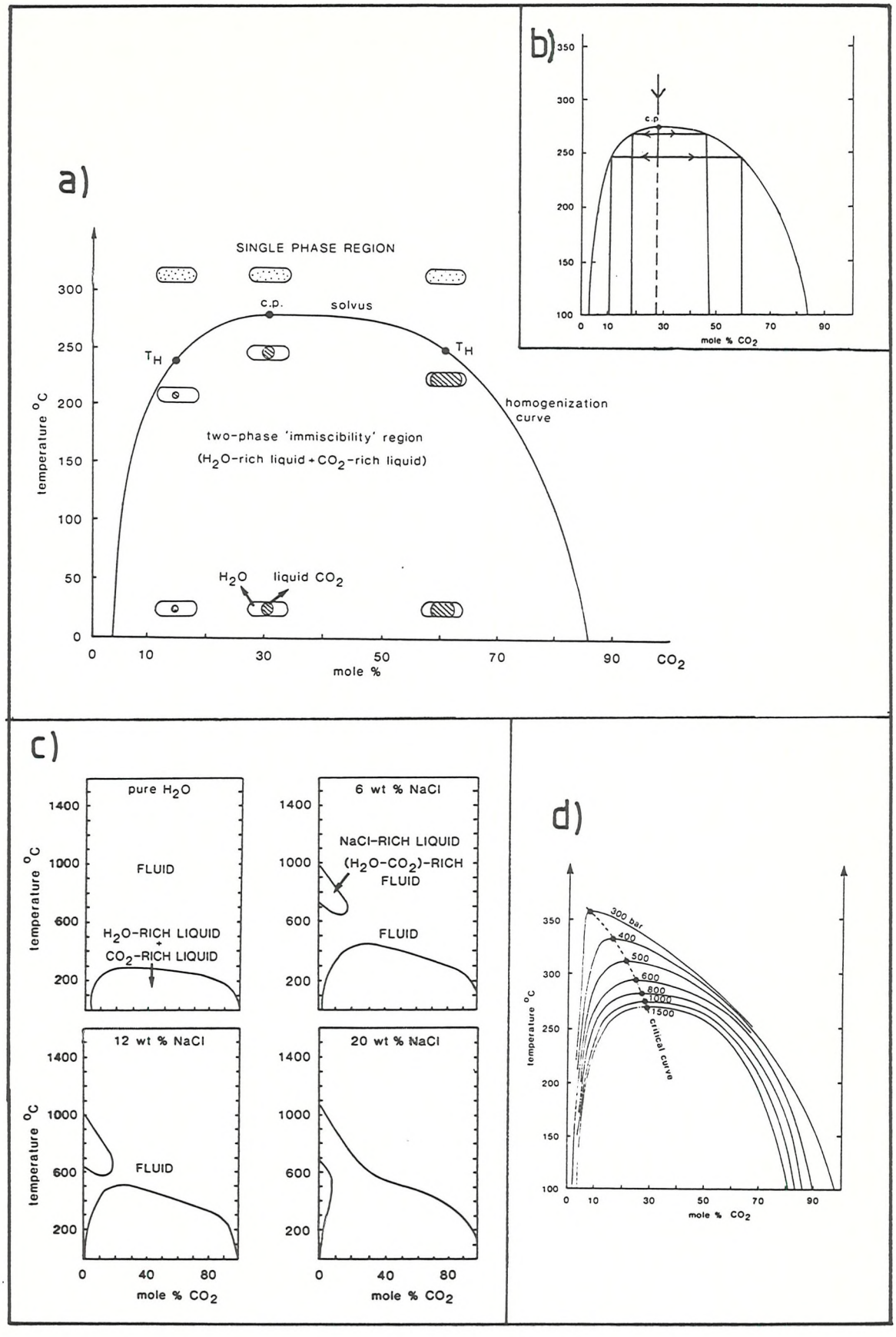

Fig.6.7 Temperature-CO_2 diagram showing the effect of CO_2 content on inclusion type (a) and the unmixing of Wadi Messesana fluids (b) close to the critical composition (c.p.). The variation of position and shape of the solvus are shown as a function of salinity (c) and pressure (d; after Shepherd et al.,1985).

density, vol.% and T_{hTOT} data indicates fluid pressures in the region of 2.0 to 3.9kb (≈7-12 km depth), consistent with evolution at the brittle-ductile transition at greenschist facies grades (Fig.6.6e).

Phase separation of H_2O-CO_2 fluids resulting in pH increase can be an efficient process for reducing gold solubility and has been demonstrated as the main precipitation mechanism in several Archaean gold deposits (e.g. Wood et al., 1986; Studemeister & Kilias,1987). The nature of the Gebeit ore fluids, their relationship to wallrock reactions, and possible precipitation mechanisms are discussed in Chapter 7 and Chapter 8.

In addition to the different inclusion types considered to be primary, the majority of inclusions in the Wadi Messesana samples are secondary aqueous inclusions (F=0.85-0.95) which give a wide range of homogenisation temperatures from 110-204°C. Plots of T_h vs. salinity and frequency (Fig.6.6c & d) suggest that two other populations (groups II & III) exist in addition to the primary inclusions (group I). Clathrate melting temperatures from 2.1-4.3°C (x=2.9, σ_n=0.82 n=6) imply a fluid salinity around 12 wt% NaCl whereas non-CO_2-bearing inclusions (T_h, 147-202°C) have low ice-melting temperatures (-0.5 to -1.9°C; x=-0.7°C, σ_n=0.5, n=8) suggesting salinities of the order of 2-3 wt% NaCl. The group III, secondary, CO_2-bearing inclusions may represent the progressive re-equilibration of group I inclusions due to fracturing during protracted post-vein deformation.

6.9.2 Vein 18

Inclusions from the quartz xenoliths within the tonalite intrusion at Vein 18 were examined in order to compare the inclusion fluids with those of Wadi Messesana and to get an impression of fluid variations closer to the main workings at Gebeit. The inclusions from this sample ranged from negative crystal to irregular in shape and were generally between 3 and 7 μm in size (Fig.6.5b). Numerous fractures and very fine secondary inclusion trails cross-cut the sample and, although the inclusions analysed appear to be primary, a secondary origin cannot be discounted. All of the primary inclusions are aqueous with a uniform 0.95 degree of fill. Final ice melt temperatures ranged between -0.3 and -3.3°C (x=-1.99°C, σ_n=1.27, n=23) indicating low salinities of 1-5 wt% NaCl (Fig.6.8a & c). Some inclusions gave final melt temperatures of 0-1.0°C, suggesting either the presence of small amounts of CO_2 (clathrates) in more saline fluids (14-16 wt% NaCl) or variations

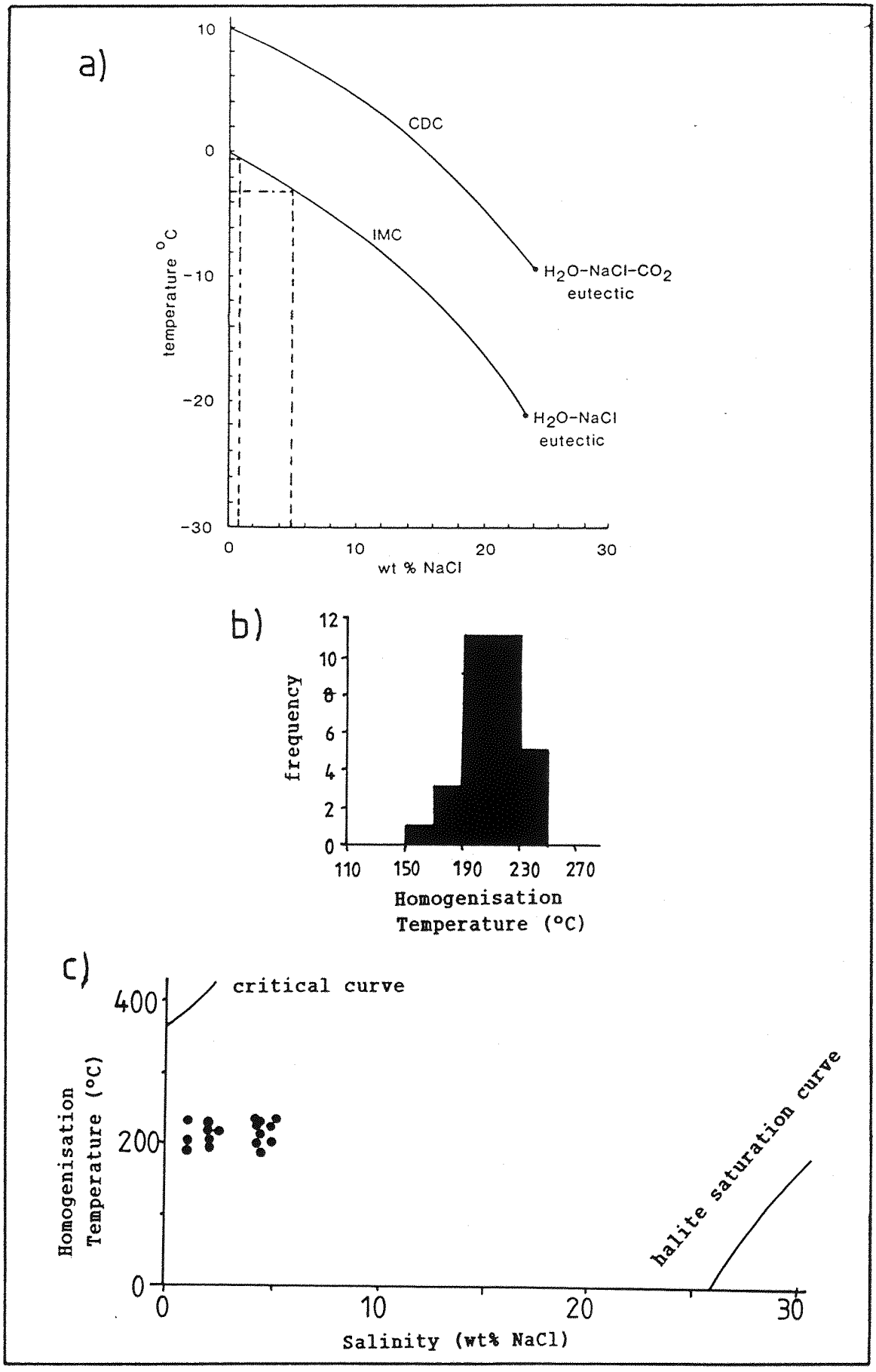

Fig.6.8 Fluid parameters determined from the Vein 18 inclusions: salinity (a; after Shepherd et al.,1985), T_h vs. frequency (b) and T_h vs. salinity.

produced by systematic machine errors. Homogenisation temperatures are fairly closely grouped between 190 and 235°C (x=214°C, σ_n=14.2, n=27) with a few, possibly secondary, inclusions homogenising at 162-190°C.

Apparent primary inclusions from the two prospect areas described above suggest that early fluids comprised low salinity (1-5 wt % $NaCl_{eq}$) aqueous and CO_2-bearing fluids, of which some may have mixed or undergone phase separation to produce CO_2-rich inclusions and CO_2-bearing aqueous inclusions with elevated salinities (9-11 wt % $NaCl_{eq}$) due to immiscibility. However, as already emphasised, the sample set is small having been taken from granitoid-hosted veins and therefore interpretation of the data must be approached with caution.

6.9.3 Quartz Colouration and Inclusions in the Gebeit Lodes

The inclusions in quartz samples taken from the Wadi, A and Y Lodes proved to be too small to be analysed but were examined at high magnifications using a petrographic microscope. Samples in which apparent primary inclusions were defined contained similar inclusions to the three main types identified in the Wadi Messesana sample: i.e. H_2O- and CO_2-bearing inclusions of variable degrees of fill. Localised freezing of the polished chip surface using acetone and liquid nitrogen confirmed the presence of CO_2 by the formation of a CO_2 gaseous phase within the liquid CO_2 phase. CO_2 homogenisation into the liquid phase below room temperature indicated a minimum CO_2 density of 0.8 gcm^{-3}. The similarity with the Wadi Messesana inclusions suggests that the main vein-forming and mineralising fluids at Gebeit may have been produced by fluid mixing or phase separation.

The intense blue to blue-black colouration of the vein quartz is particularly marked in the veins of the Wadi Lode, Y Lode and A lode and at the satellite prospects of Garabein and Walati. Blue quartz is commonly linked to the presence of very fine needle-shaped crystals, namely rutile in the case of granulite facies rocks and tourmaline in pegmatitic blue quartz (Deer et al.,1966). In addition, blue quartz colouration has been ascribed to the fine fracturing of deformed quartz (Foster, pers. comm.). The colour of smokey quartz may also be linked with the presence of Al in the quartz lattice (Deer et al.,1966).

As the blue and white quartz could be differentiated in finely powdered samples, the cause of the colour difference was considered to be due to sub-grain size (<100μm) mineral or element inclusions. Samples of blue and white quartz were analysed geochemically and by

electron microprobe to determine whether there was any significant component within the blue veins at Gebeit to account for its colour (Table 6.1). Geochemical analyses showed that TiO_2 and Al_2O_3 contents vary considerably (4-1294 ppm and 0.23-5.16%, respectively); however, the lowest TiO_2 value occurred in blue quartz and the highest Al_2O_3 value in the white quartz. Although relatively pure samples were analysed, the presence of tourmaline, arsenopyrite, and calcite, with concomitant increases in Ni, Cr, V and Sr, was detected in the blue quartz samples, reflecting fine inclusions of altered wallrock material. Conversely, sericite was found in the white quartz samples, producing higher K, Rb, Ba, and Al_2O_3 values.

Microprobe analyses of blue and white auriferous quartz types were considered to provide a more pure analysis of the vein quartz as opposed to the composition of intergrown quartz, calcite, sericite, and tourmaline. These analyses, however, produced very similar results with low Ti contents (0.0-0.02%) and only marginally higher Al values in the blue quartz (0.08-0.15% compared with 0.04%). This indicates that the blue quartz crystals contain more Al than the white quartz but overall, the white quartz veins are richer in Al_2O_3 due to the presence of intergrown sericite. However, if the colour difference was due to higher Al in the V_1 quartz lattice, the veins would tend to be smokey rather than blue in colour (Deer et al.,1966). Although altered wallrock inclusions impart some colouration to the veins, it cannot account for the pervasive colour of the dark blue veins.

Pronounced colouration of the blue lode quartz is evident in polished fluid inclusion chips and thin sections (30-100µm thick; Plate 6.7b-d). No fine crystals of tourmaline or rutile were identified by investigation of the darker areas under high magnification; however, the dark areas, unlike the clear zones, were characterised by abundant decrepitated inclusions. These dark, almost black, inclusions are generally cuspate and stellate in shape and are usually surrounded by similar but much smaller daughter inclusions. As the samples studied had not been heated at any stage after sampling, decrepitation must have been due either to subsequent deformation and uplift or a post-mineralisation thermal overprint. The dark zones of decrepitated inclusions are restricted to larger relict quartz grains which are defined by clear boundaries due to sub-grain development and recrystallisation. The relict grains are truncated by clear bands of cross-cutting, later quartz veins. The fine-grained, clear patches of deformed and recrystallised quartz also confirm that quartz colouration

	White	Blue	Blue	Blue
SiO_2 (%)	91.35	96.25	87.79	95.77
TiO_2	0.02	0.01	0.13	0.01
Al_2O_3	5.16	0.23	3.04	0.59
Fe_2O_3*	0.15	0.08	1.34	0.20
MnO	0.01	0.01	0.03	0.02
MgO	0.30	0.02	0.84	0.13
CaO	0.93	2.11	2.66	1.59
Na_2O	0.11	0.00	0.17	0.32
K_2O	1.52	0.03	0.00	0.01
P_2O_5	0.04	0.00	0.38	0.00
ΣH_2O	1.30	2.00	3.11	1.40
Total	100.88	100.73	99.49	100.05
Rb(ppm)	70	3	<2	<2
Sr	32	26	57	92
Ba	138	<10	13	<10
Pb	<3	<3	<3	<3
Th	<3	<3	<3	<3
U	<5	<5	<5	<5
La	<6	<6	<6	<6
Ce	<10	<10	<10	<10
Y	<2	<2	4	<2
Zr	6	6	14	6
Nb	2	2	2	2
Ga	5	1	5	1
Ni	5	6	60	56
Cr	13	11	29	15
V	<5	<5	52	19
Cu	<2	<2	24	13
Zn	7	8	14	<1
As	9	60	20	154

* Total Fe calculated as Fe_2O_3, ΣH_2O=Loss on Ignition
<3 = Below Lower Limit of Detection

Table 6.1a Compositions of blue and white vein quartz determined by X-ray fluorescence analysis.

	White	Blue	Blue
SiO_2 (%)	99.29	98.71	97.30
Al_2O_3	0.04	0.15	0.08
CaO	0.01	0.01	0.01
K_2O	0.04	0.02	0.02
Na_2O	0.03	0.03	0.04
FeO	0.00	0.00	0.00
MgO	0.02	0.02	0.02
MnO	0.00	0.00	0.00
TiO_2	0.00	0.02	0.02

Table 6.1b Electron probe analyses of vein quartz.

Plate 6.7 Fluid inclusions from Wadi Messesana and Wadi Lode V_1 quartz veins.

a) Primary inclusions from Wadi Messesana at highest available magnification (800x) showing mixture of H_2O-rich (i), H_2O-CO_2 (ii) and CO_2-rich (iii) inclusions. Largest inclusions = 12µm.

b) Photomicrograph (CN) of inclusion chip sample of deformed V_1 blue quartz from Garabein Mine showing the sub-grain development and recrystallisation at the margins of the large quartz grains and cross-cutting V_3 veins in optical continuity with V_1 grains (field of view = 3mm).

c) Photomicrograph (PPL) - as b) showing the dark areas of quartz which produces the blue colouration restricted to the undeformed V_1 quartz grains.

d) Photomicrograph (PPL) of the centre of the undeformed V_1 quartz grain showing the dark colouration is due to fine stellate decrepitated inclusions (field of view ≈ 100µm).

CN = crossed Nicols, PPL = plane-polarised light.

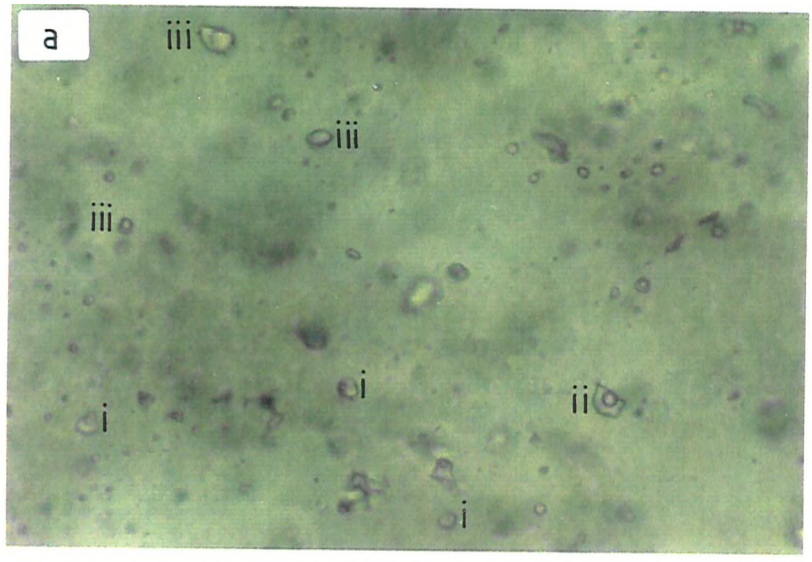
a
iii
iii
iii
i
i
ii
i

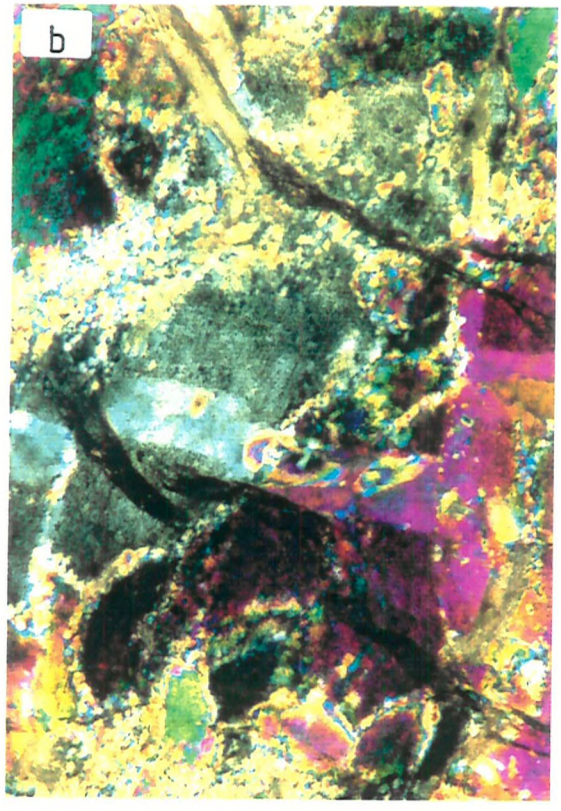
b

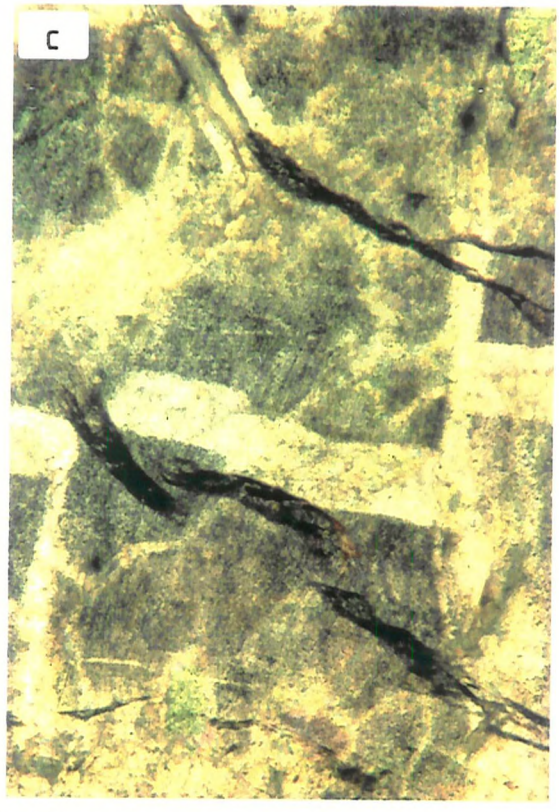
c

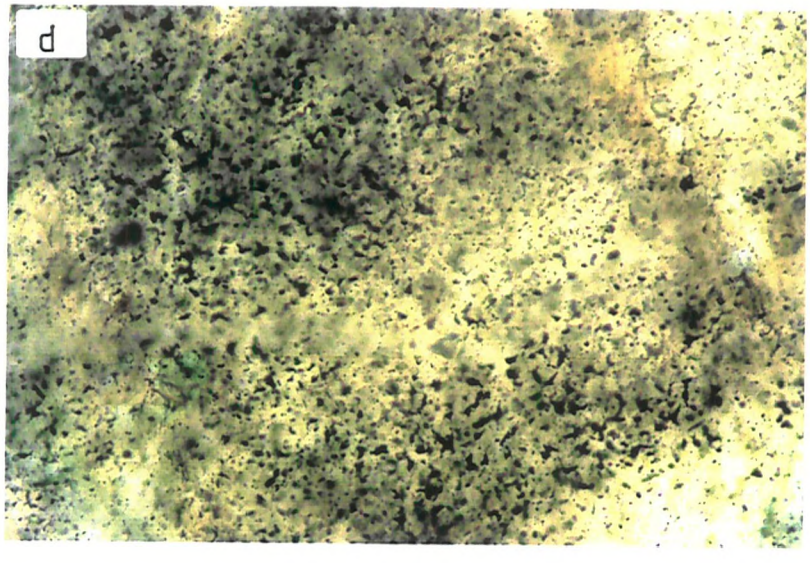
d

is related to the decrepitated inclusions and is not due to quartz deformation. Small relict inclusions found in the blue quartz suggest that the early fluids were CO_2-bearing similar to those identified at Wadi Messesana which were possibly trapped as immiscible phases. The larger, relatively high density, CO_2-bearing inclusions would tend to be more prone to decrepitate (Roedder,1984; Shepherd et al.,1985) and may account for the small size of existing inclusion populations.

6.10 Stable Isotopes

Light stable isotope analysis (namely, H, O, S, and C), when allied to geochemical and mineralogical studies, can help constrain sources of ore constituents and ore fluids. The mineralogy of lode veins and wallrock mineral assemblages at Gebeit, however, places restrictions on which isotopes can be accurately sampled, separated and measured. Virtually all carbonate phases that can be positively constrained as syn-mineralisation occur as fine intergrowths with quartz in the V_1 veins. Removal of carbonate phases from quartz can be easily achieved using warm acid digestion but the complete separation of finely intergrown quartz from calcite proved to be too time consuming to justify a carbon isotope study. Similarly, sulphide mineralisation in lode profiles tends to be fine grained and displays intricate intergrowth textures of different sulphide and silicate phases. As sulphur isotopic disequilibrium is a more common phenomenon for sulphides co-existing with pyrite and/or chalcopyrite (Ohmoto,1986), separation and analysis of sulphur isotopes is considered to be beyond the scope of this study. The lack of significant amounts of hydroxyl-bearing minerals co-existing with V_1 vein quartz therefore restricts isotope studies for the Gebeit deposit to oxygen isotope analysis of vein quartz.

6.10.1 Oxygen Isotope Signatures for the Gebeit Deposit

Quartz vein sampling for oxygen isotope analysis was concentrated on the V_1 mineralised veins and their cross-cutting white quartz stringers. All samples were examined by binocular microscope after each stage of preparation to check for sulphide/silicate impurities and were then washed and filtered several times in boiling HCl to remove any relict carbonates (sample preparation procedure given in Appendix A). Each 100µg sample size was reduced by grinding and fine sieving to

approximately 75 μm (200 mesh) for analysis. A representative set of 26 quartz vein samples covering Wadi Lode, Y Lode, Vein 18, Marble Bar and later V_3-V_5 quartz veins was sent for analysis to Dr A.E. Fallick at the Scottish Universities Research and Reactor Centre at East Kilbride. The results are given in Table 6.2 (all data are relative to SMOW).

The δO^{18} values of the samples of Wadi Lode blue and white quartz are higher than for the other subsets analysed, averaging 15.6 ± 0.7‰ compared with 14.1 ± 0.5‰ for the Y Lode. The spread in Wadi Lode δO^{18} values show regular variation when plotted on a sample location plan (Fig.6.9) and indicate a minor decrease along strike away from the main shaft. The sample area, however, comprises only a small proportion of the total zone of mineralisation and probably represents a minor fluctuation. Nevertheless, δO^{18} values for Marble Bar, Vein 18 and the large blue/white veins south of the mine complex (5300E,4450N; see Figs.5.6 & 5.13) group very closely at 14.01 ± 0.07‰. Under equilibrium conditions, δO^{18}_{quartz}, δO^{18}_{fluid}, and temperature are related between 250 and 500°C (Matsuhisa et al.,1979) by the expression:

$$10^3 \ln\alpha_{QW} = 3.34\ (10^6 T^{-2}) - 3.31 \qquad (T=°K) \qquad \ldots\ldots\ldots\ldots\ldots\ldots (1)$$

where $\ln\alpha$ is the equilibrium fractionation factor and to a good approximation, $10^3 \ln\alpha_{QW} = \delta O^{18}_{Q} - \delta O^{18}_{W}$.

Unfortunately, because of the lack of suitable fluid inclusion material, direct temperature estimates are not available for the Gebeit lode veins. However, using the temperature estimates of the Wadi Messesana and Vein 18 quartz samples as a reasonable guide to fluid temperatures, an approximate range of expected fluid δO^{18} values can be defined. Homogenisation temperatures for both prospects lie between 200 and 300°C which, using the mean δO^{18} quartz values, indicates that: assuming $T_h = T_{TOT}$,

$$\delta O^{18}_{fluid} \approx 4.0\text{-}8.7‰ \text{ for the Wadi Lode}$$
$$\approx 2.4\text{-}7.1‰ \text{ for the satellite prospects.}$$

The disparity in quartz δO^{18} values for the various mineralisation zones is probably due to variations in fluid temperature. Assuming homogeneity for δO^{18}_{W} values, from equation (1) above a difference of 1.6‰ between 200 and 300°C would reflect a fluid temperature variance

Prospect/ Lode	Vein type	δO^{18} (‰)	repeat analyses
Wadi Lode	V_3	16.15	
	V_3	15.33	
	V_1	14.51	
	V_1	15.94	
	V_1	15.29	
	V_1	15.70	
	V_3	16.04	
	V_1	15.83	
	V_1	14.34	14.41
	V_3	14.53	
	V_1	15.96	
	V_3	15.18	15.47
	V_3	16.78	
	V_1	16.47	
	V_1	15.36	
Y Lode	V_1	13.61	
	V_1	14.60	
Vein 18	V_1	14.03	
Marble Bar	V_1	14.08	
	V_5	11.63	10.88
South Gebeit	V_1	14.02	
	V_3	13.91	
Wadi Lode Extension	V_3	14.79	
	V_3	14.19	
Bishops Dam	V_3	14.22	
West Gebeit	V_3-V_5?	17.10	16.93

Standard = (Nat. Bureau Stds) NBS 28 δO^{18} = 9.60‰
All data relative to SMOW (Std Mean Ocean Water)

Table 6.2 Oxygen (δO^{18}) isotope data for Gebeit quartz veins.

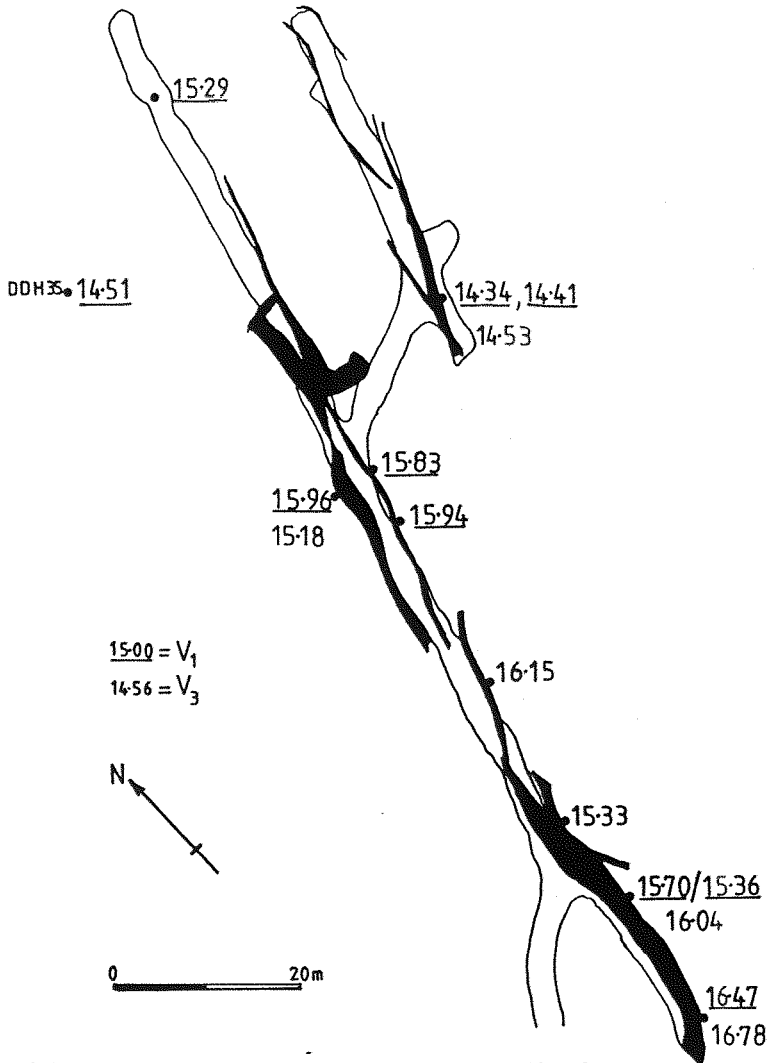

Fig.6.9 Oxygen isotope sample location plan, Wadi Lode 4-level plan (see Fig.5.23).

of 30-40°C. This suggests that there may have been a thermal gradient across the mineralised zone, possibly with fluid flow directed away from the intersections of the larger shear zones (e.g. Wadi Lode and Gebeit shear zones). However, because of the lack of direct fluid inclusion temperature measurements these figures are only a rough estimate of fluid isotope values.

Samples of V_3 and V_4 veins associated with late dextral to sinistral deformation also give similar results of 14.2-14.8‰. Likewise, the white quartz veinlets which transect the Wadi Lode blue quartz veins have almost identical δO^{18} values ($x=15.55$, $\sigma_n=0.71$, $n=9$) with the blue quartz ($x=15.42$, $\sigma_n=0.69$, $n=8$). This implies that the isotopic composition of the fluid remained relatively constant throughout the D_2 to early D_4 strike-slip deformation, unless δO^{18}_{fluid} decreased exactly in step with decreasing temperature which seems unlikely. The V_1, V_3, and V_4 veins are mineralogically, texturally and structurally distinct, ruling out the possibility that all belong to a single phase of deformation, fluid flow, and veining. The range of δO^{18} values for both quartz (14.0-15.6‰) and fluid (2.4-8.7‰) estimates are consistent with published values determined for the many Archaean lode gold deposits, i.e. δO^{18}_{quartz} = +8 to +16, δO^{18}_{fluid} = +2.5 to +10 (Perring et al.,1987; Kerrich,1986b; Roberts,1987; Foster,1988). This range cannot be used to discriminate between a metamorphic (3-20‰) or magmatic (6-12‰) fluid source but the widespread occurrence of low-salinity, CO_2-bearing fluids as observed in the Gebeit area is more typical of metamorphic fluids (Foster,1988).

Two quartz vein samples, however, did have different δO^{18} values: a white quartz vein at West Gebeit interpreted to be V_3 in age and a V_5 vein at the southern end of Marble Bar. The West Gebeit vein has higher δO^{18}_{quartz} values of 16.93-17.10‰, suggesting the influence of lower temperature metamorphic/magmatic fluids. The V_5 vein, related to late-D_4 deformation at Marble Bar, is heterogenous, showing mixed, distinctly lower, δO^{18}_{quartz} values of 10.88-11.63‰. The late tectonic control of this thrust plane-bounded vein indicates the influence of isotopically lighter, meteoric fluids; an increase in temperature relative to the V_1 veins is highly unlikely.

6.11 Thermoluminescence Analysis

Although only quartz veins of V_1 type and age are apparently mineralised in the Gebeit area, not all mineralised V_1 veins are deep

blue in colour and not all dark blue quartz veins are enriched with gold. As neither stable isotope nor fluid inclusion studies can generally be used to differentiate mineralised from non-mineralised samples, the application of other exploration techniques such as electron paramagnetic resonance (EPR; van Moort,1987) and thermoluminescence (TL; Charlet et al.,1987) have been investigated. Though EPR is a quicker and less expensive technique, Gebeit quartz vein samples were analysed by TL under a low-cost, pilot scheme. The objective of sending an initial batch of Gebeit quartz vein samples for analysis was to ascertain whether this technique could be successfully applied as part of an exploration programme in the Gebeit area to differentiate auriferous from non-auriferous veins.

Thermoluminescence is the light emission of minerals, usually quartz, which have been heated to temperatures below incandescence. This technique, pioneered by Charlet and co-workers (Charlet et al., 1987; Charlet,1987), results from the thermal activation of electrons trapped by chemical or physical crystal defects. The plotting of emission intensity (H) against temperature (T) for each sample produces a glow curve which often shows several glow peaks. The variation in distribution and relative intensity (R) of these peaks for samples of the same mineral species, e.g. quartz, can be used to characterise different generations of vein formation. Prof. Charlet and his team at the Faculte Polytechnique De Mons, Belgium, have reported that this technique has been successful in differentiating mineralised from non-mineralised vein quartz at various gold prospects in France and Canada.

From an understanding of the structural relationships of the various vein generations at Gebeit, an initial representative set of ten quartz vein samples was selected to test possible application of TL analysis (Table 6.3). The samples were submitted in random order and the laboratory at Mons was not informed of the economic potential of the respective samples. Preparation techniques are outlined in Appendix A.

All samples were analysed for natural (NTL) and artificial (ATL) thermoluminescence before and after cleaning with HF (15 mins). ATL is produced by irradiation with a Co_{60} source (5 hrs) after photodesexcitation treatment (24 hrs with UV source). Both NTL and ATL are dependent on crystallisation or recrystallisation conditions but NTL is also effected by natural irradiation doses and natural thermal activation or photodesexcitation by sunlight (Charlet et al.,1987).

Sample no.	Sample Description	Au Content
2481	V_1 Blue qtz, Y lode.	high
2482	V_4 White,vert N/S qtz,Wadi L. ext^n	----
2483	V_1 Blue qtz, Y lode.	v.high
2484	V_1 Blue qtz, Wadi lode 4 level	high
2485	V_3 White qtz,Wadi lode ext^n	----
2486	V_5 White/grey qtz, Marble Bar South	low
2487	V_4 White,vert N/S qtz,Wadi L. ext^n	----
2488	V_3 White qtz in blue qtz,Wadi Lode	----
2489	V_3 White qtz, Bishops Dam	----
2490	V_1 Blue/grey qtz,Wadi L. 4 level	v.high

Table 6.3 Description, location, and gold content of Gebeit vein quartz samples analysed by thermoluminescence.

Sample	Vein Type	Sensitivity	T_4 (°C)	I_4 (x10^{-2})	T_5 (°C)	I_5 (x10^{-2})	R_{4-5}
2486	V_5	low	262.8	14.48	342.1	14.66	49.70
2483	V_1	low	262.8	10.10	350	13.92	42.06
2488	V_3	high	262.8	26.43	338.1	26.94	49.52
2485	V_3	mean	266.7	13.96	361.9	19.31	41.96
2481	V_1	mean	270.7	17.61	373.8	18.15	49.24
2484	V_1	mean	274.7	10.87	358	22.52	32.55
2487	V_4	high	262.8	14.07	334.2	21.62	39.43
2489	V_3	low	(290.5)	9.22	350	15.71	36.99
2490	V_1	high (?)	286.8	25.7	350	52.96	32.71
2482	V_4	v.high (?)	(294.5)	821.1	---	---	---

Table 6.4 Summary of the main characteristics of thermoluminescence glow curves for Gebeit quartz samples. The samples are ordered according to glow curve evolutionary trends but show little relationship to mineralisation potential or age. (T=temperature, I=intensity (photon counts), R=relative intensity where $R_{n,\,n+1} = 100.I_n/(I_n+I_{n+1})$).

Although ATL glow curves were modified after HF attack due to the removal of impurities, intrinsic glow curve characteristics remained persistent and all samples were subsequently subjected to standard HF treatment of 15 minutes (Fig.6.10a & b). The peak intensities (H0-H5) and temperatures (T0-T5) of natural and artificial glow curve peaks produced for each of the Gebeit samples are fully tabulated in Appendix E. Analysis of the data by Charlet (1988) indicated that the samples show a progressive decrease of first peak intensity to extinction with concomitant increase in T of the second glow peak (350-400°C). They display the same variation for both NTL and ATL, indicated by a straight line correlation (r^2=0.80) for ATL and NTL intensities of the H5 high temperature glow peaks (Fig.6.10c). The glow curves reveal a continuous evolution from samples 2486,-83,-88 to samples 2484,-87,-89,-90. Samples 2487 and 2488 show higher TL sensitivities, samples 2481,-84,-85 the mean TL sensitivities, and samples 2483,-86,-89 the lower TL sensitivities. For some reason, sample 2490 was not analysed for NTL. From the range of quartz vein-types analysed, only one sample, 2482, showed a significant variation of higher intensity and sensitivity. However, an almost identical V_4 vein sample, 2487, taken very close to 2482, does not show anamalous characteristics, and there is no available evidence to explain this variation. Comparison of sample trends suggested by this technique (Table 6.4) indicates that the glow curve characteristics bear little or no relationship to the mineralisation potential, age or deformation of the quartz samples. Visibly mineralised samples (2481, -83,-84, & -90) should have distinctive glow curves if this is to be a viable technique but, in the present study, the auriferous quartz samples are spread throughout the apparent evolutionary trend. Although the V_1-V_4 quartz veins have been distinguished on a structural, mineralogical and textural basis, all bear very similar TL and oxygen isotope characteristics. Only the volumetrically minor V_5 veins show slight variations.

From the preliminary investigation of the above results it would appear that thermoluminescence analysis does not represent a viable or accurate exploration technique for the Gebeit area. Given the relatively high cost of this technique, field identification of vein types (V_1 to V_5) coupled with assaying would prove to be a more cost effective method of exploration.

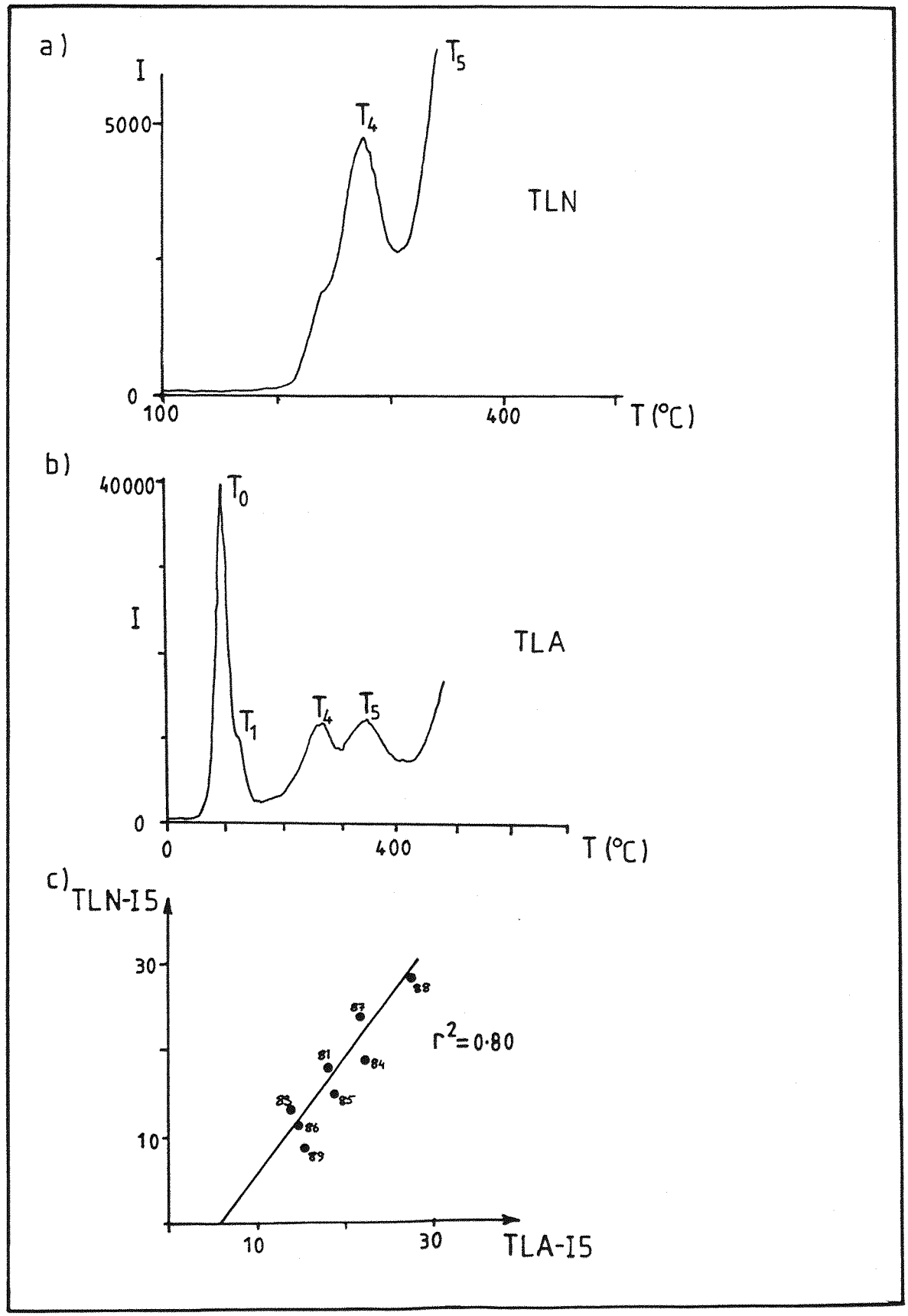

Fig.6.10 Thermoluminescence glow curves for sample 2488 produced during natural (TLN) thermoluminescence and artificial (TLA) thermoluminescence (I, intensity = number of photon counts). Correlation of intensity of glow peak 5 for TLN vs. TLA (c) shows the variation in sample sensitivity from low (-83,-86,-89) to high (-88). All data are tabulated in Appendix E.

6.12 Summary

i) From structural and mineralogical studies six phases of veining have been identified (Fig.6.11); these are designated V_1-V_6, of which phases V_1-V_5 are associated with arc accretion-related deformation episodes D_2-D_4.

ii) Gold-sulphide mineralisation is confined to V_1, north-east-trending, blue quartz veins and occurred synchronously with dextral strike-slip shearing parallel to the Wadi Lode and Wadi Tuwiya Riedel shear zones.

iii) The main sulphide mineralisation tends to be concentrated in the altered wallrock and along entrained wallrock stringers within the veins. The sulphides comprise arsenopyrite, pyrite, and pyrrhotite ±chalcopyrite, ±sphalerite, ±gersdorffite.

iv) Gold occurs as native grains adsorbed onto the surfaces of vein sulphides and as free grains in zones of strained, sulphide-poor quartz, often with calcite.

v) Altered wallrock inclusions consist of tourmaline, sericite, rutile, calcite and apatite.

vi) Fluid inclusions in all quartz phases are generally too small for quantitative thermometric studies but those observed in the V_1 lode veins appear to be CO_2-bearing. Analysis of fluid inclusions from the Wadi Messesana prospect, 5km north-west of Gebeit, revealed CO_2-aqueous inclusions which homogenise at 230-300°C and there is some evidence for immiscibility during trapping. Fluid pressure estimates of 2.0 to 3.9kb (≈7-12km depth) are consistent with evolution at the brittle-ductile transition at greenschist facies grade. Many of the fluid inclusions in the relict V_1 quartz grains have been decrepitated, producing a dark blue colouration within the veins.

vii) Stable oxygen isotope studies of vein quartz indicate that fluid compositions remained fairly constant for most of the accretion-related deformation (estimated at between 2.4 and 8.7‰) and were probably metamorphic in origin. Influx of meteoric fluids is inferred for the V_5 veins during late-tectonic D_4 deformation.

viii) Thermoluminescence analysis of each of the Gebeit quartz vein types did not produce any anomalous glow curve characteristics to differentiate vein types or auriferous from non-auriferous quartz and, hence, is not considered as a viable exploration technique for gold in the Gebeit area.

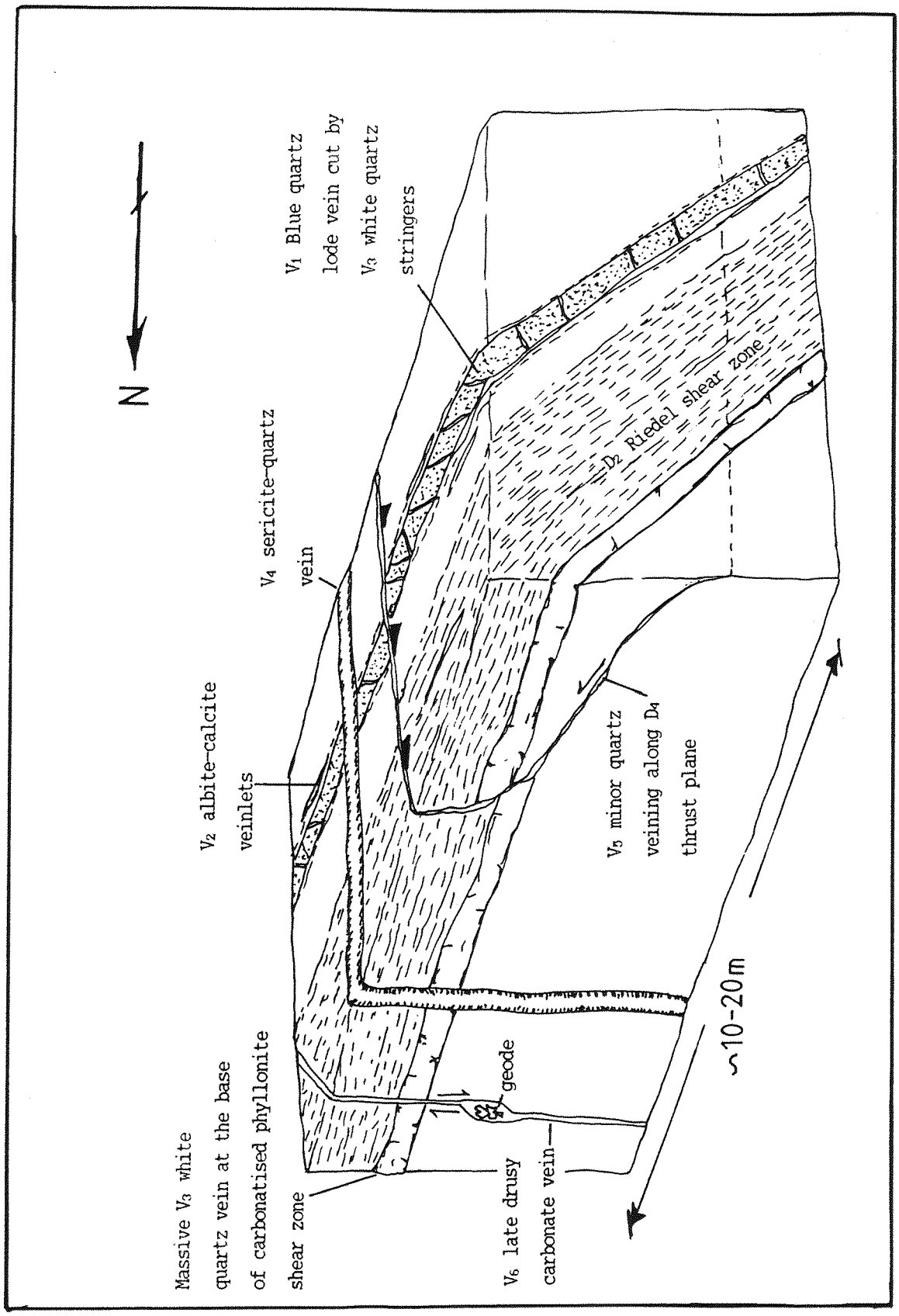

Fig.6.11 Sketch block diagram summarising the structural relationships of the various vein sets identified at Gebeit.

Chapter 7

Mineralisation II: Wallrock Alteration

7.1 Introduction

The majority of auriferous mineralisation at Gebeit occurs within the blue V_1 quartz veins and all mineralised V_1 veins display an altered wallrock envelope. The nature of vein formation and the subsequent deformation of lode veins mean that fluid inclusion studies cannot be applied directly to the Gebeit deposit, and so characterising the degree and types of alteration is important in understanding the nature of the mineralising fluids. This has been achieved using geochemical alteration profiles across the Wadi Lode taken from drill-core, augmented by thin-section and polished section petrography, X-ray diffraction studies, and electron probe micro-analysis of mineral species. Alteration profiles have been augmented by wallrock sampling from the Wadi Lode, Y Lode, and from satellite prospects with variable host lithologies (Marble Bar, Vein 18, Vein 13, and Wadi Messesana).

All V_1 veins at Gebeit are hosted by shear zones of varying width which are composed of chlorite-rich phyllonite (see section 5.5.1). In addition to the wallrock alteration associated with mineralisation, an intense and pervasive carbonate alteration occurs within the major Riedel shear zones, forming the red ridges of the Wadi Lode and Wadi Tuwiya shear zones. This type of alteration, which produces an ankerite-dominated assemblage (ankerite phyllonites), is not observed in the lode alteration profiles and may represent the product of a distinct CO_2-rich fluid phase. This intense alteration has also been characterised geochemically and petrographically in order that it can be compared and contrasted with the mineralisation-related alteration and to determine whether there is a genetic link. Background gold analyses of both altered and unaltered lithologies have been undertaken to assess any influence of syngenetic enrichment and to establish the gold distribution throughout the alteration profiles. Collation of these data, together with the other fluid parameters defined in Chapter 6, permits the formulation of a genetic model for

fluid evolution and mineralisation, as defined in Chapter 8. The controls and nature of the late-Proterozoic gold mineralisation at Gebeit can then be compared with genetic models established for the extensively studied Archaean lode gold deposits.

7.2 Wallrock Alteration

The wallrock alteration haloes observed round the lodes within the mine and in satellite prospects are highly variable. In many cases visible alteration is denoted by large-scale carbonate alteration accompanied by sulphidation and bleaching of the immediate volcanic lithologies from green to tan-brown in colour (see Plate 6.2). The carbonate alteration, however, is not solely localised around the auriferous vein margins but occurs pervasively throughout all the sheared lithologies of the Gebeit Volcanic Group. Although carbonatisation is a good regional exploration guide, it is not uniquely characteristic of economic auriferous mineralisation.

In the weathered lodes, alteration is evident by the occurrence of red-brown hematitic haloes of oxidised sulphides which stain the altered rocks enveloping the V_1 veins and also the D_2 shear zones where V_1 veins are not strongly developed. In addition to the visible alteration patterns, outer zones of cryptic alteration occur which have been determined petrographically and geochemically. The cryptic zones comprise areas of incipient carbonate and chlorite groundmass alteration including partial replacement of hornblende and pyroxene phenocrysts by fibrous actinolite ± chlorite, ± calcite (uralitisation). The cryptic zone is also marked by transitional chlorite compositions indicative of fluid influence far beyond the extent of visible alteration. This zone invariably lies between the bleached, sulphide-rich, visible alteration zones and the unaltered rocks of the Gebeit Volcanic Group which display the established greenschist facies metamorphic assemblage (see section 3.4). Uralitised pyroxene phenocrysts also occur in the incipiently altered volcanics, forming an alteration sub-zone, and the transition from visible to cryptic alteration is here defined by the first appearance of epidote. Within the aphyric and plagioclase-phyric rocks, where very fine grained pyroxene and hornblende are restricted to the groundmass, the subdivisions of alteration are difficult to delineate. Although pervasive sulphidation ± wallrock bleaching are the common signs of alteration, they are not always immediately evident. This

zone forms only a thin inner envelope (<50 cm thick) of the complete alteration profile, the intensity of which decreases gradually over several metres to the appearance of unaltered epidote, hornblende and pyroxene (see Plate 7.1e).

The widths of the visible and cryptic haloes vary considerably, ranging from 30cm to around 10m, and in many cases are controlled by the extent of shear zone fabric development. The limit of sulphidation and bleaching adjacent to relatively thick (20-60 cm) Y Lode veins is largely delineated by phyllonite envelopes which are, in places, less than 15 cm thick (see Plate 5.5f). The generally undeformed, massive volcanics which host these shears tend to display only minor cryptic alteration indicative of how efficiently the hydrothermal fluids have been channellised. The characteristic red-brown sulphidic alteration is much more extensive in the wider, more highly sheared horizons, many metres wide, where quartz stringer zones are often developed. This control of fluid access along deformation fabrics has also been demonstrated in the Wadi Lode where wallrock bleaching is concentrated along second order shears (see section 6.2.1) and also results in the fabric-parallel alignment of wallrock sulphides (see Fig.6.1, section 6.3.2, and Plate 7.1d).

The range of structures and vein mineralogies observed at Gebeit indicate that there has been a protracted deformation-related fluid history, enhancing the possibility of overlapping and overprinting of multiple hydrothermal alteration haloes. As a result, stepped alteration profiles have been augmented by detailed petrography in order to differentiate primary and secondary alteration features. The majority of altered wallrock samples contain varying amounts of fine V_1 and V_2 quartz and albite-calcite veins and stringers. These have been noted and included in the geochemical profiles as, in many cases, the development of the fine stringers proved to be too pervasive to selectively sample altered wallrock devoid of such stringers.

7.3 Wallrock Alteration Profiles

Continuous chip sampling of diamond drill core (NQ size) proved to be the best method of producing an accurate lode alteration profile, and two such profiles have been taken from lode vein intersections of the Wadi Lode where it contains visible gold (DDH 46 & DDH 35; see map sheet 3). Drill-core profiles were taken solely from the Wadi Lode for several reasons, namely:

a) the Wadi Lode lies below the oxidised weathering zone,
b) much of the early drilling of the Y and A lodes had been percussion-type drilling,
c) initial drilling on the lodes in many cases did not provide near perpendicular intersections, and
d) Wadi Lode intersections could be complemented with underground wallrock chip sampling.

The main lode profile, PF I (DDH 46, 89.4-99.9m), provided one of the few perpendicular intersections of the Wadi Lode available at the time of sampling (Fig.7.1). Due to the effects of D_1 folding, the local bedding is intersected at right angles by the V_1 veins. Bedding dips to the north-west, sub-parallel to the core, resulting in a constant host lithology throughout the footwall intersection. As a medium-grained plagioclase-phyric tuff forms the entire section, geochemical variations due to changes in protolith are avoided and altered wallrock tuffs, adjacent to the vein, can be compared directly with the relatively unaltered tuffs at the end of the profile. Although the second lode profile, PF II (DDH 35, 120.1-130.1m), also produced a perpendicular vein intersection, it was drilled towards the south-east (perpendicular to DDH 46), resulting in highly variable hanging-wall host lithologies ranging from fine, laminated andesitic tuffs to graphitic shales (Fig.7.1).

As movement during later deformation events often occurred along vein-wallrock interfaces, it is difficult to estimate how representative these profiles are, even though visible gold is present in both intersections. In some sections of the Wadi Lode (4 Level,W35) V_1 quartz veins up to 1m thick appear to be juxtaposed against incipiently altered coarse andesitic footwall lavas, suggesting that some of the veins may have been tectonically dismembered from their component alteration haloes. Generally, however, overall movement along these zones appears to be of the order of a few metres parallel to the vein margin. Intensely altered wallrocks adjacent to apparently unsheared lode veins were also sampled to act as a control when defining alteration trends.

7.4 Mineralogy of the Wallrock Alteration Profile

Continuous core-sections were taken along both of the profiles to produce average analyses for each sample interval and thus avoid

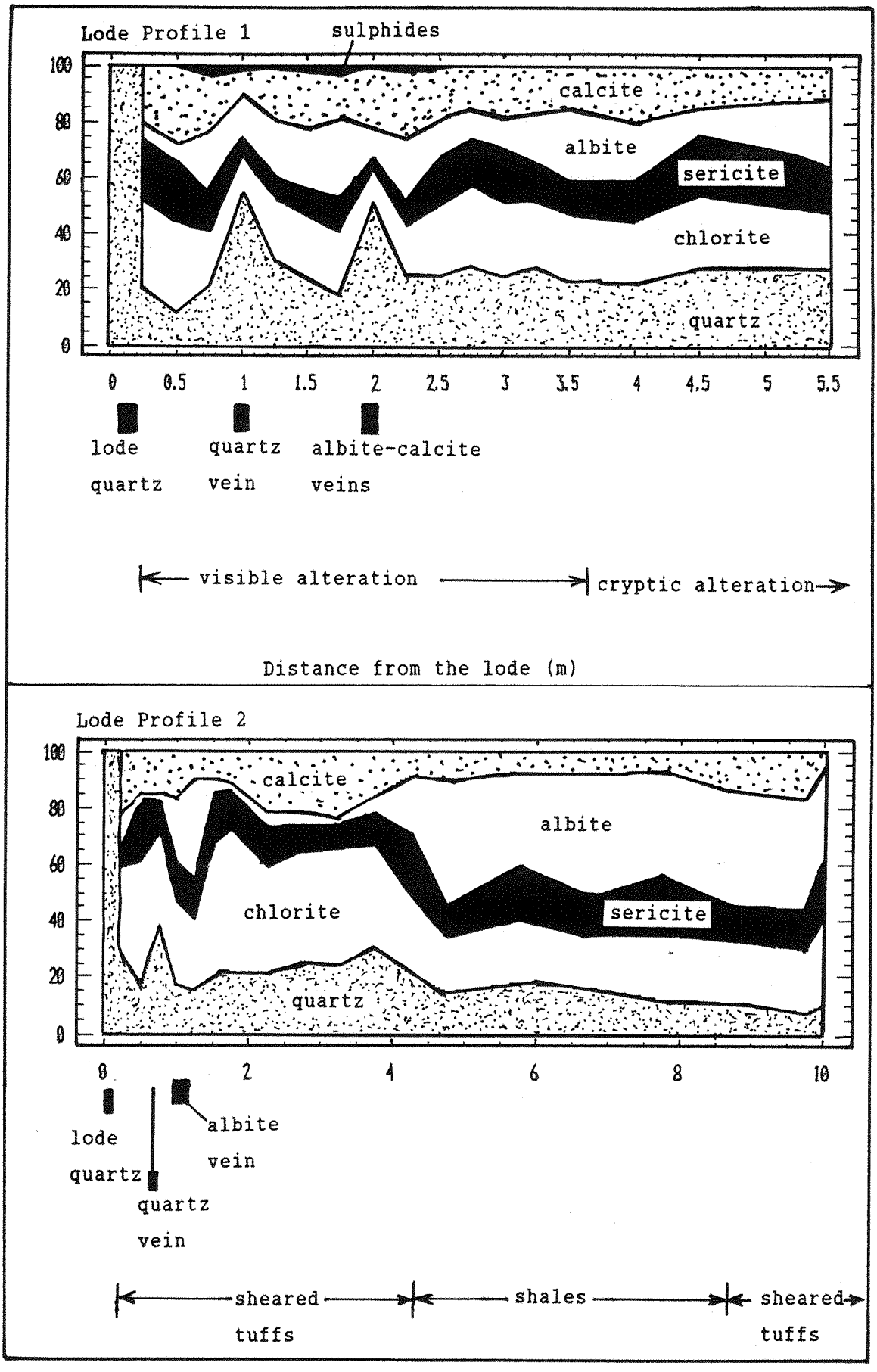

Fig.7.1 Variations in wallrock mineralogy for lode profiles 1 and 2, determined from bulk rock geochemistry and petrography.

spurious sampling errors due to preferential sampling of, for example, veins and sulphide-rich lenses. Sampling was conducted over 25cm intervals for the first 2-3m, increasing initially to 50cm and then to 1m intervals at 5-6m from the lode. Thin and polished thin sections were produced from each sample interval and were augmented by X-ray diffraction analysis to elucidate changes in bulk mineralogy. Homogenous powdered samples were analysed for major and trace element geochemistry using X-ray fluorescence techniques and variations in the chemistry of component minerals were determined by electron micro-probe analysis. All analytical data for the alteration assemblages are tabulated in Appendix F.

7.4.1 Lode Profile 1

The main minerals identified in the visible and inner cryptic alteration haloes are consistent throughout the profile, and the various alteration facies identified are defined by increases and decreases in abundance of some of these phases. All Gebeit Volcanic Group units altered adjacent to V_1 auriferous veins comprise quartz, chlorite, albite, sericite and calcite (Fig.7.1, Plate 7.1) in addition to localised patches of wallrock sulphides (section 6.3.2). The shear zones which host the V_1 veins tend to occur in the tuffaceous units of the lower part of the stratigraphic succession. Mineralisation has been shown to be synchronous with dextral, strike-slip shearing (section 6.2.1) and consequently alteration mineral assemblages tend to be fine-grained. In contrast to the vein-hosted wallrock stringers, no tourmaline has been identified in the alteration haloes. As the mineralised veins tend to be developed in the medium to very fine-grained tuffs, there is no grain size contrast to judge the extent of alteration. Relict plagioclase micro-phenocrysts are generally still evident and relict trachytic textures indicate that only small volume changes have occurred in the wallrock fabric, although the ubiquitous presence of fine extensional veinlets suggests minor overall increases in volume.

Although the component minerals are usually easily distinguished optically, the fine grain size hinders petrographic determination of modal abundances. In order to define the mineralogical changes towards auriferous veins, mineral contents have also been estimated using major element geochemistry. As albite, sericite, calcite, chlorite, and quartz form the alteration assemblage for the entire profile,

Plate 7.1 Petrography and textures of the wallrock alteration from Lode Profile 1.

a-c) Photomicrographs (CN) of the calcite-sericite-quartz-chlorite-albite mineralogy of Lode Profile 1 at 0.25-0.50m, 0.50-0.75m, and 1.5-1.75m from the lode respectively. Note euhedral, prismatic, and acicular arsenopyrite grains aligned sub-parallel. (field of view 4mm).

d) Photomicrograph (CN) of Lode Profile 1 at 2.00-2.25m from the lode showing fibrous quartz pressure shadows around larger arsenopyrite grain and alignment of fine sulphides along foliation (field of view = 3mm).

e) Photomicrograph (CN) of wallrock of Lode Profile 1 showing first appearance of epidote at 4.0m from the lode (field of view=2mm).

f) Altered hornblende-phyric andesitic flow from southern end of the Wadi Lode 4-level showing sub-parallel alignment and fracturing of altered phenocrysts (compare with Plate 3.2f).

CN = crossed Nicols, PPL = plane-polarised light.

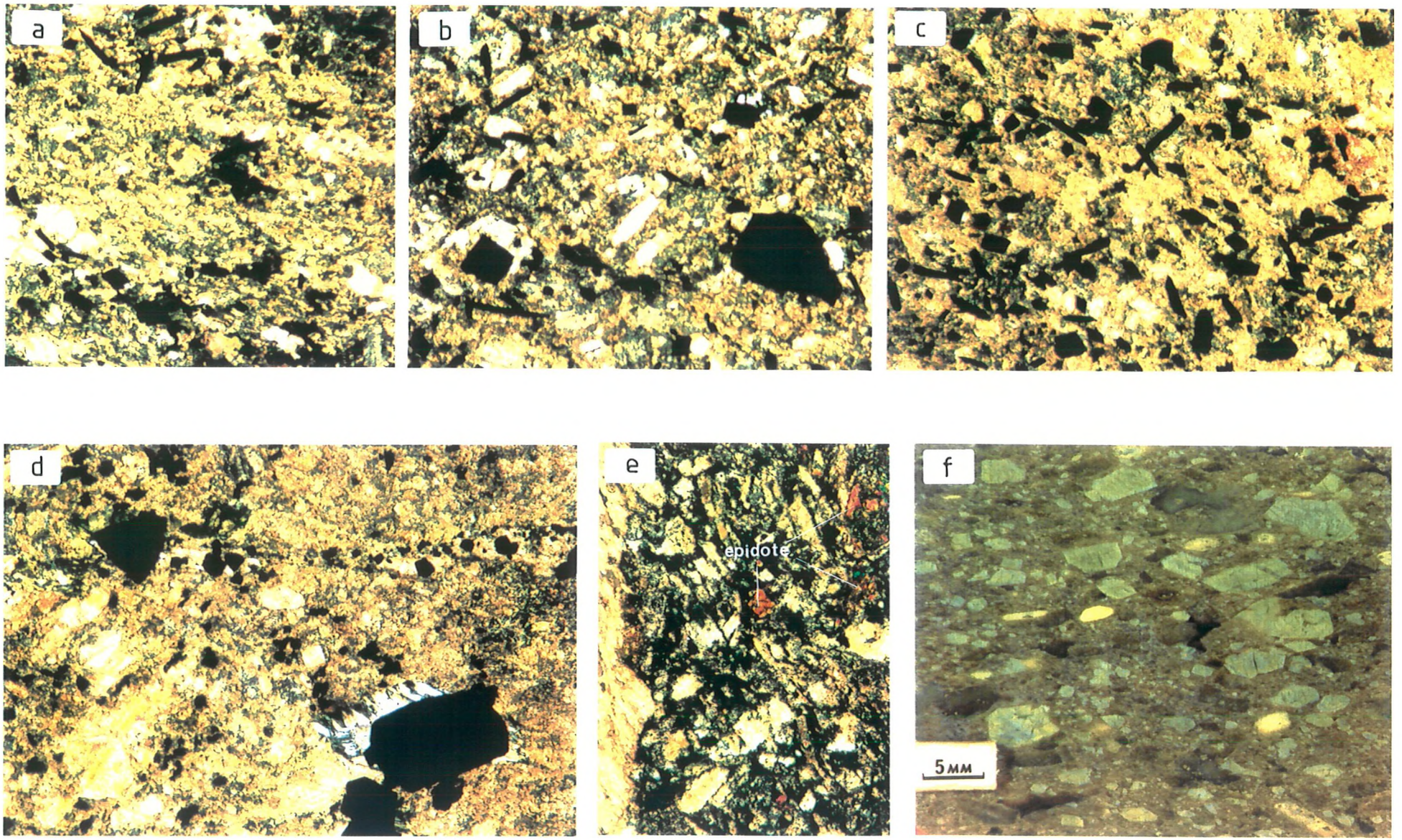
a
b
c
d
e
epidote
f
5мм

variations of modal abundance can be identified by fluctuations in Na_2O, K_2O, CaO, and MgO respectively, with residual SiO_2 determining quartz contents (Fig.7.1; Appendix G). These are produced using average mineral formulae derived from electron micro-probe data which are cross-checked against Al_2O_3 contents. Although all the modal abundances are expressed as wt% (derived from XRF data), the specific gravities of the minerals only vary by 0.34 (albite,2.62-chlorite,2.96) indicating that the maximum error between estimates of wt% and vol% of modal abundance are of the order of ±11%. This method, however, is a bulk rock estimate and does not account for changes in wallrock mineralogy alone; hence it is prone to the effects of micro-veining. From 0cm to 75cm from the vein, wallrock mineralogy is dominated by sericite, chlorite and calcite (Fig.7.2a) due to pervasive, fine-grained, carbonatisation, sericitisation of albite phenocrysts, and chloritisation of all mafic phases (e.g. hornblende and pyroxene). Residual albite comprises 5-8% of the total rock compared to ≈25% for its unaltered counterpart (Fig.7.2b) and indicates significant K^+-Na^+ exchange due to sericitisation. The matrix consists of fine grained (10-50μm) chlorite and sericite, which define the vein-parallel foliation, intergrown with calcite and quartz. Chlorite contents of 32-40% are higher than background values of 25-30%, which are matched by an increase in sericite abundance from 15% up to 25% adjacent to the lode. Combined phyllosilicates (chlorite + sericite) show an increase from background values of 30-35% up to 55% less than 50cm from the vein intersection (Fig.7.2f). This probably reflects increased hydration accompanying deformation towards the centre of the enveloping shear zone, in addition to progressive sericitic alteration. X-ray diffraction analyses were performed on clay fraction separates (<2μm) across the lode but sericite and chlorite were the only phases identified.

Abundant prismatic arsenopyrite grains occur predominantly in the matrix and are enveloped by pressure shadows of coarse, fibrous, chlorite. Calcite contents appear to reach a peak (26%) close to the lode but this is heavily influenced by calcite micro-veining. Calcite values are relatively constant at around 20%; an increase of around 10% above background values. In contrast, although quartz is enriched in the form of stringers and veins, it shows an overall decrease towards the lode from 20-25% to 10-12% (Fig.7.2a).

The main trends of this profile reflect a progressive increase in chlorite, sericite and calcite towards the lode with a concomitant

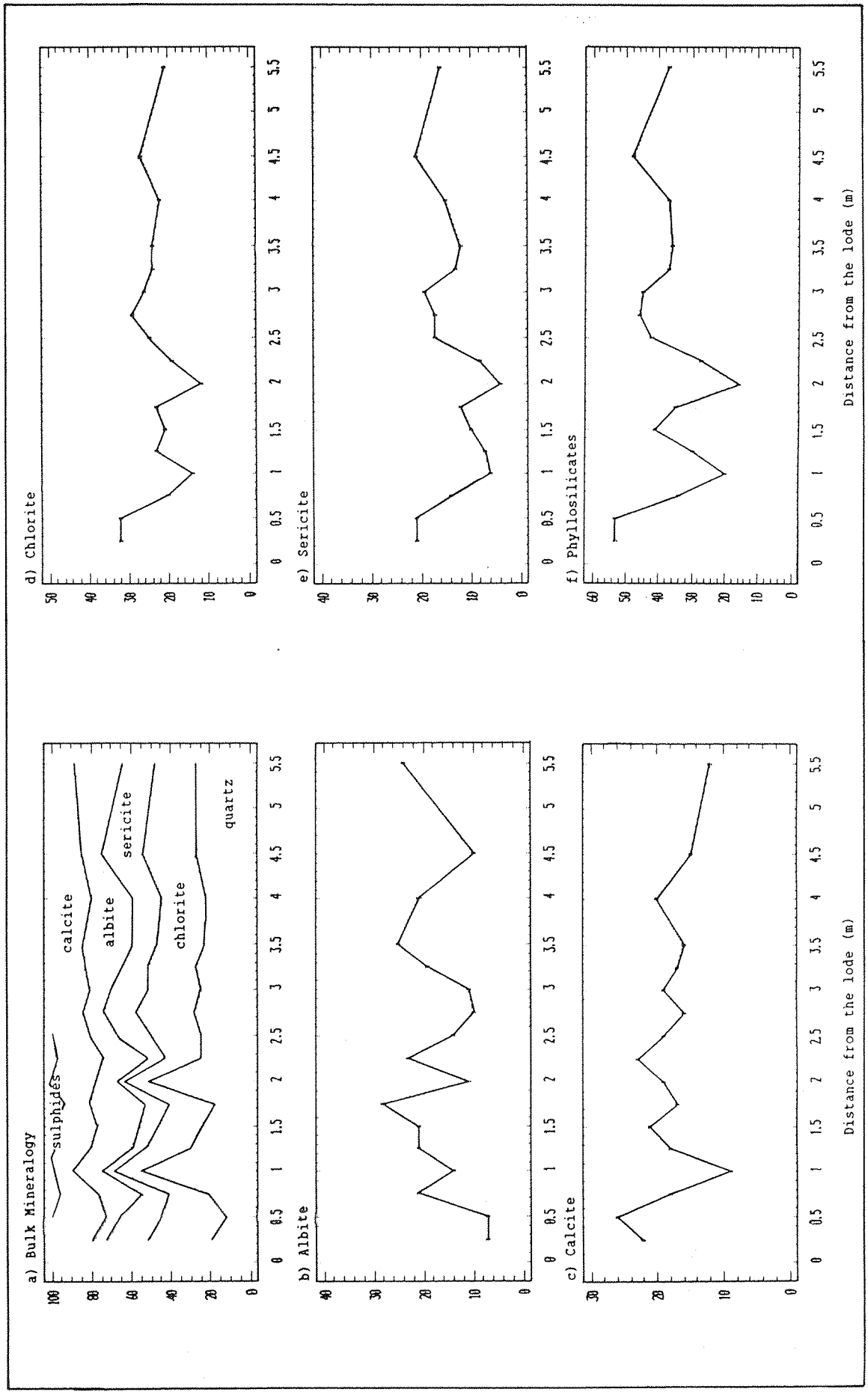

Fig.7.2 Mineralogy of lode profile 1 determined from bulk rock geochemistry, showing the variation in abundance of the component minerals.

decrease in albite and quartz. The transition from background values to abundances adjacent to the lode appears to be gradual and uniform but is interrupted by a zone of quartz (V_1 or V_3) and calcite-albite (V_2) veining at 0.75-2.50m from the lode (Fig.7.2a). In these zones, chlorite and sericite are reduced to 10-15% and 5-6% respectively, especially at the 1 and 2m intervals where quartz veining is extensive. Conversely, albite is enriched close to background levels (20-25%) due to vein albites and partial recrystallisation of groundmass albites to produce clean unsericitised grains. Although total calcite levels do not exceed those close to the lode, calcite alteration of the groundmass around 2m from the lode (Plate.7.1c) is much more pervasive. The rapid change and clear contrast in mineral abundances across these zones compared with the general lode profile trends suggests that the areas of albite-calcite enrichment represent a secondary alteration overprint related to the V_2 calcite-albite veins. Albite enrichment is also characteristic of the pervasive ankeritic alteration of the Riedel shear zones and may be coeval (section 7.7.2).

7.4.2 Wallrock Alteration Mineral Chemistry

Electron probe micro-analyses have been undertaken of the various alteration assemblage mineral phases at Oxford University, supervised by Dr N. Charnley. The aim of this study was to identify phase compositions and define any systematic variation in mineral chemistry across the alteration profile into relatively unaltered volcanics. Micro-probe studies were also carried out on the ankerite and non-carbonate altered (i.e. chlorite) shear zone phyllonites in order to compare and contrast mineral-chemistry variations due to shear deformation, mineralisation, and CO_2-rich alteration, respectively. Because of the fine grain size, profiles could not be taken across individual grains to assess sample homogeneity. All micro-probe data are expressed in the text as mineral formulae and are fully tabulated in Appendix H as component oxides.

7.4.2.1 Chlorite

The chlorites analysed from the lode alteration profile are classified as intermediate in composition between the end-members of clinochlore and chamosite (Mg_5 to Fe_5 Al)$(Si_3Al)O_{10}(OH)_8$ (Table 7.1;

Sample	THS 063	THS 064	THS 065	THS 067	THS 068	THS 069	THS 070	THS 071	THS 073	THS 075	THS 077	THS 079	TH S 081	THS 083
Si	5.820	5.583	5.383	5.482	6.018	5.582	5.587	5.470	5.552	5.410	5.408	5.449	5.382	5.321
Al	2.180	2.417	2.617	2.518	1.982	2.419	2.413	2.530	2.448	2.590	2.592	2.551	2.618	2.679
Al	2.908	2.654	2.482	2.660	3.294	2.619	2.494	2.517	2.977	2.697	2.601	2.509	2.678	2.673
Mg	4.570	5.521	5.689	5.493	4.736	5.798	5.706	5.561	4.700	4.955	5.082	5.809	4.482	4.164
Fe	3.848	3.658	3.804	3.704	2.976	3.367	3.542	3.864	3.720	4.193	4.216	3.620	4.704	5.053
Na	.022	n.a.	.022	n.a.	n.a.	n.a.	.022	.007	.007	.000	.000	.000	.000	.008
Ca	.091	n.a.	.009	n.a.	n.a.	n.a.	.006	.003	.009	.025	.016	.006	.022	.010
Ti	.014	n.a.	.006	.005	.011	.006	.055	.003	.076	.003	.005	.006	.005	.005
Mn	.050	.047	.048	.041	.034	.050	.044	.047	.035	.057	.052	.052	.067	.074
K	.260	n.a.	.025	.037	.564	.106	.090	.009	.092	.012	.009	.010	.013	.019
Cr	n.a.	n.a.	n.a.	n.a.	n.a.	n.a.	n.a.	n.a.	.061	.005	.008	.005	.000	.003
Fe/Fe+Mg	.457	.399	.401	.403	.386	.367	.383	.410	.442	.458	.453	.384	.512	.548
Si	5.990			5.565	5.505	5.415	5.671	5.276	6.453	5.446	5.429	5.585	5.389	5.807
Al	2.010			2.435	2.495	2.585	2.329	2.724	1.547	2.554	2.571	2.415	2.611	2.193
Al	3.100			2.618	2.568	2.579	2.618	2.808	2.917	2.681	2.616	2.618	2.570	3.308
Mg	4.433			5.519	5.734	5.670	5.534	4.854	4.901	4.994	5.091	5.613	4.588	3.451
Fe	3.677			3.672	3.595	3.687	3.594	4.208	3.419	4.158	4.165	3.502	4.764	4.330
Na	n.a.			n.a.	n.a.	n.a.	.007	.015	.000	.008	.007	.021	.000	.015
Ca	.039			n.a.	n.a.	n.a.	.006	.003	.006	.022	.003	.003	.006	.003
Ti	n.a.			.016	.003	.005	.008	.014	.005	.003	.008	.003	.003	.005
Mn	.046			.044	.054	.051	.037	.042	.043	.054	.074	.051	.078	.007
K	.276			.043	.012	.009	.092	.012	.030	.009	.009	.107	.009	.526
Cr	n.a.			n.a.	n.a.	n.a.	n.a.	n.a.	.002	.008	.003	.028	.003	.003
Fe/Fe+Mg	.454			.400	.385	.394	.394	.464	.411	.454	.450	.384	.509	.557
Si						5.596	5.272							
Al						2.404	2.722							
Al						2.377	2.770							
Mg						6.025	4.867							
Fe						3.531	4.494							
Na						.007	.008							
Ca						.003	.003							
Ti						.008	.003							
Mn						.051	.028							
K						.092	.006							
Cr						n.a.	n.a.							
Fe/Fe+Mg						.370	.491							
Si avge.	5.905	5.583	5.383	5.524	5.762	5.531	5.51	5.373	6.003	5.428	5.419	5.517	5.386	5.564
Fe/Fe+Mg avge.	.456	.399	.401	.402	.386	.377	.423	.437	.427	.456	.452	.384	.511	.553

Table 7.1 Composition of chlorite grains determined by electron micro-probe analysis along lode alteration profile 1. Structural formulae are based on chlorite formula of $(Mg,Al,Fe)_{12}[(Si,Al)_8O_{20}](OH)_{16}$ (Deer et al.,1966).

Bayliss, 1975) equivalent to ripidolite-pycnochlorite under the old classification (Fig.7.3; Hey,1954). The relatively unaltered epidote-bearing samples, more representative of the regional metamorphic chlorites, display higher octahedral Fe/(Fe+Mg) values of 0.45-0.55 compared to 0.37-0.45 close to the lode. When plotted in sequence along the profile to the inner edge of the cryptic alteration zone (4-5m from the lode) the variation does not appear to be systematic (Fig.7.4a); however, composition plots up to 8m from the lode (Fig. 7.4c) suggest an overall linear decrease in Fe:Mg ratios towards the lode (i.e. a decrease in Fe and an increase in Mg; Table 7.1). This shows that mineralisation-related changes in mineral chemistry extend beyond the limits of visible alteration into the apparently unaltered volcanics. Close to the lode, the lowest Fe values correspond to maxima in arsenic and total sulphides, suggesting the removal of Fe from chlorite and incorporation in wallrock iron sulphides due to reaction with H_2S in the ore fluid.

Silicon contents of chlorite are also variable and mirror the K_2O, sericite and chlorite lode variation patterns (Fig.7.5a). The corresponding drop in tetrahedral aluminium correlates (Fig.7.5b) with K_2O maxima and may be due to incorporation of tetrahedral aluminium into sericite within K-metasomatised zones. The decreases in tetrahedral aluminium are matched by increases in octahedral aluminium with a corresponding drop in total octahedral Fe+Mg (Figs. 7.4c,d). The variance in tetrahedral aluminium may, however, be due to temperature fluctuation across the profile. A solid solution chlorite geothermometer (Cathelineau & Nieva, 1985; Fig 7.6) indicates that lower tetrahedral aluminium and higher octahedral vacancy ($6-Al_{VI}-(Mg+Fe)$) represent lower fluid temperatures. Qualitative application of these criteria to the Gebeit data suggests that the chlorites associated with auriferous mineralisation may have been precipitated at lower fluid temperatures than the greenschist facies metamorphic assemblage. Chlorite potassium contents are generally low but peak at 2% adjacent to the lode and at 1.5m in sympathy with the near-lode K_2O maxima (Fig.7.5e).

Chlorites analysed from bleached and sulphidised footwall tuff samples from the Wadi Lode (4 Level,W36) have unusually high Fe values 0.47-0.55 (Fig.7.3) and variable potassium contents (0.02-0.7%). This suggests that, although reduced Fe values generally occur adjacent to the lode, iron in Fe-sulphides is not always derived by the breakdown of wallrock chlorites.

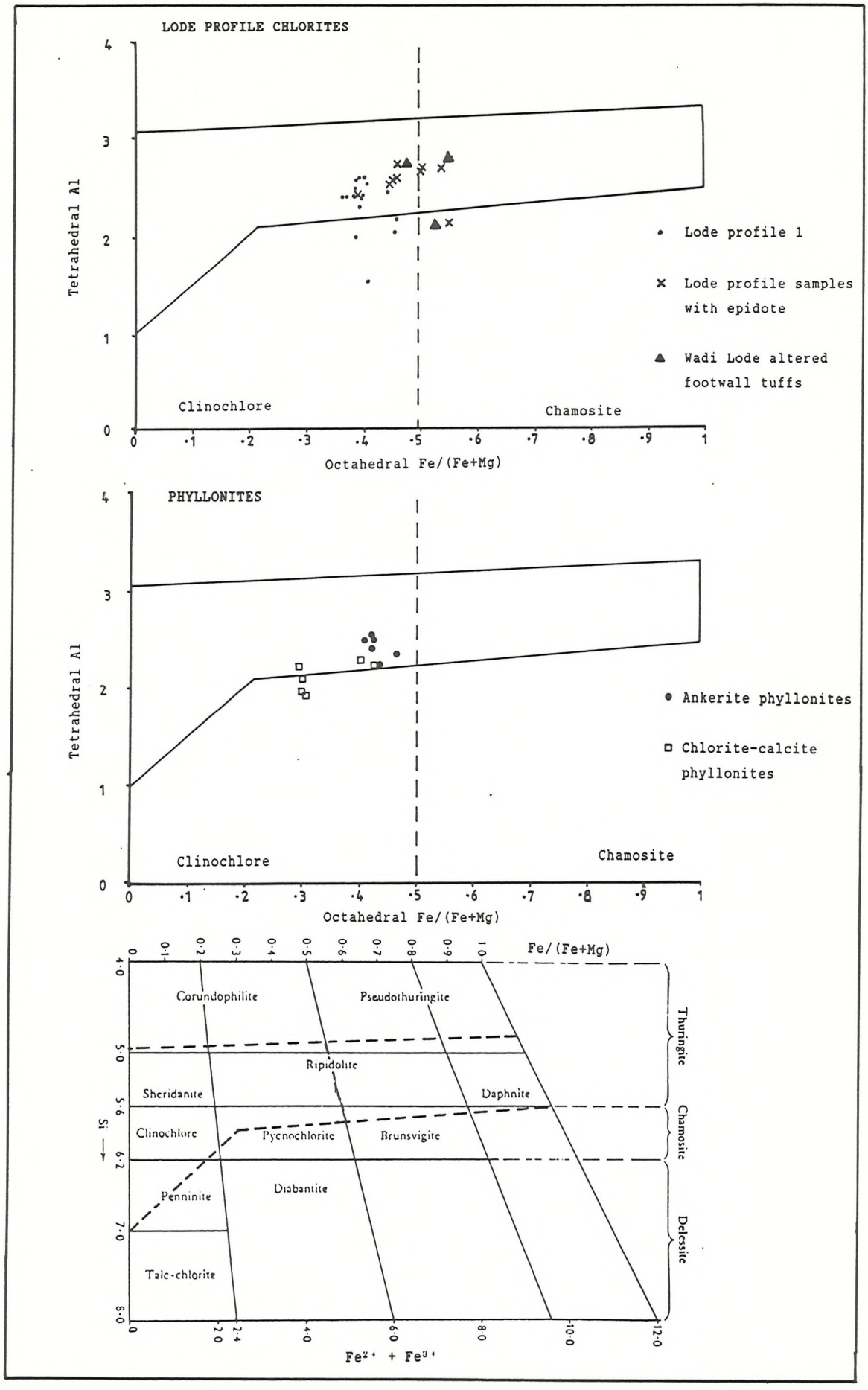

Fig.7.3 Comparison of chlorite compositions for all alteration assemblages (a,b; after Curtis et al.,1985) determined by electron micro-probe analysis. Relationships of fields are shown in comparison to chlorite classification (c) of Hey (1954).

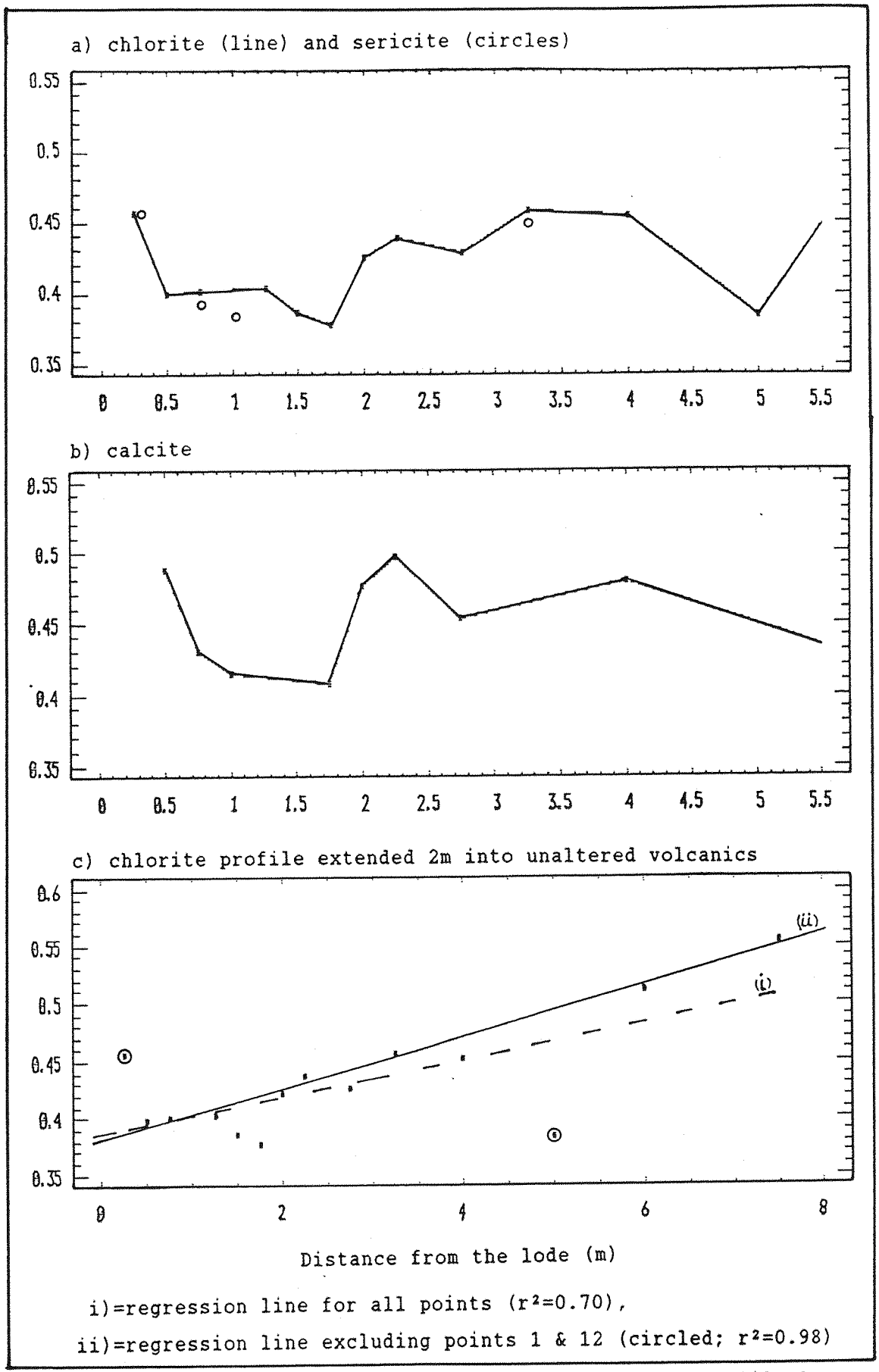

Fig.7.4 Variation in Fe/Mg ratio (Fe/Fe+Mg) along Lode Profile 1
a) chlorite (line) and sericite (circles) b) calcite
c) chlorite profile extended 2m into unaltered volcanics showing progressive decrease in Fe towards lode.

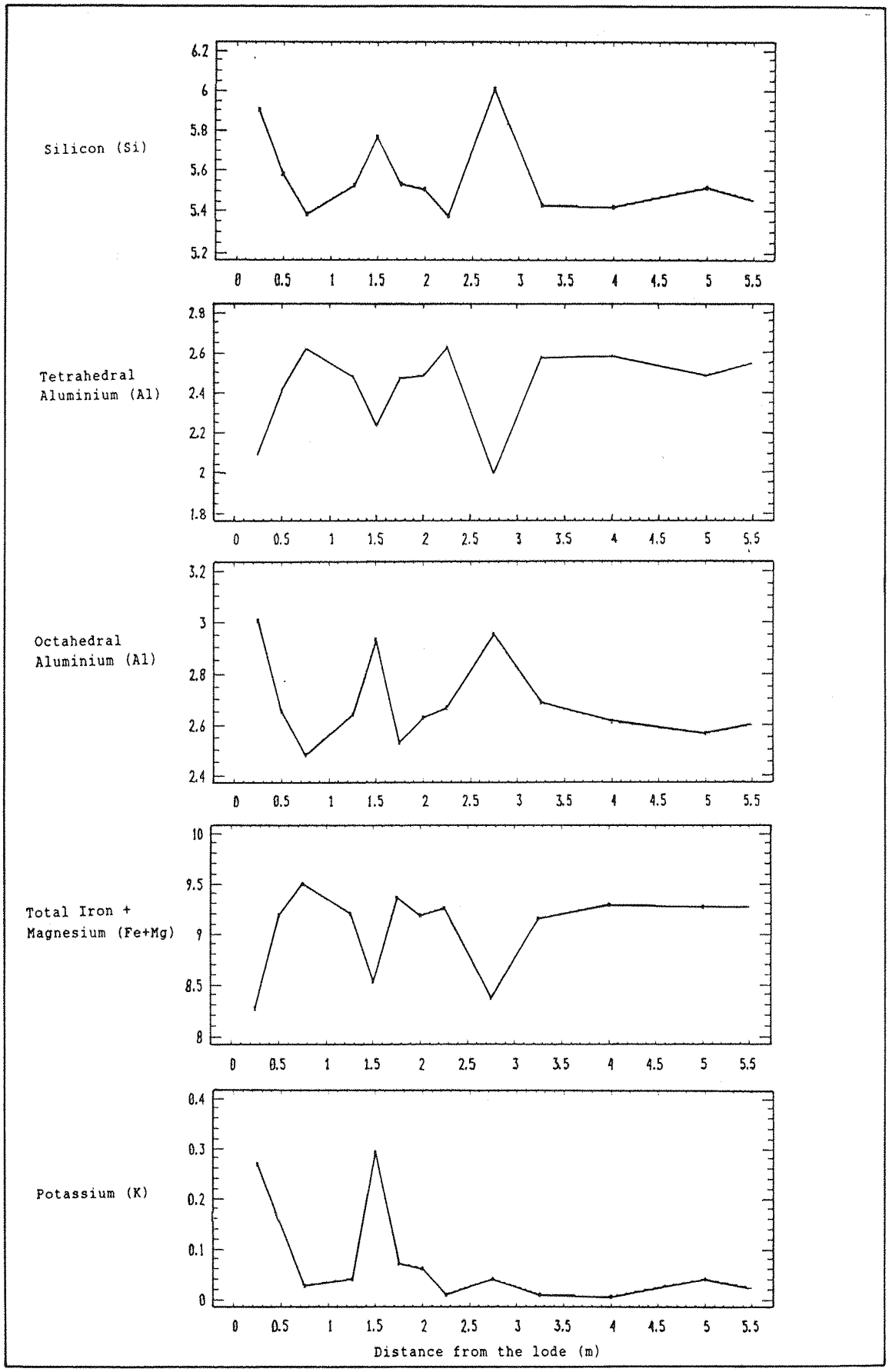

Fig.7.5 Variation in chlorite composition along Lode Profile 1 based on structural formula $(Mg,Al,Fe)_{12}[(Si,Al)_8O_{20}](OH)_{16}$

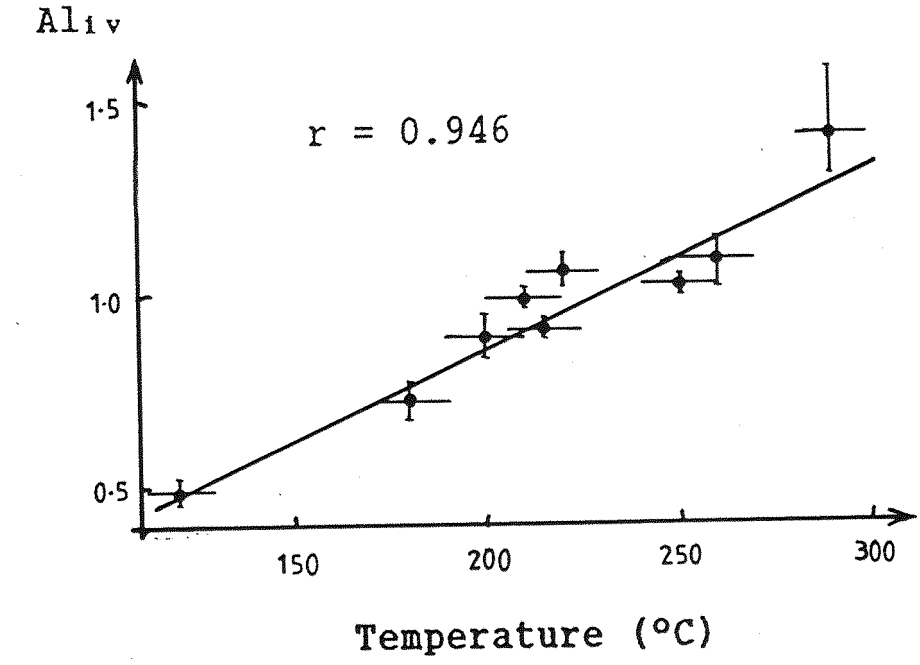

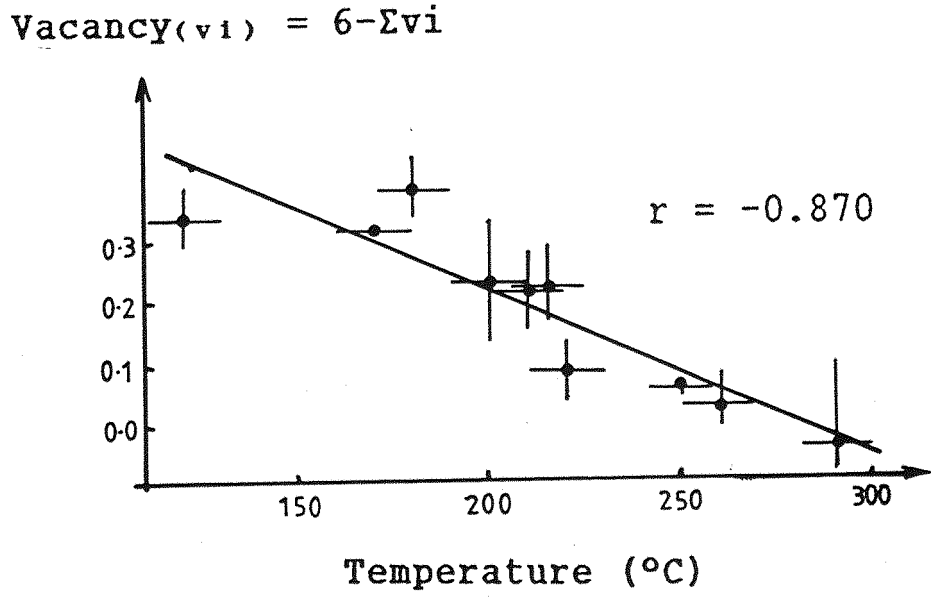

Fig.7.6 Plots showing the general correlation of tetrahedral aluminium (a) and octahedral vacancy (b) in hydrothermal chlorites with temperature (after Cathelineau and Nieva,1985).

7.4.2.2 Sericite

The white mica of the alteration assemblage tends to be fine-grained, is usually associated with altered plagioclase, and is therefore termed sericite. The sericite grains of the alteration assemblage tend to be much more fine-grained than the chlorite and proved to be difficult to analyse accurately; consequently not enough analyses were obtained to define a good variation profile (Table 7.2). The grains <25cm from the lode, however, appear to have high Fe and Mg contents (up to 7% FeO and 5% MgO) and relatively low K_2O at 3-4%. The Fe/(Fe+Mg) ratios vary between 0.37 and 0.46 and all fall on or close to the corresponding chlorite Fe/(Fe+Mg) curve (Fig.7.4a). The kinetics and thermodynamics of Fe and Mg uptake by chlorite, sericite and calcite have not been assessed and it is not known whether the parallel Fe-Mg trends shown by the various minerals indicate coeval formation and equilibrium. The combined iron and magnesium contents of sericite decrease away from the lode, ranging from 10% at 1m to 6.5% at 3.5m, coupled with a concomitant rise in K_2O. These micas, however, are too high in Al_2O_3 (27-31%) to be classified as true phengite, phlogopite or biotite (19%, 17%, and 20% Al_2O_3 respectively) and contain too much iron and magnesium to be considered as phengitic (Fe-Mg-bearing) sericites.

The above analyses conform to the muscovite structural formula but decreases in K_2O, with a corresponding increase in FeO and MgO, produce a charge imbalance which cannot be accounted for by lower Al_2O_3 values. The high Fe-Mg contents, therefore, must be due to analytical error as a result of the very fine intergrowth of chlorite and sericite which probably occurs on a scale finer than the analytical beam width (2μm). The SiO_2 and Al_2O_3 totals are variable (41-49% and 27-31% respectively) and would tend to be lower for a chlorite-sericite mix than for pure sericite. All analyses produced fairly consistent compositions, indicating the regularity of the intergrowth and this may explain the anomalous K_2O contents in the chlorite probe data. The intricately intergrown nature of the chlorite and sericite (±calcite ±albite) phases probably accounts, in part, for the wallrock bleaching effect. There is no evidence in any of the samples from Wadi Lode alteration haloes that chlorite has been altered to ferroan dolomite. The apparent decrease of Fe-Mg in sericite away from the lode suggests that the degree of chlorite-sericite intergrowth decreases and/or grain size increases in the more distal zones of the alteration halo.

Sample	TMS 063	TMS 065	TMS 066	TMS 075
Si	6.410	6.223	6.947	6.584
Al	1.590	1.777	1.053	1.416
Al	2.798	3.160	3.357	2.990
Ti	.019	.019	n.a.	n.a.
Fe	.805	.646	.322	.428
Mg	1.002	1.040	.552	.535
Mn	.008	.016	.003	.006
Ca	.263	.006	n.a.	.011
Na	.199	.041	.081	.035
K	.763	.765	1.150	1.130
Fe/Fe+Mg	.445	.383	.368	.444
Si	6.242			
Al	1.758			
Al	3.068			
Ti	.021			
Fe	.826			
Mg	.988			
Mn	.013			
Ca	.011			
Na	.026			
K	.767			
Fe/Fe+Mg	.456			

Table 7.2 Structural formulae of sericite grains determined by electron micro-probe analysis along lode alteration profile 1. Formulae are based on sericite formula $K_2Al_4[Si_6Al_2O_{20}](OH)_4$ (Deer et al.,1966).

Sample	TMS 064	TMS 065	TMS 071	TMS 079	TMS 083
Si	12.161	11.884	11.667	11.889	11.839
Al	3.842	4.119	4.316	4.148	4.128
Fe	.054	.012	n.a.	n.a.	n.a.
Mg	.014	.025	n.a.	n.a.	n.a.
Na	3.605	3.881	3.862	3.826	3.786
Ca	.008	.038	.182	.078	.194
K	.026	.062	.159	.016	.083
Si	12.004	11.893			
Al	4.057	4.083			
Fe	.013	.021			
Mg	.005	.025			
Na	3.635	3.689			
Ca	.057	.045			
K	.019	.069			
Si	11.995				
Al	4.021				
Fe	.016				
Mg	n.a.				
Na	3.753				
Ca	.035				
K	.097				
Si	11.938				
Al	4.124				
Fe	n.a.				
Mg	n.a.				
Na	3.732				
Ca	.027				
K	.090				

Table 7.4 Composition of albite determined by electron micro-probe analyses along lode alteration profile 1 based on albite formula $3Na[AlSi_3O_8]$ (Deer et al.,1966).

Sample	TMS 064	TMS 065	TMS 066	TMS 069	TMS 070	TMS 071	TMS 073	TMS 075	TMS 077	TMS 081
Mg	.0065	.0311	.0120	.0097	.0085	.0092	.0557	.0039	.0119	.0024
Fe	.0061	.0245	.0085	.0067	.0070	.0090	.0460	.0000	.0109	.0017
Mn	.0152	.0153	.0125	.0121	.0143	.0159	.0168	.0105	.0180	.0073
Ca	1.9669	1.9289	1.9670	1.9682	1.9702	1.9657	1.8813	1.9856	1.9591	1.9885
Fe/Fe+Mg	.4870	.4010	.4140	.4070	.4530	.4950	.4520		.4780	.4190
Mg		.0273			.0071					
Fe		.0224			.0070					
Mn		.0163			.0107					
Ca		1.9339			1.9751					
Fe/Fe+Mg		.4410			.4980					
Mg		.0082							Mg avge.	.0149
Fe		.0060							Fe avge.	.0120
Mn		.0146							Mn avge.	.0138
Ca		1.9711							Ca avge.	1.9586
Fe/Fe+Mg		.4500							Fe/Fe+Mg	.4496

Table 7.3 Carbonate compositions determined by electron micro-probe analyses along lode alteration profile 1 based on calcite formula $Ca_2(CO_3)_2$ (Deer et al.,1966).

7.4.2.3 Calcite

All the carbonate phases analysed within the lode profile are calcitic in composition with slight geochemical differences between vein and groundmass carbonates (Table 7.3). Iron, magnesium and manganese contents are generally low but are sufficient in most cases to cause a shift in the main {104} X-ray diffraction peak from 29.43 to 29.55 towards manganoan calcite (30.30), ankerite (30.84) and dolomite (30.99). Manganese levels remain fairly constant at 0.5-0.9% MnO in the wallrock calcite and <0.3% MnO in vein calcites. Iron and magnesium abundances vary more widely from 0.09-0.55% in the veins up to 1.1% MgO and 1.6% FeO in groundmass calcite. Although there are not enough analyses to produce a complete profile, the overall carbonate Fe/(Fe+Mg) values mirror the chlorite Fe-Mg trends (Fig.7.4b) but there is no consistent increase in Mg or decrease in Fe. These Fe/(Fe+Mg) ratios, however, are slightly higher than the chlorite and sericite values (+5%) but show the same parallel variations. Like sericite, this may suggest that the groundmass carbonates were coeval with the chlorite and sericite phases during alteration as calcite does not appear to replace them.

7.4.2.4 Albite

Most of the probe analyses of plagioclase feldspars were taken from phenocrysts (Table 7.4) as groundmass feldspars are too small to permit fully quantitative analysis. Only a limited number of analyses were undertaken in order to define the feldspar mineralogy which is consistently albitic in composition (An_1-An_7). There are no apparent major variations throughout the lode profile; however, the lowest Al_2O_3 and highest SiO_2 abundances occurred in albite adjacent to the lode with the converse in the central zone of recrystallised secondary albite. This may be due to relative excess and depletion of Al_2O_3 in albite in the respective zones of sericite destruction and formation, because of the demand for immobile Al by the more aluminous sericite.

7.4.3 Lode Profile 2

Although the wallrocks of the second lode profile are more variable in lithotype and are more highly sheared, the basic mineralogy is very similar to the first lode profile i.e. quartz, calcite, albite,

chlorite and sericite (Fig.7.7). Albite is similarly depleted to 2-3 vol% close to the lode and in the highly sheared tuffs at 1.75-3.5m. Albite contents peak significantly in two zones: at the intersection of an albitic V_3 vein at 1.25m, and at 4.0-8.5m where graphitic shales are the dominant lithology (Fig.7.7b). The very fine grained nature of the shales, coupled with the dark graphitic matrix, makes petrographic investigation very difficult but X-ray diffraction studies indicate that the same alteration assemblage occurs. In the shale zone, calcite is reduced to 8-10% and chlorite to 20% but, like albite, sericite is enriched to values similar to those adjacent to the lode (15-20%; Fig.7.7c). Calcite shows an overall increase towards the lode but is particularly enhanced (23-25%) between 2 and 3.5m in the tuffaceous phyllonites. X-ray diffraction analysis of the lode profile demonstrated that the carbonate phases, within detection limits (i.e.>4-5%), were all calcitic.

As with the first profile, chlorite is also enhanced to comprise up to 50% of the total bulk rock at the lode intersection, compared with a background level of 20-25% (Fig.7.7d). Quartz, however, shows a progressive increase from the albite-dominated shale zone towards the lode due to the presence of fine quartz stringers developed in the phyllonites (Fig.7.7a). Variation in total phyllosilicate contents is somewhat obscured by the higher sericite and lower chlorite levels in the shales but there appears to be an overall increase (Fig.7.7a) in phyllosilicate from 50% to 60% of the bulk rock content with decreasing distance from the lode.

The general trends in the alteration assemblage observed in profile 1, with increasing chlorite, calcite and sericite coupled with a drop in albite towards the lode, also occur in profile 2. Where exposed underground, the shales rarely display large-scale veining due to their comparative plasticity during deformation. Although the degree of alteration within the shales is hard to quantify, the higher albite and sericite contents compared with shales sampled away from the lodes (see Table 3.4) appear to represent normal background abundances. The apparently marked transition in intensity of alteration within the shales suggest that the shales may have been less permeable to hydrothermal fluids during deformation and mineralisation. Both profiles show quartz contents to be highly variable but, in general, quartz is depleted towards the lode except in the more highly sheared zone adjacent to the lode veins where stringer zones are developed. Native gold is visible in the blue-white quartz lode where it is

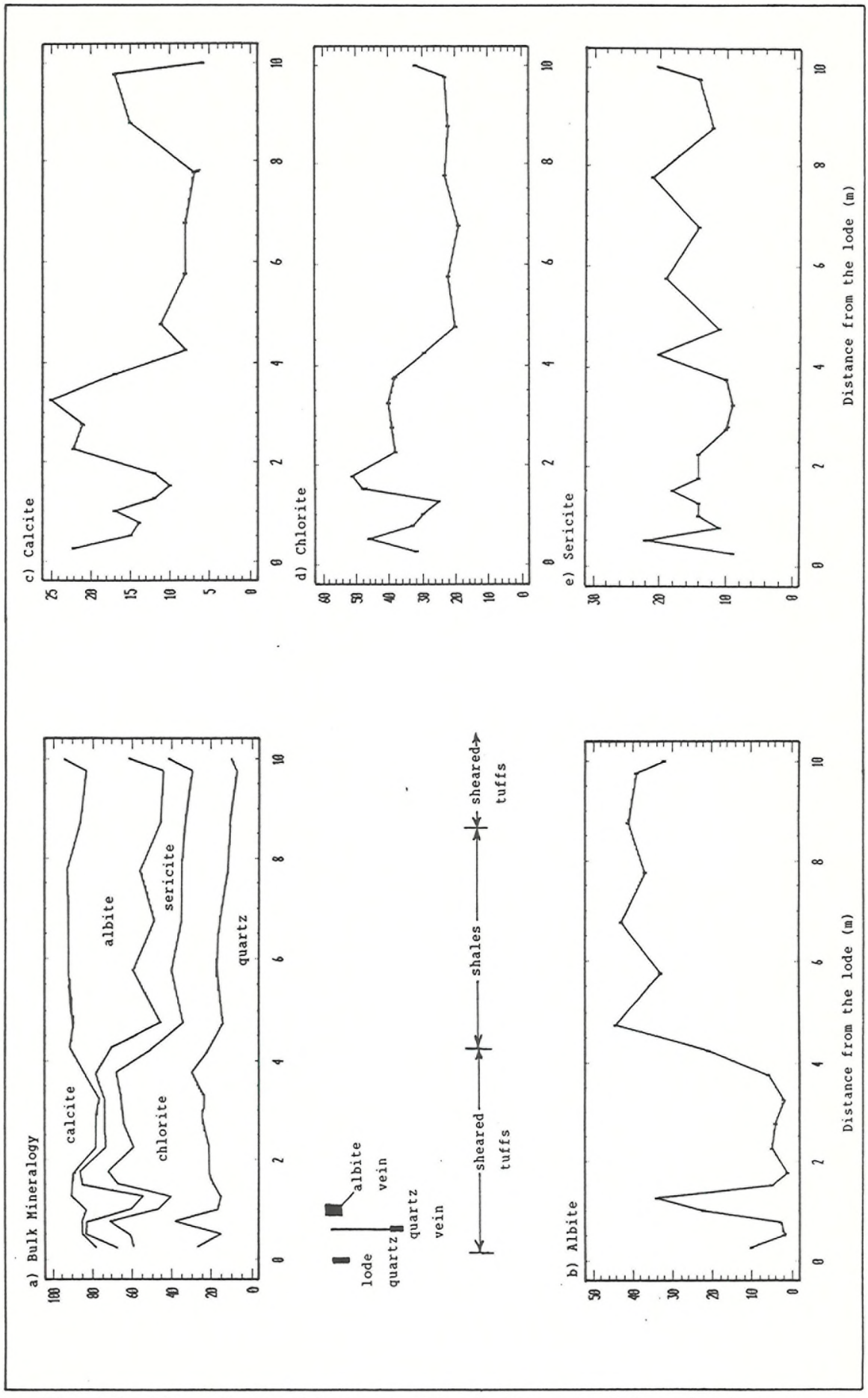

Fig.7.7 Mineralogy of lode profile 2 determined from bulk rock geochemistry, showing the variation in abundance of the component minerals.

concentrated along carbonaceous partings and on the vein margins, but it has not been identified in wallrock alteration assemblages.

7.4.4 Altered Wallrock Chip Samples

In addition to the lode drill-core profiles, several hand specimens of altered footwall and hanging-wall volcanics were taken for comparison with the profile core material. The coarse lavas and agglomerates of the upper part of the Gebeite Volcanic Group rarely host auriferous veins but a unit of hydrothermally altered hornblende- and clinopyroxene-phyric andesitic lava occurs in contact with the lode at the southern end of the Wadi Lode (4 Level). Initially this lithotype appears very different from its unaltered counterpart as the phenocrysts, although still evident, are pseudomorphed by buff to grey-green, fine-grained, chlorite, together with sericite and calcite (Plate 7.1f). The elongate phenocrysts are orientated parallel to the foliation and are often fragmented by high-angle, en echelon tension fractures (see Plate 5.3e) which are infilled by more coarse-grained chlorite and sericite. In addition, the groundmass is altered to a grey-brown colour in contrast to the original dark green matrix. The phenocrysts are harder to distinguish in the more highly sheared lavas but euhedral crystal shapes can be differentiated on foliation surfaces. This unit has been logged previously as a green lapilli tuff (Robertson Research, 1983) and this has hindered stratigraphic correlation between drillholes.

Albite, occurring in the groundmass and as phenocrysts, is strongly sericitised reducing the total plagioclase contents to 3-7%. Chlorite is enhanced (30-35%) due to the breakdown of all other ferromagnesian phases and calcite varies widely from 15 to 30%. The presence of 15-20% sericite (i.e. ≈2wt% K_2O) indicates a significant addition of K_2O as the unaltered hornblende lavas generally contain less than 0.3wt% K_2O. These mineralogical changes mirror the alteration assemblage of the lode profiles and similarly exhibit variable quartz abundances due to fine veining.

Compared to the andesite lavas, four samples of altered aphanitic tuffs adjacent to the Wadi Lode show very different trends (see Appendix G) with low chlorite (14-25%), variable calcite (8-23%) and sericite (4-21%), and high albite (27-37%) abundances. The most intensely sulphidised (3-4% sulphides) and bleached sample (TMS 144) has the lowest sericite (4%), the highest calcite contents (23%) and

background levels of albite (27%). A small peak at 30.9 on X-ray diffraction traces suggests that small amounts (3-4%) of ankerite may be present. However, no ferroan dolomite was identified by electron micro-probe analysis. The intense wallrock bleaching appears to be due to the predominance of carbonate over chlorite but the lack of Fe-Mg carbonates suggests that chlorite is not replaced. All the tuffaceous samples are too fine grained to determine a mineral paragenesis but the mineralogy conforms to the secondary albite-carbonate alteration seen in lode profile 1. Those samples (TMS 135,142,and 143) with the highest albite abundances (31-37%) have below-background levels of calcite (8-11%) and represent either weakly altered lithologies or are lithotypes which have been selectively albitised.

In addition to samples from the Wadi Lode, samples of altered wallrock were taken from the Y Lode when accessible during the first field season. Most of the samples (Appendix G) have the same mineral abundances as the Wadi Lode i.e. high chlorite and sericite, low albite and variable calcite and quartz. At some locations, however, (e.g. Y lode adit, raise 9) there are zones of intense shearing and alteration along the vein-wall rock footwall interface which are not observed in the Wadi Lode. These zones, up to 15cm thick, comprise fine-grained calcite and chlorite with rare clasts (2-8mm long) of brecciated vein quartz. Using major element geochemistry (Appendix F) to augment X-ray diffraction mineral analysis, chlorite appears to form 20-25vol% and calcite 30-40vol% of the rock, but very low K_2O and Na_2O levels (<0.2wt% each) indicate that very little sericite or albite is present. Alumina values, however, remain high (14-17%) and are accommodated by significant amounts (30-40%) of pyrophyllite ($Al_4Si_8O_{20}(OH)_4$), identified by XRD, which has extensively replaced plagioclase. The highly friable nature of this material makes petrographic studies difficult but more cohesive samples show pervasive late-stage calcite veins, 2-5mm wide, cross-cutting the foliation at high angles. The inclusion of brecciated vein fragments and the anomalous mineralogy suggest that this secondary alteration accompanied later tectonic reactivation of the vein margins and overprinted the wallrock alteration produced during the earlier mineralisation.

7.5 Lode Profile Geochemistry

All lode profile samples were analysed for major and trace elements using X-ray fluorescence techniques to identify minor as well as major element variations and to define anomalous levels of potential pathfinder elements that may aid future exploration. Although absolute major element abundances are a good guide to variations in mineralogy, volume-changes due to deformation and wallrock alteration make estimation of major and trace element mobility difficult to determine. This has been overcome using isocon diagrams.

7.5.1 Isocon Diagrams

The composition and volume relationships of metasomatic alteration were initially defined by Gresens (1967) using equations and graphs to calculate element gains and losses from chemical analyses and specific gravities of altered and unaltered rocks. This method has been simplified into a linear relationship between concentrations of components in unaltered and altered samples, termed the isocon diagram (Grant,1986). Graphically, an isocon is defined by a straight line through the origin which joins components which show no relative gains or losses (Fig.7.8a-d). The slope of the isocon determines the mass change in the alteration, and gains or losses of components can be identified by the deviation of data points from the isocon.

Isocon diagrams have been drawn for each of the Gebeit alteration profile samples in order to quantify element mobility throughout the alteration sequence. One assumption, however, has to be made in order to contruct an isocon; either a specific volume change has to be estimated or an element/group of elements must be considered to be immobile. Because of the abundant, fine-grained alteration observed in many of the Gebeit samples and the often pervasive fine microveining in alteration haloes, volume changes are likely and cannot be estimated visually. Initial plots of altered vs unaltered samples for lode profile 1 (Fig.7.8) constantly produced a large set of elements on a linear trend which defined an isocon of which Al was always a member. In addition, the Al_2O_3/Zr ratio, which was determined across the complete range of altered and unaltered lithologies, remained relatively constant at 0.29-0.33. From numerous studies of Archaean lode gold deposits (e.g. Phillips, 1985; Kerrich, 1986a), aluminium has usually been shown to be immobile even under conditions of extreme

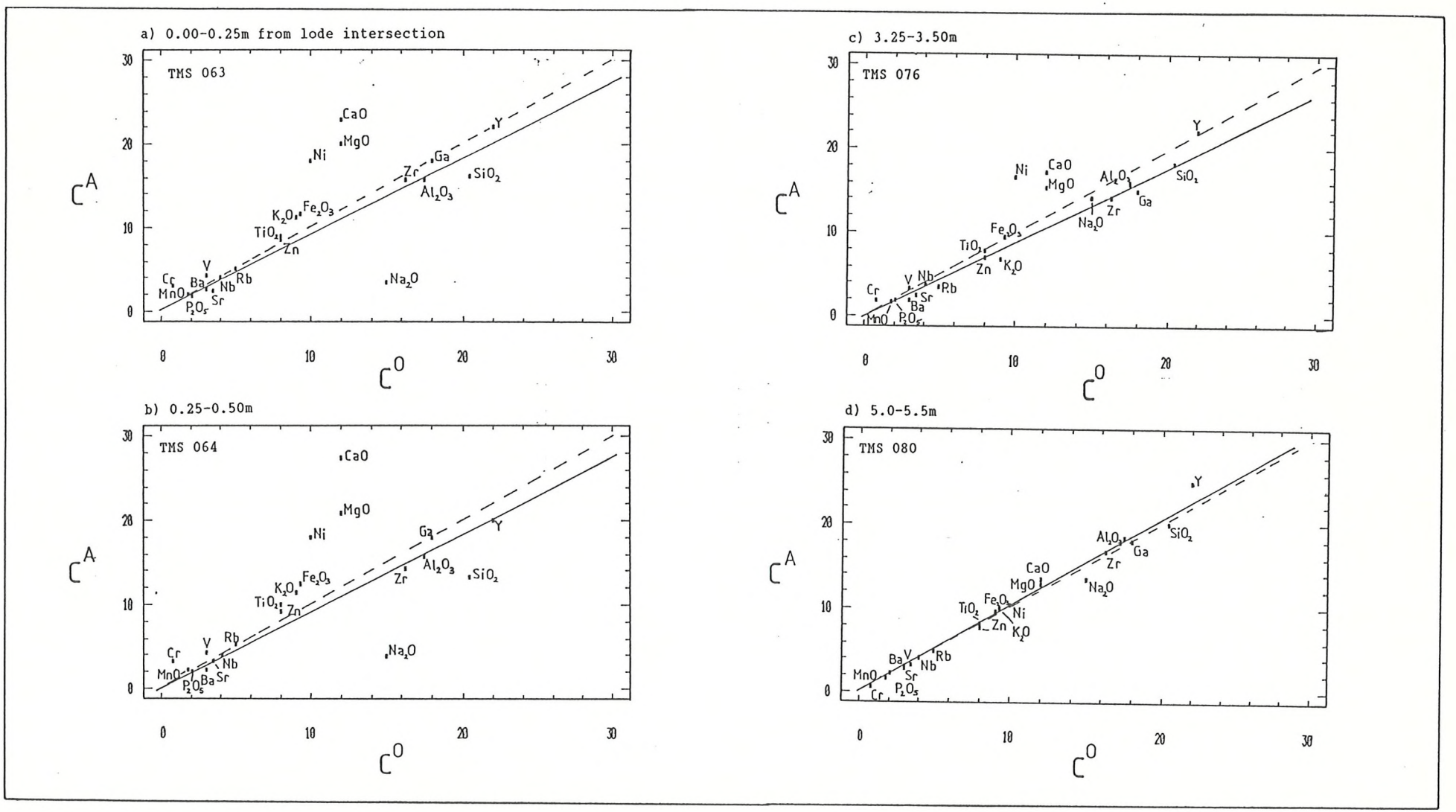

Fig.7.8 Isocon plots along lode profile 1 showing the increase in element mobility towards the lode. Isocons (solid line) are determined by Al_2O_3 and compared to line of constant mass-volume (broken line). C^A = concentration in altered sample C^o = concentration in original rock

metasomatism. Thus, all isocon plots for the Gebeit assemblages have been defined by aluminium and the relative mobilities of each element have been determined quantitatively by their deviations from the isocon.

Although variance of the slope of the isocon from 45° reflects the mass change, volume changes can be determined using specific gravities. Specific gravities have not been measured for the Gebeit samples but good estimates can be calculated using modal abundances and the specific gravities of component minerals (Appendix G). The estimated variation in specific gravity for the most and least altered samples is equivalent to a difference of ±0.4% (2.68/2.67) for the alteration profile samples and ±4% (2.77/2.67) for the carbonatised phyllonites. The mass changes for most samples can thus also be regarded as an estimate of volume change. However, there are several caveats to be considered when using isocon diagrams, namely:

i) At Gebeit the different host lithologies have significant chemical differences (especially K_2O) and therefore each protolith must be determined accurately. In examples of intense pervasive fine-grained alteration, identification of the wrong protolith can lead to large errors.

ii) Ideally, completely unaltered rocks need to be sampled in order to establish an accurate picture of element mobility. In the aphanitic tuffs, a "least-altered" protolith cannot easily be determined and the resultant isocon diagrams may reflect only the more intense phases of alteration.

iii) In order to overcome problems of original magmatic chemical variations, all unaltered samples have been sampled within the Gebeit area. As the carbonate alteration phase appears to occur on the regional scale, it may affect all lithologies. Thus any pervasive but incipient carbonatisation may not be reflected in the isocon diagrams.

iv) The accuracy of this method is only as precise as the original geochemical analyses (Appendix A) and therefore small deviations (±5-10%) as seen for example with Zr, Nb and Y, fall within the limits of systematic and analytical error.

v) Cu is highly variable in relatively unaltered protoliths and often only qualitative variations can be estimated using the known range of variability. Elements which remain below detection limit for all samples, e.g. Th and U, have not been considered.

For the Gebeit samples, three main protoliths were defined from the Gebeit Volcanic Group succession, i.e. hornblende-phyric volcanics, plagioclase-phyric and aphyric volcanics, and shales. Silicified granodiorite at the satellite prospect of Wadi Messesana was compared with less altered samples at the margin of the pluton. Similarly, epidote-bearing tuffs at the distal end of the alteration sequence was used as the protolith for lode profile 1. Many of the trace and major element abundances for both altered and unaltered samples were multiplied by a factor consistent to each element (Appendix G) in order to produce a good spread of data points along each isocon and allow an accurate isocon to be drawn. As both variables are multiplied by the same factor, the magnitude of mobility for each element is not affected (Grant,1986). Element mobilities and mass/volume changes for all samples were measured graphically and are tabled in Appendix G. Single samples have been plotted as histograms and the lode profiles displayed by line traces (see Figs.7.9A,B & 7.10A,B).

7.5.2 Lode Profile 1

Four isocon diagrams from the edge of the profile to the lode are displayed in Fig.7.8 showing the increase in element mobility towards the lode intersection. Broadly, the major element variations reflect the changes in mineralogy but, because volume changes are considered, veining can be accounted for. The mineralogy of the alteration profile is shown in Tables 7.5 and 7.6, together with the range of minor elements that are commonly found in substitution for each phase.

The total mass change (equivalent to volume change) across the profile shows only minor deviation (±10%) from zero except in the zone of secondary quartz and calcite-albite veining from 0.75-2.0m where mass increase up to +200% is due to marked influx of SiO_2 and CaO (Fig.7.9a,b & d). SiO_2 is depleted (-30%) adjacent to the lode vein whereas CaO shows a gradual increase up to +150% punctuated by a sharp rise to 430% due to the calcite veining at 2.0m. The CaO trend is very closely mirrored by MnO (Fig.7.9e) which increases to 50% by the lode and peaks at 140% at 2.0m indicating that MnO enrichment is due to the calcite alteration. Although Sr is depleted adjacent to the lode (-30% Fig.7.9f) and along the distal half of the profile, it displays a large peak at 2.0m (+240%) closely parallelling the CaO trend. As Sr occurs primarily in albite and calcite (Table 7.5), these trends suggest that Sr is depleted close to the lode due to the breakdown of albite,

Mineral	Elements	Substitutions[1]
chlorite	Si (talc layer) Al (brucite layer) Fe, Mg	Al Mg Mn, Cr, Ni, Ti
sericite	Al K	Mg, Fe, Mn, Cr, Ti, V Rb, Ba, Na, Ca
calcite	Ca	Fe, Mg, Mn, Sr, Ba, Zn
albite	Na	Ba, Sr, Ca, K, Ti, Fe, Mn, Mg
pyrite/apy	Fe, As	Zn, Ni, (± Mn)
magnetite	Fe^{2+} Fe^{3+}	Ti, Cr, V, Mn, Mg, Ca Ni, Co, Zn, (± Mg, Mn, Ca)
ilmenite	Fe	Mg, Mn
hornblende	Fe, Ca, Mg	Ti, Cr

Table 7.5 Minerals of the altered wallrock profiles and the Gebeit Volcanic Group and their potential element substitutions ([1]after Deer et al.,1966).

Distal
hornblende-pyroxene-albite-chl-epidote-ilmenite-magnetite-qtz
hornblende-albite-chl-epidote-calcite-magnetite-ilmenite-qtz
actinolite-albite-chl-calcite-magnetite-ilmenite-qtz
albite-chl-cal-ilmenite-qtz-pyrite ± sericite
chl-sericite-qtz-cal-ilmenite-pyrite-apy-po ±albite
Proximal
Vein: qtz-cal-sericite-tourmaline-apy-pyrite

Table 7.6 Summary of the progressive changes in mineralogy across the alteration profile towards an auriferous V_1 vein.

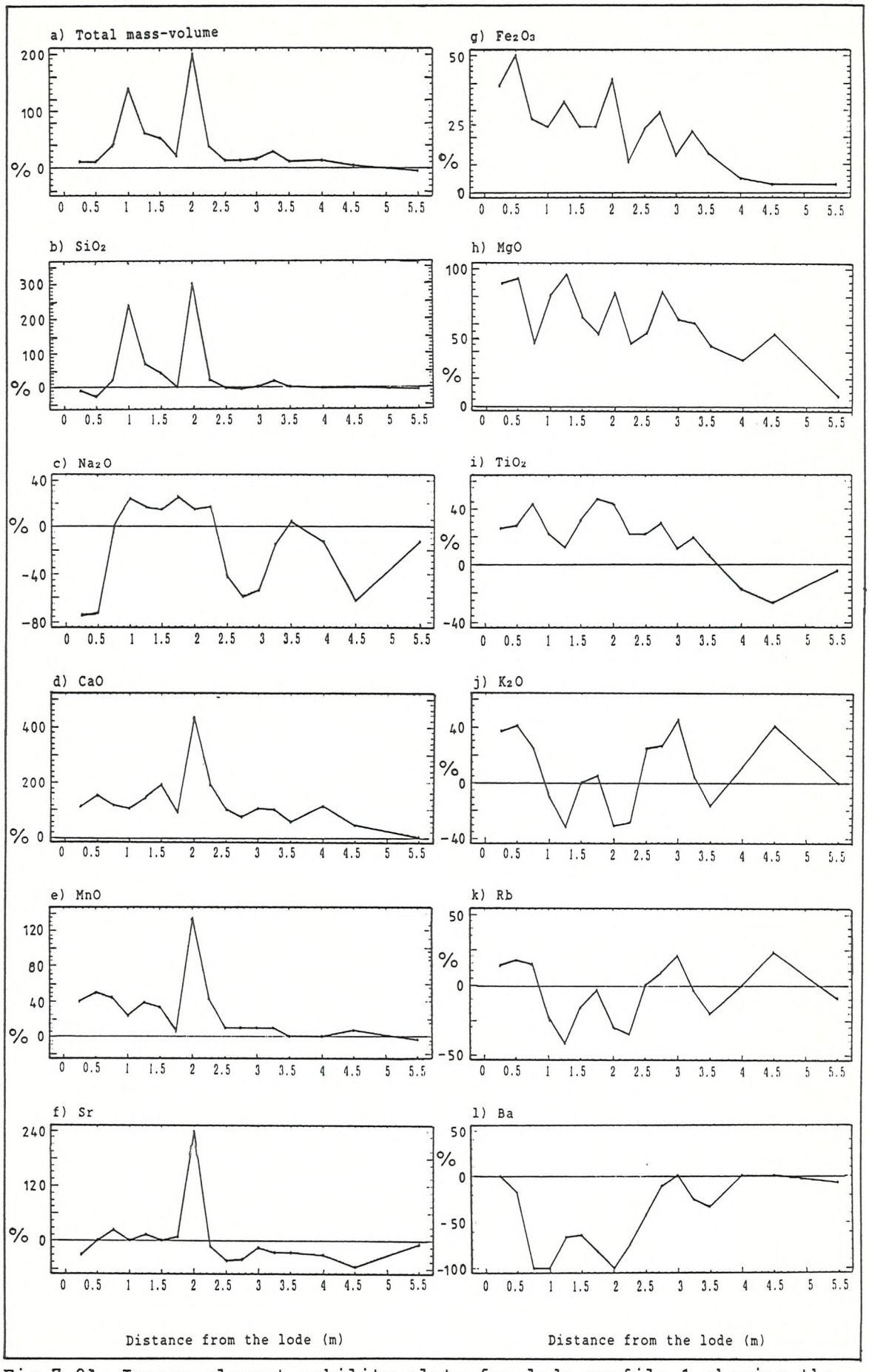

Fig.7.9A Isocon element mobility plots for lode profile 1 showing the variation of major and minor elements as a % change relative to the unaltered reference sample.

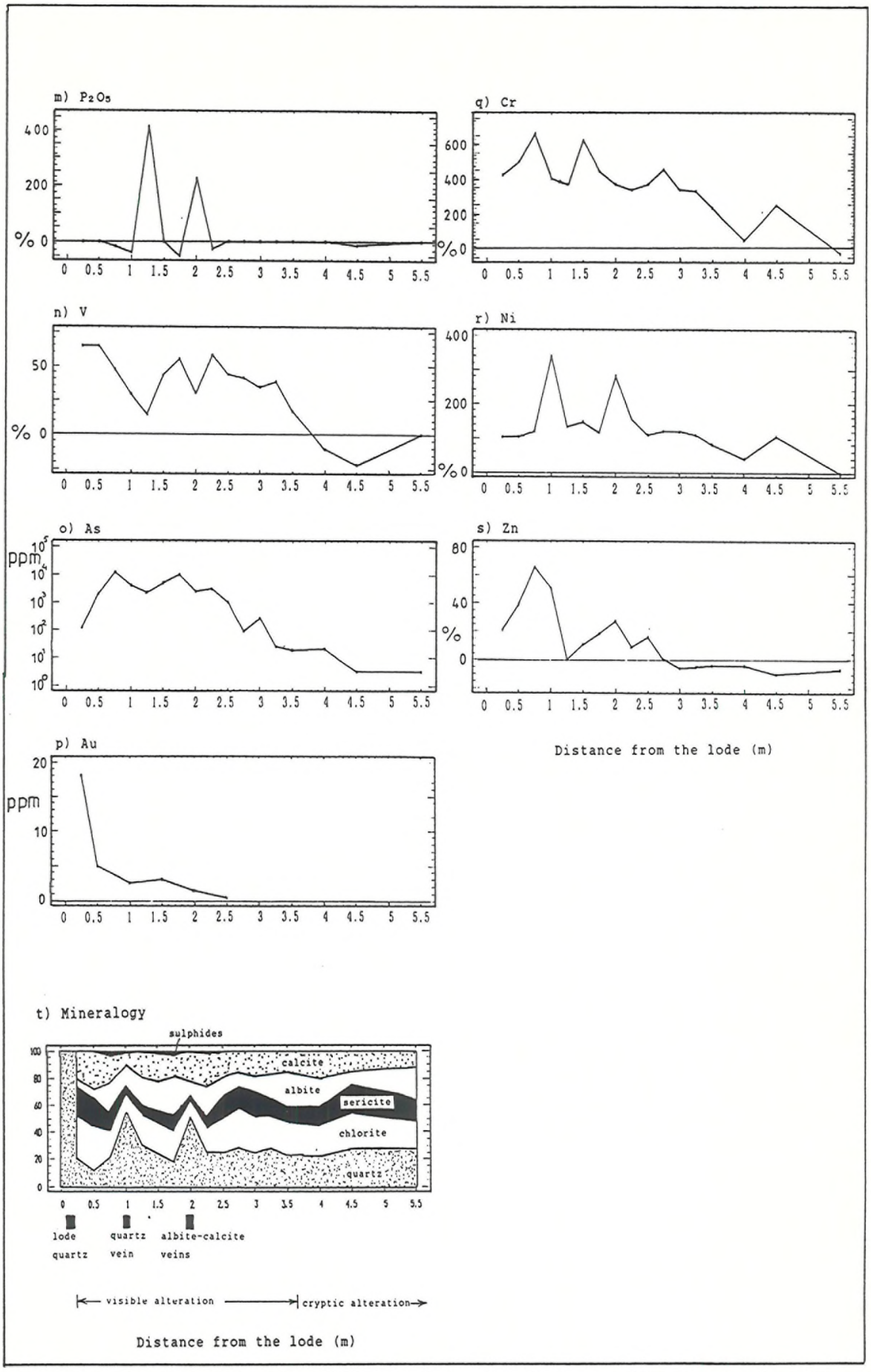

Fig.7.9B Isocon element mobility plots for lode profile 1 showing the variation of minor elements as a % change relative to the unaltered reference sample.

but is enriched (from 0.75-2.0m) by secondary albite-calcite veining.

Na_2O and K_2O consistently display antithetic trends (Fig.7.9c,j) with K_2O enriched to +40% across the profile, except in the zones of secondary albite veining (0.75-2.0m, and at 3.5m). Na_2O shows progressive depletion towards the lode up to a maximum of -80% but is enriched to around 20% where secondary albite-calcite veining occurs. Adjacent to the lode, K_2O enrichment is approximately 2x Na_2O depletion, a factor which, assuming Al is immobile, may reflect the 1:1 ratio between Na and Al in albite and the 2:1 ratio between Al and K in sericite. The K_2O trend is mirrored by both Rb and Ba (Fig.7.9k, l) as they tend to substitute for K in sericite (Table 7.5). Ba, however, also substitutes in limited amounts for Na in albite and is depleted along much of the profile, suggesting that Ba occurs in primary albite and sericite but not in the secondary vein albite.

Vanadium commonly substitutes for Fe and Al in magnetite and muscovite respectively and is enriched (+65%) close to the lode (Fig.7.9n) . As magnetite is replaced by Fe-sulphides throughout the profile, V mirrors the K_2O/sericite trend but is also depleted at the distal end of the profile (-25%) where limited substitution into sericite is offset by magnetite alteration. Titanium shows similar but minor enrichment near the lode (20-40%; Fig.7.9i) followed by depletion (-25%) at 4.0-5.5m due to its substitution in magnetite and muscovite. However, its pattern is further complicated by its incorporation in chlorite. Chromium, like titanium, is normally considered to be relatively immobile and is substituted into the same phases as Ti. It consequently shows a similar behaviour but with additions of up to 650% (Fig.7.9q). Cr contents of the unaltered lithologies (≈50-120ppm) are much lower than those observed in all of the altered lithologies, which range from 150 to 950ppm. Analytical interference during XRF analysis may be due to Ba and V which have overlapping spectra but peak abundances of Cr are not accompanied by high Ba or V contents, thus ruling out analytical error.

Fe, Mg, Zn, As, and Ni (Fig.7.9g,h,o,s) are also all enriched towards the lode with As concentrated by a factor of $1x10^4$ (11,000 ppm). Although Fe and Mg mainly occur in the groundmass chlorites, they also substitute for Al in muscovite and for Ca in calcite. Fe and Mg parallel the bulk chlorite trend except at 2.0m where enrichment accompanies calcite veining. Mg enrichment is generally twice that of Fe near the lode (90-95% cf. 40-50%) and contributes to the decrease in the Fe:Mg ratios of chlorite.

Zn and As show similar traces, bearing in mind As is plotted on a log scale (ppm), as sphalerite occurs with arsenopyrite and pyrite but Zn also peaks at 2.0m due probably to substitution in calcite. Nickel is found as a minor element in chlorite, magnetite and Fe-sulphides and would thus be expected to parallel As and chlorite trends. Ni maxima (300-350%) occur, however, at the vein intersections at 1.0m and 2.0m, suggesting that nickel sulphides (gersdorffite) and nickel-bearing sulphides (pyrite and arsenopyrite) are locally important in addition to chlorite. Chlorite and sericite enrichment at 4.5m is reflected by increases in MgO, Cr, Ni, K_2O, and Rb, with concomitant depletion in albite and magnetite indicated by a decrease in Na_2O, Sr, Ti, and V.

Zr, Y, and Ga, which all show flat trends (±10%), have not been illustrated and, like Al, often delineate the isocons. Nb was not utilised due to its very low abundances (2-5 ppm), as a variation of ±1 ppm from the standard produces an error of 20-50%. P_2O_5 likewise (Fig. 7.9m) displays a relatively flat immobile trace but peaks of 425% and 250% at 1.25m and 2.0m respectively are probably due to apatite associated with the later veins. Cu, Mo, Sn, Bi, Sb, Pb, Th, La and U were generally below detection limit and also were not utilised. Across the profile, however, the maximum values of Sb (11ppm), Pb (6ppm), and Bi (3ppm) coincided with the As maxima at 0.75 and 1.75m from the lode. Because of overlapping As and Ce peaks in XRF analytical spectra, Ce could not be determined in the lode profiles due to interference from arsenopyrite. Gold values from the lode are taken from core assays by Robertson Research on behalf of Greenwich Resources. Visible gold occurs at the margin of the main lode vein where the average gold content is 18 g/t (ppm; Fig.7.9p). This value rapidly drops to 5 g/t at 25-50cm from the lode and gradually decreases over the next 2m to 0.4 g/t, in total representing a 2m interval averaging 7.15 g/t. Although no gold can be identified in polished sections outside the main vein intersection, the anomalous values up to 2.5m from the lode are probably due to solid substitution or fine sub-micron gold grains intergrown with the wallrock sulphides. The gold enrichment adjacent to the lode is accompanied by addition of Fe, Mg, Ti, Cr, and Ni in chlorite, K, Rb, Ti and V in sericite, As and Zn in arsenopyrite, and Ca and Mn in calcite. The concomitant alteration of plagioclase is evident by depletion in Na, Ba, and Sr.

7.5.3 Lode Profile 2

The variation in lithology and veining make the correlation between elements and mineral abundances across profile 2 difficult to assess. The main trends evident in profile 1, however, seem to hold for profile 2 despite the lithological differences. A standardised unaltered tuff was used as the protolith except in the shale zone where an average of the freshest shale samples available (Table 3.4) from drillcore acted as a reference lithotype.

SiO_2 has a highly variable trace (Fig.7.10b), due to quartz veining around the lode which is influenced by the degree of deformation and the host lithotype. As with profile 1, the intervening wallrock close to the lode, which comprises predominantly chlorite and sericite at 0.50m and 1.50-1.75m, is depleted in silica (-20 to -30%). Further away in the band of highly sheared tuffaceous phyllonites (2.25-4.0m), which is calcite-dominated, silica shows variable enrichment from 0 to 15%. In the graphitic shale zone from 4.0 to 8.0m, where albite and sericite are the main phases, SiO_2 is depleted from -5 to -20%. Na_2O is strongly depleted by the lode (-50 to -95%), except in the V_3 albite vein at 1.0-1.25m, and remains markedly reduced up to 4.0m (Fig.7.10c). From the inner edge of the shale zone it shows variable enrichment and depletion (-20 to 15%) reaching a maximum (70%) at 8.75m before returning to background levels at the distal end of the profile. Like the first profile, total mass/volume change (Fig.7.10a) is determined by SiO_2 and CaO (Fig.7.10b,d) abundances, mainly due to V_1 and V_2 veining.

As with profile 1, K_2O, Rb, and Ba show identical trends as do CaO, MnO and Sr (Fig.7.10j,k,l,d,e,f) . In the vein-free zones of altered wallrock (0.50m and 1.50-1.75m) close to the lode, K_2O is enriched (20-45%) accompanied by Ba and Rb maxima, and low levels (-5 to -60%) of CaO, MnO and Sr. Rb and Ba appear depleted up to 4.0m from the lode due to the interference of veining and carbonate alteration in the tuffaceous phyllonites but are not depleted where K_2O is enriched as sericite. In the chlorite-sericite-rich zone at 1.50-1.75m, Fe and Mg maxima (70% and 80%) are accompanied by enrichments of TiO_2 and V which otherwise show relatively flat traces (Fig.7.10g,h,i,n) . In the tuffaceous phyllonites, dominated by calcite and chlorite, CaO, MnO, Sr, Mg, Fe, and especially As, Ni and Cr show enrichments. Ni, P_2O_5, and Cr are also enriched with As (Fig.7.10m,o,p,q) in and adjacent to the quartz vein at 0.75m, confirming that both Ni and Cr are hosted by

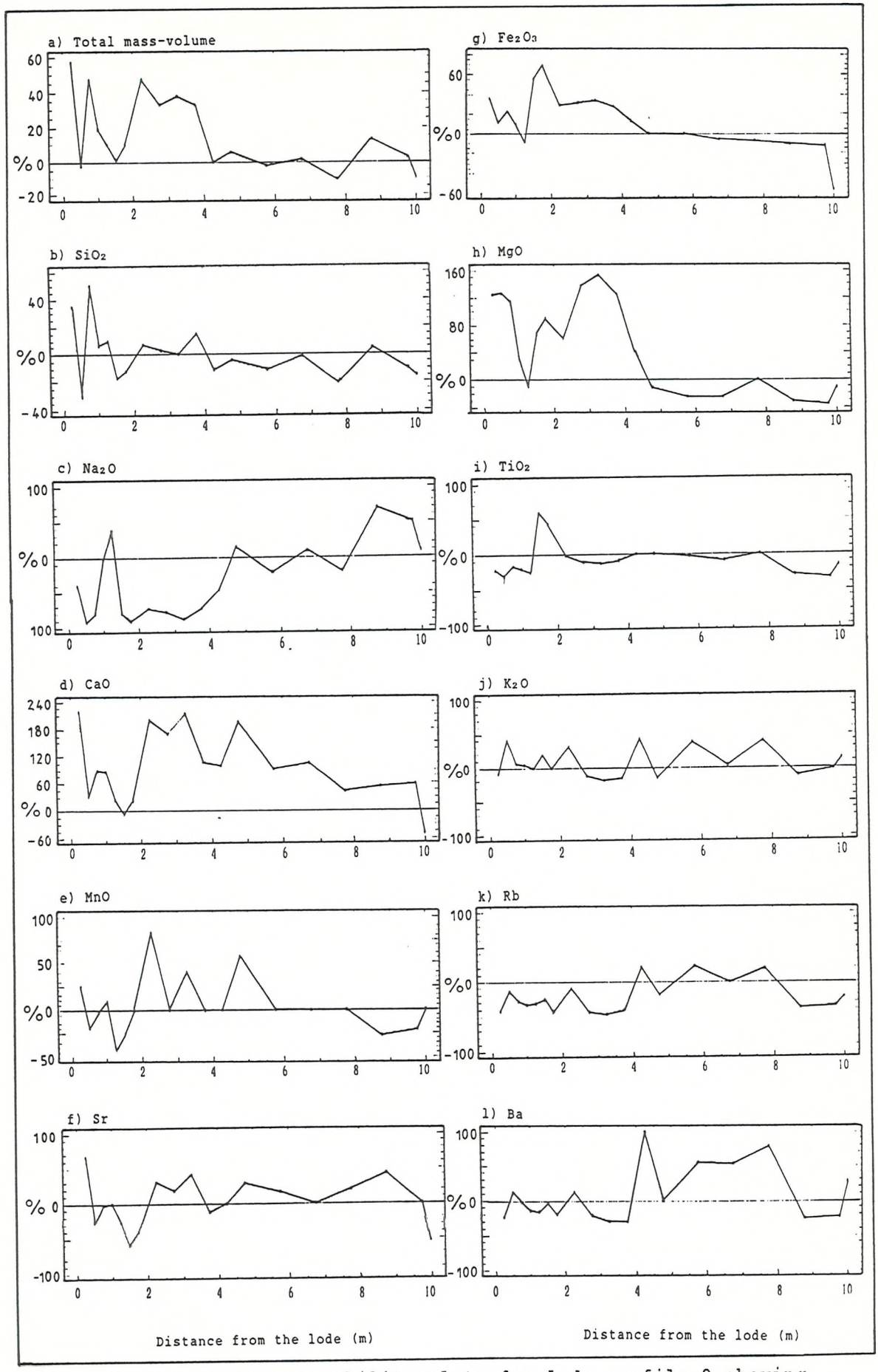

Fig.7.10A Isocon element mobility plots for lode profile 2 showing variation of major and minor elements as a % change relative to the unaltered reference sample.

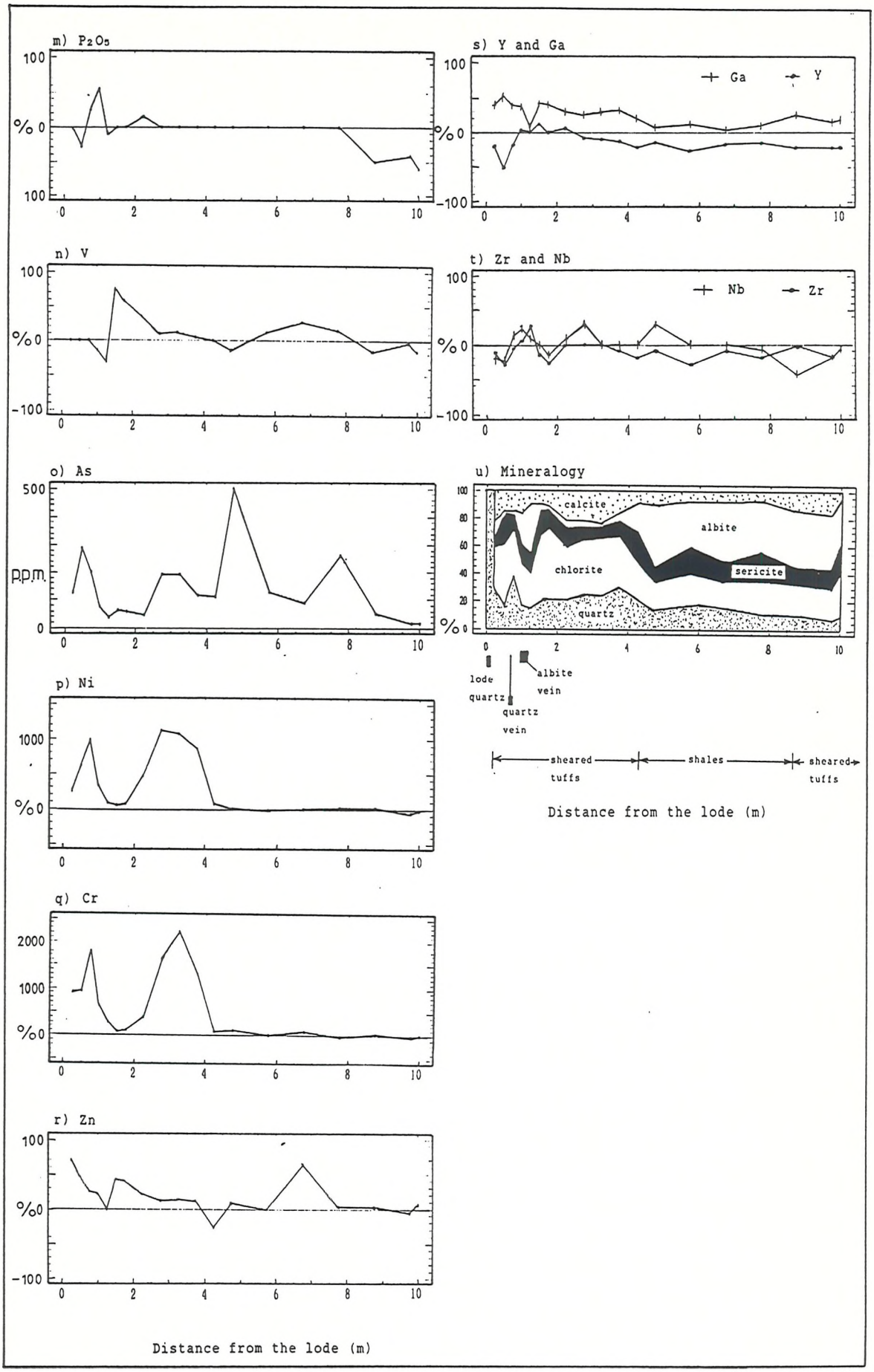

Fig.7.10B Isocon element mobility plots for lode profile 1 showing variation of minor elements as a % change relative to the unaltered reference sample.

sulphides and chlorite and that apatite occurs in the V_1 veins. Zn generally displays a flat trend (Fig.7.10r) but is enriched near the lode as seen with the enrichment of bulk rock calcite and chlorite (Fig.7.7).

Within the shale zone, where sericite and albite are the main phases, lower chlorite levels are marked by depletion in Mg and Fe (-5 to -20%) and by background abundances of Ni, Cr, and Ti. The background abundances of albite and sericite reflect minor alternating K_2O and Na_2O maxima varying between 0 and +50%, a feature which is indicative of only weak alteration. Arsenic is enriched across the profile to varying degrees but peaks adjacent to the lode, within the calcite-chlorite phyllonites, and in the shales at 4.75m and 7.75m. The As abundances are one to two orders of magnitude lower than for profile 1 but, as with the first profile, the lode-associated As peak occurs 25-50cm away from the vein-wallrock interface. This is because the majority of wallrock sulphides are dispersed around the veins rather than concentrated at the vein margin. Despite the lower As values compared to profile 1, the main vein intersection averages 111 g/t Au (average) with up to 50 g/t Au in parallel quartz stringers. The largest As peak at 4.75m (500 ppm) coincides with an enhanced Au grade of 3.3 g/t which spans the zone of minor K_2O enrichment. As the mineralogy and geochemistry of the shales is similar to the volcanics (see sections 3.4.1 & 3.6.7), the lack of intense alteration in the shale zone suggests that it was relatively less permeable and locally restricted pervasive alteration.

7.5.4 Y Lode and Wadi Lode Chip Samples

Geochemical analyses of Y lode samples taken adjacent to the lode confirm the above trends, displaying strong Na_2O depletion coupled with increases in K_2O, CaO, MgO, Fe_{tot}, total mass and SiO_2 (Fig.7.11a). The K_2O enrichment is accompanied by Ba, Rb and V, and enhanced chlorite abundances are indicated by Fe, Mg, Ni, and Cr. The increase in CaO together with Zn is not as high as in the lode profiles due to more incipient wallrock carbonatisation and is insufficient to counteract Sr, and MnO depletion.

Wadi Lode samples of altered hornblende-phyric massive lavas, formerly identified as green lapilli tuffs, display large additions of K_2O (100%) and are strongly depleted in Na_2O (-60 to -85%; Fig.7.11d). SiO_2 is consistently depleted (-20%) but CaO is variable (-25 to 45%),

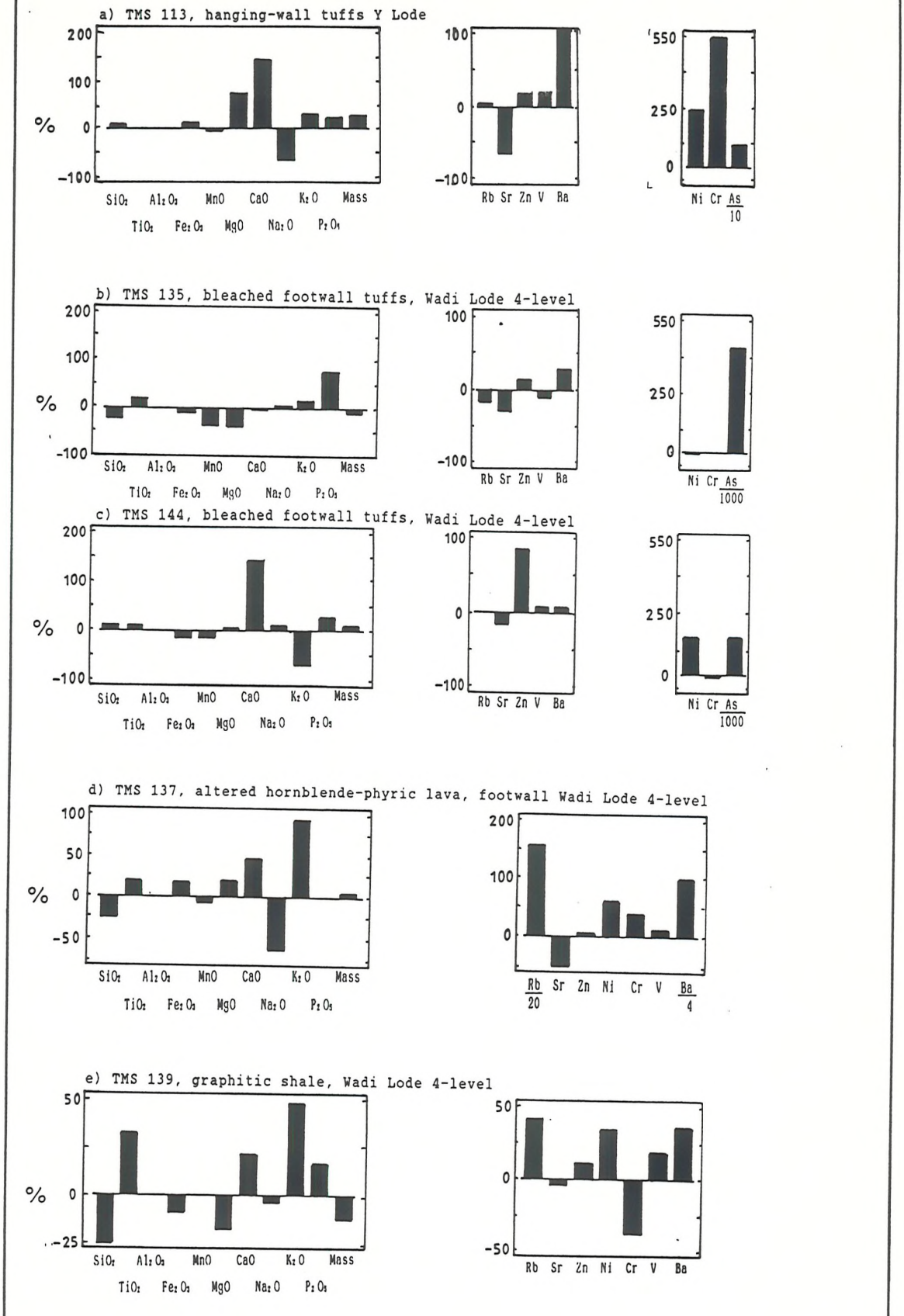

Fig.7.11 Isocon element mobility diagrams for altered wallrocks sampled from the Y Lode and Wadi Lode showing variation of major and minor elements as a % change relative to the unaltered reference sample.

producing minor positive and negative volume changes (-5 to +5%). K_2O addition is coupled with high enrichments in Rb and Ba with less V and TiO_2 enhancement. CaO enrichment and depletion is accompanied by Zn but, as CaO addition is relatively minor compared to the lode profiles, MnO and Sr are constantly depleted. Increases in chlorite and sulphide abundances are indicated by small increases in Fe and Mg, coupled with larger Cr, Ni and As additions. Shale samples taken from the Wadi Lode show the same trends as seen in profile 2 (Fig.7.11e): enrichments in K_2O, TiO_2, V, Rb and Ba in sericite; small additions of CaO with Zn and little change in MnO and Sr; and low chlorite contents reflected in depletion of Fe, Mg, and Cr. SiO_2, Na_2O, and total mass (and volume) are also depleted. The anomalous bleached tuff samples from the Wadi Lode reflect the apparent overprinting of at least two hydrothermal signatures and display highly variable CaO, K_2O, and Na_2O abundances with low to depleted Mg, Fe and Mn (Fig.7.11b,c).

7.6 Satellite Prospects

Because of the limited surface exposure and lack of underground access to all the mineralised zones at Gebeit, some of the local prospects were sampled where large scale relationships between the veins, their host shear zones, the extent of wallrock alteration, and effects of later deformation could be better assessed.

7.6.1 Vein 13, Vein 18, and Marble Bar

Drilling information and structural mapping indicate that Vein 13 and Marble Bar are part of the same structure which appears to continue to the north as Vein 18 (see Fig.5.11). This mineralised zone seems to be the northern counterpart to the Wadi Lode/A, Y, and X Lode system to the south of the Wadi Lode shear zone, thus forming a symmetrical distribution of auriferous veins about the Wadi Lode Riedel shear. The fine tuffaceous phyllonites which host the Marble Bar, Vein 18, and Vein 13 veins, therefore, have been analysed to provide a comparison with the Wadi Lode and Y Lode alteration assemblages.

Thin-section petrography could not be undertaken on these samples due to their friability owing to the high phyllosilicate contents (≈70%vol of the bulk rock). X-ray diffraction analysis indicated that the samples displayed a sequence of progressive alteration from V13 to the highly altered Marble Bar phyllonites. Mineralogy becomes

simplified with increasing alteration being denoted by decreases in albite, and calcite and concomitant increases in quartz, sericite and chlorite (Table 7.6). The resulting phyllonites at Marble Bar are devoid of albite and calcite (Appendix G) and are composed entirely of quartz (30%), sericite (25%), chlorite (42%), and Fe-sulphides (3-4%). Isocon diagrams of the alteration (Fig.7.12a-c) reflect these changes with increasing enrichment of K_2O, V, Ba, Zn, MgO, Fe_{tot}, TiO_2, Cr, and Ni together with depletion of CaO, MnO, Sr, total mass and SiO_2. Despite SiO_2 loss, quartz abundance increases, the excess SiO_2 having been released during pervasive sericitisation of albite.

Arsenic levels decrease from Vein 13 (2567ppm As) to Marble Bar (816ppm As) and all samples display relatively high gold values of 0.5 to 6.8 ppm, reflecting the broad correlation between As and Au. This is only a general association as higher As values do not neccessarily equate with high Au grades. The high gold grades and lack of pervasive quartz and calcite veining confirm that gold mineralisation occurs with Fe-sulphides in the wallrock alteration haloes and suggests that carbonate alteration does not always accompany gold mineralisation. As samples of chlorite phyllonite (TMS 032,140) from unmineralised shear zones nearby show large increases in CaO (see Fig.7.14), it is highly unlikely that the lack of calcite in these prospect samples is due to selective weathering. Whether the lack of carbonate alteration is due to the timing of gold mineralisation in the Marble Bar area or its greater distance (relative to the Wadi Lode and Y Lode) from the Wadi Lode shear zone is not certain. At Marble Bar, however, a thick, coarse, calcite vein occurs folded parallel with the auriferous blue V_1 vein. The wide variation of calcite alteration at Gebeit suggests that some of the carbonate alteration may represent a distinct CO_2-rich fluid phase which pre-dated and/or post-dated the gold mineralisation. Early pervasive, carbonatisation of the Riedel shear zones, following emplacement of the phase 1 intrusions, may have sealed these zones and prompted shear zone formation and mineralisation to continue on the Riedel shear zone margins. This would account for the distribution of the gold-bearing V_1 veins and explain the lack of gold mineralisation within the main Riedel shears. However, limited fluid inclusion evidence from the blue V_1 quartz veins indicates that primary CO_2-bearing fluids were associated with the mineralisation and that more than one phase of CO_2-related alteration occurred. The apparent lack of carbonates at some prospects and the spatial separation between gold and carbonatisation may be a result of fluid unmixing (see Chapter8).

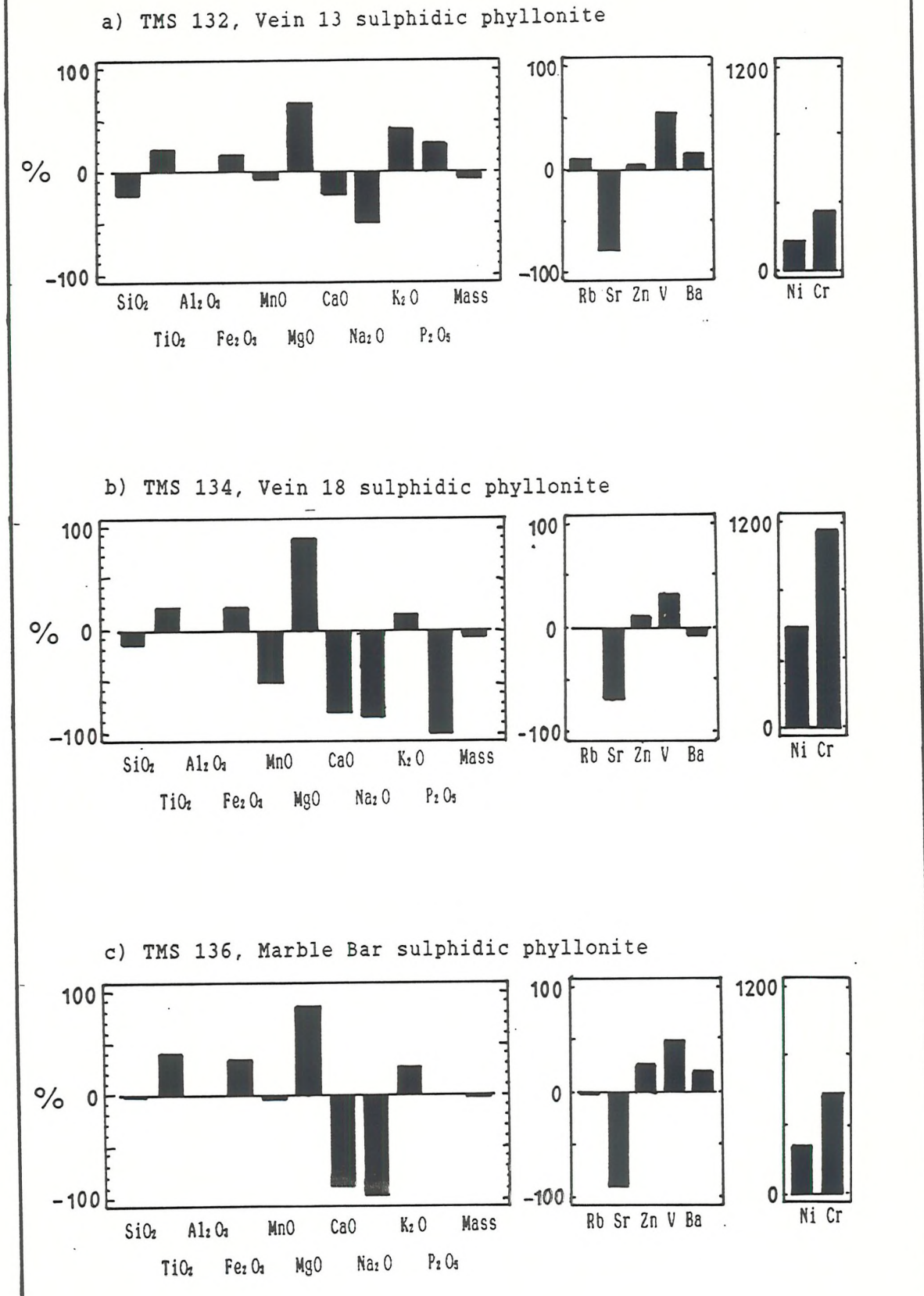

Fig.7.12 Isocon element mobility diagrams for altered wallrocks sampled from the satellite prospects of Vein 13, Vein 18, and Marble Bar showing variation of major and minor elements as a % change relative to the unaltered reference sample.

7.6.2 Wadi Messesana

The mineralisation at Wadi Messesana, although outside the Gebeit block, appears to be contemporaneous with Gebeit and is hosted by granodiorites. As the majority of fluid inclusion data available in the area are derived from this prospect, geochemical and mineralogical studies have likewise been applied to samples from Wadi Messesana.

The least altered samples at this prospect comprise biotite (≈10%) sericite (15-20%), albite (40%), quartz (25-30%), and minor calcite (2-3%). Progressive alteration towards the shear-zone-hosted quartz vein produces sericitisation of the albite feldspar, the alteration of biotite to chlorite and Fe-sulphides, and minor addition of calcite (1-2%). The most intensely sheared granodiorite adjacent to the lode is highly silicified with quartz forming up to 60% of the bulk rock composition. Calcite is removed in this zone and sericite is more abundant than albite.

Geochemically these changes are reflected in enrichment in SiO_2, K_2O, CaO, Rb, Zn, Ni, As, Ba and Cr with concomitant depletion in MnO, Na_2O, MgO, TiO_2, and Sr (Fig.7.13). In the silicification zone, large additions of SiO_2 result in significant volume increases and a decrease in Na_2O, MgO, Fe_{tot}, CaO, Ba, and TiO_2. The Messesana alteration bears many similarities compared to the Gebeit sequence, the only exception being the Fe-Mg depletion which may be a function of the relatively acidic host lithotype. As at Marble Bar and Vein 18, CO_2-rich fluid inclusions are common at this prospect (see section 6.9.1), but carbonate alteration is not prevalent, suggesting that fluid immiscibility may have occurred.

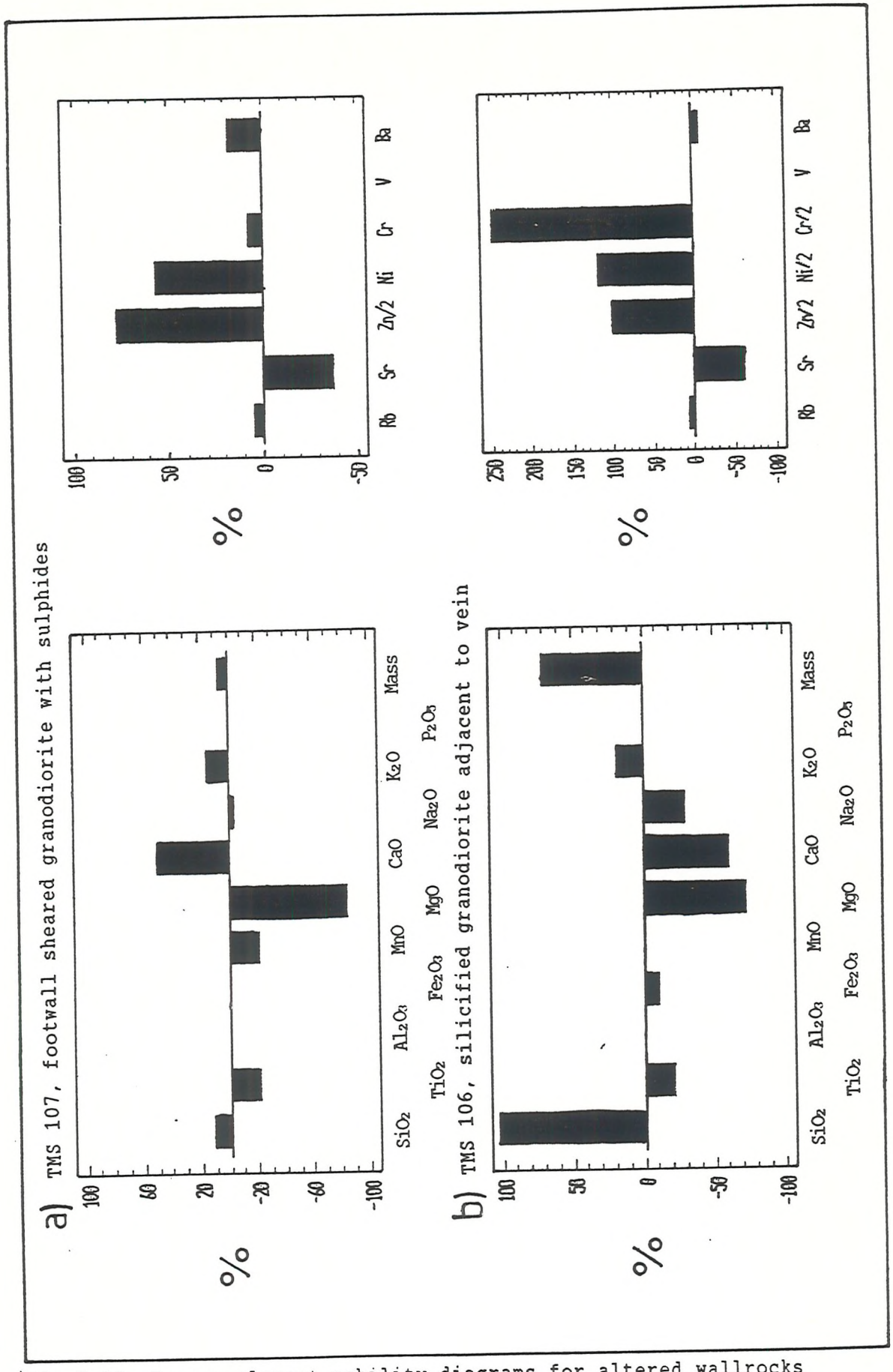

Fig.7.13 Isocon element mobility diagrams for altered wallrocks sampled from the granitoid-hosted, satellite prospect of Wadi Messesana showing variation of major and minor elements as a % change relative to the unaltered sample.

7.7 Shear Zone Phyllonites

At Gebeit the high strain zones are delineated by chlorite-calcite phyllonite shear zones. Some of these shear zones, which lie adjacent to (50m to 300m) and parallel to the Riedel shears, host the auriferous V_1 veins (Figs 6.11 & 8.6) and display bleached and sulphidised alteration haloes. The main Riedel shears which cross the Gebeit block, such as the Wadi Lode, Wadi Tuwiya, and North Gebeit shear zones, display a different mineral assemblage due to pervasive, ankerite-rich, carbonate alteration which obliterates the D_2 phyllonite fabric. The distinct alteration assemblages indicate that some of the shear zones have been altered by a separate CO_2-rich hydrothermal event. A range of samples from chloritic phyllonite to highly altered ankerite phyllonite have been taken in order to characterise this secondary alteration and to define the geochemical parameters of the unaltered and unmineralised shear zones. Geochemical analyses of both lithotypes are given in Tables 7.7 and 7.8.

7.7.1 Chlorite Phyllonites

These have been sampled from the outer margins of the Wadi Lode shear zone and from the shear zones parallel to it (grid line 4900E; see Fig.4.3, 5.18, Plate 7.2a). They are distinct from the central ankerite-rich phyllonites because carbonate alteration is relatively limited and calcite is the dominant carbonate phase. The rocks from the unmineralised shear zones display the same mineral assemblage as the lode profile alteration haloes (Appendix G), but chiefly comprise chlorite-biotite (30-50%) and quartz (30%). Albite is reduced to between 4 and 10% except in the samples taken from the margin of the Wadi Lode shear zone which have higher albite contents of 17-22%. Sericite contents are also much lower (4-11%) in comparison to the mineralised phyllonites at Marble Bar-Vein 18, and calcite is highly variable (15-30%). XRD analysis of clay fraction (<2µm) separates identified only chlorite and sericite in most samples. Mixed layer chlorite-smectite and hydrobiotite were identified in friable outcrop samples (TMS 034) and were probably introduced by recent surface weathering. Electron probe analysis of the carbonates showed all to be calcite in composition (see Table 7.11), similar to the lode-profile calcite, with Fe/(Fe+Mg) ratios of 0.34-0.50. The chlorites plot close to those of the lode profile (Fig.7.3; Table 7.9) but are marginally

	Ankerite Phyllonites					
	TMS 001	TMS 031	TMS 033	TMS 098	TMS 118	TMS 119
SiO_2 (%)	35.2	31.1	31.0	26.8	31.0	26.7
TiO_2	0.3	0.4	0.3	0.3	0.3	0.3
Al_2O_3	7.2	8.5	5.8	5.6	5.8	4.9
Fe_2O_3*	7.1	8.3	7.2	7.4	8.0	7.0
MnO	0.1	0.2	0.2	0.2	0.1	0.2
MgO	7.2	6.0	9.0	9.8	7.9	8.3
CaO	15.6	17.7	16.3	18.2	17.0	19.1
Na_2O	1.7	1.2	2.5	2.9	2.3	0.0
K_2O	1.0	1.4	0.3	0.1	0.6	1.5
P_2O_5	0.2	0.2	0.1	0.2	0.1	0.1
ΣH_2O	22.4	23.2	25.2	27.0	25.0	29.4
Total	98.1	98.0	97.8	98.2	98.1	97.5
Rb(ppm)	25	49	5	<2	11	22
Sr	239	188	248	247	183	239
Ba	88	89	88	82	257	245
Pb	<3	3	<3	<3	<3	<3
Th	<3	<3	<3	<3	<3	<3
U	<5	<5	<5	<5	<5	<5
La	6	<6	<6	<6	6	<6
Y	9	10	8	6	7	6
Zr	22	34	26	25	24	22
Nb	2	3	3	2	2	2
Ga	9	14	7	7	6	5
Ni	167	137	243	299	305	270
Cr	555	362	710	765	808	703
V	167	217	154	132	164	144
Cu	36	57	36	68	74	71
Zn	51	62	46	38	49	52
As	262	208	42	137	363	302
Sb	<3	<3	<3	262	<3	<3

* Total Fe calculated as Fe_2O_3
ΣH_2O = Loss on Ignition
<3 = Below Lower Limit of Detection

Table 7.7 Major and trace element geochemistry of the ankerite phyllonites from the Wadi Lode and Wadi Tuwiya shear zones. Sample localities are given in Fig.7.17.

	Chlorite Phyllonites				
	TMS 004	TMS 005	TMS 032	TMS 034	TMS 140
SiO_2 (%)	34.3	42.4	44.8	46.5	40.9
TiO_2	0.3	0.7	0.8	0.7	0.9
Al_2O_3	6.8	15.0	16.4	12.8	14.3
Fe_2O_3*	8.5	8.9	10.3	11.0	10.9
MnO	0.2	0.2	0.2	0.2	0.2
MgO	10.7	7.0	6.9	8.4	6.2
CaO	18.2	10.6	8.9	7.9	10.0
Na_2O	0.5	0.8	2.5	1.1	1.9
K_2O	0.4	1.3	0.4	1.1	0.9
P_2O_5	0.1	0.3	0.2	0.2	0.2
ΣH_2O	18.2	12.2	8.0	9.8	12.5
Total	98.2	99.2	99.3	99.7	98.0
Rb(ppm)	14	26	10	27	16
Sr	173	188	186	178	200
Ba	43	352	240	193	160
Pb	<3	<3	6	<3	<3
Th	<3	<3	<3	<3	<3
U	<5	<5	<5	<5	<5
La	<6	<6	<6	7	<6
Y	8	19	15	15	15
Zr	24	46	37	46	39
Nb	3	3	3	3	3
Ga	8	17	20	17	19
Ni	281	77	63	154	59
Cr	967	214	128	527	123
V	192	297	334	317	427
Cu	22	27	118	82	105
Zn	59	73	69	87	82
As	<7	38	32	13	60
Sb	<3	<3	<3	<3	<3

* Total Fe calculated as Fe_2O_3
ΣH_2O = Loss on Ignition
<3 = Below Lower Limit of Detection

Table 7.8 Major and trace element geochemistry of the chlorite phyllonites. Sample localities are given in Fig.7.14.

a) Sample	PTMS 044	PTMS 043	PTMS 037
Si	5.747	5.504	5.665
Al	2.253	2.496	2.335
Al	2.410	2.337	2.458
Mg	4.915	5.444	4.779
Fe	3.725	3.897	4.179
Na	.000	.015	.023
Ca	.022	.065	.015
Ti	.388	.008	.008
Mn	.005	.002	.002
K	.139	.025	.183
Cr	.327	.199	.257
Fe/Fe+Mg	.431	.417	.467
Si	5.581	5.499	
Al	2.419	2.501	
Al	2.238	2.139	
Mg	5.353	5.396	
Fe	3.939	4.008	
Na	.038	.023	
Ca	.028	.009	
Ti	.008	.003	
Mn	.017	.007	
K	.016	.016	
Cr	.314	.397	
Fe/Fe+Mg	.424	.426	
Si	5.471		
Al	2.529		
Al	2.229		
Mg	5.514		
Fe	4.035		
Na	.000		
Ca	.006		
Ti	.008		
Mn	.000		
K	.012		
Cr	.228		
Fe/Fe+Mg	.423		

b) Sample	PTMS 035	PTMS 036	PTMS 042
Si	6.044	5.789	5.680
Al	1.956	2.211	2.320
Al	2.059	2.057	2.246
Mg	6.688	6.917	5.699
Fe	2.887	2.916	3.961
Na	.464	.000	.038
Ca	.024	.014	.025
Ti	.008	.006	.005
Mn	.023	.010	.067
K	.036	.014	.016
Cr	n.a.	.094	n.a.
Fe/Fe+Mg	.302	.297	.410
Si	6.098	5.917	
Al	1.902	2.083	
Al	2.151	2.275	
Mg	6.569	6.651	
Fe	2.943	2.900	
Na	.013	.014	
Ca	.043	.012	
Ti	.024	.005	
Mn	.019	.005	
K	.190	.015	
Cr	n.a.	.023	
Fe/Fe+Mg	.309	.304	
Si	5.732		
Al	2.268		
Al	1.842		
Mg	7.448		
Fe	2.857		
Na	.013		
Ca	.020		
Ti	.005		
Mn	.015		
K	.024		
Cr	n.a.		
Fe/Fe+Mg	.433		

Table 7.9 Chlorite compositions determined by electron micro-probe analyses of ankerite phyllonite (a) and chlorite-calcite phyllonite (b). Structural formulae are based on chlorite formula of $(Mg,Al,Fe)_{12}[(Si,Al)_8O_{20}](OH)_{16}$ (Deer et al.,1966).

Sample	TMS 038	TMS 037	TMS 043	TMS 044
Si	6.530	6.536	6.568	6.756
Al	1.470	1.464	1.432	1.244
Al	3.759	2.945	3.320	3.470
Ti	n.a.	.024	.015	.023
Fe	.107	.207	.282	.218
Mg	.281	.433	.580	.493
Mn	n.a.	.003	.006	.000
Cr	n.a.	.158	.068	n.a.
Ca	.002	.002	.013	.002
Na	.069	.043	.047	.039
K	1.343	1.401	1.397	1.278
Fe/Fe+Mg	.276	.324	.327	.306
Si	6.553	6.637	6.585	
Al	1.447	1.363	1.415	
Al	3.677	3.324	2.651	
Ti	n.a.	.019	.028	
Fe	.118	.215	.414	
Mg	.348	.463	.748	
Mn	n.a.	.002	.000	
Cr	n.a.	.178	.138	
Ca	.015	.004	.006	
Na	.063	.023	.028	
K	1.392	1.391	1.351	
Fe/Fe+Mg	.254	.317	.356	
Si	6.458			
Al	1.542			
Al	3.629			
Ti	.027			
Fe	.157			
Mg	.332			
Mn	.002			
Cr	n.a.			
Ca	.002			
Na	.069			
K	1.532			
Fe/Fe+Mg	.321			

Table 7.10 Structural formulae of sericite grains from the ankerite phyllonites determined by electron micro-probe analysis. Formulae are based on sericite formula $K_2Al_4[Si_6Al_2O_{20}](OH)_4$ (Deer et al.,1966).

more clinochlore-rich having lower Fe/(Fe+Mg) ratios of 0.28-0.41. They also contain less Al (≈17% Al_2O_3) than the chlorites of the lode profile (≈21.5% Al_2O_3) due to the limited availability of immobile Al in the chlorite-rich phyllonite zones.

Isocon plots of these samples indicate that all have increased in volume (10-50%) with the largest increase (150%) occurring in the sample with the highest calcite contents (Fig.7.14). The more chlorite-rich samples display significant enrichment in K_2O and Rb with variable increases in Ba, V, CaO, MnO, Zn, SiO_2, MgO, Fe_{tot}, Ni, As and Cr. As with the lode profile, Na_2O is variably depleted along with Sr. The two samples (TMS 032 & 140) taken at the margin of the Wadi Lode shear zone, however, show a reversal of this trend and are strongly depleted in K_2O. The higher albite abundances in these rocks suggest replacement of sericite in the phyllonite by secondary albite coupled with a marked depletion in Rb and Ba, thus forming a transition zone between the shearing- and mineralisation-related alteration and the ankerite-rich phyllonites.

7.7.2 Ankerite Phyllonites

The pervasive carbonate alteration at the centre of the main Reidel shear zones is sufficient to produce a blocky cohesive lithology (Plate.7.2) and the degree of fabric-replacement appears to decrease progressively (≈5m to 10m) to the friable calcite-rich samples at the shear zone margins. Incipiently carbonatised rocks (Plate 7.2d) display preferential alteration along the chloritic cleavage domains with fine (10-50μm) ferroan dolomite rhombs replacing chlorite. In the most intensely altered samples, the majority of the rock is composed of fine-grained ankerite together with quartz and albite ± sericite ± chlorite, and cleavage domains are largely obliterated (Plate 7.2e,f). Estimates of bulk mineralogy using major element geochemistry indicate that the ankerite rich samples comprise 55-62wt% ankerite (equivalent to vol%), 10-20% quartz, 5-26% albite and up to 13% sericite. Bulk X-ray diffraction analyses confirm that in most cases ankerite is the only carbonate phase. Chlorite has not been identified in the most altered samples due to its complete replacement by ankerite. The more weakly carbonatised samples (TMS 001 & 031) also contain minor amounts (5-10%) of calcite. Separation of clay fractions (<2μm) for XRD analysis generally produced very poor returns owing to the very low chlorite and sericite abundances, thus confirming their widespread

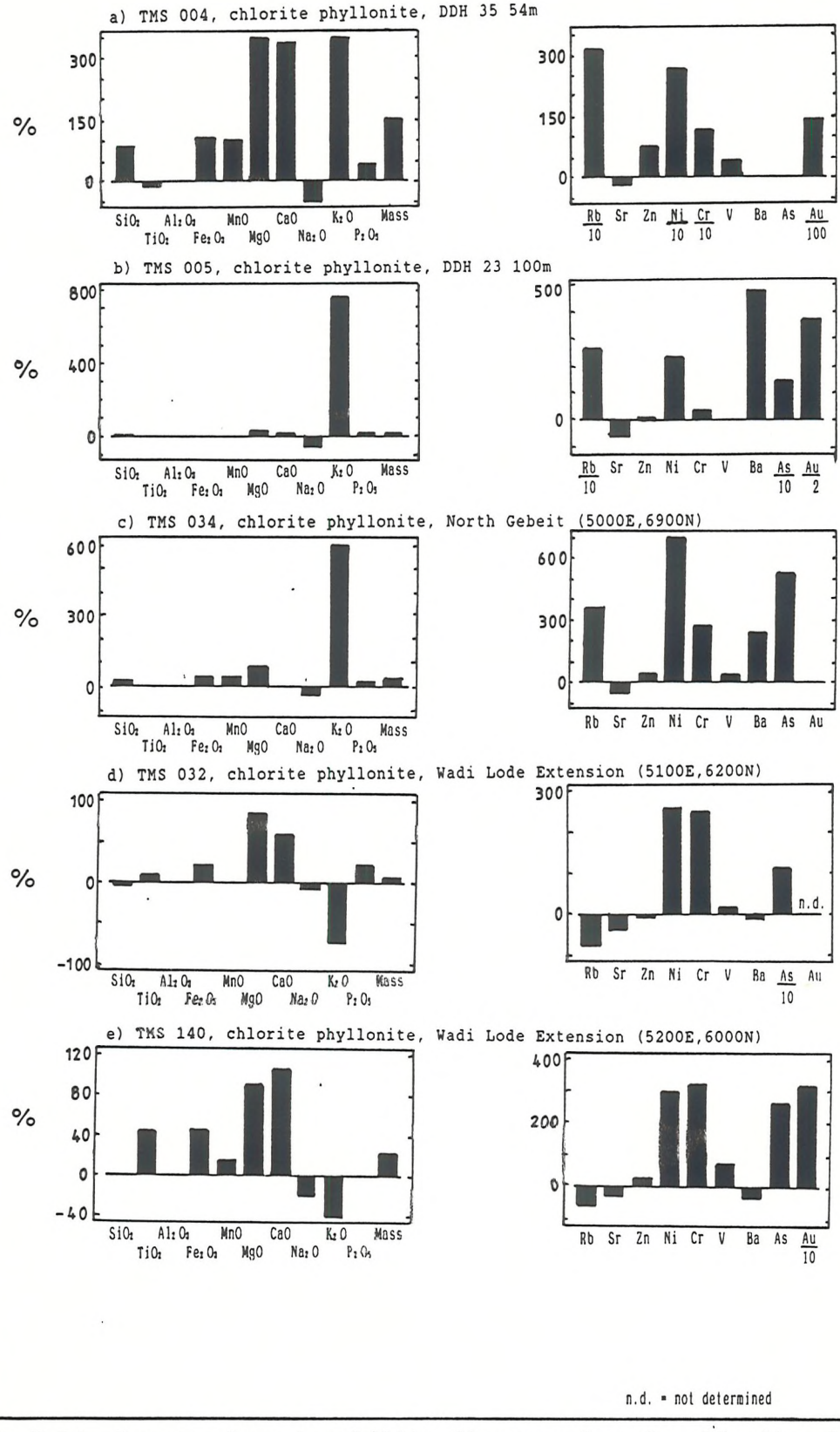

Fig.7.14 Isocon element mobility diagrams for the chlorite phyllonites showing variation of major and minor elements as a % change relative to the unaltered reference sample.

Plate 7.2 Petrography and textures from the chlorite and ankerite phyllonites.

a) Chlorite-calcite phyllonite derived from sheared andesitic lapillistone at the margins of the Wadi Tuwiya shear zone (5000E,6900N).

b) Ankerite phyllonite showing partial replacement of phyllonite fabric, Wadi Lode Extension (5200E,6000N).

c) Blocky, cohesive ankerite phyllonite showing near-complete replacement of phyllonite S_2 foliation with only minor traces remaining, Bishops Dam (4300E,6500N).

d-f) Photomicrographs (CN) of chlorite-(d) and ankerite-phyllonites from the Wadi Lode shear zone showing progressive replacement of chlorite foliation to produce a blocky cohesive ankerite rich lithotype (field of view = 2.5mm)

CN = crossed Nicols, PPL = plane-polarised light.

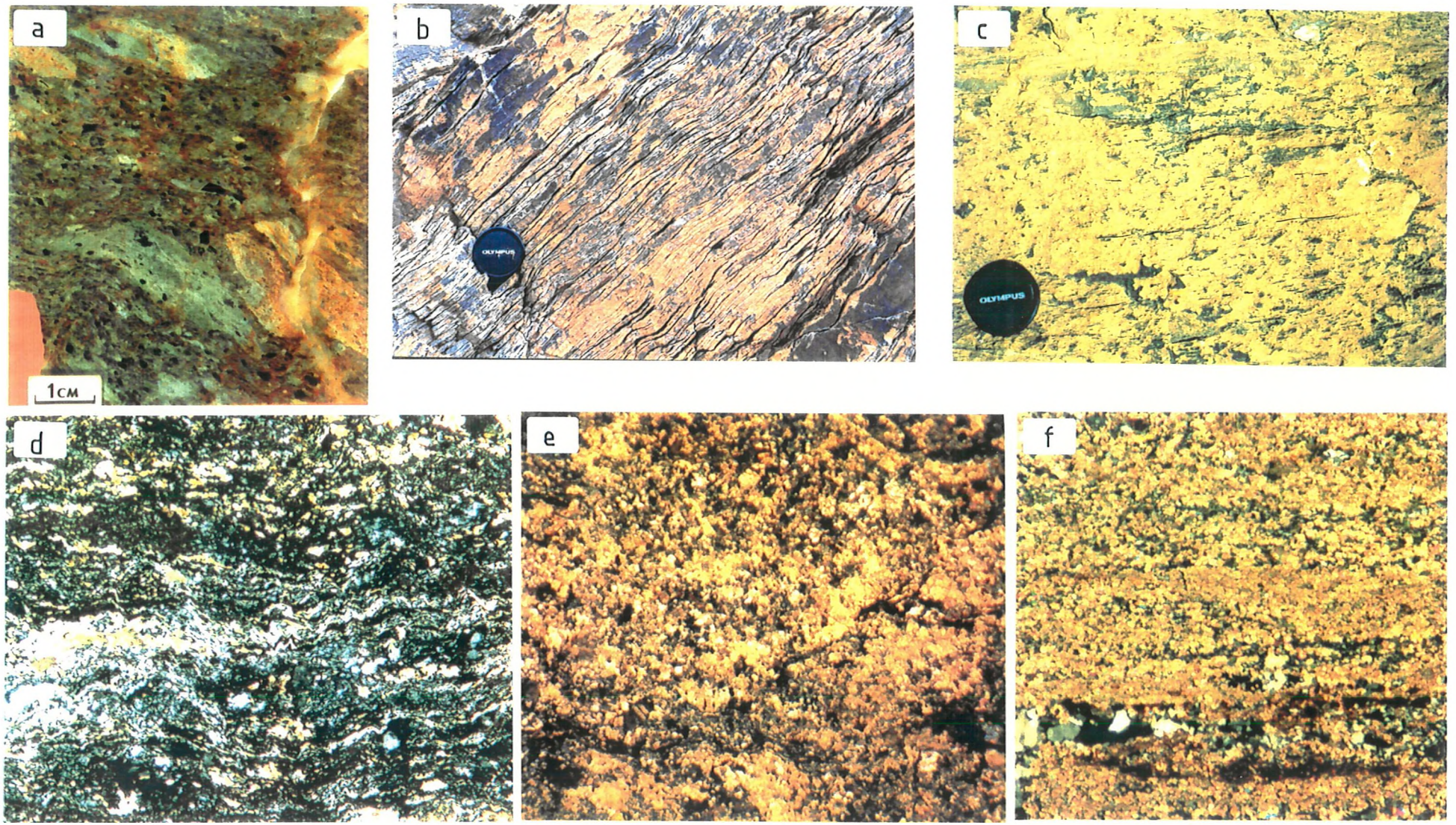
a
1см
b
c
d
e
f

replacement by ankerite and albite. Electron microprobe studies of relict chlorite grains show that they are of the same composition as the lode profile chlorite (Table 7.9a) with Fe/(Fe+Mg) ratios of 0.42-0.47 but total Al (4.6-4.8) intermediate between that of the lode profile chlorite (4.9-5.4) and the chlorite phyllonites (4.0-4.6). However, in contrast to the other chlorites analysed, the chlorites in ankerite phyllonites contain significant amounts of Cr up to 2.5%. Sericite analyses from the same samples also contain high Cr contents (1-2%) together with 2-4% Fe and Mg (Table 7.10). Nonetheless, the Fe/(Fe+Mg) ratios (0.25-0.36) of the sericite are much lower than for the chlorites, suggesting they may not have been coeval. All carbonate phases analysed are ferroan dolomites (Table 7.11) with just above the minimum 20% Fe to be classified as ankerite (Deer et al.,1966). Fe/(Fe+Mg) ratios of 0.21-0.36 are in the same range as the sericites, indicating that they were in equilibrium during formation and suggesting that ankerite and sericite were produced from the interaction of foliation chlorites and a CO_2-rich fluid. In most samples, sericite is replaced by secondary albite and the depletion of hydrous phases in this assemblage is in direct contrast to the hydration reactions observed in the lode profile assemblages.

Six samples of pervasively altered ankerite-rich phyllonite, from both the Wadi Lode and Wadi Tuwiya shear zones, were analysed for major and minor elements and the data subsequently plotted on isocon diagrams. All isocons show a wide displacement of points from the line of constant mass (slope=1) regardless of the reference sample used and indicate large mass/volume increases (Fig.7.15a). Using the end members of the compositional range (i.e. 61% ankerite, 9% quartz, 26% albite or 62% ankerite, 21% quartz, 13% sericite), calculated specific gravities of this lithotype vary from 2.72 to 2.77. As the quartz-albite-chlorite-calcite-sericite assemblage potentially has the lowest specific gravity of any of the observed mineral associations, the maximum difference between mass change defined by the isocon and estimates of volume change during this phase of alteration is calculated at ±4% (2.67/2.77; see section 7.5.1). Thus, as the total mass changes are relatively large, they also approximate to the total volume change.

There is comparatively little variation in the immobile trace elements Zr, Nb, Y, and TiO_2, and discrimination plots of the ankerite phyllonites are congruent with those of unaltered Gebeit Volcanic Group (Fig.7.16), indicating that the diverse geochemistry is not due to

	Ankerite phyllonite						Chlorite phyllonite		
a) Sample	PTMS 038	PTMS 034	PTMS 043	PTMS 037	PTMS 044	PTMS 036	b) PTMS 035	PTMS 033	PTMS 042
Mg	.7454	.7121	.7391	.6849	.7480	.7172	.0121	.0109	.0000
Fe	.2167	.2782	.2298	.3287	.2219	.2140	.0105	.0071	.0026
Mn	.0075	.0053	.0063	.0022	.0055	.0252	.0121	.0065	.0144
Ca	1.0302	1.0043	1.0246	.9839	1.0243	1.0434	1.9653	1.9753	1.9829
Fe/Fe+Mg	.2250	.2910	.2370	.3240	.2290	.2300	.5000	.3950	
Mg	.7512	.7589	.7382	.6715	.7429		.0227		
Fe	.2225	.2363	.2704	.3329	.2611		.0173		
Mn	.0091	.0081	.0052	.0030	.0052		.0139		
Ca	1.0171	.9965	.9860	.9923	.9906		1.9459		
Fe/Fe+Mg	.2280	.2370	.2680	.3310	.2600		.4330		
Mg		.7893	.7153				.0204		
Fe		.2059	.2515				.0103		
Mn		.0067	.0059				.0067		
Ca		.9979	1.0271				1.9625		
Fe/Fe+Mg		.2070	.2600				.3350		
Mg		.6141						Mg avge.	.0165
Fe		.3392						Fe avge.	.0113
Mn		.0122						Mn avge.	.0098
Ca		1.0344						Ca avge.	1.9623
Fe/Fe+Mg		.3560						Fe/Fe+Mg	.4158

Ankerite	
Mg avge.	.7239
Fe avge.	.2612
Mn avge.	.0063
Ca avge.	1.0084
Fe/Fe+Mg	.2648

Table 7.11 Carbonate compositions determined by electron micro-probe analyses of ankerite phyllonite (a; $Ca(Mg,Fe,Mn)(CO_3)_2$) and chlorite-calcite phyllonite (b; $Ca_2(CO_3)_2$).

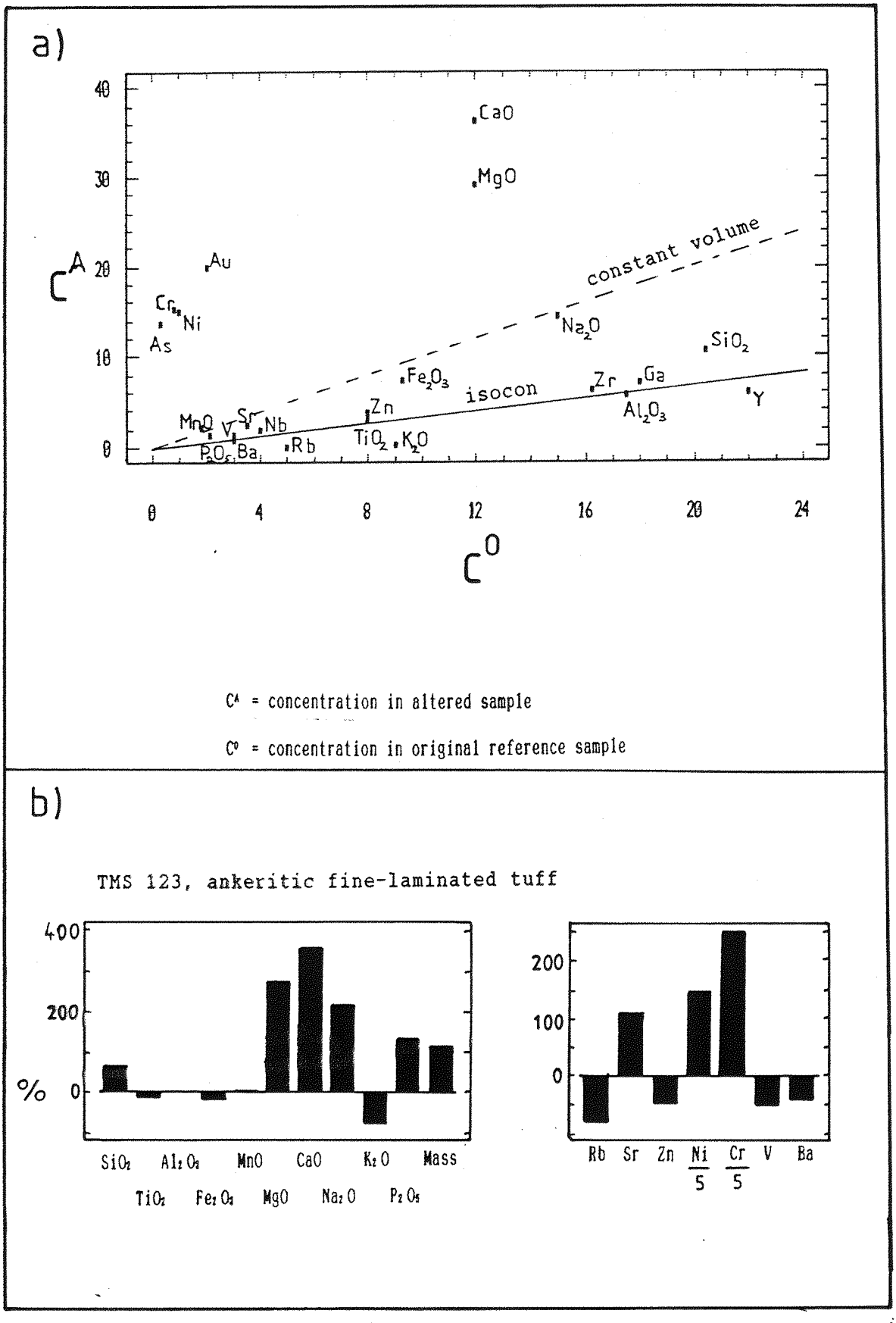

Fig.7.15 a) Isocon plot of an ankerite phyllonite (TMS 098) showing significant element mobility and increase in volume.

b) Isocon element mobility diagram for an ankerite altered fine-laminated tuff sampled from the footwall of the Wadi Tuwiya shear zone.

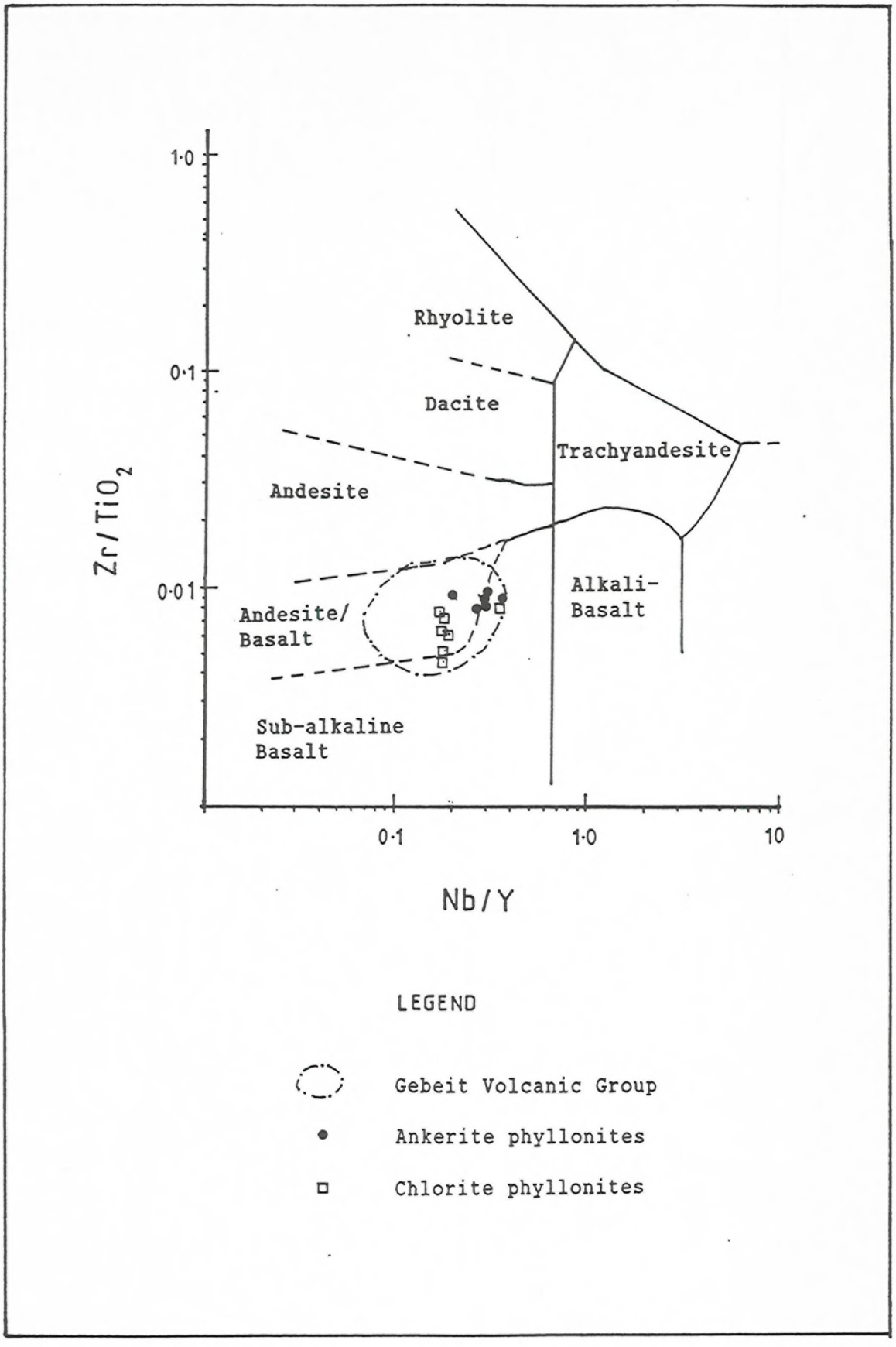

Fig.7.16 Zr/TiO_2 vs. Nb/Y discrimination diagram (after Winchester & Floyd,1977) showing the compositions of the volcanic protoliths of the ankerite and chlorite phyllonites relative to the Gebeit Volcanic Group.

preferential shearing of a geochemically anomalous lithology, e.g. an ultrabasic unit.

Variation in the degree of volume change and element enrichment in the sample set (Fig.7.17) displays the scale of element mobility during progressive carbonate alteration. With increasing volume, there is progressive enrichment of CaO (500-970%), MgO (200-750%), MnO (50-280%), and Na_2O (-20% to 200%). The sample with the highest volume increase (TMS 119), however, shows an anomalous enrichment in K_2O and depletion in Na_2O along with increases in Rb and Ba. Neither albite nor sericite are evident from XRD analysis, and so the anomalous K_2O may be due to localised enrichment from cross-cutting V_4 veins or later sericitic alteration of relict albite. This suggests that the albitic alteration may not have been synchronous with the CO_2 alteration. Sample TMS 098, which exhibits the greatest enrichment in Na_2O (200%) and the strongest depletion in K_2O (-90%), has very low contents of sericite and chlorite and contains high levels of Sb (262 ppm). With increasing CaO and MgO, Sr, Zn, V, and Ba are enriched together with depletion in Rb. The largest element increases, however, are displayed by Cr (1500-6500%), Ni (1000-4150%) and As which is concentrated up to 425x background. P_2O_5, Fe_{tot} and SiO_2 are enriched in all samples to the same degree. Although Cu contents are highly variable in the unaltered volcanics (30-80ppm), similar and higher values (50-120ppm) occur in the chlorite and ankerite phyllonites. As large volume increases would deplete immobile phases, Cu is evidently enriched in these lithotypes and the most common sulphide observed in the ankerite phyllonites is chalcopyrite.

A further sample of ankeritic finely laminated tuffs was taken from the thrust window at the southern margin of the Wadi Tuwiya shear zone (4500E,6600N). Although original sedimentary lamination is still evident, it displays the geochemical trends observed in the ankerite phyllonites together with a volume increase of 120% (Fig.7.15b). This indicates that outside the Riedel shears, localisation of ankeritic metasomatism was chiefly controlled by proximity to these Reidel shear zones and to a much lesser degree the extent of fabric development. The Reidel shears must, therefore, have also controlled the introduction of the CO_2-rich fluids.

Volume increases vary from 100-250% but consistent Al:Zr ratios across the alteration spectrum confirm Al immobility with only low alumina contents of 5.0-8.5% evident. The ankerite-rich phyllonites have comparable CaO values to the most calcite-rich rocks which occur

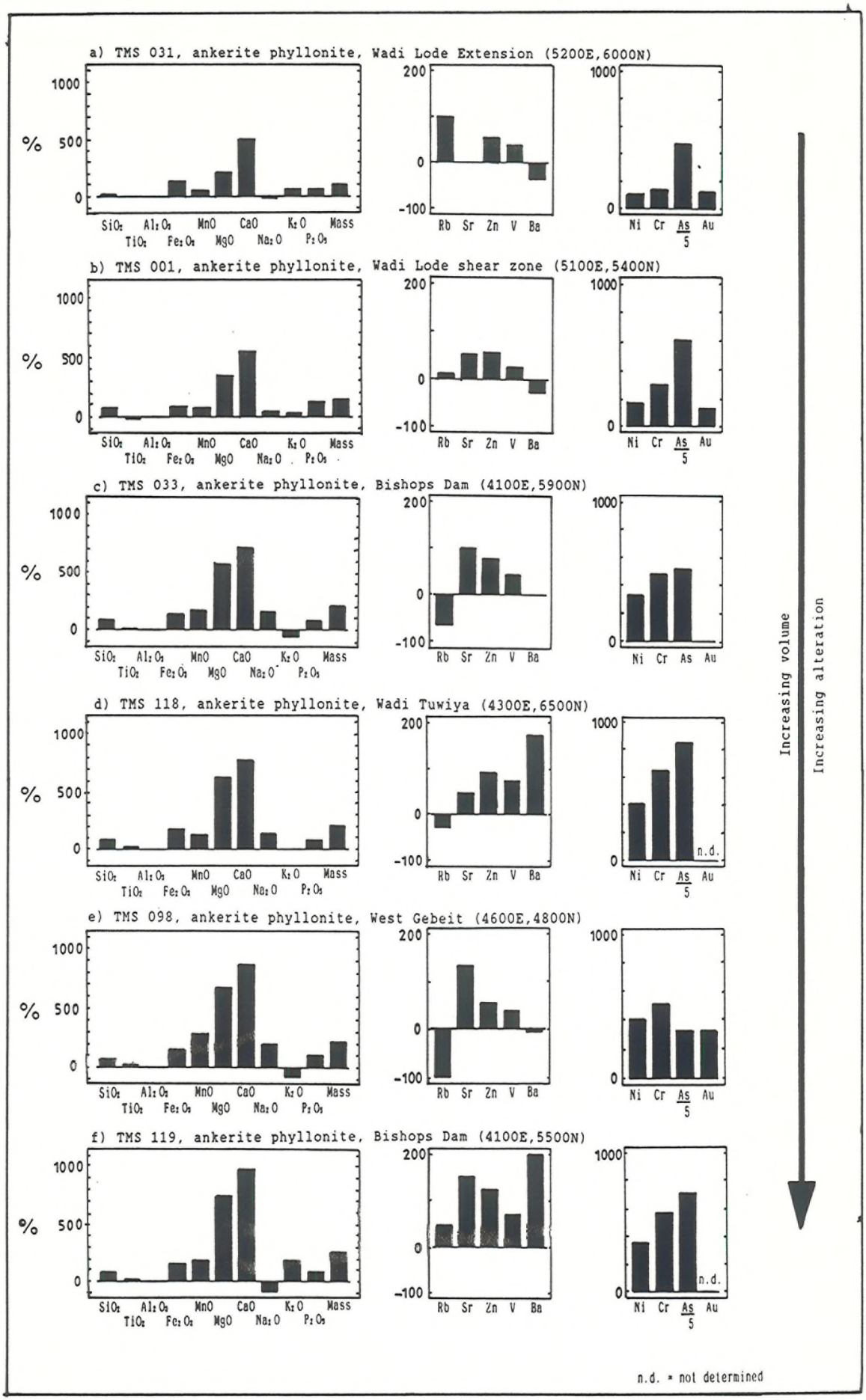

Fig.7.17 Isocon element mobility diagrams for the ankerite phyllonites displayed in order of increasing volume change and alteration showing variation of major and minor elements as a % change relative to the unaltered reference sample.

on the periphery of the main shear zones but show significantly higher loss on ignition values (22-27%) indicative of substantially larger volumes of CO_2.

The Wadi Lode shear zone, which is approximately 2000m long by 150m wide, is bounded at both ends by major shear zones (Wadi Gebeit and Wadi East Gebeit) and, as a Riedel shear, lies sub-perpendicular to the regional extension direction. As the average volume increase of the ankerite phyllonites is around 200%, a minimum extension of 100m, increasing from 50m to 150m, is anticipated across the zone. In addition, the cross-sectional area of the shear zone parallel to strike has then increased from $1x10^5$ to $3x10^5$ m^2, equivalent to an addition of $2x10^5$ m^3 of rock per m depth. With a specific gravity of 2.7 (2700 kg m^{-3}) this equates to an increase of $54x10^6$ tonnes of rock per 100m depth. Calculations of the relative abundances of the enriched components indicate that CO_2 comprises approximately 40% of the total added mass, i.e. $21.6x10^6$ tonnes per 100m depth, amounting to a minimum volume of 0.2km^3 CO_2.

XRD analyses of the phase 1 microdiorite dykes which intrude the Riedel shear zones show varying degrees of minor alteration with, in some cases, the replacement of chlorite and biotite by ankerite as well as calcite (TMS 019, 092, 101, & 112), indicating emplacement prior to or synchronous with carbonate alteration. Petrographic studies of these incipiently altered dykes show little apparent volume change, an observation which is supported by the lack of any depletion in Al, Zr or Ti, suggesting that the dykes remained relatively impervious to the hydrothermal fluids compared to the phyllonites. Many dykes and ankerite phyllonites contain cross-cutting quartz-albite veinlets, some of which have thin alteration haloes 10-30mm wide. These haloes show replacement of altered groundmass plagioclase grains by unsericitised albite and indicates that part or all of the Na_2O enrichment in the ankerite phyllonites may have been secondary. This later Na_2O enrichment may represent redeposition of leached Na_2O derived from altered wallrocks lower in the crust and transported by residual ore fluids depleted in K_2O and relatively Na_2O-rich (see 8.4.3).

7.8 Gold Grade Distribution

In current models of Archaean lode gold deposits (e.g. Phillips, 1985; Kerrich,1986a), pervasive carbonatisation is associated with gold mineralisation with economic grades centred on the ankeritic zones

representing maximum CO_2 alteration (Phillips & Brown,1987). At Gebeit, however, though the mineralised zones are located symmetrically around a central ankerite-bearing shear zone, economic gold grades are restricted to the V_1 blue quartz veins in calcite-rich marginal areas. 30 samples taken throughout the alteration spectrum were sent to Anamet Services (Bristol) for background gold analysis (Appendix A). The aims were to determine background gold grades for the unaltered volcanics and to identify whether there is any disseminated auriferous mineralisation associated with the ankeritic alteration.

Samples of unaltered volcanics taken from drillcore all show low Au abundances, ranging from <1 to 7 ppb (n=9), with the majority of samples (n=5) containing <1 ppb to produce an average background concentration of ≤2 ppb (Table 7.12). The more altered, sheared andesites and chlorite-calcite phyllonites display a wide range of values from background concentrations (TMS 034,& 149) to much higher, anomalous levels of 15-153 ppb. Altered footwall shale and hornblende-phyric andesite samples taken 2-3m from the Wadi Lode (4 Level) show similar enrichment of 54-57 ppb Au. Replicate analyses (Table 7.12) of two of the above samples showed wide variations from <1-57 ppb (TMS 011) and 60-153 ppb (TMS 004) in the chlorite phyllonites and lode footwall andesites, indicating heterogenous distribution of fine sulphide-hosted gold.

Anomalous and high grades from carbonate-deficient samples adjacent to the Wadi Lode (TMS 011) and at Vein 18, Vein 13 and Marble Bar (see section 7.6.1), confirm that auriferous mineralisation is not directly associated with carbonate alteration. Analyses of the ankerite-phyllonites show background to anomalous Au concentrations of <1-20 ppb. Because of the large volume increase associated with this lithology, either this gold enrichment was synchronous with carbonate alteration or pre-dated the alteration and has been significantly diluted. As the chlorite-calcite phyllonites contain up to 153 ppb Au, enrichment during early shearing prior to carbonatisation is feasible.

Two samples of microdiorite dykes, emplaced along the Wadi Lode shear zone during the same interval of D_2 deformation as the auriferous mineralisation, yielded Au values of 1 and 9 ppb with the higher value occurring in an ankerite-bearing dyke. The low gold contents of the dykes eliminates them as a potential source of the gold.

Visible gold is common in the blue V_1 quartz veins, which can grade up to 2000 g/t Au, but has not been observed within the wallrock alteration haloes. However, gold distribution around veins and at the

Sample Description	Sample Location	Au (ppb)	As (ppm)	Geochemical Sample Number
Plagioclase-phyric tuff	DDH 22, 08m	<1	28	TMS 002
Hb-Cpx-phyric andesite	DDH 21, 130m	<1	8	TMS 003
Aphyric tuff	DDH 21, 21m	3	<7	TMS 006
Graphitic shale	DDH 34, 79m	<1	14	TMS 007
Laminated aphyric tuff	DDH 25, 110m	1	9	TMS 008
Hb-Cpx-phyric tuff	DDH 23, 130m	7	<7	TMS 009
Aphyric tuff	DDH 28, 98m	<1	20	TMS 010
Andesite debris flow	Garabein	5	<7	TMS 147
,, repeat	Garabein	<1	<7	TMS 147
Oxidised sulphidic phyllonite	Vein 18	6805	1588	TMS 134
,, repeat	Vein 18	6840	1588	TMS 134
Oxidised sulphidic phyllonite	Vein 13	520	2567	TMS 132
,, repeat	Vein 13	510	2567	TMS 132
Oxidised sulphidic phyllonite	Marble Bar N.	5200	816	TMS 136
Altered Hb-phyric andesite	DDH 28, 98m	24	18	TMS 013
Altered Hb-phyric andesite	DDH 26, 131m	<1	66	TMS 011
,, repeat	DDH 26, 131m	57	66	TMS 011
Graphitic shale	Wadi Lode 4L.	54	83	TMS 139
Ankerite phyllonite	Wadi Lode Extn.	13	261	TMS 001
Ankerite phyllonite	5200E,6000N	14	208	TMS 031
Ankerite phyllonite	4100E,5900N	<1	42	TMS 033
Ankerite phyllonite	West Gebeit	20	137	TMS 098
Chlorite phyllonite	DDH 35, 54m	153	<7	TMS 004
,, repeat	DDH 35, 54m	60	<7	TMS 004
Chlorite phyllonite	DDH 23, 100m	15	38	TMS 005
Chlorite phyllonite	5000E,6900N	<1	13	TMS 034
Chlorite phyllonite	5200E,6000N	8	60	TMS 140
Chlorite phyllonite	5000E,6900N	<1	9	TMS 149
Phase 1 diorite dyke	5100E,5500N	1	9	TMS 088
Phase 1 diorite dyke	Bishops Dam	9	25	TMS 092

Table 7.12 Summary of background gold analyses of main rock types at Gebeit comprising unaltered volcanics, altered wallrocks, ankerite and chlorite phyllonites and altered phase 1 diorite dykes. Analytical techniques are described in Appendix A.

satellite prospects indicates that auriferous mineralisation extends at sub-economic grades for several metres from vein intersections. Extensive trenching and sampling was carried out by Robertson Research and Greenwich Resources (1982-1990) across the shear zones parallel to the Wadi Lode and Wadi Tuwiya shear zones, especially in the prospect areas of East Gebeit (4900E,6000-6700N), Vein 18, Vein 13, Marble Bar, Arsenic Lode (5300E,5200N-5200E,5400N) and Southern Extension (5300E,5000N-5600E,4800N). These shear zones range from 10m to 40 m in width with varying degrees of foliation-parallel quartz and calcite veins developed as occasional thin stringers up to veins 5-30 m long and 5-30 cm wide. Gold grades tend to peak at 5-20 g/t at vein intersections but anomalous grades of 0.1-3.6 g/t generally occur across the whole shear horizon. At East Gebeit, samples of unaltered volcanics and cross-cutting dolerite dykes were consistently below 0.1 g/t Au.

Relative As and Au contents and concentration factors for the complete range of alteration and mineralisation (Table 7.13) show the broad correlation between As and Au, although, high As values do not imply economic Au grades and vice-versa (e.g. Arsenic Lode and lode profile 2). Au and As abundances in the economically mineralised zones show concentration factors of up to 5000x background for As and between 3000 (≈5 g/t) and $1x10^6$ (2000 g/t) for Au. Comparison with enrichment factors for the chlorite-calcite and ankerite phyllonites reflect a difference of at least one order of magnitude.

7.8.1 Supergene Alteration

The relict pre-Nubian oxidised weathering zone at Gebeit is variable in thickness and in places extends to 30m below the present ground surface (Fletcher,1985). Ore-grade material from the upper parts of the Y Lode, X Lode, A Lode and the satellite prospects is pervasively oxidised, producing a characteristic red-brown limonite/ hematite gossan in the shear zones hosting the V_1 veins. This contrasts with the sulphide-rich, unweathered rocks from the Wadi Lode, 80m below surface. Deep soil profiles are developed in the area and widespread gold values indicate that gold has been transported for a considerable distance within the soil horizon (Fletcher,1985). Percolating ground waters appear to have preferentially altered the intricate shear zone network, so increasing maximum weathering depths. The oxidised lodes are consequently amenable to heap leaching and

Rock Type	As		Au	
	Range (ppm)	CF	Range (ppb)	CF
Lode profile 1	11-11639	10-5000	400-18100	200-9000
Lode Profile 2	16-500	10-150	$0.1\text{-}1.15\times10^5$	$300\text{-}6\times10^4$
Wadi Lode	116-7374	38-4400	avge. 3×10^4 max. 2×10^6	1.5×10^4 1.0×10^6
Arsenic Lode	up to 2400	1000	$0.2\text{-}10\times10^4$	2-5000
V13, V18, M.B.	816-2567	258-800	520-6800	245-3089
Shales	83-500	20-150	54-3300	15-920
Chl-phylls.	<7-66	0-26	<1-153	0-203
Ank-phylls.	42-363	51-426	<1-20	0-32

Table 7.13 Arsenic (As) and gold (Au) contents of alteration facies lithotypes and their relative concentration factors (CF) expressed as a multiple of background abundances.

provided the focus of early mining activity.

Auriferous vein material sampled within the oxidation zone often displays gold intimately intergrown with scorodite ($8[FeAsO_4.2H_2O]$), a hydrated iron-arsenic oxide developed after arsenopyrite (Robertson Research,1983). The green alteration colour associated with oxidation to scorodite can easily be confused with malachite staining; however, chalcopyrite is only rarely observed in V_1 quartz veins. As the bulk of free gold occurs in zones of deformed quartz or on the margins of calcite-filled fractures, gold on freshly broken vein material commonly coats fracture surfaces. In highly oxidised specimens, leaching of the calcite from auriferous fractures generally produces a vuggy texture in the ore. Intense leaching of outcrop vein samples may readily liberate any free gold and could account for slightly lower grades encountered in some of the V_1 surface veins. This would in addition enhance eluvial and colluvial deposits which have been extensively exploited at Gebeit by Pharonic activity. Deep weathering has given rise to zones of secondary enrichment at several prospects in the Northern Red Sea Hills e.g. Um Nabardi close to the Nile (Fletcher,1985). High gold grades have been recorded from the upper old mine levels at Gebeit (Robertson Research,1983) but there is no evidence for a discrete enrichment blanket.

7.9 Summary of Wallrock Alteration

At Gebeit the high strain zones are delineated by chlorite-phyllonite shear zones. Some of these shear zones host the auriferous V_1 blue quartz veins and display intense wallrock alteration. These shear zones lie adjacent and parallel to the main Wadi Lode and Wadi Tuwiya Riedel shear zones (see Figs.6.11 & 8.6). However, the phyllonites which form the main Riedel shear zones (i.e. Wadi Lode and Wadi Tuwiya) have been intensively carbonatised, resulting in a cohesive, blocky, ankerite-rich rock type. Mineralogical and geochemical studies of the various types of alteration have permitted characterisation of the alteration envelopes and fluids:

i) wallrock alteration adjacent to the veins comprises quartz, chlorite, sericite, calcite and albite. Albite is pervasively sericitised and chlorite is relatively abundant together with highly variable calcite contents (-80% to +200%) Quartz is depleted in the wallrock but forms the majority of veins and stringers.

ii) Wallrock bleaching due to finely intergrown chlorite, sericite, and calcite, forms a thin 10-50 cm envelope around the veins and visible alteration extends up to 8m from the lode. The width of cryptic alteration haloes are variable but occur up to 25m from the lode intersection.

iii) Geochemically, wallrock alteration is marked by significant additions of K_2O, MgO, Fe_{tot}, Cr, Ni, As, Au, ± CaO and MnO with concomitant depletion of Na_2O and Sr. Volume changes are not large (±25%) except in the zones of pervasive vein development (+50% to +200%).

iv) Economic gold mineralisation represents gold enrichment of 10^3 to 10^6 and As concentration of 10^2 to 10^3 above background, accompanied by minor enrichment in Sb and Bi, with B confined to the veins.

v) The alteration assemblage is commonly overprinted by later CO_2-rich hydrothermal signatures associated with V_2 calcite-albite veins which were synchronous with D_2 shearing. Intense carbonate alteration which may represent an early, pre-mineralisation, CO_2-rich fluid phase is concentrated along the main Reidel shear zones. High CO_2 levels resulted in pervasive ankeritic metasomatism of the chlorite-sericite phyllonites.

vi) Volume changes associated with carbonate alteration average +200% and indicate extension across the Wadi Lode shear zone of about 100m. If the effects of extension across the Wadi Tuwiya and North Gebeit shear zones are considered together with the extension accompanying V_1-V_3 vein formation, the total extension across the 10km long Gebeit block is in the order of several hundred metres (≈+3%).

viii) Although fluid inclusion evidence indicates that the ore fluids were CO_2-H_2O-rich , the variation in chlorite-sericite-, ankerite-, and albite-dominated alteration assemblages is suggestive of two or more distinct fluids. However, stable isoptope evidence shows that fluid composition remained fairly constant throughout much of the deformation.

"Tectonic and Chemical Evolution of a Late Proterozoic Gold Deposit, Gebeit Mine, Northern Red Sea Hills, Sudan."

PART FIVE

SUMMARY, DISCUSSION, AND CONCLUSIONS

"Science is nothing but trained and organised common sense."

(T.H. Huxley; Collected Essays, iv,"The Method of Zadig")

Chapter 8

Discussion

8.1 Introduction

The magmatic, tectonic, and hydrothermal histories presented in the preceding chapters can now be integrated to produce an evolutionary model for the Gebeit deposit. The resulting model can be compared and contrasted to deposits of the Archaean and Phanerozoic and ultimately utilised as the basis for an exploration model for new prospects in the Northern Red Sea Hills and other similar terranes.

8.2 Magmatic and Tectonic Evolution of the Gebeit Area

The Gebeit Volcanic Group, which hosts the mineralisation at Gebeit, has been shown to comprise a shallowing-upward succession of basaltic andesite tuffs, flows and agglomerates, intercalated at the base with minor graphitic shales. All of these volcanic lithologies plot as oceanic, island arc rocks transitional between low-K tholeiite and calc-alkaline in affinity, suggesting that they formed part of the back-arc area of an immature, emergent arc, dated at 871-832Ma. The hornblende, chlorite, actinolite, calcite, albite, epidote, and magnetite mineral assemblage of the unaltered volcanics show that peak metamorphic grade reached lower greenschist facies.

Regional studies, based mainly in the Arabian Shield, indicate that the volcanic rocks of the Gebeit area formed the western edge of the late-Proterozoic, north-east-trending, Hijaz-Gebeit arc system, which was orientated parallel to both the Midyan-Northern Red Sea Hills arc system to the north and the Asir-Southern Red Sea Hills arc system to the south (see Figs. 2.11 & 2.15). These arc terranes were bounded to the east and west by north-south-trending terranes of continental affinity and of pre-Pan-African age. Suturing of these terranes culminated in the simultaneous collision of the northern arc terranes and the marginal continental terranes around 670-630Ma, resulting in a complex tectonic history.

At Gebeit, the earliest phase of accretion-related deformation, D_1, formed regional, upright, F_1 folds which imparted a strong north-east-trending structural grain to the basement (Fig.8.1a). The north-east trend and regional extent of these folds suggest that D_1 deformation accompanied early obduction and accretion of the central arc terranes. This deformation phase was followed by the main episode of D_2, dextral, strike-slip shearing (Fig.8.1b). The dextral strike-slip deformation was accommodated along regional, north-east-trending, brittle-ductile, phyllonite shear zones, subdividing the Gebeit Volcanic Group into a series of elongate tectonic blocks. Estimates of movement along one of these shears (Wadi Adarit) indicate a minimum displacement of ≈2km.

Post-obduction dextral shearing has been identified at Nakasib, along the Bi'r Umq-Port Sudan suture to the south of Gebeit and probably occurred to the north, in the Eastern Desert of Egypt, where extensive south-west-directed thrusting has been observed. Extrapolation of the accretion model of Stoeser and Camp (1985; see Fig.2.14) to the western Shield, suggests that the dextral deformation, which appears to have occurred throughout the northern arc terranes, was probably prompted by the onset of collision of the north-south-trending, marginal continental terranes with the north-east-trending island arcs (Fig.8.1). Protracted interaction between the arc terranes and the continental terranes produced a complex tectonic evolution of repeated north-west-directed folding and thrusting (arc-arc collision) and strike-slip deformation (arc-continent collision). Synchronous collision of the Mozambique Belt, the Pharusian-Dahomeyan Belt and the Nubian-Arabian Shield also appears to have produced dextral wrench faulting along the north-east-trending, reactivated Trans-African and Central African lineaments of central north Africa.

At Gebeit, the D_2 phyllonite shear zones are terminated to the south-west by north-west-trending, low-angle, thrust zones which separate the overlying Gebeit Volcanic Group from the Sasa Plain tuffaceous slate assemblages in the west. The Sasa Plain tuffaceous slates appear to represent the distal volcanogenic sediments derived from a north-south-trending marginal arc. Thus, the phyllonite shear zones at Gebeit, locally, represent the lateral ramps of south-west-directed thrusts. During D_2 shearing, secondary Riedel and P-shear zones, conforming to a dextral shear zone array, were developed across many of the tectonic blocks but were most pronounced in the Gebeit block. Subsequent intrusive magmatism and hydrothermal fluid flow were

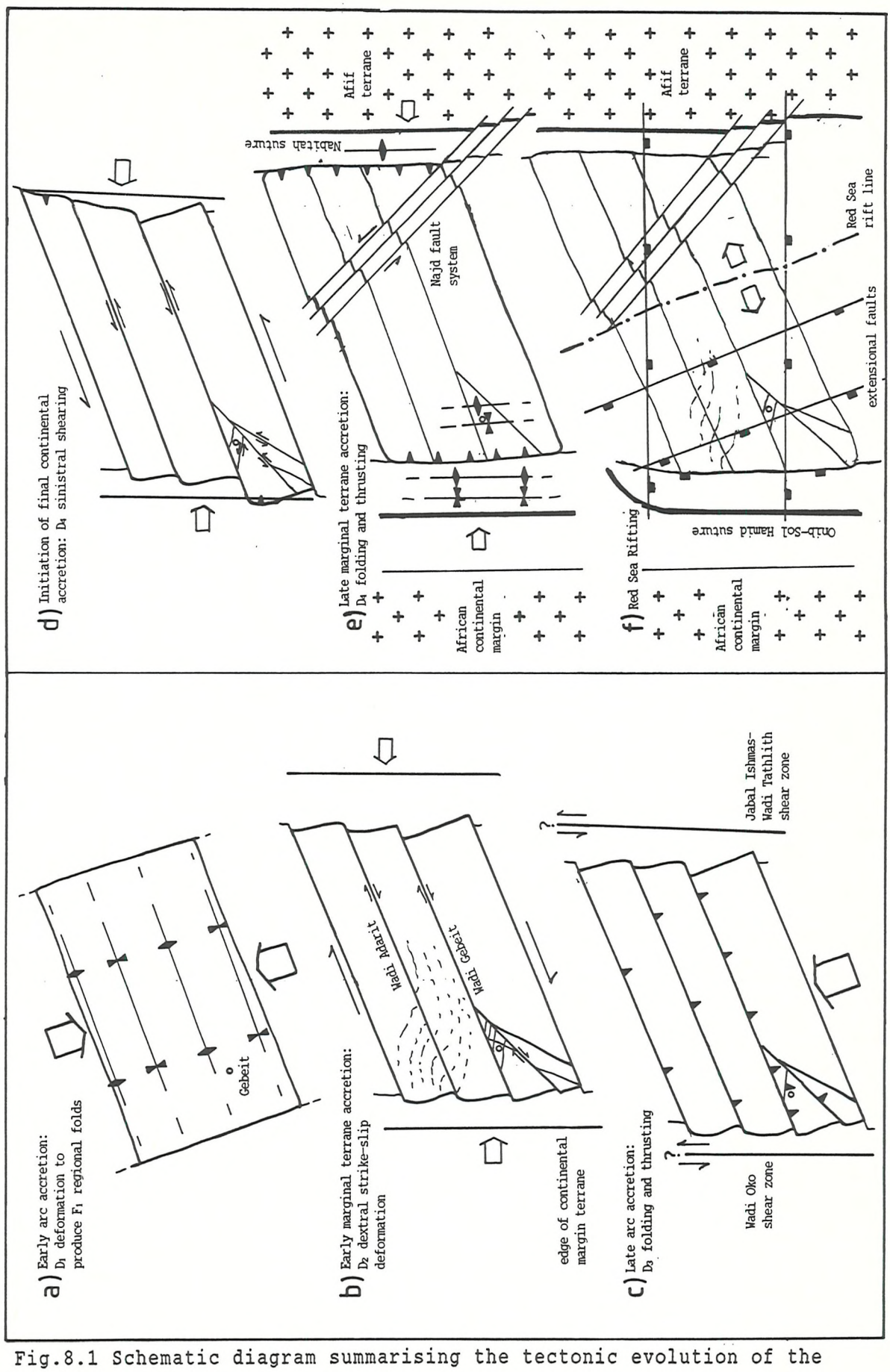

Fig.8.1 Schematic diagram summarising the tectonic evolution of the Gebeit-Hijaz arc terrane in the Northern Red Sea Hills, Sudan, and its relation to other terranes in the Nubian-Arabian Shield (see Fig.5.7; the size of the Gebeit block is exaggerated for clarity).

controlled and focussed mainly by the extensional Riedel shear zones.

The first phase of intrusive magmatism observed in the Gebeit block occurred during D_2 shearing. This produced a series of low-K, calc-alkaline dolerites, diorites, and tonalite dykes and stocks that were confined parallel to the fabric of the Riedel shear zones. Sheared, calc-alkaline, granodiorite intrusions to the north of Gebeit, at Wadi Messesana and Tikraneit, indicate that some intrusive magmatism pre-dated D_2 shearing. Emplacement of the phase 1 intrusions was followed by a phase of intense carbonatisation which was largely confined to the extensional Riedel and major block-bounding shear zones. This alteration appears to have pre-dated gold mineralisation, confining the thick V_1, auriferous, blue quartz veins to more minor shear zones adjacent to the ankeritic Riedel shear zones (see Fig.8.6). Replacement of epidote in the alteration zones indicate that the peak of metamorphism pre-dated the carbonatisation and mineralisation.

Late-D_2 dextral shearing was interrupted by a phase of north-west-directed, D_3 folding and thrusting which reactivated the main shear zones (Fig.8.1c) and fragmented the auriferous V_1 quartz lodes. The effects of D_3 deformation are not restricted to the Gebeit block and extensive north-west-directed thrusting has been observed in the Eastern Desert of Egypt. This deformation phase was probably due to the final stages of arc-arc collision and may be related to the post-obduction sinistral shearing, parallel to the plate boundary, along the north-south-trending Wadi Oko shear zone.

Late-D_3 deformation reverted to dextral strike-slip shearing, which again reactivated the shear zones and controlled the emplacement of the east-west-trending phase 2 dolerites. Geochemically, these dykes are transitional between calc-alkaline and within-plate magmatism and post-dated the V_1, vein-hosted, gold mineralisation. Late-D_3 structures also controlled the massive V_3 white quartz veins which cross-cut and lie parallel to the V_1 blue quartz veins.

The transition from D_3 to D_4 deformation was marked by a switch from dextral to sinistral strike-slip shearing along the D_2 shear zones (Fig.8.1d). During this phase of sinistral shearing, emplacement of the alkaline phase 3 dolerites and formation of the V_4 quartz-sericite veins was controlled by brittle reactivation of D_2 and D_3 structures. As with the D_3 strike-slip shearing, the D_4 shearing further fragmented the V_1-V_3 veins and phase 1 and phase 2 dykes.

The main phase of D_4 deformation, however, comprised NNW-trending folding and north-east-directed thrusting and was probably related to

the final stages of collision of the central arc terranes with the marginal continental terranes (Fig.8.1e). This final phase of accretion-related deformation folded the V_1 lode veins about NNW-trending upright antiforms and synforms, resulting in a sinuous lode outcrop pattern.

Approximately 100km west of Gebeit, the Abirkitib-Onib and Oko shear zones clearly mark a change in structural trends from north-east-trending arc-related structures to the tight, upright north-south-trending folding of the continental margin terranes to the west. A similar change to north-south-trending structures occurs on the eastern side of the Arabian Shield along the Nabitah suture. Gebeit occurs at the western margin of the arc terranes and it appears to lie in an interference zone where both arc and continental terrane accretion structures interact and are superimposed. The bulk of the deformation appears to have been accommodated by continental collision to the south along the Mozambique Belt, resulting in the preservation of the relatively weakly deformed central arc terranes of the Nubian-Arabian Shield.

Following cratonisation of the Nubian-Arabian Shield, the Gebeit area was regionally peneplaned and remained inactive until the Mesozoic when rifting commenced due to the break-up of Pangea. From ≈150-89Ma the Wadi Oko shear zone and the north-south-trending sections of some of the Gebeit shear zones were reactivated and intruded by alkaline trachyte dykes of lamproitic affinity. Reactivation of the Wadi Oko shear zone also controlled the sedimentation of the continental sheet sandstones of the Nubian Formation within north-south-trending graben. Subsequent phases of rifting at Gebeit produced normal faulting and joints on north-west and east-west trends (Fig.8.1f). The north-west faults and joint surfaces were generally infilled by coarse drusy carbonates. Extensive development of carbonate calcretes along wadi bases and fault surfaces suggests that the carbonates have been locally remobilised from the alteration assemblages. The east-west faults are post-Nubian in age and many extend to the Red Sea coast. These faults contain the phase 4 undersaturated, analcime-olivine dolerites which transect all other structures and may be ≈30Ma in age.

8.3 Fluid Evolution

Although the mineralisation at Gebeit is largely restricted to the rocks of the lower half of the stratigraphic succession, the

confinement of mineralisation to shear zone-hosted quartz veins and the low background gold contents of the unaltered host rocks (<7ppb) indicate an epigenetic origin. At Gebeit, five phases of veining synchronous with accretion-related deformation have been identified based on structural and petrographic criteria. Variation in the degree and type of alteration exhibited by the wallrock alteration profiles and the ankerite phyllonites initially suggests that fluid composition changed during terrane accretion.

The first phase of alteration observed within the Gebeit block resulted in the intense and pervasive carbonatisation of the main chlorite phyllonite shear zones. The replacement of virtually all the chlorite by ankerite is indicative of a CO_2-rich fluid phase, and the removal of all hydrous phases (chlorite and sericite) contrasts with the mineral assemblages of the lode alteration profiles. Carbonate alteration is also common in the lode profiles and the V_1 veins but only calcite has been observed, indicating much lower amounts of CO_2 in the ore fluids. However, in the V_1 lode veins the fracture-hosted calcite appears to post-date the formation of the gold-quartz veins. In contrast to the Fe-carbonate association observed in many Archaean lode gold deposits, the lode veins at Gebeit are restricted to the margins of the main Riedel shears, outside the zones of ankerite metasomatism. Although the exact timing of the ankerite alteration cannot be defined, no significant quartz veining occurs along the centres of the main Riedel shears and suggests that this alteration pre-dated the gold-quartz mineralisation. The pervasive metasomatism of the chlorite fabric of the shear zone phyllonites by ankerite may have "sealed" the central Riedel shear zones and prompted the development of parallel, adjacent shears (see Fig.8.6). These later shears subsequently hosted the V_1, auriferous, blue quartz veins, confining economic mineralisation to ENE-trending zones parallel and adjacent to the carbonatised Riedel shear zones. Three further phases of quartz veining (V_3-V_5) during D_3 and D_4 deformation show that the complex tectonic evolution resulted in a protracted fluid history.

8.4 Gebeit Ore Fluid Characteristics

From the wallrock alteration, fluid inclusion, and oxygen isotope investigations in this study, the general parameters of the ore fluids at Gebeit can be assessed. In the lode profiles, the changes in the mineral assemblages with progressive redox reactions denoted by:

hornblende -> actinolite -> chlorite,
epidote -> chlorite + calcite, and
magnetite -> pyrite,

indicate a relatively reducing (low Eh) ore fluid. Fluid pH was buffered by wallrock alteration which resulted in sericitisation of albitic plagioclase. Fluid pH is difficult to determine but the predominance of sericite over plagioclase and kaolinite in the alteration assemblage suggests a neutral to slightly acidic pH (≈5.5-6.0; Montoya & Hemley,1975). The overprint of the regional greenschist facies assemblage by the alteration facies early in the deformation cycle indicates that mineralisation slightly post-dated peak metamorphism. Correlation with temperature estimates derived from fluid inclusion data at Wadi Messesana and Vein 18 suggests the ore fluids were low salinity, H_2O-CO_2 fluids at temperatures around 250-300°C. Correlation of fluid inclusion homogenisation temperatures with $\delta^{18}O$ isotope analyses of the lode veins suggest that $\delta^{18}O$ values of the fluids were in the region of +2.5 to +10‰. Vein and wallrock mineralogical and geochemical changes show that gold mineralisation is characterised by significant addition of K_2O (±Rb,Ba), MgO, Fe_{tot}, Cr, Ni, H_2O, CO_2, S, and As in the wall rocks with enrichment of SiO_2, CaO, and B in the veins. This was accompanied by considerable wallrock depletion of Na_2O and SiO_2.

8.4.1 Source of the Fluids

As a result of incomplete evidence and the varying styles of lode gold mineralisation in Zimbabwe, Australia and Canada, there has been a dichotomy of opinion on the origin of the mineralising fluids in Archaean lode gold deposits with workers divided between metamorphic dewatering fluids (e.g. Groves et al.,1984; Colvine et al.,1984; Phillips,1985) and magmatic fluids (e.g. Burrows et al.,1986). Compilation of exisiting data has reconciled the main features of the two fluid processes extant in Archaean deposits and resulted in a metamorphogenic model incorporating modification by a juvenile fluid component (Kerrich,1986b; Perring et al.,1987). The magmatic component has recently been attributed to the close association along major crustal structures of lode gold deposits and deep seated, gold-bearing lamprophyres (Rock et al.,1987; Rock & Groves,1988a,b; Wyman & Kerrich, 1988). The lamprophyre association satisfies the main problems related to a purely metamorphic fluid source (Kerrich,1986b) namely, the common

occurrence of mantle carbon isotope signatures and mineralisation which, in many cases, significantly post-dates the peak of metamorphism (i.e. lack of prograde metamorphism). Recent studies in Canada suggest that isotopically evolved, deep circulating meteoric fluids may be involved in the genesis of some Archaean mesothermal gold deposits (Nesbitt et al.,1986; Nesbitt,1988). These deposits appear to be restricted to the brittle regime and it is not known how efficient this process is within the brittle-ductile regime.

Oxygen isotope analyses of the V_1-V_4 quartz veins at Gebeit show that they all have relatively consistent quartz δO^{18} values of 14.0-15.6‰. Although the low salinity, CO_2-bearing fluid characteristics appear to be more typical of metamorphic fluids (see section 6.10.1), there is insufficient evidence to unequivocally determine whether the fluids are magmatic or metamorphic in origin. The timing of gold mineralisation (and carbonate alteration) is immediately pre-dated by the intrusion of the phase 1 dykes and post-dated by the emplacement of the transitional phase 2 dolerites. Although neither phase of magmatism is lamprophyric in character (i.e. enriched in K_2O, Ba, Rb, Sr, LREE, and Th), a parental lamprophyre source cannot be ruled out. These dykes are hosted by the same Riedel structures as the V_1 lode veins, indicating the association with major crustal structures. The close relationship between mineralisation and minor intrusions showing similar strong structural controls is also charactersitic of a large number of Archaean lode gold deposits (e.g. Hodgson & MacGeehan 1982; Foster,1984,1985, 1987; Colvine et al.,1984; Groves et al.,1987). Lamproite dykes are present at Gebeit but are likely to be Mesozoic in age.

8.4.2 Source of the Fluid Components and Fluid-Rock Access

The source of the gold and other elements enriched in the Gebeit lode alteration profiles cannot unequivocally be identified. Lateral secretion of material into veins from their enclosing wallrocks (Boyle, 1976) has been discounted for mesothermal lode gold deposits on several grounds (see Kerrich,1986b) and, given the low background gold contents of the unaltered Gebeit volcanics, has not been considered as a mechanism for the Gebeit mineralisation. Deep hydrothermal fluids in the crust are usually of low oxidation potential (Seward,1984,1988) and the mineralogy of the Gebeit alteration assemblages indicates that the ore fluids were relatively reducing, unlike the Archaean Hemlo deposit

in Ontario and the Kalgoorlie deposit in W.Australia (Cameron & Hattori,1985). The limited evidence at Gebeit suggests that the gold was probably derived by some form of metamorphic devolatilisation of the underlying arc volcanics and possibly modified by a magmatic component. Although the reduced alteration assemblages indicate that the gold was not derived by oxidative granulite metamorphism (Cameron & Hattori,1987; Cameron,1988,1989a, b,c), oxidising auriferous fluids are evident in some Archaean lode gold deposits (Foster,1985). The presence of graphite in the black carbonaceous shales may have locally reduced an otherwise moderately oxidised fluid (above the FMQ buffer).

Gold in unaltered calc-alkaline volcanics has been shown to be in neither the groundmass nor the phenocrysts but partitioned into tiny sulphide blebs (Bornhorst & Rose,1985). However, Henley (1986) has shown that gold-saturated ore fluids (≈10ppb Au) can be produced from fluid circulation through rocks with low gold contents, such as greywackes, and hence the source of the gold is largely irrelevant. The gold at Gebeit, therefore, has not necessarily been derived from special Au-enriched source rocks lower in the crust, although deep-seated lamprophyres with anomalously high gold contents may exist. However, lamporphyres also tend to be enriched in S, CO_2, LIL (large ion lithophile) elements and may account for the anomalous enrichment of Cr, Mg, and Ni associated with the Gebeit mineralisation.
Cr enrichment has been described from a few Archaean lode gold deposits (e.g. Golden Mile; Phillips,1985; Macassa Mine, Kirkland Lake and Lamaque Mine, Val d'Or, Canada, Kerrich, 1986a) but in many cases the deposits are hosted by or lie close to ultramafic rocks [e.g. in the Kerr Addison, Dome, and Hollinger mines, Canada (Kerrich,1986b); Kanowna in W.Australia (Groves et al.,1984); and Gaika, Zimbabwe (Viljoen,1984)]. Although there is no evidence for ultramafic rocks in the vicinity of Gebeit, high abundances of Mg (20.4 wt%), Cr (1440 ppm), and Ni (502 ppm) occur in the rare basal cumulate flows around Gebeit and may have been remobilised into the alteration profiles by the circulating hydrothermal fluids.

The confinement of the mineralised V_1 veins and their alteration assemblages to the Riedel shear zones indicates that fluid circulation at Gebeit was controlled and focussed by these structures (Fig.8.2). As with many lode gold deposits in Western Australia (Vearncombe et al.,1988; Barley et al., 1988; Eisenlohr et al.,1989), economic gold mineralisation is restricted to these subsidiary extensional Riedel shears. Although the north-east-trending regional ductile shear zones,

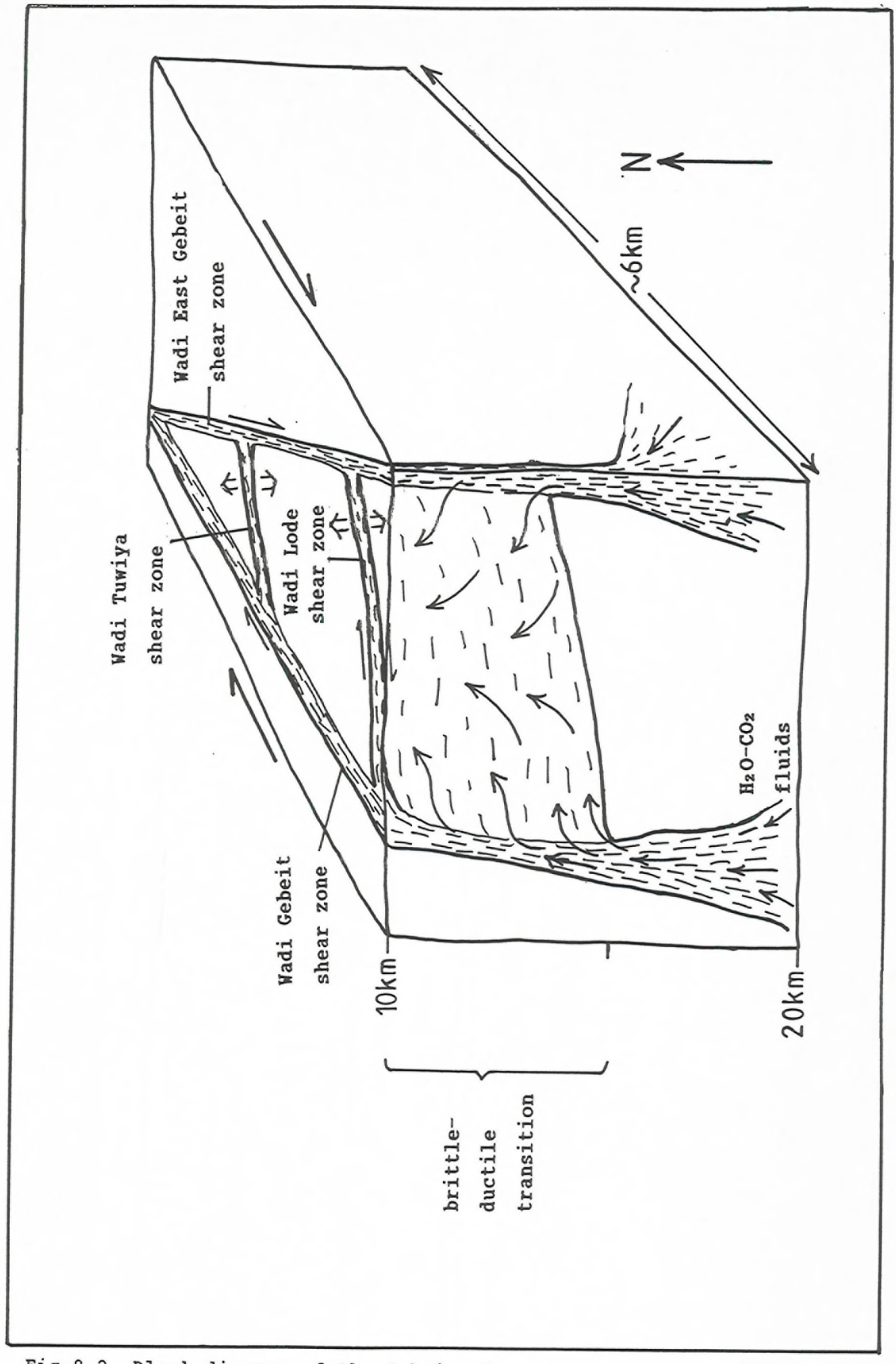

Fig.8.2 Block diagram of the Gebeit shear zone array showing the focussing of fluids from the major ductile shear zones into the second order extensional (Riedel) shear zones at the brittle-ductile transition (horizontal scale exaggerated).

such as Wadi Gebeit and Wadi Adarit, probably focussed hot fluids rising from the lower crust, they appear to be barren suggesting that physico-chemical gradients caused preferential fluid migration into the second order structures (Fig.8.2).

Due to the decrease in viscosity with depth, shear zones widen with depth towards the ductile regime (Sibson,1977) to a depth where temperature $>0.75T_m$ (T_m= melting temperature) and deformation is distributed throughout the rock (White & Baxter,1987). The permeable wedge-shaped profiles of these first order shear zones focus fluids from the upper mantle and lower crust. Fluid movement in the ductile regime is believed to be controlled along grain boundaries (White & White,1982) and/or micro-cracking and dilatation during deformation (Etheridge et al.,1983) and may act as a host to disseminated gold deposits (e.g. Golden Mile; Boulter et al.,1987). The change from quasi-plastic to brittle deformation is spread across the brittle-ductile transition zone due to the upward movement of ductile shearing as a result of fluid metasomatism and reaction softening.

Deformation textures in the phyllonite shear zones are predominantly ductile in nature but vein formation synchronous with deformation in the wallrock alteration profiles suggests that gold precipitation occurred at the brittle-ductile transition (as opposed to purely ductile) following lower greenschist facies peak metamorphism. Pressure estimates from fluid inclusions indicate ore fluid pressures of ≈2.5 to 4kb (equivalent to 10-15km depth) and are compatible with inclusion formation at the brittle-ductile transition. The antitaxial crack-seal textures observed in the V_1 veins suggest that fluid movement by seismic pumping (i.e. repeated fluid overpressuring and transient porosity; Sibson et al.,1975, 1988; Sibson, 1989) occurred along the Riedel shear zones due to enhanced fluid flow coupled with dilatation and fracturing.

8.4.3 Gold Transport and Precipitation Mechanisms

In nature, gold usually occurs in one of three oxidation states A° (native state), Au^+, and Au^{3+}. Due to their high oxidation potentials Au^+ and Au^{3+} are unstable in water and form complex ions, depending on the type and concentration of ligands available in aqueous fluids. The Au^+ ion is a "soft" electron acceptor and energetically is most likely to interact with "soft" donor ligands such as the hydrosulphide ligand, HS^-, which is exceptionally stable (Seward,1988). Up to temperatures

of 400°C, gold solubility mechanisms have been shown to be dominated by thiosulphide complexing (Au^{+} complexes; Seward,1973) but at higher temperatures are likely to be dominated by chloride complexes (Au^{3+} complexes; Henley,1973). Below 300°C, HS^{-} and H_2S ligands are the most abundant sulphur species, suggesting that gold transport occurs as bisulphide complexes. Maximum dissolution is achieved as the fluid pH approaches neutral (Fig.8.3; Seward, 1973,1979) and probable complexes have been identified as:

$$pH < N : Au(HS)^{\circ} \qquad (1)$$

$$pH = N : Au(HS)_2^{-} \qquad (2)$$

$$pH > N : Au(HS)_2S^{2-} \qquad (3)$$

A common and noticeable characteristic of mesothermal lode gold deposits is the very minor quantities of base metals which is in contrast to the base metal-rich volcanogenic massive sulphide deposits which usually contain little or no gold. This dichotomy is also evident in the distinction between base metal-rich and gold-rich epithermal deposits. This phenomenon was originally explained in terms of variations in fluid-rock ratios at the sites of metal leaching (Kerrich & Fryer,1981) but is now commonly attributed to differences in fluid salinities and ligands (Henley,1986). Base metal solubility is related to chloride complexing and is a direct function of salinity, i.e.

$$ZnS + 2H^{+} + 2Cl^{-} \rightarrow ZnCl_2 + H_2S \qquad (4)$$

whereas up to 400°C, gold solubility is a function of thiosulphide complexing and is independent of Cl^{-}, i.e.

$$Au + 2H_2S \rightarrow Au(HS)_2^{-} + H^{+} + 0.5H_2 \qquad (5)$$

At Gebeit, the estimated temperature range (250-300°C) and low salinity of the ore fluids suggest that bisulphide ligands were probably (but not certainly) the complexing agents for gold transport. This is supported by the broad association of gold with Fe-As-sulphides and the lack of any base metal enrichment. Enrichments of As and Sb associated with gold mineralisation indicate that arsenothio and, to a lesser degree, antimonothio complexes may have played an important role in gold transport:

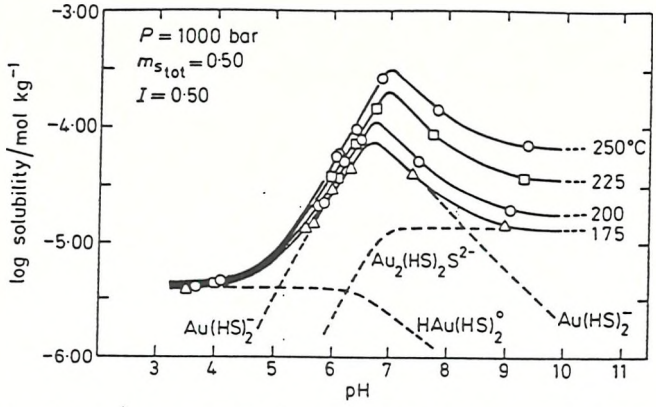

Fig.8.3 Plot of log solubility of gold in sulphide solutions as a function of temperature and pH (from Seward,1985).

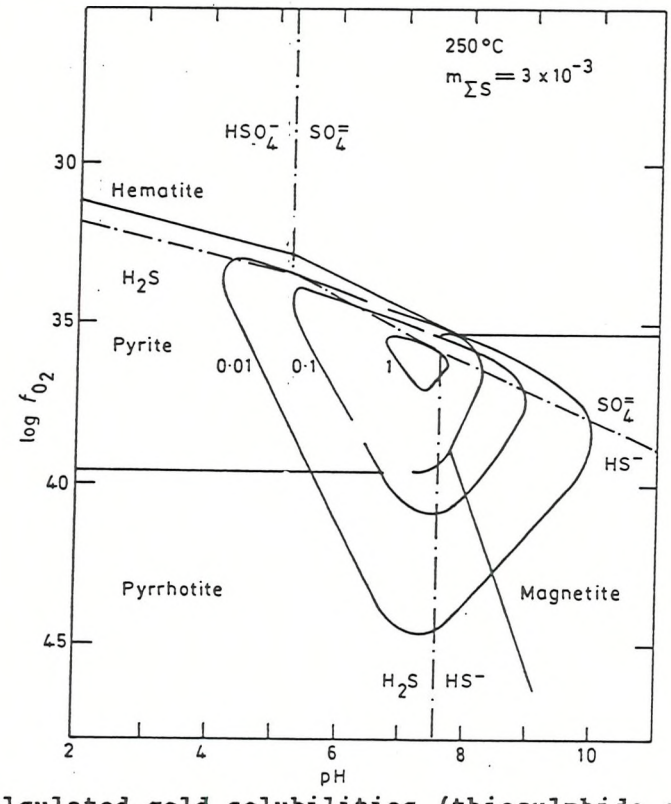

Fig.8.4 Calculated gold solubilities (thiosulphide complex $Au(HS)_2^-$) as a function of pH and fO_2 (contours in ppm) (from Seward,1973).

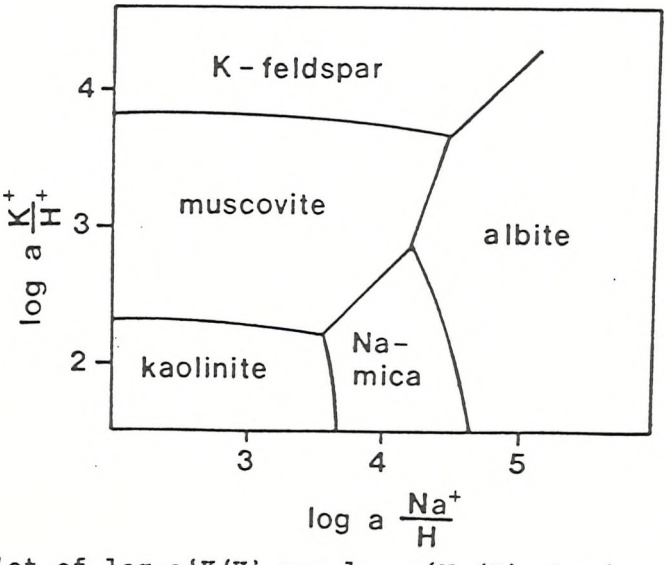

Fig.8.5 Plot of log a{K/H} vs. log a{Na/H} showing equlilibria relations for the sericitisation of albite during wallrock alteration. (from Montoya & Hemley,1975).

$$Au^{+} + As^{3+} + 3H_2S \rightarrow Au(AsS_3)^{2-} + 6H^{+} \quad (6)$$

$$Au^{+} + 2Sb^{3+} + 4H_2S \rightarrow Au(Sb_2S_4)^{-} + 8H^{+} \quad (7)$$

Wallrock enrichments in Cr, Ni, Fe, and Mg suggest that minor chloride complexing of these elements occurred but was not sufficient to produce base metal enrichments.

Gold transported as a thiosulphide complex should be precipitated in response to changes in T, P, Eh, pH, and decreasing activities of the bisulphide ligands (Fig.8.4; Seward,1973), however, simple cooling does not cause gold deposition (Seward,1988). Consistent $\delta^{18}O$ isotope signatures also preclude cooling and oxidation due to the interaction of cooler near surface meteoric waters. The auriferous veins show no evidence for significant decreases in pressure (e.g. extensive brecciation) and Seward (1973) has shown that a pressure decrease above 250°C leads to an increase in gold solubility. A pure H_2O fluid at 250 to 300°C will boil at 600-1200m depth and any increase in salinity tends to reduce the depth at which boiling occurs (Haas, 1971). Therefore, the estimates of pressure and temperature of the Gebeit fluids during deposition are too high for boiling to have occurred (i.e. separation into coexisting vapour and liquid phases) as seen in near-surface epithermal systems.

Gold deposition at Gebeit may have been initiated by any process which causes a reduction in the activity of the reduced sulphur species ($a\{H_2S\}$). Many lode gold deposits in Western Australia and Zimbabwe (Foster,1987) show a strong association with Fe-rich host rocks (i.e. tholeiitic basalts and BIF) and fluid-wallrock reaction is considered to be the main destabilising process (e.g. Phillips & Groves,1983; Groves et al.,1984; Neall & Phillips,1987; Groves,1988). These wallrock redox reactions produce iron sulphides from destabilised wallrock Fe-Mg silicates (e.g. chlorite, magnetite)

$$2Au(HS)_2^{-} + Fe^{2+} \rightarrow 2Au^{\circ} + FeS_2 + 2H_2S \quad (8)$$
(silicate) (sulphide)

which usually occur as a pyritic alteration zone seen with, or immediately adjacent to, the gold mineralisation in many mesothermal deposits (e.g. Phillips,1985). Wide-scale wallrock carbonatisation due to the presence of CO_2-rich fluids also commonly occurs and is volumetrically the most extensive and important wallrock reaction. In

mafic-hosted deposits, it represents the hydrolysis of amphibole to calcite and chlorite and, with further carbonatisation closer to the vein, to Fe-carbonate (ankerite; Phillips & Brown,1987):

$$3Ca_2(FeMg)_5Si_8O_{22}(OH)_2 + 6CO_2 + 7H_2O = 5(FeMg)_3Si_2O_5(OH)_4 + 6CaCO_3 + 14SiO_2 \quad (9)$$

(calcic amphibole) (chlorite-calcite)

$$(FeMg)_3Si_2O_5(OH)_4 + 3CaCO_3 + 3CO_2 = 3(FeMg)Ca(CO_3)_2 + 2SiO_2 + 2H_2O \quad (10)$$

(chlorite-calcite) (ankerite)

Fluid pH during mineralisation is buffered by alteration of host rock feldspar, and lower fluid Na/H ratios commonly result in sericitisation (Fig.8.5) or, in cases of high a{K/H} in basic lithologies, biotite. This reflects the high fluid K/Na ratio observed in many lode gold deposits (≈0.1; Kerrich,1986a).

This characteristic alteration of carbonatisation, sulphidation and sericitisation, common to the majority of mesothermal lode gold deposits, is evident at Gebeit but with several differences. Firstly, the zones of ankerite metasomatism do not envelop the lode veins but occur along the centres of the main Riedel shears (Wadi Lode, Wadi Tuwiya, and North Gebeit shear zones) with the auriferous veins restricted to adjacent, calcite-rich shear zones (see Fig.8.6). Carbonate alteration haloes <u>do</u> occur around most of the V_1 veins but calcite is the dominant phase, indicating that the zones of gold enrichment are not congruent with the zones of most intense CO_2 metasomatism. In all lode profile samples studied, there was no evidence of replacement of wallrock chlorite by ankerite but there was a decrease in the Fe/Fe+Mg ratio of chlorite towards the lode intersection, suggesting incorporation of chlorite-Fe into wallrock Fe-sulphides.

Secondly, unlike many Archaean deposits where gold mineralisation occurs in the sulphidised zones, the lode alteration profiles show that the bulk of the calcite and sulphides occur in the altered wallrocks whereas gold and tourmaline are restricted to the lode quartz veins. The majority of the gold grains observed in this study occur in sulphide-poor quartz, often at the margins of fractures infilled by late calcite. This may, in part, be due to the preferential formation of fractures towards and away from ductile gold grains hosted by a brittle quartz matrix during deformation of the V_1 lode veins. Much of the gold that is associated with vein sulphides appears to occur on the

sulphide surfaces and is not intergrown with the sulphides (see section 6.8.3). This has been attributed to the physical adsorption and reduction-driven chemisorption of the charged gold species to precipitate the native gold (Starling et al.,1989). This indicates that at Gebeit fluid-wallrock reaction occurred as a result of gold mineralisation and was not the main depositional mechanism.

Although the textural and structural evidence indicates that CO_2-rich fluids both pre-dated and post-dated auriferous mineralisation, oxygen isotope data for all the phases of quartz veining show that fluid compositions were fairly constant isotopically up to the end of the accretion-related deformation. The influx of an separate CO_2-rich fluid phase without modifying fluid isotopic signatures is difficult to account for unless the CO_2-rich phase was coeval but immiscible with the aqueous fluid phases. Fluid inclusion studies of lode quartz veins from Gebeit Mine and Wadi Messesana have shown coexisting CO_2-rich and H_2O-rich, low salinity fluids with congruent homogenisation temperatures. However, at the satellite prospects of Wadi Messesana and Marble Bar there is no associated carbonate alteration but at Marble Bar the V_1 vein lies parallel to a thick calcite vein. Although fluid inclusions indicate an H_2O-CO_2-rich fluid phase, the alteration patterns suggest that the fluid separated due to immiscibility into an H_2O-rich fluid and a CO_2-rich fluid which behaved as two discrete phases.

Most models for the formation of Archaean lode gold deposits invoke the focusing of H_2O-CO_2 fluids along shear zones to dilational sites where changes in the fluid parameters prompt gold precipitation under suitable P-T conditions. The relatively flat shape of the H_2O-CO_2 solvus at higher pressures (i.e. 2-3kb) indicates that phase separation would result in an H_2O-rich fluid and a CO_2-rich fluid (Bowers & Helgeson,1983) which for low salinity fluids (2-6wt% NaCl) occurs around 275 to 400°C (see Fig.6.7). Several studies have suggested that H_2O-rich and CO_2-rich fluids are capable of independent flow once immiscibility has occurred (e.g. Trommsdorff & Skippen,1986; Watson & Brennan,1987; Yardley & Bottrell,1988). The apparent temporal and spatial separation of CO_2-rich and H_2O-rich alteration assemblages and the occurrence of coexisting H_2O-CO_2-rich fluids could, therefore, be explained in terms of phase separation and independent flow. At Gebeit, a CO_2-rich alteration phase preceded gold mineralisation and may have been due to the separation and removal of a less dense CO_2 vapour phase together with the retardation of the H_2O-rich phase by

wetting of the fracture surfaces. Similarly, the late infilling of fractured blue quartz by calcite may represent the immiscible CO_2-rich fluid component of the V_3 quartz veins.

Although phase separation in an H_2O-CO_2-rich fluid results in an increase in pH for the aqueous liquid (i.e. increasing gold solubility), the removal of H_2S into the CO_2-rich phase results in the destabilisation of the thiosulphide complexes. Gold (and presumably SiO_2 and B) is partitioned into the aqueous liquid, accounting for the restriction of gold and tourmaline to the lode veins. This reaction is not buffered chemically and therefore is relatively instantaneous, explaining the occurrence of randomly distributed, high grade gold zones (up to 2000ppm; DDH 16, 130m) in sulphide-deficient blue quartz veins. The reduced sulphur species react with the iron in the wallrock silicates to produce the zones of Fe-As-sulphides adjacent to the lode veins. The CO_2-rich fluid produces relatively minor wallrock alteration (i.e. calcite metasomatism) but the majority appears to leave the system to produce the intense carbonatisation of the ankerite phyllonite shear zones higher in the crust (Fig.8.6). As phase separation does not result in complete fluid separation (i.e. an H_2O-rich and a CO_2-rich phase), the bulk of the calcite alteration around the lode veins is probably due to the residual CO_2 in the H_2O-rich ore fluid.

Thus, at any given level in the crust above the brittle-ductile transition, the main phase of carbonatisation appears to pre-date the phase of gold mineralisation (Fig.8.6). As described above, the sites of gold mineralisation at the brittle-ductile transition can move upwards through the crust due to progressive reaction-softening of the shear zone fabrics but will also tend to move to deeper parts of the crust with progressive uplift and erosion of the terrane. Similarly, K-metasomatism and Na-leaching of wallrocks adjacent to lode veins lower in the crust tend to decrease the K/Na ratio of the residual fluid. Redeposition of the leached Na higher in the crust probably produced the V_2 veins and the albitic alteration seen in the ankerite phyllonites and some of the fractured V_1 veins. The combination of these processes results in the repeated overprinting of fluids of apparently differing composition. If this process accounts for the separation of the locus of gold mineralisation and ankerite metasomatism, then auriferous lode veins may occur along the main Riedel shears at depth below the zone of ankeritic carbonatisation (Fig.8.6).

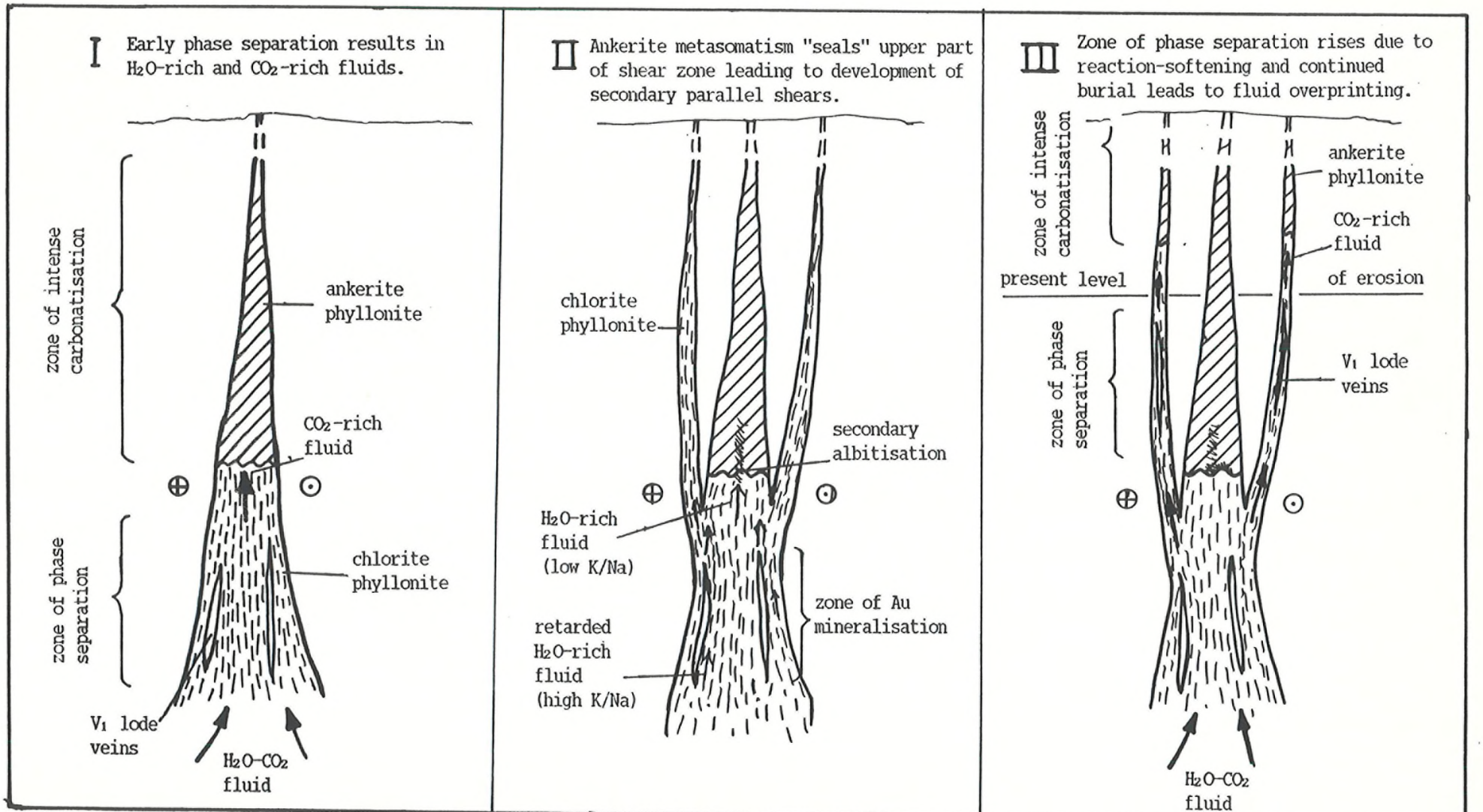

Fig.8.6 Sketch-sections of a second order extensional (Riedel) shear zone showing the effects of phase separation on alteration assemblages and location of lode veins.

Phase separation appears to be an efficient gold depositional mechanism and accounts for the anomalous characteristics of the Gebeit mineralisation. Similar features have been described from the Archaean gold deposit at Sigma Mine in the Abitibi greenstone belt, Quebec (Robert & Brown,1986a,b) where phase separation is also considered to be the dominant depositional mechanism (Robert & Kelly,1987). Evidence for phase separation has been described from a number of lode gold deposits from the Archaean (e.g. Groves et al.,1984; Studemeister & Kilias,1987; Walsh et al.,1988) and the Mesozoic (Read & Meinert,1986; Shelton et al.,1988) suggesting that fluid unmixing is a significant and widespread process.

From records and estimates of gold recovery up to 1975 and ore reserve calculations by Greenwich Resources, the minimum gold content in the lodes of the Gebeit block is in the region of 20×10^6g Au. If it is assumed that this mass is derived by 50%-efficient leaching of the underlying Gebeit volcanics with an estimated Au abundance of ≈2ppb, then the source rock volume would be about 7 km^3 (1km^3 contains 5.6×10^6g Au at 2ppb; method after Kerrich,1986b). The release of around 5 wt% structural water from hydrated andesitic basalt of the arc volcanics would produce a solvent volume of about 1 km^3. Estimates of the volume increase of the carbonatised phyllonites indicate that about 0.2km^3 of CO_2 has been added. If the H_2O-rich and CO_2-rich fluid phases at Gebeit were coeval, the combined solvent volume would amount to 1.2km^3 with CO_2 forming 17-20% of the total volume. This is equivalent to an X_{CO_2} of ≈0.1, which agrees with the fluid inclusion estimates and supports a phase separation precipitation mechanism.

8.5 Controls on Mineralsation and Guides for Further Exploration

The evidence derived from this study indicates that the epigenetic, mesothermal, lode gold mineralisation at Gebeit Mine in the Northern Red Sea Hills, Sudan, was controlled primarily by the formation of extensional Riedel shears as secondary structures to major north-east-trending, dextral, strike-slip shear zones. Gold mineralisation was synchronous with late-D_2 dextral shearing, during the main phase of arc accretion-related deformation, and slightly post-dated peak lower greenschist facies metamorphism. It is bracketed by an early phase of calc-alkaline, low-K dykes and a later phase of transitional calc-alkaline to alkaline dolerites.

Wallrock alteration data, integrated with fluid inclusion and

stable isotope studies, indicate that the ore fluids at Gebeit comprised H_2O-CO_2 fluids of low salinity and Eh, and near-neutral pH, at 250-300°C. Gold transport was probably achieved by thiosulphide complexes and the available evidence, although limited, suggests that phase separation was the main gold precipitation mechanism. Approximations of the gold and carbonate contents of the Gebeit block suggest that the minimum total solvent volume was $\approx 1.2 km^3$, with X_{CO_2} at around 0.1. Mineralisation was pre-dated by the main phase of carbonatisation which sealed the main Riedel shears, prompting the development of parallel shear zones at the margins. Economic gold grades are confined to these peripheral north-east-trending shear zones with mineralisation largely confined to the zones of maximum fluid flow delineated by the blue V_1 quartz veins. The complex interaction of the arc and continental terranes resulted in a protracted tectonic history and mineralisation was post-dated by two further phases (D_3 and D_4) of accretion-related deformation which fragmented the V_1 lode veins.

There have been several attempts at grouping the regional location of mineral deposits of the Nubian-Arabian Shield into metallogenic provinces (e.g. Al-Shanti & Roobol,1979; Sillitoe,1979; Petrascheck, 1979; Pohl,1982; Vail,1985 ,1987). These studies are of limited use as there is relatively little information on the environments and controls of mineralisation for specific deposits in the Nubian-Arabian Shield. Hundreds of gold prospects have been identified throughout the Shield and most appear to be mesothermal gold-quartz vein type deposits (e.g. Vail,1985a,b). Less commonly, the gold deposits are associated with base metal epithermal deposits (e.g. Mahd adh Dhahab; Worl,1979; Huckerby,1983) and weathered volcanogenic massive sulphide mineralisation (e.g. the Ariab Belt, southern Sudan, Cortial et al., 1985; Nuqrah, Saudi Arabia; Sabir,1979). In the Northern Red Sea Hills, the majority of the gold prospects appear to be mesothermal, shear zone-hosted, gold-quartz vein deposits usually, but not always, confined to the greenschist facies volcanic lithologies (Vail,1978; Fletcher,1985, Morteani et al.,1986). However, of the few gold deposits in the Shield which have been evaluated structurally, all appear to be related to accretion-related strike-slip deformation.

In Sudan, the evidence for early formation of the Gebeit mineralisation during D_2 dextral shear contrasts with the apparently late-accretion-related mesothermal mineralisation of the Abirkitib Mine, Sudan (Almond et al.,1984). Gold mineralisation at Abirkitib post-dates both collision along the N-S-trending Onib-Sol Hamid suture

and the emplacement of the Serakoit batholith, and appears to have been synchronous with late sinistral shearing along the reactivated suture (Almond et al.,1984; Stern et al.,1989). This strike-slip event was coeval with sinistral shearing along the Wadi Oko shear zone (Almond et al.,1987; see Fig.2.20) and was probably due to post-collisional ductile shearing parallel to the plate boundary, as described from the Mozambique Belt by Shackleton and Ries (1984). This phase of shearing may have been related to the D_3 deformation seen at Gebeit or possibly may be related to post-collisional Najd faulting (Stern et al.,1989; see Fig.2.17), therefore, post-dating the D_4 deformation at Gebeit.

Gold deposits along the Jabal Ishmas-Wadi Tath Lith shear zone in eastern Saudi Arabia (i.e. the southern half of the Nabitah suture; see Fig.2.13) show similar characteristics to the Abirkitib mineralisation (Worl,1980). All of these mesothermal, gold-quartz vein deposits occur along secondary Riedel shears related to post-collisional sinistral shearing along the reactivated N-S-trending Nabitah suture. These deposits have been shown to be pre-Najd in age and the gold-quartz vein mineralisation associated with massive sulphides in some of these deposits appears to be epigenetic in origin (Worl,1980). The epithermal base metal-gold-telluride mineralisation at Mahd adh Dahb, in the northern Asir terrane of Saudi Arabia, has been shown to be complex (e.g. Worl, 1979; Huckerby,1983) and appears to be due to several hydrothermal episodes. Mineralisation was controlled by secondary N-S-trending Riedel shears related to major, NE-trending, sinistral, strike-slip shears. If this NE-trending sinistral shearing event is synchronous with the early-D_4 sinistral shearing seen at Gebeit, then the limited available evidence suggests that phases of gold mineralisation occurred throughout the protracted and complex tectonic evolution of the Nubian-Arabian Shield during accretion. Generally, the predominant control on mineralisation in the Shield appears to be the availability of second order extensional shears produced during strike-slip deformation. From recent studies (e.g. Almond & Ahmed, 1987; this study), strike-slip deformation is now being widely recognised throughout the Shield. The predominantly strike-slip mode of deformation is due to the complex oblique collisions of the various arc and continental terranes which form the Nubian-Arabian Shield. As these strike-slip events are not restricted to a single deformation phase, each area under consideration for gold exploration must be evaluated in terms of its local tectonic evolution.

Likewise, further exploration for similar deposits in the Northern

Red Sea Hills should be concentrated on the delineation of major Riedel shears within the late-Proterozoic tectonic framework. These zones are likely to be defined by resistant red ridges due to ankerite metasomatism but economic vein-type mineralisation may occur adjacent to or below these zones. The veins are also likely to display a marked As anomaly (Khalil,1973; Fletcher,1985) but As values do not show a direct correlation with gold grade. The auriferous V_1 quartz veins usually (but not always) display a definitive blue colouration due to decrepitation of the CO_2-rich fluid inclusions. The cause of the decrepitation is unknown but is probably due to rapid uplift associated with D_3 folding and thrusting rather than to a thermal overprint. However, the close association of the quartz-hosted gold with calcite-infilled fractures may result in apparent low grades for quartz vein samples taken from surface due to the weathering of the calcite.

The Gebeit deposit bears all the characteristics common to most Archaean and many Mesozoic mesothermal lode gold deposits:

a) the gold in quartz vein mineralisation is hosted by shear zones developed in a mafic volcanic sequence,
b) siting of the veins was controlled by second order extensional brittle-ductile shears associated with regional ductile shear zones,
c) mineralisation occurred at the brittle-ductile transition immediately after lower greenschist facies peak metamorphism,
d) the mineralisation is associated with wide-scale carbonatisation and local wallrock sulphidation and sericitisation, and
e) deformation that accompanied gold mineralisation, also controlled intrusive magmatism and was part of a protracted tectonic history.

This suggests that the principal mechanisms of gold mineralisation have remained consistent throughout the geological record. Similarly, the depositional and tectonic environments of the arc terranes ofthe central Shield have often been compared to the multiple arc terranes of the SW-Pacific (Brown,1980), and late-Proterozoic epithermal as well as mesothermal mineralisation is evident. The concentration of the majority of the world's gold deposits in late-Archaean terranes and in the Tertiary circum-Pacific belt appears to be due to the rate and extent of crustal formation and, possibly, the physical accessibility of these areas. Due to its remoteness and arid environment, the Nubian-Arabian Shield is a relatively poorly prospected terrain. However, as the same processes extant in the formation of the majority of the world's gold deposits are evident in this region, it is possible that significant deposits have yet to be discovered.

Chapter 9

Conclusions

The main conclusions of this study on the tectonic and chemical evolution of the late-Proterozoic gold deposit at Gebeit Mine can now be summarised:

1) The volcanic rocks which host the mineralisation have been designated as the Gebeit Volcanic Group and three petrographic groups have been distinguished:

   a) plagioclase-phyric and aphyric fine and coarse tuffs,
   b) hornblende- and clinopyroxene-phyric tuffs, flows, lapilli-tuffs and agglomerates.
   c) minor carbonaceous shales,

All these Upper-Proterozoic volcanic lithologies plot as oceanic, island arc, basaltic andesites, transitional between low-K tholeiite and calc-alkaline in affinity.

2) The stratigraphy represents a shallowing sequence from the submarine-deposited aphyric and plagioclase-phyric tuffs and black shales at the base, to the predominantly subaerial hornblende-phyric flows, tuffs and agglomerates at the top. The Gebeit Volcanic Group appears to have been deposited in a shallow, marginal back-arc basin on the south-eastern flank of a relatively immature, palaeo-oceanic arc.

3) The earliest phase of arc accretion recognised, D_1, produced regional, north-east-trending F_1 folds throughout the Northern Red Sea Hills. This was followed by the main D_2 phase of dextral, strike-slip deformation which was accommodated by major, north-east-trending, brittle-ductile, chlorite-phyllonite shear zones. These shear zones subdivided the rocks of the Gebeit Volcanic Group into a series of discrete, north-east-trending, elongate tectonic blocks. Several Riedel and P shears were formed across the Gebeit block and fluid flow was preferentially focussed by the extensional Riedel shears. Strike-

slip deformation appears to have occurred on a regional scale and was probably induced by east-west-directed compression due to the simultaneous collision of the northern arc terranes and the north-south-trending continental terranes to the east and west.

4) The first phase of intrusive activity exposed at Gebeit was synchronous with late-D_2 dextral shearing and comprised a gabbro-diorite-tonalite-trondjhemite, low-K, calc-alkaline suite, predominantly consisting of dolerite and microdiorite dykes. These intrusions were confined to the S_2 fabrics of the main Gebeit Riedel shear zones and probably pre-dated the gold mineralisation. These phase 1 dykes were accompanied, or possibly post-dated, by a more evolved, calc-alkaline, diorite-granodiorite suite which contains shear zone-hosted auriferous mineralisation at two satellite prospects but is not observed within the Gebeit mine area.

5) Following intrusion of the phase 1 dykes, the extensional Wadi Lode and Wadi Tuwiya shear zones, and to a lesser extent the phase 1 dykes, were altered by an early, pre-mineralisation, CO_2-rich fluid phase concentrated along the main Reidel shear zones. High fCO_2 resulted in pervasive ankeritic metasomatism of the chlorite-sericite phyllonites to produce a blocky, cohesive, rock type containing up to 60 vol.% ankerite. The quartz-albite-chlorite-calcite mineral assemblage of the phase 1 dykes indicates that the peak of regional metamorphism was lower greenschist facies grade and post-dated phase 1 dyke emplacment but pre-dated carbonatisation. Volume changes associated with carbonate alteration average +200% and indicate extension across the Wadi Lode shear zone of about 100m. If the effects of extension across the Wadi Lode, Wadi Tuwiya and North Gebeit shear zones are considered together with the extension accompanying V_1-V_3 vein formation, the total extension across the 10km long Gebeit block is in the order of several hundred metres ($\approx$+3%). This pervasive alteration appears to have sealed the main Riedel shears prompting development of parallel, adjacent extensional shears. These secondary shear zones subsequently hosted the auriferous V_1 blue quartz veins, and the minor V_2 calcite-albite veins, thus effectively confining economic gold mineralisation to the margins of the main Riedels.

6) Gold-sulphide mineralisation was confined to V_1, north-east-trending, blue quartz veins and occurred synchronous with late-D_2

dextral strike-slip shearing, parallel to the Wadi Lode and Wadi Tuwiya Riedel shear zones. Gold occurs as native grains associated with vein sulphides and as free grains in zones of strained, sulphide-poor quartz, often with calcite. Sulphide mineralisation tends to be concentrated in the altered wallrocks and along entrained wallrock stringers within the veins and comprises arsenopyrite, pyrite, and pyrrhotite ±chalcopyrite, ±sphalerite, ±gersdorffite.

7) Wallrock alteration adjacent to the V_1 veins comprises quartz, chlorite, sericite, calcite and albite. Albite is pervasively sericitised and chlorite is relatively abundant together with highly variable calcite contents (-80% to 200%) Quartz is depleted in the wallrock but forms the majority of veins and stringers. Wallrock bleaching, due to finely intergrown chlorite, sericite, and calcite, forms a thin 10-50 cm envelope around the veins and visible alteration extends up to 8m from the lode. The widths of cryptic alteration haloes are variable but occur up to 25m from the lode intersection. Geochemically, wallrock alteration is marked by significant additions of K_2O (± Rb, Ba), MgO, Fe_{tot}, Cr, Ni, As, Au, ± CaO and MnO with concomitant depletion of Na_2O and Sr. As the veins formed along extensional shear zones, wallrock volume changes were minor (±25%) except in the zones of fine and pervasive vein development (50% to 200%). In contrast to the altered wallrocks, wallrock laminae entrained within the lode veins consist of tourmaline, sericite, rutile, calcite and apatite. Economic gold mineralisation represents gold enrichment of 10^3 to 10^6 and As concentration of 10^2 to 10^3 above background, also accompanied by minor enrichment in Sb and Bi, with B confined to the veins.

8) From structural and mineralogical studies, six phases of veining have been identified (see Fig.6.11); these are designated V_1-V_6, of which phases V_1-V_5 are associated with arc accretion-related deformation episodes, D_2-D_4. Fluid inclusions in all quartz phases are generally too small for quantitative thermometric studies (<5µm) but those observed in the V_1 lode veins are CO_2-rich. Analysis of fluid inclusions from the Wadi Messesana prospect, 5km north-west of Gebeit, revealed CO_2-aqueous inclusions which homogenise at 230-300°C and there is evidence of immiscibility during trapping. Fluid pressure estimates of 2.0 to 3.9kb (≈7-12km depth) are consistent with evolution within the brittle-ductile transition at greenschist facies grade. Many of

the fluid inclusions in the relict V_1 quartz grains have been decrepitated, possibly due to deformation and rapid uplift during D_3 thrusting, producing a dark blue colouration within the vein quartz. Stable oxygen isotope studies of vein quartz indicate that fluid compositions remained fairly constant for most of the accretion-related deformation (estimated at between 2.4 and 8.7‰) and were probably metamorphic (± magmatic input?) in origin. Influx of meteoric fluids is inferred for the V_5 veins during late-tectonic D_4 deformation.

9) Wallrock alteration assemblages incorporated with fluid inclusion and stable isotope data indicate the ore fluids at Gebeit comprised H_2O-CO_2 fluids of low salinity and Eh, and near-neutral pH, at 250-300°C. Gold transport was probably achieved by thiosulphide complexing and the available evidence, although limited, suggests that phase separation was the main gold precipitation mechanism. Estimates of the gold and carbonate contents of the Gebeit block suggest that the minimum total solvent volume was $\approx 1.2 km^3$, with X_{CO_2} at around 0.1. The range of alteration styles and apparent separation of the CO_2-H_2O fluids is thus attributed to progressive fluid unmixing followed by overprinting due to changes in crustal depth.

10) Following gold mineralisation, the D_2 deformation was interrupted by a relatively minor phase of north-west-directed, D_3 folding and thrusting which was concentrated along the D_2 shear zones and resulted in deformation of the V_1 veins and phase 1 dykes. D_3 deformation was followed by renewed north-east dextral shearing which further fragmented the V_1 lodes. This late D_3 shearing reactivated the D_2 shear zones, controlling the emplacement of phase 2, transitional calc-alkaline to alkaline, dolerite dykes and V_3, massive, white quartz veins. The block-bounding shear zones formed the south-west margin to the Gebeit Volcanic Group where they are thrust over the Sasa Plain tuffaceous slate assemblages, believed to represent part of a continental margin arc terrane (El Nadi,1984).

11) The final stages of arc accretion commenced with a switch from dextral to sinistral strike-slip deformation, probably due to collision with the marginal arc terranes to the west. This phase of strike-slip deformation once again reactivated the D_2 shears, controlling the emplacement of the phase 3 alkaline dolerite dykes and V_4 quartz-sericite veins and deforming the earlier veins and dykes. Accretion-

related deformation ended with the D_4 phase of eastward-directed folding and thrusting which folded the north-east-trending, V_1 lodes into NNW-trending open, upright, antiforms and synforms.

12) Following accretion and cratonisation of the Nubian-Arabian Shield around 670-630 Ma, the area remained tectonically inactive until the Mesozoic. At least four phases of extension, related to the break-up of Pangea and the rifting of the Red Sea, produced faults on E-W and NW-SE trends and reactivated many of the N-S-trending Pan-African structures. At Gebeit, several phases of normal faulting and anorogenic, alkaline, within-plate, plutonism have been identified but have not been accurately dated. These comprise:

a) Reactivation of N-S-trending sections of the major shear zones which hosted ultra-potassic, alkaline trachyte dykes similar to the Oko shear zone (see section 4.4.3). These dykes are of lamproitic affinity and are probably Mesozoic (150-89 Ma) in age.

b) NW-trending normal faults which cross-cut and partially reactivate the late-Proterozoic structures but usually have displacements of <50cm. Some of these NW structures may have been coeval with reactivation of the N-S shear zones and controlled the siting of many of the post-tectonic ring complexes (e.g. Salala)

c) E-W faults, which transect all structures, hosted the late, phase 4, undersaturated, alkaline, analcime-olivine dolerites which are probably of Cainozoic age (<30 Ma).

13) Gold mineralisation at Gebeit was primarily controlled by the availability of extensional sites (Riedel shears) for fluid access during D_2 dextral strike-slip shearing. Although structural data in the region are limited, dextral shearing appears to have occurred throughout the Red Sea Hills and probably in the northern arc terranes of the Arabian Shield. Mineralisation is broadly associated with a phase of intense carbonatisation which can be identified on aerial photographs and may prove to be a useful exploration guide. Sparse data from other Shield deposits suggest that gold mineralisation was not restricted to any specific phase of arc accretion and deformation. The Gebeit deposit bears many similarities with Archaean and Mesozoic-Tertiary mesothermal lode gold deposits, suggesting that the concentration of gold deposits in the Archaean and Tertiary is due to the rate and extent of crustal formation and is not due to differences in ore fluids or depositional mechanisms.

REFERENCES

ABDEL-MONEM A.A. and HURLEY P.M. 1979. U-Pb dating of zircons from psammitic gneisses, Wadi Abu Rosheid-Wadi Sikait area, Egypt. In "Evolution and Mineralisation of the Nubian-Arabian Shield", 2, Al-Shanti A.M.S. and Tahoun S.A. (eds), Pergamon Press, Oxford,pp 165-170.

AGAR R.A. 1985. Stratigraphy and palaeogeography of the Siham group : direct evidence for a late proterozoic continental microplate and active continental margin in the Saudi Arabian shield. Jour. Geol. Soc. Lond., **142**, pp 1205-1220.

AGAR R.A. 1987. The Najd fault system revisited; a two-way strike-slip orogen in the Saudi Arabian Shield. J. Struct. Geol., **9**, pp 41-48.

AHMED T.E-D.S. 1984. Methods and criteria of prospecting for Au deposits in the Northern Red Sea Hills, Sudan. Unpubl. Ph.D. thesis, Univ. Moscow, 229pp.

ALMOND D.C. 1979. Younger granite complexes of Sudan. In "Evolution and Mineralisation of the Nubian-Arabian Shield",1, Tahoun S.A. (ed), Pergamon Press, Oxford, pp 151-164.

ALMOND D.C. 1980. Precambrian events of Sabaloka, Near Khartoum, and their significance in the chronology of the basement complex of northeast Africa. Precambrian Res., **13**, pp 43-62.

ALMOND D.C. 1982. New ideas in the Geological history of the basement complex of northeast Sudan. Sudan Notes & Records 1982 Vol., **59**, pp 106-136.

ALMOND D.C., AHMED F., and SHADDAD M.Z. 1984. Setting of gold mineralisation in the northern Red Sea Hills of Sudan. Econ Geol, **79**, pp 389-392.

ALMOND D.C. and AHMED F. 1987. Ductile shear zones in the northern Red Sea Hills; Sudan and their implication for crustal collision. Geol. Jour., Thematic Issue, **22**, pp 175-184.

AL-REHAILI M.H. and WARDEN A.J. 1980. Comparison of the Bir Umq and Hamdah ultrabasic complexes, Saudi Arabia. In "Evolution and Mineralisation of the Nubian-Arabian Shield", 4, Al-Shanti A.M.S. (ed), Pergamon Press, Oxford, pp 143-156.

AL-SHANTI A.M., ABDEL-MONEM A.A., and MARZOUKI F.H. 1984. Geochemistry, petrology and Rb-Sr dating of trondjhemite and granophyre associated with the Jabal Tays ophiolite, Idsas area, Saudi Arabia. Precamb. Res., **24**, pp 321-334.

AL-SHANTI A.M. and GASS I.G. 1983. The upper proterozoic ophiolite melange zones of the eastern most Arabian shield. Jour. Geol. Soc. Lond., **140**, pp 867-876.

AL-SHANTI A.M.S. and MITCHELL A.H.G. 1976. Late Precambrian subduction and collision in the Al-Amar-Idsas region, Arabian Shield, Kingdom of Saudi Arabia. Tectonophysics, 30, pp 41-47.

AL-SHANTI A.M.S. and ROOBOL M.J. 1979. Some thoughts on metallogenesis and evolution of the Arabian-Nubian Shield. In "Evolution and Mineralisation of the Nubian-Arabian Shield",1, Tahoun S.A. (ed), Pergamon Press, Oxford, pp 87-96.

BAKOR A.R., GASS I.G., and NEARY C.R. 1976. Jabal al Wask, Northwest Saudi Arabia: an Eocambrian back-arc ophiolite. Earth Planet. Sci. Lett., 30, pp 1-9.

BALL E. 1980. An example of very consistent brittle deformation over a wide intercontinental area; the late Pan-African fracture system of the Touareg and Nigerian Shields. Tectonophysics, 61, pp 363-379.

BARKER F. 1979. Trondjhemite - definition, environment and hypothesis of origin. In "Trondjhemites, Dacite and Related Rocks". Barker F. (ed) Elsevier, Amsterdam, pp 1-12.

BARLEY M.E., EISENLOHR B., GROVES D.I., PERRING C.S., and VEARNCOMBE J.R. 1988. The Norseman-Wiluna Belt: hydrothermal gold mineralisation in a Late Archaean oblique-slip mobile belt. Geology, 17, pp 826-829.

BAUBRON J.C., DELFOUR J., and VIALETTE Y. 1976. Geochronological measurements (Rb/Sr; K/Ar) on rocks of the Arabian Shield, Kingdom of Saudi Arabia. Bur. Rech. Geol. Min. Open File Rept. 76-JED-22, 152pp.

BAYLISS P. 1975. Nomenclature of the trioctahedral chlorites. Can. Mineral., 13, pp 178-180.

BENT J.T. 1896. A visit to northern Sudan. Proc. Roy. Geog. Soc. London, pp 335-355.

BERGMAN S.C. 1987. Lamproites and other potassium-rich igneous rocks: a review of their occurrence, mineralogy and geochemistry. In "Alkaline Igneous Rocks" Fitton & Upton (eds) Geol. Soc. Sp. Pub., 30, pp103-190.

BERHE S.M. and ROTHERY D.A. 1986. Interactive processing of satellite images for structural and lithological mapping in north east Africa. Geol. Mag., 123, pp 393-403.

BERTHE D., CHOUKROUNE P., and JEGOUZO P. 1979. Orthogneiss, mylonite and non-coaxial deformation of a granite: the example of the South Armorican Shear Zone. J. Struct. Geol., 1, pp 31-42.

BERTRAND J.M.L. and CABY R. 1978. Geodynamic evolution of the Pan-African orogenic belt: a new interpretation of the Hoggar Shield (Algerian Sahara). Geol. Rund., 67, pp 357-388.

BEURRIER M. and VILLEY M. 1982. Polyphase tectonometamorphic and magmatic evolution in the northeast part of the Arabian Shield. Abstract. Precamb. Res., 16, A47.

BLACK R., CABY R., MOUSSINE-POUCHKINE A., BAYER R., BERTRAND J.M., BOUILLIER A.M., FABRE J., and LESQUER A. 1979. Evidence for late-Precambrian plate tectonics in West Africa. Nature, 278, pp 223-227.

BOKHARI F.Y. and KRAMERS J.D. 1982. Lead isotope data from massive sulphide deposits in the Saudi Arabian Shield. Econ. Geol., **77**,pp 1766-1769.

BORNHORST T.J. and ROSE W.I. 1986. Patitioning of gold in young calc-alkalic volcanic rocks from Guatemala. J. Geology, **94**, pp 412-418.

BOULTER C.A., FOTIOS M.G., and PHILLIPS G.N. 1987. The Golden Mile Kalgoorlie: A giant gold deposit localised in ductile shear zones by structurally induced infiltration of an auriferous metamorphic fluid. Econ. Geol., **82**, pp 1661-1678.

BOWERS T.S. and HELGESON H.C. 1983. Calculation of the thermodynamic and geochemical consequences of nonideal mixing in the system H_2O-CO_2-NaCl on phase relations in geologic systems: equation of state for H_2O-CO_2-NaCl fluids at high pressures and temperatures. Geochim. Cosmochim. Acta, **47**, pp 1247-1275.

BOYLE R.W. 1976. Mineralization processes in Archaean greenstone and sedimentary belts. Geol. Surv. Canada, Paper, 75-15.

BROWN G.C. 1980. Calc-alkaline magma genesis: the Pan-African contribution to crustal growth? In "Evolution and Mineralisation of the Nubian-Arabian Shield",3, Al-Shanti A.M.S. and Tahoun S.A. (eds), Pergamon Press, Oxford, pp 19-30.

BROWN G.C. 1982. Calc-alkaline intrusive rocks: their diversity, evolution, and relation to volcanic arcs. in "Andesites", R.S. Thorpe (Ed), Wiley, London, pp 437-459.

BROWN G.C., THORPE R.S., and WEBB P.C. 1982. The geochemical characteristics of granitoids in contrasting arcs and comments on magma sources. J. geol. Soc. London, **141**, pp 413-426.

BROWN G.F. 1972. Tectonic map of the Arabian peninsula. Saudi Arabian Dir. Gen. Miner. Resour. Map AP-2.

BROWN G.F. and COLEMAN R.G. 1972. The tectonic framework of the Arabian Peninsula. Int. Geol. Congr. XXIV, 3, pp 300-305.

BROWN G.F. and JACKSON R.O. 1960. The Arabian Shield. Rep. 21st Int. Geol. Congr., 9, pp 69-77.

BROWN P.E. and LAMB W.M. 1986. Mixing of H_2O-CO_2 in fluid inclusions; geobarometry and Archaean gold deposits. Geochim. Cosmochim. Acta, **50**, pp 847-852.

BURROWS D.R., WOOD P.C., and SPOONER E.T.C. 1986. Carbon isotope evidence for a magmatic origin for Archaean gold-quartz vein ore deposits. Nature, 321, pp 851-854.

BURROWS D.R. and SPOONER E.T.C. 1987. Generation of a magmatic H_2O-CO_2 fluid enriched in Mo, Au, and W within an Archaean sodic granodiorite stock, Mink Lake, Northwestern Ontario. Econ. Geol., **82**, pp 1931-1957.

CABY R. 1982. Pan-African evolution of the Touareg Shield (Central Sahara). Abstract. Precamb. Res., **16**, A10-11.

CABY R. and ANDREOPOULOS-RENAUD U. 1987. Le Hoggar oriental, bloc cratonisé a 730 Ma dans la chaîne Pan-Africaine du nord du continent Africain. Precambrian Research, 36, pp 335-344.

CABY R., BERTRAND J.M.L., and BLACK R. 1981. Pan-African ocean closure and continental collision in the Hoggar-Iforas segment, central Sahara. In "Precambrian Plate Tectonics", Kröner A (ed), Elsevier, pp 407-431.

CALVEZ J.Y., ALSAC C., DELFOUR J., KEMP J., and PELLATON C. 1983. Geologic evolution of western, central, and eastern parts of the northern Precambrian Shield, Kingdom of Saudi Arabia. Saudi Arabian Dep. Min. Min. Res. Open File Report BRGM-OF-03-17, 57pp.

CAMERON E.I. 1988. Archaean gold: relation to granulite formation and redox zoning in the crust. Geology, **16**, pp 109-112.

CAMERON E.I. 1989a. Scouring of gold from the lower crust. Geology, **17**, pp 26-29.

CAMERON E.I. 1989b. Derivation of gold by oxidative metamorphism of a deep ductile shear zone: Part 1. Conceptual model. J. Geochem. Explor., **31**, pp 135-147.

CAMERON E.I. 1989c. Derivation of gold by oxidative metamorphism of a deep ductile shear zone: Part 2. Evidence from the Bamble Belt, south Norway. J. Geochem. Explor., **31**, pp 149-169.

CAMERON E.I. and HATTORI K. 1985. The Hemlo gold deposit, Ontario: a geochemical and isotopic study. Geochim. Cosmochim. Acta, **49**,pp2041-50.

CAMERON E.I. and HATTORI K. 1987. Archaean gold mineralisation and oxidised hydrothermal fluids. Econ. Geol. **82**, pp 1177-1191.

CAMP V.E. 1984. Island arcs and their role in the evolution of the Western Arabian Shield. Geol. Soc. Am. Bull., **95**, pp 913-921.

CAMP V.E., JACKSON N.J., RAMSAY C.R., ROOBOL M.J., STOESER D.B., and WHITE D.L. 1984. Discussion on the upper proterozoic ophiolite melange zones of the eastern most Arabian shield. Jour. Geol. Soc. Lond., **141**, pp 1083-1087.

CANN J.R. 1970. Rb, Sr, Y, Zr, and Nb in some ocean floor basaltic rocks. Earth Planet. Sci. Lett., **10**, pp 7-11.

CAS R.A.F. and WRIGHT J.V. 1987. "Volcanic Successions- Modern and Ancient". Allen and Unwin, London, 519pp.

CATHELINEAU M. and NIEVA D.N. 1985. A chlorite solid solution geothermometer. The Los Azufres (Mexico) geothermal system. Contrib. Mineral. Petrol., **91**, pp 235-244.

CHARLET J.M. 1987. La thermoluminescence des quartz du district auroantimonifère de Saint-Yrieix (Haute-Vienne, France), application à la prospection et à l'évaluation des indices minéralisés. C.R. Acad. Sci. Paris, **305**, pp 281-285.

CHARLET J.M. 1988. Report on thermoluminescence study of Gebeit quartz veins for Greenwich Resources plc, 9pp.

CHARLET J.M., QUINIF Y., and LAIR Ph. 1987. Thermoluminescence in mineral and energetic resources exploration, some case of applications. Bull. Soc. belge Géol., **96**, pp 15-21.

CLAESSON S., PALLISTER J.S., and TATSUMOTO M. 1984. Samarium-neodymium data on two late Proterozoic ophiolites of Saudi Arabia and implications for crustal and mantle evolution. Contrib. Mineral. Petrol., **85**, 244-252.

CLARK M.D. 1985. Late Proterozoic crustal evolution of the Midyan region, northwestern Saudi Arabia. Geology, **13**, pp 611-615.

CLIFFORD T.N. 1970. The structural framework of Africa. In "African Magmatism and Tectonics". Clifford T.N. and Gass I.G. (eds). Oliver and Boyd, Edinburgh, pp 1-26.

COLLINS W.J., BEAMS S.D., WHITE A.J.R., and CHAPPELL B.W. 1982. Nature and origin of A-type granites with particular reference to southeastern Australia. Contrib. Miner. Petrol., **80**, pp 189-200.

COLVINE A.C. 1988. Gold mineralisation in the Superior Province, Canada: a product of terminal Archaean cratonisation. Bicentennial Gold 88, Melbourne. Geol. Soc. Aust. Abs. **22**, pp 36-44.

COLVINE A.C., ANDREWS A.J., CHERRY M.E., DUROCHER M.E., FYON A.J., LAVIGNE M.J., MACDONALD A.J., MARMONT S., POULSEN K.H., SPRINGER J.S., and TROOP D.G. 1984. An integrated model for the origin of Archaean lode gold deposits. Ontario Geol. Surv. O.F.R. 5524, 99pp.

CORTIAL P., LEFEVRE J.C., and SALIH H.M. 1985. Gold deposits related to the volcanosedimentary sequence of Ariab, Sudan. In "Prospecting in Areas of Desert Terrain", IMM Conf. report, pp 155-159.

CURTIS C.D., HUGHES C.R., WHITEMAN J.A., and WHITTLE C.K. 1985. Compositional variation within some sedimentary chlorites and some comments on their origin. Min. Mag., **49**, pp 375-386.

DARBYSHIRE D.P.F., JACKSON N.J., RAMSAY C.R., and ROOBOL M.J. 1983. Rb-Sr Isotope study of the latest proterozoic volcano sedimentary belts in the central Arabian shield. Jour. Geol. Soc. Lond., **140**, pp 203-213.

DAVIES B.F. 1984. Strain analysis of wrench faults and collision tectonics of the Arabian-Nubian Shield. J. Geology, **92**, pp 37-54.

DEER W.A., HOWIE R.A., and ZUSSMAN J. 1966. "An Introduction to the Rock-forming Minerals". Longman, Harlow, Essex, 528pp.

DELANY F.M. 1955. Ring structures in the northern Sudan. Eclog. Geol. Helv., **48**, pp 133-148.

DELFOUR J. 1979. Upper Proterozoic volcanic activity in the northern Arabian Shield, Kingdom of Saudi Arabia. In "Evolution and Mineralisation of the Nubian-Arabian Shield", 2, Al-Shanti A.M.S. and Tahoun S.A. (eds), Pergamon Press, Oxford, pp 59-76.

DIXON T.H. 1981. Age and chemical characteristics of some pre-Pan-African rocks in the Egyptian shield. Precambrian Res., **14**, pp 119-133.

DIXON T.H. and GOLOMBEK M.P. 1988. Late Precambrian crustal accretion rates in northeast Africa and Arabia. Geology, **16**, pp 991-994.

DOSTAL J. and DUPUY C. 1987. An in late proterozoic andesites from northwest Africa. Econ. Geol., **82**, pp 762-766.

DUYVERMAN H.J. and HARRIS N.B.W. 1982. Late Precambrian evolution of Afro-Arabian crust from ocean arc to craton. Discussion and reply. Geol. Soc. Am. Bull., **93**, pp 174-178.

DUYVERMAN H.J., HARRIS N.B.W., and HAWKESWORTH C.J. 1982. Crustal accretion in the Pan-African : Nd & Sr isotope evidence from the Arabian Shield. Earth Planet. Sci. Lett., **59**, pp 315-326.

EISENLOHR B.N., GROVES D., and PARTINGTON G.A. 1989. Crustal-scale shear zones and their significance to Archaean gold mineralisation in Western Australia. Mineral. Deposita, **24**, pp 1-8.

ELBAYOUMI R.M.A. and GREILING R.O. 1984. Tectonic evolution of a Pan-African plate margin in southeast Egypt - a suture zone overprinted by low angle thrusting? In "African Geology", (ed) J. Klerkx and J. Michot Musée Royal de l'Afrique Centrale - Tervuren, pp 47-56.

EL-BOUSHI I.M. 1972. Geology of the Gebeit gold mine, Democratic Republic of the Sudan. Econ. Geol., **67**, pp 481-486.

EL-NADI A.H. 1984. The geology of the late Precambrian metavolcanics, Red Sea Hills, NE Sudan. Ph.D. Thesis, Univ. Nottingham, 244pp.

EL-NADI A.H. 1987. New subdivision of the basement complex, Northeast Sudan. In "Current Research in African Earth Sciences", Matheis and Schandelmeier (eds) Balkema, Rotterdam,1987, pp 95-99.

EMBLETON J.C.B., HUGHES D.J., KLEMENIC P.M., POOLE S., and VAIL J.R. 1982. A new approach to the stratigraphy and tectonic evolution of the Red Sea Hills, Sudan. Abstract. Precamb. Res., **16**, A19.

ENGEL A.E.J., DIXON T.H., and STERN R.J. 1980. Late Precambrian evolution of Afro-Arabian crust from ocean arc to craton. Bull. geol. Soc. Am., **91**, pp 699-706.

ENGEL C.G. and SHARP R.P. 1958. Chemical data on dessert varnish. Bull. geol. Soc. Am., **69**, pp 487-518.

ETHERIDGE M.A., WALL V.J., and COX S.F. 1984. High fluid pressures during regional metamorphism and deformation: implications for mass transport and deformation mechanisms. J. Geophys. Res., **89**, pp 4344-58.

FISHER R.V. 1985. Submarine volcaniclastic rocks. In "Sedimentology - Recent Developments and Applied Aspects". Brenchley P.J. and Williams B.P.J.(eds), Blackwell, Oxford, pp 5-27.

FISHER R.V. and SCHMINCKE H.-U. 1984. "Pyroclastic Rocks". Springer-Verlag, Berlin, 472pp.

FITCHES W.R., GRAHAM R.H., HUSSEIN I.M., RIES A.C., SHACKLETON R.M., and PRICE R.C. 1983. The late-Proterozoic ophiolite of Sol Hamed north east Sudan. Precamb. Res., **19**, pp 385-411.

FLECK R.J. 1984. Age of diorite-granodiorite gneisses of the Jiddah-Makkah region, Kingdom of Saudi Arabia. Open file Rep. Saudi Arabian Dir. Miner. Resour., USGS-OF-01-1, 18pp.

FLECK R.J., COLEMAN R.G., CORNWALL H.R., GREENWOOD W.R., HADLEY D.G., PRINZ W.C., RATTE V.C. and SCHMIDT D.L. 1976. Geochronology of the Arabian Shield, Western Saudi Arabia: K-Ar results. Bull. Geol. Soc. Am., **87**, pp 9-21.

FLECK R.J., GREENWOOD W.R., HADLEY D.G., ANDERSON R.E. and SCHMIDT D.L. 1980. Age and evolution of the southern part of the Arabian Shield. In "Evolution and Mineralisation of the Nubian-Arabian Shield", 3, Al-Shanti A.M.S. & Tahoun S.A. (eds), Pergamon Press, Oxford, pp 1-18.

FLETCHER R.J. 1985. Geochemical exploration for gold in the Red Sea Hills, Sudan. In "Prospecting in Areas of Desert Terrain", IMM Conf. report, pp 79-94.

FLOYD P.A. and WINCHESTER J.A. 1975. Magma type and tectonic setting discrimination using immobile elements. Earth and Planet Sci. Lett., **27**, pp 211-218.

FOSTER R.P. 1985. Major controls of Archaean gold mineralisation in Zimbabwe. Trans. Geol. Soc. Afr., **88**, pp 109-133.

FOSTER R.P. 1987. Archaean gold metallogenesis and exploration in Zimbabwe. Afr. Mining, IMM, pp 103-126.

FOSTER R.P. 1988. Archaean gold mineralisation in Zimbabwe, implications for metallogenesis and exploration. Bicentennial Gold 88, Melbourne. Geol. Soc. Aust. Abs. **22**, pp 62-72.

FRISCH W. and AL-SHANTI A. 1977. Ophiolite belts and the collision of island arcs in the Arabian Shield. Tectonophysics, **43**, pp 293-306.

GABERT G., RUXTON B.P., and VENZLAFF H. 1960. Über untersuchungen im Kristallin der nördlichen Red Sea Hills im Sudan. Geol. Jb., **77**, pp 241-270.

GAMMOND J.F. 1983. Displacement features associated with fault zones: a comparison between examples and experimental models. J. Struct. Geol., **5**, pp 33-45.

GARSON M.S. and SHALABY I.M. 1976. Precambrian to Lower Palaeozoic plate tectonics and metallogenesis in the Red Sea region. Geol. Assoc. of Canada Spec. Paper No. **14**, pp 573-593.

GASKELL J.L. 1985. Reappraisal of Gebeit Gold Mine, north east Sudan: a case history. In" Prospecting in Areas of Desert Terrain", IMM conf report, pp 49-58.

GASKELL J.L. 1986. Recent developments in gold mining activity in the Arabian-Nubian Shield rocks of Egypt and Sudan. Report.

GASS I.G. 1955. The geology of the Dunganab area, Anglo-Egyptian Sudan. MSc Thesis, University of Leeds.

GASS I.G. 1977. The evolution of the Pan-African crystalline basement in north east Africa and Arabia. Jour. Geol. Soc. Lond.,**134**,pp 129-138.

GASS I.G. 1979. Evolutionary model for the Pan-African crystalline basement. In "Evolution and Mineralisation of the Nubian-Arabian Shield",1, Tahoun S.A. (ed), Pergamon Press, Oxford, pp 11-20.

GASS I.G. 1981. Pan-African (Upper Proterozoic) plate tectonics of the Arabian-Nubian Shield. In "Precambrian Plate Tectonics", Kröner A (ed), Elsevier, pp 387-402.

GASS I.G. 1982. Upper Proterozoic (Pan-African) calc-alkaline magmatism in north eastern Africa and Arabia. In "Andesites" ed R.S. Thorpe, Wiley, pp 591-609.

GASS I.G. and NASSEEF A.O. 1980. Arabian Shield granite traverse. In "Evolution and Mineralisation of the Nubian-Arabian Shield", 4, Al-Shanti A.M.S. (ed), Pergamon Press, Oxford, pp 77-82.

GEOSURVEY 1982. A geologic interpretation of Landsat MSS imagery of the Red Sea Hills, Sudan. Report for Minex Sudan.

GILL J. 1981. "Orogenic Andesites and Plate Tectonics". Springer - Verlag, Minerals and Rocks Series, v16.

GILLESPIE J.G. and DIXON T.H. 1983. Lead isotpoe systematics of some igneous rocks from the Egyptian Shield. Precamb. Res., **20**, pp 63-77.

GIRDLER R.W. 1985. The opening of the Red Sea. In "Geology in the Real World - the Kingsley Dunham volume". Nesbitt R.W. and Nichol I. (eds), IMM, pp 143-153.

GOLDING S.D. and WILSON A.F. 1987. Oxygen and hydrogen isotope relationships in Archaean gold deposits of the Eastern Goldfields Province, Western Australia: constraints on the source of Archaean gold-bearing fluids. Uni. WA Geol. Dept. Extn. Publ., **11**, pp 203-213.

GRANT J.A. 1986. The isocon diagram - a simple solution to Gresens' equation for metasomatic alteration. Econ. Geol., 81, pp 1976-1982.

GREENWICH RESOURCES 1985-87. Maps of the Gebeit mine area: Surface geology (1:1000), Y Lode and 4-level, 5-level of the Wadi Lode (1:250).

GREENWOOD W.R. and BROWN G.F. 1973. Petrology and chemical analysis of selected plutonic rocks from the Arabian Shield, Kingdom of Saudi Arabia. Saudi Arabian Dir. Gen. Min. Res. Bull. 9.

GREENWOOD W.R., HADLEY D.G., ANDERSON R.E., FLECK R.J., and SCHMIDT D.L 1976. Late Proterozoic cratonization in south western Saudi Arabia. Phil. Trans. R. Soc. Lond., A, **280**, pp 517-527.

GREILING R.O. 1987. Directions of Pan-African thrusting in the Eastern Desert of Egypt derived from lineation and strain data. In "Current Research in African Earth Sciences", Matheis and Schandelmeier (eds) Balkema, Rotterdam,1987, pp 83-86.

GREILING R.O., EL RAMLY M.F., EL AKHAL H., and STERN R.J. 1988. Tectonic evolution of the northwestern Red Sea margin as related to basement structure. Tectonophysics, **153**, pp 179-191.

GRESENS R.L. 1967. Composition-volume relationships of metasomatism. Chem. Geol., 2, pp 47-65.

GROVES D.I. 1988. Gold mineralisation in the Yilgarn Block, Western Australia. Bicentennial Gold 88, Melbourne. Geol. Soc. Aust. Abs. **22**, pp 13-18.

GROVES D.I., PHILLIPS G.N., HO S.E., HENDERSON C.A., CLARK M.E., and WOOD G.M. 1984. Controls on distribution of Archaean hydrothermal gold deposits in Western Australia. In "Gold '82: The Geology and Genesis of Gold Deposits." Foster (ed.), A.A. Balkema, Rotterdam, pp 689-712.

GROVES D., PHILLIPS G.N., HO S.E., and HOUSTOUN S.M. 1985. The nature, genesis and regional controls of gold mineralisation in Archean greenstone belts of the western Australian shield, a brief review. Trans. geol. Soc. S. Afr., **88**, pp 148-158.

GROVES D., PHILLIPS G.N., HO S.E., HOUSTOUN S.M., and STANDING C.A. 1987. Craton-scale distribution of Archaean greenstone gold deposits: predictive capacity of the metamorphic model. Econ. Geol., **82**, pp 2045-2058.

HAAS J.L. 1971. The effect of salinity on the maximum geothermal gradient of a hydrothermal system at hydrostatic pressure. Econ. Geol., **66**, pp 940-946.

HARRIS N.B.W. 1982. The petrogenesis of alkaline intrusives from Arabia and northeast Africa and their implications for within-plate magmatism. Tectonophysics, **83**, pp 243-258.

HARRIS N.B.W., HAWKESWORTH C.J., and RIES A.C. 1984. Crustal evolution in northeast and east Africa from model Nd ages. Nature, **309**, pp 773-776.

HART S.R., ERLANK A.J. and KABLE E.J.D. 1974. Sea floor basalt alteration:some chemical and strontium isotope effects. Contrib. Mineral. Petrol., **44**, pp 219-230.

HEDGE C.E. 1984. Precambrian geochronology of part of northwestern Saudi Arabia. Open file Rep. Saudi Arabian Dir. Miner. Resour., USGS-OF-04-31, 12pp.

HENDEL E.M. and HOLLISTER L.S. 1981. An empirical solvus for CO_2-H_2O-2.6 wt% salt. Geochim. Cosmochim. Acta, **45**, pp 225-228.

HENLEY R.W. 1973. Solubility of gold in hydrothermal chloride solutions. Chem. Geol., **11**, pp 73-87.

HENLEY R.W. 1986. The geothermal framework of epithermal deposits. In "Fluid-Mineral Equilibria in Hydrothermal Systems". Henley R.W., Truesdell A.H., and Barton P.B. (eds), Reviews in Econ. Geol., **2**, Soc. Econ. Geol., pp 1-24.

HEY M.H. 1954. A new review of the chlorites. Min. Mag., **30**, p 277.

HILDRETH W. 1981. Gradients in silicic magma chambers; implications for lithospheric magmatism. J. geophys. Res., **86**, pp 10153-10192.

HODGSON C.J. and MacGEEHAN P.J. 1982. A review of the geological characteristics of "gold only" deposits in the superior province of the Canadian Shield. In "Geology of Canadian Gold Deposits" Hodder R.W. and Petruk W. (eds), CIM Special Vol., **24**, pp 211-229.

HOLMES A. 1951. The sequence of Precambrian orogenic belts in south and central Africa. Int. Geol. Congr. XVIII., 14, pp254-269.

HUCKERBY J.A., MOORE J.McM. and DAVIS G.R. 1983. Tectonic control of mineralisation at Mahd adh Dhahab gold mine, western Saudi Arabia. Trans. Instn. Min. Metall., 92, B171-B182.

HUME W.F. 1934. Geology of Egypt, v2, Pt.1: The Metamorphic Rocks. Geol. Survey of Egypt, 293pp.

HUSSEIN I.M. 1977. Geology of the Halaib area of the northern Red Sea Hills, Sudan, with special reference to the Sol Hamed basic complex. M.Phil. thesis, Portsmouth Polytechnic (unpubl.).

HUSSEIN I.M., KRONER A., and DURR S. 1984. Wadi Onib - a dismembered Pan-African ophiolite in the Red Sea Hills of Sudan. Bull. Fac. Earth Sci., King Abdulaziz Univ., Jeddah, 6, pp319-327.

HUSSEINI M.I. 1988. The Arabian infracambrian extensional system. Tectonophysics, 148, pp 93-103.

HUTCHINSON R.W. 1987. Metallogeny of Precambrian gold deposits: space and time relationships. Econ. Geol., 82, pp 1993-2007.

JACKAMAN B. 1972. Genetic and environmental factors controlling the formation of massive sulphide deposits of Wadi Bidah and Wadi Wassat. Saudi Arabian Dir. Gen. Mineral. Resources Tech. Record. TR-1972-1.

JACKSON N.J. 1980. Correlation of late-Proterozoic stratigraphies, northeast Africa and Arabia: Summary of an IGCP Project 164 Report. J. geol. Soc. London, 137, pp 629-634.

JACKSON N.J. 1986a. Petrogenesis and evolution of Arabian felsic plutonic rocks. J. Afr. Earth Sci., 4, pp 47-59.

JACKSON N.J. 1986b. Distribution nature and origin of trondjhemite in the Arabian Shield; a reconnaissance survey. J. Afr. Earth Sci., 4, pp 99-103.

JACKSON N.J. and RAMSAY C.R. 1980. Time space relationships of Upper Precambrian volcanic and sedimentary units in the Central Arabian Shield. J. geol. Soc. London, 137, pp 617-628.

JACKSON N.J., WALSH J.N., and PEGRAM E. 1984. Geology, geochemistry and petrogenesis of late-Precambrian Granitoids in the Central Hijaz region of the Arabian Shield. Contrib. Min. Pet., 87, pp 205-219.

JENSEN L.S. 1976. Regional stratigraphy and structure of the Timmins-Kirkland Lake area, District of Timiskaming. Misc. Pap. Ont. Dept. Mines, 67, 183pp.

JOHNSON P.R., SCHEIBNER E., and SMITH E.A. 1987. Basement fragments, accreted tectonostratigraphic terraines and overlap sequences: elements in the tectonic evolution of the Arabian Shield. In "Terrane Accretion and Orogenic Belts" AGU Geodynamics series volume, .

JOHNSON P.R. and VRANAS G.J. 1984. The geotectonic environments of Late Proterozoic mineralisation in the southern Arabian Shield. Precamb. Res., 25, pp 329-384.

KABESH M.L. 1962. Geology of the Muhammad Qol Sheet. Mem. Geol. Surv. Sudan., 3, 61pp.

KAZMIN V. 1971. Precambrian of Ethiopia. Nature, 230, pp 176-177.

KAZMIN V., SHIFERAW A., and BALCHA T. 1978. The Ethiopian basement: stratigraphy and possible manner of evolution. Geol. Rdsch., 67, pp 531-546.

KEMP J. 1981. Geologic map of the Wadi al Ays quadrangle, sheet 25C, Kingdom of Saudi Arabia. Saudi Arabia. Dep. Minist. Miner. Resour. Geol. Map GM-53C, 39pp.

KENNEDY W.O. 1964. The structural differentiation of Africa in the Pan-African (500 m.y.) tectonic episode. Res. Inst. Afr. Geol., Univ. Leeds, 8th Annu. Rep., 1962-1963, pp 48-49.

KERRICH R. 1986a. Archaean lode gold deposits of Canada. Part 1: Synthesis of geochemical data from selected mining camps with emphasis on patterns of alteration. Univ. Witwatersrand, Econ. Geol. Res. Unit, Inf. Circ. 182, 30pp.

KERRICH R. 1986b. Archaean lode gold deposits of Canada. Part II: Characteristics of the hydrothermal systems, and models of origin. Univ. Witwatersrand, Econ. Geol. Res. Unit, Inf. Circ. 183, 34pp.

KERRICH R. and FRYER B.J. 1981. The separation of rare elements from abundant base metals in Archaean lode gold deposits: implications of low water/rock source regions. Econ. Geol., 76, pp 160-166.

KHALIL B.E.D. 1973. Quantitative interpretation of secondary dispersion patterns of gold deposits in the Red Sea Hills, Sudan. Bull. Geol. Miner. Resour. Dept. Sudan, 24, 63pp.

KLEMENIC P.M. 1985. New geochronological data on volcanic rocks from northeast Sudan and their implication for crustal evolution. Precamb. Res., 30, pp 263-276.

KLEMENIC P.M. 1987. Variable intra-plate igneous activity in central and north-east Sudan. J. Afr. Earth Sci., Vol 6, No 4, pp 465-474.

KLEMENIC P.M. and POOLE S. 1988. The geology and geochemistry of Upper Proterozoic granitoids from the Red Sea Hills, Sudan. J. geol Soc. London, Vol 145, pp 635-643.

KLEMENIC P.M., POOLE S., and ALI S.E.M. 1985. The geochemistry of late upper-Proterozoic volcanic groups in the Red Sea Hills of northeast Sudan - evolution of a late-Proterozoic volcanic arc system. J. geol. Soc. London, 142, pp 1221-1233.

KLERKX J. and DEUTSCH S. 1977. Résultats préliminaires obtenus par la méthode Rb/Sr sue l'âge des formations precambriennes de la région D'Uweinat (Libye). Rapp. annu. Mus. roy. Afr. centr. Tervuren (Belg.) Dept. Géol. Min. (1976), pp 83-94.

KLITSCH E.H. 1987. The palaegeographic development of NE-Africa. In "Current Research in African Earth Sciences", Matheis and Schandelmeier (eds) Balkema, Rotterdam,1987, pp 155-158.

KRAUSKOPF K.B. 1967. "Introduction to Geochemistry". McGraw-Hill.

KRONER A. 1977. Precambrian mobile belts of southern and eastern Africa - ancient sutures or sites of ensialic mobility? A case for crustal evolution towards plate tectonics. Tectonophysics, **40**, pp 101-135.

KRONER A. 1979. Pan African plate tectonics and its repercussions on the crust of northeast Africa. Geol. Rund., **68**, pp 565-583.

KRONER A. 1985. Ophiolites and the evolution of tectonic boundaries in the late-Proterozoic Arabian-Nubian shield of north east Africa and Arabia. Precamb. Res., **27**, pp 277-300.

KRONER A., HALPERN M., TEGTMEYER A., and BASAHEL A. 1984. Age and significance of metavolcanic sequences and granitoid gneisses from the Al Lith area, south-western Arabian Shield. Proceedings Vol. IGCP 164, Pan-African Crustal Evolution in the Arabian-Nubian Shield, King Abdulaziz Univ. Fac. Earth. Sci. Res. Ser., 6, pp380-388.

KRONER A., ROOBOL M.J., RAMSAY C.R., and JACKSON N.J. 1979. Pan African ages of some gneissic rocks in the Saudi Arabian Shield. J. geol. Soc. London, **136**, pp 455-461.

KRONER A., STERN R.J., DAWOUD A.S., COMPSTON W., and REISCHMANN T. 1987. The Pan-African continental margin in northeast Africa: evidence from a geochronological study of granulites at Sabaloka, Sudan. Earth Planet Sci. Lett., 85, pp 91-104.

LANDEFELD L.A. 1988. The geology of the Mother Lode Gold Belt, Sierra Nevada Foothills Metamorphic Belt, California. Bicentennial Gold 88, Melbourne. Geol. Soc. Aust. Abs. **22**, pp 167-172.

LEBLANC M. 1981. The late Proterozoic ophiolites of Bou Azzer (Morocco): Evidence for Pan-African plate tectonics. In "Precambrian Plate Tectonics", Kröner A (ed.), Elsevier, pp 435-448.

LESHER C.M., GIBSON H.L., and CAMPBELL I.H. 1986. Composition-volume changes during hydrothermal alteration of andesite at Buttercup Hill, Noranda District, Quebec. Geochim. Cosmochim. Acta, **50**, pp 2693-2705.

LIEGOIS J.P., BERTRAND J.M., and BLACK R. 1987. The subduction- and collision-related Pan-African composite batholith of the Adrar des Iforas (Mali): a review. Geol. Jour., 22, Thematic Issue, pp 185-211.

LISTER G.S. and SNOKE A.W. 1984. S-C mylonites. J. Struct. Geol., **6**, pp 617-638.

LUDDEN J.N., DAIGNEAULT R., ROBERT F., and TAYLOR R.P. 1984. Trace element mobility in alteration zones associated with Archaean Au lode deposits. Econ. Geol., **79**, pp 1131-1141.

LUDDEN J.N. and THOMPSON G. 1979. An evaluation of the behaviour of the rare earth elements during the weathering of sea floor basalt. Earth Planet. Sci. Lett., **43**, pp 85-92.

MACLEAN W.H. and KRANIDIOTIS P. 1987. Immobile elements as monitors of mass transfer in hydrothermal alteration: Phelps Dodge massive sulphide deposit, Matagami, Quebec. Econ. Geol., **82**, pp 951-962.

MARZOUKI F.M.H., JACKSON N.J., RAMSAY C.R., and DARBYSHIRE D.P.F. 1982. Composition age and origin of two Proterozoic diorite -tonalite complexes in the Arabian shield. Precamb. Res., **19**, pp 31-80.

MATSUHISA Y., GOLDSMITH J.R., and CLAYTON R.N. 1979. Oxygen isotope fractionation in the system quartz-albite-anorthite-water. Geochim. Cosmochim. Acta, **43**, pp 1131-1140.

MAWSON R. and WILLIAMS M.A.J. 1984. A wetter climate in eastern Sudan 2000 years ago? Nature, **309**, pp 49-51.

McCAIG A.M. 1988. Deep fluid circulation in fault zones. Geology, **16**, pp 867-870.

McWILLIAMS M.O. 1981. Palaeomagnetic and Precambrian tectonic evolution of Gondwana. In "Precambrian Plate Tectonics", Kröner A (ed.), Elsevier, pp 649-687.

MEDANI A.H. and VAIL J.R. 1974. Post-Cretaceous faulting in Sudan and its relationship to the East African Rift System. Nature, **248**, pp133-5.

MIRONOV A.C., KHMODIK S.M., and MAKSIMOVA E.A. 1981. An experimental investigation of the sorption of gold by pyrites with different thermo-electric properties. Geochem. Int., **18**, pp 153-160.

MESCHEDE M. 1986. A method of discriminating between different types of mid-ocean ridge basalts and continental tholeiites with the Nb-Zr-Y diagram. Chem. Geol., **56**, pp 207-218.

MITCHELL W.S. and AUMENTO F. 1977. Uranium in oceanic rocks: Deep Sea Drilling Project Leg 37. Can. J. Earth. Sci., **14**, pp 794-808.

MIYASHIRO A. 1973. "Metamorphism and Metamorphic Belts". George Allen and Unwin, London, 492pp.

MOLNAR P. and TAPPONIER P. 1975. Cainozoic tectonics of Asia: the effects of a continental collision. Science, **189**, pp 419-426.

MONTOYA J.W. and HEMLEY J.J. 1975. Activity relations and stabilities in alkali feldspar and mica alteration reactions. Econ. Geol., **70**, pp 577-594.

MOORE J.McM. 1979. Tectonics of the Najd transcurrent fault system, Saudi Arabia. J. geol. Soc. London, **136**, pp 441-454.

MOORE J.McM. 1982. Strcuture, stratigrphy and mineralization in the southern Arabian Shield: a study in satellite image interpretation. Abstract. Precamb. Res., **16**, A53-54.

MOORE J.McM. 1983. Tectonic fabric and structural control of mineralization in the southern Arabian Shield: a compilation based on satellite imagery interpretation. Open file Rep. Saudi Arabian Dir. Miner. Resour., USGS-OF-03-105.

van MOORT J.C. 1987. Electron spin resonance of auriferous and barren quartz at Beaconsfield, Northern Tasmania. J. Geochem. Exploration, **27**, pp 1-11.

MORGEN G.E. and BRIDEN J.C. 1981. Aspeccts of Precambrian palaeomagnetism with new data from the Limpopo Mobile Belt and Kaapvaal craton in Southern Africa. Phys. Earth. Planet. Int., **24**, pp 142-168.

MORTEANI G., GRUNDMANN G., and FUGANTI A. 1986. Gold-bearing quartz veins in the northwestern Nubian Desert, northern Sudan. Abs. Geocongress, J'berg, pp 571-572.

MOSELEY F. 1983. "The Volcanic Rocks of the Lake District". Macmillan, London, 111pp.

NAGY R.M., GHUMA M.A., and ROGERS J.J.W. 1976. A crustal suture and lineament in north Africa. Tectonophysics, **31**, T67-72.

NASSEEF A.O., BAKOR A.R., and HASHAD A.H. 1980. Petrography of possible ophiolite rocks along the Qift-Quseir road, Eastern Desert, Egypt. In "Evolution and Mineralisation of the Nubian-Arabian Shield", 4, Al-Shanti A.M.S. (ed), Pergamon Press, Oxford, pp 157-168.

NASSEEF A.O. and GASS I.G. 1977. Granitic and metamorphic rocks of the Taif area, western Saudi Arabian. Bull. Geol. Soc. Am., **88**, pp 1721-1730.

NASSIEF M.O., MACDONALD R., and GASS I.G. 1984. The Jebel Thurwah Upper Proterozoic ophiolite complex, western Saudi Arabia. J. geol Soc. London, **141**, pp 537-546.

NAWAB Z.A. 1979. Geology of the Al Amar-Idsas region of the Arabian Shield. In "Evolution and Mineralisation of the Nubian-Arabian Shield", 2, Al-Shanti A.M.S. and Tahoun S.A. (eds), Pergamon Press, Oxford, pp 29-40.

NEARY C.R., GASS I.G., and CAVANAGH R.J. 1976. Granitic association of north-east Sudan. Bull. Geol. Soc. Am., **87**, pp 1501-1512.

NEALL F.B. and PHILLIPS G.N. 1987. Fluid-wallrock interaction in an Archaean hydrothermal gold deposit: a thermodynamic model for the Hunt Mine, Kambalda. Ecn. Geol., **82**, pp 1679-1694.

NESBITT B.E. 1988. Gold deposit continuum: a genetic model for lode Au mineralization in the continental crust. Geology, **16**, pp 1044-1048.

NESBITT B.E., MUROWCHICK J.B. and MUEHLENBACHS K. 1986. Dual origins of lode gold deposits in the Canadian Cordillera. Geology, **14**, pp 506-509.

NEUERBERG G. 1961. A method of mineral separation using hydrofluoric acid. J. Am. Miner., **72**, pp 1241-1250.

NUR A. 1982. The origin of tensile fracture lineaments. J. Struct. Geol., **4**, pp 31-40.

O'HALLORAN D. 1985. Ras ed Dom migrating ring complex: A-type granites and syenites from the Bayuda Desert, Sudan. J. Afr. Earth Sci., **3**, pp 61-75.

OHMOTO H. 1986. Stable isotope geochemistry of ore deposits. In "Stable Isotopes in High Temperature Geological Processes." Valley J.W., Taylor H.P., and O'Neil J.R. (eds), Min. Soc. Am., Reviews in Mineralogy, **16**, pp 491-560.

PALLISTER J.S., STACEY J.S., FISCHER L.B., and PREMO W.R. 1987. Arabian Shield ophiolites and Late Proterozoic microplate accretion. Geology, 15, pp 320-323.

PALLISTER J.S., STACEY J.S., FISCHER L.B., and PREMO W.R. 1988. Precambrian ophiolites of Arabia : Geologic settings, U-Pb Geochronology, Pb-isotope characteristics, and implications for continental accretion. Precamb. Res., 38, pp 1-54.

PEARCE J.A. 1982. Trace element characteristics of lavas from destructive plate boundaries. In "Andesites", R.S. Thorpe (ed.), J. Wiley and Sons.

PEARCE J.A. 1983. Role of the sub-continental lithosphere in magma genesis at active continental margins. In "Continental Basalts and Mantle Xenoliths". Hawkesworth C.J. and Norry M.J. (eds), Shiva, Cheshire, pp 230-249.

PEARCE J.A. and CANN J.R. 1973. Tectonic setting of basic volcanic rocks determined using trace element analyses. Earth Planet Sci. Lett., 19, pp 290-300.

PEARCE J.A., HARRIS N.B.W., and TINDLE A.G. 1984. Trace element discrimination diagrams for the tectonic interpretation of granitic rocks. Jour. Petrol., 25, pp 956-983.

PERRING C.S., GROVES D.I., and HO S.E. 1987. Constraints on the source of auriferous fluids for Archaean gold deposits. Uni. WA Geol. Dept. Extn. Publ., 11, pp 287-306.

PHILLIPS G.N. 1985. Archaean gold deposits of Australia. Univ. Witwatersrand, Econ. Geol. Res. Unit, Inf. Circ. 175, 41pp.

PHILLIPS G.N. and GROVES D.I. 1983. Fluid access and fluid-wallrock interaction in the genesis of the Archaean gold-quartz vein deposit at Hunt Mine, Kambalda, western Australia. In "Gold '82: The Geology and Genesis of Gold Deposits." Foster (ed), A.A. Balkema, pp 389-416.

PHILLIPS G.N. and BROWN I.J. 1987. Host rock and fluid control on carbonate assemblages in the Golden Mile Dolerite, Kalgoorlie Gold Deposit, Australia. Can. Miner., 25, pp 265-273.

PHIPPS D. and PLAYFORD G. 1984. Laboratory techniques for the extraction of palynomorphs from sediments. Dept. Geol. Univ. Queensland, 11, 1, 22pp.

PICHAVANT M., RAMBOZ C. and WEISBROD A. 1982. Fluid immiscibility in natural processes: use and misuse of fluid inclusion data. I. Phase equilibria analysis - a theoretical and geometrical approach. Chem. Geol., 37, pp 1-27.

PLATT J.P. 1979. Extensional crenulation cleavage. J. Struct. Geol., 1, pp 95.

PLATT J.P. 1984. Secondary cleavages in ductile shear zones. J. Struct. Geol., 6, pp 439-442.

PLATT J.P. and VISSERS R.L.M. 1980. Extensional structures in anisotropic rocks. J. Struct. Geol., 2, pp 397-410.

POHL W. 1982. Large-scale metallogenic features of the Precambrian in northeast Africa and Arabia. Abstract. Precamb. Res., **16**, A32-33.

RAMBOZ C., PICHAVANT M., and WEISBROD A. 1982. Fluid immiscibility in natural processes: use and misuse of fluid inclusion data. II. Interpretation of fluid inclusion data in terms of immiscibility. Chem. Geol., **37**, pp 28-48.

RAMSAY C.R., JACKSON N.J., and ROOBOL M.J. 1979. Structural/ lithological provinces in a Saudi Arabian Shield geotraverse. In "Evolution and Mineralisation of the Nubian-Arabian Shield", 1, Al-Shanti A.M.S. and Tahoun S.A. (eds), Pergamon Press, Oxford, pp 63-84.

RAMSAY C.R., STOESER D.B., and DRYSDALL A.R. 1986. Guidelines to classification and nomenclature of Arabian felsic plutonic rocks. J. Afr. Earth Sci., Vol **4**, pp 13-20.

RAMSAY J.G. 1967. "Folding and Fracturing of Rocks". McGraw-Hill, New York, 567pp.

RAMSAY J.G. 1980a. The crack-seal mechanism of rock deformation. Nature, **284**, pp 227-238.

RAMSAY J.G. 1980b. Shear zone geometry: a review. J. Struct. Geol., **2**, pp 83-89.

READ J.J. and MEINERT L.D. 1986. Gold-bearing quartz vein mineralisation at the Big Hurrah Mine, Seward Peninsula, Alaska. Econ. Geol., **81**, pp 1760-1774.

REISCHMANN T. 1986. Geologie und Genese spätproteroischer Vulkanite der Red Sea Hills, Sudan. PhD Thesis (unpubl.), Univ. Mainz, 202pp.

REISCHMANN T., KRONER A., and HOFMANN A.W. 1986. Nd isotope characteristics of late-Proterozoic rocks from the Red Sea Hills, Sudan, and their significance for the evolution of the Arabian-Nubian Shield (ANS). Absract U5, Terra Cognita, Vol 6, No. 2, pp 234.

REYMER A. and SCHUBERT G. 1984. Phanerozoic addition rates to the continental crust and crustal growth. Tectonics, 3, pp 63-77.

REYMER A. and SCHUBERT G. 1986. Rapid growth of some major segments of continental crust. Geology, **14**, pp 299-302.

RIEDEL W. 1929. Zur Mechanik geologischer Brucherscheinungen. Centralbl. f. Mineral. Geol. u. Pal., 1929B, pp 354-368.

RIES A.C. and SHACKLETON R.M. 1985. Geochronology, geochemistry and tectonics of the northeast Bayuda desert, north Sudan: Implications for the western margins of the late-Proterozoic fold belt of north-east Africa. Precamb. Res., **30**, pp 43-62.

RIES A.C., SHACKLETON R.M., GRAHAM R.H., and FITCHES W.R. 1983. Pan-African structures, ophiolites and melange in the east desert of Egypt: a traverse at 26°N. J. geol. Soc. London, **140**, pp 75-95.

RINGWOOD A.E. 1974. The petrological evolution of island arc systems. J. geol. Soc. London, **130**, pp 183-204.

ROBERT F. and BROWN A.C. 1986a. Archaean gold-bearing quartz veins at the Sigma Mine, Abitibi Greenstone Belt, Quebec: Part I. Geologic relations and formation of the vein system. Econ. Geol., **81**,pp 578-592.

ROBERT F. and BROWN A.C. 1986b. Archaean gold-bearing quartz veins at the Sigma Mine, Abitibi Greenstone Belt, Quebec: Part II. Vein paragenesis and hydrothermal alteration. Econ. Geol., **81**, pp 593-616.

ROBERT F. and KELLY W.C. 1987. Ore-forming fluids in Archaean gold-bearing quartz veins at the Sigma Mine, Abitibi Greenstone Belt, Quebec Canada. Econ. Geol., **82**, pp 1464-1482.

ROBERTON A. 1987. An account of the Gebeit Mine, from records at the mine office. Unpubl. report.

ROBERTS R.G. 1987. Ore deposit models £1. Archaean lode gold deposits. Geoscience Canada, **14**, pp 37-52.

ROBERTSON RESEARCH INTERNATIONAL 1983-1985. Reports on the Sudan-Minex gold project, 3916, 3184.

ROCK N.M.S. 1987. The nature and origin of lamprophyres: an overview. In "Alkaline Igneous Rocks" Fitton and Upton (eds) Geol. Soc. Sp. Pub., **30**, pp 191-226.

ROCK N.M.S., DULLER P., HASZELDINE R.S., and GROVES D.I. 1987. Lamprophyres as potential gold exploration targets: some preliminary observations and speculations. Uni. WA Geol. Dept. Extn. Publ., **11**, pp 271-286.

ROCK N.M.S. and GROVES D.I. 1988. Can lamprophyres resolve the genetic controversy over mesothermal gold deposits? Geology, **16**, pp 538-541.

ROEDDER E. 1984. "Fluid Inclusions". Min. Soc. Am., Reviews in Mineralogy, **12**, 644pp.

ROGERS J.J.W., GHUMA M.A., NAGY R.M., GREENBERG J.K., and FULLAGAR P.D. 1978. Plutonism in Pan-African belts and the geologic evolution of northeastern Africa. Earth Planet. Sci. Lett., **39**, pp 109-117.

ROOBOL M.J., RAMSAY C.R., JACKSON N.J., and DARBYSHIRE D.P.F. 1983. Late-Proterozoic lavas of the central Arabian shield - evolution of an ancient volcanic arc system. J. geol. Soc. London, **140**, pp 185-202.

RUXTON B.P. 1956. The major rock groups of the northern Red Sea Hills, Sudan. Geol. Mag., **193**, pp 314-330.

SAUNDERS A.D. and TARNEY J. 1979. The geochemical of basalts from a back-arc spreading centre in the East Scotia Sea. Geochim. Cosmochim. Acta, **43**, pp 555-572.

SAUNDERS A.D. and TARNEY J. 1984. Geochemical characteristics of basaltic volcanism within back-arc basins. In "Marginal Basin Geology". Kokelaar B.P. and Howells M.F. (eds), Blackwell, Oxford, pp 59-76.

SCHANDELMEIER H. and HARMS U. 1987. The Northern Zalingei fold zone: an intracontinental mobile belt of mid-Proterozoic age in northeast Africa. In "Current Research in African Earth Sciences", Matheis and Schandelmeier (eds) Balkema, Rotterdam,1987, pp 45-48.

SCHANDELMEIER H., RICHTER A., and HARMS U. 1987. Proterozoic deformation of the east Saharan craton in southeast Libya, south Egypt and north Sudan. Tectonophysics, **140**, pp 233-246.

SCHMID R. 1981. Descriptive nomenclature and classification of pyroclastic deposits and fragments: recommendations of the IUGS Subcommision on the systematics of Igneous rocks. Geology, **9**, pp 41-43.

SCHMIDT D.L., HADLEY D.G., and STOESSER D.B. 1979. Late Proterozoic crustal history of the Arabian Shield, Southern Najd Province, Kingdom of Saudi Arabia. In "Evolution and Mineralisation of the Nubian-Arabian Shield", 2, Al-Shanti A.M.S. and Tahoun S.A. (eds), Pergamon Press, Oxford, pp 41-58.

SCHULL T.J. 1988. Rift basins of interior Sudan: Petroleum exploration and discovery. Bull. Am. Ass. Petrol. Geol., **72**, pp 1128-1142.

SCHURMANN H.M.E. 1966. "The Precambrian along the Gulf of Suez and the northern part of the Red Sea". Publ. Leiden, E J Brill.

SEWARD T.M. 1973. Thio complexes of gold in hydrothermal ore solutions. Geochim. Cosmochim. Acta., **37**, pp 379-399.

SEWARD T.M. 1979. Hydrothermal transport and deposition of gold. Uni. WA Geol. Dept. Extn. Publ., **3**, pp 45-55.

SEWARD T.M. 1984. The transport and deposition of gold in hydrothermal systems. In "Gold '82: The Geology and Genesis of Gold Deposits." Foster (ed.), A.A. Balkema, Rotterdam, pp 165-181.

SEYFERT C.K. and SIRKIN L.A. 1973. "Earth History and Plate Tectonics." Harper & Row, New York, 504pp.

SHACKLETON R.M. 1977. Possible late-Precambrian ophiolites in Africa and Brazil. Ann. Rep. Res. Inst. Afr. Geol. Univ. Leeds, **20**, pp 3-7.

SHACKLETON R.M. 1979. Precambrian tectonics of north-east Africa. In "Evolution and Mineralisation of the Nubian-Arabian Shield", 2, Al Shanti A.M.S. and Tahoun S.A. (eds), Pergamon Press, Oxford, pp 1-6.

SHACKLETON R.M. 1986. Precambrian collision tectonics in Africa. In "Collision Tectonics", Coward M P,Ries A C (eds) Geol. Soc. Spec. Publ. No. **19**, pp 329-349.

SHACKLETON R.M., RIES A.C., GRAHAM R.H., and FITCHES W.R. 1980. Late Precambrian ophiolitic mélange in the eastern desert of Egypt. Nature, **285**, pp 472-474.

SHACKLETON R.M. and RIES A.C. 1986. The relationship between regionally consistent stretching lineations and plate motions. J. Struct. Geol., **6**, pp 111-117.

SHANTI M. and ROOBOL M.J. 1979. A Late Proterozoic ophiolite complex at Jabal Ess in northern Saudi Arabia. Nature, **279**, pp 488-491.

SHELTON K.L., SO C-S., and CHANG J-S. 1988. Gold-rich mesothermal vein deposits of the Republic of Korea: geochemical studies of the Jungwon Gold Area. Econ. Geol., **83**, pp 1221-1237.

SHEPHERD T., RANKIN A.H., and ALDERTON D.H.M. 1985." A Practical Guide to Fluid Inclusion Studies". Blackie, Glasgow, 239pp.

SHIMAMOTO T. 1989. The origin of s-c mylonites. J. Struct. Geol., **11**, pp 51-64.

SHIMRON A.E. 1980. Proterozoic island arc volcanism and sedimentation in Sinai. Precamb. Res., **12**, pp 437-458.

SIBSON R.H. 1977. Fault rocks and mechanisms. J. geol. Soc. London, **133**, pp 191-213.

SIBSON R.H. 1989. Earthquake faulting as a structural process. J. Struct. Geol., **11**, pp 1-14.

SIBSON R.H., MOORE R.McM., and RANKIN AH. 1975. Seismic pumping - a hydrothermal fluid transport mechanism. J. geol. Soc. London, **131**, pp 653-659.

SIBSON R.H., ROBERT F., and POULSEN K.H. 1988. High-angle reverse faults, fluid-pressure cycling, and mesothermal gold-quartz deposits. Geology, **16**, pp 551-555.

SIMPSON C. and SCHMID S.M. 1983. An evaluation of criteria to deduce the sense of movement in sheared rocks. Bull. Geol. Soc. Am., **94**, pp 1281-1288.

SOLIMAN F.A., EL-SHARKAWI M.A., HUSSEIN A.A.A., and GAD M.A. 1982. Geology, geochemistry and mineralisation of the Umm Samiuki area, Eastern Desert, Egypt. Abstract. Precamb. Res., **16**, A38-39.

STACEY J.S. and AGAR R.A. 1985. U-Pb isotopic evidence for the accretion of a continental microplate in the Saudi Arabian Shield. J. geol. Soc. London, **142**, pp 1189-1203.

STACEY J.S., DOE B.R., ROBERTS R.J., DELEVAUX M.H., and GRAMLICH J.W. 1980. A lead isotope study of mineralisation in the Saudi Arabian Shield. Contrib. Min. Pet., **74**, pp 175-188.

STACEY J.S. and HEDGE C.E. 1984. Geochronologic and isotope evidence for early Proterozoic crust in the eastern Arabian shield. Geology **12**, pp 310-313.

STACEY J.S. and STOESER D.B. 1983. Distribution of oceanic and continental leads in the Arabian-Nubian Shield. Contrib. Min. Pet., **84**, pp 91-105.

STACEY J.S., STOESER D.B., GREENWOOD W.R., and FISCHER L.B. 1984. U-Pb Zircon Geochronology and geological evolution of the Halaban-Al Amar region of the eastern Arabian Shield, Kingdom of Saudi Arabia. J. geol. Soc. London, **141**, pp 1043-1055.

STARLING A., GILLIGAN J.M., CARTER A.H.C., FOSTER R.P., and SAUNDERS R.A. 1989. High-temperature hydrothermal precipitation of precious metals on the surface of pyrite. Nature, **340**, pp 298-300.

STECKLER M.S. and ten BRINK U.S. 1986. Lithospheric strength variations as a control on new plate boundaries. Earth Planet. Sci. Lett., **79**, pp 120-132.

STEINER L. 1987. The Nuba ophiolite and its geological setting. In "Current Research in African Earth Sciences", Matheis and Schandelmeier (eds) Balkema, Rotterdam,1987, pp 101-104.

STERN R.J. 1979. Late Precambrian ensimatic volcanism in the central eastern desert of Egypt. PhD thesis, Univ. Calif., San Diego, 210pp.

STERN R.J. 1981. Petrogenesis and tectonic setting of late-Precambrian ensimatic volcanic rocks, Central Eastern Desert Egypt. Precamb. Res., **1.6**, pp 195-230.

STERN R.J. and HEDGE C.E. 1985. Geochronologic and isotopic constraints on late-Precambrian crustal evolution in the Eastern Desert of Egypt. Am. Jour. Sci., **285**, pp 97-127.

STERN R.J. and MANTON W.I. 1987. Age of Feiran basement rocks, Sinai: implications for late Precambrian crustal evolution in the northern Arabian-Nubian Shield. J. geol. Soc. London, **144**, pp 569-575.

STERN R.J., KRONER A., MANTON W.I., REISCHMANN T., MANSOUR M., and HUSSEIN I.M. 1989. Geochronology of the late Precambrian Hamisana shear zone, Red Sea Hills, Sudan and Egypt. J. geol. Soc. London, **146**, pp 1017-1029.

STOESER D.B. 1986. Distribution and tectonic setting of plutonic rocks of the Arabian shield. J. Afr. Earth Sci., Vol **4**, pp 21-46.

STOESER D.B. and CAMP V.E. 1985. Pan-African microplate accretion of the Arabian Shield. Bull. Geol. Soc. Am., **96**, pp 817-826.

STOESER D.B. and ELLIOT J.E. 1980. Post-orogenic peralkaline and calc-alkaline ranites and associted mineralization of the Arabian Shield, Kingdom of Saudi Arabia. In "Evolution and Mineralisation of the Nubian-Arabian Shield", 4, Al-Shanti A.M.S. (ed), Pergamon Press, Oxford, pp 1-24.

STOESER D.B., STACEY J.S., GREENWOOD W.R., and FISCHER L.B. 1984. U/Pb zircon geochronology of the southern portion of the Nabitah mobile belt and Pan-African continental collision in the Saudi Arabian Shield. Saudi Arabian Dep. Min. Min. Res. Tech. Rec. USGS-TR-04-5, 88pp.

STRECKEISEN A. 1976. To each plutonic rock its proper name. Earth Sci. Rev., **12**, pp 1-33.

STUCKLESS J.S. 1987. Fractionation of geochemically similar elements in A-type granites from the Arabian Shield. Geol. Soc. Am. Abs., **19**, p858.

STUDEMEISTER P.A. and KILIAS S. 1987. Alteration pattern and fluid inclusions of gold-bearing quartz veins in Archaean trondjhemite near Wawa, Ontario, Canada. Econ. Geol., **82**, pp 429-439.

STURCHIO N.C., SULTAN M., and BATIZA R. 1983. Geology and origin of the Meatiq Dome, Egypt: a Precambrian metamorphic core complex? Geology, **11**, pp 72-76.

SUTHREN R.J. 1985. Facies analysis of volcaniclastic sediments: a review. In "Sedimentology - Recent Developments and Applied Aspects". Brenchley P.J. and Williams B.P.J.(eds), Blackwell, Oxford, pp 123-146.

TAPPONIER P. and MOLNAR. P. 1976. Slip-line field theory and large scale continental tectonics. Nature, **264**, pp 319-324.

TAYLOR S.R. and McCLENNAN S.M. 1985. "The Continental Crust: its Composition and Evolution." Blackwell, Oxford, 312pp.

TCHALENKO J.S. 1970. Similarities between shear zones of different magnitudes. Bull. Geol. Soc. Am., **81**, pp 1625-1640.

TECHNOEXPORT 1978. Geological map of the Red Sea Hills of Sudan (1:1000 000) Technoexport final report. Geol. Miner. Resour. Dept. Khartoum. (unpubl.)

TERRELL D.J., PAL S., LOPEZ M.M., and PEREZ R.J. 1979. Rare earth elements in basalt samples, Gulf of California. Chem. Geol., **26**, pp 267-275.

TRELOAR P.J. 1988. The geological evolution of the Magondi Mobile Belt, Zimbabwe. Precamb. Res., **38**, pp 55-73.

TROMMSDORFF V. and SKIPPEN G. 1986. Vapour loss ("boiling") as a mechanism for fluid evolution in metamorphic rocks. Contrib. Mineral. Petrol., **94**, pp 317-322.

VAIL J.R. 1973. Distribution of igneous ring complexes and Sudan and vicinity. 17th Ann. Rep. Inst. Afr. Geo., pp 27-30.

VAIL J.R. 1976. Location and geochronology of igneous ring complexes and related rocks in northeast Africa. Geol. Jahrb., **20**, pp 97-114.

VAIL J.R. 1978. The outline of the Geology of mineral deposits of the Dem. Rep. of Sudan and adjacent areas. Overseas Geol. Miner. Resour., London (IGS & NERC), No. 49, HMSO.

VAIL J.R. 1979. Outline of Geology and mineralisation of the Nubian Shield east of the Nile Valley, Sudan. In "Evolution and Mineralisation of the Nubian-Arabian Shield", 1, Tahoun S.A. (ed), Pergamon Press, Oxford, pp 97-107.

VAIL J.R. 1982. Distribution and tectonic setting of post-kinematic igneous complexes in the Red Sea Hills of Sudan and the Arabian-Nubian Shield. Abstract. Precamb. Res., **16**, A41.

VAIL J.R. 1983. Pan-African crustal accretion in north-east Africa. J. Afr. Earth Sci., 1, pp 285-294.

VAIL J.R. 1985a. Relationship between tectonic terrains and favourable metallogenesis domains in the central Arabian-Nubian Shield. Trans. Inst. Min. Metall. (Sect B Appl. Earth Sci.), **94**, pp B1-B5.

VAIL J.R. 1985b. Pan-African (late Precambrian) tectonic terrains and the reconstruction of the Arabian-Nubian Shield, Geology,**13**,pp 839-842.

VAIL J.R. 1985c. Alkaline ring complexes in Sudan. J. Afr. Earth Sci. 3, pp 51-59.

VAIL J.R. 1987a. Late-Proterozoic tectonic terranes in the Arabian-Nubian Shield and their characteristic mineralisation. Geol. Jour., **22**, Thematic Issue, pp 161-174.

VAIL J.R. 1987b. Tectonics and evolution of the Proterozoic basement of northeastern Africa. In "The Pan-African Belt of Northeast Africa and Adjacent Areas - Tectonic Evolution and Economic Aspects of a Late-Proterozoic Orogen". El-Gaby and Greiling (eds), Braunschweig, Wiesbaden, pp 195-226.

VAIL J.R. 1989. Ring complexes and related rocks in Africa. J. Afr. Earth Sci., 8, pp 19-40.

VAIL J.R. and HUGHES D.J. 1977. Tholeiite derivative dyke swarms near Erkowit, Red Sea Hills, Sudan. Geol. Rdsch., 66, pp 228-237.

VAIL J.R. and KURON J.L. 1978. High level igneous emplacements in the Red Sea Hills, Sudan. Geol. Rdsch., 67, pp 521-530.

VAIL J.R., ALMOND D.C., HUGHES D.J., KLEMENIC P.M., POOLE S., NOUR S.E.M., and EMBLETON J.C.B. 1984. Geology of the Wadi Oko-Khor Hayet area, Red Sea Hills, Sudan. Bull. Geol. Miner. Resour. Dept. Sudan, 34, pp 1-20.

VAIL J.R. and HUGHES D.J. 1987. The contact between the continental Sudan Shield and the orogenic Nubian Shield in Blue Nile Province, Sudan. In "Current Research in African Earth Sciences", Matheis and Schandelmeier (eds) Balkema, Rotterdam,1987, pp 105-108.

VEARNCOMBE J.R. 1983. A dismembered ophiolite from the Mozambique Belt, West Pokot, Kenya. J. Afr. Earth Sci., 1, pp 285-294.

VERCOUTTER J. 1959. The gold of Kush. J. Sudan Antiquities Service, 7 pp120-153.

VILJOEN M.J. 1982. Archaean gold mineralisation and komatiites in southern Africa. In "Gold '82: The Geology and Genesis of Gold Deposits." Foster (ed.), A.A. Balkema, Rotterdam, pp 595-627.

WALSH J.F., KESLER S.E., DUFF D., and CLOKE P.I. 1988. Fluid inclusion geochemistry of high-grade, vein-hosted gold ore at the Paramour Mine, Porcupine Camp, Ontario. Econ. Geol., 83, pp 1347-1367.

WARDEN A.J. 1982. The northeast branch of the Mozambique Belt. Abstract. Precamb. Res., 16, A41-A42.

WARDEN A.J. and DANIELS J.L. 1982. Evolution of the Precambrian of Northern Somalia. Abstract. Precamb. Res., 16, A42-A43.

WARDEN A.J. and DANIELS J.L. 1984. Evolution of the Precambrian of Northern Somalia. Bull. Fac. Earth Sci., King Abdulaziz Univ., Jeddah, 6, pp 145-164.

WATSON E.B. and BRENAN J.M. 1987. Fluids in the lithosphere,1. Experimentally-determined wetting characteristics of CO_2-H_2O fluids and their implications for fluid transport, host-rock physical properties, and fluid inclusion formation. Earth Planet. Sci. Lett., 85, pp 497-515

WHITE D.L. 1985. The significance of continental derivation of the Proterozoic Mahanid Formation, southeast Arabian Shield. J. geol. Soc. London, 142, pp 1235-1238.

WHITE S.H. and BAXTER J.L. 1987. Gold mineralisation in shear zones. Hermitage Holdings Pty Ltd., Strctural Geology Workshop Manual pp 55.

WHITE S.H., BURROWS S.E., CARRERAS J., SHAW N.D., and HUMPHREYS F.J. 1980. On mylonites in ductile shear zones. J. Struct. Geol., 2, pp 175-187.

WHITE C.J. and WHITE S.H. 1981. The structure of grain boundaries in tectonites. Tectonophysics, 78, pp 613-628.

WHITEMAN A.J. 1968. Formation of the Red Sea depression. Geol. Mag., 105, pp 231-246.

WHITEMAN A.J. 1971. "Geology of the Sudan Republic". Clarendon Press, Oxford. 290 pp.

WINCHESTER J.A. and FLOYD P.A. 1977. Geochemical discrimination of different magma series and their differentiation products using immobile elements. Chem. Geol., 20, pp 325-345.

WINDLEY B.F. 1984. "The Evolving Continents." 2nd Ed., J. Wiley, Chichester, 399pp.

WOOD P.C., BURROWS D.R., THOMAS A.V. and SPOONER E.T.C. 1986. The Hollinger-McIntyre Au-quartz vein system, Timmins, Ontario, Canada; geologic characteristics, fluid properties and light stable isotopes. In "Proceedings of Gold '86 - an International Symposium on the Geology of Gold: Toronto". Macdonald A.J. (ed), pp 58-80.

WOODALL R. 1988. Gold in 1988. Bicentennial Gold 88, Melbourne. Geol. Soc. Aust. Abs. 22, pp 1-12.

WOODCOCK N.H. and FISCHER M. 1986. Strike-slip duplexes. J. Struct. Geol., 8, pp 725-735.

WYCISK P. 1987. Sequential arrangement of cratonic sedimentation since Silurian time (northwest Sudan/southwest Egypt). In "Current Research in African Earth Sciences", Matheis and Schandelmeier (eds), 1987, pp 211-216.

WYMAN D. and KERRICH R. 1988. Alkaline magmatism, major structures, and gold deposits: implications for greenstone belt gold metallogeny. Econ. Geol., 83, pp 454-461.

YARDLEY B.W.D. and BOTTRELL S.H. 1988. immiscible fluids in metamorphism: implications for two=phase flow for reaction history. Geology, 16, pp 199-202.

YASSIN A.A. and AHMED A.H. 1984. Gold mineralisation in north eastern Sudan. Bull. Geol. Miner. Resour. Dept., Sudan. 15pp.

APPENDIX A

Analytical operating conditions

---

1) Oxygen Isotopes

Visibly pure 100mg samples of Gebeit vein quartz were crushed using a mortar and pestle and sieved using 150μm (100 mesh) and 74μm (200 mesh) nylon filters to obtain a 100-200 mesh-sized sample. These grains were boiled in industrial grade HCl for 2-3 hours and washed at each stage of processing using 3- and 5-times distilled water and finally dried at 105°C. All samples were examined by binocular microscope for contaminant minerals and 2 random samples analysed by XRD as a cross-check. Oxygen isotope analyses were performed at the Scottish Universities Research and Reactor Centre using standard techniques under the auspices of Dr T. Fallick. For each analysis, 20mg of quartz was reacted with BrF_5 or ClF_3 overnight at 3-5 atmospheres in a Ni bomb liberating gaseous O_2 which was analysed on a double collector mass spectrometer (ISOSPEC 44). The routine internal standard used was Standard NBS 28 with an isotopic value of $\delta^{18}O$ = 9.6‰, and within run precision for pure homogenous quartz is ±0.1‰ (1σ). All results are given in the text (Table 6.2).

2) X-Ray Fluorescence Analysis

XRF analyses were carried out using a Philips PW1400 wavelength dispersive X-ray fluorescence machine using a 3kW rhodium anode X-ray tube. Data processing was performed on a dedicated DEC PDP-11/23 running under the MICRO-RSX operating system. Voltage, current settings and analyte line wavelength are element specific. For major element analysis, powdered samples were fused with a 5:1 mixture of eutectic flux (Spectroflux 100B) to produce a homogenous glass bead. Trace elements were analysed using a pressed pellet of pulverised rock mixed with a few drops of 7% PVA solution. Estimates of bias precision are given overleaf and analyses tabulated in Appendices B and F.

Accuracy and Precision Estimates for X-Ray Fluorescence Analysis.

International standards used in this study:

NIM-G : granite, Bushveld Igneous Complex,
AC-E : granite, Ailsa Craig, Scotland,
BE-N : basalt, old volcano near Essey-La-Côte, Nancy, France,
BHVO-1 : basaltic lava, Kilauea Caldera, Hawaii,
BCR : basalt, Columbia River Group, Bridal Veil Flow Quarry, Washington, USA.

Trace element values (ppm) in BCR, BEN, NIM-G, & GnA reference material.

Element	Line	Proposed values	LLD	n	This work Mean	SD	Precision (%)
Pb	Pb Lβ	13	3	5	14.6	1.20	8.22
Th	Th Lα	6	3	5	6.2	0.98	15.80
Rb	Rb Kα	47	2	5	45	2.00	4.44
U	U Lα	1.7	5	5	1.4	1.02	72.90
Sr	Sr Kα	330	2	5	323.6	3.50	1.08
Y	Y Kα	38	2	5	37.2	1.17	3.15
Zr	Zr Kα	191	2	5	188.6	2.80	1.48
Nb	Nb Kα	14	2	5	12	0.89	7.42
Ga	Ga Kα	19	1	5	26.2	2.14	8.17
Zn	Zn Kα	127	1	5	128	2.00	1.56
Ni	Ni Kα	13	2	5	14	1.79	12.79
Cr	Cr Kα	360	4	4	329.8	8.07	2.45
V	V Kα	404	5	4	411.8	5.85	1.42
Ba	Ba Lβ	678	10	4	702.8	14.80	2.11
La	La Lα	25	6	3	27.7	0.94	3.39
Ce	Ce Lβ	54	10	3	56.7	4.50	7.94
As	As Kβ	17	7	1	15	0.00	—
Cu	Cu Kα	72	2	2	56.5	1.50	2.65
Mo	Mo Kα	97	2	5	92.6	4.32	4.67
Sn	Sn Kα	1920	3	5	1902.6	11.11	0.58
Bi	Bi Lα	230	3	5	195.2	9.64	4.94

Standards BEN & BCR used for elements Pb to Ce, NIM-G & GnA for elements As to Bi.
Lower limit of detection, LLD (2σ) = $3m.\ \sqrt{R_b/T_b}$,
where: m = slope factor (conc units/counts/s), R_b = background count rate,
T_b = background counting time.

Precision and bias for major elements in AC-E and BHVO reference materials

Reference Material	Accepted Value	Batch 1	2	3	4	5	6	Mean	SD (σ_{n-1})	Precision (%)
BHVO										
SiO_2 (%)	49.99		49.22	49.28	49.39	48.88	49.43	49.24	0.22	0.44
TiO_2	2.68		2.61	2.68	2.62	2.63	2.69	2.65	0.04	1.35
Al_2O_3	13.74		13.40	13.28	13.38	13.60	13.62	13.46	0.15	1.11
Fe_2O_3*	12.15		12.07	12.09	12.11	12.11	12.16	12.11	0.03	0.25
MnO	0.17		0.17	0.17	0.17	0.17	0.17	0.17	0.00	0.00
MgO	7.07		7.07	7.24	7.19	7.16	7.22	7.18	0.07	1.00
CaO	11.35		11.35	11.30	11.32	11.38	11.37	11.34	0.03	0.30
Na_2O	2.20		2.49	2.25	2.28	2.30	2.54	2.37	0.13	5.61
K_2O	0.53		0.54	0.50	0.50	0.51	0.53	0.52	0.02	3.49
P_2O_5	0.28		0.28	0.25	0.25	0.25	0.26	0.26	0.01	5.00
AC-E										
SiO_2 (%)	70.35	70.77		68.60	69.65	69.39	70.66	69.81	0.91	1.30
TiO_2	0.11	0.10		0.10	0.10	0.10	0.11	0.10	0.004	3.92
Al_2O_3	14.70	14.88		14.46	14.46	14.72	14.84	14.67	0.20	1.38
Fe_2O_3*	2.53	2.75		2.49	2.49	2.51	2.56	2.56	0.11	4.30
MnO	0.06	0.06		0.06	0.06	0.06	0.07	0.06	0.004	7.50
MgO	0.03	0.05		0.00	0.00	0.00	0.01	0.01	0.02	220.0
CaO	0.34	0.38		0.36	0.36	0.36	0.38	0.37	0.01	2.97
Na_2O	6.54	6.81		6.59	6.56	6.49	6.75	6.64	0.13	2.03
K_2O	4.49	4.57		4.44	4.44	4.43	4.61	4.50	0.09	2.00
P_2O_5	0.01	0.05		0.00	0.00	0.00	0.00	0.01	0.02	200.00

WITHIN BATCH MEAN					OVERALL BIAS (%)	OVERALL PRECISION (%)
SiO_2 (%)	58.94	59.52	59.29	60.05	- 1.20	0.78
TiO_2	1.39	1.36	1.37	1.40	- 1.40	1.30
Al_2O_3	13.87	13.92	14.16	14.23	- 1.20	1.26
Fe_2O_3*	7.29	7.30	7.31	7.36	- 0.30	0.42
MnO	0.12	0.12	0.12	0.12	0.00	0.00
MgO	3.62	3.60	3.58	3.62	+ 1.50	0.53
CaO	5.83	5.84	5.87	5.88	+ 0.09	0.41
Na_2O	4.42	4.42	4.40	4.65	+ 2.20	2.66
K_2O	2.47	2.47	2.47	2.57	- 0.60	2.00
P_2O_5	0.13	0.13	0.13	0.13	-15.00	0.00

* Total Fe calculated as Fe_2O_3. SD= standard deviation (σ_{n-1}) to 95% confidence level
Precision low for MgO and P_2O_5 for AC-E as very close to detection limit.
Overall precision for major element analysis of the Gebeit lithologies = ±3%

3) X-Ray Diffraction

XRD analyses were performed using a Philips 1700 series X-ray diffraction machine with Cu Kα radiation at a tube voltage of 40 kV and a tube current of 36mA, running at 1° per minute with 1° slits.

4) Microprobe Analysis

a) Qualitative analyses and high-resolution back-scattered electron (BSE) photography were carried out using an I.S.I. model 60A scanning electron microscope fitted with a ROBINSON back-scatterd electron detector and a PRINCETON GAMMA-TECH energy dispersive (EDS) analyser under an accelerating voltage of 20 kV.

b) Quantitative analyses of Gebeit wallrock alteration mineral assemblages (i.e. chlorite, quartz, albite, sericite, aclcite, ankerite and tourmaline) were performed on a CAMBRIDGE INSTRUMENTS Microscan Mark 9 wavelength dispersive microprobe at the Department of Earth Sciences, Oxford University.

5) Background Gold Analysis

Low level gold analyses were carried out by the Anamet laboratory using acid digestion techniques. 25-50g of pulverised rock was subjected to aqua regia (HNO_3 and HCl) to dissolve the gold. Gold was extracted from the resulting solution by absorption into DIBK-ALIQUAT 336 (di-isobutyl ketone) mixed organic solvent using a low (5-10%) acid strength to minimise iron extraction. The solvent gold content is determined by carbon furnace atomic absorption (A.A.) with standard solutions and the gold content back-calculated. The precision from replicate analyses of international reference material is ±15% at 300 ppb and the detection limit of the method is 1 ppb. Results are fully tabulated in Table 7.12.

6) Fluid Inclusion Analysis

Twenty-two double-sided polished chip samples (50-100μm thick) were produced for this study covering vein phases V_1-V_4 for the Gebeit area and most of the satellite prospects (Garabein, Halal Hindeib, Um Arad, Tagoti, Wadi Messesana). In virtually all samples, the fluid

inclusion populations were too small for thermometric analysis (<5µm) and only two samples WM011 (Wadi Messana) and V1810 (Vein 18) had inclusions large enough to be analysed. Heating and freezing measurements were performed using a Linkam TH 1500 heating-freezing stage and a microscope fitted with a long working distance condenser lens and cooled using liquid N_2. Data are tabulated in Appendix D.

7) Thermoluminescence

Thermoluminescence analyses were performed by the GEP Group, Faculté de Polytechnique de Mons, Belgium, under the auspices of Prof. J.M. Charlet. Relatively pure samples of Gebeit vein quartz were obtained by moderate crushing, washing and sieving of 100-125µm size grains followed by heavy liquid separation (density <2.83) and final washing in HF to cleanse the grains. TL properties were defined from the glow curve characteristics by plotting light intensity against temperature for heated samples. This was determined using a high sensitivity photon counting machine (ATL 2000) TL machine with a linear heating programme (2°C/s) connected with a microcomputer. Samples were measured for both natural (NTL) and artificial thermoluminescence (ATL; photodesexcitation for 24h with a UV source followed by irradiation with a Co^{60} source for 5h) and are fully tabulated in Appendix E and summarised in Table 6.4.

Sample No.	Rock type	Sample Location
TMS 001	ankerite phyllonite	WLE 5100E,5400N
TMS 002	plag. phyric tuff	DDH 22 08m
TMS 003	Hb-cpx-phyric andesite	DDH 21 130m
TMS 004	chlorite phyllonite	DDH 35, 54m
TMS 005	chlorite phyllonite	DDH 23 100m
TMS 006	fine aphyric tuff	DDH 21 21m
TMS 007	shale	DDH 34 79m
TMS 008	fine laminated tuff	DDH 25 110m
TMS 009	Hb-cpx-phyric andesite	DDH 23 130m
TMS 010	Hb-cpx-phyric andesite	DDH 28 98m
TMS 011	altd Hb-cpx-phyric andesite	DDH 26 131m
TMS 012	chlorite phyllonite	DDH 28 74m
TMS 013	Hb-cpx-phyric andesite	DDH 28 98m
TMS 014	Phase 3 dolerite dyke (altd)	5400E,6020N
TMS 015	Phase 1 diorite dyke	5450E,5800N
TMS 016	altered basic intrusion	4800E,6670N
TMS 017	ultra-potassic trachyte dyke	5150E,6350N
TMS 018	alkali granite	6500E,5500N
TMS 019	Phase 1 diorite dyke	5000E,5600N
TMS 020	basalt	5475E,6400N
TMS 021	tuffaceous slate	Sasa Plain
TMS 022	gabbro	5500E,6500N
TMS 023	ultra-potassic trachyte dyke	4100E,5900N
TMS 024	tonalite	VEIN 18
TMS 025	Phase 1 dolerite dyke	4850E,6000N
TMS 026	Phase 3 dolerite dyke (altered)	5600E,4900N
TMS 027	Phase 1 dolerite dyke	5000E,6500N
TMS 028	ultra-potassic trachyte dyke	5100E,6400N
TMS 029	Phase 1 diorite dyke	5250E,6300N
TMS 030	Hb-cpx-basal cumulate flow	stratigraphic section
TMS 031	ankerite phyllonite	5200E,6000N
TMS 032	chlorite phyllonite	5100E,6200N
TMS 033	ankerite phyllonite	4100E,5900N
TMS 034	chlorite phyllonite	5000E,6900N
TMS 035	altered footwall tuffs	4352E,4735N
TMS 036	aphyric basalt	4950E,6400N
TMS 037	Hb-cpx-phyric andesite	Marble Bar South
TMS 038	Phase 4 dolerite dyke	4600E,6150N
TMS 039	white V_3 quartz vein	5100E,5700N
TMS 040	blue V_1 quartz vein	Garabein
TMS 041	shale sample for pyrolysis	DDH 35 127m
TMS 042	blue V_1 quartz vein	DDH 35 120.11-120.36m
TMS 043		120.36-120.61m
TMS 044		120.61-120.86m
TMS 045		120.86-121.11m
TMS 046		121.11-121.36m
TMS 047		121.36-121.61m
TMS 048	Lode Profile 2	121.61-121.86m
TMS 049		121.86-122.11m
TMS 050		122.11-122.61m
TMS 051		122.61-123.11m
TMS 052		123.11-123.61m
TMS 053		123.61-124.11m
TMS 054		124.11-124.61m
TMS 055		124.61-125.11m

Sample No.	Rock type	Sample Location
TMS 056		DDH 35 125.11-126.11m
TMS 057		126.11-127.11m
TMS 058	Lode Profile 2	127.11-128.11m
TMS 059		128.11-129.11m
TMS 060		129.11-130.11m
TMS 061		130.11-130.40m
TMS 062	Pyrolysis shale sample	DDH 35 115m
TMS 063		DDH 46 89.50-89.75m
TMS 064		89.75-90.00m
TMS 065		90.00-90.25m
TMS 066		90.25-90.50m
TMS 067		90.50-90.75m
TMS 068		90.75-91.00m
TMS 069		91.00-91.25m
TMS 070		91.25-91.50m
TMS 071		91.50-91.75m
TMS 072		91.75-92.00m
TMS 073		92.00-92.25m
TMS 074	Lode Profile 1	92.25-92.50m
TMS 075		92.50-92.75m
TMS 076	Fine to coarse	92.75-93.00m
TMS 077	andesitic tuff	93.00-93.50m
TMS 078		93.50-94.00m
TMS 079		94.00-94.50m
TMS 080		94.50-95.00m
TMS 081		95.00-95.50m
TMS 082		95.50-96.00m
TMS 083		96.00-97.00m
TMS 084		97.00-98.00m
TMS 085		98.00-99.00m
TMS 086		99.00-100.00m
TMS 087		5000E,5300N
TMS 088	Phase 1 diorite dyke	5000E,5300N
TMS 089	Phase 2 dolerite dyke	5000E,5300N
TMS 090	Phase 1 gabbro	4250E, 8250N
TMS 091	Phase 2 granite	Sasa Plain
TMS 092	Phase 1 diorite dyke	4200E,6500N
TMS 093	Phase 3 dolerite	5050E,5950N
TMS 094	Phase 2 granodiorite	West Gebeit
TMS 095	Na-trachyte dyke	Yemomt
TMS 096	Phase 1 granodiorite	Wadi Messesana
TMS 097	Phase 4 dolerite dyke	5000E,6750N
TMS 098	ankerite phyllonite	4600E,4800N
TMS 099	Phase 1 diorite dyke	4600E,4800N
TMS 100	amphibolite	Sasa Plain
TMS 101	Phase 1 diorite dyke	4400E,6500N
TMS 102	quartzite	Wadi Yemomt
TMS 103	acid gneiss	Sasa Plain
TMS 104	Phase 2 dolerite dyke	4-level
TMS 105	fine laminated tuffs	Eastern Gebeit
TMS 106	silicified granodiorite	Wadi Messesana
TMS 107	sulphidised granodiorite	Wadi Messesana
TMS 108	altered footwall tuffs	Halal Hindeib
TMS 109	altered footwall tuffs	Halal Hindeib
TMS 110	Phase diorite dyke	Tagoti West

Sample No.	Rock type	Sample Location
TMS 111	carbonatised andesite bomb	4000E,6000N
TMS 112	Phase 1 dolerite dyke	4100E,6200N
TMS 113	altered footwall tuffs	Y Lode
TMS 114	andesite tuff	Sadareit
TMS 115	andesite tuff	Sadareit
TMS 116	red calcrete	5300E,6000N
TMS 117	white calcrete	5100E,6400N
TMS 118	ankerite phyllonite	4300E,6500N
TMS 119	ankerite phyllonite	4100E,5500N
TMS 120	Hb-cpx-phyric andesite	DDH 43 223.7m
TMS 121	Hb-cpx-phyric andesite	DDH 41
TMS 122	fine laminated tuffs	DDH 24 14m
TMS 123	carbonatised aphyric tuffs	4600E,6750N
TMS 124	granodiorite	Tikraneit
TMS 125	altered granodiorite	Tikraneit
TMS 126	pink post-tectonic granite	Tikraneit
TMS 127	Phase 1 diorite dyke	5000E,5300N
TMS 128	chlorite phyllonite	5300E,5600N
TMS 129	chloritised granodiorite	Tikraneit
TMS 130	fine laminated tuffs	Y Lode
TMS 131	tuffaceous slates	Sasa Plain
TMS 132	oxidised sulphidic schists	Vein 13
TMS 133	altered footwall tuffs	Y Lode Raise 9
TMS 134	oxidised sulphidic schists	Vein 18
TMS 135	altered footwall tuffs	4-level W37
TMS 136	oxidised sulphidic schists	Marble Bar N
TMS 137	Hb-cpx-phyric andesite (altd)	4-level W33
TMS 138	blue V_1 quartz vein	Garabein
TMS 139	shale	4-level W38
TMS 140	chlorite phyllonite	5200E,6000N
TMS 141	Cu-rich altered granodiorite	Tikraneit
TMS 142	altered footwall tuffs	4-level W36
TMS 143	altered footwall tuffs	4-level W36
TMS 144	altered footwall tuffs	4-level W35
TMS 145	Hb-cpx-phyric andesite	4400E,5900N
TMS 146	Hb-cpx-phyric andesite	Yemomt
TMS 147	Andesite pyroclastic flow	Garabein
TMS 148	Plagioclase-phyric tuffs	4650E,6400N
TMS 149	chlorite phyllonite	5000E,6900N
TMS 150	blue V_1 quartz vein	4-level W35

APPENDIX B

Geochemistry of the Volcanics and Intrusions at Gebeit

Gebeit Volcanics - Average Compositions

Sample	Basaltic Andesite Tuffs TMS 059-061 n=3	TMS 006,008 n=2	Plag. Phyric Volcanics n=6	Hb/Cpx Ph Volcanics n=7
SiO2	46.44	47.36	50.87	47.14
TiO2	.58	1.29	.82	.83
Al2O3	17.39	19.07	17.01	17.01
Fe2O3	8.54	14.00	9.51	10.19
MnO	.11	.16	.15	.18
MgO	2.92	4.28	4.60	6.07
CaO	6.85	4.94	6.19	10.77
Na2O	4.15	2.20	2.72	2.33
K2O	1.79	1.30	1.87	.20
P2O5	.10	.37	.21	.24
L.O.I.	6.51	4.75	7.03	4.51
TOTAL	95.37	99.72	101.01	99.47
Trace elements (ppm)				
As	28	<7	<7	14
Cu	42	65	19	58
Mo	<2	<2	<2	<2
Sn	<6	<6	<6	<6
Bi	<3	<3	<3	<3
Sb	<3	<3	<3	<3
Pb	<3	<3	4	4
Th	<3	<3	<3	<3
Rb	33	28	48	<2
U	<5	<5	<5	<5
Sr	323	412	301	560
Y	17	34	22	22
Zr	58	79	73	57
Nb	3	4	5	3
Ga	21	24	19	20
Zn	80	118	81	81
Ni	15	27	19	52
Cr	38	50	41	180
V	240	354	283	317
Ba	298	299	308	73
La	6	8	9	<6
Ce	<10	31	16	<10
Trace element Totals	1209	1534	1236	1453
TiO2	7921	14744	7601	9328
MnO	1139	1615	1607	1798

Hornblende, Pyroxene, Plagioclase Phyric Basaltic Andesites

Sample	TMS 003	TMS 009	TMS 010	TMS 013	TMS 020	TMS 030	TMS 036	TMS 037	TMS 120	TMS 121	TMS 145	TMS 146
SiO2	45.0	42.7	50.2	50.3	43.7	44.5	50.5	46.1	47.4	48.5	45.8	50.4
TiO2	.8	.7	.8	.9	.8	.4	.9	.7	1.0	.9	.8	.9
Al2O3	16.9	16.0	17.5	16.2	8.6	8.0	18.8	13.3	17.5	16.3	18.7	19.9
Fe2O3	10.1	10.7	10.1	10.0	8.8	12.2	10.3	8.9	10.2	9.4	10.9	11.2
MnO	.2	.2	.2	.2	.2	.2	.2	.2	.2	.2	.2	.2
MgO	8.3	6.8	4.8	6.1	7.6	19.5	4.2	5.5	5.4	5.5	5.7	4.5
CaO	10.2	13.0	9.4	8.9	20.3	9.8	8.5	12.0	11.4	13.0	9.6	8.9
Na2O	1.6	1.5	2.8	3.1	2.0	.3	3.1	1.8	2.3	2.1	3.1	2.6
K2O	.0	.4	.1	.1	.7	.1	.2	.3	.0	.1	.7	.2
P2O5	.3	.2	.2	.2	.2	.2	.1	.3	.2	.2	.2	.1
L.O.I.	6.1	6.9	3.3	3.2	5.6	4.5	2.7	10.0	4.3	3.2	4.6	1.3
TOTAL	99.4	99.0	99.4	99.1	98.5	99.6	99.6	99.1	99.8	99.4	100.2	100.2
Trace elements (ppm)												
As	8	<7	20	18	12	<7	9	7	25	10	17	<7
Cu	30	64	28	68	85	76	46	50	82	80	56	90
Mo	<2	<2	<2	<2	2	<2	<2	<2	<2	<2	<2	<2
Sn	<6	<6	<6	<6	<6	<6	<6	<6	<6	<6	<6	<6
Bi	<3	<3	<3	<3	<3	<3	<3	<3	<3	<3	<3	<3
Sb	3	<3	<3	<3	<3	<3	<3	<3	<3	<3	5	<3
Pb	<3	<3	3	3	<3	<3	<3	<3	3	4	5	<3
Th	<3	<3	<3	<3	<3	<3	<3	<3	<3	<3	<3	<3
Rb	<2	8	2	<2	12	<2	4	6	<2	<2	10	19
U	<5	<5	<5	<5	<5	<5	<5	<5	<5	<5	<5	<5
Sr	987	545	355	289	212	53	309	279	618	313	811	527
Y	20	21	26	25	14	10	28	15	23	20	19	15
Zr	48	40	70	57	67	32	87	38	63	58	65	55
Nb	3	3	4	3	8	2	3	3	3	3	3	3
Ga	18	18	22	19	12	13	23	17	23	21	18	22
Zn	78	85	95	95	66	85	90	81	85	74	56	93
Ni	84	39	28	57	243	502	19	40	48	67	44	49
Cr	330	210	74	318	799	1443	38	171	64	124	138	86
V	275	351	306	350	210	226	239	291	365	324	246	312
Ba	26	132	71	60	238	25	72	94	50	37	138	145
La	<6	<6	<6	8	<6	8	<6	<6	6	<6	<6	9
Ce	<10	<10	<10	<10	18	<10	<10	<10	11	26	11	10
Trace element Totals	1910	1516	1104	1370	1998	2475	967	1092	1469	1161	1642	1435
TiO2	8868	9409	10425	10456	9638	3729	8954	6838	9812	8593	7703	7479
MnO	1832	2072	2049	1749	1911	2036	1635	2361	1995	1659	1228	1757

Trace Element Ratios Hornblende/ Clinopyroxene Phyric Basaltic Andesites

	TMS 003	TMS 009	TMS 010	TMS 013	TMS 020	TMS 030	TMS 036	TMS 037	TMS 120	TMS 121	TMS 145	TMS 146
Zr/TiO2	.0054	.0043	.0067	.0055	.0070	.0086	.0097	.0056	.0064	.0067	.0084	.0074
Nb/Y	.1500	.1429	.1538	.1200	.5714	.2000	.1071	.2000	.1304	.1500	.1579	.2000
Ti	5320.80	5645.40	6255.00	6273.60	5782.80	2237.40	5372.40	4102.80	5905.20	5155.80	4621.80	4487.40
Ti/Y	266.04	268.83	240.58	250.94	413.06	223.74	191.87	273.52	256.75	257.79	243.25	299.16
Ti/Nb	1773.60	1881.80	1563.75	2091.20	722.85	1118.70	1790.80	1367.60	1968.40	1718.60	1540.60	1495.80
Ti/Cr	16.12	26.88	84.53	19.73	7.24	1.55	141.38	23.99	92.27	41.58	33.49	52.18
Ti/V	19.35	16.08	20.44	17.92	27.54	9.90	22.48	14.10	16.18	15.91	18.79	14.38
Zr/Y	2.400	1.905	2.692	2.280	4.786	3.200	3.107	2.533	2.739	2.900	3.421	3.667
Zr/Nb	16.00	13.33	17.50	19.00	8.38	16.00	29.00	12.67	21.00	19.33	21.67	18.33
Zr/Cr	.1455	.1905	.9459	.1792	.0839	.0222	2.2895	.2222	.9844	.4677	.4710	.6395
Zr/V	.1745	.1140	.2288	.1629	.3190	.1416	.3640	.1306	.1726	.1790	.2642	.1763
Zr/Ga	2.667	2.222	3.182	3.000	5.583	2.462	3.783	2.235	2.739	2.762	3.611	2.500
Ba/La	<L.L.D.	<L.L.D.	<L.L.D.	7.50	<L.L.D.	3.13	<L.L.D.	<L.L.D.	8.33	<L.L.D.	<L.L.D.	16.11
La/Th	<L.L.D.	<L.L.D.	<L.L.D.	<L.L.D.	<L.L.D.	<L.L.D.	<L.L.D.	<L.L.D.	<L.L.D.	<L.L.D.	<L.L.D.	<L.L.D.
La/Nb	<L.L.D.	<L.L.D.	<L.L.D.	2.67	<L.L.D.	4.00	<L.L.D.	<L.L.D.	2.00	<L.L.D.	<L.L.D.	3.00
K/Rb	<L.L.D.	396.27	361.46	<L.L.D.	477.11	<L.L.D.	505.12	361.02	<L.L.D.	<L.L.D.	573.57	69.99
FeO*/MgO	1.09	1.42	1.91	1.48	1.04	.56	2.22	1.47	1.71	1.53	1.72	2.25
Y.3	60	63	78	75	42	30	84	45	69	60	57	45
Ti/100	53.21	56.45	62.55	62.74	57.83	22.37	53.72	41.03	59.05	51.56	46.22	44.87
Ti%	33.01	35.40	29.71	32.22	34.66	26.52	23.91	33.08	30.91	30.41	27.48	30.97
Y%	37.22	39.51	37.05	38.51	25.18	35.56	37.38	36.28	36.12	35.39	33.88	31.06
Zr%	29.78	25.09	33.25	29.27	40.16	37.93	38.71	30.64	32.98	34.21	38.64	37.96

Fine Laminated Basaltic Andesite Tuffs

				Altered		Lode Alteration Profile 2			
Sample	TMS 008	TMS 105	TMS 122	TMS 006	TMS 123	TMS 058	TMS 059	TMS 060	TMS 061
SiO2	50.4	44.8	50.5	44.33	43.0	50.4	47.3	43.7	48.3
TiO2	1.4	1.3	.8	1.20	.3	.6	.5	.5	.7
Al2O3	17.3	20.7	17.1	20.87	8.1	18.5	15.7	16.9	19.6
Fe2O3	13.0	11.7	9.5	15.05	3.5	8.1	7.4	7.9	10.3
MnO	.2	.2	.2	.14	.1	.1	.1	.1	.1
MgO	5.2	4.1	4.9	3.34	7.5	2.3	2.4	2.5	3.9
CaO	5.4	10.7	5.7	4.44	12.4	3.6	8.2	9.2	3.2
Na2O	1.1	1.8	5.2	3.26	4.4	4.1	4.5	4.4	3.6
K2O	1.1	.0	.2	1.53	.2	2.5	1.4	1.7	2.3
P2O5	.2	.1	.3	.52	.2	.1	.1	.1	.1
L.O.I.	4.3	4.1	6.0	5.20	19.2	6.5	7.0	7.7	4.8
TOTAL	99.6	99.5	100.5	99.87	98.9	96.9	94.5	94.6	97.0
Trace elements (ppm)									
As	9	23	<7	<7	104	261	51	16	16
Cu	66	61	78	63	53	47	26	32	68
Mo	<2	<2	<2	<2	<2	5	<2	<2	<2
Sn	<6	<6	<6	<6	<6	<6	<6	<6	<6
Bi	<3	<3	<3	<3	<3	3	<3	<3	<3
Sb	<3	<3	<3	<3	<3	6	<3	<3	<3
Pb	<3	<3	6	<3	15	15	7	<3	<3
Th	<3	<3	<3	<3	<3	<3	<3	<3	<3
Rb	22	<2	2	33	4	46	27	30	42
U	<5	<5	<5	<5	<5	5	<5	<5	<5
Sr	379	356	221	445	351	215	444	349	177
Y	31	26	22	37	10	27	15	16	19
Zr	78	85	78	80	35	102	56	51	66
Nb	3	2	4	4	3	4	2	3	4
Ga	23	30	21	25	4	25	20	20	24
Zn	113	97	81	122	19	129	73	72	96
Ni	34	33	53	20	75	42	19	9	17
Cr	33	49	106	66	217	100	45	28	41
V	400	328	260	307	71	292	222	225	273
Ba	346	50	55	251	78	290	198	275	421
La	7	<6	<6	9	9	7	<6	6	6
Ce	25	10	13	36	12	22	<10	17	<10
Trace element Totals	1569	1150	1000	1498	1060	1633	1213	1143	1270
TiO2	16270	12865	7860	13218	3491	8083	7039	7188	9536
MnO	1792	1634	1749	1437	1090	683	1229	1326	862

Trace Element Ratios — Fine Laminated Basaltic Andesite Tuffs

	TMS 008	TMS 105	TMS 122	TMS 006	TMS 123	TMS 058	TMS 059	TMS 060	TMS 061
Zr/TiO2	.0048	.0066	.0099	.0061	.0100	.0126	.0080	.0071	.0069
Nb/Y	.0968	.0769	.1818	.1081	.3000	.1481	.1333	.1875	.2105
Ti	9762.00	7719.00	4716.00	7930.80	2094.60	4849.80	4223.40	4312.80	5721.60
Ti/Y	314.90	296.88	214.36	214.35	209.46	179.62	281.56	269.55	301.14
Ti/Nb	3254.00	3859.50	1179.00	1982.70	698.20	1212.45	2111.70	1437.60	1430.40
Ti/Cr	295.82	157.53	44.49	120.16	9.65	48.50	93.85	154.03	139.55
Ti/V	24.41	23.53	18.14	25.83	29.50	16.61	19.02	19.17	20.96
Zr/Y	2.52	3.27	3.55	2.16	3.50	3.78	3.73	3.19	3.47
Zr/Nb	26.00	42.50	19.50	20.00	11.67	25.50	28.00	17.00	16.50
Zr/Cr	2.36	1.73	.74	1.21	.16	1.02	1.24	1.82	1.61
Zr/V	.1950	.2591	.3000	.2606	.4930	.3493	.2523	.2267	.2418
Zr/Ga	3.39	2.83	3.71	3.20	8.75	4.08	2.80	2.55	2.75
Ba/La	49.43	<L.L.D.	<L.L.D.	27.89	8.67	41.43	<L.L.D.	45.83	70.17
La/Th	<L.L.D.	<L.L.D.	<L.L.D.	<L.L.D.	<L.L.D.	<L.L.D.	<L.L.D.	<L.L.D.	<L.L.D.
La/Nb	2.33	<L.L.D.	<L.L.D.	2.25	3.00	1.75	<L.L.D.	2.00	1.50
K/Rb	401.27	<L.L.D.	820.98	384.39	435.41	450.10	430.27	460.46	453.19
FeO*/MgO	2.23	2.57	1.72	4.05	.42	3.22	2.81	2.87	2.36
Y.3	93.00	78.00	66.00	111.00	30.00	81.00	45.00	48.00	57.00
Ti/100	97.62	77.19	47.16	79.31	20.95	48.50	42.23	43.13	57.22
Ti%	36.34	32.14	24.67	29.34	24.37	20.95	29.49	30.34	31.75
Y%	34.62	32.47	34.53	41.06	34.91	34.99	31.42	33.77	31.63
Zr%	29.04	35.39	40.80	29.60	40.72	44.06	39.10	35.88	36.62

Plagioclase Phyric Basaltic Andesites

Lode Alteration Profile 2

Sample	TMS 002	TMS 147	TMS 148	TMS 079	TMS 080	TMS 081	TMS 082	TMS 083
SiO2	54.3	55.1	51.2	48.9	50.1	50.1	48.9	50.6
TiO2	.6	.8	.8	.6	.9	.9	.8	.9
Al2O3	16.5	17.6	14.1	16.7	18.4	18.0	17.2	17.8
Fe2O3	8.3	8.7	10.7	10.0	10.1	9.1	9.2	9.7
MnO	.1	.1	.1	.2	.2	.2	.2	.2
MgO	3.3	3.7	8.0	7.4	4.5	4.1	3.8	4.0
CaO	5.0	5.0	4.5	6.0	6.4	6.0	8.4	6.9
Na2O	3.8	3.4	2.6	2.6	2.7	2.2	2.4	2.6
K2O	.8	1.6	1.3	1.0	1.9	2.7	2.3	2.2
P2O5	.2	.2	.2	.2	.2	.2	.2	.2
L.O.I.	5.9	3.9	6.7	8.1	6.5	6.9	8.9	7.3
TOTAL	98.9	100.1	100.1	101.8	102.0	100.4	102.2	102.4
Trace elements (ppm)								
As	28	<7	29	11	<7	<7	<7	<7
Cu	42	65	39	31	7	<2	4	4
Mo	<2	<2	<2	<2	<2	2	<2	<2
Sn	<6	<6	<6	<6	<6	<6	<6	<6
Bi	<3	<3	<3	<3	<3	<3	<3	<3
Sb	<3	<3	<3	<3	<3	<3	<3	<3
Pb	<3	9	4	<3	4	3	<3	3
Th	<2	<3	<2	<3	<3	3	<3	3
Rb	19	2	35	26	48	72	55	56
U	<5	<5	<5	<5	<5	<5	<5	<5
Sr	287	305	256	213	333	246	368	314
Y	19	21	20	13	25	25	23	22
Zr	84	66	100	38	67	67	59	63
Nb	4	3	4	4	5	5	5	4
Ga	18	20	21	14	18	19	17	18
Zn	77	107	88	78	77	73	83	86
Ni	24	49	19	68	21	16	12	22
Cr	115	90	24	207	25	33	26	23
V	254	255	206	210	311	310	298	316
Ba	173	148	196	142	283	449	380	364
La	9	<6	11	<6	9	9	6	<6
Ce	22	<10	13	<10	11	<10	<10	19
Trace element Totals	1175	1140	1065	1055	1224	1323	1330	1298
TiO2	7360	7985	7590	5767	8139	7913	7454	7148
MnO	1434	2056	1292	1844	1673	1598	1840	1806

Trace Element Ratios Plagioclase Phyric Basaltic Andesites

	TMS 002	TMS 147	TMS 148	TMS 079	TMS 080	TMS 081	TMS 082	TMS 083
Zr/TiO2	.0114	.0083	.0132	.0066	.0082	.0085	.0079	.0088
Nb/Y	.2105	.1429	.2000	.3077	.2000	.2000	.2174	.1818
Ti	4416.00	4791.00	4554.00	3460.20	4883.40	4747.80	4472.40	4288.80
Ti/Y	232.42	228.14	227.70	266.17	195.34	189.91	194.45	194.95
Ti/Nb	1104.00	1597.00	1138.50	865.05	976.68	949.56	894.48	1072.20
Ti/Cr	38.40	53.23	189.75	16.72	195.34	143.87	172.02	186.47
Ti/V	17.39	18.79	22.11	16.48	15.70	15.32	15.01	13.57
Zr/Y	4.42	3.14	5.00	2.92	2.68	2.68	2.57	2.86
Zr/Nb	21.00	22.00	25.00	9.50	13.40	13.40	11.80	15.75
Zr/Cr	.7304	.7333	4.1667	.1836	2.6800	2.0303	2.2692	2.7391
Zr/V	.3307	.2588	.4854	.1810	.2154	.2161	.1980	.1994
Zr/Ga	4.67	3.30	4.76	2.71	3.72	3.53	3.47	3.50
Ba/La	19.22	<L.L.D.	17.82	<L.L.D.	31.44	49.89	63.33	<L.L.D.
La/Th	<L.L.D.	<L.L.D.	<L.L.D.	<L.L.D.	<L.L.D.	3.00	<L.L.D.	<L.L.D.
La/Nb	2.25	<L.L.D.	2.75	<L.L.D.	1.80	1.80	1.20	<L.L.D.
K/Rb	349.54	6646.77	318.07	323.81	329.39	312.34	341.02	329.68
FeO*/MgO	2.27	2.12	1.20	1.21	2.01	2.01	2.21	2.18
Y.3	57	63	60	39	75	75	69	66
Ti/100	44.16	47.91	45.54	34.60	48.83	47.48	44.72	42.89
Ti%	23.85	27.08	22.16	31.00	25.59	25.06	25.89	24.95
Y%	30.78	35.61	29.19	34.95	39.30	39.58	39.95	38.40
Zr%	45.37	37.31	48.65	34.05	35.11	35.36	34.16	36.65

Spider Plot Data Pearce Norms

Hornblende, Pyroxene, Plagioclase Phyric Basaltic Andesites

	TMS 003	TMS 009	TMS 010	TMS 013	TMS 020	TMS 030	TMS 036	TMS 037	TMS 120	TMS 121	TMS 145	TMS 146
Sr	8.23	4.54	2.96	2.41	1.77	.44	2.58	2.33	5.15	2.61	6.76	4.39
K	.06	2.55	.58	.78	4.60	.45	1.62	1.74	.26	.65	4.61	1.07
Rb	.00	4.00	1.00	.00	6.00	.00	2.00	3.00	.00	.00	5.00	9.50
Ba	1.30	6.60	3.55	3.00	11.90	1.25	3.60	4.70	2.50	1.85	6.90	7.25
Th	.00	.00	.00	.00	.00	.00	.00	.00	.00	.00	.00	.00
Ta	.00	.00	.00	.00	.00	.00	.00	.00	.00	.00	.00	.00
Nb	.86	.86	1.14	.86	2.29	.57	.86	.86	.86	.86	.86	.86
Ce	.00	.00	.00	.00	1.80	.00	.00	.00	1.10	2.60	1.10	1.00
P	2.51	2.02	2.02	1.86	1.58	1.76	.98	2.40	2.08	1.70	1.59	.67
Zr	.53	.44	.78	.63	.74	.36	.97	.42	.70	.64	.72	.61
Hf	.00	.00	.00	.00	.00	.00	.00	.00	.00	.00	.00	.00
Sm	.00	.00	.00	.00	.00	.00	.00	.00	.00	.00	.00	.00
Ti	.59	.63	.70	.70	.64	.25	.60	.46	.66	.57	.51	.50
Y	.67	.70	.87	.83	.47	.33	.93	.50	.77	.67	.63	.50
Yb	.00	.00	.00	.00	.00	.00	.00	.00	.00	.00	.00	.00

Pearce Norms M.O.R.B. Normalised Data
Spider Plot Data

Plagiocalse Phyric Basaltic Andesites

					Lode Alteration Profile 1				
	M.O.R.B.	TMS 002	TMS 147	TMS 148	TMS 079	TMS 080	TMS 081	TMS 082	TMS 083
Sr	120.00	2.39	2.54	2.13	1.78	2.78	2.05	3.07	2.62
K	1245.00	5.33	10.68	8.94	6.76	12.70	18.06	15.07	14.83
Rb	2.00	9.50	1.00	17.50	13.00	24.00	36.00	27.50	28.00
Ba	20.00	8.65	7.40	9.80	7.10	14.15	22.45	19.00	18.20
Th	.20	.00	.00	.00	.00	.00	15.00	.00	15.00
Ta	.18	.00	.00	.00	.00	.00	.00	.00	.00
Nb	3.50	1.14	.86	1.14	1.14	1.43	1.43	1.43	1.14
Ce	10.00	2.20	.00	1.30	.00	1.10	.00	.00	1.90
P	523.00	1.96	2.01	1.34	1.54	1.88	1.87	1.76	1.79
Zr	90.00	.93	.73	1.11	.42	.74	.74	.66	.70
Hf	2.40	.00	.00	.00	.00	.00	.00	.00	.00
Sm	3.30	.00	.00	.00	.00	.00	.00	.00	.00
Ti	9000.00	.49	.53	.51	.38	.54	.53	.50	.48
Y	30.00	.63	.70	.67	.43	.83	.83	.77	.73
Yb	3.40	.00	.00	.00	.00	.00	.00	.00	.00

Spider Plot Data - Normalised To M.O.R.B. (after Pearce et al 1981)
Fine Andesitic Tuffs

Fine Laminated Basaltic Andesite Tuffs Spider Plot Data

				Altered			Lode Alteration Profile 2			
Pearce Norms	M.O.R.B.	TMS 008	TMS 105	TMS 122	TMS 123	TMS 006	TMS 058	TMS 059	TMS 060	TMS 061
Sr	120.00	3.16	2.97	1.84	2.93	3.71	1.79	3.70	2.91	1.48
K	1245.00	7.09	.13	1.32	1.40	10.19	16.63	9.33	11.10	15.29
Rb	2.00	11.00	.00	1.00	2.00	16.50	23.00	13.50	15.00	21.00
Ba	20.00	17.30	2.50	2.75	3.90	12.55	14.50	9.90	13.75	21.05
Th	.20	.00	.00	.00	.00	.00	.00	.00	.00	.00
Ta	.18	.00	.00	.00	.00	.00	.00	.00	.00	.00
Nb	3.50	.86	.57	1.14	.86	1.14	1.14	.57	.86	1.14
Ce	10.00	2.50	1.00	1.30	1.20	3.60	2.20	.00	1.70	.00
P	523.00	1.84	.80	2.36	1.89	4.36	1.25	.77	.92	.79
Zr	90.00	.87	.94	.87	.39	.89	1.13	.62	.57	.73
Hf	2.40	.00	.00	.00	.00	.00	.00	.00	.00	.00
Sm	3.30	.00	.00	.00	.00	.00	.00	.00	.00	.00
Ti	9000.00	1.08	.86	.52	.23	.88	.54	.47	.48	.64
Y	30.00	1.03	.87	.73	.33	1.23	.90	.50	.53	.63
Yb	3.40	.00	.00	.00	.00	.00	.00	.00	.00	.00

Geochemistry Data

	Shales	Wadi Lode 4 Level	Shales from Alteration Profile 2			
Sample	TMS 007	TMS 139	TMS 054	TMS 055	TMS 056	TMS 057
SiO2	56.65	48.27	50.21	51.34	51.52	53.95
TiO2	.54	.79	.54	.51	.52	.47
Al2O3	16.42	18.84	16.55	15.51	16.91	15.93
Fe2O3	7.85	8.09	8.84	7.21	8.10	7.11
MnO	.06	.07	.07	.08	.06	.06
MgO	2.06	1.92	3.82	1.70	1.56	1.48
CaO	2.33	3.22	4.66	6.32	4.52	4.61
Na2O	4.55	4.99	2.38	4.89	3.68	4.80
K2O	1.60	2.68	2.33	1.25	2.24	1.60
P2O5	.14	.13	.16	.12	.13	.14
L.O.I.	4.70	9.92	7.11	7.91	8.01	7.21
TOTAL	96.91	98.92	96.67	96.85	97.25	97.37
Trace elements (ppm)						
As	14	83	108	497	129	89
Cu	57	100	44	61	41	59
Mo	5	4	2	3	3	10
Sn	<6	<6	<6	<6	<6	<6
Bi	3	<3	<3	<3	<3	<3
Sb	3	11	4	7	9	6
Pb	8	12	12	19	27	21
Th	<3	<3	<3	<3	<3	<3
Rb	34	57	43	25	43	32
U	<5	<5	<5	<5	<5	<5
Sr	167	181	163	210	196	257
Y	29	25	22	23	21	23
Zr	114	93	91	96	82	100
Nb	4	4	4	5	4	4
Ga	20	24	24	20	23	20
Zn	110	143	81	112	112	176
Ni	35	53	54	27	27	32
Cr	118	83	238	216	140	228
V	227	299	232	179	266	223
Ba	156	248	298	144	238	201
La	7	<6	9	10	10	14
Ce	11	12	15	24	17	11
Trace element Totals	1122	1432	1443	1670	1384	1504
TiO2	7572	8299	8004	6952	7937	7101
MnO	570	696	799	892	612	604

Phase 1 Dykes: Calc-alkaline Dolerites and Diorites

	Dolerites				Diorites						
Sample	TMS 025	TMS 027	TMS 099	TMS 112	TMS 015	TMS 019	TMS 029	TMS 088	TMS 092	TMS 101	TMS 127
SiO2	55.19	46.93	47.19	48.92	57.03	54.73	57.00	56.72	54.57	56.88	54.54
TiO2	.61	.85	.78	.68	.66	.53	.78	.53	.50	.50	.75
Al2O3	15.32	20.29	14.45	15.19	16.06	15.62	17.04	15.52	14.77	15.11	15.86
Fe2O3	7.33	10.66	8.17	7.93	6.19	5.90	6.67	5.78	5.17	5.53	6.16
MnO	.13	.17	.16	.14	.09	.08	.09	.09	.09	.10	.09
MgO	6.22	4.85	5.60	5.23	4.93	4.02	5.68	4.17	4.13	3.89	3.91
CaO	7.30	9.99	7.74	5.87	2.98	4.69	1.49	4.43	4.51	4.91	4.65
Na2O	4.91	2.38	2.90	3.47	6.14	5.25	6.27	6.21	6.71	6.65	7.04
K2O	.89	.46	2.63	2.14	.41	1.09	.30	.25	.57	.67	.11
P2O5	.14	.17	.19	.16	.24	.23	.27	.16	.16	.17	.24
L.O.I.	1.60	2.10	9.47	10.24	4.40	6.90	3.50	5.80	8.23	8.17	5.63
TOTAL	99.63	99.02	99.40	100.13	99.12	99.04	99.08	99.66	99.41	102.57	98.97
Trace elements (ppm)											
As	8	51	17	199	17	275	38	9	25	17	15
Cu	<2	<2	80	52	<2	<2	10	27	32	32	40
Mo	<2	<2	<2	<2	<2	<2	<2	<2	<2	<2	<2
Sn	<6	<6	<6	6	<6	6	<6	<6	<6	<6	<6
Bi	<3	<3	<3	<3	<3	<3	<3	<3	<3	<3	<3
Sb	<3	<3	<3	<3	<3	<3	<3	<3	<3	<3	<3
Pb	<3	5	<3	3	7	<3	5	5	4	<3	8
Th	<3	<3	<3	<3	<3	<3	<3	<3	<3	<3	<3
Rb	8	8	31	59	5	43	3	3	7	7	2
U	<5	<5	<5	<5	<5	<5	<5	<5	<5	<5	<5
Sr	420	799	165	178	286	289	379	210	177	183	285
Y	13	24	14	17	15	13	14	9	9	9	13
Zr	55	80	67	95	110	112	124	93	89	88	111
Nb	2	3	3	3	5	5	4	4	4	3	4
Ga	18	29	15	17	23	22	25	23	20	19	20
Zn	64	82	73	69	78	67	85	79	58	66	76
Ni	54	30	39	80	37	67	35	34	28	24	57
Cr	342	87	160	208	217	275	135	186	182	166	132
V	166	312	229	186	185	171	185	125	118	112	183
Ba	231	149	329	467	434	289	547	620	297	289	224
La	<6	<6	<6	9	8	15	14	9	6	11	11
Ce	19	<10	<10	11	18	45	23	<10	10	10	23
Trace element Totals	1400	1659	1222	1659	1445	1694	1626	1436	1066	1036	1204
TiO2	6171	9468	7635	6943	6816	6475	6531	4912	4951	4810	6854
MnO	1262	1681	1670	1503	951	947	869	931	892	1029	1019
K2O/Na2O	.181	.193	.909	.617	.067	.208	.048	.040	.085	.101	.016
K2O+Na2O	5.79	2.84	5.53	5.60	6.56	6.34	6.57	6.45	7.28	7.32	7.15
Na2O+K2O/Al2O3	.378	.140	.383	.369	.408	.406	.386	.416	.493	.485	.451
K/Rb	1108	575	849	362	823	254	998	818	813	962	567
CaO+MgO	13.52	14.85	13.34	11.10	7.90	8.70	7.17	8.60	8.64	8.80	8.56
FeOt	6.60	9.59	7.35	7.13	5.57	5.31	6.00	5.20	4.65	4.98	5.54
Al/(Na+K+Ca/2)	.56	.99	.61	.65	.55	.48	.65	.48	.39	.40	.47

Phase 1 Intrusions: Calc-alkaline Gabbros and Granodiorites

	Gabbro	Granodiorites		
Sample	TMS 090	TMS 024	TMS 096	TMS 124
SiO2	45.50	66.38	67.61	66.23
TiO2	1.15	.38	.54	.69
Al2O3	14.38	16.15	16.15	15.00
Fe2O3	13.05	3.30	3.61	3.87
MnO	.18	.07	.06	.06
MgO	8.09	2.42	.98	1.69
CaO	11.15	3.19	1.32	2.52
Na2O	2.43	4.94	4.48	4.24
K2O	.24	.36	3.16	3.64
P2O5	.16	.14	.17	.19
L.O.I.	3.41	2.10	1.71	.76
TOTAL	99.74	99.44	99.78	98.89
Trace elements (ppm)				
As	<7	<7	81	9
Cu	138	30	25	20
Mo	<2	2	<2	<2
Sn	<6	<6	<6	<6
Bi	<3	<3	<3	<3
Sb	<3	<3	<3	<3
Pb	<3	6	8	7
Th	<3	<3	5	10
Rb	3	7	93	90
U	<5	<5	<5	<5
Sr	480	535	312	340
Y	16	11	17	17
Zr	36	110	220	234
Nb	2	4	9	7
Ga	14	19	25	23
Zn	82	41	40	33
Ni	62	41	26	30
Cr	31	368	24	43
V	399	69	43	68
Ba	55	174	677	716
La	<6	<6	25	14
Ce	<10	<10	36	33
Trace element Totals	1318	1417	1666	1694
TiO2	8019	3600	5445	6524
MnO	1863	708	622	583
K2O/Na2O		.07	.70	.86
K2O+Na2O		5.30	7.63	7.88
K2O+Na2O/Al2O3		.33	.47	.53
CaO+MgO		5.61	2.30	4.21
K/Rb		518	339	404
FeOt		2.97	3.25	3.48
Al/(Na+K+Ca/2)		.34	.30	.29

	Gabbros/Dolerites			Granitoids		
Sample	TMS 022	TMS 089	TMS 104	TMS 091	TMS 094	TMS 110
SiO2	37.45	49.33	45.33	58.23	54.62	65.54
TiO2	1.31	2.39	1.81	1.21	1.49	.82
Al2O3	17.87	15.02	14.14	16.35	15.71	14.90
Fe2O3	9.97	11.31	11.71	6.05	8.75	5.53
MnO	.14	.11	.15	.11	.13	.09
MgO	4.05	5.38	8.22	1.63	3.80	1.11
CaO	18.81	5.17	8.54	4.16	4.27	1.62
Na2O	1.46	2.35	2.03	4.69	3.73	4.46
K2O	.69	2.68	.98	2.73	2.62	3.40
P2O5	.89	.96	.42	.44	.69	.23
L.O.I.	5.60	4.50	5.45	3.06	3.71	1.89
TOTAL	98.24	99.45	98.96	98.66	99.74	99.59
Trace elements (ppm)						
As	10	<7	<7	<7	<7	<7
Cu	268	44	59	20	42	33
Mo	<2	3	<2	2	2	2
Sn	<6	<6	<6	<6	<6	<6
Bi	<3	<3	<3	<3	<3	<3
Sb	<3	<3	<3	<3	3	<3
Pb	<3	5	<3	6	8	8
Th	<3	<3	<3	<3	<3	6
Rb	13	44	26	52	31	61
U	<5	<5	<5	<5	<5	<5
Sr	806	439	450	516	503	177
Y	15	47	28	37	31	53
Zr	86	352	176	462	366	462
Nb	5	27	16	23	13	10
Ga	18	25	22	27	24	24
Zn	58	140	101	93	129	97
Ni	114	53	196	29	48	40
Cr	212	75	244	22	83	18
V	114	188	199	61	163	46
Ba	248	779	226	794	661	887
La	15	43	18	38	35	28
Ce	16	83	22	78	65	67
Trace element Totals	1998	2347	1783	2260	2207	2019
TiO2	14179	25052	18507	12386	14343	8141
MnO	1363	1116	1511	1018	1249	811
K2O/Na2O	.47	1.14	.48	.58	.70	.76
K2O+Na2O	2.14	5.03	3.01	7.42	6.34	7.86
Na2O+K2O/Al2O3	.12	.34	.21	.45	.40	.53
CaO+MgO	22.87	10.55	16.76	5.79	8.07	2.73
FeOt	8.97	10.18	10.53	5.44	7.87	4.98
K/Rb	531	610	378	525	845	558
Al/(Na+K+Ca/2)	.63	1.03	1.15	.44	.72	.44

	Alkaline Dolerites					
Sample	TMS 014	TMS 026	TMS 038	TMS 087	TMS 093	TMS 097
SiO2	42.42	40.22	44.73	42.17	45.66	43.58
TiO2	2.77	2.55	3.93	2.89	2.50	4.12
Al2O3	13.36	15.90	15.84	15.26	14.42	15.39
Fe2O3	11.45	12.71	14.89	11.98	11.61	15.65
MnO	.13	.23	.18	.11	.08	.21
MgO	3.23	6.00	5.55	4.58	6.49	4.70
CaO	11.36	17.62	7.98	7.45	7.43	7.49
Na2O	2.50	.02	3.66	2.20	2.69	3.62
K2O	.65	.00	1.16	3.28	1.31	1.20
P2O5	.63	.37	.75	.65	.45	.86
L.O.I.	10.60	2.20	.50	8.57	6.48	2.33
TOTAL	99.10	97.82	99.16	99.14	99.14	99.15
Trace elements (ppm)						
As	<7	<7	<7	<7	34	<7
Cu	22	10	30	36	58	52
Mo	2	<2	2	2	<2	<2
Sn	<6	<6	<6	<6	<6	<6
Bi	<3	<3	<3	<3	<3	<3
Sb	<3	<3	<3	<3	<3	<3
Pb	3	<3	<3	<3	<3	3
Th	<3	<3	3	4	4	3
Rb	9	<2	15	74	24	17
U	<5	<5	<5	<5	<5	<5
Sr	493	176	690	288	432	651
Y	28	23	31	27	18	34
Zr	178	143	249	277	206	264
Nb	30	21	35	45	34	38
Ga	23	19	30	25	28	25
Zn	107	77	120	105	164	138
Ni	66	66	54	24	151	68
Cr	102	116	43	18	152	37
V	202	128	148	147	159	172
Ba	262	65	596	827	375	410
La	22	13	40	39	30	31
Ce	63	33	62	63	43	63
Trace element Totals	1612	890	2148	2001	1912	2006
TiO2	27138	21870	43343	30712	26172	42667
MnO	1389	1723	1576	1098	803	1855
K2O/Na2O	.26	.00	.32	1.49	.49	.33
K2O+Na2O	3.16	.02	4.82	5.48	4.00	4.81
K2O+Na2O/Al2O3	.24	.00	.30	.36	.28	.31
K/Rb	726		773	443	547	703
FeOt	10.30	11.44	13.40	10.78	10.45	14.08
CaO+MgO	14.59	23.62	13.53	12.03	13.92	12.20

Post-tectonic alkaline intrusions

	Trachyandesite /Basalt	K-rich trachyte		Na-trachyte	Commendite
Sample	TMS 023	TMS 017	TMS 028	TMS 095	TMS 018
SiO2	47.78	61.92	62.02	62.72	70.73
TiO2	1.60	.05	.07	.07	.30
Al2O3	15.68	15.58	15.79	17.41	9.63
Fe2O3	8.04	3.63	3.81	4.26	7.50
MnO	.06	.11	.10	.19	.09
MgO	3.29	.94	.82	.00	.26
CaO	5.34	2.07	2.10	.65	1.41
Na2O	.41	2.24	1.86	7.92	.87
K2O	9.91	9.29	9.89	4.69	6.53
P2O5	.98	.02	.05	.01	.04
L.O.I.	5.90	3.20	3.10	1.32	2.20
TOTAL	98.98	99.04	99.60	99.24	99.57
Trace elements (ppm)					
As	<7	<7	<7	15	<7
Cu	2	<2	<2	<2	<2
Mo	<2	2	<2	24	8
Sn	<6	12	7	14	18
Bi	<3	<3	<3	<3	<3
Sb	<3	<3	<3	<3	<3
Pb	3	11	10	21	9
Th	6	9	13	43	22
Rb	185	162	161	224	146
U	<5	<5	5	10	6
Sr	119	62	57	25	22
Y	36	39	37	107	186
Zr	385	762	810	1742	1742
Nb	62	141	133	275	173
Ga	24	33	35	60	40
Zn	118	133	140	247	96
Ni	20	11	8	15	14
Cr	14	168	10	7	286
V	10	<5	<5	<5	10
Ba	1291	892	901	62	264
La	51	87	93	200	88
Ce	98	147	150	368	190
Trace element Totals	2424	2671	2570	3459	3320
TiO2	19304	647	610	637	4544
MnO	574	1106	1052	1975	1048
K2O/Na2O	23.89	4.14	5.33	.59	7.48
K2O+Na2O	10.32	11.53	11.74	12.61	7.41
K2O+Na2O/Al2O3	.66	.74	.74	.72	.77
K/Rb	536	573	614	210	448
FeOt	7.24	3.27	3.43	3.83	6.75
CaO+MgO	8.63	3.01	2.91	.65	1.68
Al/(Na+K+Ca/2)	.79	.82	.81	.92	.77

APPENDIX C

Structural Data (not contained on maps)

Estimation of the strain in deformed volcanic clasts by measurements of ratios (R) axial dimensions (where X>Y>Z, and ø'= angle to stretching lineation).

Millsite, East Gebeit (measurements in cm)

X	Rf(X/Y)	Y	Rf(Y/Z)	Z	ø'	X	Rf(X/Y)	Y	Rf(Y/Z)	Z	ø'
8.7	2.6	3.4	1.5	2.3	0	5.0	2.4	2.1	1.5	1.4	0
7.9	2.8	2.8	1.0	2.8	0	2.2	2.2	1.0	1.3	0.8	0
4.5	2.5	1.8			-17						
7.8	2.9	2.7			0	18.5	1.9	9.9	1.4	7.0	-34
4.6	2.9	1.6	1.3	1.2	4	7.8	1.9	4.2	1.0	4.2	-70
4.9	1.8	2.8	1.9	1.5	6	12.3	2.8	4.4	1.9	2.3	0
11.7	2.5	4.6	1.4	3.4	- 4	6.2	1.1	5.4	1.6	3.3	0
		5.4	1.5	3.6	0	7.6	1.9	4.1	1.6	2.6	0
26.6	2.3	11.7	1.5	7.6	-10	2.2	1.8	1.2	1.7	0.7	0
17.7	3.2	5.5	1.3	4.4	- 8	17.1	2.9	6.0	1.0	6.0	0
16.4	2.1	7.8	1.3	6.0	9	7.6	1.6	4.8	1.2	4.0	30
18.6	1.8	10.3	1.2	8.7	4	14.6	2.1	7.0	1.0	7.0	-25
				6.5				2.4	1.6	1.7	
9.8	2.5	3.9	1.6	2.4	- 8	6.1	1.4	4.5	1.1	4.3	-40
12.8	2.1	6.1	1.2	4.9	-20	7.7	2.2	3.5	3.5	1.0	0
16.2	2.7	5.9	1.4	4.2	3	12.7	1.5	8.2	1.4	6.0	0
7.0	2.9	2.4	1.0	2.8	0	6.2	1.1	5.5	1.4	4.0	0
		8.0	1.4	5.8		10.9	1.8	6.1	1.6	3.8	0
9.9	1.9	5.1			0						
15.0	2.7	5.5			-66						

Initial ellipticity of the clasts = Ri, Rf = final ratio
Strain ellipse ratio = Rs and Rf_{max} = Rs.Ri_{max}; Rf_{min} = Rs/Ri_{max}
For X/Y, Rf_{max} = 3.2, Rf_{min} = 1.1, Rs = 1.88 Ri = 1.71
For Y/Z, Rf_{max} = 1.9, Rf_{min} = 1.1, Rs = 1.44 Ri = 1.31
Thus, Rs (X:Y:Z) = 1.88:1:0.69; Ri = 1.71:1: 0.77

Garabein

X	Rf(X/Y)	Y	Rf(Y/Z)	Z	ø'	X	Rf(X/Y)	Y	Rf(Y/Z)	Z	ø'
5.6	2.0	2.8	1.2	2.4	9	4.7	1.4	3.4	1.3	2.7	12
8.7	1.4	6.3	1.8	3.5	6	5.3	1.8	2.9	1.5	1.9	-32
7.6	2.2	3.4	1.1	3.1	6	3.4	2.0	1.7	1.2	1.4	-5
5.4	2.6	2.1	2.1	1.0	6	2.4	1.5	1.6	1.1	1.4	-15
3.9	1.6	2.4	2.0	1.2	13	3.8	1.5	2.5	1.3	2.0	4
2.4	1.3	1.9	1.3	1.5	11	1.2	1.3	0.9	1.3	0.7	20
4.2	1.7	2.5	1.3	1.9	17	3.8	2.4	1.6	2.0	0.8	3
6.7	1.7	3.9	2.2	1.8	13	2.5	1.4	1.8	1.1	1.7	28
3.2	1.9	1.7	1.3	1.3	7	5.9	1.8	3.2	1.3	2.4	12
7.9	1.8	4.3	1.4	3.0	-3	2.1	1.8	1.2	1.2	1.0	26
4.7	2.0	2.4	1.0	2.4	14	2.0	2.0	1.0	1.4	0.7	6
5.2	2.2	2.4	1.8	1.3	-4	5.8	1.9	3.0	1.4	2.2	0

Garabein (cont)

X	Rf(X/Y)	Y	Rf(Y/Z)	Z	ø'	X	Rf(X/Y)	Y	Rf(Y/Z)	Z	ø'
6.6	3.1	2.1	1.1	1.9	0	5.5	1.6	3.4	1.4	2.5	-13
2.7	1.7	1.6	1.3	1.2	11	5.5	2.0	2.8	1.3	2.1	-5
2.2	1.8	1.2	1.5	0.8	-3	8.6	3.2	2.7	1.7	1.6	13
6.8	2.4	2.9	1.3	2.3	-7	7.1	2.4	2.9	1.2	2.4	13
2.9	1.6	1.8	1.3	1.4	4	5.6	1.6	3.5	1.4	2.5	-7
11.6	2.2	5.3	1.3	4.0	-2	5.2	2.2	2.4	1.1	2.1	-16
8.9	2.3	3.9	1.6	2.4	21	5.5	1.9	2.9	1.3	2.3	-11
3.4	1.7	2.0	1.3	1.5	-18	9.6	2.2	4.3	1.2	3.5	0

For X/Y, Rf_{max} = 3.2, Rf_{min} = 1.3, Rs = 2.04 Ri = 1.57
For Y/Z, Rf_{max} = 1.8, Rf_{min} = 1.1, Rs = 1.41 Ri = 1.28
Thus, Rs (X:Y:Z) = 2.00:1:0.71; Ri = 1.60:1: 0.78

West Gebeit

X	Rf(X/Y)	Y	Rf(Y/Z)	Z	ø'	X	Rf(X/Y)	Y	Rf(Y/Z)	Z	ø'
9.0	1.6	5.5	1.8		-7	9.2	1.7	5.3	2.3	2.3	36
14.5	1.6	9.0	2.6		-10	11.0	1.7	6.5	2.2	3.0	-16
8.8	2.0	4.5	1.5		0	10	1.9	5.3	2.8	1.9	23
3.2	1.7	1.8	1.1		0	8.2	1.9	4.4	1.4	3.2	0
9.0	1.7	5.3	1.7		-20	12	1.5	8	2.7	3.0	29
10.5	1.6	6.5			-4	24.6	2.6	9.4	4.7	2.0	0
3.4	1.8	1.9			0	9.8	2.0	5.0	2.8	1.8	-6
17.7	1.6	11.4			-42	10.2	2.1	4.8	2.3	2.1	0
6.2	2.6	2.4	1.5	1.6	3	34.6	2.9	10	2.4	5.1	0
7.2	1.9	3.8			-2	9.6	2.1	4.6	1.5	3.1	11
5.9	1.7	3.5			-33	22.5	2.3	10	2.9	3.4	0
1.8	1.8	1.0			0	32.6	3.0	11.0	2.4	4.6	-12
5.3	1.3	4.2			-54	4.0	1.3	3.1	2.6	1.2	0
12.5	1.9	6.5			-11			3.9	1.5	2.6	0
5	1.2	4.3	2.0		-5	14.4	2.3	6.0	2.6	2.3	0
12.5	1.7	7.2	1.2		22	9.9	1.9	5.2	1.9	2.9	0
9.9	1.9	5.2			0	12	1.4	8.5	1.8	4.6	0
3.5	2.9	1.2			-10	7.6	1.9	4.0	3.0	1.2	0
11.4	3.3	3.5			-4	10	2.9	3.5	2.0	1.7	0
10.4	2.2	4.8	1.2		26						

For X/Y, Rf_{max} = 2.9, Rf_{min} = 1.3, Rs = 1.94 Ri = 1.49
For Y/Z, Rf_{max} = 2.8, Rf_{min} = 1.2, Rs = 1.83 Ri = 1.53
Thus, Rs (X:Y:Z) = 1.94:1:0.55; Ri = 1.50:1: 0.65

APPENDIX D

Fluid Inclusion Data

F=Degree of fill, T_h=Homogenisation Temperature, T_m=Melting Temperature

wt% CO_2 =

$$\frac{(\text{vol\%}CO_2 \times \rho CO_2)}{(\text{vol\%}CO_2 \times \rho CO_2) + (\text{vol\%}H_2O \times \rho H_2O)}$$

where: ρH_2O assumed =1, ρCO_2 determined by T_h CO_2 vol% = visual estimate.

Sample V1810

F	T_h (°C)	T_m (°C)	F	T_h (°C)	T_m (°C)
0.90	210	-6.0	0.90	225	-1.0
0.90	223	-1.0	0.95	220	-1.5
0.90	202	1.0	0.95	206	0.0
0.90	228	-2.8	0.85	191	0.4
0.95	215	-2.8	0.85	211	-0.9
0.95	202	-2.4	0.85	206	-1.0
0.90	218	-1.4	0.90	228	0.4
0.95	228	-3.2	0.90	234	0.0
0.90	232	-2.6	0.90	201	5.0
0.90	230	-2.6	0.95	177	-0.3
0.85	238	-3.3	0.90	175	-0.5
0.95	201	-3.2	0.85	189	0.5
0.90	198	-1.1	0.90	162	0.8
0.80	190	-2.6	0.90	218	-1.0
0.90	190	-2.5	0.95	230	-1.0
0.95	207	-1.1			

T_h: n=27, x=214.15, σ_n=14.2, σ_{n-1}=14.46, Σx=5782

T_m n=23, x=-1.99, σ_n=1.27, σ_{n-1}=1.30, Σx=45.8

Sample WM011

Aqueous inclusions

F	T_h (°C)	T_m (°C)	F	T_h (°C)	T_m (°C)
0.80	204	10.1	0.80	180	- 0.7
0.55	262	3.7	0.90	170	2.0
0.80	200	4.6	0.95	168	- 0.2
0.75	263	3.7	0.80	147	- 0.5
0.90	235	3.3	0.85	159	- 0.9
0.65	253	4.9	0.90	159	- 0.7
0.95	192	- 1.9	0.95	145	
0.85	186	2.1	0.85	144	- 0.5
0.85	183	- 0.5	0.90	137	3.2
0.90	189		0.90	120	3.3
0.80	192	- 1.9	0.95	110	2.3
0.95	113	4.3			

(see text for statistics and discussion on inclusion populations)

CO_2-rich inclusions

F	T_h (°C)	T_{hco2} (°C)	F	T_h (°C)	T_{hco2} (°C)
0.20	270	18.6	0.20		6.2
0.35	280	12.9	0.30		- 2.2
0.30	278	6.5	0.45		12.2
0.15	294	9.2	0.15		15.4
0.30	275	17.4	0.25		6.0
0.20	230	19.2	0.30		18.8
0.40	335	19.7			

T_{hco2}: n=13, x=12.3, σ_n=6.5

$$\text{mol\% } CO_2 \ (X_{co2}) = \frac{(\text{wt\% } CO_2/\text{mol.wt } CO_2)}{(\text{wt\% } CO_2/\text{mol.wt } CO_2) + (\text{wt\% } H_2O/\text{mol.wt } H_2O)}$$

where: mol.wt H_2O = 18.02, mol.wt CO_2 = 44.01

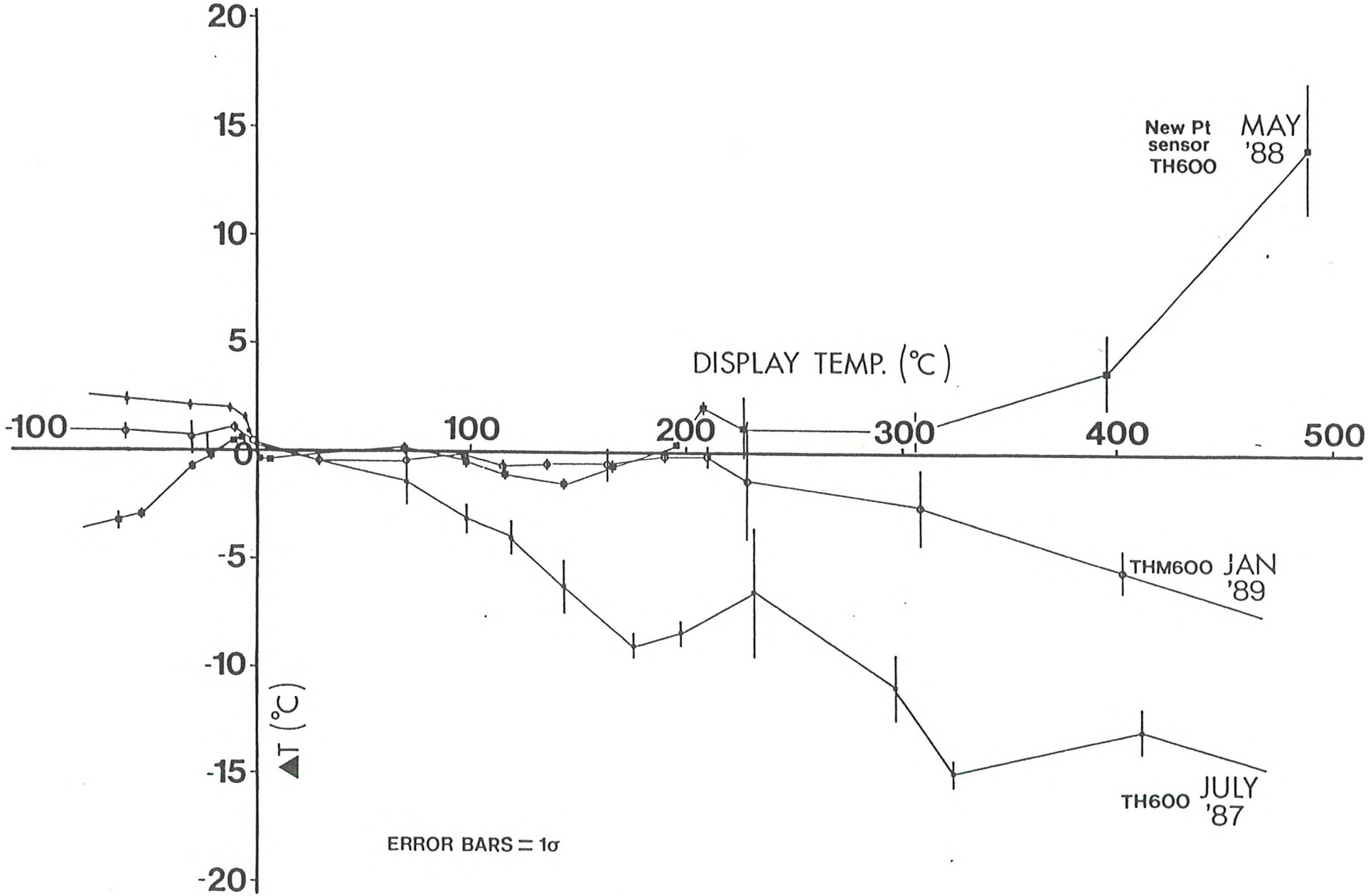

Calibration curves used in the present study for Linkam TH600 and THM600 heating-freezing stages. $\Delta T = T_{true} - T_{obs}$.

APPENDIX E

Thermoluminescence data

A	2481	2482	2483	2484	2485
B	001	002	003	004	005
A	2486	2487	2488	2489	2490
B	006	007	008	009	010

Table 1

Sample	T4	T5	H4	H5	R4-5	treatment
2483	278,6	346,1	2668	5113	34,29	sans HF
	286	354	2780	5584	33,24	15' HF
2488	286,6	342,1	3687	7772	32,18	sans HF
	278,6	346,1	4849	11753	29,21	15' HF
2486	274,7	346,1	2065	3009	40,70	sans HF
	286,6	358	3450	5021	40,73	15'HF

Table 2. Natural thermoluminescence

	T4	T5	$H4^{*}$ 10^{-2}	$H5^{*}$ 10^{-2}	R4-5
2486	286,6	358	8,21	11,95	40,73
2483	286	354	6,62	13,3	33,24
2488	278,6	346,1	11,5	27,98	29,21
2485	290,5	377,8	5,63	14,68	27,72
2481	278,6	373,8	4,66	18,04	20,53
2484	-	385,7		18,71	0
2487	-	401,6		24,57	0
2489	-	393,7		8,05	0
2482	306,4	-	759,3	-	

Table 4. Natural thermoluminescence after HF treatment
* glow peak intensity relative to a standard.

	T0	T1	T4	T5	H0	H1	H4	H5	R4-5	treatment
2483	96,2		250,9	342,1	73317		8325	6814	54,99	sans HF
	96,2		262,8	350	50254		4244	5847	42,06	15'HF
2488	96,2	116	254,8	338,1	33787	14270	14289	9529	59,99	sans HF
	96,2	116	262,8	338,1	37993	9964	11100	11314	49,52	15' HF
2486	96,2		250,9	342,1	16116	-	5269	3988	56,92	sans HF
	96,2	116	262,8	342,1	14701	4531	6082	6156	49,7	15' HF

Table 3. Artificial thermoluminescence

	T0	T1	T2	T4	T5	$H0_2^{*}$ 10^{-2}	$H1_2^{*}$ 10^{-2}	$H2_2^{*}$ 10^{-2}	$H4_2^{*}$ 10^{-2}	$H5_2^{*}$ 10^{-2}	R4-5
2486	96,2	116		262,8	342,1	35	10,8		14,48	14,66	49,7
2483	96,2			262,8	350	119,65			10,10	13,92	42,06
2488	96,2	116		262,8	338,1	90,46	23,72		26,43	26,94	49,52
2485	104,1	127,9		266,7	361,9	19	9,59		13,96	19,31	41,96
2481	104,1		195,3	270,7	373,8	54		13,06	17,61	18,15	49,24
2484	104,1	127,9	191,4?	274,7	358	27,3	13,34	4,40	10,87	22,52	32,55
2487	104,1		207,2	262,8	334,2	58,77		6,37	14,07	21,62	39,43
2489	100,1	123,9	(155,7)	(290,5)	350	41,36	9,68	2,03	9,22	15,71	36,99
2490	104,1	123,9		286,8	350	43,54	19,14	0,50	25,7	52,96	32,71
2482	108,1		191,4	(294,5)	-	3391,8			821,1	-	-

Table 5. Artificial thermoluminescence after HF treatment * glow peak intensity relative to a standard

APPENDIX F

Geochemistry of the Gebeit Alteration Assemblages

Granitoid Hosted Satellite Prospects

	Wadi Mesessana			Tikraneit			
Sample	TMS 096	TMS 106	TMS 107	TMS 124	TMS 125	TMS 129	TMS 141
SiO2	67.61	80.55	70.20	66.23	60.23	52.02	72.92
TiO2	.54	.25	.38	.69	1.24	1.62	.43
Al2O3	16.15	9.58	14.47	15.00	13.51	16.27	12.28
Fe2O3	3.61	1.86	2.48	3.87	5.32	8.61	2.79
MnO	.06	.05	.04	.06	.14	.13	.10
MgO	.98	.17	.11	1.69	.91	5.54	.63
CaO	1.32	.30	1.61	2.52	4.75	6.72	.17
Na2O	4.48	1.82	3.94	4.24	4.26	4.20	.14
K2O	3.16	2.19	3.38	3.64	2.16	.90	4.18
P2O5	.17	.08	.13	.19	.35	.49	.21
L.O.I.	1.71	1.86	2.47	.76	5.74	2.54	3.47
TOTAL	99.78	98.70	99.20	98.89	98.61	99.03	97.31
Trace elements (ppm)							
As	81	432	176	9	12	10	8
Cu	25	14	19	20	23	52	15510
Mo	<2	<2	<2	<2	2	<2	4
Sn	<6	<6	<6	<6	<6	<6	<6
Bi	<3	<3	<3	<3	<3	<3	<3
Sb	<3	<3	<3	<3	<3	<3	<3
Pb	8	7	9	7	<3	6	8
Th	5	4	7	10	8	<3	11
Rb	93	60	89	90	42	19	74
U	<5	<5	5	<5	<5	<5	<5
Sr	312	57	171	340	121	713	28
Y	17	11	19	17	18	23	13
Zr	220	130	211	234	355	194	268
Nb	9	6	9	7	9	7	6
Ga	25	17	22	23	18	24	22
Zn	40	71	85	33	24	71	56
Ni	26	55	48	30	50	91	56
Cr	24	76	20	43	85	213	114
V	43	23	29	68	97	180	94
Ba	677	348	721	716	480	285	1158
La	25	13	16	14	23	16	15
Trace element Totals	1630	1324	1656	1661	1367	1904	17445
TiO2	5445	2528	3806	6524	12054	15631	4695
MnO	622	561	388	583	1526	1213	1302
Ce	36	27	45	33	28	34	34

GEOCHEMISTRY DATA

Lode Alteration Profile 1

Sample	TMS 063	TMS 064	TMS 065	TMS 066	TMS 067	TMS 068	TMS 069	TMS 070	TMS 071	TMS 072	TMS 073	TMS 074	TMS 075	TMS 076	TMS 077	TMS 078	TMS 079	TMS 080	TMS 081	TMS 082	TMS 083	TMS 084	TMS 085	TMS 086
SiO2	40.51	33.41	45.75	70.68	54.01	48.12	42.63	65.61	44.82	43.11	41.39	43.63	47.92	45.63	43.27	47.27	48.89	50.13	50.08	48.88	50.60	48.61	46.42	48.23
TiO2	1.11	1.10	.83	.41	.66	.65	.87	.33	.68	.91	1.02	.83	.85	.84	.63	.60	.64	.95	.90	.83	.87	.85	.81	.82
Al2O3	15.65	15.71	12.79	7.10	11.10	11.62	14.52	5.62	12.69	15.17	15.23	15.19	14.01	15.90	15.50	16.59	16.74	18.43	17.98	17.21	17.84	17.12	16.24	17.22
Fe2O3	11.56	12.45	8.61	4.74	7.72	7.56	9.46	4.23	7.61	10.08	10.35	9.02	8.94	9.43	8.60	9.19	10.02	10.08	9.09	9.21	9.67	9.69	9.10	9.30
MnO	.21	.23	.16	.09	.16	.17	.16	.13	.19	.18	.17	.17	.16	.16	.17	.18	.18	.17	.16	.18	.18	.19	.19	.18
MgO	6.70	6.93	4.24	2.96	4.91	4.30	5.06	2.44	4.25	5.41	6.35	5.63	5.10	5.12	4.79	5.87	7.43	4.50	4.07	3.75	3.99	4.06	3.89	3.68
CaO	11.42	13.71	9.63	5.00	9.25	11.62	9.56	10.45	12.73	10.77	9.16	10.58	9.53	8.61	11.35	8.24	6.00	6.43	6.05	8.38	6.88	8.19	9.60	8.50
Na2O	.71	.77	2.20	1.54	2.20	2.27	3.06	1.14	2.52	1.53	1.07	1.18	2.05	2.83	2.30	1.08	2.59	2.71	2.19	2.40	2.63	2.43	1.61	1.59
K2O	2.22	2.27	1.64	.66	.77	1.19	1.56	.39	.95	1.96	1.95	2.25	1.50	1.34	1.78	2.40	1.01	1.91	2.71	2.26	2.22	2.04	2.61	2.81
P2O5	.18	.19	.11	.06	.66	.15	.07	.23	.12	.18	.16	.18	.16	.19	.17	.16	.18	.23	.22	.21	.21	.21	.21	.21
L.O.I.	10.00	11.90	10.10	6.00	9.10	10.60	10.10	9.90	11.90	11.40	11.20	12.40	10.70	9.80	12.10	9.90	8.10	6.50	6.90	8.90	7.30	8.10	10.60	9.00
TOTAL	100.29	98.67	96.07	99.24	100.53	98.25	97.05	100.46	98.46	100.70	98.05	101.04	100.93	99.85	100.66	101.48	101.80	102.03	100.35	102.22	102.41	101.50	101.27	101.55
Trace elements (ppm)																								
As	129	2022	11639	4171	2095	4845	9313	2547	3066	989	96	272	25	18	20	<7	11	<7	<7	<7	<7	9	<7	<7
Cu	<2	12	41	<2	<2	16	2	<2	21	40	2	<2	21	<2	12	32	31	7	<2	4	4	<2	31	67
Mo	<2	<2	<2	<2	<2	2	2	<2	<2	<2	<2	<2	<2	<2	<2	<2	<2	<2	2	<2	<2	<2	<2	<2
Sn	<6	<6	<6	<6	<6	<6	<6	<6	<6	<6	<6	<6	<6	<6	<6	<6	<6	<6	<6	<6	<6	<6	<6	<6
Bi	<3	<3	3	<3	<3	0	3	<3	<3	<3	<3	<3	<3	<3	<3	<3	<3	<3	<3	<3	<3	<3	<3	<3
Sb	<3	4	11	5	3	6	7	3	6	5	<3	<3	<3	<3	<3	<3	<3	<3	<3	<3	<3	<3	<3	<3
Pb	3	4	6	3	4	5	6	4	3	4	3	7	3	3	3	<3	<3	4	3	<3	3	3	3	3
Th	<3	<3	3	<3	3	<3	3	3	3	<3	3	<3	3	<3	<3	<3	<3	<3	3	<3	3	3	<3	<3
Rb	50	52	41	16	18	28	39	10	23	45	47	52	38	35	44	59	26	48	72	55	56	50	64	68
U	<5	<5	<5	<5	<5	<5	<5	<5	<5	<5	<5	<5	<5	<5	<5	<5	<5	<5	<5	<5	<5	<5	<5	<5
Sr	238	321	304	140	262	248	316	336	227	172	172	256	198	235	223	138	213	333	246	368	314	401	221	467
Y	22	20	18	9	15	19	14	9	20	22	21	19	22	22	15	12	13	25	25	23	22	21	21	22
Zr	63	57	48	27	39	41	51	23	52	58	56	48	51	56	44	36	38	67	67	59	63	61	61	58
Nb	4	5	4	4	4	4	5	3	4	5	5	4	4	5	3	4	4	5	5	5	4	5	5	5
Ga	18	18	15	8	11	12	16	5	13	16	16	15	16	15	16	15	14	18	19	17	18	17	17	17
Zn	86	99	95	50	50	59	79	35	65	83	70	64	61	69	68	68	78	77	73	83	86	86	73	71
Ni	36	36	32	26	29	33	36	24	36	37	38	38	33	33	25	40	68	21	16	12	22	17	12	14
Cr	155	167	142	75	102	211	165	63	116	144	158	141	126	92	47	103	207	25	33	26	23	98	35	38
V	426	432	312	160	227	293	378	123	298	377	353	341	328	319	233	217	210	311	310	298	316	281	282	310
Ba	258	218	<10	<10	46	65	35	<10	49	180	225	251	182	180	264	271	142	283	449	380	364	316	366	433
La	7	8	<6	7	<6	7	<6	<6	<6	<6	<6	6	<6	7	<6	<6	<6	9	9	6	<6	<6	9	<6
Trace Totals	1488	3467	12714	4694	2908	5887	10470	3188	4002	2177	1265	1508	1111	1082	1017	995	1055	1224	1323	1330	1298	1368	1191	1573
MnO	2105	2361	2023	1077	1694	1947	2000	1380	2008	1846	1743	1720	1665	1648	1678	1798	1844	1673	1598	1840	1806	1895	1908	1779
TiO2	8961	9198	8112	4134	5551	6861	9784	3641	7452	8688	9051	7598	7529	7654	5896	5587	5767	8139	7913	7454	7148	7626	7172	7704
S (residual)	1.86	3.48	.95		.93	1.91	1.58	1.41	1.82	2.08	.54	.56	.06						.10				.04	
Ce	21	63	358	131	81	130	270	74	101	50	32	16	<10	13	26	<10	<10	11	<10	<10	19	13	31	<10
		2		4		6		8		10		12		14		16		18		20		22		24
Metres from Vein	0			1				2				3			4		5		6				9	

GEOCHEMISTRY DATA

Lode Alteration Profile 2

Sample	TMS 042	TMS 043	TMS 044	TMS 045	TMS 046	TMS 047	TMS 048	TMS 049	TMS 050	TMS 051	TMS 052	TMS 053	TMS 054	TMS 055	TMS 056	TMS 057	TMS 058	TMS 059	TMS 060	TMS 061
SiO2	88.63	43.69	36.49	52.37	45.63	50.73	41.44	40.98	36.91	39.39	36.65	44.64	50.21	51.34	51.52	53.95	50.39	47.33	43.68	48.29
TiO2	.01	.39	.55	.46	.54	.55	1.25	1.03	.53	.54	.50	.54	.54	.51	.52	.47	.62	.49	.51	.73
Al2O3	.62	11.11	17.93	11.99	14.92	15.93	17.17	15.94	11.95	13.13	12.68	13.15	16.55	15.51	16.91	15.93	18.55	15.69	16.87	19.61
Fe2O3	.42	8.00	10.61	7.91	8.58	7.70	14.15	14.32	11.71	9.24	8.91	9.05	8.84	7.21	8.10	7.11	8.12	7.37	7.90	10.34
MnO	.04	.15	.14	.11	.13	.09	.14	.16	.17	.16	.17	.13	.07	.08	.06	.06	.07	.11	.13	.09
MgO	.10	5.66	9.33	6.59	4.54	3.29	6.97	7.95	4.97	7.82	8.19	7.51	3.82	1.70	1.56	1.48	2.27	2.35	2.47	3.94
CaO	5.52	12.07	8.07	7.70	9.40	6.64	5.35	6.68	12.30	11.91	13.63	9.47	4.66	6.32	4.52	4.61	3.63	8.17	9.21	3.18
Na2O	.18	1.11	.26	.38	2.45	3.72	.57	.19	.56	.49	.22	.61	2.38	4.89	3.68	4.80	4.10	4.51	4.36	3.58
K2O	.02	1.04	2.55	1.32	1.58	1.65	2.11	1.62	1.59	1.17	1.05	1.13	2.33	1.25	2.24	1.60	2.49	1.40	1.66	2.29
P2O5	.01	.12	.15	.19	.27	.18	.23	.20	.17	.16	.15	.16	.16	.12	.13	.14	.15	.09	.11	.10
L.O.I.	4.92	12.42	11.98	10.29	10.77	7.46	8.87	10.42	9.52	13.70	14.43	10.52	7.11	7.91	8.01	7.21	6.51	7.01	7.71	4.81
TOTAL	100.45	95.76	98.06	99.30	98.82	97.93	98.25	99.49	90.38	97.71	96.59	96.91	96.67	96.85	97.25	97.37	96.90	94.53	94.61	96.96
Trace elements (ppm)																				
As	<7	126	288	201	76	35	62	60	44	194	191	116	108	497	129	89	261	51	16	16
Cu	11	106	6	12	28	40	156	120	100	30	39	39	44	61	41	59	47	26	32	68
Mo	<2	<2	<2	<2	<2	2	2	<2	<2	<2	<2	<2	2	3	3	10	5	<2	<2	<2
Sn	<6	<6	<6	<6	<6	<6	<6	<6	<6	<6	<6	<6	<6	<6	<6	<6	<6	<6	<6	<6
Bi	<3	<3	<3	<3	<3	<3	<3	<3	<3	<3	<3	3	<3	<3	<3	<3	3	<3	<3	<3
Sb	<3	<3	<3	<3	<3	<3	3	<3	5	<3	<3	<3	4	7	9	6	6	<3	<3	<3
W	12	16	15	8	12	10	13	<7	13	<7	12	15	14	16	13	9	12	8	11	<7
Pb	3	6	3	<3	3	<3	3	<3	7	3	<3	3	12	19	27	21	15	7	<3	<3
Th	<3	<3	<3	<3	<3	<3	<3	<3	<3	<3	<3	<3	<3	<3	<3	<3	<3	<3	<3	<3
Rb	3	18	44	24	27	30	36	26	30	21	19	22	43	25	43	32	46	27	30	42
U	<5	<5	<5	<5	<5	<5	<5	<5	<5	<5	<5	<5	<5	<5	<5	<5	5	<5	<5	<5
Sr	255	377	260	221	287	235	142	176	331	320	354	227	163	210	196	257	215	444	349	177
Y	2	11	11	12	19	20	24	20	16	15	14	14	22	23	21	23	27	15	16	19
Zr	10	36	46	41	58	75	54	42	44	49	47	44	91	96	82	100	102	56	51	66
Nb	2	2	3	3	4	4	4	3	3	4	3	3	4	5	4	4	4	2	3	4
Ga	2	16	28	17	21	19	25	23	16	17	17	18	24	20	23	20	25	20	20	24
Zn	14	85	121	73	83	74	112	102	68	68	66	69	81	112	112	176	129	73	72	96
Ni	6	44	143	145	72	33	28	30	76	171	169	148	54	27	27	32	42	19	9	17
Cr	76	229	471	521	257	144	80	71	154	618	559	504	238	216	140	228	100	45	28	41
V	7	202	304	212	217	187	530	429	293	257	249	244	232	179	266	223	292	222	225	273
Ba	<10	138	343	196	216	228	286	218	230	171	140	153	298	144	238	201	290	198	275	421
La	<6	7	7	<6	7	6	<6	<6	9	<6	<6	<6	9	10	10	14	7	<6	6	6
Trace element Totals	403	1419	2093	1686	1387	1142	1560	1320	1439	1938	1879	1622	1443	1670	1384	1504	1633	1213	1143	1270
MnO	354	1612	1352	1128	1352	1021	1317	1573	1810	1618	1773	1415	799	892	612	604	683	1229	1326	862
TiO2	60	6090	7007	6111	6855	7222	15552	12341	8361	7046	6060	6871	8004	6952	7937	7101	8083	7039	7188	9536
Ce	10	<10	<10	<10	11	10	27	<10	14	<10	24	<10	15	24	17	11	22	<10	17	<10

Altered Wallrocks - Wadi Lode 4 Level

Sample	TMS 135	TMS 137	TMS 142	TMS 143	TMS 144
SiO2	43.68	33.11	46.81	46.96	50.03
TiO2	1.07	.93	1.10	1.13	.78
Al2O3	19.46	16.18	18.49	17.65	15.76
Fe2O3	9.23	8.94	9.87	11.74	7.02
MnO	.12	.19	.10	.10	.12
MgO	2.65	6.97	2.69	2.89	3.81
CaO	6.36	14.87	4.51	4.79	12.94
Na2O	3.46	.79	4.05	3.43	2.97
K2O	2.33	1.70	1.66	2.36	.47
P2O5	.41	.24	.42	.48	.24
L.O.I.	8.51	15.75	10.46	8.57	6.38
TOTAL	97.27	99.66	100.17	100.11	100.52
Trace elements (ppm)					
As	7374	171	390	116	4081
Cu	110	39	82	73	132
Mo	<2	<2	<2	<2	<2
Sn	<6	<6	<6	<6	<6
Bi	<3	<3	<3	<3	<3
Sb	<3	<3	<3	<3	<3
Pb	<3	<3	4	<3	20
Th	<3	<3	<3	<3	<3
Rb	45	32	22	33	45
U	<5	<5	<5	<5	<5
Sr	271	261	346	218	247
Y	29	18	16	29	27
Zr	77	53	50	78	78
Nb	4	3	4	4	5
Ga	30	19	15	25	29
Zn	101	82	58	107	134
Ni	21	78	73	27	46
Cr	45	227	346	33	28
V	293	334	207	262	276
Ba	230	275	167	215	278
La	10	6	<6	10	11
Trace element Totals	8640	1598	1780	1230	5437
TiO2	12523	9746	6201	11747	12534
MnO	1357	1724	1350	965	1053
Ce	125	11	18	12	62

Altered Wallrocks - Y Lode

Sample	TMS 035	TMS 113	TMS 133
SiO2	40.45	44.52	29.40
TiO2	.37	.64	.57
Al2O3	16.88	13.72	14.39
Fe2O3	4.38	8.25	6.62
MnO	.06	.13	.13
MgO	3.29	5.43	4.38
CaO	16.32	11.44	21.14
Na2O	.15	.78	.12
K2O	.16	1.86	.02
P2O5	.05	.20	.14
L.O.I.	16.80	12.73	21.63
TOTAL	98.91	99.70	98.52
Trace elements (ppm)			
As	97	24	103
Cu	28	74	111
Mo	<2	<2	<2
Sn	<6	<6	<6
Bi	<3	<3	<3
Sb	<3	<3	<3
Pb	3	<3	<3
Th	<3	<3	<3
Rb	5	41	<2
U	<5	<5	<5
Sr	125	81	89
Y	16	15	14
Zr	28	39	32
Nb	3	3	2
Ga	19	15	17
Zn	36	73	51
Ni	23	54	24
Cr	163	180	50
V	159	285	160
Ba	343	497	181
La	7	<6	9
Trace element Totals	1055	1381	843
TiO2	3852	6125	5886
MnO	644	1323	1319
Ce	14	<10	17

Satellite Prospects - Volcanics Hosted

	Oxidised Phyllonite			Altered Tuffs	
Sample	V 13 TMS 132	V 18 TMS 134	M.B.N. TMS 136	Halal Hindeib TMS 108	TMS 109
SiO2	42.38	46.90	50.44	51.94	57.02
TiO2	1.04	1.05	1.16	.83	.41
Al2O3	18.83	18.84	18.00	19.63	20.64
Fe2O3	11.58	12.09	12.99	9.49	6.85
MnO	.16	.10	.17	.17	.18
MgO	7.12	7.98	7.53	3.11	1.82
CaO	4.87	1.18	.65	6.56	3.81
Na2O	1.58	.40	.06	2.73	4.43
K2O	2.69	2.21	2.36	1.00	2.22
P2O5	.26	.00	.24	.10	.19
L.O.I.	8.95	8.21	6.28	4.70	3.32
TOTAL	99.45	98.95	99.88	100.25	100.87
Trace elements (ppm)					
As	2567	1588	816	30	<7
Cu	92	44	89	66	30
Mo	<2	<2	<2	<2	<2
Sn	<6	<6	<6	<6	<6
Bi	<3	<3	<3	<3	<3
Sb	<3	<3	<3	<3	<3
Pb	<3	3	<3	<3	<3
Th	<3	<3	<3	<3	<3
Rb	58	51	51	22	51
U	<5	<5	<5	<5	<5
Sr	71	105	40	280	541
Y	23	15	20	18	19
Zr	56	62	62	62	78
Nb	3	4	4	2	4
Ga	24	27	24	19	21
Zn	90	94	113	76	78
Ni	58	146	77	39	18
Cr	164	595	285	79	26
V	473	413	458	269	59
Ba	354	276	262	180	404
La	7	<6	<6	<6	<6
Trace element Totals	4040	3423	2301	1142	1329
TiO2	10556	9657	11339	8142	3575
MnO	1732	974	1677	1753	1842
Ce	42	17	18	<10	18

Chlorite Phyllonites

Sample	TMS 004	TMS 005	TMS 011	TMS 012	TMS 032	TMS 034	TMS 128	TMS 140	TMS 149
SiO2	34.31	42.39	40.00	52.58	44.80	46.50	35.69	40.94	56.28
TiO2	.29	.73	.93	.69	.80	.65	.63	.93	.13
Al2O3	6.78	14.99	17.85	17.18	16.36	12.84	11.82	14.29	11.41
Fe2O3	8.52	8.85	10.46	8.46	10.33	10.95	7.82	10.86	5.85
MnO	.16	.15	.14	.15	.17	.21	.21	.17	.29
MgO	10.68	7.00	7.70	3.39	6.87	8.40	5.71	6.22	2.50
CaO	18.22	10.55	8.43	6.18	8.85	7.88	16.80	10.04	7.43
Na2O	.47	.79	.31	3.16	2.49	1.11	2.86	1.92	4.08
K2O	.44	1.33	2.21	1.21	.43	1.08	1.33	.87	4.27
P2O5	.13	.25	.30	.24	.24	.23	.23	.17	.38
L.O.I.	18.20	12.20	11.00	6.20	8.00	9.80	14.90	12.47	7.51
TOTAL	98.20	99.24	99.33	99.44	99.34	99.66	98.00	98.88	100.13
Trace elements (ppm)									
As	5	38	66	17	32	13	45	60	9
Cu	22	27	50	30	118	82	100	105	112
Mo	<2	<2	<2	<2	<2	<2	<2	<2	<2
Sn	<6	<6	<6	<6	<6	<6	<6	<6	<6
Bi	<3	<3	<3	<3	<3	<3	<3	<3	<3
Sb	<3	<3	<3	<3	<3	<3	<3	<3	<3
Pb	<3	<3	<3	<3	6	<3	3	<3	13
Th	<3	<3	<3	3	<3	<3	<3	<3	<3
Rb	14	26	41	28	10	27	13	16	36
U	<5	<5	<5	<5	<5	<5	<5	<5	<5
Sr	173	188	128	567	186	178	229	200	85
Y	8	19	21	22	15	15	16	15	16
Zr	24	46	55	96	37	46	46	39	52
Nb	3	3	4	4	3	3	3	3	3
Ga	8	17	21	22	20	17	15	19	16
Zn	59	73	75	80	69	87	71	82	96
Ni	281	77	88	24	63	154	85	59	112
Cr	967	214	264	70	128	527	258	123	218
V	192	297	350	220	334	317	273	427	307
Ba	43	352	438	244	240	193	258	160	178
La	<6	<6	6	13	<6	7	7	<6	8
Trace element Totals	1799	1377	1607	1440	1261	1666	1422	1308	1261
TiO2	3768	8394	10251	7155	6559	6251	5776	8815	6557
MnO	1501	1518	1461	1628	1798	2074	2240	1615	904
Ce	<10	<10	11	25	<10	<10	<10	<10	<10

Carbonate Altered Phyllonites (Ankerite)

Sample	TMS 001	TMS 031	TMS 033	TMS 098	TMS 118	TMS 119
SiO2	35.22	31.11	30.97	26.75	30.96	26.65
TiO2	.26	.40	.29	.29	.31	.26
Al2O3	7.23	8.52	5.81	5.59	5.81	4.91
Fe2O3	7.13	8.15	7.19	7.37	8.00	7.01
MnO	.13	.15	.16	.23	.13	.16
MgO	7.24	5.96	8.97	9.76	7.93	8.33
CaO	15.61	17.68	16.29	18.18	17.04	18.14
Na2O	1.65	1.16	2.52	2.89	2.26	.02
K2O	.99	1.42	.27	.06	.57	1.46
P2O5	.22	.18	.13	.15	.11	.10
L.O.I.	22.40	22.20	25.20	26.95	25.00	27.38
TOTAL	98.08	96.93	97.79	98.21	98.13	94.41
Trace elements (ppm)						
As	262	208	42	137	363	302
Cu	36	57	36	68	74	71
Mo	<2	<2	<2	3	<2	<2
Sn	<6	<6	<6	<6	<6	<6
Bi	<3	3	<3	<3	<3	<3
Sb	<3	<3	<3	262	<3	<3
W	27	24	9	n.a.	n.a.	n.a.
Pb	<3	3	<3	<3	<3	<3
Th	<3	<3	<3	<3	<3	<3
Rb	25	49	5	<2	11	22
U	<5	<5	<5	<5	<5	<5
Sr	239	188	248	247	183	239
Y	9	10	8	6	7	6
Zr	22	34	26	25	24	22
Nb	2	3	3	2	2	2
Ga	9	14	7	7	6	5
Zn	51	62	46	38	49	52
Ni	167	137	243	299	305	270
Cr	555	362	710	765	808	703
V	167	217	154	132	164	144
Ba	88	89	88	82	257	245
La	6	<6	<6	<6	6	<6
Trace element Totals	1665	1460	1625	2073	2259	2083
TiO2	3522	4117	2885	3037	3281	2774
MnO	1368	1563	1603	2457	1323	1839
Ce	23	32	<10	<10	<10	<10

APPENDIX G

Isocon Data and Modal Abundances

---

1) Calculation of approximate specific gravity of selected specimens showing the widest range of mineralogical variations:

Assumed specific gravities, quartz = 2.65 sericite = 2.90
albite = 2.62 calcite = 2.70
chlorite = 2.75 ankerite = 2.95

Sample	TMS 098	TMS 119	TMS 136	TMS STD
Quartz	0.09x2.65	0.20x2.65	0.29x2.65	0.19x2.65
Albite	0.26x2.62			0.27x2.62
Chlorite			0.39x2.75	0.25x2.75
Sericite		0.15x2.90	0.29x2.90	0.16x2.90
Calcite				0.11x2.70
Ankerite	0.61x2.95	0.61x2.95		
Total	2.72	2.77	2.68	2.67

For isocon plots, maximum error in calculation of volume change =
2.67/2.77 i.e. ±4% for the ankerite phyllonites,
2.68/2.67 i.e. ±0.4% for the alteration profiles.

Modal abundances for the main types of alteration assemblage are listed below:

MODAL ABUNDANCES

Chlorite Phyllonites

Sample	TMS 004	TMS 005	TMS 011	TMS 032	TMS 034	TMS 140
Quartz	14	33	30	29	31	31
Albite	4	7	3	22	10	17
Sericite	4	11	19	4	9	8
Chlorite	45	30	33	29	36	26
Calcite	33	19	15	16	14	18
TOTAL	100.00	100.00	100.00	100.00	100.00	100.00

MODAL ABUNDANCES

Altered Wallrocks - Wadi Lode 4 Level

Sample	TMS 135	TMS 137	TMS 142	TMS 143	TMS 144
Quartz	24	17	28	27	27
Albite	31	7	36	30	27
Sericite	20	15	15	20	4
Chlorite	14	34	13	14	19
Calcite	11	27	8	9	23
TOTAL	100.00	100.00	100.00	100.00	100.00

MODAL ABUNDANCES

Altered Wallrocks - Y Lode

Sample	TMS 035	TMS 113	TMS 133
Quartz	4	30	4
Albite	1	7	1
Sericite	2	20	0
Chlorite	19	22	25
Calcite	29	21	38
Pyrophyllite	45	0	32
TOTAL	100.00	100.00	100.00

MODAL ABUNDANCES

Oxidised Sulphidic Phyllonite
Vein 13, Vein 18, Marble Bar

Sample	TMS 132	TMS 134	TMS 136
Quartz	13	26	30
Albite	13	4	0
Sericite	26	23	25
Chlorite	37	42	42
Calcite	9	2	0
Sulphides	2	3	3
TOTAL	100	100	100

MODAL ABUNDANCES

Lode Alteration Profile 1

Sample	TMS 063	TMS 064	TMS 065	TMS 066	TMS 067	TMS 068	TMS 069	TMS 070	TMS 071
Quartz	18	12	21	55	30	25	18	52	25
Albite	7	7	21	14	21	21	27	11	23
Sericite	21	22	15	6	7	10	12	4	8
Chlorite	32	32	21	14	23	21	23	13	19
Calcite	22	26	18	9	18	21	17	19	23
Sulphides	0	1	4	2	1	2	3	1	2
Total	100	100	100	100	100	100	100	100	100

Sample	TMS 072	TMS 073	TMS 074	TMS 075	TMS 076	TMS 077	TMS 078	TMS 080
Quartz	25	28	25	27	23	22	27	27
Albite	14	10	11	19	25	21	10	24
Sericite	17	17	19	13	12	15	21	16
Chlorite	25	29	26	24	24	22	27	21
Calcite	19	16	19	17	16	20	15	12
Sulphides	.5	0	0	0	0	0	0	0
Total	100.5	100	100	100	100	100	100	100

MODAL ABUNDANCES

Lode Alteration Profile 2

Sample	TMS 043	TMS 044	TMS 045	TMS 046	TMS 047	TMS 048	TMS 049	TMS 050	TMS 051	TMS 052
Quartz	27	15	38	17	15	19	21	21	25	25
Albite	10	2.5	4	22	34	5	2	5	4.5	2
Sericite	9	22	11	14	14	18	14	14	10	9
Chlorite	32	46	33	30	25	48	51	38	39	40
Calcite	22	14.5	14	17	12	10	12	22	21.5	24
Total	100	100	100	100	100	100	100	100	100	100

Sample	TMS 053	TMS 054	TMS 055	TMS 056	TMS 057	TMS 058	TMS 059	TMS 060	TMS 061
Quartz	30	21	14	18	16	12	11	7	10
Albite	5	21.5	43	33	43	37	40	39	32
Sericite	10	20	11	19	14	21	12	14	20
Chlorite	38	29	20	22	19	23	22	23	32
Calcite	17	8.5	12	8	8	7	15	17	6
Total	100	100	100	100	100	100	100	100	100

Isocon Data

Standards and Scaling Factors

Element	Scaling Factor	TMS STD	STDTUFF	STDHBPX
SiO2	x0.4	20.40	18.57	18.85
TiO2	x10	8.00	5.77	8.35
Al2O3	x1	17.50	17.39	17.01
Fe2O3	x1	9.30	8.54	10.19
MnO	x10	1.80	1.09	1.80
MgO	x3	12.00	8.77	18.20
CaO	x2	12.00	13.71	21.54
Na2O	x5	15.00	20.74	11.67
K2O	x5	9.00	8.93	1.02
P2O5	x10	2.10	.99	2.36
Rb	x0.1	5.00	3.30	.00
Sr	x0.01	3.50	3.23	5.60
Y	x1	22.00	16.67	22.00
Zr	x0.25	16.25	14.42	14.32
Nb	x1	4.00	3.00	3.14
Ga	x1	18.00	21.33	19.86
Zn	x0.1	8.00	8.03	8.11
Ni	x0.05	1.00	.75	2.62
Cr	x0.02	.80	.76	3.59
V	x0.01	3.00	2.40	3.17
Ba	x0.01	3.00	2.98	.73

Isocon Data

Lode Alteration Profile 1

Element	Scaling Factor	TMS 063	TMS 064	TMS 065	TMS 066	TMS 067	TMS 068	TMS 069	TMS 070	TMS 071	TMS 072
SiO2	x0.4	-10	-27	22	239	69	43	1	300	21	-4
TiO2	x10	26	28	43	22	12	31	47	43	22	22
Al2O3	x1	0	0	0	0	0	0	0	0	0	0
Fe2O3	x1	39	50	27	24	33	24	24	41	11	23
MnO	x10	40	50	44	23	38	33	8	133	43	9
MgO	x3	89	93	46	81	95	65	53	82	46	54
CaO	x2	114	154	119	104	146	194	92	433	192	103
Na2O	x5	-74	-72	0	24	17	15	25	15	17	-42
K2O	x5	37	41	24	-10	-32	0	5	-31	-28	24
P2O5	x10	0	0	-18	-40	412	0	-50	225	-25	0
Rb	x0.1	13	17	14	-23	-42	-16	-4	-30	-35	0
Sr	x0.01	-30	0	25	0	13	0	8	240	-11	-43
Y	x1	12	0	11	0	9	30	-22	23	25	13
Zr	x0.25	9	-1	0	0	-3	-3	-4	7	9	0
Nb	x1	8	42	39	144	59	50	58	129	38	42
Ga	x1	9	11	12	7.3	0	0	8	-14	0	0
Zn	x0.1	20	38	65	50	0	11	18	27	9	16
Ni	x0.5	102	102	118	340	133	146	116	282	154	110
Cr	x0.02	420	500	667	400	367	625	440	367	333	367
V	x0.01	64	64	47	29	14	43	55	30	57	44
Ba	x0.1	0	-18	-100	-100	-67	-64	-83	-100	-75	-42
Total Mass Change		11.25	10	37.5	140	60	52	21.25	200	37.5	12.5

Element	Scaling Factor	TMS 073	TMS 074	TMS 075	TMS 076	TMS 077	TMS 078	TMS 080	TMS 082	TMS 084	TMS 086
SiO2	x0.4	-7	0	18	0	-4	-3	-6	-2	-2	-4
TiO2	x10	29	11	19	6	-17	-27	-4	-6	-2	-2
Al2O3	x1	0	0	0	0	0	0	0	0	0	0
Fe2O3	x1	29	13	22	14	5	3	3	0	6	0
MnO	x10	10	10	10	0	0	7	-4	0	0	0
MgO	x3	83	63	61	44	34	53	7	-5	4	-6
CaO	x2	76	106	100	60	114	44	2	42	40	43
Na2O	x5	-59	-54	-15	4	-13	-62	-13	-18	-17	-46
K2O	x5	26	45	4	-16	11	41	0	28	15	60
P2O5	x10	0	0	0	0	0	-13	0	0	0	0
Rb	x0.1	8	20	-4	-20	0	23	-9	12	0	40
Sr	x0.01	-40	-14	-26	-24	-29	-56	-8	0	14	33
Y	x1	9	0	26	12	-23	-42	8	7	-2	1
Zr	x0.25	0	-14	0	-4	-23	-40	-2	-7	-3	-9
Nb	x1	46	17	25	42	-13	3	18	26	30	0
Ga	x1	2	-3	11	-7	0	-12	-5	-3	-3	-3
Zn	x0.1	0	-6	-5	-4	-4	-10	-7	6	11	-9
Ni	x0.5	118	120	109	82	41	106	0	-39	-13	-28
Cr	x0.02	450	333	325	229	44	240	-33	-30	160	0
V	x0.01	41	34	38	17	-11	-22	0	0	0	0
Ba	x0.1	-11	0	-25	-33	0	0	-7	24	0	45
Total Mass Change		13.75	15	27	11.25	12.5	3.75	-5	1.25	2.5	1.25

Isocon Data

Lode Alteration Profile 2

Element	Scaling Factor	TMS 043	TMS 044	TMS 045	TMS 046	TMS 047	TMS 048	TMS 049	TMS 050	TMS 051	TMS 052
SiO2	x0.4	35	-30	50	6	10	-17	-12	7	3	0
TiO2	x10	-22	-31	-17	-19	-25	58	42	-3	-11	-13
Al2O3	x1	0	0	0	0	0	0	0	0	0	0
Fe2O3	x1	36	12	23	9	-9	55	68	29	31	33
MnO	x10	25	-20	-3	9	-43	-25	0	83	0	40
MgO	x3	124	126	114	34	-9	68	91	61	137	153
CaO	x2	218	31	89	86	23	-8	22	200	168	214
Na2O	x5	-41	-92	-81	-3	38	-80	-93	-73	-78	-89
K2O	x5	-9	40	6	4	0	19	0	30	-13	-19
P2O5	x10	-3	-30	25	54	-11	0	0	15	0	0
Rb	x0.1	-43	-14	-29	-34	-32	-27	-42	-11	-44	-47
Sr	x0.01	67	-27	-3	0	-27	-59	-41	31	18	40
Y	x1	-22	-50	-20	2	0	11	0	6	-9	-12
Zr	x0.25	-13	-30	-8	5	26	-15	-29	0	0	0
Nb	x1	-22	-25	13	21	8	0	-16	8	31	0
Ga	x1	39	52	39	37	7	42	41	31	25	30
Zn	x0.1	70	48	25	21	0	43	40	22	12	13
Ni	x0.2	248	614	967	326	80	37	66	456	1117	1058
Cr	x0.02	900	940	1800	620	300	83	100	400	1600	2200
V	x0.01	0	0	0	-14	-32	75	58	36	10	11
Ba	x0.01	-23	12	-2	-14	-16	-5	-19	11	-22	-30
Total Mass		57	-2.5	47	19	10	1.25	10	47	33	37.5

Element	Scaling Factor	TMS 052	TMS 053	TMS 054	TMS 055	TMS 056	TMS 057	TMS 058	TMS 059	TMS 060	TMS 061
SiO2	x0.4	0	15	-11	-4	-11	-2	-21	4	-10	-15
TiO2	x10	-13	-10	0	0	-5	-9	0	-31	-33	-16
Al2O3	x1	0	0	0	0	0	0	0	0	0	0
Fe2O3	x1	33	28	13	0	0	-6	-7	-11	-12	-57
MnO	x10	40	0	0	57	0	0	0	-27	-21	0
MgO	x3	153	125	42	-12	-25	-25	0	-32	-35	-11
CaO	x2	214	108	100	196	92	103	43	53	59	-52
Na2O	x5	-89	-73	-48	13	-21	8	-20	68	50	7
K2O	x5	-19	-17	43	-16	38	3	39	-13	-3	13
P2O5	x10	0	0	0	0	0	0	0	-50	-43	-61
Rb	x0.1	-47	-40	20	-19	21	0	19	-39	-36	-23
Sr	x0.01	40	-13	0	29	17	0	20	42	0	-55
Y	x1	-12	-15	-24	-16	-29	-18	-17	-23	-24	-23
Zr	x0.25	0	-10	-20	-10	-30	-9	-20	-3	-18	-8
Nb	x1	0	0	0	28	0	0	-8	-44	-19	-8
Ga	x1	30	32	20	6	12	2	10	25	15	19
Zn	x0.1	13	12	-26	7	0	63	3	3	-6	6
Ni	x0.2	1058	8588	53	-16	-25	-7	7	6	-52	-23
Cr	x0.02	2200	1300	94	100	13	95	-21	33	-20	0
V	x0.01	11	4	0	-14	12	27	15	-17	-4	-17
Ba	x0.01	-30	-31	100	0	55	52	78	-25	-23	26
Total Mass		37.5	33	0	5	-2.5	1.25	-11	12.5	2.5	-10

Isocon Data

Element	Halal Hindeib TMS 108	Altd Tuffs TMS 123	Wadi Messesana TMS 106	TMS 107	Altd Hb/Px TMS 137	Altd Shale TMS 139
SiO2	-3.00	68.00	103.00	12.00	-26.00	-26.00
TiO2	111.00	-13.00	-21.00	-22.00	19.00	32.00
Al2O3	.00	.00	.00	.00	.00	.00
Fe2O3	44.00	-18.00	-12.00	.00	18.00	-9.00
MnO	.00	4.00	.00	-22.00	-8.00	.00
MgO	78.00	275.00	-74.00	-86.00	20.00	-18.00
CaO	80.00	356.00	-61.00	50.00	46.00	21.00
Na2O	-35.00	218.00	-30.00	-5.00	-64.00	-4.00
K2O	-52.00	-74.00	18.00	15.00	933.00	48.00
P2O5	-46.00	133.00	.00	.00	.00	17.00
Rb	-53.00	-80.00	8.00	.00	--	41.00
Sr	-46.00	109.00	-63.00	-38.00	-52.00	-5.00
Y	.00	.00	9.00	21.00	-14.00	-25.00
Zr	-16.00	17.00	.00	5.00	-3.00	-28.00
Nb	-48.00	58.00	14.00	5.00	.00	-12.00
Ga	-4.00	-52.00	13.00	-5.00	.00	5.00
Zn	4.00	-46.00	200.00	156.00	7.00	11.00
Ni	133.00	733.00	235.00	57.00	62.00	34.00
Cr	214.00	1250.00	500.00	7.00	39.00	-38.00
V	350.00	-50.00	.00	.00	13.00	19.00
Ba	-54.00	-40.00	-9.00	18.00	400.00	36.00
Tot. Mass	5.00	117.50	70.00	6.00	5.00	-12.50

Isocon Data

Element	Scaling Factor	Satellite Prospects TMS 132	TMS 134	TMS 136	Wadi Lode TMS 135	TMS 142	TMS 143	Y Lode TMS 144	TMS 113	TMS 133
SiO2	x0.4	-22.5	-14	-3	-23	-13	-9	9	11	-29
TiO2	x10	21	22	40	20	29	41	10	0	-12
Al2O3	x1	0	0	0	0	0	0	0	0	0
Fe2O3	x1	17	22	35	-11	0	26	-15	13	-14
MnO	x10	-10	-50	-5	-36	-44	-45	-17	-5	-10
MgO	x3	67	88	86	-40	-37	-28	5	74	36
CaO	x2	-23	-81	-88	-4	-29	-20	141	144	334
Na2O	x5	-51	-85	-98	4	27	13	9	-67	-95
K2O	x5	40	15	26	16	-13	31	-70	31	-98
P2O5	x10	26	-100	0	77	89	136	29	22	-25
Rb	x0.1	10	0	-2	-18	-60	-35	0	5	-100
Sr	x0.01	-80	-69	-90	-29	-5	-39	-18	-68	-68
Y	x1	-2	-36	-11	19	-31	30	37	-14	-22
Zr	x0.25	-19	-11	-7	7	-27	19	32	-24	-40
Nb	x1	-28	-6	-5	-8	-3	0	40	-3	-36
Ga	x1	25	40	23	50	-21	38	79	6	17
Zn	x0.1	5	11	27	14	-31	34	85	18	-21
Ni	x0.5	174	584	276	-6	246	32	157	244	50
Cr	x0.02	350	1150	571	0	625	-5	-13	550	75
V	x0.01	53	31	48	-11	-35	-13	7	19	-19
Ba	x0.01	15	-7	19	28	-48	-28	7	108	-31
Total Mass Change		-7.5	-7.5	-2.5	-10	-5	-2.5	11	28	22.5

Isocon Data

Chlorite Phyllonites

Element	TMS 004	TMS 005	TMS 011	TMS 012	TMS 032	TMS 034	TMS 128	TMS 140	TMS 149
SiO2	86	2	-19	4	-6	31	4	0	70
TiO2	-15	0	7	-14	8	0	18	43	-75
Al2O3	0	0	0	0	0	0	0	0	0
Fe2O3	106	0	-1	-8	20	43	25	45	-2
MnO	100	0	-21	-17	0	43	80	15	150
MgO	350	30	21	-14	83	84	112	91	-3
CaO	333	12	-25	4	57	-2	318	106	92
Na2O	-50	-62	-86	7	-10	-37	43	-20	107
K2O	350	760	110	-31	-73	600	8	-40	259
P2O5	43	15	21	13	21	26	39	0	183
Rb	3125	2667	260	-43	-78	3590	-57	-61	9
Sr	-22	-63	-79	63	-41	-57	0	-30	-63
Y	-7	-3	-9	1	-27	-9	8	-16	11
Zr	-5	-9	-8	50	-38	7	4	-26	23
Nb	130	-5	25	0	-19	24	9	-5	17
Ga	1	-3	0	24	16	14	23	30	37
Zn	77	-5	-11	0	-7	41	30	28	83
Ni	2650	233	235	15	258	700	600	300	756
Cr	1167	35	42	67	250	267	760	325	900
V	40	0	4	-24	15	32	41	76	62
Ba	0	475	480	-17	-13	233	35	-31	-7
Tot Mass%	153	13.75	-5	-1.25	6.25	33	48	23	54

Carbonate Altered Phyllonites (Ankerite)

Isocon Values

Element	TMS 001	TMS 031	TMS 033	TMS 098	TMS 118	TMS 119
SiO2	68	24	85	66	85	85
TiO2	-21	0	9	14	18	17
Al2O3	0	0	0	0	0	0
Fe2O3	84	131	131	150	175	155
MnO	71	50	160	280	120	180
MgO	345	204	570	674	633	742
CaO	543	506	712	865	775	968
Na2O	36	-20	158	199	129	-94
K2O	32	61	-52	-88	0	182
P2O5	125	56	83	100	67	80
Rb	14	100	-64	-100	-29	50
Sr	54	0	100	133	45	150
Y	0	-28	10	14	-3	-2
Zr	-16	6	20	21	14	21
Nb	14	47	127	50	60	78
Ga	23	58	18	21	3	0
Zn	56	55	77	55	91	126
Ni	1625	1040	3267	4033	4133	3633
Cr	2933	1400	4750	5167	6500	5700
V	27	38	44	38	75	71
Ba	-27	-38	0	-5	175	200
Total Mass%	147	105	203	213	206	257

APPENDIX H

Probe Data

All data ~~is~~ are presented as apparent % (App%), element % (%Elmnt), and oxide % (%Oxide).

Chlorite - Ankerite phyllonites.

044

Std	App.%	%Elmnt	%Oxide
NA	0.05	0.07	0.09
MG	7.75	10.27	17.03
AL	7.56	9.91	18.73
SI	10.06	12.37	26.46
KK	0.05	0.05	0.06
CA	0.09	0.09	0.13
TI	0.03	0.03	0.05
CR	1.20	1.29	1.88
MN	0.07	0.07	0.09
FE	15.85	17.36	22.33
O	57.29	48.49	0.00
Tot	100.00	100.00	86.85

044

Std	App.%	%Elmnt	%Oxide
NA	0.00	0.00	0.00
MG	8.03	10.63	17.63
AL	7.74	10.18	19.24
SI	9.87	12.19	26.08
KK	0.04	0.04	0.05
CA	0.02	0.02	0.03
TI	0.03	0.03	0.05
CR	0.88	0.94	1.38
MN	0.00	0.00	0.00
FE	16.33	17.88	23.00
O	57.06	48.09	0.00
Tot	100.00	100.00	87.46

044

Std	App.%	%Elmnt	%Oxide
NA	0.02	0.03	0.03
MG	10.43	13.14	21.80
AL	7.30	9.56	18.06
SI	11.00	13.51	28.90
KK	0.05	0.05	0.06
CA	0.04	0.04	0.06
TI	0.02	0.02	0.04
CR	0.09	0.10	0.14
MN	0.02	0.02	0.03
FE	11.93	13.17	16.94
O	59.10	50.36	0.00
Tot	100.00	100.00	86.06

037

Std	App.%	%Elmnt	%Oxide
NA	0.03	0.04	0.06
MG	6.96	9.29	15.41
AL	7.93	10.34	19.54
SI	10.36	12.73	27.23
KK	0.59	0.57	0.69
CA	0.05	0.05	0.07
TI	0.03	0.03	0.05
CR	1.00	1.07	1.56
MN	0.01	0.01	0.01
FE	17.08	18.67	24.02
O	55.96	47.20	0.00
Tot	100.00	100.00	88.64

043

Std	App.%	%Elmnt	%Oxide
NA	0.02	0.03	0.04
MG	8.04	10.59	17.56
AL	7.96	10.43	19.72
SI	10.02	12.37	26.47
KK	0.08	0.08	0.09
CA	0.21	0.21	0.29
TI	0.03	0.03	0.05
CR	0.77	0.83	1.21
MN	0.01	0.01	0.01
FE	15.90	17.42	22.41
O	56.96	48.00	0.00
Tot	100.00	100.00	87.85

043

Std	App.%	%Elmnt	%Oxide
NA	0.03	0.04	0.06
MG	7.75	10.30	17.09
AL	7.48	9.83	18.58
SI	9.86	12.13	25.96
KK	0.05	0.05	0.06
CA	0.03	0.03	0.04
TI	0.01	0.01	0.02
CR	1.51	1.62	2.37
MN	0.03	0.03	0.04
FE	16.06	17.58	22.62
O	57.19	48.38	0.00
Tot	100.00	100.00	86.84

Sericite - Ankerite Phyllonites.

043

Std	App.%	%Elmnt	%Oxide
NA	0.12	0.13	0.18
MG	1.54	1.74	2.88
AL	14.71	15.79	29.84
SI	19.82	22.72	48.61
KK	6.74	6.73	8.10
CA	0.06	0.06	0.09
TI	0.08	0.09	0.15
CR	0.37	0.44	0.64
MN	0.04	0.04	0.05
FE	1.73	1.94	2.49
O	54.79	50.32	0.00

Tot	100.00	100.00	93.03

043

Std	App.%	%Elmnt	%Oxide
NA	0.07	0.08	0.11
MG	1.96	2.24	3.71
AL	13.64	14.84	28.04
SI	19.86	22.74	48.66
KK	6.52	6.50	7.83
CA	0.03	0.03	0.04
TI	0.15	0.17	0.28
CR	0.75	0.88	1.29
MN	0.00	0.00	0.00
FE	2.54	2.84	3.66
O	54.48	49.68	0.00

Tot	100.00	100.00	93.62

037

Std	App.%	%Elmnt	%Oxide
NA	0.06	0.07	0.09
MG	1.24	1.40	2.32
AL	14.68	15.68	29.63
SI	20.25	23.12	49.46
KK	6.76	6.75	8.13
CA	0.02	0.02	0.03
TI	0.10	0.11	0.19
CR	0.97	1.15	1.68
MN	0.01	0.01	0.01
FE	1.33	1.49	1.92
O	54.58	50.20	0.00

Tot	100.00	100.00	93.46

037

Std	App.%	%Elmnt	%Oxide
NA	0.11	0.12	0.16
MG	1.16	1.31	2.16
AL	15.20	16.21	30.64
SI	19.85	22.75	48.67
KK	6.80	6.79	8.17
CA	0.01	0.01	0.01
TI	0.13	0.14	0.24
CR	0.86	1.02	1.49
MN	0.02	0.02	0.03
FE	1.28	1.43	1.85
O	54.58	50.20	0.00

Tot	100.00	100.00	93.42

044

Std	App.%	%Elmnt	%Oxide
NA	0.10	0.11	0.15
MG	1.30	1.46	2.42
AL	14.53	15.50	29.29
SI	20.28	23.12	49.47
KK	6.09	6.09	7.34
CA	0.01	0.01	0.01
TI	0.12	0.13	0.22
MN	0.00	0.00	0.00
FE	1.32	1.48	1.90
O	56.25	52.10	0.00

Tot	100.00	100.00	90.80

038

Std	App.%	%Elmnt	%Oxide
NA	0.18	0.20	0.26
MG	0.90	1.00	1.66
AL	16.39	17.30	32.69
SI	19.55	22.49	48.11
KK	7.43	7.43	8.95
CA	0.01	0.01	0.01
TI	0.09	0.10	0.17
MN	0.01	0.01	0.01
FE	0.97	1.09	1.40
O	54.47	50.37	0.00

Tot	100.00	100.00	93.26

038

Std	App.%	%Elmnt	%Oxide
NA	0.17	0.18	0.25
MG	0.96	1.06	1.76
AL	16.52	17.38	32.85
SI	20.13	23.15	49.52
KK	6.83	6.84	8.24
CA	0.07	0.07	0.10
FE	0.74	0.83	1.07
O	54.58	50.49	0.00

Tot	100.00	100.00	93.79

038

Std	App.%	%Elmnt	%Oxide
NA	0.18	0.20	0.26
MG	0.76	0.84	1.40
AL	16.55	17.41	32.90
SI	19.68	22.63	48.42
KK	6.47	6.48	7.80
CA	0.01	0.01	0.01
FE	0.66	0.74	0.95
O	55.69	51.69	0.00

Tot	100.00	100.00	91.74

Quartz - V_1 Quartz Veins

001

Std	App.%	%Elmnt	%Oxide
NA	0.02	0.02	0.03
MG	0.01	0.01	0.02
AL	0.08	0.08	0.15
SI	47.77	46.14	98.71
KK	0.02	0.02	0.02
CA	0.01	0.01	0.01
TI	0.01	0.01	0.02
MN	0.00	0.00	0.00
FE	0.00	0.00	0.00
O	52.08	53.71	0.00
Tot	100.00	100.00	98.96

003

Std	App.%	%Elmnt	%Oxide
NA	0.03	0.03	0.04
MG	0.01	0.01	0.02
AL	0.04	0.04	0.08
SI	47.04	45.48	97.30
KK	0.02	0.02	0.02
CA	0.01	0.01	0.01
TI	0.01	0.01	0.02
MN	0.00	0.00	0.00
FE	0.00	0.00	0.00
O	52.84	54.40	0.00
Tot	100.00	100.00	97.49

007

Std	App.%	%Elmnt	%Oxide
NA	0.02	0.02	0.03
MG	0.01	0.01	0.02
AL	0.02	0.02	0.04
SI	48.10	46.41	99.29
KK	0.03	0.03	0.04
CA	0.01	0.01	0.01
TI	0.00	0.00	0.00
MN	0.00	0.00	0.00
FE	0.00	0.00	0.00
O	51.81	53.50	0.00
Tot	100.00	100.00	99.43

Tourmaline - V_1 Quartz Veins

001

Std	App.%	%Elmnt	%Oxide
NA	1.59	1.84	2.47
MG	3.34	3.97	6.59
AL	15.13	17.33	32.75
SI	14.20	17.17	36.74
KK	0.05	0.05	0.06
CA	0.07	0.07	0.10
TI	0.50	0.55	0.91
MN	0.00	0.00	0.00
FE	4.75	5.29	6.81
O	60.37	53.73	0.00
Tot	100.00	100.00	86.43

Calcite - V_1 Quartz Veins

003

Std	App.%	%Elmnt	%Oxide
MG	0.04	0.05	0.09
CA	44.45	42.86	59.97
MN	0.21	0.23	0.29
FE	0.11	0.12	0.16
O	55.19	56.74	0.00
Tot	100.00	100.00	60.51

003

Std	App.%	%Elmnt	%Oxide
MG	0.05	0.07	0.11
CA	44.58	42.98	60.14
MN	0.22	0.24	0.30
FE	0.11	0.12	0.16
O	55.04	56.59	0.00
Tot	100.00	100.00	60.71

007

Std	App.%	%Elmnt	%Oxide
MG	0.09	0.12	0.20
CA	43.59	42.04	58.82
MN	0.32	0.34	0.44
FE	0.25	0.28	0.36
O	55.75	57.22	0.00
Tot	100.00	100.00	59.82

007

Std	App.%	%Elmnt	%Oxide
MG	0.12	0.16	0.27
CA	47.02	45.26	63.32
MN	0.35	0.38	0.48
FE	0.38	0.43	0.55
O	52.13	53.77	0.00
Tot	100.00	100.00	64.62

001

Std	App.%	%Elmnt	%Oxide
MG	0.04	0.05	0.09
CA	40.33	38.96	54.52
MN	0.30	0.32	0.41
FE	0.24	0.27	0.35
O	59.09	60.40	0.00
Tot	100.00	100.00	55.37

Calcite - Lode Alteration Profile

064

Std	App.%	%Elmnt	%Oxide
NA	0.00	0.00	0.00
MG	0.07	0.09	0.15
AL	0.03	0.04	0.07
SI	0.01	0.01	0.02
KK	0.04	0.03	0.04
CA	48.48	46.63	65.25
TI	0.00	0.00	0.00
MN	0.46	0.49	0.64
FE	0.18	0.20	0.26
O	50.73	52.51	0.00

Tot	100.00	100.00	66.43

065

Std	App.%	%Elmnt	%Oxide
MG	0.33	0.44	0.73
CA	46.84	45.07	63.06
MN	0.46	0.49	0.64
FE	0.71	0.80	1.03
O	51.66	53.20	0.00

Tot	100.00	100.00	65.46

069

Std	App.%	%Elmnt	%Oxide
MG	0.08	0.11	0.18
AL	0.01	0.01	0.02
SI	0.01	0.01	0.02
CA	36.66	35.49	49.66
MN	0.28	0.30	0.39
FE	0.15	0.17	0.22
O	62.81	63.91	0.00

Tot	100.00	100.00	50.49

071

Std	App.%	%Elmnt	%Oxide
MG	0.07	0.09	0.15
CA	44.69	43.08	60.28
MN	0.30	0.32	0.42
FE	0.19	0.21	0.28
O	54.75	56.30	0.00

Tot	100.00	100.00	61.13

075

Std	App.%	%Elmnt	%Oxide
MG	0.49	0.66	1.09
CA	37.91	36.64	51.27
MN	0.42	0.45	0.58
FE	1.11	1.25	1.61
O	60.07	61.00	0.00

Tot	100.00	100.00	54.55

079

Std	App.%	%Elmnt	%Oxide
MG	0.12	0.16	0.27
CA	45.00	43.35	60.66
MN	0.51	0.55	0.71
FE	0.30	0.34	0.43
O	54.07	55.60	0.00

Tot	100.00	100.00	62.07

065

Std	App.%	%Elmnt	%Oxide
MG	0.08	0.11	0.18
CA	43.68	42.12	58.94
MN	0.40	0.43	0.55
FE	0.16	0.18	0.23
O	55.68	57.16	0.00

Tot	100.00	100.00	59.90

065

Std	App.%	%Elmnt	%Oxide
MG	0.29	0.39	0.64
CA	47.05	45.27	63.33
MN	0.49	0.52	0.68
FE	0.65	0.73	0.94
O	51.52	53.09	0.00

Tot	100.00	100.00	65.59

066

Std	App.%	%Elmnt	%Oxide
MG	0.12	0.16	0.27
CA	44.77	43.15	60.38
MN	0.35	0.37	0.48
FE	0.23	0.26	0.33
O	54.53	56.06	0.00

Tot	100.00	100.00	61.46

071

Std	App.%	%Elmnt	%Oxide
MG	0.08	0.11	0.18
CA	42.38	40.90	57.22
MN	0.38	0.41	0.53
FE	0.18	0.20	0.26
O	56.98	58.38	0.00

Tot	100.00	100.00	58.19

073

Std	App.%	%Elmnt	%Oxide
MG	0.09	0.12	0.20
CA	43.83	42.26	59.13
MN	0.44	0.47	0.61
FE	0.24	0.27	0.35
O	55.40	56.88	0.00

Tot	100.00	100.00	60.29

077

Std	App.%	%Elmnt	%Oxide
MG	0.03	0.04	0.07
CA	35.04	33.96	47.52
MN	0.23	0.25	0.32
FE	0.00	0.00	0.00
O	64.70	65.75	0.00

Tot	100.00	100.00	47.91

083

Std	App.%	%Elmnt	%Oxide
MG	0.02	0.03	0.04
CA	37.37	36.18	50.62
MN	0.17	0.18	0.23
FE	0.04	0.05	0.06
O	62.40	63.56	0.00

Tot	100.00	100.00	50.95

Chlorite - Lode Alteration Profile (cont).

075

Std	App.%	%Elmnt	%Oxide
NA	0.00	0.00	0.00
MG	7.73	9.99	16.56
AL	7.85	10.10	19.08
SI	12.48	15.20	32.51
KK	0.10	0.10	0.12
CA	0.02	0.02	0.03
TI	0.02	0.02	0.04
CR	0.01	0.01	0.02
MN	0.19	0.20	0.25
FE	14.58	16.01	20.60
O	57.02	48.35	0.00

Tot	100.00	100.00	89.21

075

Std	App.%	%Elmnt	%Oxide
NA	0.01	0.01	0.02
MG	7.07	9.24	15.33
AL	9.20	11.84	22.38
SI	10.22	12.62	27.00
KK	0.30	0.29	0.35
CA	0.03	0.03	0.04
TI	0.28	0.30	0.49
CR	0.24	0.26	0.38
MN	0.15	0.16	0.20
FE	15.34	16.81	21.63
O	57.16	48.44	0.00

Tot	100.00	100.00	87.82

077

Std	App.%	%Elmnt	%Oxide
NA	0.00	0.00	0.00
MG	7.20	9.56	15.85
AL	8.68	11.32	21.39
SI	9.73	12.06	25.79
KK	0.04	0.04	0.05
CA	0.08	0.08	0.11
TI	0.01	0.01	0.02
CR	0.02	0.02	0.03
MN	0.24	0.25	0.32
FE	17.00	18.58	23.90
O	57.00	48.08	0.00

Tot	100.00	100.00	87.46

077

Std	App.%	%Elmnt	%Oxide
NA	0.01	0.01	0.02
MG	7.27	9.64	15.98
AL	8.60	11.22	21.19
SI	9.81	12.15	25.99
KK	0.03	0.03	0.04
CA	0.07	0.07	0.10
TI	0.01	0.01	0.02
CR	0.03	0.03	0.05
MN	0.23	0.24	0.31
FE	16.87	18.44	23.73
O	57.07	48.16	0.00

Tot	100.00	100.00	87.43

079

Std	App.%	%Elmnt	%Oxide
NA	0.01	0.01	0.02
MG	7.54	10.00	16.58
AL	8.64	11.31	21.36
SI	9.92	12.32	26.35
KK	0.03	0.03	0.04
CA	0.01	0.01	0.01
TI	0.03	0.03	0.05
CR	0.01	0.01	0.02
MN	0.32	0.33	0.43
FE	17.20	18.79	24.17
O	56.29	47.16	0.00

Tot	100.00	100.00	89.03

079

Std	App.%	%Elmnt	%Oxide
NA	0.00	0.00	0.00
MG	7.35	9.76	16.19
AL	8.47	11.07	20.92
SI	9.69	12.00	25.68
KK	0.03	0.03	0.04
CA	0.05	0.05	0.07
TI	0.02	0.02	0.04
CR	0.03	0.03	0.05
MN	0.22	0.23	0.29
FE	17.02	18.60	23.93
O	57.12	48.21	0.00

Tot	100.00	100.00	87.21

081

Std	App.%	%Elmnt	%Oxide
NA	0.00	0.00	0.00
MG	8.28	10.76	17.84
AL	7.98	10.40	19.65
SI	9.47	11.66	24.95
KK	0.03	0.03	0.04
CA	0.02	0.02	0.03
TI	0.02	0.02	0.04
CR	0.02	0.02	0.03
MN	0.21	0.22	0.28
FE	14.02	15.40	19.82
O	59.95	51.47	0.00

Tot	100.00	100.00	82.68

081

Std	App.%	%Elmnt	%Oxide
NA	0.03	0.04	0.05
MG	8.61	11.13	18.45
AL	8.50	11.07	20.92
SI	10.34	12.80	27.37
KK	0.35	0.34	0.41
CA	0.01	0.01	0.01
TI	0.01	0.01	0.02
CR	0.11	0.12	0.17
MN	0.22	0.23	0.29
FE	14.53	15.95	20.52
O	57.29	48.30	0.00

Tot	100.00	100.00	88.21

083

Std	App.%	%Elmnt	%Oxide
NA	0.00	0.00	0.00
MG	6.31	8.54	14.16
AL	8.57	11.20	21.15
SI	9.57	11.85	25.34
KK	0.04	0.04	0.05
CA	0.07	0.07	0.10
TI	0.02	0.02	0.03
CR	0.00	0.00	0.00
MN	0.28	0.29	0.37
FE	18.90	20.59	26.49
O	56.24	47.40	0.00

Tot	100.00	100.00	87.69

083

Std	App.%	%Elmnt	%Oxide
NA	0.00	0.00	0.00
MG	6.49	8.80	14.59
AL	8.41	11.03	20.84
SI	9.64	11.95	25.56
KK	0.03	0.03	0.04
CA	0.02	0.02	0.03
TI	0.01	0.01	0.02
CR	0.01	0.01	0.02
MN	0.33	0.34	0.44
FE	19.29	21.00	27.01
O	55.77	46.81	0.00

Tot	100.00	100.00	88.55

085

Std	App.%	%Elmnt	%Oxide
NA	0.02	0.03	0.04
MG	5.06	6.78	11.23
AL	9.41	11.99	22.65
SI	10.75	13.17	28.18
KK	1.71	1.66	2.00
CA	0.01	0.01	0.01
TI	0.02	0.02	0.04
CR	0.01	0.01	0.02
MN	0.28	0.29	0.37
FE	17.91	19.53	25.13
O	54.82	46.51	0.00

Tot	100.00	100.00	89.67

085

Std	App.%	%Elmnt	%Oxide
NA	0.01	0.01	0.02
MG	5.75	7.88	13.06
AL	8.59	11.24	21.23
SI	9.39	11.63	24.88
KK	0.06	0.06	0.07
CA	0.03	0.03	0.04
TI	0.02	0.02	0.03
CR	0.01	0.01	0.02
MN	0.31	0.32	0.41
FE	20.21	21.96	28.25
O	55.62	46.84	0.00

Tot	100.00	100.00	88.01

Chlorite - Lode Alteration Profile

063

Std	App.%	%Elmnt	%Oxide
NA	0.03	0.04	0.06
MG	6.73	8.84	14.67
AL	8.50	10.93	20.65
SI	10.63	13.02	27.84
KK	0.83	0.81	0.97
CA	0.29	0.29	0.41
TI	0.05	0.05	0.09
MN	0.21	0.22	0.28
FE	15.62	17.11	22.01
O	57.11	48.69	0.00

Tot	100.00	100.00	86.98

063

Std	App.%	%Elmnt	%Oxide
NA	0.00	0.00	0.00
MG	6.81	8.88	14.73
AL	8.88	11.37	21.48
SI	11.32	13.87	29.67
KK	0.91	0.89	1.07
CA	0.13	0.13	0.18
TI	0.04	0.04	0.07
MN	0.20	0.21	0.27
FE	15.45	16.93	21.78
O	56.26	47.68	0.00

Tot	100.00	100.00	89.25

064

Std	App.%	%Elmnt	%Oxide
MG	8.29	10.77	17.87
AL	8.43	10.98	20.75
SI	10.18	12.59	26.93
MN	0.20	0.21	0.27
FE	14.95	16.40	21.10
O	57.95	49.05	0.00

Tot	100.00	100.00	86.92

065

Std	App.%	%Elmnt	%Oxide
NA	0.03	0.04	0.05
MG	8.35	10.91	18.09
AL	8.29	10.85	20.51
SI	9.63	11.93	25.52
KK	0.08	0.08	0.09
CA	0.03	0.03	0.04
TI	0.02	0.02	0.04
MN	0.20	0.21	0.27
FE	15.29	16.76	21.57
O	58.08	49.17	0.00

Tot	100.00	100.00	86.18

067

Std	App.%	%Elmnt	%Oxide
MG	8.35	10.86	18.01
AL	8.71	11.36	21.47
SI	10.09	12.52	26.79
KK	0.12	0.12	0.14
TI	0.02	0.02	0.04
MN	0.18	0.19	0.24
FE	15.35	16.83	21.65
O	57.18	48.10	0.00

Tot	100.00	100.00	88.34

067

Std	App.%	%Elmnt	%Oxide
MG	8.36	10.87	18.02
AL	8.47	11.05	20.87
SI	10.23	12.66	27.09
KK	0.14	0.14	0.16
TI	0.06	0.06	0.11
MN	0.19	0.20	0.25
FE	15.15	16.61	21.37
O	57.40	48.41	0.00

Tot	100.00	100.00	87.87

068

Std	App.%	%Elmnt	%Oxide
MG	7.60	9.62	15.96
AL	9.40	11.90	22.48
SI	11.55	14.13	30.23
KK	1.88	1.84	2.22
TI	0.04	0.04	0.07
MN	0.15	0.16	0.20
FE	12.62	13.89	17.88
O	56.76	48.42	0.00

Tot	100.00	100.00	89.04

068

Std	App.%	%Elmnt	%Oxide
MG	8.56	11.10	18.40
AL	8.33	10.87	20.55
SI	9.95	12.31	26.33
KK	0.04	0.04	0.05
TI	0.01	0.01	0.02
MN	0.23	0.24	0.31
FE	14.56	15.98	20.56
O	58.32	49.45	0.00

Tot	100.00	100.00	86.22

069

Std	App.%	%Elmnt	%Oxide
NA	0.01	0.01	0.02
MG	9.18	11.87	19.67
AL	7.96	10.45	19.74
SI	10.29	12.73	27.24
KK	0.03	0.03	0.04
CA	0.01	0.01	0.01
TI	0.03	0.03	0.05
MN	0.22	0.23	0.29
FE	14.55	15.98	20.55
O	57.72	48.66	0.00

Tot	100.00	100.00	87.61

069

Std	App.%	%Elmnt	%Oxide
MG	8.67	11.26	18.68
AL	8.70	11.39	21.52
SI	9.99	12.43	26.59
KK	0.03	0.03	0.04
TI	0.02	0.02	0.04
MN	0.22	0.23	0.29
FE	15.35	16.83	21.65
O	57.02	47.81	0.00

Tot	100.00	100.00	88.81

069

Std	App.%	%Elmnt	%Oxide
MG	8.28	10.67	17.69
AL	7.94	10.29	19.43
SI	9.68	11.86	25.38
KK	0.32	0.31	0.38
TI	0.02	0.02	0.04
MN	0.20	0.21	0.27
FE	12.93	14.23	18.31
O	60.63	52.41	0.00

Tot	100.00	100.00	81.50

071

Std	App.%	%Elmnt	%Oxide
NA	0.01	0.01	0.02
MG	6.69	8.97	14.87
AL	8.98	11.71	22.13
SI	9.43	11.72	25.07
KK	0.02	0.02	0.02
CA	0.01	0.01	0.01
TI	0.01	0.01	0.02
MN	0.12	0.12	0.16
FE	18.19	19.84	25.53
O	56.54	47.59	0.00

Tot	100.00	100.00	87.83

071

Std	App.%	%Elmnt	%Oxide
NA	0.01	0.01	0.02
MG	8.46	10.97	18.18
AL	8.35	10.88	20.55
SI	10.51	12.98	27.78
KK	0.30	0.29	0.35
CA	0.02	0.02	0.03
TI	0.03	0.03	0.05
MN	0.16	0.17	0.21
FE	14.91	16.36	21.05
O	57.25	48.29	0.00

Tot	100.00	100.00	88.22

071

Std	App.%	%Elmnt	%Oxide
NA	0.03	0.04	0.05
MG	8.65	11.20	18.57
AL	8.19	10.69	20.20
SI	10.26	12.67	27.11
KK	0.29	0.28	0.34
CA	0.02	0.02	0.03
TI	0.20	0.21	0.35
MN	0.19	0.20	0.25
FE	14.55	15.97	20.55
O	57.62	48.72	0.00

Tot	100.00	100.00	87.45

073

Std	App.%	%Elmnt	%Oxide
NA	0.01	0.01	0.02
MG	8.24	10.79	17.89
AL	8.30	10.87	20.53
SI	9.90	12.26	26.24
KK	0.03	0.03	0.04
CA	0.01	0.01	0.01
TI	0.01	0.01	0.02
MN	0.20	0.21	0.27
FE	15.72	17.22	22.16
O	57.58	48.59	0.00

Tot	100.00	100.00	87.18

073

Std	App.%	%Elmnt	%Oxide
NA	0.02	0.03	0.04
MG	7.08	9.40	15.58
AL	9.13	11.89	22.46
SI	9.49	11.80	25.24
KK	0.04	0.04	0.05
CA	0.01	0.01	0.01
TI	0.05	0.05	0.09
MN	0.18	0.19	0.24
FE	17.13	18.72	24.08
O	56.87	47.87	0.00

Tot	100.00	100.00	87.79

Albite - Lode Alteration Profile

064

Std	App.%	%Elmnt	%Oxide
NA	8.04	8.17	11.01
AL	9.77	10.59	20.01
SI	28.83	31.92	68.29
KK	0.33	0.34	0.40
CA	0.10	0.10	0.15
O	52.93	48.88	0.00
Tot	100.00	100.00	99.86

064

Std	App.%	%Elmnt	%Oxide
NA	8.22	8.33	11.22
AL	9.66	10.47	19.78
SI	29.40	32.51	69.55
KK	0.36	0.37	0.44
CA	0.13	0.14	0.19
FE	0.08	0.09	0.12
O	52.15	48.09	0.00
Tot	100.00	100.00	101.30

064

Std	App.%	%Elmnt	%Oxide
NA	7.93	8.05	10.85
MG	0.01	0.01	0.02
AL	9.74	10.54	19.92
SI	29.37	32.48	69.47
KK	0.07	0.07	0.09
CA	0.21	0.22	0.31
TI	0.01	0.01	0.02
MN	0.00	0.00	0.00
FE	0.06	0.07	0.09
O	52.60	48.55	0.00
Tot	100.00	100.00	100.77

064

Std	App.%	%Elmnt	%Oxide
NA	8.14	8.23	11.09
MG	0.02	0.02	0.04
AL	9.93	10.74	20.30
SI	29.45	32.62	69.78
KK	0.24	0.24	0.29
CA	0.05	0.05	0.07
TI	0.01	0.01	0.02
MN	0.00	0.00	0.00
FE	0.05	0.06	0.07
O	52.11	48.03	0.00
Tot	100.00	100.00	101.66

065

Std	App.%	%Elmnt	%Oxide
NA	6.09	6.35	8.56
MG	0.46	0.54	0.90
AL	10.81	11.75	22.21
SI	25.94	29.04	62.12
KK	1.37	1.39	1.67
CA	0.21	0.22	0.31
TI	0.04	0.04	0.07
MN	0.03	0.03	0.04
FE	0.53	0.60	0.77
O	54.52	50.04	0.00
Tot	100.00	100.00	96.65

065

Std	App.%	%Elmnt	%Oxide
NA	8.23	8.31	11.21
MG	0.05	0.06	0.10
AL	9.97	10.80	20.40
SI	29.54	32.74	70.05
KK	0.26	0.26	0.32
CA	0.17	0.18	0.25
TI	0.25	0.28	0.47
MN	0.00	0.00	0.00
FE	0.10	0.11	0.14
O	51.43	47.26	0.00
Tot	100.00	100.00	102.94

065

Std	App.%	%Elmnt	%Oxide
NA	8.47	8.57	11.55
MG	0.05	0.06	0.10
AL	9.82	10.67	20.17
SI	28.89	32.06	68.59
KK	0.23	0.23	0.28
CA	0.14	0.15	0.20
TI	0.01	0.01	0.02
MN	0.00	0.00	0.00
FE	0.06	0.07	0.09
O	52.33	48.18	0.00
Tot	100.00	100.00	101.00

066

Std	App.%	%Elmnt	%Oxide
NA	8.07	8.25	11.12
AL	9.94	10.82	20.45
SI	27.40	30.47	65.17
KK	0.57	0.58	0.70
CA	0.65	0.68	0.95
O	53.37	49.20	0.00
Tot	100.00	100.00	98.39

081

Std	App.%	%Elmnt	%Oxide
NA	8.31	8.42	11.35
AL	9.87	10.71	20.24
SI	28.82	31.97	68.39
KK	0.06	0.06	0.07
CA	0.29	0.30	0.42
O	52.65	48.54	0.00
Tot	100.00	100.00	100.47

085

Std	App.%	%Elmnt	%Oxide
NA	7.97	8.15	10.99
AL	9.59	10.43	19.70
SI	28.12	31.14	66.61
KK	0.30	0.30	0.37
CA	0.70	0.73	1.02
O	53.32	49.25	0.00
Tot	100.00	100.00	98.69

Epidote - Lode Alteration Profile

079

Std	App.%	%Elmnt	%Oxide
NA	0.01	0.01	0.02
MG	0.14	0.18	0.29
AL	10.29	11.72	22.15
SI	15.77	17.95	38.41
KK	0.81	0.76	0.92
CA	15.51	15.53	21.73
TI	0.14	0.16	0.26
CR	0.00	0.00	0.00
MN	0.03	0.03	0.04
FE	9.17	10.17	13.08
O	48.13	43.49	0.00
Tot	100.00	100.00	96.90

Sericite - Lode Alteration Profile

063

Std	App.%	%Elmnt	%Oxide
NA	0.47	0.55	0.74
MG	2.48	2.91	4.83
AL	12.65	14.16	26.75
SI	18.59	21.53	46.06
KK	3.59	3.57	4.29
CA	1.22	1.26	1.76
TI	0.10	0.11	0.18
MN	0.05	0.05	0.07
FE	4.82	5.38	6.92
O	56.03	50.48	0.00
Tot	100.00	100.00	91.60

063

Std	App.%	%Elmnt	%Oxide
NA	0.06	0.07	0.09
MG	2.42	2.83	4.69
AL	13.76	15.34	28.99
SI	17.69	20.66	44.20
KK	3.55	3.53	4.26
CA	0.05	0.05	0.07
TI	0.11	0.12	0.20
MN	0.08	0.08	0.11
FE	4.88	5.44	7.00
O	57.40	51.88	0.00
Tot	100.00	100.00	89.61

065

Std	App.%	%Elmnt	%Oxide
NA	0.10	0.11	0.15
MG	2.67	3.07	5.09
AL	14.63	16.19	30.58
SI	18.13	21.24	45.45
KK	3.64	3.63	4.38
CA	0.03	0.03	0.04
TI	0.10	0.11	0.18
MN	0.10	0.11	0.14
FE	3.93	4.39	5.64
O	56.67	51.12	0.00
Tot	100.00	100.00	91.65

066

Std	App.%	%Elmnt	%Oxide
NA	0.21	0.23	0.31
MG	1.49	1.68	2.78
AL	13.90	14.90	28.15
SI	21.48	24.43	52.27
KK	5.62	5.63	6.78
MN	0.02	0.02	0.03
FE	2.01	2.25	2.90
O	55.27	50.86	0.00
Tot	100.00	100.00	93.22

077

Std	App.%	%Elmnt	%Oxide
NA	0.09	0.10	0.14
MG	1.43	1.62	2.68
AL	15.14	16.28	30.76
SI	19.97	23.02	49.25
KK	5.50	5.50	6.63
CA	0.05	0.05	0.07
MN	0.04	0.04	0.05
FE	2.66	2.98	3.83
O	55.12	50.41	0.00
Tot	100.00	100.00	93.41

Chlorite - Chlorite Phyllonites.

035

Std	App.%	%Elmnt	%Oxide
NA	0.69	0.88	1.19
MG	10.59	13.44	22.28
AL	6.79	8.95	16.92
SI	11.43	14.03	30.02
KK	0.12	0.12	0.14
CA	0.08	0.08	0.11
TI	0.03	0.03	0.05
MN	0.10	0.10	0.13
FE	12.08	13.33	17.14
O	58.09	49.04	0.00
Tot	100.00	100.00	87.98

035

Std	App.%	%Elmnt	%Oxide
NA	0.02	0.03	0.03
MG	10.34	13.06	21.66
AL	6.83	8.95	16.90
SI	11.47	14.01	29.98
KK	0.62	0.61	0.73
CA	0.14	0.14	0.20
TI	0.09	0.10	0.16
MN	0.08	0.08	0.11
FE	12.19	13.45	17.30
O	58.22	49.57	0.00
Tot	100.00	100.00	87.07

042

Std	App.%	%Elmnt	%Oxide
NA	0.05	0.07	0.09
MG	8.30	10.93	18.13
AL	7.39	9.72	18.37
SI	10.23	12.59	26.94
KK	0.05	0.05	0.06
CA	0.08	0.08	0.11
TI	0.02	0.02	0.04
MN	0.28	0.29	0.37
FE	15.94	17.46	22.46
O	57.66	48.79	0.00
Tot	100.00	100.00	86.57

045

Std	App.%	%Elmnt	%Oxide
NA	0.03	0.04	0.06
MG	5.35	7.07	11.72
AL	10.12	12.82	24.22
SI	11.13	13.70	29.30
KK	0.63	0.61	0.74
CA	0.07	0.07	0.10
TI	0.04	0.04	0.07
MN	0.10	0.10	0.13
FE	16.88	18.45	23.73
O	55.65	47.10	0.00
Tot	100.00	100.00	90.07

035

Std	App.%	%Elmnt	%Oxide
NA	0.02	0.03	0.03
MG	12.38	15.48	25.67
AL	7.11	9.48	17.91
SI	11.08	13.77	29.45
KK	0.08	0.08	0.09
CA	0.07	0.07	0.10
TI	0.02	0.02	0.04
MN	0.07	0.07	0.09
FE	12.37	13.64	17.55
O	56.80	47.36	0.00
Tot	100.00	100.00	90.93

045

Std	App.%	%Elmnt	%Oxide
NA	0.03	0.04	0.06
MG	6.93	9.23	15.31
AL	9.04	11.78	22.25
SI	9.43	11.72	25.07
KK	0.02	0.02	0.02
CA	0.00	0.00	0.00
TI	0.02	0.02	0.03
MN	0.13	0.13	0.17
FE	17.47	19.08	24.55
O	56.93	47.98	0.00
Tot	100.00	100.00	87.46

Calcite - Chlorite Phyllonites.

035

Std	App.%	%Elmnt	%Oxide
MG	0.11	0.15	0.24
CA	40.79	39.40	55.13
MN	0.27	0.29	0.37
FE	0.30	0.34	0.44
O	58.53	59.82	0.00
Tot	100.00	100.00	56.18

035

Std	App.%	%Elmnt	%Oxide
MG	0.16	0.21	0.35
CA	34.96	33.88	47.41
MN	0.15	0.16	0.21
FE	0.22	0.25	0.32
O	64.51	65.50	0.00
Tot	100.00	100.00	48.29

035

Std	App.%	%Elmnt	%Oxide
MG	0.23	0.31	0.51
CA	45.15	43.49	60.86
MN	0.40	0.43	0.55
FE	0.48	0.54	0.70
O	53.74	55.23	0.00
Tot	100.00	100.00	62.62

042

Std	App.%	%Elmnt	%Oxide
MG	0.00	0.00	0.00
CA	44.63	43.02	60.19
MN	0.40	0.43	0.55
FE	0.07	0.08	0.10
O	54.90	56.47	0.00
Tot	100.00	100.00	60.84

Altered Tuffs - Wadi Lode 4-level

045

Std	App.%	%Elmnt	%Oxide
MG	0.29	0.39	0.65
CA	42.28	40.76	57.03
MN	0.67	0.72	0.92
FE	0.82	0.92	1.19
O	55.94	57.21	0.00
Tot	100.00	100.00	59.79

045

Std	App.%	%Elmnt	%Oxide
MG	0.25	0.34	0.56
CA	44.07	42.45	59.40
MN	0.47	0.50	0.65
FE	0.91	1.02	1.32
O	54.30	55.69	0.00
Tot	100.00	100.00	61.93

Ankerite, calcite, and albite - Ankerite Phyllonites.

Ankerite

044

Std	App.%	%Elmnt	%Oxide
MG	6.87	9.31	15.45
CA	21.01	20.48	28.65
MN	0.14	0.15	0.19
FE	6.75	7.52	9.68
O	65.23	62.54	0.00
Tot	100.00	100.00	53.97

044

Std	App.%	%Elmnt	%Oxide
MG	6.99	9.40	15.59
CA	21.75	21.22	29.69
MN	0.15	0.16	0.20
FE	5.74	6.41	8.24
O	65.37	62.81	0.00
Tot	100.00	100.00	53.72

037

Std	App.%	%Elmnt	%Oxide
MG	6.14	8.46	14.02
CA	20.60	20.03	28.02
MN	0.06	0.06	0.08
FE	8.39	9.32	12.00
O	64.81	62.13	0.00
Tot	100.00	100.00	54.12

037

Std	App.%	%Elmnt	%Oxide
MG	5.97	8.23	13.65
CA	20.64	20.06	28.07
MN	0.08	0.08	0.11
FE	8.44	9.38	12.07
O	64.87	62.25	0.00
Tot	100.00	100.00	53.90

034

Std	App.%	%Elmnt	%Oxide
MG	6.44	8.77	14.55
CA	20.95	20.40	28.55
MN	0.14	0.15	0.19
FE	7.07	7.87	10.13
O	65.40	62.81	0.00
Tot	100.00	100.00	53.42

034

Std	App.%	%Elmnt	%Oxide
MG	5.38	7.46	12.36
CA	21.34	20.71	28.97
MN	0.32	0.34	0.43
FE	8.52	9.46	12.17
O	64.44	62.03	0.00
Tot	100.00	100.00	53.93

034

Std	App.%	%Elmnt	%Oxide
MG	7.09	9.56	15.85
CA	21.22	20.70	28.96
MN	0.22	0.23	0.30
FE	6.13	6.84	8.80
O	65.34	62.67	0.00
Tot	100.00	100.00	53.91

034

Std	App.%	%Elmnt	%Oxide
MG	7.41	9.91	16.44
CA	21.15	20.66	28.91
MN	0.18	0.19	0.25
FE	5.32	5.94	7.65
O	65.94	63.30	0.00
Tot	100.00	100.00	53.25

043

Std	App.%	%Elmnt	%Oxide
MG	6.84	9.22	15.29
CA	21.60	21.07	29.48
MN	0.17	0.18	0.23
FE	5.90	6.59	8.47
O	65.49	62.94	0.00
Tot	100.00	100.00	53.47

043

Std	App.%	%Elmnt	%Oxide
MG	6.79	9.23	15.30
CA	20.85	20.32	28.43
MN	0.14	0.15	0.19
FE	6.97	7.76	9.99
O	65.25	62.54	0.00
Tot	100.00	100.00	53.91

043

Std	App.%	%Elmnt	%Oxide
MG	6.59	8.93	14.81
CA	21.70	21.14	29.59
MN	0.16	0.17	0.22
FE	6.47	7.21	9.28
O	65.08	62.55	0.00
Tot	100.00	100.00	53.90

036

Std	App.%	%Elmnt	%Oxide
MG	6.59	8.89	14.74
CA	21.87	21.32	29.83
MN	0.67	0.71	0.91
FE	5.46	6.09	7.84
O	65.41	62.99	0.00
Tot	100.00	100.00	53.32

038

Std	App.%	%Elmnt	%Oxide
MG	6.88	9.25	15.33
CA	21.59	21.07	29.48
MN	0.20	0.21	0.27
FE	5.53	6.18	7.94
O	65.80	63.29	0.00
Tot	100.00	100.00	53.02

038

Std	App.%	%Elmnt	%Oxide
MG	7.12	9.58	15.88
CA	21.92	21.38	29.92
MN	0.25	0.26	0.34
FE	5.84	6.52	8.39
O	64.87	62.26	0.00
Tot	100.00	100.00	54.53

Calcite

038

Std	App.%	%Elmnt	%Oxide
MG	0.09	0.12	0.20
CA	36.85	35.68	49.92
MN	0.15	0.16	0.21
FE	0.16	0.18	0.23
O	62.75	63.86	0.00
Tot	100.00	100.00	50.56

Albite

038

Std	App.%	%Elmnt	%Oxide
NA	8.45	8.52	11.49
AL	9.56	10.36	19.57
SI	29.86	32.99	70.57
KK	0.06	0.06	0.07
CA	0.06	0.06	0.09
O	52.01	48.01	0.00
Tot	100.00	100.00	101.79

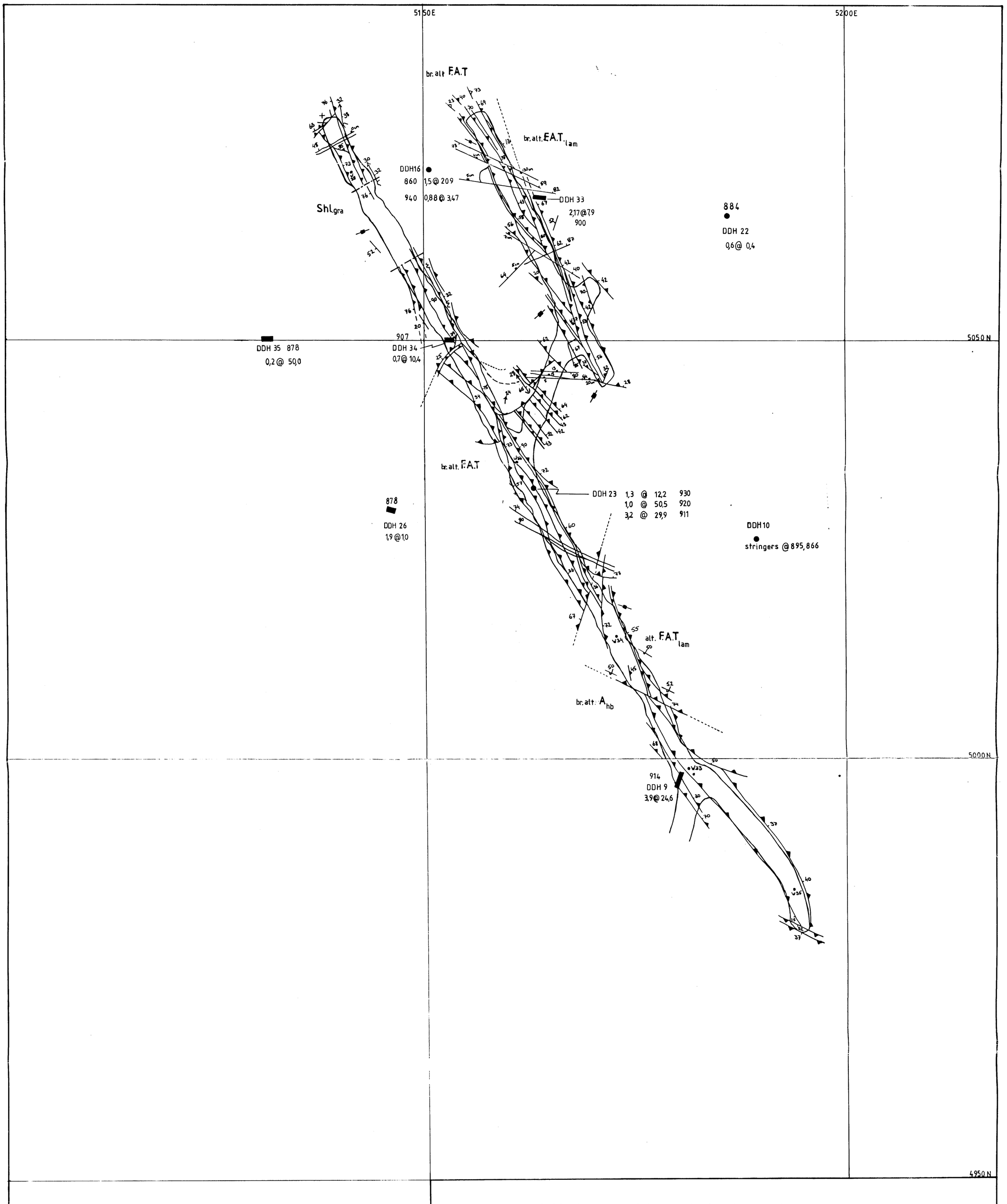

GEBEIT GOLD MINE, SUDAN

WADI LODE : 4 LEVEL PLAN

GEOLOGY 1:250

LEGEND

- Lode
- Thrust/Strike-slip Fault
- Normal Fault
- Lithological Boundary
- Fold Axis
- Bedding, normal/ inverted
- Cleavage
- Joint
- No Exposure
- Survey Stn. ●W34
- Drillhole Intersection — vertical ● inclined

FAT.....Fine Andesitic Tuff
Shl .....Shale
A_{hb}.....Hornblende-Phyric Andesite

br. ..... brown
alt. ..... altered
lam_f..... laminated
gra. ..... graphitic

Tony Starling 05/1987

Um Arad

Wadi Messesana

KHOR MESSESANA

KHOR ADARIT

KHOR HALAL HINDEIB

Halal Hindeib

Garabein/Odhaf

WADI GEBEIT

Walati

KHOR YEMOMT

KHOR ADAR NAKASHEB

GEBEIT

21°05′

21°00′

36°15′

36°20′

DRAINAGE AND GENERAL GEOLOGY OF THE GEBEIT AREA, NORTHERN RED SEA HILLS, SUDAN

- Gebeit Volcanic Gp.
- N. Sasa Plain Tuffaceous Slates
- Syn-tectonic Granitoids
- Wadi/Khor
- Au Mine (disused)
- Au Prospect
- Fault/Thrust Pan-African Age
- Post-Pan-African Faults
- F_1 Fold Axes
- Bedding

N Azm

1°44′

200m 0 1km

T. STERLING 07/1990

GEOLOGY OF THE GEBEIT BLOCK (NORTH), NORTHERN RED SEA HILLS, SUDAN.

4000E

5000E

8000N

7000N

6000N

WADI GEBEIT

WADI EAST GEBEIT

NORTH GEBEIT

GEBEIT SHEAR ZONE

WADI TUWIYA SHEAR ZONE

WADI TUWIYA

VEIN 18

VEIN 13

MARBLE BAR

BISHOPS DAM

WADI LODE SHEAR ZONE

WADI LODE EXTENSION

A LODE SHEAR ZONE

EAST GEBEIT

WESTERN BOUNDARY FAULT

GEBEIT MINE

WEST GEBEIT

LEGEND

A	Gebeit Volcanic Group (upper)
a	Gebeit Volcanic Group (lower)
P	Ankerite Phyllonite
	Intrusion
Do	Dolerite
Di	Diorite
T	Tonalite
Gb	Gabbro
uK	ultra-Potassic
i	Phase 1
ii	" 2
iii	" 3
iv	" 4

	Limit of Exposure
	Fault
	Shear Zone (chlorite phyllonite)
56	Bedding
23	Foliation
	Fold Axes
	Thrust
12	Fold vergence & plunge
5000E	Mine Grid

MINE GRID N

MAG N

TRUE N

1°44' E

45°

Scale 1:5000

0 500m

T. STARLING 1990

GEOLOGY OF THE WADI LODE EXTENSION AND BISHOPS DAM PROSPECT AREAS, GEBEIT MINE, SUDAN.

LEGEND

EXTRUSIVE

FAT	Fine Andesitic Tuff		Shear Zone
CAT	Coarse " "		Lithological Boundary
A_{hb}	Hornblende-phyric Andesite		Limit of exposure
A_{pl}	Plagioclase- " "		Foliation
A_{gg}	Andesite Agglomerate		Bedding
A_{lap}	" Lapillistone		Thrust
Shl	Shale	-------	Vein
aP	Ankerite Phyllonite	Q,q,Ct	Blue, white quartz, Calcite
cP	Chlorite "	cc	Calcrete
lam	laminated		

INTRUSIVE

Do	Dolerite
Di	Diorite
Gb	Gabbro
Gr	Granite
T	Tonalite
uK	ultra-Potassic
i,ii,iii,iv	Phase 1,2,3,4

MINE GRID N / MAG N / TRUE N — 7°44' — 45°

Scale 1:2000

0 200m

T.STARLING 1990

WADI GEBEIT

BISHOPS DAM

VEIN 18

VEIN 13

MARBLE BAR

WADI EAST GEBEIT

6500N

6000N

5500N

4000E

4500E

5000E

5500E